



HAL
open science

Reforming of toluene formed during the gasification of biomass with alumina based catalysts prepared by aqueous sol-gel processes.

Vincent Claude

► **To cite this version:**

Vincent Claude. Reforming of toluene formed during the gasification of biomass with alumina based catalysts prepared by aqueous sol-gel processes.. Chemical engineering. Université de Liège, 2017. English. NNT: . tel-03211049

HAL Id: tel-03211049

<https://hal.science/tel-03211049>

Submitted on 28 Apr 2021

HAL is a multi-disciplinary open access archive for the deposit and dissemination of scientific research documents, whether they are published or not. The documents may come from teaching and research institutions in France or abroad, or from public or private research centers.

L'archive ouverte pluridisciplinaire **HAL**, est destinée au dépôt et à la diffusion de documents scientifiques de niveau recherche, publiés ou non, émanant des établissements d'enseignement et de recherche français ou étrangers, des laboratoires publics ou privés.

Université
de Liège



UNIVERSITÉ DE LIÈGE
Faculté des Sciences Appliquées
Department of Chemical Engineering
Nanomaterials, Catalysis and Electrochemistry

Reforming of toluene formed during the gasification of biomass with alumina based catalysts prepared by aqueous sol-gel processes

Dissertation présentée par
Vincent CLAUDE
le mardi 14 Février 2017
en vue de l'obtention du grade de Docteur en
Sciences de l'Ingénieur

Composition du jury :

Benoît Heinrichs, Professeur à l'Université de Liège, Président

Stéphanie Lambert, Chercheur qualifié FRS-FNRS, Chargé de cours adjoint à l'Université de Liège,
Promotrice

Dominique Toye, Professeur à l'Université de Liège

Grégoire Léonard, Chargé de cours à l'Université de Liège

Jean-Paul Pirard, Professeur Émérite à l'Université de Liège

Claire Courson, Maître de Conférences à l'Université de Strasbourg

Sébastien Testu, Enseignant-Chercheur à l'Université de Lorraine

Christian Meyers, Consulting Engineer chez Carbon-Hydrogen-Minerals sprl

Remerciements

Cette thèse de doctorat s'inscrit dans le contexte général des travaux de recherche effectués au Department of Chemical Engineering - Nanomaterials, Catalysis and Electrochemistry de l'Université de Liège (ULg-NCE). Cette thèse a été financée par le FRS-FNRS, dans le cadre du crédit FRFC n°2.4541.12 (2012-2016).

Je tiens à remercier très vivement Dr. Stéphanie Lambert-Jamouille, Chercheur qualifiée FRS-FNRS, Chargée de cours adjointe et promotrice de ce travail. Je la remercie de m'avoir proposé un sujet aussi vaste que la synthèse de catalyseurs par voie sol-gel pour le reformage catalytique de goudrons lors de la gazéification de la biomasse. Je lui exprime ma reconnaissance pour la rigueur scientifique à laquelle elle m'a formé, ainsi que pour le temps qu'elle a consacré à la définition des objectifs, à la planification des expériences, à l'analyse critique des résultats et à la supervision de la rédaction de la thèse et des articles parus dans les journaux scientifiques.

Je remercie Pr. Benoît Heinrichs, Pr. Dominique Toye et M. Christian Meyers pour leur encadrement et leurs conseils pertinents tout au long de ce doctorat.

Lors des réunions scientifiques internes au laboratoire, j'ai eu la chance de recevoir de nombreuses et judicieuses suggestions émises par Dr. Christelle Alié, Dr. Cédric Calberg, Dr. Ludvine Tasseroul, Dr. Carlos Paez, Dr. Sigrid Douven, M^{lle} Géraldine Léonard et M. Julien Mahy. Pour cela, je leur en suis reconnaissant.

Ma reconnaissance s'adresse aussi à M. Jérémy Geens, Premier agent spécialisé au Department of Chemical Engineering, pour ses conseils pratiques et pour avoir réalisé les mesures de porosimétrie au mercure et de TPD-NH₃ au moment où le temps m'était compté.

Le montage de l'installation expérimentale n'aurait jamais pu être possible sans l'aide technique de M. Jean-Pol Deschamps, Premier agent spécialisé en chef au Department of Chemical Engineering. Dans ce cadre, je suis aussi reconnaissant à M. Patrick Kreit, Directeur technique du site CRYO du Department of Chemical Engineering.

Ma reconnaissance s'adresse aussi à M^{me} Marlène Goffin, Secrétaire exécutive au Department of Chemical Engineering, qui a toujours fait de son mieux pour que les commandes de pièces matérielles soient effectuées dans les délais les plus brefs.

Je tiens à remercier ma collègue de bureau, Dr. Sophie Pirard, pour son aide scientifique concernant les calculs cinétiques et diffusionnels, ainsi que pour sa bonne humeur au quotidien.

Ma reconnaissance s'adresse aussi à M. Timothée Lohay, Ingénieur civil en chimie et science des matériaux. Les expériences et discussions scientifiques qui ont eu lieu lors de l'encadrement de son travail de fin d'étude furent très constructives pour l'avancement de ce projet.

Je suis également redevable à M^{me} Alice Dubus, Premier agent spécialisé à l'atelier de soufflage de verre de l'ULg, pour son aide et sa rapidité à m'avoir fourni des pièces nécessaires au bon fonctionnement des appareils de notre laboratoire.

Je tiens également à remercier Dr. Alexandre Léonard, Dr. Marie-Laure Piedboeuf, Pr. Jean-Paul Pirard, Dr. Christophe Servais, Pr. Grégoire Léonard, Dr. Cédric Gomme, Dr. Pierre-Yves Olu, Dr. Charline Malengreaux, Dr. Marie-Noelle Dumont, Dr. Sandra Belboom, M. Tristant Asset, M. Artium Belet, M^{lle} Anne Delamotte, M. Anthony Zubiaur, M. Fabien Deschamps, M. Angel Merchan, M. Dimitri Liquet, Pr. Nathalie Job et M. François Noville avec qui j'ai eu l'occasion de partager des discussions intéressantes et enrichissantes durant ces quatre années.

Je suis reconnaissant à M^{me} Martine Dejeneffe, à Pr. Philippe Compère et à Pr. Bénédicte Vertruyen pour leur disponibilité et leurs conseils quant à l'utilisation des microscopes TEM/SEM et de l'appareil de mesures de diffraction par rayons X.

Je tiens très vivement à remercier Dr. Claire Courson, pour m'avoir accueilli au sein du laboratoire de l'Institut de Chimie et Procédés pour l'Energie, l'Environnement et la Santé de l'Université de Strasbourg en 2014. Ce séjour d'un mois fut décisif pour l'avancement de ma thèse et pour le montage d'une installation expérimentale à l'ULg. Ma reconnaissance s'adresse en particulier à M. Yvan Zimmermann, Technicien de laboratoire, qui m'a formé à l'utilisation d'une des installations expérimentales de l'ICPEES. Je suis également profondément reconnaissant envers Dr. Francesca Micheli, alors doctorante en fin de thèse, qui a accepté de m'accorder de son précieux temps pour m'encadrer. Je remercie aussi cette dernière pour ses conseils et ses encouragements tout au long de ma thèse. Ce séjour fut pour moi très riche d'un point de vue scientifique et humain. Je suis reconnaissant à Dr. Charlotte Lang, Dr. Dmitri Komissarenko et Dr. Kilian Kobl de m'avoir intégré à leur groupe. Finalement, je voudrais remercier toutes les autres personnes que j'ai eues l'occasion de croiser durant ce séjour.

Je suis profondément reconnaissant à M. Alain Kiennemann, Professeur Émérite à l'Université de Strasbourg, pour avoir effectué la relecture de ma thèse et m'avoir fait part de ses remarques constructives.

Je me dois également de remercier les organismes publics et privés qui financent le Department of Chemical Engineering et grâce auxquels j'ai pu disposer des équipements et des moyens nécessaires à la réalisation de ma thèse de doctorat : le Ministère de la Région Wallonne, Direction générale des Technologies, de la Recherche et de l'Energie (DG06), le Ministère de la Communauté Française, le Fonds National de la Recherche Scientifique (FRS-FNRS) et le Fonds de Bay.

Bien évidemment, je me dois de remercier ma famille et mes amis pour le soutien qu'ils m'ont apporté.

Dernier point, qui n'est pas des moindres, je tiens à remercier ma compagne, Pricillia Collin, pour son immense soutien moral et sa bonne humeur au quotidien lors de ces quatre années de travail intense.

“It is not the critic who counts; not the man who points out how the strong man stumbles, or where the doer of deeds could have done them better. The credit belongs to the man who is actually in the arena, whose face is marred by dust and sweat and blood; who strives valiantly; who errs, who comes short again and again, because there is no effort without error and shortcoming; but who does actually strive to do the deeds; who knows great enthusiasms, the great devotions; who spends himself in a worthy cause; who at the best knows in the end the triumph of high achievement, and who at the worst, if he fails, at least fails while daring greatly, so that his place shall never be with those cold and timid souls who neither know victory nor defeat.”

«Ce n'est pas le critique qui importe ; tout ce qu'il fait c'est pointer du doigt l'homme fort quand il chute ou quand il se trompe en faisant quelque chose. Le vrai crédit revient à l'homme qui se trouve réellement dans l'arène ; avec le visage sali de poussière, de sueur et de sang, luttant courageusement. Le vrai crédit va vers celui qui commet des erreurs, qui se trompe mais, qui au fur et à mesure, réussit, car il n'existe pas d'effort sans erreur. Lui qui connaît de grands enthousiasmes, de grandes dévotions et qui se dépense dans une cause noble. Lui qui, au mieux, connaît à sa fin le triomphe du haut accomplissement, et qui, au pire, s'il échoue, échoue au moins en ayant grandement osé, si bien que sa place ne se trouve jamais parmi ces froides et timides âmes qui ne connaissent ni la victoire, ni la défaite.»

Extrait du discours: “The Man in the Arena: Citizenship in a Republic”

Université de la Sorbonne, Paris, 23 Avril 1910

Theodore ROOSEVELT

«Plus la science accroît le cercle de ses connaissances et plus grandit autour le cercle d'ombre.»

Henri POINCARÉ

Résumé

La gazéification de biomasse en bio-syngas ($\text{CO}+\text{H}_2$) s'accompagne généralement de formation de goudrons (toluène, naphthalène) qui peuvent causer des problèmes techniques en aval du réacteur. Le reformage de ces goudrons via un catalyseur primaire (à l'intérieur du réacteur) ou secondaire (en sortie du réacteur) apparaît actuellement comme la méthode la plus intéressante d'un point de vue pratique et économique.

L'utilisation de catalyseurs constitués de nanoparticules métalliques supportées sur $\gamma\text{-Al}_2\text{O}_3$ est une association efficace pour le reformage catalytique de goudrons. Une méthode de synthèse de support $\gamma\text{-Al}_2\text{O}_3$ par voie sol-gel aqueuse est mise au point durant ce projet. Dans l'optique de synthétiser des catalyseurs composés de nanoparticules métalliques finement dispersées, des supports en $\gamma\text{-Al}_2\text{O}_3$ sont modifiés avec un précurseur de silice fonctionnalisé : l'EDAS (3-(2-aminoéthylamino)propyltriméthoxysilane). L'addition d'EDAS modifie les propriétés texturales du support $\gamma\text{-Al}_2\text{O}_3$. Des échantillons préparés avec d'autres types de précurseurs de silice (non-fonctionnalisés ou fonctionnalisés avec d'autres chaînes que celle présente dans l'EDAS) mettent en évidence le fait que la réactivité du précurseur de silice influence la cristallinité du support. La présence d'une chaîne fonctionnalisée modifie quant à elle la forme des cristallites d'alumine, menant ainsi à une distribution de taille de mésopores plus étroite et centrée à 4 nm et une plus grande surface spécifique du support.

Afin de déterminer quel type de catalyseurs synthétiser (primaires ou secondaires), le reformage catalytique de 8000 ppmv de toluène en conditions primaires ($T = 750\text{-}850\text{ }^\circ\text{C}$) est effectué avec des supports constitués de $\gamma\text{-Al}_2\text{O}_3$ ou d'olivine, dopés avec 2 % Ni ou 10 % Fe. L'olivine, catalyseur primaire de référence, présente de meilleurs résultats pour le reformage du toluène. Dans le cas de $\gamma\text{-Al}_2\text{O}_3$, le faible dopage en Ni conduit à la formation d'un spinelle NiAl_2O_4 difficile à réduire, et le dopage avec Fe favorise la transition de phase de $\gamma\text{-Al}_2\text{O}_3$ vers $\alpha\text{-Al}_2\text{O}_3$. Les travaux suivants sont donc axés sur le développement de catalyseurs de type 10 % Ni/ $\gamma\text{-Al}_2\text{O}_3$ testés en conditions secondaires.

La réduction de catalyseurs constitués d'une unique phase de NiAl_2O_4 ne s'initie qu'à partir de $T = 680\text{ }^\circ\text{C}$ lors de mesures en température programmée sous H_2 (TPR). Cependant, ceux-ci sont réduits lors du reformage catalytique de 24.000 ppmv de toluène à $T = 650\text{ }^\circ\text{C}$. Il est démontré que dans ces conditions, le toluène est un meilleur agent réducteur que H_2 ou CO , et que la réduction des espèces NiAl_2O_4 par le toluène permet de convertir celui-ci en syngas tout en prévenant la formation de coke. Lors de la présence de NiO réduit à plus basse température ($T \sim 450\text{ }^\circ\text{C}$), le catalyseur ne tire pas avantage du phénomène de réduction spécial des oxydes métalliques par le toluène, ce qui entraîne ainsi la désactivation rapide du catalyseur par cokage.

L'ajout d'un surfactant (acide stéarique) lors de la préparation par voie sol-gel aqueuse s'avère efficace afin de modifier la morphologie (mésopores, macropores) de catalyseurs Ni/ $\gamma\text{-Al}_2\text{O}_3$. Malgré une activité catalytique nettement plus élevée, attribuée à une meilleure diffusion des réactifs, l'échantillon montre des tendances beaucoup plus importantes à se désactiver par cokage. On émet l'hypothèse que cette faiblesse est due à une combinaison de plusieurs faits: déséquilibre entre la réaction de cracking du toluène et les réactions de dissociation-migration des espèces HO^* et O^* + meilleure réductibilité empêchant de tirer avantage du phénomène de réduction spécial par le toluène + présence de larges pores ne restreignant pas la croissance de carbone filamentaire.

Un large screening de catalyseurs 10 % Ni/ $\gamma\text{-Al}_2\text{O}_3$ dopés avec des métaux (Cu, Mn, Fe, Mo ou Mn) ou des oxydes (CaO , K_2O , MgO ou CeO_2) est effectué. Les échantillons contenant les éléments Mn, Mo, Ca ou K s'avèrent les plus intéressants de par leur activité catalytique et leur résistance au cokage. Pour une même quantité massique ajoutée, les échantillons constitués d'associations de dopants (Co+Mo, Mn+Mo, Ca+K ou Ce+K) affichent de meilleures performances catalytiques que ceux effectués avec un seul dopant.

Les résultats obtenus avec les meilleurs catalyseurs lors de tests catalytiques de longue durée (30 h) ou en présence de H_2S sont prometteurs. Ceci porte à croire que ces catalyseurs pourraient convenir à une application industrielle.

Summary

The gasification of biomass into bio-syngas ($\text{CO}+\text{H}_2$) usually goes along with the formation of tars (toluene, naphthalene) which can cause technical problems at the outlet of the reactor. The reforming of these tars via primary catalysts (inside the reactor) or secondary catalysts (outside the reactor) currently appears as the most interesting way from practical and economical point of views.

The use of catalysts made of metallic nanoparticles deposited on $\gamma\text{-Al}_2\text{O}_3$ is an efficient combination for tar reforming applications. During this project, an aqueous sol-gel method for the synthesis of $\gamma\text{-Al}_2\text{O}_3$ supports is developed. In the aim of developing catalysts with metallic nanoparticles finely dispersed, supports of $\gamma\text{-Al}_2\text{O}_3$ are modified with a functionalized silicon precursor (3-(2-aminoethylamino)propyltrimethoxysilane, EDAS). The addition of EDAS modifies the properties of $\gamma\text{-Al}_2\text{O}_3$. Samples prepared with other silicon precursors (non-functionalized or functionalized with other chains than the ones of EDAS) highlight that the reactivity of the precursor influences the crystallinity of the support. The presence of a functionalized chain modifies the shape of the crystallites, which leads to a narrower pore size distribution centered on 4 nm and to a higher specific surface area of the support.

In order to orientate the project towards the development of either primary or secondary catalysts, catalytic tests are performed with 8000 ppmv of toluene under primary conditions ($T = 750\text{-}850\text{ }^\circ\text{C}$) with either $\gamma\text{-Al}_2\text{O}_3$ or olivine supports, doped with either 2 wt. % Ni or 10 wt. % Fe. The olivine, known as primary catalyst of reference, shows better performances. In the case of $\gamma\text{-Al}_2\text{O}_3$, the low loading of Ni leads to the formation of a spinel of NiAl_2O_4 which shows low reducibility, and the doping with Fe favors the $\gamma\text{-Al}_2\text{O}_3$ to $\alpha\text{-Al}_2\text{O}_3$ phase transition of the support. Therefore, the next studies focus on the development of 10 wt. % Ni/ $\gamma\text{-Al}_2\text{O}_3$ catalysts tested in secondary conditions.

The reduction of catalysts entirely composed of NiAl_2O_4 only starts at $T = 680\text{ }^\circ\text{C}$ during H_2 -TPR measurements. However, these samples are reduced during the catalytic reforming of 24.000 ppmv of toluene at $T = 650\text{ }^\circ\text{C}$. It is demonstrated that under these conditions, toluene is a better reducing agent than H_2 or CO , and that the reduction of NiAl_2O_4 oxide with toluene enables its conversion with a very little formation of coke. For bulk NiO, reduced at low temperatures ($T \sim 450\text{ }^\circ\text{C}$), the catalyst does not take advantage of the anti-coking effect brought by the phenomenon of special reduction by toluene, which leads to a quick deactivation of the catalyst by formation of carbon deposit.

The addition of a surfactant (stearic acid) during the aqueous sol-gel synthesis efficiently modifies the morphology (mesopores, macropores) of Ni/ $\gamma\text{-Al}_2\text{O}_3$ catalysts. Despite a much higher catalytic activity, attributed to a better diffusion of the gaseous reagents, the sample shows a much higher sensibility towards deactivation by coking. It is hypothesized that this weakness is the consequence of the combination of several facts: loss of balance between the reaction rates of toluene cracking and the rates of dissociation-migration of the HO^* and O^* species + better reducibility of the catalyst, which avoids the phenomenon of special reduction by toluene + presence of large pores, which do not prevent the growth of filamentous carbon.

A vast screening of catalysts composed of 10 % Ni/ $\gamma\text{-Al}_2\text{O}_3$ and doped with metals (Cu, Mn, Fe, Mo or Mn) or oxides (CaO, K_2O , MgO or CeO_2) is performed. The samples doped with Mn, Mo, Ca ou K show the most interesting catalytic activities and resistances against coking. It is to notice that, for an identical amount, the samples doped with two different elements (Co+Mo, Mn+Mo, Ca+K or Ce+K) show better catalytic performances compared to those doped with only one type of dopant.

The tests of the best catalysts in long-term conditions (30 h) or in presence of H_2S are promising. Hence, these catalysts might be adequate for industrial applications.

Table of contents

Chapter I

Biomass gasification technology and its tar reforming catalysts	5
I.1. INTRODUCTION	6
I.2. BIOMASS VALORIZATION PROCESSES	7
I.2.1. Overview of the different technologies	7
<i>I.2.1.1. Physico-chemical transformations</i>	8
<i>I.2.1.2. Thermo-chemical transformations</i>	8
I.2.2. Gasification processes	9
<i>I.2.2.1. Gasification reactions</i>	9
<i>I.2.2.2. Syngas empowering</i>	11
I.3. TECHNOLOGICAL ASPECTS OF BIOMASS GASIFICATION	11
I.3.1. Overview of the processes implied in the fabrication and purification of bio-syngas	11
I.3.2. Types of gasifier reactors	12
I.3.3. Gasification products	13
<i>I.3.3.1. General composition of gas at the outlet of gasifiers</i>	13
<i>I.3.3.2. Undesirable gasification compounds</i>	14
<i>I.3.3.2.1. Tars</i>	14
<i>I.3.3.2.2. Other contaminants</i>	15
I.3.4. Influences of experimental parameters	15
I.4. CATALYTIC PURIFICATION OF BIO-SYNGAS	16
I.4.1. Tar reforming	16
<i>I.4.1.1. Catalytic reforming mechanisms</i>	16
<i>I.4.1.2. Kinetic approach</i>	16
I.4.2. Influences of operating parameters on the catalyst performances	18
<i>I.4.2.1. Influences of the temperature</i>	18
<i>I.4.2.2. Influences of the gas composition</i>	18
<i>I.4.2.3. Influences of the space velocity</i>	19
I.4.3. Deactivation and regeneration of catalysts	19
<i>I.4.3.1. Mechanisms of coking</i>	19
<i>I.4.3.1.1. Mechanisms of carbon deposition</i>	20
<i>I.4.3.1.2. Reduction of coking by adjustment of parameters</i>	21
<i>I.4.3.1.3. Regeneration of carbon deactivated catalysts</i>	22
<i>I.4.3.2. Poisoning of metallic active sites</i>	22
<i>I.4.3.2.1. Sulfide compounds</i>	22
<i>I.4.3.2.2. Poisoning with salts</i>	24
<i>I.4.3.3. Thermal degradation</i>	24
<i>I.4.3.3.1. Sintering</i>	24

I.4.3.3.2. Phase transformation	25
I.4.3.3.3. Volatilization	25
I.4.4. Catalysts developed for the bio-syngas purification	25
I.4.4.1. Influences of porous structure and shaping of catalysts	27
I.4.4.2. Influences of support composition	27
I.4.4.2.1. Carbon supports	27
I.4.4.2.2. Basic supports	28
I.4.4.2.3. Acid supports	30
I.4.4.2.4. γ -Al ₂ O ₃ promoted supports	31
I.4.4.3. Influences of the composition of the metallic active sites	33
I.4.4.3.1. General trends	33
I.4.4.3.2. Noble metal-based catalysts	34
I.4.4.3.3. Ni-based catalysts	35
I.4.4.4. Influences of the dispersion of the active sites	37
I.4.4.5. Influences of the synthesis method the catalysts	37
I.5. CONCLUSIONS	38
<u>Chapter II</u>	
Elaboration of an aqueous sol-gel method for the synthesis of γ-Al₂O₃ supports	40
II.1. INTRODUCTION	41
II.1.1. The sol-gel chemistry	41
II.1.1.1. Organic path	42
II.1.1.2. Aqueous path	43
II.1.2. Formation of aluminum hydroxides and calcined alumina	44
II.1.3. Cogelation and coprecipitation methods	46
II.2. EXPERIMENTAL	47
II.2.1. Preparation of samples	47
II.2.2. Characterization techniques	48
II.3. RESULTS	49
II.4. DISCUSSION	53
II.4.1. Influences of the aluminum precursor type on the textural properties of γ -Al ₂ O ₃ supports	53
II.4.2. Modifications of the properties of γ -Al ₂ O ₃ supports caused by EDAS	54
II.5. CONCLUSIONS	55
<u>Chapter III</u>	
Influences of the aqueous synthesis way and of the organosilane nature on the physico-chemical properties of alumina supports	57
III.1. INTRODUCTION	58
III.1.1. Modifications of γ -Al ₂ O ₃ with different silicon precursors	58

III.1.2. Thermal stabilization of γ -Al ₂ O ₃ by silica addition	59
III.2. EXPERIMENTAL	60
III.2.1. General parameters	60
III.2.2. Synthesis procedures	60
III.2.2.1. <i>Classic preparation method</i>	60
III.2.2.2. <i>Modifications of the Classic method</i>	61
III.2.3. Additional calcination and steaming treatments	61
III.2.4. Characterization techniques	61
III.3. RESULTS AND DISCUSSION	62
III.3.1. Formation, composition and morphology of Al ₂ O ₃ -SiO ₂ materials	62
III.3.1.1. <i>Precipitation curves</i>	62
III.3.1.2. <i>Thermal behaviors</i>	63
III.3.1.3. <i>Compositions of samples</i>	64
III.3.1.4. <i>Morphology of the supports</i>	65
III.3.2. Effect of EDAS concentration on Al ₂ O ₃ -SiO ₂ materials	66
III.3.3. Influences of the addition step of EDAS on Al ₂ O ₃ -SiO ₂ materials	68
III.3.4. Influences of the silicon alkoxide reactivity on Al ₂ O ₃ -SiO ₂ materials	70
III.3.5. Influences of the length and composition of the silicon alkoxide functional chain on the properties of Al ₂ O ₃ -SiO ₂ materials	72
III.3.6. External surface area of the crystallites	75
III.3.7. Evolution of physico-chemical properties of the supports with additional thermal and steaming treatments	76
III.4. CONCLUSIONS	78

Chapter IV

Performances of nickel and iron doped materials used as primary catalysts	81
IV.1. INTRODUCTION	82
IV.2. EXPERIMENTAL	83
IV.2.1. Catalysts preparation	83
IV.2.1. <i>Sol-gel synthesis of Ni- and Fe/γ-Al₂O₃ catalysts</i>	83
IV.2.2. <i>Impregnation of olivine with Ni and Fe</i>	84
IV.2.2. Characterization techniques	84
IV.2.3. Catalytic experiments	85
IV.2.4. Use of toluene as tar model compound	86
IV.3. RESULTS AND DISCUSSIONS	87
IV.3.1. Characterizations of catalysts	87
IV.3.1.1. <i>Compositions of samples</i>	87
IV.3.1.2. <i>Textural and physico-chemical properties of samples</i>	88
IV.3.2. Catalytic activities and post-test characterizations	93
IV.3.2.1. <i>Catalytic performances at T = 750 °C</i>	93
IV.3.2.2. <i>Catalytic performances at T = 850 °C</i>	97

IV.4. CONCLUSIONS	100
<u>Chapter V</u>	
Development of Ni-based secondary catalysts supported on γ-Al₂O₃	103
V.1. INTRODUCTION	104
V.2. EXPERIMENTAL	106
V.2.1. Synthesis of Ni/ γ -Al ₂ O ₃ catalysts	106
V.2.1.1. <i>Ni/γ-Al₂O₃ catalysts prepared by sol-gel method</i>	106
V.2.1.2. <i>Ni/γ-Al₂O₃ catalysts prepared by impregnation method</i>	106
V.2.2. Characterization techniques	107
V.2.3. Catalytic tests	107
V.3. RESULTS AND DISCUSSION	109
V.3.1. Compositions of Ni/ γ -Al ₂ O ₃ catalysts	109
V.3.2. Influences of the catalysts preparation method	109
V.3.2.1. <i>Properties of Ni/γ-Al₂O₃ catalysts prepared by impregnation or by sol-gel methods</i>	109
V.3.2.2. <i>Catalytic performances of Ni/γ-Al₂O₃ catalysts prepared by impregnation or by sol-gel methods</i>	111
V.3.3. Influences of the syngas composition	113
V.3.4. Influences of the nickel loading	117
V.3.4.1. <i>Properties of Ni/γ-Al₂O₃ catalysts with different Ni loadings</i>	117
V.3.4.2. <i>Catalytic performances of Ni/γ-Al₂O₃ catalysts with different Ni loadings</i>	119
V.3.5. Influences of the temperature on the catalytic performances	122
V.4. CONCLUSIONS	125
<u>Chapter VI</u>	
Influence of the support texture on the performances of 10 wt. % Ni/γ-Al₂O₃ catalyst	128
VI.1. INTRODUCTION	129
VI.2. EXPERIMENTAL	129
VI.2.1. Synthesis of Ni/ γ -Al ₂ O ₃ catalysts modified with stearic acid	129
VI.2.2. Characterization techniques	130
VI.2.3. Catalytic tests	131
VI.3. RESULTS AND DISCUSSION	131
VI.3.1. Compositions	131
VI.3.2. Influences of synthesis method on 10 wt. % Ni/ γ -Al ₂ O ₃ catalysts tailored with stearic acid	131
VI.3.3. Further characterizations and catalytic performances of the most promising Ni/ γ -Al ₂ O ₃ sample synthesized with stearic acid	136
VI.3.2.2.1. <i>Textural properties of sample N-10Ni-PS-eth</i>	136
VI.3.2.2.1. <i>Catalytic performances of sample N-10Ni-PS-eth</i>	137
VI.4. CONCLUSIONS	140

Chapter VII

Enhancement of the catalytic performances and lifetime of nickel/alumina catalysts via addition and combination of dopants

	142
VII.1. INTRODUCTION	143
VII.2. EXPERIMENTAL	145
VII.2.1. Synthesis of doped Ni/ γ -Al ₂ O ₃ catalysts	145
VII.2.2. Characterization techniques	145
VII.2.3. Catalytic experiments	146
VII.3. RESULTS AND DISCUSSION	147
VII.3.1. γ -Al ₂ O ₃ supports doped as reference materials	147
VII.3.2. Catalysts doped with 2 wt. % of metal or 1.5 wt. % of oxide	147
VII.3.2.1. <i>Composition and textural properties</i>	147
VII.3.2.2. <i>Doping with 2 wt. % of metal</i>	148
VII.3.2.2.1. <i>Properties of Ni/γ-Al₂O₃ catalysts doped with 2 wt. % of metal</i>	148
VII.3.2.2.2. <i>Catalytic performances of Ni/γ-Al₂O₃ catalysts doped with 2 wt. % of metal</i>	150
VII.3.2.3. <i>Doping with 1.5 wt. % of oxide</i>	153
VII.3.2.3.1. <i>Properties of Ni/γ-Al₂O₃ catalysts doped with 1.5 wt. % of oxide</i>	153
VII.3.2.3.2. <i>Catalytic performances of Ni/γ-Al₂O₃ catalysts doped with 1.5 wt. % of oxide</i>	155
VII.3.3. Double doping and synergistic effects	158
VII.3.3.1. <i>Catalysts doped with two different metals</i>	158
VII.3.3.1.1. <i>General trends</i>	158
VII.3.3.1.2. <i>Properties of samples doped with Co+Mo or Mn+Mo</i>	159
VII.3.3.1.3. <i>Catalytic performances of samples doped with Co+Mo or Mn+Mo</i>	161
VII.3.3.2. <i>Catalyst catalysts doped with two oxides</i>	162
VII.3.3.2.1. <i>General trends</i>	162
VII.3.3.2.2. <i>Properties of samples doped with Ca+K or Ce+K</i>	163
VII.3.3.2.3. <i>Catalytic performances of samples doped with Ca+K or Ce+K</i>	164
VII.3.4. Influences of dopant loadings	165
VII.3.4.1. <i>Catalysts doped with Mn or Mo</i>	166
VII.3.4.1.1. <i>Properties of 10 wt. % Ni/γ-Al₂O₃ catalysts doped with 4 wt. % of Mn or Mo</i>	166
VII.3.4.1.2. <i>Catalytic performances of 10 wt. % Ni/γ-Al₂O₃ catalysts doped with 4 wt. % of Mn or Mo</i>	167
VII.3.4.2. <i>Catalysts doped with Ca or K</i>	168
VII.3.4.2.1. <i>Properties of 10 wt. % Ni/γ-Al₂O₃ catalysts doped with 3 wt. % of Ca or K</i>	168
VII.3.4.2.2. <i>Catalytic performances of 10 wt. % Ni/γ-Al₂O₃ catalysts doped with 3 wt. % of Ca or K</i>	169
VII.3.5. Catalytic performances of the most promising catalysts at different temperatures	171

VII.3.5.1. <i>Evolution of the performances of the best Ni/γ-Al₂O₃ catalysts promoted with metal dopants</i>	171
VII.3.5.2. <i>Evolution of the performances of the best Ni/γ-Al₂O₃ catalysts promoted with oxide dopants</i>	175
VII.4. CONCLUSIONS	179
<u>Chapter VIII</u>	
Catalytic performances of the most promising Ni/γ-Al₂O₃ catalysts during long-term tests and in presence of H₂S	183
VIII.1. INTRODUCTION	184
VIII.2. EXPERIMENTAL	185
VIII.2.1. Ni-based catalysts selected	185
VIII.2.2. Characterization techniques	185
VIII.2.3. Catalytic tests	185
VIII.3. RESULTS AND DISCUSSION	186
VIII.3.1. Characterization of the commercial catalyst	186
VIII.3.2. Long-term tests	188
VIII.3.3. Catalytic performances in sulphidic conditions	191
VIII.4. CONCLUSIONS	193
General conclusions and perspectives	196
ANNEXES	A.1
<u>Annex 1:</u> Additional information relative to Chapter I	A.2
<u>Annex 2:</u> Formulae, characterization techniques, calculations, amount of reagents and X-Ray references	A.8
<u>Annex 3:</u> Experimental installation used for catalytic tests	A.20
<u>Annex 4:</u> Additional information relative to Chapter VII	A.23
<u>Annex 5:</u> Complementary study about the optimization of operating variables for the synthesis of γ -Al ₂ O ₃ based catalysts	A.26
<u>Annex 6:</u> Complementary study about 10 wt. % Ni/ γ -Al ₂ O ₃ catalysts modified with different silicon precursors	A.33
<u>Annex 7:</u> Complementary study about the coating of honeycomb cordierite support with Ni/boehmite gels	A.42
REFERENCES	A.55

Structure of the thesis

The goal of this thesis is to develop for the first time in the Department of Chemical Engineering-Nanomaterials, Catalysis and Electrochemistry of the University of Liège, heterogeneous nickel-based alumina catalysts for the reforming of tars during the gasification of the biomass.

Chapter I presents the processes involved during the gasification of the biomass and the catalytic purification of the bio-syngas. More than an introduction, this study is essential in order to target the needs of the industry, to understand the functioning of the tar reforming catalysts and to determine the conditions of the catalytic tests.

Chapter II details the development of an aqueous sol-gel method for the synthesis of γ -Al₂O₃ supports. The first aim of this chapter is to determine the influences of two different aluminum precursors (Al(NO₃)₃ or Al-*sec*-butoxide) and of the synthesis operating variables (*pH*, calcination temperature ...) on the textural and crystallographic properties of Al₂O₃ supports. In order to use these alumina materials as catalytic supports, only the formation of γ -Al₂O₃ is aimed, because it presents high specific surface area and pore volume values. The second aim of this chapter concerns the synthesis of γ -Al₂O₃ with the addition of a functionalized silicon precursor, 3-(2-aminoethylamino)propyltrimethoxysilane, called EDAS. By the presence of an ethylenediamine group in this molecule, it is possible to chelate metallic ions and to highly increase their dispersion at a molecular level, which is an asset for catalytic applications.

Chapter III aims at getting a better understanding about how silicon precursors modify the final properties of γ -Al₂O₃ supports. It highlights the influences of the amount and of the step of addition of the EDAS molecules during the synthesis. Furthermore, in this chapter, γ -Al₂O₃ supports are synthesized with non-functionalized silicon precursors of different reactivity (tetraethoxysilane or tetramethoxysilane) and with silicon precursors containing other functional chains than the ones of EDAS, such as 3-aminopropyltrimethoxysilane, trimethoxypropylsilane or trimethoxyoctylsilane. The aim is to understand the influences of the reactivity of the silicon precursor and the presence of functional chains on the final properties of γ -Al₂O₃-SiO₂ supports. Additional treatments at high temperatures ($T = 600/1000/1200$ °C) or under steam conditions ($T = 700$ °C, 10 vol. % H₂O) show how the properties of pure γ -Al₂O₃ supports and of γ -Al₂O₃ supports modified with a silicon precursor evolve under conditions similar to the ones encountered during catalytic tests .

Chapter IV presents catalytic tests performed under primary catalytic conditions ($T = 750$ - 850 °C) with 8000 ppmv of toluene. The catalysts are either constituted of γ -Al₂O₃ or olivine, with either 2 wt. % Ni or 10 wt. % Fe as metallic dopant. The objective is to determine

whether to orientate the thesis towards the development of primary (inside the gasifier) or secondary (outside the gasifier) catalysts.

Chapter V describes the catalytic performances of Ni/ γ -Al₂O₃ catalysts tested under secondary conditions ($T = 650$ °C) with 24.000 ppmv of toluene. The chapter details how the preparation method (sol-gel or impregnation) and the loading of Ni influence the formation of nickel oxides with different interactions with the alumina support (NiO, NiO/Al₂O₃ or NiAl₂O₄). Catalytic tests show the decisive influences of the presence of NiO or NiAl₂O₄ on the performances of the catalysts. This chapter also presents catalytic tests performed with different compositions of syngas, thus in order to understand why the catalysts are reduced at lower temperatures during catalytic tests ($T = 650$ °C) than during TPR measurements ($T = 680$ °C). Finally, the catalytic performances of quartz, pure γ -Al₂O₃ and 10 wt. % Ni/ γ -Al₂O₃ samples are also evaluated at $T = 900 \rightarrow 600$ °C, in order to compare their kinetic parameters with the literature and to determine the influences of a pre-reduction step.

Chapter VI presents the synthesis of Ni/ γ -Al₂O₃ catalysts prepared with stearic acid by aqueous sol-gel methods. The influences of different synthesis operating parameters (type of solvent, addition step of surfactant) on the morphology of the catalysts are studied. The most promising Ni/ γ -Al₂O₃ catalyst modified with stearic acid is tested for the reforming of 24.000 ppmv of toluene at $T = 650$ °C.

The purpose of **Chapter VII** is to highlight which dopants and combinations of dopants increase the catalytic activity and the resistance against coking of 10 wt. % Ni/ γ -Al₂O₃ catalysts tested for the reforming of 24.000 ppmv toluene at $T = 650$ °C. The most promising catalysts are also tested at $T = 900 \rightarrow 600$ °C in order to determine their kinetic parameters and their resistance against several deactivation phenomena (coking, sintering, phase transformation).

In order to be as close as possible to real conditions of industrial biomass gasification processes, **Chapter VIII** studies the catalytic performances of the most promising catalysts during long-term tests (30 h) or in the presence of H₂S. The catalysts developed in this thesis are also compared to the commercial catalyst *Hifuel*.

Being aware that numerous samples are synthesized, characterized and tested in the body of the manuscript, a part of the results is set in annexes. **Annexes 1, 2, 3, 4** and **5** are information directly linked to the studies presented in the body of the manuscript. **Annexes 6** and **7** are complementary studies relative to this thesis.

Annex 1 is complementary to **Chapter I**. It gives additional economic and technical information relative to the gasification of biomass.

Annex 2 reminds the formulae used in this work, gives details about all characterization techniques, shows some calculations, lists the amounts of reagents used for the synthesis of catalysts and gives the references of all the compounds determined by X-Ray analysis.

One important objective of this project was to build-up an experimental installation able to recreate the conditions during biomass gasification (temperature, gas composition). **Annex 3** gives details about the assembly and the functioning of this experimental installation.

Annex 4 is complementary to **Chapter VII**. It gives information about a new drying method used to prepare homogeneous catalysts doped with two different oxides. It also presents the characterizations of the reference γ -Al₂O₃ supports doped with metals or Ce.

The aqueous sol-gel method used for the preparation of catalysts is improved throughout the project. **Annex 5** presents the optimization of the operating variables used for the synthesis of γ -Al₂O₃ based catalysts.

Annex 6 is a complementary study inspired by the results obtained in **Chapter III**. This annex studies the properties and catalytic performances of 10 wt. % Ni/ γ -Al₂O₃ catalysts modified with different type of silicon precursors.

The prices of sol-gel procedures being much higher than those of classic impregnation, and the project being focused on the design of catalysts for secondary catalytic applications, the development of an efficient coating method appears essential for the future utilization of the catalysts at large scale. In this way, **Annex 7** sets the bases of a procedure for the coating of Ni/boehmite gel on a commercial honeycomb cordierite.

Chapter I corresponds to a review published in the journal **Energy & Fuels** (V. Claude, C. Courson, M. Köhler and S.D. Lambert, “*Overview and essentials of biomass gasification technologies and their catalytic cleaning methods*”, Energy & Fuels, (2016), vol. 30, n° 11, p. 8791-8814).

Chapter III corresponds to an article published in the journal **European Journal of Inorganic Chemistry** (V. Claude, M. Vilaseca, A.S. Tatton, C. Damblon and S.D. Lambert, “*Influence of the method of aqueous synthesis and the nature of the silicon precursor on the physicochemical properties of porous Alumina*”, Eur. J. Inorg. Chem., (2016), p.1678-1689).

The results from **Chapters VII** and **VIII** were presented during an oral communication carried out at the **11th Natural Gas Conversion Symposium**, June 2016, Tromsø, Norway.

A part of the results presented in **Chapter VI** and in **Annex 7** were obtained during the management of the **Master’s thesis** of Timothée Lohay (academic year 2015-2016), whose report is entitled: “*Synthesis, characterization and shaping of alumina-based catalysts for toluene reforming*”.

Chapter I

Biomass gasification technology and its tar reforming catalysts

- Positioning of the biomass gasification technologies among the other bio-energies;
- Description and influences of the different processes involved during the biomass gasification;
- Functioning, properties and factors influencing the performances and lifespan of tar reforming catalysts;
- Review of the most common catalysts used for the production of a clean bio-syngas.

This chapter aims at first at presenting the basis of biomass gasification technology and positioning them among other bio-energies.

Obtaining a tar free bio-syngas from biomass gasification processes has been the subject of many studies in the last two decades, and it still remains a major technologic and economic challenge. Though the bio-syngas quality improvement can be obtained through different operating processes (reactor design, gasifying ratio, feedstock, temperature and space ratio), the purification of the bio-syngas by the use of catalysts has proved to be one of the most convenient and efficient way to eliminate undesirable tars.

In this way, after setting the essential details relative to the gasification of biomass (temperature, composition of bio-syngas, type and amount of tars and other pollutants), the rest of this chapter mostly focuses on the processes and mechanisms involved during the catalytic reforming of bio-syngas tars. Furthermore, this chapter also makes an inventory of the numerous studies conducted in order to understand the influences of different properties, especially support and active site compositions, on the tar reforming activity and on the lifetime of the catalysts.

I.1. INTRODUCTION

Adapted from old coal gasification technologies developed during the industrial revolution, the biomass gasification appears nowadays as an interesting and versatile way to take advantage of different sources (e.g. agricultural and urban wastes, energy crops, food and industrial processing residues). If managed conscientiously, these processes can therefore lead to the sustainable and renewable production of a bio-syngas, which can either be used directly as combustible or converted into storable and high valuable chemical compounds such as methanol.^{[1], [2]} However, despite the fact that bio-syngas is predicted to be an economically viable energy and that some industrial plants are already in action, bio-syngas technologies still encounter some technical problems, which seriously hinder their commercial development.^{[3], [4]} In this way, the tar presence at the gasifier outlet, which results from the incomplete degradation of aromatic rings contained in the biomass, still remains a major problem that the industry has to face. Modifications of the gasifier reactor design and of the gasification operating conditions (temperature, space ratio, gasifying reagent) have proved to substantially reduce the tar concentration.^{[5]-[9]} Furthermore, the catalytic reforming of tars at the inside or at the outside of the gasifier reactors also appears as a convenient and economical solution to obtain a clean bio-syngas, which explains the numerous studies conducted during the last two decades on this topic. The catalytic tar reforming has been carried out with numerous types of catalysts, the researchers modifying several aspects such as the acido-basicity, the texture, the crystallinity or the elementary composition of the supports and active sites. Furthermore, catalytic operating conditions such as the temperature, space ratio or gas mixture also proved to be of significant importance for the sustainability and performances of the catalysts.

The first part of this chapter aims at situating the biomass gasification processes among other biomass derived technologies. Thereafter, the economic and technical advantages as well as the drawbacks of different gasifier reactors and operating conditions are described. Finally, among the several existing syngas cleaning operations, this chapter emphasizes the basic notions and recent progresses achieved in the catalytic tar reforming field.

I.2. BIOMASS VALORIZATION PROCESSES

I.2.1. Overview of the different technologies

The term “biomass” covers the raw (wood, energy crops, agricultural residues ...) or processed (effluents, food processing residues, green wastes ...) organic matter, which can either be of vegetal or animal origin.^{[10], [11]} Depending strongly on its origins, biomass materials are generally composed of cellulose, hemicellulose, lignin, lipids, proteins, simple sugars and starches. In the case of woody biomass, cellulose, hemicellulose and lignin are the three main constituents.^[11] The renewable aspect that is attributed to biomass can be explained by the carbon cycle: the carbon dioxide emitted during its use is compensated by the carbon stock accumulated during its growing stage. Therefore, the biomass can only be considered as a clean and renewable energy if obtained in a sustainable way. In case of CO₂ emission not compensated by its natural growth (for example an overexploited forest), the biomass cannot and must not be considered as a clean and renewable energy.^[10] The term “bio-energies” refers to all the processes (industrial or not) which can produce energy from biomass. Figure A1.1 presented in Annex 1 gives a general view of the part of bio-energy in the worldwide energy consumption in 2013.^[12]

Despite the fact that the energy production from biomass becomes more interesting in developed countries, its actual part in the total global energy consumption is still very low (~3.3 %). In this way, in the European Union, the “bio-electricity” (issued from solid or liquid biomass, biogas or wastes) has generated 121 TWh in 2010, which corresponds to 3.6 % of the total electric production of the E.U..^[13] According to a report from the International Energy Agency (IEA), the part of bio-electricity has been growing at an average rate of 2.5 % per year over the 2000-2010 decade.^[11] From an economical aspect, the supplying costs can be low, when agricultural or urban residues are collected and transported over short distances. However, expenses can quickly arise when raw materials are imported (ex: wood pellets).^[14] Following these observations, the biomass valorization sector is more inclined to develop itself into small interconnected installations, rather than huge centralized complexes. Biomass can be converted into energy or by-products via versatile transformation technologies: Figure I.1 gives an overview of the principal processes. Basically, two different operations of biomass transformation are performed: physico-chemical or thermo-chemical.

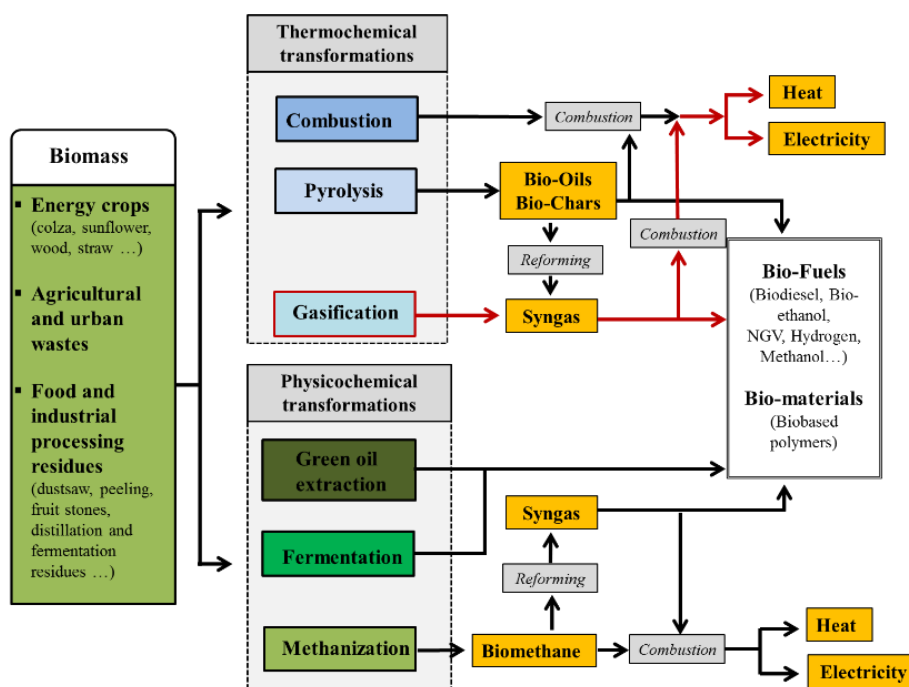


Figure I.1: Overview of main biomass valorizations, inspired from the literature.^[2]

According to a study made by the International Renewable Agency, *IRENA*, biomass gasification technologies can provide power with relatively low costs compared to other renewable resources (such as bio-diesel) (Figure A1.2 presented in Annex 1).^{[15], [16]} A study made by the International Energy Agency, *IEA*, showed a cost estimate for different fuels: gasoline from petroleum, conventional and advanced biodiesel, bio-synthetic gas and ethanol from different sources (Figure A1.3 presented in Annex 1).^[15] Despite the conventional gasoline price being predicted to increase, some renewable solutions, such as conventional or advanced bio-diesel, do not seem to be economically interesting alternatives. In comparison, bio-synthetic gas obtained from gasification was on the third position below ethanol, which means that bio-syngas could really be an efficient alternative.

1.2.1.1. Physico-chemical transformations

Three main technologies of physicochemical transformations can be distinguished: oil extraction, fermentation and anaerobic digestion. Details about these processes are given in part I of Annex 1.

1.2.1.2. Thermo-chemical transformations

Though less developed, the thermo-chemical processes are generally more efficient than the physico-chemical ones. The reasons are as follows: 1) a shorter reaction time (a few seconds or minutes for thermo-chemical processes vs. several days, weeks or even longer for bio-chemical/biological processes); 2) a higher ability to destroy most of the organic compounds. Lignin materials are typically considered to be non-fermentable and thus cannot be completely decomposed via biological processes, whereas they can be fully converted thanks to thermo-

chemical transformations.^[11] In comparison to fossil fuels, biomass has lower heating values (LHV) for a similar weight. In fact, the heating value of biomass ranges from 15-19 GJ/t, compared to 20-30 GJ/t for coals. Furthermore, the bulk density, also known as energy density, is only 10-40 % of most fossil fuels. However, in comparison to fossil fuels, biomass contains much higher volatile matter contents (80 % in biomass instead of 20 % for fossil fuels), which means that biomass has a high ignition stability and can easily be thermo-chemically processed towards other higher value fuels (syngas).^[11] The thermo-chemical transformation processes are summarized in Figure I.2. They can be classified into three different paths: combustion, pyrolysis and gasification processes. The main difference lies in the amount of oxygen used during the operations, thus modifying the thermo-chemical reactions and reaction products.^[10] ^[17] Details about the valorization of the biomass by other thermo-chemical transformations than gasification (combustion and pyrolysis) are given in part I of Annex 1.

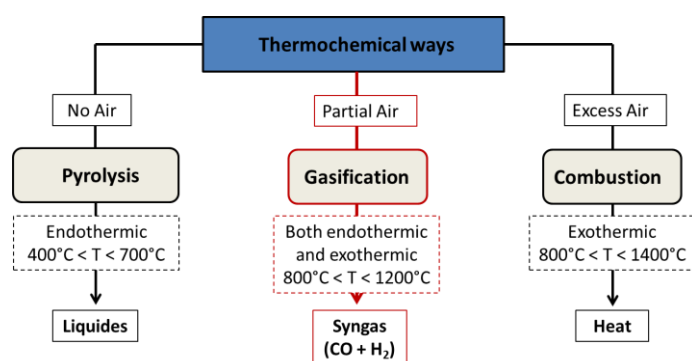


Figure I.2: Scheme of the three different thermo-chemical ways.^[17], ^[18]

I.2.2. Gasification processes

The biomass gasification is a sum of complex thermo-chemical processes, which include biomass drying, pyrolysis, char gasification and reforming of gaseous products formed by pyrolysis.^[17] Its final product is a combustible gas, called syngas or bio-syngas, which is mainly composed of H_2 and CO , and whose lower heating value (LHV) is situated between 5 and 20 MJ/Nm^3 (depending on the biomass and gasification vector: air, steam or pure O_2).^[19] Common gasifying agents used in industrial gasifiers include a mixture of steam and air or oxygen, with the amount of oxygen being generally 1/5 to 1/3 of the amount theoretically required for complete combustion. The necessary heat for gasification is produced by a partial combustion of the biomass in the same reaction chamber. In addition to the typical biomass products and wastes described above, it is important to note that the gasification operations can also be performed with plastics, coal or a mixture of plastics/coal/biomass, thus increasing the versatile aspect of the gasification.^{[20]–[24]}

I.2.2.1. Gasification reactions

At temperatures between $T = 800\text{ °C}$ and $T = 1200\text{ °C}$, several parallel gasification reactions take place inside the gasifier (Table I.1). The produced tars are converted by further

partial oxidation, reforming, hydrogenation and thermal cracking with highly endothermic reaction enthalpies comprised between + 200 kJ/mol to + 300 kJ/mol (Equations I.1 - I.5). The combustion of char and volatile compounds (CO, H₂, CH₄) via partial or complete oxidation reactions occurs in the presence of air or oxygen (Equations I.6 - I.7 and Equations I.13 - I.16). These reactions are highly exothermic and allow generating the necessary heat for the drying, pyrolysis and gasification reactions. The produced H₂O and CO₂ molecules are thereafter consumed during the char gasification (Equations I.8 - I.11). Reactions of water-gas shift (Equation I.17) and methanation (Equations I.18 – I.19) take place in either direction, depending on the specific temperature, pressure and reactants concentrations. Water-gas shift is of great importance since it plays a significant role for the generation of H₂, and therefore for the LHV of the syngas. The methanation reactions occur slowly at low temperatures and in the absence of any catalysts.^{[17], [25]} The Gibb's energy for the Boudouard (Equation I.8) and water-gas shift (Equation I.17) reactions are negative at temperatures above $T = 720$ °C and up to $T = 820$ °C, respectively.^{[26], [27]}

Table I.1: Main reactions involved in the biomass gasification process.^{[25], [28], [29]}

Equations	Heat of reaction (kJ/mol) at 298 K	Name	Equation n°
Tars general equations			
$C_n H_m + \left(\frac{n}{2}\right) \cdot O_2 \rightarrow n \cdot CO + \left(\frac{m}{2}\right) \cdot H_2$	Highly endothermic + (200 to 300)	Tars partial oxidation	I.1
$C_n H_m + n \cdot CO_2 \rightarrow 2n \cdot CO + \left(\frac{m}{2}\right) \cdot H_2$		Tars dry reforming	I.2
$C_n H_m + n \cdot H_2O \rightarrow 2 \cdot CO + \left(\frac{m}{2} + n\right) \cdot H_2$		Tars steam reforming	I.3
$C_n H_m + \left(2n - \frac{m}{2}\right) \cdot H_2 \rightarrow n \cdot CH_4$		Tars hydrogenation	I.4
$C_n H_m \rightarrow \left(n - \frac{m}{4}\right) \cdot C + \left(\frac{m}{4}\right) \cdot CH_4$		Tars thermal cracking	I.5
Char combustion			
$C + O_2 \rightarrow CO_2$	-394	Complete combustion	I.6
$C + \left(\frac{1}{2}\right) \cdot O_2 \rightarrow CO$	-111	Partial combustion	I.7
Char gasification			
$C + CO_2 \leftrightarrow 2 \cdot CO$	+173	Boudouard reaction	I.8
$C + H_2O \leftrightarrow CO + H_2$	+131	Water-Gas reaction 1	I.9
$2 \cdot C + 2 \cdot H_2O \leftrightarrow CH_4 + CO_2$	+16	Water-Gas reaction 2	I.10
$C + 2 \cdot H_2O \leftrightarrow CO_2 + 2 \cdot H_2$	-91	Water-Gas reaction 3	I.11
$C + 2 \cdot H_2 \leftrightarrow CH_4$	-75	Hydrogasification reaction	I.12
Homogeneous volatile oxidation			
$CO + \left(\frac{1}{2}\right) \cdot O_2 \rightarrow CO_2$	-283	Carbon monoxide combustion	I.13
$H_2 + \left(\frac{1}{2}\right) \cdot O_2 \rightarrow H_2O$	-242	Hydrogen combustion	I.14
$CH_4 + 2 \cdot O_2 \rightarrow CO_2 + 2 \cdot H_2O$	-283	Methane combustion	I.15
$CH_4 + \left(\frac{1}{2}\right) \cdot O_2 \rightarrow CO + 2 \cdot H_2$	-35	Methane partial oxidation	I.16
$CO + H_2O \leftrightarrow CO_2 + H_2$	-41	Water-Gas Shift reaction	I.17
Methanation reactions			
$CO + 3 \cdot H_2 \leftrightarrow CH_4 + H_2O$	-204	Methanation reaction 1	I.18
$2 \cdot CO + 2 \cdot H_2 \leftrightarrow CH_4 + CO_2$	-248	Methanation reaction 2	I.19

1.2.2.2. Syngas empowering

Currently, most of the syngas obtained from the biomass gasification is used for the generation of power. The cogeneration method is the more current method to convert syngas into energy: thanks to a few technical adjustments, the syngas can replace gasoline or natural gas in internal or external combustion machines normally used for electricity production.^[30] At the same time, the heat emitted during these processes is collected and used for household heating or for additional electricity production thanks to steam turbines.^{[30], [31]}

However, as depicted in Figure A1.4 presented in Annex 1, the bio-syngas produced can also be processed to a variety of useful compounds, mainly thanks to the Fischer-Tropsch and methanol synthesis processes.^{[1], [17]} The methanol, which is one of the easiest product formed by the Fischer-Tropsch process, becomes growingly interesting since it could be a practical alternative to gasoline and diesel.^{[32], [33]}

1.3. TECHNOLOGICAL ASPECTS OF BIOMASS GASIFICATION

1.3.1. Overview of the processes implied in the fabrication and purification of bio-syngas

Seeing all the promising studies presented in the previous part, one could wonder why gasification technologies are not more developed. In fact, the Achilles' heel of gasification technology lies in its cleaning processes. Indeed, according to previous studies,^{[3], [4]} the gas cleaning operations for a fluidized bed make up for 65-85 % of the total costs. These cleaning costs, mainly due to the elimination of tars, are the main obstacles to the commercialization of these technologies. This explains why they are less interesting in comparison to the low costs of oil, gas and coal.^{[14], [34]}

The global processes involved in biomass gasification are presented in Figure I.3. At first, the biomass undergoes upstream processes such as milling and drying. Thereafter, the biomass is converted into gaseous products during the gasification step.

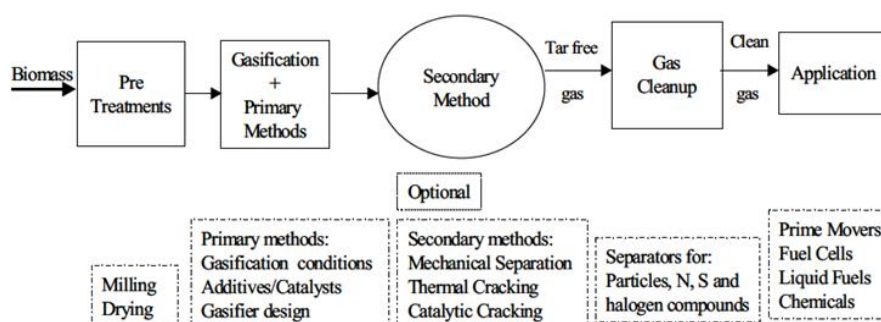


Figure I.3: Main processes involved in biomass gasification.^[35]

The primary methods consist in modifications inside the gasification reactor, allowing obtaining a cleaner syngas with more interesting general composition (higher LHV).^{[10], [35]} In theory, if the primary methods were perfect, the syngas exiting the gasifier would be tar-free, thus eliminating the need of downstream secondary methods. An optimization of the gasification can be reached through three different technical modifications: 1) it can be done by

modifying the gasification conditions, such as temperature, pressure, gasifying medium (air/steam/O₂), residence time, and equivalence ratio (defined in Annex 1, Equation A1.1). The selection of these parameters also depend on the type of gasifier.^{[10], [35]} A homogeneous bed temperature profile and a well-functioning bed fluidization are of utmost importance in case of a fluidized-bed gasifier; 2) it can be performed with the use of bed additives, also known as “primary catalysts”. These catalysts, located inside the reactor, promote the different gasification reactions via different catalytic paths, allowing obtaining a tar-free syngas with higher LHV. Furthermore, the addition of primary catalysts also prevents the agglomeration of solid products such as slag and subsequent choking of the bed;^[35] 3) the kind of reactor also strongly influences the gasification processing parameters, resulting in an important tar reduction and a modification of the final gas composition.^{[19], [36], [37]}

At the gasifier outlet, the syngas usually undergoes various downstream processes in order to be purified from undesirable compounds. These processes can be divided into two categories:

1) the secondary methods, which aim at removing the remaining tars at the reactor outlet. These processes can be conducted at low temperatures and consist of mechanical methods such as the use of a cyclone, baffle filter, ceramic filter, rotating particle separator, electrostatic filter and scrubber. Although these methods are reported to be very effective, in most cases, they are neither convenient, nor economically viable.^{[10], [38]} Indeed, most of these operations are performed with physical separations, which result in the problematic creation of large amounts of toxic condensates. Therefore, instead of transferring the tars into a solid/liquid phase, it is largely preferred to destroy them by catalytic reforming methods, which take advantage of the high temperatures of the exiting syngas ($T = 500\text{-}700\text{ }^{\circ}\text{C}$). These techniques result in an increase of efficiency and lower operational costs.^{[10], [19]} Indeed, more than destroying the tars, using a catalyst permits the improvement of several useful reactions such as the reverse methanation or Water-Gas shift reactions, which allow obtaining a syngas with a high LHV.^[19] Some other tar cleaning methods, such as the use of plasma arc, could also be used but currently remain technological curiosities.^{[19], [39]}

2) the second downstream cleaning method aims at purifying the syngas from undesirable gaseous (mainly H₂S) and solid (dusts, ashes) compounds. The elimination of H₂S and other sulfide compounds is usually done at lower temperatures ($T = 150\text{-}300\text{ }^{\circ}\text{C}$) thanks to the adsorption on specific metallic oxide (for example ZnO) doped ceramic filters. Once these filters are saturated, they can undergo air regeneration.^[40] The solid separation is finally done thanks to physical methods similar to the ones presented above: cyclones, filters and scrubber. Due to a tar-free syngas at this stage, the mechanical cleaning methods are no hindrances.^[10]

I.3.2. Types of gasifier reactors

The type of reactor has a strong impact on gasification processes and on the final gas composition. In 2012, the European Biomass Industry Association made an inventory of the 50

manufacturers identified in the U.S.A, Canada and Europe offering “commercial” gasification plants, resulting in the following occurrence of gasifier kinds^[41]:

- 75% of the designs used a downdraft fixed bed;
- 20% of the designs used fluidized bed systems (bubbling/ circulating or dual);
- 2.5% of the designs used an updraft fixed bed;
- 2.5% were of other designs.

Each type of reactor has its own economic and technologic strengths and weaknesses. As a general point, air-based gasifiers are relatively cheap and typically produce a syngas with a high N₂ content, resulting in a low energy content (5-6 MJ/m³ on a dry basis). In comparison, oxygen or steam-based gasifiers tend to produce a syngas with a high concentration of CO and H₂ resulting in a much higher energy content (9-19 MJ/m³).^[14] The gasifier capacities and their typical particulate/tar loadings (Figure I.4) are the two major technical aspects taken into account in a gasifier design.^{[19], [36]}

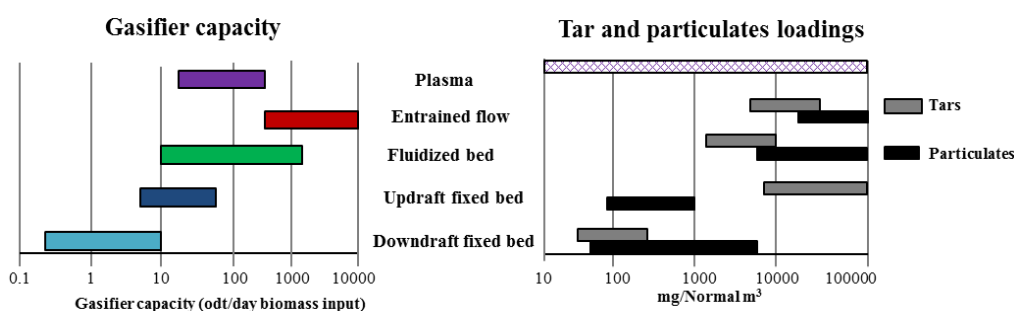


Figure I.4: Technological gasifier capacity range and tars/particulate loadings, adapted from the literature.^{[19], [36]}

Details about the main commercial and pilot gasifiers currently in activity, as well as the processes, advantages and drawbacks of each type of gasifier are given in part II of Annex 1.

I.3.3. Gasification products

I.3.3.1. General composition of gas at the outlet of gasifiers

Table I.2 presents the composition of outlet gas which can be obtained depending on the gasifying agents (air, steam or pure O₂). Plasma gasifiers are also presented because their operating parameters are different from the other gasifiers. The exiting gas compositions depend on various operating parameters, making it unique for each installation.^{[19], [34], [39]} The highest H₂ and CO concentrations are obtained under steam conditions, whereas the gasification made with air (the most common for fixed-bed reactors) leads to weak CO and H₂ concentrations.

Table I.2: General composition of biomass gasification syngas.^{[6], [34]}

Gasifying agent	Gas product (vol. %)					
	H ₂	CO	CO ₂	CH ₄	N ₂	H ₂ O
Air	5-16	10-22	9-19	2-6	42-62	11-34
Steam	38-56	17-32	13-17	7-12	0	52-60
Steam+O ₂	14-32	43-52	14-36	6-8	0	38-61
Plasma	16-52	26-47	1-37	0	3-16	0-4

1.3.3.2. Undesirable gasification compounds

1.3.3.2.1. Tars

The major issue in biomass gasification is dealing with the tar formed during the process. Milne & Evans came up with a good definition of tar in the biomass gasification^[42]: “*Tar is a complex mixture of condensable hydrocarbons, which includes single ring to multiple ring aromatic compounds along with other oxygen containing hydrocarbons and complex polycyclic aromatic hydrocarbons.*”

Tars are formed during the biomass gasification by a serie of complex reactions which depend on gasification conditions such as the gasifying reagent (air, pure O₂, steam), the kind of reactor, the temperature of the gasification, the raw material moisture and the biomass feedstock.^{[36], [37], [42]–[45]} Elliott *et al.*^[43] was the first to establish a scheme of the formation and evolution of the tars composition with the temperature. Milne *et al.*^[42] improved this scheme and showed the influence of residential time on the tar formation. They also introduce an important concept: the tar ranking. Figure I.5 is inspired by these two major studies and describes the different tar families as a function of temperature.^{[42], [43]}

At low temperatures ($T \sim 400$ °C), primary tars, derived from the biomass decomposition through pyrolysis and gasification, are present. They are composed of molecules rich in oxygen such as alcohols, aldehydes, ketones, carboxylic acids, phenols and furans. With increasing temperatures ($T > 500$ °C), the primary tars further decompose into secondary tars: aromatic compounds with one ring, two rings, three rings and a small concentration of compounds with more than three rings. Gasification ranging from $T = 700$ - 900 °C produces tertiary tars, which are polyaromatic compounds with four and five rings.^{[36], [44], [45]}

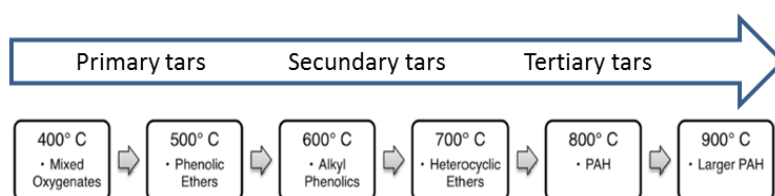


Figure I.5: Tar ranking as a function of temperature, adapted from the literature.^{[36], [42], [45]}

According to Coll *et al.*^[46] (Figure I.6), the majority of the hydrocarbons present are toluene and other one ring aromatics (46 wt. %), followed by naphthalene and two ring aromatic hydrocarbons (28 wt. %).

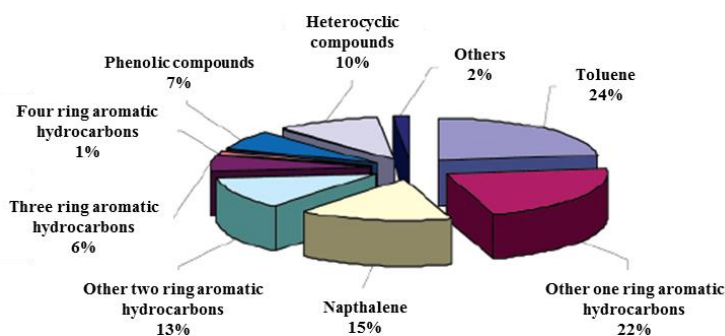


Figure I.6: Typical composition of biomass tars (wt. %).^{[46], [47]}

A study conducted by the Energy Research Center of the Netherlands (ECN), the Toegepast Natuurwetenschappelijk Onderzoek (TNO) and the University of Twente (UT), proposed a more elaborated classification in order to rank the multitude of unconverted tar compounds present at the exit of a gasifier.^[48] Tars were classified according to their molecular weight, solubility and condensability. Table I.3 presents the five different classes of tars established, their properties and representative compounds. Coll *et al.*^[46] studied the catalytic reforming of five typical biomass tars with two commercial catalysts (UCI G90-C and ICI 46-1), both containing about 15 wt. % of nickel on alumina. The results showed that the order of reactivity for the reforming of tars was the following: benzene > toluene >> anthracene >> pyrene > naphthalene. Therefore, according to this study, since it has the lowest reactivity, naphthalene appears to be the most adequate molecule as biomass tar model.

Table I.3: Classification of tars based on molecular weight (wt. %).^[45]

Tar class	Class name	Property	Representative compounds
1	GC-undetectable	Very heavy tars	
2	Heterocyclic aromatics	Highly water-soluble	Pyridine, phenol
3	Light aromatic (1 ring)	Do not pose a problem regarding condensability and solubility	Toluene, benzene
4	Light PAH (2-3 rings)	Condense at low temperature, even at very low concentrations	Naphthalene, anthracene, fluorine, indene
5	Heavy PAH (4-7 rings)	Condense at high temperature and very low concentration	Fluoranthene, chrysene, coronene, pyrene

1.3.3.2.2. Other contaminants

A variety of other gas contaminants may cause technical and environmental problems (Table I.4). Nitrogen may lead to the formation of toxic compounds such as ammonia (NH₃) or cyanide (HCN). Hydrogen sulfide (H₂S) is a major problem since it can provoke corrosion of the pipes and cause acid rain if emitted into the atmosphere. This is also the case for other elements such as alkali metals or chlorine.^{[14], [34], [49]}

Table I.4: Other contaminants than tars.^{[14], [49]}

Contaminant	NH ₃ (ppmv)	H ₂ S (ppmv)	HCN (ppmv)	Alkali metals (Na/K)	Chlorine
Concentration	1000-14.000	20-200	5-500	#	#
Potential problem	Emissions	Corrosion + Emissions	Emissions	Corrosion	Corrosion + Emissions

#: not available

1.3.4. Influences of experimental parameters

Further information concerning the influences of the biomass feedstock, of the gasification temperature, of the gasifying reactants (equivalence ratio, steam to biomass ratio), of the gasifying pressure and of the gasification time on the final bio-syngas composition are detailed in part II of Annex 1.

I.4. CATALYTIC PURIFICATION OF BIO-SYNGAS

I.4.1. Tar reforming

I.4.1.1. Catalytic reforming mechanisms

Figure I.7 presents the different mechanisms of catalytic steam and dry reforming of hydrocarbons (methane, polyaromatic hydrocarbons, alkanes, ...) with a catalyst based on ceramic support (Al_2O_3 , SiO_2 , ...) with metallic active sites (Ni, Co, Pt, ...).^{[49]–[53]} On the metallic active site, tar molecules are adsorbed and hydrocracking, catalytic thermal cracking, hydrodealkylation and various hydrogenation reactions take place. These reactions decompose the tar molecules into active surface species: carbon C^* , hydrogen H^* and tar-derived fragments C_xH_y^* . $\text{H}_2\text{O}_{(\text{g})}$ and $\text{CO}_{2(\text{g})}$ molecules are dissociated on the support and metal sites to generate active species such as H^* , HO^* and O^* . $\text{CO}_{2(\text{g})}$ molecules can also react with the adsorbed H^* to produce $\text{CO}_{(\text{g})}$ and HO^* . The active species generated on the support surface can migrate towards the metallic active sites and decompose the activated carbon C^* and the tar fragments C_xH_y^* into $\text{CO}_{(\text{g})}$ and $\text{H}_{2(\text{g})}$ via several oxidation reactions. Finally, $\text{CO}_{(\text{g})}$ and $\text{H}_{2(\text{g})}$ molecules, resulting from these several reactions, are desorbed from the metallic active sites. Nevertheless, other mechanisms than presented in Figure I.7 can occur: for example, active surface species (C^* , O^* , HO^* and H^*) can reassemble according to reverse activations to produce again $\text{H}_2\text{O}_{(\text{g})}$ and $\text{CO}_{2(\text{g})}$ molecules. Furthermore, H^* species can also react to form $\text{H}_{2(\text{g})}$ molecules.

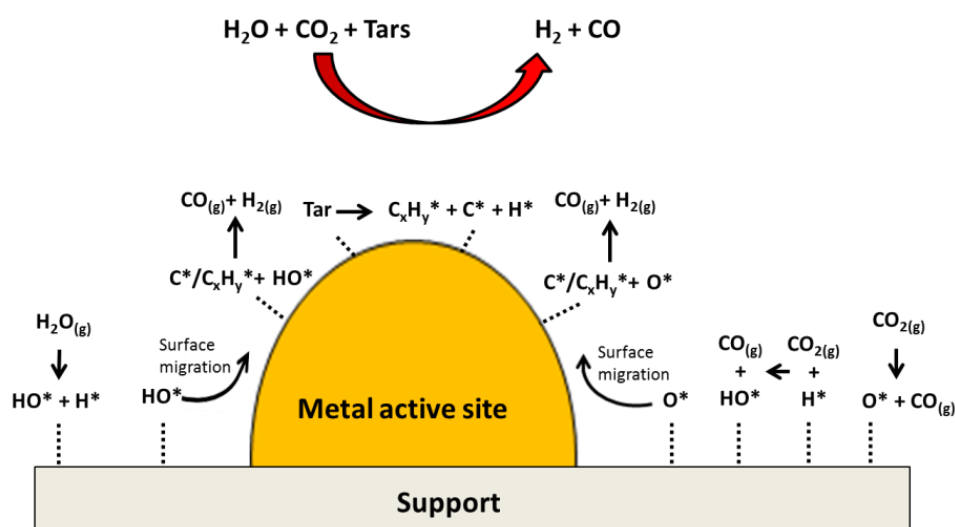


Figure I.7: General scheme of catalytic tar steam and dry reforming.^{[50], [51], [54]}

I.4.1.2. Kinetic approach

Numerous studies about toluene steam- and dry- reforming conducted at laboratory scale used some catalysts with a diameter of particles of 300-800 μm . It is generally assumed that heat and mass transfer limitations do not take place, and that the reactor is a plug flow without any gas expansion (the flow rate is constant). It was shown by different authors^{[55]–[58]} that the activity of the catalyst for the tar removal can be expressed with respect only to the tar concentration (Equation I.20):

$$-r = k \cdot C_{rt,Tar}^n \quad (I.20)$$

when r is the reaction rate ($\text{mol}_{\text{Tar}}/(\text{g}_{\text{Cata}} \cdot \text{h})$), k is the apparent kinetic constant ($\text{m}^3/(\text{g}_{\text{Cata}} \cdot \text{h})$) and $C_{rt,Tar}$ is the concentration of tar ($\text{mol}_{\text{Tar}}/\text{m}^3$). It is also generally assumed that the decomposition of tar is a first order ($n = 1$), which leads to (Equation I.21):

$$-r = k \cdot C_{rt,Tar} \quad (I.21)$$

Under plug flow conditions, using the residence time t (h) and the conversion of tar, f_{Tar} , the apparent rate constant k becomes (Equation I.22):

$$k = \frac{-\ln(1-f_{Tar})}{t} \quad (I.22)$$

Combined with the Arrhenius law, the activation energy, E_a , is obtained as a function of the residence time and the conversion (Equation I.23):

$$\ln \left(\frac{-\ln(1-f_{Tar})}{t} \right) = \ln(k_0) - \frac{E_a}{RT} \quad (I.23)$$

where E_a is the activation energy (kJ/mol), k_0 is the pre-exponential factor ($\text{m}^3/(\text{g}_{\text{Cata}} \cdot \text{h})$), R is the gas constant ($8.314 \cdot 10^{-3} \text{ kJ}/(\text{K} \cdot \text{mol})$) and T is the temperature (K).

It is important to note that the hypothesis of the first order reaction for the decomposition of tar is only possible when the $(\text{CO}_2 + \text{H}_2\text{O})/\text{C}$ ratio is higher than the stoichiometric ratio.^{[55], [56]} Moreover, this assumption is less accurate when the size of the aromatic compound increases. Indeed, the decomposition of large aromatic compounds takes place according to multiple reaction pathways.^{[58]–[60]}

The comparison of activation energies and apparent constants is an important criterion for the determination of the catalyst performances.^{[45], [56], [58], [61]} Li et al.^[45] compared the activation energy required for the steam reforming of a tar mixture at the outlet of a biomass gasifier reactor studied from different authors. The activation energies were comprised between 70 and 100 kJ/mol depending on the type of gasifier (air, steam) and on the type of catalysts used. As element of comparison, the thermal conversion of naphthalene, toluene and benzene without any catalysts was 350, 247 and 443 kJ/mol respectively.

Table I.5: Activation energies and constant rates from different studies.^[45]

Kinetic values	Commercial nickel-based catalyst	Calcined dolomite		No catalysts		
	Tar generated in a gasifier with air	Tars generated in a gasifier with steam	Tars generated in a gasifier with air	Naphtalene	Toluene	Benzene
E_a (kJ/mol)	72	84	97	350	250	440
k ($\text{m}^3/(\text{g} \cdot \text{h})$)	$1.4 \cdot 10^8$	$2.6 \cdot 10^6$	$1.2 \cdot 10^9$	$1.7 \cdot 10^{17}$	$3.3 \cdot 10^{13}$	$2.0 \cdot 10^{19}$

1.4.2. Influences of operating parameters on the catalyst performances

1.4.2.1. Influences of the temperature

Though promoting the gasification reactions, increasing the temperature in gasifiers or in unities situated at the outlet of the gasifiers also has significant drawbacks: 1) in the case of catalysts situated inside the gasifier (primary catalyst), a temperature increase can damage and reduce the reactor lifetime. Furthermore, increasing the temperature will directly impact the biomass reactions and the final gas composition. As explained previously, in a reactor without any catalysts, a temperature increase leads to a lower concentration of tars, but which are more stable (HAP). Generally, the optimum temperature for primary catalysts is situated at $T \sim 850$ °C, which matches with the bed reactor temperature;^{[55], [62]–[64]} 2) in the case of catalysts situated at the outlet of the gasifier (secondary catalyst), heating the catalytic cleaning units includes additional costs. Therefore, efficient units with secondary catalysts are expected to work at the lowest temperature possible ($T = 500\text{--}700$ °C) in order to be economically interesting.^{[39], [63]}

The temperature has a strong effect on the kinetic parameters. Narvaez *et al.*^[58] studied the influences of different operating parameters (temperature, space time, equivalence ratio and steam to carbon ratio) on the kinetic constant for the degradation of a tar mixture at the exit of a fluidized gasifier with a commercial nickel-based catalyst. They showed that the apparent kinetic constant, k_{app} , was multiplied by 5 between $T = 650$ °C and $T = 800$ °C. This trend was confirmed by Aznar *et al.*^[61], who conducted a kinetic comparison between different nickel based catalysts as a function of the temperature and space ratio.

In previous studies about the development of secondary catalysts used at low temperatures ($T = 500\text{--}650$ °C), a pre-reduction step is usually undertaken at higher temperatures ($T = 750$ °C, $t = 1$ h, H_2) in order to reduce the metallic nanoparticles.^[63] For a classic commercial catalyst with 10 wt. % of Ni on alumina at temperatures up to $T = 650$ °C, the nickel oxide particles are usually reduced to $Ni^{(0)}$ by the H_2 and CO molecules that are naturally present in the exiting syngas.^{[3], [9]} However, below $T = 650$ °C, even if the catalyst has been previously reduced, deactivation can occur due to the presence of oxidant molecules in the syngas (CO_2 and H_2O), which convert active $Ni^{(0)}$ particles into less efficient NiO particles.^[65] Therefore, $T = 650$ °C appears to be the minimum working temperature for catalysts at the exit of a gasifier.

1.4.2.2. Influences of the gas composition

Usually the tar concentration is situated around 500–10.000 ppmv, whereas the reagents (H_2O and CO_2) are present in a much higher concentration ranging from 9 to 36 vol. %. So, the H_2O/C and CO_2/C ratios are always higher than the stoichiometric ratios. However, some authors showed that the degradation reactions strongly depend on the gas compositions. Laosiripojana *et al.*^[66] studied the effect of H_2O/C and CO_2/C ratios on the degradation of naphthalene with Ni and Ni–Fe bimetallic based catalysts supported on palygorskite

(magnesium aluminum phyllosilicate). $\text{H}_2\text{O}/\text{C}$ and CO_2/C ratios were increased from 0 to 3 at $T = 700\text{ }^\circ\text{C}$. The results were similar for each catalyst and for both oxidants. Indeed, in both cases, the maximum H_2 yield, which is linked to the general conversion of naphthalene, reached a maximum value corresponding to $\text{H}_2\text{O}/\text{C}$ and CO_2/C ratios situated between 1.0 and 1.5. The authors also noticed that the carbon deposition was higher after dry-reforming ($5.7\text{ mmol}_{\text{Carbon}}/\text{g}_{\text{Cata}}$) than after steam-reforming ($3.9\text{ mmol}_{\text{Carbon}}/\text{g}_{\text{Cata}}$). According to the authors, the water present in the feed gas reacts with CH_4 to form CO and H_2 , and with CO to form H_2 and CO_2 , thus reducing the selectivity of the Boudouard and methane decomposition reactions. Moreover, as explained above, H_2O molecules are dissociated into HO^* radicals on the surface of the catalysts, allowing the degradation of tars into CO and H_2 , whereas the dissociation of CO_2 molecules is always associated to a risk of carbon deposition. Narvaez *et al.*^[58] studied the performance of a nickel-based commercial catalyst (BASF G1-25S) for the catalytic conversion of a tars mixture at the outside of a bubbling fluidized bed reactor. The authors studied the influences of the $\text{H}_2\text{O}/\text{C}$ ratio (1.4-2.4) on the apparent kinetic constants (k_{app}). The results showed that for two different temperatures ($T = 750\text{ }^\circ\text{C}$ and $T = 800\text{ }^\circ\text{C}$), the apparent kinetic constants were multiplied by a factor of around 2 when the $\text{H}_2\text{O}/\text{C}$ ratio increases from 1.4 to 2.4.

1.4.2.3. Influences of the space velocity

Space velocity (or *GHSV*, in h^{-1}) is defined as the inverse of the residence time and therefore corresponds to the quotient of the incoming reagents divided by the reactor/catalyst bed volume. Generally, as the residence time increases, reactions in the catalytic reformer have a greater opportunity to proceed, and the system tends towards thermodynamic equilibrium.

Kinoshita *et al.*^[62] highlighted the importance of the residence time on the composition of the produced gas and the tar degradation with a commercial nickel-based catalyst. The authors showed that increasing the residence time has similar effects as increasing the temperature: a rise of the volume percentage of H_2 and CO and a decrease of the CO_2 concentration. It is noteworthy that the tar concentration at $T = 750\text{ }^\circ\text{C}$ was divided by 10 (from $20\text{ g}/\text{m}^3$ to $2\text{ g}/\text{m}^3$) when the residence time was increased from 0.7 to 1.7 s. Furthermore, Li *et al.*^[67] found similar trends when studying the decomposition of toluene on Ni-doped mayenite (calcium aluminate). They showed that the H_2 yield and toluene conversion increased with the residence time until reaching a maximum value where an equilibrium was reached. By comparing the results obtained at $T = 650\text{ }^\circ\text{C}$ and $T = 800\text{ }^\circ\text{C}$, they also confirmed that the optimum residence time varies for every temperature (when T increases, the optimum space ratio decreases).

1.4.3. Deactivation and regeneration of catalysts

1.4.3.1. Mechanisms of coking

Catalyst deactivation by coking is the most significant problem that catalysts encounter since the carbon deposits reduce the activity of the metallic active sites and can block the pores

of the support, decreasing the active specific surface area. Furthermore, the carbon deposits increase the pressure drop in the reactor, resulting in frequent regeneration or early shutdown of the reactor.

1.4.3.1.1. Mechanisms of carbon deposition

Carbon deposits result from the dissociation of hydrocarbons or reverse reactions between gaseous species and the catalyst surface. Figure I.8 resumes the different type of carbon deposit that can be encountered: adsorbed hydrocarbons, atomic carbons adsorbed on the surface (C_{α}^*), graphitic carbons (C_{β}^*), metal carbides or filamentous carbon.^{[68]–[73]}

Adsorbed hydrocarbons do not deactivate the catalysts, but they can be transformed into more problematic species. When Thermal Programmed Oxidation (TPO) or Thermogravimetric (TG) measurements are carried out under air, adsorbed hydrocarbons are generally oxidized below $T = 400$ °C. Due to their important activity, most of atomic carbons adsorbed on the surface of the catalyst (C_{α}^*) are gasified into CO and CH₄. Polymerizations and rearrangements of C_{α}^* species can lead to graphitic carbons (C_{β}^*). C_{β}^* species are less reactive, but they can still be gasified. If not, they can either combine to form polymeric amorphous films, which encapsulate the metallic active sites and clog the substrate pores, or dissolve into the metallic active site to form metal carbides or filamentous carbon.^{[68],[69]} Using air, TPO or TG, amorphous carbon deposits are generally oxidized below $T = 550$ °C, whereas filamentous carbons are removed above $T = 550$ °C. C_{β}^* species can interact with the lattice of the metal active site to form metal carbides (Ni₃C, Fe₃C, Co₂C...). More than altering the efficiency of the active site, the metallic carbides can become nucleation points for the growth of amorphous and filamentous carbons. The metal carbides are very difficult to re-gasify (their combustion under TPO or TG takes place at $T > 700$ °C).

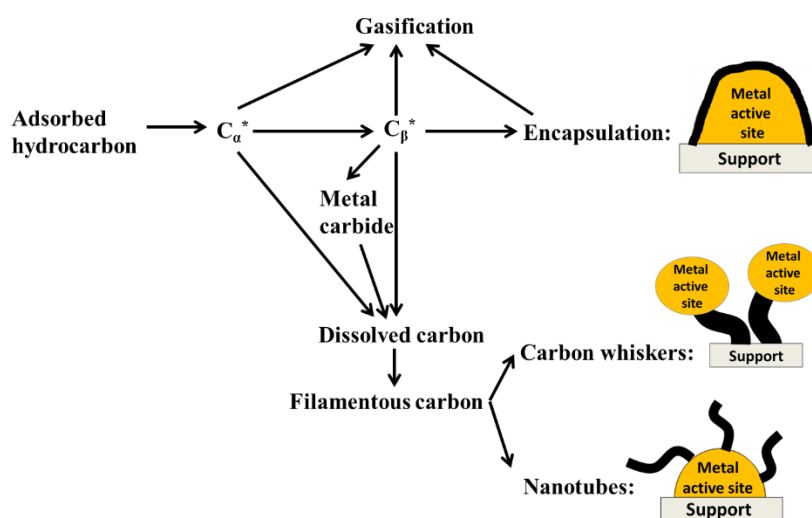


Figure I.8: Mechanisms of carbon formation, inspired from Trimm *et al.*^[68].

It can be seen in Figure I.8 that filamentous carbons are divided in two categories: nanotubes and carbon whiskers. Nanotubes are formed when the metal/support interactions are

high. Carbon whiskers formation occurs because carbon species dissolved into the metallic active site can also diffuse through the metallic particle in order to nucleate and precipitate at the interface crystallite/support.^{[68], [69]} This effect results in the formation of carbon whiskers, which lift the metallic nanoparticles from the surface and lead to the fragmentation of the catalysts. The ejection of metallic nanoparticles due to the formation of carbon whiskers is usually present in catalysts with low nanoparticles/support interactions. Whereas the other types of carbon deposit can be eliminated thanks to regeneration steps, the formation of carbon whiskers is the most problematic case because it destroys physically the catalyst.^{[68], [69]}

In order to quantify the resistance of the catalysts towards coking, Azadi *et al.*^[74] defined the “coke formation rate” parameter, which is the weight loss of the used catalysts, measured by TGA analysis, divided by the testing time. Further studies have permitted the establishment of kinetic laws of deactivation. Bain *et al.*^[75] investigated the reforming and coking kinetics during the steam degradation of benzene, toluene and light alkanes using a Ni-alkali-Al₂O₃ catalyst. First order rate equations were found to represent both the kinetics of reforming and deactivation. A similar study was conducted by Dou *et al.*^[60]: the authors established a kinetic model of the deactivation through coking during the steam reforming of 1-methylnaphtalene on Ni-Mo/Al₂O₃ catalysts.

1.4.3.1.2. Reduction of coking by adjustment of parameters

The formation of coke results from a destabilization of the balance between the rate of the hydrocarbon decomposition and the gasification rate of the carbon species on the metallic active site.^[65] To prevent the coking of catalysts, two main improvements can be carried out: decreasing the rate of hydrocarbons adsorption-decomposition, or increasing the gasification rate of the carbon species.^[65]

Increasing the concentration of oxidants (H₂O, CO₂) of the feedstock enables a higher gasification rate of the carbon species on the catalyst surface, resulting in a lower carbon deposition.^{[46], [58], [66]} According to several authors^{[46], [70], [76], [77]}, the most significant factors influencing the carbon deposition are the concentration and type of hydrocarbons in the gas phase. It was shown that the carbon deposit formation increases with the unsaturation, molecular weight and aromaticity of the hydrocarbons since the compound structure becomes more similar to the carbon deposit composition. Coll *et al.*^[46] highlighted that the minimum H₂O/C ratio to avoid the formation of coke increased with the tar compound aromaticity (from 2.5 for toluene to 8.4 for pyrene at $T = 780$ °C).

Low temperatures ($T = 500-700$ °C) favor the formation of coke on the catalysts and the catalyst deactivation.^{[58], [61], [76]} Indeed, the thermal equilibrium of the Boudouard reaction is achieved at $T \sim 700$ °C. At $T > 700$ °C, the adsorbed or deposited carbon reacts with CO₂ to form CO.^{[54], [78]} Therefore, a temperature increase has generally more impact on the gasification rate of the carbon species than on the hydrocarbon decomposition on the active site.^{[76], [78], [79]}

1.4.3.1.3. Regeneration of carbon deactivated catalysts

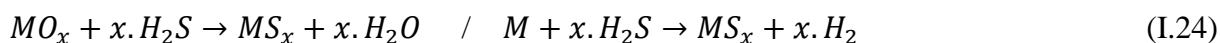
The catalysts can be regenerated by removing the carbon deposit thanks to gasification reactions with O₂, H₂O, CO₂ or H₂. It is to notice that using reagents such as O₂, H₂O or CO₂ leads to an oxidization of the metallic active sites. Thanks to its rate and simplicity, air regeneration is the most common regeneration process. One major drawback of air regeneration is the deactivation of the catalyst due to the formation of hot spots during the burning of carbon.^[79] That is why some authors, such as McCulloch^[80], recommend operating the regeneration at temperatures lower than $T = 450$ °C, in order to avoid the conversion of γ - to α -alumina and formation of nickel aluminate spinels (NiAl₂O₄). Steam regeneration is also a common regeneration technique. However, the sensitivity of supports towards hydrolysis can be then a major problem.^{[79], [80]}

1.4.3.2. Poisoning of metallic active sites

According to Forzatti *et al.*^[81], poisoning is the loss of activity due to the strong chemisorption on the active sites of impurities present in the feed stream. A poison may simply act by blocking an active site (geometric effect), or it may alter the sorption capacity of other species by an electronic effect. Poisons can also modify the chemical nature of the active sites or result in the formation of new compounds so that the performances of the catalyst are strongly altered.

1.4.3.2.1. Sulfide compounds

As showed in Table I.4, sulfur compounds, such as sulfur-organic species (thiophene, thiols ...) or simple sulfur species (H₂S, SO₂), are usually present in the bio-syngas. Following the availability of electrons in the molecular orbital of sulfur compounds, H₂S is a stronger poison than SO₂. The poisoning reactions on metal-based catalysts are generally stronger for metallic active sites, but can also occur on oxides as presented in the following equations (Equation I.24).^{[9], [81]}



The sensitivity of the reforming catalysts to chemisorption of sulfur compounds increases when the temperature decreases.^[9] Forzatti *et al.*^[81] reported that 5 ppm of H₂S in the feed poisoned a Ni/Al₂O₃ catalyst working at $T = 800$ °C, whereas less than 0.01 ppm of H₂S poisoned the same catalyst at $T = 500$ °C. It is possible to shift the equilibrium of the adsorption-desorption reactions to the desorption of sulfur compounds if H₂ pressure is increased or if the physico-chemical characteristics of the catalyst are modified: 1) modification of the metallic active site by alloying with a second metal allows creating electron-deficient metallic sites, which lowers the strength of the M-S bond;^{[82], [83]} 2) modification of the acid properties of the support, and therefore the interactions between the metallic active sites and the Brönsted acid sites.^[9]

Bakker *et al.*^[84] studied the interactions between Ni and H₂S when temperature increases with Thermal Programmed Sulfidation (TPS) measurements. They showed that for metallic (Ni/Al₂O₃) and oxide (NiO/Al₂O₃) catalysts, the Ni-S surface species were converted into stable Ni₃S₂ compounds. The main difference between both catalysts was the transition phase temperature of Ni₃S₂ which takes place around $T = 270$ °C for metallic oxides and around $T = 110$ °C for metallic catalysts. This temperature difference is due to a higher dissociation rate of H₂S at the surface of Ni⁽⁰⁾ particles and a higher diffusion rate of adsorbed sulfur atoms in the reduced nickel core.^[84] Furthermore, NiS and Ni₃S₂ compounds indicate lower melting points and a higher surface mobility, thus increasing the sintering of the Ni⁽⁰⁾ nanoparticles.^{[85], [86]}

It was shown that the presence of H₂S in the feed allows decreasing the coke formation rate on nickel active sites.^{[9], [65], [87]} This was attributed to two facts: 1) the adsorption of S atoms at the surface of nickel active sites slow down the adsorption of tars and their decomposition; 2) it is suspected that a certain number of neighboring nickel sites is required to form an aromatic graphite precursor. Hence, the presence of S atoms on the metallic surface prevents the number of Ni atoms required for carbon deposit polymerization reactions to take place. This phenomenon depicted in Figure I.9 is called “ensemble control”^{[9], [88], [89]} In this way, sulfur-passivated catalysts such as Ni₃S₂/Al₂O₃^[87] and Co₂S/Al₂O₃^[90] presented lower tar conversions compared to classic catalysts, but had longer lifetimes.

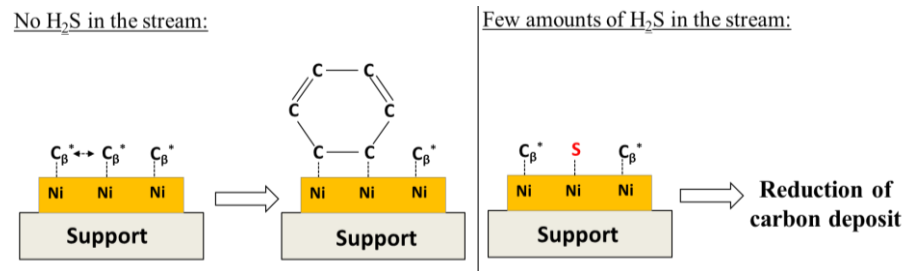


Figure I.9: Reduction of the coking by "ensemble control" caused by presence of H₂S in the stream, inspired by the work of Nielsen *et al.*^[65] and Alstrup *et al.*^[89].

The regeneration of catalysts poisoned with sulfur compounds is possible thanks to H₂O (Equation I.25), H₂ (Equation I.26) or O₂ injection (Equation I.27).^{[9], [40], [91]} These desorption reactions are favored at high temperatures. However, the reactions are usually not complete, even at high temperatures, due to too strong interactions between adsorbed –S atoms and metallic active sites. In this way, it is easier to desorb sulfur species from NiS than Ni₃S₂ compounds.^{[9], [84]} Usually, regeneration with steam injection is the most practical and efficient solution.^[79]



According to Westmoreland *et al.*^[92], the elements Fe, Zn, Cu, Mo, Mn, V, Ca, Sr, Ba, Co and W are more suitable for H₂S adsorption and regeneration in reforming applications. A metallic alloy formation (for example with Ni) with these components is supposed to lead to the formation of electron-deficient metallic sites, thus lowering the M-S bonds.

According to Ryu *et al.*^[93], the sulfur resistance of the elements from group 8-10 increases in the following order: Pt < Pd < Ni << Rh < Ru. Their sulfur resistance can be increased thanks to the synergetic effect of a bimetallic alloy with Mo^[94]. Indeed, the positive effect of molybdenum doping was confirmed by Rodriguez *et al.*^[82], who researched the affinity for sulfur compounds of different alloys such as Mo+Zn, Mo+Cu, Mo+Fe, Mo+Co and Mo+Ni.

1.4.3.2.2. Poisoning with salts

Some compounds (K, Cl, Zn, Cl, Na ...) present in the fly ashes are known to decrease the performances of classic catalysts. Alkali react with the acid support (such as alumina) to form crystalline phases. Alkali may cause extensive sintering of the support crystallites.^[9] Salts and fly ash compounds can also aggregate and clog the pores, leading to a decrease of the specific surface area.^{[9], [65]}

Albertazzi *et al.*^[95] studied the influence of KCl, K₂SO₄ and ZnCl₂ compounds on a Ni/MgO-Al₂O₃ catalyst. They concluded that the lifetime of catalysts was shortened because the sintering of Ni nanoparticles was favored by salts.

1.4.3.3. Thermal degradation

1.4.3.3.1. Sintering

Sintering phenomena decreases the activity of the catalysts through the reduction of the specific surface area of both support and metallic active sites. Since the sintering effects are generally irreversible or difficult to reverse, preventing sintering is of great importance. The driving force of the sintering mechanism is the surface energy, which varies inversely with the particle size.^[65] Therefore, sintering provokes the agglomeration and the coalescence of small crystallites (metallic or oxides) into larger ones with lower surface-to-volume ratios. In the case of a single phase, the “Huettig” and “Tamman” temperatures estimate if the material is situated in its sintering temperature range: 1) the “Huettig” temperature corresponds to 30 % of the melting temperature of the compound (in Kelvin). It is defined as the temperature in which the surface atoms near the crystallite defects exhibit a first significant mobility; 2) the “Tamman” temperature corresponds to 50 % of the melting temperature of the compound (in Kelvin). Around this temperature, bulk atoms become increasingly mobile up to the melting point.^{[79], [96]}

In the case of supported metallic catalysts, two general mechanisms are proposed for the agglomeration of metallic particles: 1) the atomic migration or Ostwald ripening. In that case, the sintering occurs via a transfer of metallic atoms from one crystallite to another by a transport

of atoms across the surface of the support (or in the gas phase). Metal-to-metal bonds being more stable than metal-to-support bonds, the small crystallites decrease in size whereas the larger ones growth; 2) the crystallite migration. In this case, the entire metallic crystallites migrate along the surface of the support and coalesce with each other.^{[81], [97], [98]}

Despite the fact that temperature is the key variable of the sintering rate, the mechanisms are also influenced by many other parameters. In this way, the atmosphere around the catalysts is also of great importance. Indeed, it has been proved that increasing the steam concentration accelerates the sintering process of Ni nanoparticles supported on MgAl₂O₄. The higher rate was attributed to the formation of Ni₂-OH surface species with lower melting points.^{[9], [99]} More generally, sintering is favored under a reducing atmosphere since the melting point of the metallic nanoparticles is always lower than the melting point of the metallic oxides. The support morphology (crystallite shape and size, pore size and distribution ...) may have a significant influence on the mobility of the metallic particle. In this way, increasing the support microporosity is usually decreasing the metallic nanoparticles sintering rate.^{[9], [65]}

As presented in the upper section, some poisoning species such as S, Pb, Bi, Cl or F can increase the mobility of the metallic particles. For example, the “Tamman” temperature for nickel compounds decreases from $T = 863$ °C for pure nickel to $T = 641$ °C for NiCl₂ and $T = 127$ °C for Ni(CO)₄.^[79] The opposite effect of sintering is also possible since the addition of Ca, Ba, Ce or Ge decreases the metallic atom mobility.^[81]

1.4.3.3.2. Phase transformation

Operating at high temperatures ($T > 700$ °C) can provoke phase transformations. One common example is the phase transition of γ -Al₂O₃ towards α -Al₂O₃, which drastically reduces the specific surface area of the catalytic supports from about 250 m²/g to circa 1 m²/g.

1.4.3.3.3. Volatilization

Due to their low sublimation points, some compounds like MoO₃, P₂O₅ or Bi₂O₃ can be emitted during biomass gasification. Other elements like Ni can be transformed into volatile compounds (Ni(CO)₄, NiCl₂).^[97] Fortunately, Ni(CO)₄ compounds only form at temperatures below $T = 300$ °C.^[79]

1.4.4. Catalysts developed for the bio-syngas purification

Despite the fact that catalysts designed for the purification of bio-syngas are closely linked to the catalysts used for the steam and dry reforming of CH₄ to syngas^[65], studies on obtaining the most appropriate materials are still topical. Several types of catalysts have been designed and tested.^{[3], [39], [100]} The best results were obtained by catalysts situated inside the gasifiers (primary catalysts). In fact, the high operational temperatures ($T > 800$ °C) improve the conversion of tars and prevent the catalytic deactivation by H₂S. However, the use of catalysts located at the outlet of the gasifiers (secondary catalyst) remains the only resort for cleaning

syngas out of gasifiers with fixed/entrained beds. Since the working temperatures of secondary catalysts are lower ($T = 550\text{-}700\text{ }^{\circ}\text{C}$), the complete conversion of tars is more difficult to achieve. In that case, catalytic deactivations through coking and sulfidation are more threatening. The ideal case would consist in the presence of a primary catalyst inside the reactor (ex.: olivine), in order to convert the high aromatic tars into smaller molecules such as toluene or benzene, followed by a secondary catalyst (ex.: Ni/Al₂O₃) in order to completely eliminate the remaining tars.^[101] Therefore, this part focuses on the description of basic notions and recent advances of secondary catalysts.

Several studies^{[9], [39], [100], [102], [103]} agree on ranking the following properties required by bio-syngas catalysts:

- 1) Effective tar reforming capacity, even at low temperatures ($T = 550\text{-}700\text{ }^{\circ}\text{C}$);
- 2) High CH₄ reforming capacity;
- 3) Resistance towards deactivation by coking, sulfidation and sintering;
- 4) Easy regeneration;
- 5) Cheap materials (especially for primary catalysts);
- 6) Strong resistance against attrition (especially for primary catalysts used in fluidized bed);
- 7) High H₂ production, notably through the Water-Gas Shift reaction;
- 8) Use of non-toxic materials (especially for primary catalysts).

Richardson introduced an overview of the usual catalyst properties (Figure I.10). The catalyst design can be operated through three main parts: the morphological and mechanical properties (meaning size, shape and strength); the chemico-physical properties (meaning surface area, porosity, acidity, composition and density) and the catalytic properties (meaning activity, selectivity and stability).^[104]

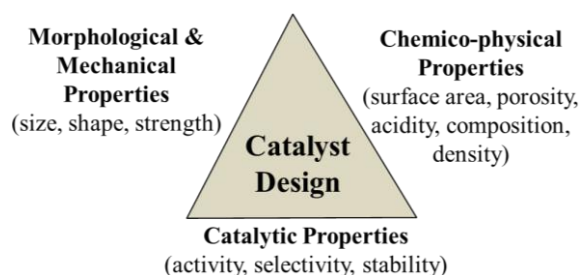


Figure I.10: Catalyst design triangle introduced by Richardson.^[104]

Yung *et al.*^[100] made an exhaustive literature review in order to list and classify the different elements used for catalytic tar reforming (Figure I.11). The authors ranked the performances of different active site promoter and support. Some elements such as P, S and Cl were classified as biomass derived poisons.

The figure shows a periodic table where elements are color-coded and marked with symbols to indicate their role in bio-syngas purification catalysts. The legend below the table defines these symbols:

- bold text** = tested as base catalyst
- = good promoter
- = moderate promoter
- = poor promoter
- = biomass-derived poisons
- = good support
- = moderate support
- = poor support

Figure I.11: Overview of the different elements used for bio-syngas purification catalysts.^[100]

The catalysts used for tar reforming are divided into two groups: synthetic catalysts and minerals (Figure A1.5 presented in Annex 1). Synthetic catalysts are usually more performant due to a high control of their properties (porosity, specific surface area, metal dispersion and interactions with the support ...), but they are usually too expensive and fragile to be used in primary conditions. As for natural catalysts, their biggest advantage resides in their extremely low cost, but also sometimes in their mechanical strengths (example: olivine).^[105] In both cases, the supports are usually doped with metallic elements.

1.4.4.1. Influences of porous structure and shaping of catalysts

The micro- (< 2 nm), meso- (2-50 nm) and macro- (> 50 nm) porosity of a catalyst are strongly influencing its performance. An adequate pore size distribution is essential for a good diffusion of the reagent molecules. Indeed, since the common tar molecule size lies at around 0.5-1 nm (toluene: 0.68 nm; naphthalene: 0.72 nm), it has been proved that catalysts with a pore opening below 0.7 nm are inefficient for this application.^{[49], [103]} In addition, a good hierarchical pore size distribution favors a better metal particle dispersion.^{[103], [106]} A controlled pore structure may also reduce the sintering ability of the metallic nanoparticles. This effect has been illustrated by the study conducted by Tian *et al.*^[107], who managed to block Ni nanoparticles in alumina nano-honeycombs, thus permitting to avoid the migration and coalescence mechanisms at high temperatures.

The catalyst macroscopic shaping is also known to have influences. In this way, it was proved that the estimated rate of deactivation ranks as follows: nets > pellets > monoliths.^[9]

1.4.4.2. Influences of support composition

1.4.4.2.1. Carbon supports

Activated carbons, *i.e.* non-graphitic and microcrystalline forms of carbon, can be used as catalytic supports. Their neutral surface properties make them more resistant towards the deactivation by coke deposition than acid supports.^[108] Their hierarchical pore structure is a

strong asset since it greatly improves the dispersion of metallic particles and especially facilitates the transport of reactant molecules.^[103]

Fuentes-Cano *et al.*^[56] studied the kinetics of toluene and naphthalene steam reforming at different temperatures ($T = 750-950$ °C) over commercial coconut char, coal char, and char prepared in a laboratory. They observed similar conversions for every types of char they used. Naphthalene and toluene were completely removed at temperatures up to $T = 850$ °C.

El-Rub *et al.*^[109] compared the activity of char to other common catalysts (dolomite, olivine, 70 wt. % Ni/Al₂O₃-SiO₂ and sand) for the reforming of phenol and naphthalene at temperatures from $T = 700$ °C to $T = 900$ °C and in the presence of CO₂ and H₂O. At $T = 700$ °C, the phenol conversion was in the following order: Ni/Al₂O₃ > dolomite > char > olivine > sand. At $T = 900$ °C, the degradation conversions were as follows: Ni/Al₂O₃ > char > dolomite > olivine > sand.

Despite their interesting properties, chars do not seem to be the most appropriate support for long term operations since they are slowly consumed by the CO₂ and H₂O present in the syngas composition.^{[39], [103]}

1.4.4.2.2. Basic supports

By definition, a basic solid catalyst shows the ability to extract a proton from a molecule. Alkaline-earth metallic oxides, alkali ion-added zeolites, alkali metallic ions supported on silica or alumina and some clay minerals are examples of basic solids.^[49] It is known that the support basicity plays an important role by increasing the ability of the catalyst to chemisorb CO₂, thus improving the oxidation of the surface carbon.^{[3], [110], [111]}

- Pure calcium and magnesium oxides

CaO and MgO are the most commonly used basic catalysts for tar reforming. The basicity of MgO and CaO oxides is attributed to their O²⁻ ions: the sites with the highest basicity are located at the morphological defects of the polycrystalline solid, where each O²⁻ anion is coordinated to only three or four metallic cations.^[49] CaO has a higher basicity because of its larger lattice constant.^[49] In this way, the electrons around O²⁻ ions in CaO are more labile than the electrons around O²⁻ ions in MgO, favoring their overlap with the orbitals of the incoming molecules.^{[112], [113]} The ability of CaO and MgO to adsorb CO₂ and H₂O molecules is defined by their carbonation and hydration equations (Equations I.28 and I.29).^[114] The carbonation reactions of MgO and CaO are possible only below $T = 700$ °C.^{[115], [116]}



Despite the most used mixture of these oxides is a natural mineral (dolomite: CaMg(CO₃)₂), various synthetic mixtures have also been synthesized.^[117] Despite its interesting reforming properties, dolomite is not convenient as a primary catalyst due to its low attrition

resistance, leading to dust formation.^[35] An addition of pure calcite into the feedstock has also proved to have important influences on the LHV of the syngas (the H₂ concentration went from 23 to 55 vol. % when CaO was added).^[118]

According to Delgado *et al.*^[119], the activity towards tar reforming is the following: MgO-CaO > CaO > MgO. Li *et al.*^[120] studied the toluene reforming of Ni supported on MgO-CaO with different weight percentages of magnesium (30 / 50 / 70). Their results showed that the MgO_{70%}CaO_{30%} support mixture was showing the highest activity. According to Zhao *et al.*^[121], CaO degrades heavy tars very effectively, but it is less efficient for cracking and reforming of smaller aromatics such as benzene or naphthalene. The authors also demonstrated that *in situ* CO₂ capture by CaO favors the Water-Gas shift reaction beyond equilibrium limitations, resulting in a syngas with high H₂ and low CO content. A study on the reforming catalytic activity of iron and nickel based catalyst supported over CaO, MgO and calcined dolomite was conducted by Di Felice *et al.*^[117]: the authors highlighted the fact that Ni-CaO was more efficient than Ni-MgO, mostly because MgO reacts with Ni to form a solid solution, which decreases the catalytic activity. A similar effect was also shown for Fe-CaO materials, on which Fe was less active due to the formation of a Ca₂Fe₂O₅ solid solution. Wang *et al.*^[122] carried out a comparative study of CH₄ steam reforming with nickel catalysts and showed that the deactivation rates of the catalysts was in the following order: Ni/MgO < Ni/ γ -Al₂O₃ < Ni/SiO₂ < Ni/ α -Al₂O₃. The long term stability of Ni/MgO was attributed to the low sintering of nickel crystallites, thus limiting carbon formation.

- Olivine

Thanks to its non-toxic, cheap and high attrition resistance properties, olivine has proved to be the best natural support for primary catalyst application.^{[39], [100]} Its general formula is (Mg,Fe)₂SiO₄, but its composition varies depending from where it is extracted.^[101] However, this support exhibits a very low specific surface area ($S_{BET} < 5 \text{ m}^2/\text{g}$).

Virginie *et al.*^[64] studied the reforming activity of olivine doped with iron and calcined at different temperatures ($T = 400\text{-}1400 \text{ }^\circ\text{C}$). The calcination temperature strongly influenced the iron metallic state (0, +II, +III) and its diffusion through the olivine support, thus resulting in a different reforming activity. It was shown that the highest activities were obtained after calcination at $T = 1000 \text{ }^\circ\text{C}$. In the same laboratory, Swierczynski *et al.*^[55] studied this influence of the calcination on Ni/olivine catalysts. The interactions of Ni with the intrinsic Fe and MgO elements naturally present in olivine were supposed to explain the high resistance towards carbon formation. These trends were confirmed by other studies using Ni and olivine.^{[123], [124]} The association of CaO or Ca₁₂Al₁₄O₃₃ with olivine was studied by Zamboni *et al.*^[115]: carbonation-decarbonation cycles highlighted a better stability of the CO₂ sorption ability of Ca₁₂Al₁₄O₃₃ compared to CaO. The authors also showed that the dispersion of the iron naturally present in the olivine structure was improved by the Ca₁₂Al₁₄O₃₃ phase.^[115]

- *Other natural supports*

Guan *et al.*^[51] investigated the use of scallop shell as a raw support for tar catalysis applications. This cheap support composed of basic element (CaO) presents interesting macro- and microporosity. Doped with Fe or Ni salts, and promoted with potassium,^[105] this support was efficient for the tar reforming at $T = 650$ °C. However, its fragility made it inappropriate for an application as primary catalyst.

1.4.4.2.3. *Acid supports*

Acid catalysts are materials which are able to provide a proton. Many chemical processes (ex.: cracking) are catalyzed by solid acids, usually using their ability to break C-C bonds. Most materials used are zeolites, alumina and various pure and sulfated metal oxides.^{[65], [81]}

- *Silica*

Pure silica supports are always avoided in steam reforming applications.^[65] Indeed, the hydrolysis of SiO₂ leads to volatile Si(OH)₄ species which cause various technical problems in downstream unities. However, this effect can be countered by the addition of alkali, which is known to reduce the volatility of SiO₂ supports.^[65] Magnesium doped nickel silicates have proved to be valuable for the destruction of CH₄, C₂+ alkanes and NH₃.^[125] The magnesium-silicate synergy was supposed to explain the good resistance to H₂S during hydrocarbons reforming. However, even though the catalyst seems to have interesting properties, one should consider that the authors carried out the tests at high temperature ($T = 900$ °C) and with a low H₂S content (20 ppm).^[125]

- *Zeolites*

Zeolites are alumina-silica materials commonly used for catalytic applications. They are either natural or synthetic. It is easy to modify their Al/Si ratios, their amounts of acid sites and their mesostructures thanks to surfactant assisted synthesis (SBA, MCM-41...)^[126] Unfortunately, zeolite materials do not seem to be appropriated for tar reforming purposes.^[49] In fact, according to Forzatti *et al.*^[81], the Brønsted acid sites stabilize the carbon intermediates (carbonium ions), which can condensate and form polyaromatic compounds. This fact was confirmed by Buchireddy *et al.*^[127], who researched the reforming of naphthalene at $T = 750$ °C with different zeolites impregnated with 7.5 %wt. of Ni. It was observed that the tar yield of zeolite containing Na (chabazite) was low due to the disappearance of acids sites. The authors highlighted the fact that the acidic nature of zeolites increased the naphthalene conversion via cracking reactions, and that the more acidic the zeolites were, the faster they were deactivated through coking. Nevertheless, when doped with other elements, zeolites can achieve very interesting results. Tao *et al.*^[128] developed a Ni (3 wt. %)-CeO₂ (0-3 wt. %)/SBA-15 catalyst, which showed very good results for the catalytic reforming of toluene between $T = 700$ °C and $T = 850$ °C. The positive anti-coking results were attributed to CeO₂ doping.

- Iron oxide supports

The catalytic activity of iron depends on its oxidation state (Fe_2O_3 , Fe_3O_4 or $\text{Fe}^{(0)}$). When iron is in a metallic state, it achieves its maximum tar destruction yield thanks to the ability of $\text{Fe}^{(0)}$ to break the C-C and C-H bonds.^[51] The magnetite (Fe_3O_4) is known to enhance the Water-Gas Shift reaction.^{[129], [130]}

Uddin *et al.*^[131] studied the degradation of tars formed during the cedar wood gasification at $T = 850\text{ }^\circ\text{C}$ with catalysts composed of mixtures of Fe_2O_3 and Al_2O_3 . It was found that Al_2O_3 permitted to achieve a higher specific surface area, without decreasing the Fe_2O_3 activity. The Fe_2O_3 (50 wt. %)/ Al_2O_3 (50 wt. %) composition showed the more interesting results (up to 90 % of converted tars at $T = 850\text{ }^\circ\text{C}$). Other Fe-minerals were studied, such as natural iron ore^[132] and ilmenite (FeTiO_3)^[133]. Generally, iron based catalysts show interesting properties when used at high temperatures ($T > 800\text{ }^\circ\text{C}$), *i.e.* inside the reactor. However, due to low temperatures at the gasifier outlet, Fe can not be reduced to its metallic state.

- Al_2O_3 supports

Various studies agree on the fact that $\gamma\text{-Al}_2\text{O}_3$ seems to be the best support for secondary catalyst applications.^{[39], [65], [100], [122], [134]} Interesting catalytic properties of $\gamma\text{-Al}_2\text{O}_3$ were highlighted by Miyazawa *et al.*^[135], who studied the steam reforming of a tar mixture derived from the pyrolysis of cedar wood with different supports. They found out that the order of activity at $T = 600\text{ }^\circ\text{C}$ was the following: $\text{Ni}/\gamma\text{-Al}_2\text{O}_3 > \text{Ni}/\text{ZrO}_2 > \text{Ni}/\text{TiO}_2 > \text{Ni}/\text{CeO}_2 > \text{Ni}/\text{MgO} > \text{no catalyst}$.

$\gamma\text{-Al}_2\text{O}_3$ appears to be an interesting support because of its large specific surface area (200-500 m^2/g), high mechanical strength and good sintering resistance. However, if the temperature is too high ($T > 800\text{ }^\circ\text{C}$), $\alpha\text{-Al}_2\text{O}_3$ phase formation can occur. The catalytic activity is much lower for $\alpha\text{-}$ compared to the $\gamma\text{-}$ phase principally because of the drastic pore volume and specific surface area reduction (S_{BET} of $\alpha\text{-Al}_2\text{O}_3$ usually about 20 m^2/g).^{[3], [122]} When $\gamma\text{-Al}_2\text{O}_3$ supports are doped with transition metals (Co, Ni, Cu ...), the calcination and operating temperatures become critical factors due to the formation of strong metal-aluminate interactions, which occurs at temperatures higher than 800 $^\circ\text{C}$. This decreases the reducibility and activity of the active species. However, these strong metal-alumina interactions can be interesting since they reduce the metallic nanoparticles sintering and therefore the catalyst coking, resulting in a longer lifetime of the catalyst.^{[9], [136]}

1.4.4.2.4. $\gamma\text{-Al}_2\text{O}_3$ promoted supports

As $\gamma\text{-Al}_2\text{O}_3$ appears as one of the most adapted supports, many doping attempts have been conducted in order to optimize its properties (acidity/basicity) and its resistance towards sintering.

- Calcium doped alumina supports

Used as pure material, CaO particles tend to agglomerate and can be evacuated by the stream. In contrary, adding CaO to γ -Al₂O₃ allows keeping a high dispersion of particles and provides a synergy of the interesting properties of CaO and alumina.^[115] Furthermore, when the calcination temperature is sufficiently high ($T \sim 900$ °C)^[137], mayenite structure (Ca₁₂Al₁₄O₃₃) can be formed. Mayenite shows a very good anti-coking and anti-sulfur properties thanks to the presence of “free oxygen” in its structure.^[138] The sulfur-resistance property provided by calcium was confirmed by Engelen *et al.*^[139], who washcoated Ni and Ca salts on α -Al₂O₃ support used for the benzene steam reforming with H₂S concentrations of 0/50/100 ppm.

- Magnesium doped alumina supports

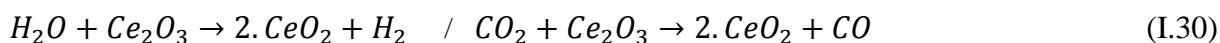
In addition to the interesting properties of magnesium (Ni-MgO interactions, CO₂ adsorption), under the adequate calcination temperature ($T \sim 800$ °C)^{[140], [141]}, the formation of magnesium aluminate spinel (MgAl₂O₄) considerably increases the mechanical strength and the sintering resistance of the catalyst.^[50] Li *et al.*^[142] studied the degradation of rice straw derived tars on nickel catalysts (Ni from 2 to 20 wt. %) with different supports (CaO, TiO₂ or γ -Al₂O₃ + 0.5/1/2 wt. % of MgO). The best results were obtained with 7.5 wt. % of Ni supported on γ -Al₂O₃ + 1 wt. % of MgO.

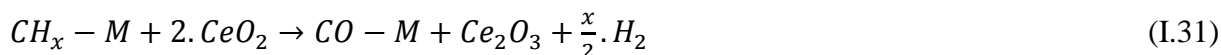
- Potassium doped alumina supports

Among a serie of different additives (Na, K, Mg, Ca, Ba, La, Zr or Ce) deposited on γ -Al₂O₃ support, Seok *et al.*^[143] showed that K was the most efficient against coking. This effect was researched thoroughly by Gálvez *et al.*^[144], who suggested that after calcination at $T > 650$ °C, the formation of K₂O was possible. Under a syngas atmosphere, K₂O is immediately transformed into K₂CO₃ or KOH, which favors the formation of reactive O* and HO* species. Hou *et al.*^[145] showed that the combination of 0.5 wt. % of K and 0.5 wt. % of Ca on nickel-alumina catalysts had a beneficial influence against the coke deposition during the dry reforming of methane. Zhenissova *et al.*^[111] observed that K doping can promote the CO₂ sorption ability of both CaO and MgO in hydrotalcite supports.

- Cerium doped alumina supports

Despite its high price, cerium oxide appears to be the most promising support doping element discovered in the last two decades. Indeed, cerium oxide can easily stock and destock oxygen, which increases its redox properties and its oxygen lability, thus strongly inhibiting the surface carbon formation. Furthermore, CeO₂ is known to facilitate the surface dissociation of H₂O and CO₂ (Equation I.30). The O* radicals are then easily stabilized and integrated into the CeO₂ structure until they can react with adsorbed hydrocarbon species (Equation I.31). This high oxygen lability is apparently also efficient for protecting the catalyst from sulfur deactivation by converting H₂S compounds into less threatening SO₂ species.^{[146], [147]}





Li *et al.*^[146] experimented the reforming of a tar mixture at $T = 550$ °C on different supports (γ -Al₂O₃, ZrO₂, TiO₂, CeO₂, MgO) doped with 4 wt. % of Ni. The catalytic activity was found to be ranked accordingly: Ni/ γ -Al₂O₃ > Ni/ZrO₂ > Ni/TiO₂ > Ni/CeO₂ > Ni/MgO. The pure cerium support showed a remarkable anti-coking effect since the carbon deposition was as follows: Ni/ZrO₂ > Ni/MgO > Ni/ γ -Al₂O₃ > Ni/TiO₂ > Ni/CeO₂.

Roh *et al.*^[148] and Chang *et al.*^[147] both compared the efficiency of Ni/ZrO₂, Ni/CeO₂ and Ni/Ce_{0.8}-ZrO_{2.0.2} for the dry reforming of methane. In both studies, the best catalysts were the ones combining CeO₂ and ZrO₂. Same trends were obtained by Park *et al.*^[149] for the steam reforming of benzene with different supports (γ -Al₂O₃, ZrO₂, CeO₂, ZrO_{2.0.25}-CeO_{2.0.75}) doped with 15 wt. % of Ni. According to these authors, the cubic Ce-ZrO₂ support provides more stable catalysts than raw CeO₂ or ZrO₂ for Ni-based catalysts because ZrO₂ stabilizes the cubic structure at high temperatures and increases the CO₂ and H₂O dissociation by increasing the oxygen storage capacity.

Wang *et al.*^[150] investigated the dry reforming of methane with Ni catalysts supported on γ -Al₂O₃, CeO₂ and CeO₂/ γ -Al₂O₃. The catalytic performances were the best for the composition Ni/CeO₂/ γ -Al₂O₃, followed by Ni/ γ -Al₂O₃ and finally Ni/CeO₂. The authors highlighted the fact that adding CeO₂ to γ -Al₂O₃ generates strong metal-support interactions, resulting in a better dispersion of Ni nanoparticles and a better resistance against sintering.

More recently, Quitete *et al.*^[151] investigated the catalytic performances of different supports (LaAl₁₁O₁₈, La_{0.8}Ce_{0.2}Al₁₁O₁₉ and CaAl₁₂O₁₉) doped either with 6 or 14 wt. % of Ni for the steam reforming of toluene. The composition Ni (14 wt. %)/La_{0.8}Ce_{0.2}Al₁₁O₁₉, followed by Ni (6 wt. %)/La_{0.8}Ce_{0.2}Al₁₁O₁₉, showed the longer lifetime with almost no deactivation after $t = 18$ h of catalytic tests. In comparison, the composition Ni (6 wt. %)/LaAl₁₁O₁₈ was almost completely deactivated after $t = 10$ h, thus exhibiting the beneficial synergy of La and Ce doping.

1.4.4.3. Influences of the composition of the metallic active sites

1.4.4.3.1. General trends

Among the entire metallic elements commonly used, transition metals are the more recurrent. By definition, a transition metal is a metal that forms one or more stable ions which has not completely filled its d orbitals. This particularity enables them to change their oxidation states and therefore to easily lend or take electrons from other molecules. The metallic active states possess a greater capacity to decompose tars in the produced gas in comparison to the oxidized states.^{[65], [129], [152]}

Bimetallic catalysts are often used and have shown several beneficial influences. In this way, it has been shown by Fajin *et al.*^[153] that the “*doping of metallic surfaces with atoms of other metals leads to a stabilizing cooperative effect of both in the adsorption of water, its dissociation products, and transition state configuration.*” The authors showed that the

activation barriers calculated for H_2O dissociation on some bimetallic surfaces were significantly lowered when compared with the activation energies for the reaction of H_2O dissociation on pure surfaces of each metal. This would explain why several authors found out that Ni-based bimetallic materials showed better resistance against coking or H_2S deactivation.^{[3], [66], [94], [121], [154], [155]} One other interesting effect of bimetallic catalysts lies in the fact that one metal can increase the reduction of the second one by the “spillover effect” of the H_2 molecules. In this way, it has been shown that the activated species (H^*) can migrate on distances up to micrometers, which explains why only a few amount of second dopant may greatly influence the reducibility of the catalyst.^{[156], [157]} Finally, formation of bimetallic can also in some case reduce the formation of carbon deposit thanks to the “ensemble control” effect.^{[65], [89], [158]}

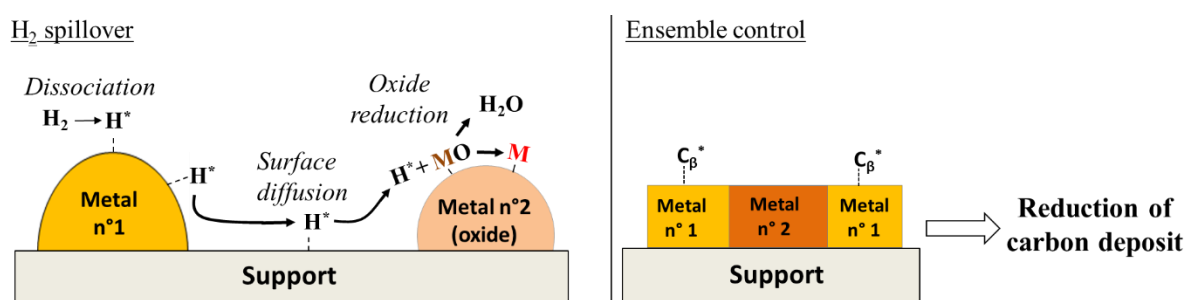


Figure I.12: H_2 “spillover” and “ensemble control” mechanisms on bimetallic catalysts.^{[65], [89], [156]–[158]}

1.4.4.3.2. Noble metal-based catalysts

Experimental results showed that group VIII metals exhibit a good resistance against carbon formation during CH_4 steam^[159] and dry reforming^[160]. Nishikawa *et al.*^[161] investigated the influences of different noble metals (Pt, Pd, Rh, Ru) on the performances of Ni (12 wt. %) / CeO_2 (30 wt. %) / $\gamma\text{-Al}_2\text{O}_3$ catalysts during the steam reforming of gasifier tar mixture. The noble metal loading was very small (0.01-0.1 wt. %). The conversions and the carbon deposits did not drastically differ between the different catalysts. The authors highlighted the fact that, thanks to a better reducibility, the Pt-doped catalyst showed similar performances with and without the pre-reduction step. TPR and EXAFS characterizations suggested that Ni can alloy with Pt much easier than with other noble metals, thus enabling an easier reduction of Ni. Furusawa *et al.*^[76] studied the steam reforming of benzene/naphthalene with either Pt (1 wt. %) or Ni (20 wt. %) or Co (20 wt. %) supported on MgO or $\gamma\text{-Al}_2\text{O}_3$. Their conclusions were that Pt (1 wt. %) and Ni (20 wt. %) catalysts showed similar results and in both cases higher conversions than Co (20 wt. %) catalysts. Moreover, $\gamma\text{-Al}_2\text{O}_3$ seemed to be the most adapted support, limiting the sintering of Pt and Ni nanoparticles.

Miyazawa *et al.*^[162] and Asadullah *et al.*^[163] showed the interesting tar destructing properties of rhodium supported on $\text{CeO}_2\text{-SiO}_2$. According to the authors, Rh catalysts exhibited higher conversions, were more stable and had lower carbon deposits than Ni based catalysts. Nevertheless, the authors admitted that the high price of Rh made these catalysts difficult for large scale applications. Furthermore, Asadullah *et al.*^[164] also investigated the cellulose

conversion with noble metals supported on CeO₂ and concluded that the performances were the following: Rh > Ru > Pd > Pt > Ni.

More recently, Dagle *et al.*^[165] researched the synergic influence of iridium doped Ni/Al₂O₃ catalysts for naphthalene steam reforming. More than simply increasing the catalyst activity, the addition of Ir also permitted to counter the coke formation.

1.4.4.3.3. Ni-based catalysts

Although widely used industrially, Ni is not the most effective catalyst for steam reforming. However, it is the element showing the most interesting activity/price ratio compared to other more precious metals such as Ru or Rh.^[3] The optimum Ni loading is situated around 15 wt. % for impregnated and 20 wt. % for precipitated catalysts.^[9] Nickel active sites are extremely sensible towards deactivation via coking and sulfur poisoning.^{[9], [124]} In order to counter these drawbacks, Ni nanoparticles are either dispersed on a support doped with oxides (CaO, MgO, K₂O, CeO₂...) or alloyed with another metallic element. These alloys avoid the formation of aromatic carbon precursors at the surface and the carbon dissolution inside the nickel structure, or decrease the Ni-S bonds energy, in order to facilitate the regeneration of the catalysts.^[158]

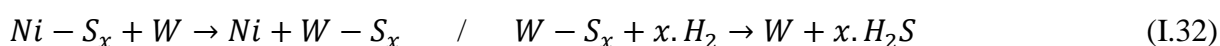
The synergy between nickel and cobalt for the steam reforming of toluene at $T = 600$ °C was investigated by Wang *et al.*^[166]. Different loadings of Co, Ni and Ni-Co supported on γ -Al₂O₃ were tested. Surprisingly, pure Co catalysts (12 wt. %) were more efficient than pure Ni catalysts (12 wt. %). In the case of bimetallic catalysts, characterizations (EXAFS, XRD) highlighted the formation of a homogeneous Ni-Co alloy. The addition of Co to Ni showed interesting results up to a doping of 25 wt. % of Co, after which a lower activity was attributed to an important decrease of the Ni surface area. The synergic effects of Ni-Co were also highlighted by Zhao *et al.*^[121], who studied the steam reforming of cellulose on Ni-Co supported on SBA-15, either or not doped with CaO. According to the authors, a CaO addition is very useful for the cracking of large aromatic tars, whereas Ni-Co bimetallic catalysts are only highly effective for the cracking and steam reforming of small tar molecules and water-gas shift reaction.

Alstrup *et al.*^[158] showed that copper and nickel easily form a solid solution, which appeared to reduce the carbon deposit during methane reforming. A Cu addition would hinder the aromatic carbon formation at the surface and make the carbon diffusion through the Ni-Cu alloy more difficult compared to pure Ni. Furthermore, several studies showed that a Cu addition favors the reduction of the Ni nanoparticles by the H₂ “spillover effect”. Thus, it was possible to obtain metallic Ni nanoparticles and therefore a better activity at lower temperatures.^{[167], [168]}

Guan *et al.*^[51] studied the steam reforming of biomass tars over Ni-Fe catalyst supported on scallop shell. According to the authors, the activity of Ni-Fe catalysts were high due to the synergy between the activation of tars on Ni active sites and the oxygen atoms supplied by the

carbonaceous intermediates (CO_3^{2-}) available on neighboring Fe atoms. Ashok *et al.*^[169] also investigated the toluene reforming over Ni-Fe/ Al_2O_3 catalysts with a 10 wt. % of Ni and a Fe/Al ratio of 1/2. Three calcination temperatures ($T = 500, 700$ or 900 °C) were applied for the pure supports ($\text{Fe}_2\text{O}_3\text{-Al}_2\text{O}_3$) before adding Ni by wet impregnation. The authors highlighted the formation of Ni-Fe alloy. They showed that Fe oxides increase the coverage of oxygen species during the reforming reaction, thus enhancing the degradation of toluene and suppressing coke formation. The calcination temperature influenced the Ni/ $\text{Fe}_2\text{O}_3\text{-Al}_2\text{O}_3$ interactions. Indeed, the supports calcined at $T = 500\text{-}700$ °C showed the highest tar conversions, whereas supports calcined at $T = 900$ °C showed a high carbon deposit and lower tar conversions.

Metals of group VIB such as Mo and W are known to prevent the deactivation of Ni-based catalysts in sulfur containing conditions.^[170] It was found that the addition of Mo to Ni decreased the interactions between Ni oxide and alumina, thus increasing the reducibility of Ni. Mo oxides were also assumed to serve as barrier, thus preventing the growth of Ni nanoparticles. Furthermore, the incorporation of a small amount of Mo permits to greatly enhance the resistance of Ni catalysts towards coke formation. Indeed, Mo oxide are supposed to decrease the coking rate and also prolong the induction period of the coke formation.^[171] Finally, some authors presume that MoO_x species can prevent coking by undergoing redox cycles during the catalytic test, thus contributing to oxygen mobility on the catalyst surface.^[172] Furthermore, according to Maluf *et al.*^[173], an electron transfer occurs from MoO_x species to Ni, leading to an increase in the electron density of metallic Ni, and hence, the catalytic activity. Sato *et al.*^[57] researched the sulfuring resistance of Ni (25 wt. %)/CaO-MgO catalysts doped with different tungsten concentrations (0 - 23 wt. %) for the reforming of a toluene/naphthalene mixture at $T = 850$ °C. Pure Ni (20 wt. %)/ $\gamma\text{-Al}_2\text{O}_3$ and Ru (2 wt. %)/ $\gamma\text{-Al}_2\text{O}_3$ catalysts were also tested under the same conditions. The authors highlighted the fact that W enables the most remarkable stability of Ni against sulfur poisoning, even after $t = 10$ h of testing with 500 ppmv of H_2S . W was supposed to promote the dissociation of the Ni-S compounds and accelerate the regeneration reactions (Equation I.32).



Chaiprasert *et al.*^[174] studied the reforming of a biomass gasifier tar mixture with Pt, Fe or Co (1 wt. %) doped Ni (10 wt. %)/Dolomite catalysts. According to the authors, an addition of Pt increases the steam reforming and the Water-Gas shift reactions. Addition of Fe only influenced the Water-Gas shift reaction. A co-promoted catalyst was more effective for the methane reforming reaction. The carbon deposition increased as follows: Ni+Pt (6.5 wt. %) < Ni+Fe (8.3 wt. %) < Ni+Co (9.3 wt. %) < pure Ni (16.5 wt. %).

Addition of Mn also proved to have very interesting anti-coking properties. Seok *et al.*^[143] studied the coking tendencies of Ni-based catalysts (17 wt. % of Ni) during the dry methane reforming on Al_2O_3 , La_2O_3 , CeO_2 , ZrO_2 , MnO and Ni-MnO_x/MnAl₂O₄. The Ni-MnO_x/MnAl₂O₄ composition showed the most stable activity with almost no carbon deposition (0.003 g_{Carbon}/g_{Cata} after 25 h of reaction). Oh *et al.*^[175] also showed the anti-coking properties

of Mn during the steam reforming of toluene with Ni/Ru-Mn/ α -Al₂O₃. The authors used Ru to enhance the catalytic performances of Ni, and Mn to prevent the coking. Koike *et al.*^[176] investigated the performances of Ni+MnO_x/Al₂O₃ catalysts on the steam reforming of tars during the pyrolysis of cedar wood. The synergetic association of Ni and MnO_x allowed obtaining higher catalytic performances compared to pure Ni or MnO_x on alumina. According to the authors, the Ni particles were partially covered with MnO_x species, which were able to supply oxygen atoms to the carbonaceous intermediates formed on the Ni active sites. These oxygen supplying properties were confirmed by Mendiara *et al.*^[70], who attributed them to the ability of Mn to dissociate CO₂ and H₂O molecules.

1.4.4.4. Influences of the dispersion of the active sites

More than simply increasing the activity thanks to a higher surface area and therefore more accessible active sites^[122], the nanoparticles sizes have proved to strongly influence the resistance of the catalyst against coking. Baker and Mudge^[177] established a linear correlation between the metal surface area and the lifetime of the catalysts. This trend was further explained by Lercher *et al.*^[178], who suggested that the rate of the formation of carbon whiskers is proportional to the particle size. Below a critical Ni particle size, carbon deposit is strongly reduced due to a more efficient transfer of O* and HO* from the support to the metallic active site. Xu *et al.*^[179] and Kim *et al.*^[180] also confirmed this fact and assumed that the Ni particle size must be lower than 7 nm in order to prevent carbon formation during the reforming of methane. Quitete *et al.*^[151] confirmed these trends during their attempt to convert toluene with nickel hexa-aluminates and managed to establish a linear equation between the Ni particle size and the coking rate. Mohsenzadeh *et al.*^[181] performed a DFT study of the adsorption-dissociation of H₂O on Ni (1 1 1), Ni (1 1 0) and Ni (1 0 0) surfaces. The authors found out that the water dissociation rate was favored on Ni (1 1 0) and Ni (1 0 0) sites in comparison with Ni (1 1 1) sites. This observation was correlated with previous studies which showed that the coking was favored on Ni (1 1 1) faces. Hence, the coking is favored on the Ni crystal sites for which the water dissociation is low. A corroboration of these results and the fact that the proportion of Ni (1 1 0) and Ni (1 0 0) sites increases when the nanoparticle size decreases was made by Goodman *et al.*^[182].

1.4.4.5. Influences of the synthesis method of the catalysts

Studies were carried out to determine the influence of the two most common catalyst preparation methods, *i.e.* the incipient wetness impregnation and the sol-gel process. It appears that due to weaker active site/support interactions, the metallic nanoparticles from impregnated catalysts are more inclined to sinter and submit coke deactivation, especially by carbon whiskers formation. Although generally showing lower activity, sol-gel synthesized catalysts are therefore more interesting in terms of lifetime.^{[3], [183]–[185]}

I.5. CONCLUSIONS

Though the type of gasifier (fluidized bed, fixed bed ...) and the processing parameters (temperature, gas composition, gasifying time ...) may play important roles on the final quality of the bio-syngas, it appears that the spread of the gasification technologies are mostly depending on the elimination of the tars produced with low-cost and technically convenient methods.

The use of catalyst appears as the most interesting method to obtain a tar-free clean bio-syngas. Primary catalysts (situated inside the reactor) such as doped-olivine have shown very interesting results. However, some improvements still need to be done for the development of secondary catalysts (situated at the outlet of the reactor) with high catalytic activities and good resistances against deactivation by coking and sulphidation. Though interesting results have been obtained with catalysts doped with noble elements such as Pt, Rh, Ru, Re, the researchers must keep in mind that the objectives consist at reducing the total costs of the cleaning operations. So, the new studies should focus on the development of materials based on economically interesting elements.

Ni/ γ -Al₂O₃ materials developed by sol-gel method appears as one of the most promising investigation path to follow for the development of secondary catalysts. Indeed, the sol-gel methods enable higher metal/support interactions, which prevent sintering and coke deactivation. However, the higher costs and the more complicated apparatus required for the preparation of catalysts by sol-gel methods compared to a classic impregnation has to be taken into account. Furthermore, the use of sol-gel catalysts at large scale is also more problematic compared to impregnated catalysts and hence requires more adaptations (e.g. coating of the catalysts on monolithic support).

The influence of simple doping with cheap and available element such as Mn, Mo, Fe, Co, Mg, Ca or K should be also considered.

Chapter II

Elaboration of an aqueous sol-gel method for the synthesis of γ -Al₂O₃ supports

- Introduction to the sol-gel process;
- Synthesis of γ -Al₂O₃ supports by aqueous precipitation;
- Influences of the use of either Al-nitrate or Al-*sec*-butoxide on the properties of γ -Al₂O₃ supports;
- Preparation of boehmite functionalized with a silicon precursor (EDAS).

As depicted in Chapter I, γ -Al₂O₃ appears to be the best support for the synthesis of secondary catalysts situated at the outlet of biomass gasifiers. In this project, instead of using commercially available γ -Al₂O₃ materials, it is decided to develop a synthesis method of γ -Al₂O₃ supports based on literature references, in order to be able to tailor the micro- and mesoporosity of future catalysts supported on γ -Al₂O₃.

First, this chapter aims at outlining the theoretical and experimental notions of the fabrication of alumina materials by the sol-gel process. Thereafter, the experimental validation of an aqueous precipitation method for the synthesis of pure Al₂O₃ support is done. Furthermore, the influences of two different precursors of aluminum, aluminum *sec*-butoxide (Al[OCH(CH₃)CH₂CH₃]₃) or aluminum nitrate (Al(NO₃)₃), on the final properties of the alumina supports are investigated, in order to set synthesis instructions for the future syntheses of catalysts.

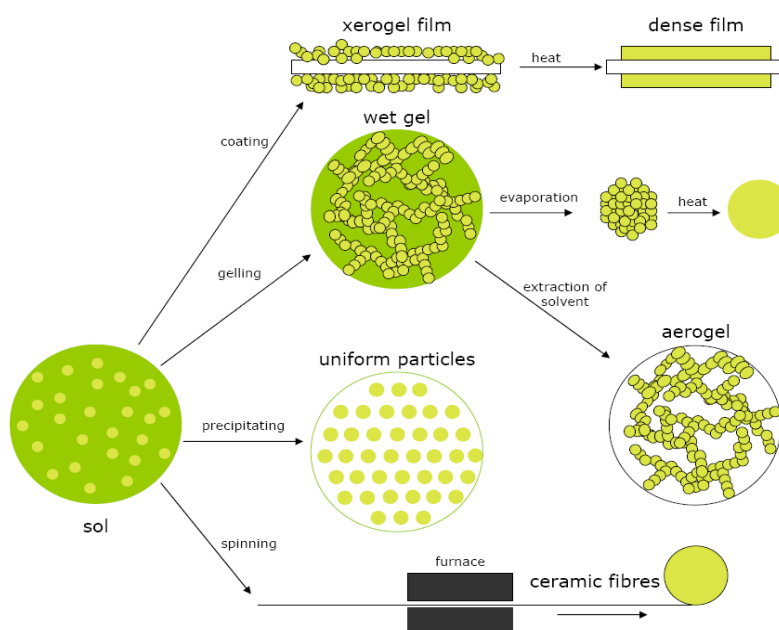
Some amino-functionalized compounds are known to chelate metallic ions, which leads to a high dispersion of metallic active sites and which increases catalytic performances. Keeping that in mind, this chapter also aims at developing a synthesis procedure for the cogelation between a functionalized silicon alkoxide (3-(2-aminoethylamino)propyltrimethoxysilane, EDAS) and alumina hydroxide.

II.1. INTRODUCTION

II.1.1. The sol-gel chemistry

The sol-gel term was defined several years ago by Brinker and Scherrer in the book “*The Physics and Chemistry of Sol-Gel Processing*” edited in 1990.^[186] These processes were further developed for the synthesis of inorganic materials, and especially for metallic oxides with porous and tailored morphologies, and a homogeneous particle size distribution of crystallites (SiO₂, Al₂O₃). By definition, a sol is a colloidal suspension of solid particles (1-1000 nm) in a liquid, in which the dispersed phase is present in a low amount. Therefore, gravitational forces are negligible, and short-range forces, such as Van der Waals bonds and the surface charge electrostatic forces, dominate the interactions. A gel is obtained by the cross-linking of the sol colloid and results in a solid network with a high liquid amount in its pores. In this way, a sol-gel process can simply be summarized as an inorganic polymerization performed in solution media.^[186]

The starting materials used for the sol-gel process can be various reagents such as metallic salts, metallic oxides, metallic hydroxides, metallic complexes or metallic alkoxides. They should be soluble in the reaction medium and reactive enough to participate in the gel forming process. Though offering many applications, the sol-gel processes can be divided into the following basic elementary steps: solution formation, gelation, aging, drying and densification by final heat treatments (Figure II.1).^[186]

Figure II.1: Scheme of different sol-gel pathways.^[186]

Though being defined by the same syntheses steps, *i.e.* hydrolysis and condensation, depending on the type of precursors and solvent used, the sol-gel polymerization can be performed in two different paths: organic or aqueous.

II.1.1.1. Organic path

The organic paths are performed in non-water media (alcohols, toluene...) and use precursors sensitive to water, the most common ones being the metallic alkoxides (ex: $Si(OC_2H_5)_4$, $Al(OCH(CH_3)_2)_3$, $Ti(OCH(CH_3)_2)_4$...). The polymerization is started when water is added to the mixture and occurs as follows^[186]:

First, an initial hydrolysis step, where the alkoxide precursor reacts with water:

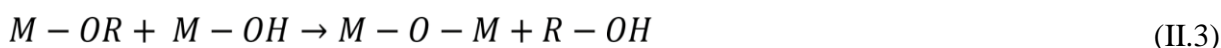


where M is a metal (Si, Al, Ti ...) and R is an alkyl group (CH_3 , CH_2CH_3 ...)

The inorganic network is thereafter formed via the condensation step. The hydroxyl group reacts with another hydroxyl group to form water:



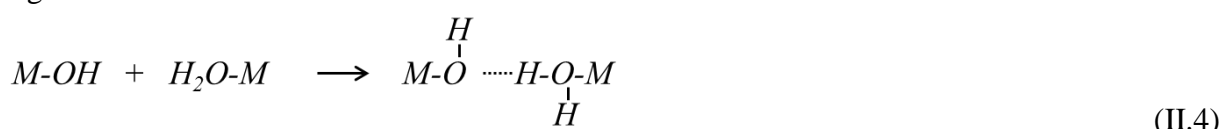
or with an initial precursor to form alcohol:



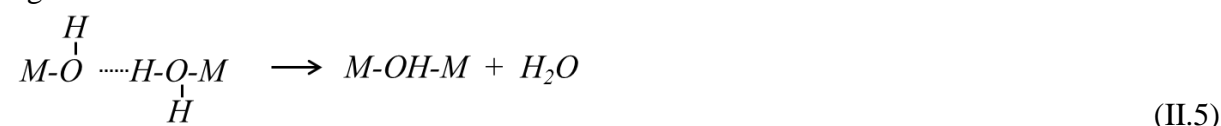
Numerous studies have shown that it is possible to influence the hydrolysis and condensation rates through the control of various experimental parameters (temperature, pH , H_2O /solvent ratio, agitation time).^{[186]–[189]} A "gel" obtained with a very fast hydrolysis will consist of small particles, which are highly reticulated, whereas a slower hydrolysis will present larger grains, with less interconnections.

II.1.1.2. Aqueous path

Inorganic sol-gel mechanisms via aqueous paths were thoroughly studied by Jolivet^[190] and Livage^[191]. The first principle to obtain a “gel” via an aqueous method consists in the solubilization of metallic cations (Na^+ , Fe^{2+} , Ca^{2+} , Al^{3+} , Y^{3+} , La^{3+} ...) in water. In the formed solution, hydrolyzed oxides and hydroxides bond, initiate complexes such as aquo ($[\text{M}(\text{OH}_2)_N]^{z+}$), hydroxo ($[\text{M}(\text{OH})_N]^{(N-z)-}$) or oxo ($[\text{M}(\text{O})_N]^{(2N-z)-}$) compounds, with $2 < N < 8$ and $1 < z < 7$. The initiating complexes can thereafter be combined according to two different condensation mechanisms: the olation and the oxolation.^{[190], [191]} The olation reaction occurs between complexes composed of hydroxo (-OH) and aquo-hydroxo (-OH₂) groups as follows: In a first step, an interaction is formed by the hydrogen bond between the OH and the H₂O ligands:



Thereafter, the M-OH₂ bond is broken, a hydroxo bridge M-OH-M is formed and the aquo ligand H₂O is eliminated:



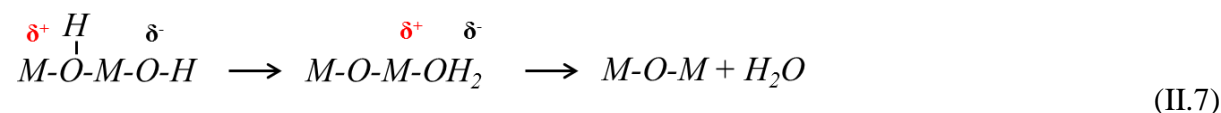
The bridging -OH ligands are called “ol” in order to differentiate them from hydroxo ligands at the extremity. So, the “olation” is therefore the reaction leading to the formation of an “ol” bridge (-OH-) between two metals. Olation kinetics are generally fast and depend mainly on the lability, *i.e.* the ability of bond cleavage, of the M-OH₂ bond. The lability of the M-OH₂ bond depends on the polarization of the cation: the bond is more inclined to be undone for cations with low formal charge z or for large cations. The olation reaction is supposed to occur according to a nucleophilic substitution of type S_N1 (the reaction rate is of first-order and depends only on the electrophile).^{[190], [191]}

The second condensation mechanism is called “oxolation”. It occurs when both precursors do not contain any aquo ligands (-OH₂) coordinated to the metallic cation. It involves the condensation of two hydroxo (-OH) groups to form one water molecule as follows:

At first, a nucleophilic addition with formation of an “-ol” bridge leads to an unstable transition state:



Thereafter, a proton is transferred to a terminal -OH ligand to form an aquo group which is finally eliminated:



By definition, condensation mechanisms by oxolation lead to “-oxo” (-O-) bridges. However, contrary to ololation, oxolation reactions are usually influenced by the acidity of the environment. Oxolation generally presents lower reaction rates than ololation. The oxolation reaction is supposed to occur according to a nucleophilic substitution of type SN2 (the reaction rate is of second-order and depends on the two reacting species). Two essential conditions are required for the oxolation reaction to take place: 1) the presence of a hydroxo (-OH) ligand carrying a negative charge ($\delta(OH) < 0$) in the coordination sphere of a cation; 2) the possibility of a cation to undergo the nucleophilic attack from a hydroxo ligand, *i.e.* the cation must be sufficiently electrophile to undergo the attack ($\delta(M) > + 0.3$).^{[190], [191]}

II.1.2. Formation of aluminum hydroxides and calcined alumina

The comparison of aqueous and organic paths for the synthesis of γ - Al_2O_3 was studied by Rajaeiyan *et al.*^[192] in 2013. The authors showed that after a classic calcination under air at $T = 750$ °C, better structural and textural properties were obtained for the aqueous method than for the organic path. Indeed, the specific surface area was higher (200 m²/g for aqueous path, while 30 m²/g for organic path). Furthermore, γ - Al_2O_3 rays were visible on XRD spectrum for the sample synthesized by the aqueous method, whereas the sample synthesized by the organic method showed amorphous alumina rays. Taking these results into consideration and in the aim of developing an easy, safe and relatively cost-effective method for the synthesis of alumina catalytic supports, it was decided to focus on alumina synthesis via aqueous sol-gel paths for the future syntheses of this project.

When dissolved into water, the aluminum ions can form different complexes depending on the *pH*-value (Figure II.2). Once formed, these aqueous complexes will condense and form cross-linking networks via oxolation and ololation reactions previously described. The final material properties (crystallinity, specific surface area and pore volume) depend strongly on the experimental conditions such as the temperature, the type of precursors, the agitation or the aging conditions.^{[190], [191], [193], [194]}

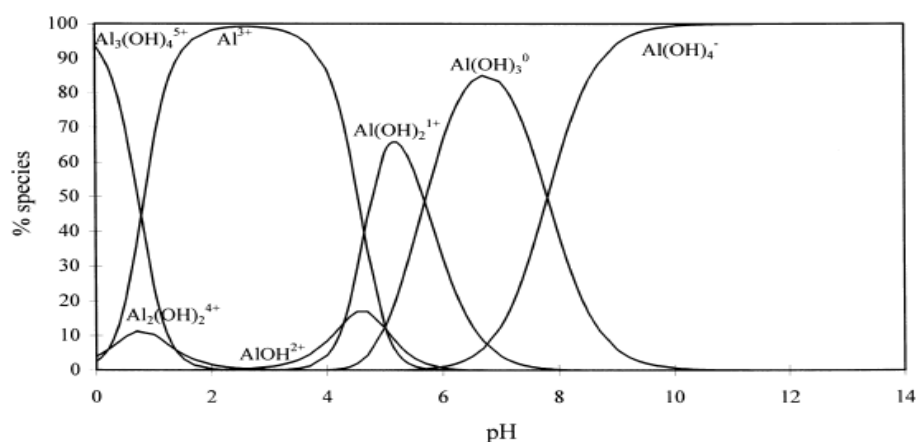


Figure II.2: Speciation diagram of aluminum ions as a function of the *pH* at $T = 25$ °C and $P = 1$ atm.^[195]

Depending on the synthesis conditions, the basic brick of aluminum hydroxide ($Al(OH)_3(OH_2)$) can either be aggregated into amorphous alumina hydroxide ($Al(OH)_3$),

diaspore (α - AlOOH) or boehmite (γ - AlOOH) (Figure II.3). Controlling these hydroxides paths is therefore of major relevance. Indeed, after a classic calcination under air at $T = 500\text{ }^\circ\text{C}$, $\text{Al}(\text{OH})_3$ leads to η - Al_2O_3 , whereas diaspore leads to α - Al_2O_3 and only boehmite leads to γ - Al_2O_3 .^{[190], [196], [197]} Figure II.4 shows the complexity of the different crystalline phases which can be obtained depending on the starting hydroxyde type and the thermal treatments.^{[196], [197]}

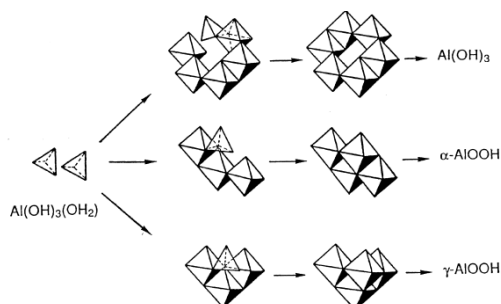


Figure II.3: Possible paths for the formation of aluminum hydroxides or oxhydroxide solid complexes.^[190]

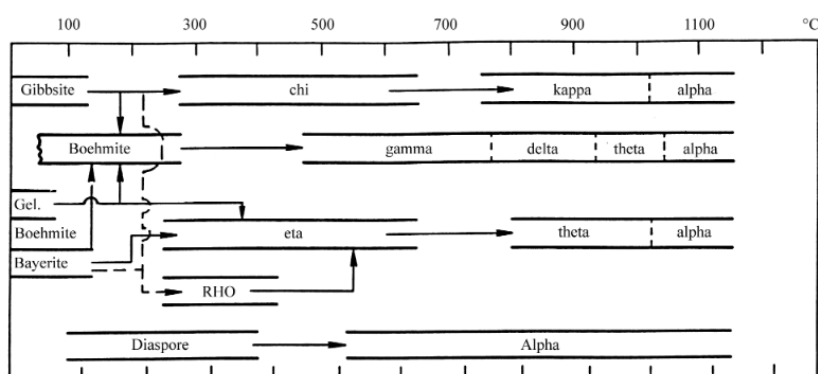


Figure II.4: Thermal transformation sequences of aluminum hydroxides.^{[196], [197]}

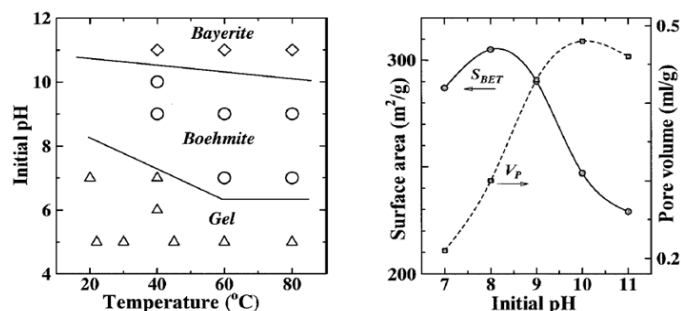


Figure II.5: Field map of the alumina crystalline phase produced by precipitation method as a function of the initial pH -value and temperature (left side) and the textural properties of obtained gels as a function of the hydrolysis pH (right side) according to Okada *et al.*^[198].

Okada *et al.*^[198] highlighted the importance of the operating variables: the formation of boehmite under atmospheric pressure is guaranteed only for temperatures of $T = 70$ - $100\text{ }^\circ\text{C}$, and for pH -values comprised between 7.5 and 10 (Figure II.5). Indeed, under these aging conditions, the amorphous and diaspore aluminum hydroxide crystals formed during the precipitation are inclined to undergo dissolution/reprecipitation mechanisms to form $\text{Al}(\text{OH})_4^-$ complexes, which are thereafter rearranged to form the boehmite phase. This phenomenon was confirmed by several authors^{[190], [191]}, notably Lee *et al.*^[199], who also highlighted the fact that by allowing

the formation of γ -AlOOH, these conditions allow obtaining the alumina hydroxide gels with the highest specific surface area and pore volume (Figure II.5).

Under classic calcination (air, $T = 500$ - 700 °C), the boehmite crystallites are converted via a topotactic transformation (similar crystalline structure of the starting and final material, no variation of the volume) into γ -Al₂O₃ crystallites according to the three following steps: 1) at around $T = 100$ °C, elimination of physisorbed water; 2) between $T = 250$ °C and $T = 500$ °C, transformation of boehmite into γ -Al₂O₃ with water evacuation; 3) up to $T = 500$ °C, elimination of the residual hydroxyls.^{[200], [201]}

II.1.3. Cogelation and coprecipitation methods

The methods of cogelation (done by organic path) and of coprecipitation (done by aqueous path) allow the synthesis of homogenous supports from the hydrolysis and condensation of different kind of precursors.

The syntheses by cogelation can be performed with two alkoxides of the same element, for example the formation of SiO₂ with tetramethoxysilane (TMOS; Si(OCH₃)₄) and tetraethoxysilane (TEOS; Si(OC₂H₅)₄).^{[202], [203]} It is also possible to start from one alkoxide and one salt, for example the synthesis of Al₂O₃ with a mixture of Al-isopropoxide (Al(OC₃H₇)₃) and aluminum nitrate (Al(NO₃)₃)^[204], or Al-isopropoxide (Al(OC₃H₇)₃) and aluminum acetylacetonate (Al(C₅H₇O₂)₃)^[205]. The more interesting aspect of the cogelation lies in the possibility to create homogeneous inorganic materials with different elements. The most famous application is the formation of aluminosilicates, and especially zeolites, made of aluminum and silica precursors. It is common to synthesize these materials with an organic sol-gel path using two alkoxides (TEOS and Al-isopropoxide, or TEOS and Al-*sec*-butoxide)^[206].

Similar materials can be obtained by coprecipitation by using a combination of TEOS and aluminum salts (Al(NO₃)₃, Al(Cl₃)₃).^{[207], [208]} Coprecipitation of more than two different types of precursors has also proved to be possible with for example the synthesis of La₂O₃ doped mullite using Al(NO₃)₃, TEOS and La(NO₃)₃ reagents^[209] or the synthesis of ZrO₂ doped mullite using Al(NO₃)₃, Al-isopropoxide, TEOS and Zr acetate reagents^[210].

Cogelation with a functionalized precursor is also possible in order to tailor the morphology of the material. In this way, the use of silicon alkoxide containing a functional organic group made of one or several amino groups, which are able to form a chelate with a metallic cation (Figure II.6), has proved to be an innovative and efficient way to improve the performances of catalytic materials. Indeed, the amino-metal complex of the functional chain allows an efficient dispersion of the metallic nanoparticles on the inorganic support, thus improving the activity and lifetime of the catalyst. In this way, Heinrichs *et al.*^[211] synthesized finely dispersed Pd and Pd-Ag/SiO₂ by the homogeneous cogelation of a common silicon alkoxide (TEOS) and an amino-group functionalized silicon alkoxide (3-(2-aminoethylamino)propyltrimethoxysilane, (CH₃O)₃Si(CH₂)₃NHCH₂CH₂NH₂, called EDAS). Lambert *et al.* also investigated the beneficial effect of EDAS, notably for selective

hydrodechlorination performed on Pd-Ag/SiO₂ and Pd-Cu/SiO₂ cogelled catalysts^[212], and for the volatile organic compounds combustion performed on Ag/SiO₂, Cu/SiO₂ and Pd/SiO₂ cogelled catalysts.^[213]

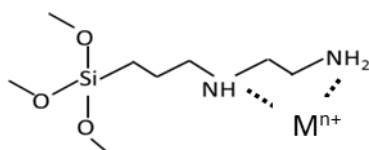


Figure II.6: Complex formation between amino groups of EDAS and a metallic cation M^{n+} .

Since no functionalized aluminum precursors are commercially available, the functionalization of alumina supports is nowadays only performed via grafting methods. The usual methods consist in the mixing of a functionalized silica precursor with an alumina support in an organic solvent. Thereafter, a small quantity of water is added to hydrolyze the alkoxy groups and form silanol groups, which graft onto the alumina support by condensation reactions.^{[214]–[216]} These methods are nevertheless not convenient and difficult to scale up, principally because of the required synthesis conditions (inert and dry atmosphere, toxic organic solvents). The aim of this chapter is to perform the synthesis of γ -Al₂O₃ supports modified by EDAS molecules thanks to a simple and classic aqueous coprecipitation method.

II.2. EXPERIMENTAL

II.2.1. Preparation of samples

Two synthesis methods were experimented for the synthesis of γ -Al₂O₃ and EDAS modified γ -Al₂O₃ supports. The first method, called method *A* (related to “alkoxide”), used Al-*sec*-butoxide (Al[OCH(CH₃)CH₂CH₃]₃) as aluminum source. The second one, called method *N* (related to “nitrate”), used aluminum nitrate (Al(NO₃)₃) as aluminum source. For both methods, the reagents were dissolved in a media solution with H₂O/(Al + $\frac{3}{4}$ Si) and Ethanol/(Al + Si) molar ratios fixed at 50 and 5 respectively. The presence of the fraction $\frac{3}{4}$ in the first ratio was justified by the fact that only the three methoxy groups in the EDAS molecule are hydrolyzed by water. Ethanol was added to the media solution in order to prevent a direct contact of the silicon precursor with pure water, which is known by experience to lead to macroscopic silicate aggregates. The different amounts of reagent (Al-*sec*-butoxide, Al nitrate, EDAS, water, ethanol) used for the synthesis of 10 g of calcined material are listed in part V of Annex 2.

It is to recall that this chapter aimed at developing procedure for the synthesis of catalysts supports, which will be doped with metals (Ni, Fe ...). Therefore, the amount of EDAS was set in order to allow the synthesis of future catalysts doped with 2 wt. % of Ni and with Ni/EDAS ratio equal to 4. Hence, this led to calcined supports with loading of 8.2 wt. % of SiO₂.

The preparation of a sol by the method *A* was performed as follows: Al-*sec*-butoxide was quickly (1 mL/s) injected into the solution (water + ethanol) under vigorous stirring. The sol was then stirred for $t = 30$ min. The variant method consisted in adding EDAS to the solution

under vigorous stirring for $t = 5$ min before adding Al-*sec*-Butoxide. After the stirring, the pH value was increased to 9.5 by a dropwise (1 mL/min) addition of a NH_4OH solution (30 wt. %, *i.e.* 15 M). Samples synthesized via this method contain the prefix “A” in their names.

The preparation of a sol by the method *N* was performed as follows: aluminum nitrate was dissolved in the solution (water + ethanol) and the sol was then stirred for $t = 30$ min. A variant method consisted in adding EDAS to the solution under vigorous stirring for $t = 5$ min before adding $\text{Al}(\text{NO}_3)_3$. The sol was then stirred for $t = 30$ min. After the stirring, the pH value was increased to 9.5 by a stepwise (1 mL/min) addition of a NH_4OH ammonia solution (30 wt. %, *i.e.* 15 M). Samples synthesized via this method contain the prefix “N” in their names. The general schemes of the method *A* or *N* are depicted in Figure II.7.

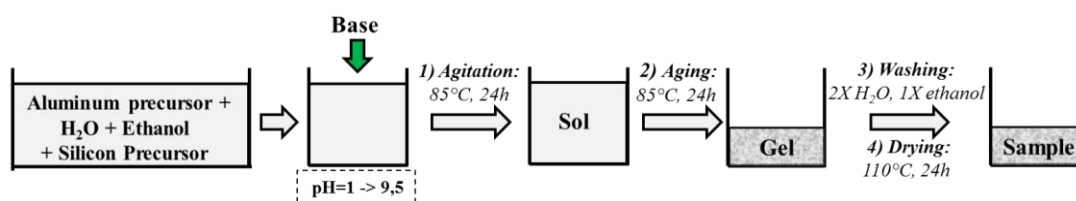


Figure II.7: General scheme of the pure alumina and EDAS modified alumina supports starting from aluminum nitrate or Al-*sec*-butoxide.

For both methods, right after the precipitation step, the vessels were closed and the solutions were put under vigorous stirring in a heated oil bath at $T = 85$ °C for $t = 24$ h. After the agitation step, the bottle was opened and put into an oven for aging ($t = 24$ h, $T = 85$ °C, $P = 700$ mbar). The obtained gels were washed twice with water and once with ethanol using the centrifuge ($t = 15$ min, 10.000 rpm) in order to eliminate undesirable compounds such as nitrates and ammonia. The ethanol washing step is believed to prevent the pore collapse during the drying steps, allowing keeping a high mesoporous structure.^{[217], [218]} The clean gels were thereafter put into an oven for drying ($t = 24$ h, $T = 110$ °C, $P = 900$ mbar). A temperature of $T = 110$ °C was set because it is believed to favor the formation of the boehmite phase.^[219] During the drying step, the gels were transformed into monolith-like solids. The dried samples were thereafter calcined under air for $t = 4$ h at $T = 500$ °C. The calcination is known to be the most important synthesis operation since it modifies the structure and crystallinity of the samples (cf. Figure II.4). In this way, some studies have highlighted the fact that a too high heating rate (> 2 °C/min) can affect the mesoporous structure, notably because of the presence of heterogeneous hot spots and a too high evacuation rate of water.^{[220], [221]} Accordingly, the heating rate was fixed to 2 °C/min. Although some literature^[220] has demonstrated some advantages on the final support properties by using calcination ramp steps under a N_2 flux, for practical purpose, it was decided to perform the calcination under classic air conditions.

II.2.2. Characterization techniques

In this chapter, thermogravimetric-differential scanning calorimetry (TG-DSC), mercury porosimetry (Poro-Hg), nitrogen adsorption-desorption (BET), microscope analyses (SEM-BSE, SEM-EDX), transmission electron microscopy (TEM), X-Ray diffraction (XRD)

measurements were performed. The crystallites sizes were calculated by using the Scherrer equation centered on the (4 0 0) ray of γ - Al_2O_3 ($2\theta = 67.0^\circ$) of the XRD spectra. Deeper information about the characterizations techniques and variables quoted are provided in part II of Annex 2. X-Ray references cards are given in part VI of Annex 2.

II.3. RESULTS

Figure II.8 presents the precipitation curves of samples *A*, *N*, *A-EDAS8* and *N-EDAS8*. The samples precipitated with *Al-sec*-butoxide (*A* and *A-EDAS8*) required minimal NH_4OH additions (around 1 mL) in order to reach a *pH* value of 9.5. In contrary, the samples synthesized with aluminum nitrate (*N* and *N-EDAS8*) presented very similar aqueous precipitation curves typical for aqueous alumina precipitation with a base.^[222] Indeed, *N* and *N-EDAS8* curves were characterized by three distinct fields:

1) for the field I, *i.e.* $pH < 4$, the titration curve was almost horizontal, which indicates that the polymerization rate of the small size Al aggregates was fast and continuous. Mononuclear Al complexes condensed to form Al_2 - Al_{12} species such as $\text{Al}_2(\text{OH})_4^{2+}$, $\text{Al}_6(\text{OH})_{12}^{6+}$ and $\text{Al}_{10}(\text{OH})_{22}^{8+}$;

2) for the field II, *i.e.* $4 < pH < 7$, the main Al species were large polymeric Al and amorphous $\text{Al}(\text{OH})_3$. Mononuclear Al species were replaced by larger polymers (Al_{13} - Al_{54}). In this field, the rate of polymerization was very slow, so an addition of OH^- importantly raised the *pH* value;

3) for the field III, *i.e.*, $pH > 9$, most of the species were converted into crystalline alumina hydroxide, such as boehmite AlOOH . A part of the Al species dissolved and formed $\text{Al}(\text{OH})_4^-$ species.^{[222]–[224]}

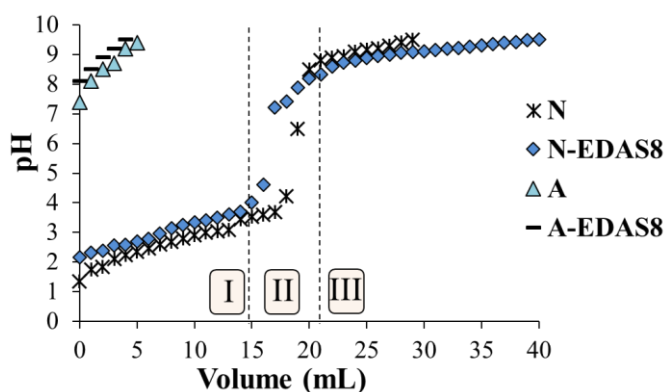


Figure II.8: Precipitation curves for samples *A*, *A-EDAS8*, *N* and *N-EDAS8*.

Though presenting similar shapes, one can notice slight differences between the *N* and *N-EDAS8* precipitation curves. Indeed, the initial *pH* value was higher for *N-EDAS8*: at $V_{\text{NH}_4\text{OH}} = 0$, $pH_{N-EDAS} = 2.2$ whereas $pH_N = 1.3$. This difference of *pH* was due to the intrinsic basic properties of the amino groups of EDAS molecules caused by their non-binding electron doublet.^[225] Consequently, sample *N-EDAS8* entered the field II at a lower NH_4OH volume addition than sample *N* ($V_{\text{NH}_4\text{OH}, I \rightarrow II} = 14$ mL for *N-EDAS8*, whereas $V_{\text{NH}_4\text{OH}, I \rightarrow II} = 17$ mL for *N*). However, the field III of sample *N-EDAS8* was much longer than for sample *N*, thus

resulting in a higher total NH_4OH volume needed for *N-EDAS8* to reach a *pH* value of 9.5 (29 mL for *N* and 40 mL for *N-EDAS8*).

TG-DSC tests were performed on dried gels in order to understand the thermal behaviors of the materials (Figure II.9). The samples made of raw alumina (samples *A* and *N*) presented similar TG and DSC curves, *i.e.* a first endothermic peak at about $T = 100$ °C, which corresponded to the evaporation of water, followed by a second peak located between $T = 250$ °C and $T = 500$ °C, which corresponded to the transformation of boehmite into γ - Al_2O_3 .^{[200], [201], [226]} This second peak was more pronounced for sample *N* than for sample *A*. From $T = 500$ °C to $T = 800$ °C, the evacuation of hydroxyl groups retained in the alumina network was evidenced by a slow and constant increase of the DSC curves associated with a slow decrease of the TG curves.^{[227], [228]}

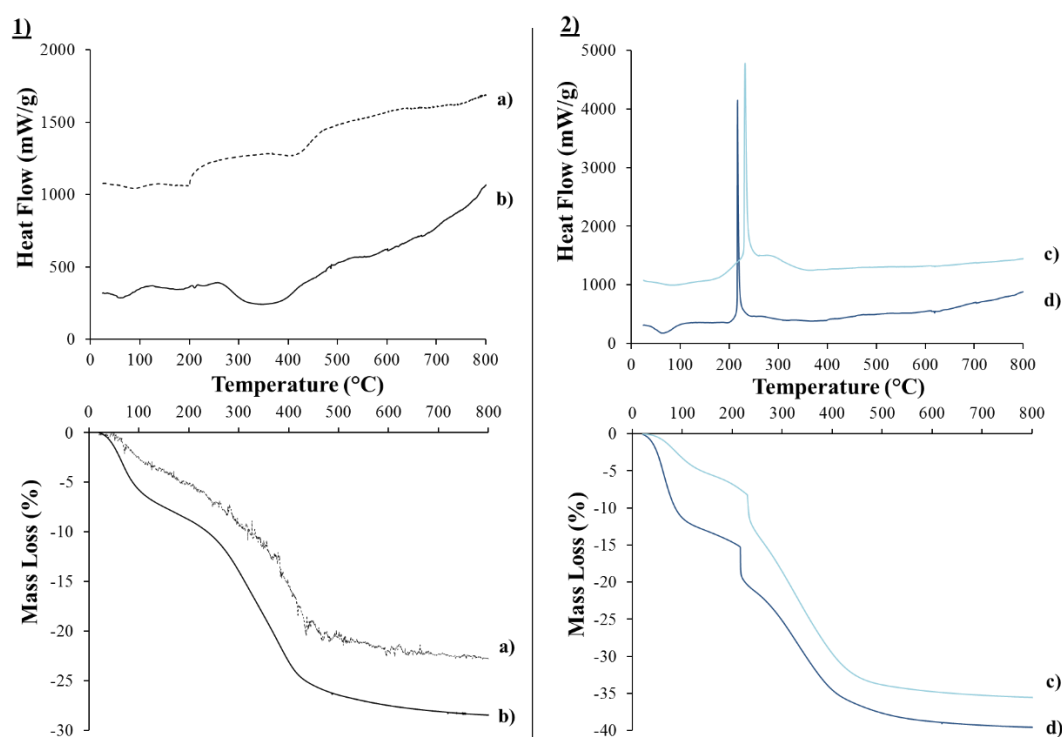


Figure II.9: TG-DSC curves of calcined samples; a. *A*, b. *N*, c. *A-EDAS8*, d. *N-EDAS8*.

It was observed in Figure II.9 that, though presenting similar thermal behaviors, EDAS doped supports (samples *A-EDAS8* and *N-EDAS8*) were characterized by an additional weight loss of about 5 wt. % associated with a high exothermic peak situated between $T = 210$ °C and $T = 220$ °C, which was caused by the degradation of the organic compounds of their functionalized chains. One can notice that samples synthesized by the method *A* presented lower total weight losses (around 5 wt. %) than the ones synthesized by the method *N*. Though being dried under the same conditions ($t = 24$ h at $T = 110$ °C), samples from the method *N* apparently had a more important quantity of adsorbed water and hydroxyl groups.

Figure II.10 shows SEM-BSE pictures of calcined samples. The samples presented similar microscopic surface aspects, composed of aggregates of micrograins with sizes between 0.5 and 10 μm . Though the surfaces of samples were rough, all the grains were dense and showed no

macroporosity. Indeed, the macroporous volume, V_{Hg} , calculated from mercury porosimetry measurements were below $0.1 \text{ cm}^3/\text{g}$ for all the samples.

SEM-EDX mapping measurements were made on samples *N-EDAS8* and *A-EDAS8* and confirmed the homogeneity of the samples at microscale (Figure II.11).

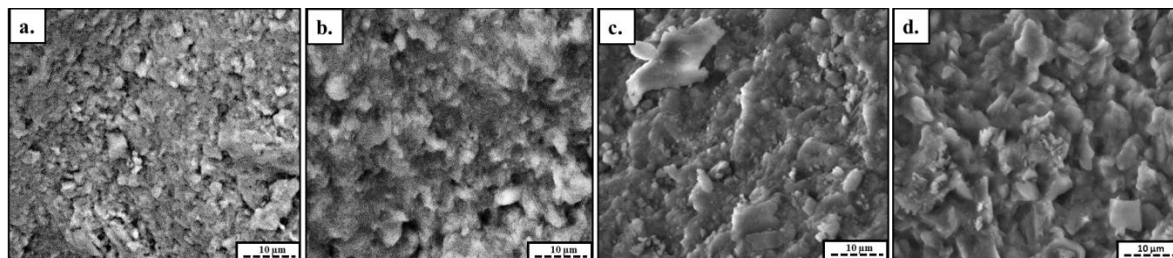


Figure II.10: SEM pictures of calcined samples *A*, *A-EDAS8*, *N*, *N-EDAS8*. Analysis conditions: 15 kV, 2000 X, SEM-BSE.

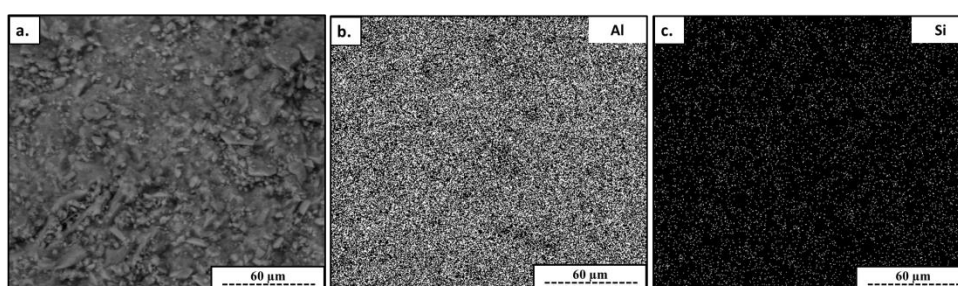


Figure II.11: Al and Si element mapping of calcined *N-EDAS8* sample. Analysis condition: 15 kV, 400 X, SEM-EDX.

Figure II.12 shows TEM micrographs of the calcined samples. The samples made of pure alumina (samples *A* and *N*) presented platelet-like crystallites assembled in a random way, which is apparently characteristic for γ - Al_2O_3 supports synthesized by sol-gel methods.^[192] In comparison, EDAS modified supports presented very peculiar morphologies, with small elliptical crystallites assembled in a dense and compact way.

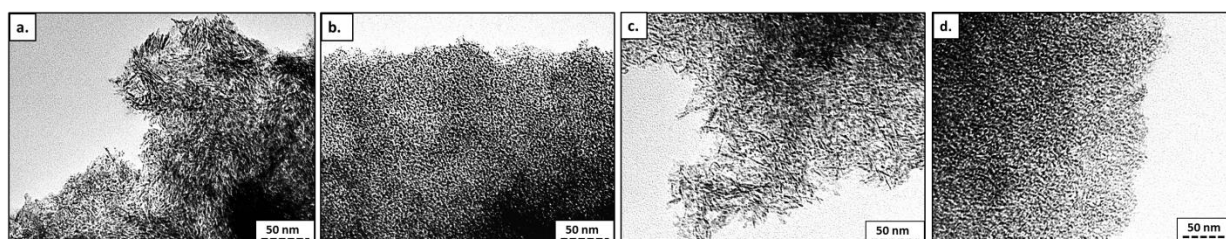


Figure II.12: TEM pictures of calcined samples; a. *A*, b. *A-EDAS8*, c. *N*, d. *N-EDAS8*; 245.000 X.

Table II.1 lists the textural and crystallographic properties of the calcined samples obtained from the nitrogen adsorption-desorption isotherms (S_{BET} , V_p , S_{meso} , $V_{Dubinin}$), X-Ray diffraction (d_{XRD}) and helium pycnometry analyses (ρ).

Table II.1: Textural and crystallographic properties of the calcined samples.

Samples	S_{BET} (m ² /g)	V_p (cm ³ /g)	S_{meso} (m ² /g)	$V_{Dubinin}$ (cm ³ /g)	ρ (cm ³ /g)	d_{XRD} (nm)
A	230	0.50	195	0.09	3.15	4.5
A-EDAS8	395	0.35	200	0.13	2.73	3.6
N	340	0.60	280	0.12	2.97	4.4
N-EDAS8	530	0.30	225	0.17	2.84	3.3

S_{BET} : specific surface area, V_p : porous volume, S_{meso} : mesoporous surface area, $V_{Dubinin}$: microporous volume, ρ : apparent density; d_{XRD} : size of γ - Al_2O_3 crystallites determined by XRD.

The nitrogen adsorption-desorption isotherms and their respective pore size distributions are shown in Figure II.13. All isotherms were characterized by: 1) at low relative pressure (p/p_0), a sharp increase of the adsorbed volume followed by a plateau, which corresponds to a type I isotherm according to BDDT classification, is characteristic of microporous adsorbents. Furthermore, the microporous volume, $V_{Dubinin}$, was important for all samples (> 0.05 cm³/g); 2) at higher pressure ($p/p_0 > 0.4$), the samples exhibited a broad hysteresis which is characteristic of a nitrogen adsorption-desorption type IV isotherm according to the BDDT classification; 3) a high pore volume, V_p .^{[229], [230],[231]} All the samples presented a mesoporous pore size distribution comprised between 2 and 30 nm. It is to notice that raw alumina (samples A and N) presented specific surface areas and pore volumes similar to samples synthesized under similar operating conditions in the literature.^{[194], [199]}

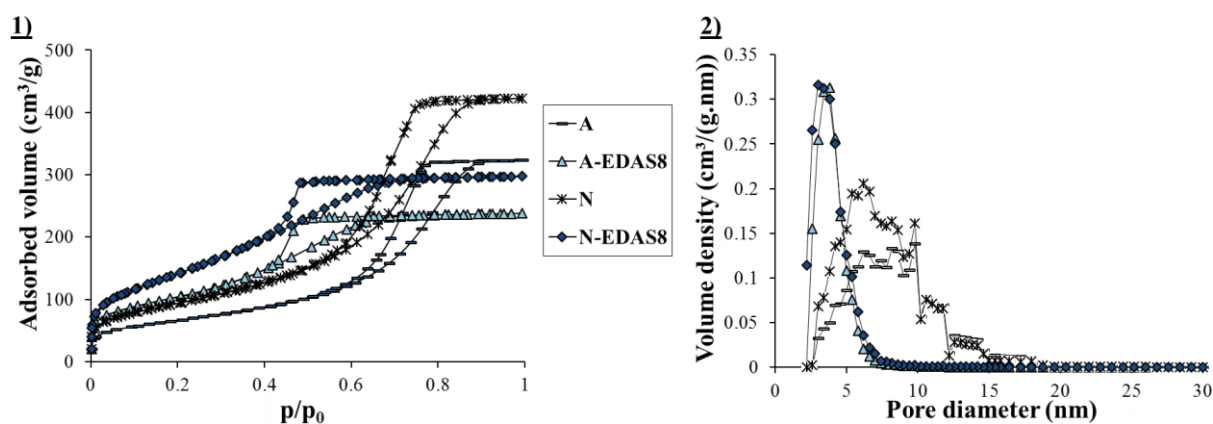


Figure II.13: Nitrogen adsorption-desorption curves (left side) and pore size distribution (right side) of calcined samples A, A-EDAS8, N and N-EDAS8.

Despite showing nitrogen adsorption-desorption isotherms and pore size distributions with similar shapes, it is to notice that the sample N was more porous than sample A (+ 32 % of S_{BET} , + 18 % of V_p , + 25 % of $V_{Dubinin}$, Table II.1).

In corroboration with TEM observations, one can notice that an EDAS addition modified the pore size distribution of both A-EDAS8 and N-EDAS8 samples in a similar way (Figure II.13, Table II.1). Indeed, both samples presented an isotherm hysteresis shifted to a lower p/p_0 value, higher specific surface areas (+ 41 % of S_{BET} for A-EDAS8 and + 36 % of S_{BET} for N-EDAS8), a lower total porous volume and a notable microporous volume increase (- 29 % of V_p and + 30 % of $V_{Dubinin}$ for A-EDAS8; - 48 % of V_p and + 29 % of $V_{Dubinin}$ for N-EDAS8) in comparison with the respective pure alumina samples A and N. The influences of the nature of the aluminum precursor were the following: higher specific surface area and higher microporous volume values for sample N-EDAS8 compared to sample A-EDAS8 (+ 25 % of

S_{BET} , + 23 % of V_{Dubinin}); and almost identical pore size distributions. In this way, whatever the kind of aluminum precursor, doping the sample with EDAS allowed obtaining a narrow pore size distribution centered on 4 nm with a maximal value of 10 nm.

X-Ray diffraction patterns made on calcined samples are shown in Figure II.14. The support crystallite sizes, d_{XRD} , were obtained using the Scherrer equation from the γ - Al_2O_3 ray located at $2\theta = 67.0^\circ$, which corresponds to the (4 4 0) planar direction (Table II.1). According to rigorous XRD techniques, measuring crystallite sizes below 10 nm is not considered to yield quantitative data because of the various approximations required. However, one can notice that for both aluminum precursors, an EDAS addition had a significant influence on the decrease of the γ - Al_2O_3 crystallites size (from 4.5 to 3.6 nm for the method A and from 4.4 to 3.3 nm for the method N). It is also to notice that samples with similar compositions (*i.e.* samples A and N, or samples A-EDAS8 and N-EDAS8) presented similar diffraction patterns.

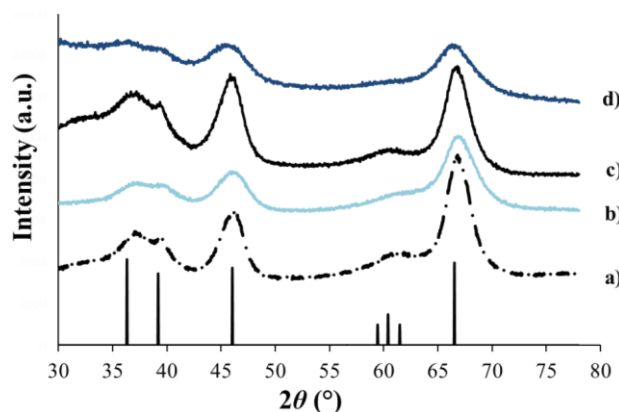


Figure II.14: X-Ray patterns of γ - Al_2O_3 reference rays and calcined samples; a. A, b. A-EDAS8, c. N, d. N-EDAS8.

The apparent density, ρ , of the samples (Table II.1), *i.e.* the density including opening pores accessible to the gas according to IUPAC^[231], were very close to the true density of calcined alumina gels which is about 3.0 g/cm^3 . The true density of calcined silica gels being about 2.2 g/cm^3 ,^[232] this could explain why the samples A-EDAS8 and N-EDAS8 presented lower values than the pure alumina samples.

II.4. DISCUSSION

II.4.1. Influences of the aluminum precursor type on the textural properties of γ - Al_2O_3 supports

In the synthesis conditions used in this work, it seemed that samples starting from two fundamentally different aluminum precursors such as Al-*sec*-butoxide (sample A) and Al-nitrate (sample N) presented equivalent thermal behavior (Figure II.9), morphology (Figures II.10 and II.12) and crystallinity (Figure II.14).

The textural and crystallographic similarities between samples A and N were attributed to the operating variables ($pH = 9.5$, $T = 85^\circ\text{C}$) (cf. Figure II.5). Whereas the aqueous precipitation of aluminum nitrate is known to favor the formation of boehmite (γ - AlOOH)^{[191], [198], [199]}, the

hydrolysis of Al-*sec*-butoxide is in the contrary known to lead to amorphous alumina hydroxide species (Al(OH)₃)^[233]. However, in this case, sample A exhibited X-Ray rays of well-crystallized γ -Al₂O₃ (Figure II.14), which means that the synthesis conditions (*pH*, *T*) used can successfully convert the amorphous alumina hydroxide species into crystalline boehmite.

II.4.2. Modifications of the properties of γ -Al₂O₃ supports caused by EDAS

When EDAS is added during the preparation, similar modifications of the alumina supports can be observed:

1) Though starting from different aluminum precursors, both samples *A-EDAS8* and *N-EDAS8* appeared to be homogeneous (Figures II.11 and II.12). This observation was particularly interesting for sample *A-EDAS8* since the hydrolysis rates of silicon alkoxides are lower than the ones of aluminum alkoxides, which without adequate preparation steps may lead to inhomogeneous materials.^{[126], [234]} Nevertheless, the formation of homogeneous aluminosilicate with different precursor types was shown by Sinko *et al.*^[235]. In line with the present results, the authors showed that starting from a mixture of TEOS+Al(NO₃)₃ or TEOS+Al(OCH(CH₃)₂)₃ reagents in water+ethanol media leads to homogeneous materials with similar textural and crystalline properties. Furthermore, other studies showed that the cogelation of Al-*sec*-butoxide and trimethoxysilane also allowed obtaining homogenous aluminosilicate supports.^[236]

In this case, the formation of homogenous aluminosilicate supports via the method A was assumed to be possible thanks to the pre-hydrolysis step of EDAS before the Al-*sec*-butoxide addition. Indeed, pre-hydrolysis steps are known to counterbalance the difference of alkoxide reactivity, thus allowing the formation of homogeneous cogelled materials.^[234]

The formation of homogenous supports via the method N could be explained by oxolation/olation reactions between hydrolyzed Si-OH groups from EDAS and alumina hydroxide complexes such as Al₂(OH)₂⁴⁺ or Al₃(OH)₄⁵⁺ (Figure II.2). It was supposed that these condensation reactions occurred before the precipitation and led to the formation of submicronic aggregates since the sol remained transparent before the precipitation.

2) Comparing the properties of samples *N-EDAS8* and *A-EDAS8* revealed that starting from Al-nitrate or Al-*sec*-butoxide also led to materials with similar properties. Indeed, despite the lower textural properties (*V*_{Dubinin}, *V*_P and *S*_{BET}) of sample *A-EDAS8* compared to sample *N-EDAS8*, both samples exhibited similar thermal behavior (Figure II.9), morphology (Figure II.10 and Figure II.12) and crystallinity (Figure II.14).

3) Both EDAS modified supports were characterized by a strong modification of their crystalline properties. Indeed, samples *A-EDAS8* and *N-EDAS8* showed less defined alumina X-Ray patterns (Figure II.14) compared to the pure alumina samples (sample A and N). Due to its methoxy groups, the EDAS molecule is classified as a high reactive silicon precursor.^[237] This high reactivity could lead to an insertion of Si atoms inside the bulk alumina structure, thus modifying the γ -Al₂O₃ crystallinity.

4) The most interesting aspect concerning EDAS lied in its influence of the peculiar tuning of the support crystallites. Indeed, for samples *A-EDAS8* and *N-EDAS8*, TEM observations (Figure II.12) revealed the presence of spherical crystallites, which apparently explains the very narrow pore size distribution obtained from the nitrogen adsorption-desorption isotherms (Figure II.13). Two hypotheses were formulated to interpret these observations: i) the high reactivity of the EDAS molecule (presence of methoxy- groups), which could lead to the quick formation of numerous nucleation points; ii) the propylethylenediamine chain (NH₂CH₂CH₂NH(CH₂)₃-) of EDAS molecule, which could act as a template. However, the current results of this section were not sufficient to confirm or deny these hypotheses.

II.5. CONCLUSIONS

In this chapter, the experimental procedure for the synthesis of pure γ -Al₂O₃ supports was established. Though presenting similar textural and crystalline properties, the alumina supports synthesized from Al-nitrate presented higher porous values than the ones obtained from Al-*sec*-butoxide. Since nitrate salts are much easier to handle than alkoxides, these observations permit to validate Al(NO₃)₃ as aluminum source for the future synthesis procedures.

The aqueous sol-gel synthesis of homogeneous γ -Al₂O₃ supports modified by a functionalized silicon precursor (EDAS) was successfully performed with both aluminum sources. Hence, the synthesis of boehmite functionalized with a silicon precursor can be performed thanks to a simple aqueous sol-gel method, which could be an useful alternative to common grafting methods. However, more work needs to be done in order to find a clear explanation for the formation of the spherical crystallites and of the narrow pore size distribution observed for EDAS modified supports.

Chapter III

Influences of the aqueous synthesis way and of the organosilane nature on the physico-chemical properties of alumina supports

- Influences of the EDAS concentration on the textural properties of silicon modified γ -Al₂O₃ supports;
- Impact of the addition step of EDAS during the synthesis of silicon modified γ -Al₂O₃ supports;
- Impact of the nature of the silicon precursor alkoxide groups (methoxy-/ethoxy-) during the synthesis of silicon modified γ -Al₂O₃ supports;
- Investigation of γ -Al₂O₃ supports modified with silicon precursors containing different natures of functional chains (APTMS, EDAS, TOPS or TOOS);
- Resistance of pure and silicon modified γ -Al₂O₃ supports against steaming treatments and high calcination temperatures.

It was observed in Chapter II that the addition of the amino-functionalized silicon precursor called EDAS (3-(2-aminoethylamino)propyltrimethoxysilane) during the aqueous precipitation of aluminum hydroxide had a strong influence on the mesoporous structure and the crystallinity of alumina. In fact, the samples modified with EDAS were less crystallized compared to pure alumina, with smaller γ -Al₂O₃ crystallites, leading to a narrow mesopore size distribution. These modifications could be either due to: 1) the high reactivity of the EDAS molecule (presence of methoxy- groups), which could lead to the quick formation of numerous nucleation points; 2) the propylethylenediamine chain of EDAS molecule, which could act as a template.

In order to get a better understanding of the aqueous coprecipitation between a silicon alkoxide and alumina hydroxide on the final properties of γ -Al₂O₃-SiO₂ supports, different influences are studied in this chapter: 1) the consequence of the EDAS amount and of the EDAS addition step (before, just after or a long time after the precipitation); 2) the influence of the silicon alkoxide reactivity either with the high reactive tetramethoxysilane (TMOS) or with the lower reactive tetraethoxysilane (TEOS); 3) the impact of the chain length and silicon alkoxide nature: 3-aminopropyltrimethoxysilane (APTMS) with a lower chain length and a chemical composition similar to the EDAS molecule (presence of one amino group); trimethoxypropylsilane (TOPS), trimethoxyoctylsilane (TOOS) with different chain lengths and with chains of different chemical compositions (alkyl chains).

The final part of this chapter investigates the resistance of pure alumina support and of alumina supports modified with either TMOS, TEOS or EDAS during thermal ($T = 700, 1000$ or 1200 °C) and hydrothermal ($T = 700$ °C, 10 % vol. H₂O) treatments. The tests were performed in order to get a better understanding of the resistances of the materials in conditions close to the one encountered during catalytic tests.

III.1. INTRODUCTION

III.1.1. Modifications of γ -Al₂O₃ supports with different silicon precursors

The influence of the nature of different silicon precursors during the sol-gel synthesis of SiO₂ is relatively well referenced in the literature. The reactivity of the inorganic precursor is known to have a strong impact: some precursors are more reactive than others, and therefore are more quickly hydrolysable.^{[237], [238]} According to Niederberger & Pinna^[239], “*The chemical reactivity of metal alkoxides towards hydrolysis and condensations depends mainly on the electronegativity of the metal atom, its ability to increase the coordination number, the steric hindrance of the alkoxy group, and on the molecular structure of the metal alkoxide (monomeric or oligomeric)*”. Therefore, any branching of alkoxy groups or lengthening of the chain slows down the hydrolysis rate of the metallic alkoxide. For silicon alkoxides, the reaction rate increases in this order: Si(OⁱPr)₄ < Si(OⁿPr)₄ < Si(OEt)₄ < Si(OMe)₄.^[240] A ¹⁷O NMR study about the hydrolysis and condensation of SiO₂ xerogels made of a mixture of EDAS/TEOS in ethanol-water media was performed by Alié *et al.*^[237]. The authors evidenced the fact that, due

to their high reactivity, the EDAS molecules quickly formed nucleation points onto which TEOS condensed later to form the silica particles.

Most of the synthesis procedures of aluminosilicates use TEOS as silicon precursor.^{[208], [241]–[244]} It is to notice that though the literature about the aluminosilicate synthesis by organic path is thoroughly detailed^{[126], [186], [245]}, there is less information about the synthesis of these materials via an aqueous precipitation.

Some studies were performed in order to functionalize Al₂O₃ supports by grafting alkyl functionalized (octadecyltrimethoxysilane)^[214] or organo-amino functionalized (aminopropyltrimethoxysilane)^[215] silicon alkoxide precursors. However, the influence of such functionalized silicon alkoxides on the properties of γ -Al₂O₃ synthesized by aqueous precipitation is yet to be understood.

III.1.2. Thermal stabilization of γ -Al₂O₃ by silica addition

The thermal stabilization effect of silica on alumina has already been studied, notably by Yoldas *et al.*^[246]. The authors highlighted the fact that low loadings of silica (1-10 wt. %) allowed reducing the sintering of the support and delaying the formation of the α -Al₂O₃ phase, which shows a low specific surface area ($S_{BET} < 20 \text{ m}^2/\text{g}$). These observations have been corroborated by Kosuge *et al.*^[243], which confirmed the fact that a Si doping (ca. 8 mol. %) allows keeping the γ -Al₂O₃ phase up to $T = 1000 \text{ }^\circ\text{C}$, thus providing samples with higher S_{BET} values (260 m²/g instead of 165 m²/g without Si doping) and a narrower pore size distribution (centered on 8 nm instead of 11 nm) compared to pure alumina samples. Pérez *et al.*^[242] studied the influence of the addition method of SiO₂ during the sol-gel synthesis of alumina. The first method involved the addition of a colloidal silica suspension, whereas the second method involved a co-hydrolysis of TEOS with Al-*sec*-butoxide precursor in *sec*-butanol. The authors highlighted the fact that, in comparison to samples prepared by using the silica colloid doping method, samples synthesized with TEOS, and therefore with a more intimate mixing of the Al- and Si- hydrolyzed species, were more inclined to maintain the mesostructure and the γ -Al₂O₃ phase at high temperatures.

Silica addition has also proved to stabilize alumina against sintering under steaming conditions. According to Beguin *et al.*^[247], the formation of a silica layer firmly bonded to the alumina surface was able to fill the anionic vacancies of alumina responsible for the thermal sintering in the presence of water. Johnson *et al.*^[248] highlighted that an addition of Si allowed decreasing the surface area rate loss (m²/(g.h)) up to 50 times compared to the rate loss of non-stabilized alumina samples. According to the authors, SiO₂ replaces the surface hydroxyl groups (Al-OH), which tend to be eliminated during the sintering process to form Al-O-Al bonds. Figure III.1 reminds the evolution of the γ -Al₂O₃ crystalline phase with typical calcination under air at different temperatures.

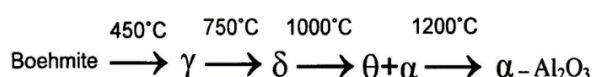


Figure III.1: Evolution of the Al₂O₃ crystalline phase with air calcination at different temperatures.^[249]

III.2. EXPERIMENTAL

III.2.1. General parameters

The prefix “N” refers to the use of ammonium hydroxide (NH₄OH) as precipitant. As already used in the literature, the concentration of the NH₄OH solution was settled to 15 M, *i.e.* 30 wt. %, which corresponds to a *pH* of 12.2.^{[250], [251]} Samples precipitated with different EDAS addition steps either contains the “BA” prefix, which refers to “Before Agitation” or the “AA” prefix, which refers to “After Agitation”. Samples precipitated with different types of silicon alkoxides contain the prefixes “APTMS”, “EDAS”, “TMOS”, “TEOS”, “TOPS” and “TOOS”, which refers to the silicon precursor used (Table III.1).

Table III.1: Name, abbreviation and linear formula of the different silicon precursors.

Name	Abbreviation	Linear formula
3-aminopropyltrimethoxysilane	APTMS	NH ₂ (CH ₂) ₃ Si(OCH ₃) ₃
3-(2-aminoethylamino)propyltrimethoxysilane	EDAS	NH ₂ CH ₂ CH ₂ NH(CH ₂) ₃ Si(OCH ₃) ₃
Tetramethoxysilane	TMOS	Si(OCH ₃) ₄
Tetraethoxysilane	TEOS	Si(OC ₂ H ₅) ₄
Trimethoxypropylsilane	TOPS	CH ₃ (CH ₂) ₂ Si(OCH ₃) ₃
Trimethoxyoctylsilane	TOOS	CH ₃ (CH ₂) ₇ Si(OCH ₃) ₃

The numbers “2, 8, 16” used with the different silicon precursors refer to the theoretical loading of SiO₂ after calcination. The reagent type and amounts are listed in part V of Annex 2.

III.2.2. Synthesis procedures

III.2.2.1. Classic preparation method

The *Classic* synthesis method is depicted in Figure III.2 and is identical to the synthesis procedures presented in Chapter II. Aluminum nitrate, water, ethanol and the silicon precursors were mixed together in a 500 mL bottle. The solution was stirred for $t = 30$ min, after which the precipitation was performed with NH₄OH. As the *pH* increased, the solution became cloudy due to the formation of aluminum hydroxide species [Al(OH)₃]_n. The vessel was then closed and set in an oil bath at $T = 85$ °C for $t = 24$ h under stirring. After the agitation step, the bottle was opened and put into an oven for aging ($t = 24$ h, $T = 85$ °C, $P = 700$ mbar). The resulting gels were washed twice with water and once with ethanol by centrifugation ($t = 15$ min, 10.000 rpm). The gels were thereafter put into an oven for drying ($t = 24$ h, $T = 110$ °C, $P = 900$ mbar). Finally, the dried samples were calcined under air for $t = 4$ h at $T = 500$ °C with a heating rate of 2 °C/min.

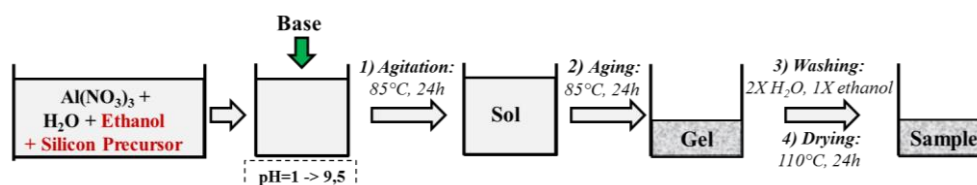


Figure III.2: Scheme of the *Classic* preparation method.

III.2.2.2. Modifications of the Classic method

The steps of the *BA* preparation method (as “Before Agitation”) are shown in Figure III.3. The first step consisted in the dissolution of aluminum nitrate in water. Thereafter, the precipitation step occurred by dropwise adding the precipitant (NH_4OH). After this step, EDAS previously dissolved in ethanol was quickly added to the mixture at room temperature. Following steps were identical to those used during the *Classic* preparation method.

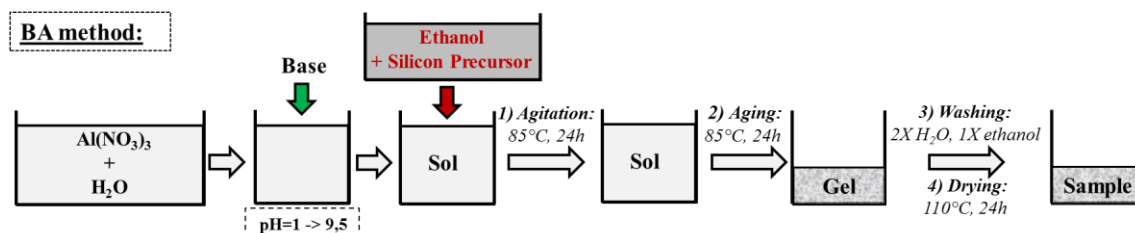


Figure III.3: Scheme of the *BA* preparation method.

The steps of the *AA* preparation method (as “After Agitation”) are depicted in Figure III.4. For this method, aluminum nitrate was dissolved in water, the precipitation step was performed, the bottle was closed and set in the oil bath at $T = 85\text{ }^\circ\text{C}$ for $t = 24\text{ h}$ under stirring. Only then, the mixture of EDAS/ethanol was added and the solution was mixed at room temperature for $t = 30\text{ min}$. Thereafter, the bottle was opened and put into an oven for the aging step. Next steps were identical to the *Classic* method described above.

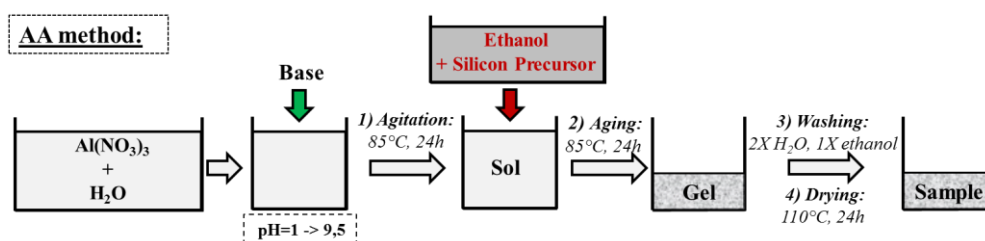


Figure III.4: Scheme of the *AA* preparation method of $\gamma\text{-Al}_2\text{O}_3$ material.

III.2.3. Additional calcination and steaming treatments

The additional calcination treatments were performed under air for $t = 6\text{ h}$ at either $T = 700, 1000$ or $1200\text{ }^\circ\text{C}$, with a heating rate of $5\text{ }^\circ\text{C}/\text{min}$. The steaming treatments were performed thanks to the experimental installation described in Annex 3. The samples were placed in a quartz reactor inside an oven for $t = 6\text{ h}$ at $T = 700\text{ }^\circ\text{C}$. During this time, a flux containing a mix of 10/90 vol. % of $\text{H}_2\text{O}/\text{N}_2$ circulated through the sample.

III.2.4. Characterization techniques

Composition analysis (ICP–AES), thermogravimetric-differential scanning calorimetry (TG–DSC), nitrogen adsorption-desorption (BET), microscope analyses (SEM–BSE, SEM–EDX), transmission electron microscopy (TEM), ^{27}Al Nuclear Magnetic Resonance (^{27}Al NMR) and X-Ray diffraction (XRD) measurements were performed on the samples of this

chapter. The crystallites sizes were calculated by using the Scherrer equation centered on the (4 0 0) ray of γ - Al_2O_3 ($2\theta = 67.0^\circ$) of the XRD spectra. Deeper information about the characterizations techniques and variables quoted are provided in part II of Annex 2. X-Ray references cards are given in part VI of Annex 2.

- Note about the interpretation of the ^{27}Al NMR spectra:

The γ - Al_2O_3 phase is defined by a crystallographic arrangement of its atoms under a spinel structure with a cubic $\text{Fd}\bar{3}m$ space group.^[252] One elementary lattice is composed of 32 oxygen anions organized in a face-centered cubic packing (f.c.c.). The 64/3 Al cations are distributed over the tetrahedral and octahedral interstitial sites in the oxygen sublattice.^{[253], [254]} Figure III.5 shows the tetrahedral and octahedral site positions on a f.c.c. cubic structure and a typical ^{27}Al NMR spectra. ^{27}Al NMR peaks encountered at 6 ppm and 64 ppm are assigned as tetrahedral (Al^{IV}) and octahedral (Al^{VI}) aluminum sites respectively.^{[255], [256]} However, in some particular cases, pentahedral (Al^{V}) aluminum sites can be encountered around 33 ppm. These sites evidence a modification of tetrahedral aluminum clusters to compensate the excess negative charge in the network caused by the substitution of Al^{3+} by Si^{4+} .^{[257]-[259]}

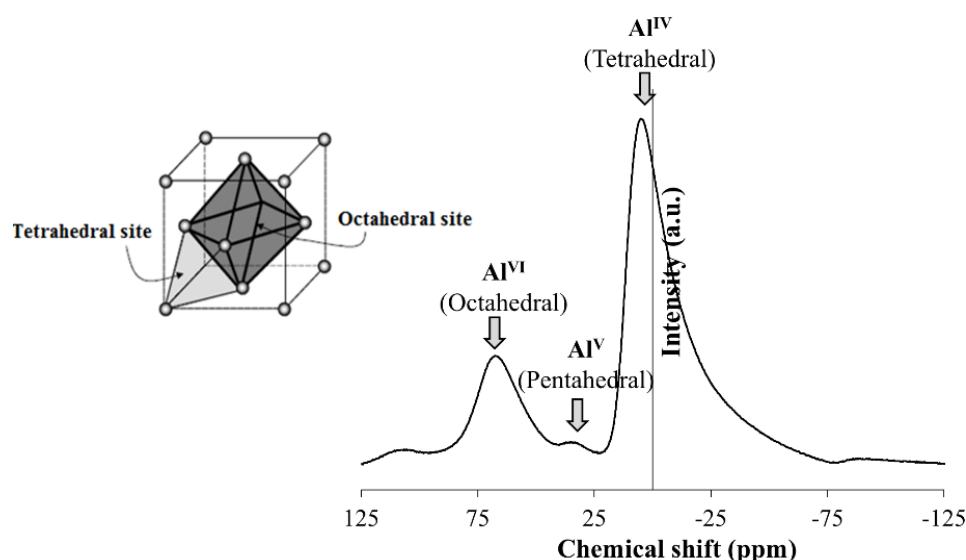


Figure III.5: Visual presentation of tetrahedral and octahedral sites in face-centered cubic (f.c.c.) crystal lattice (left side) and typical ^{27}Al NMR spectra of γ - Al_2O_3 modified with SiO_2 (right side).

III.3. RESULTS AND DISCUSSION

III.3.1. Formation, composition and morphology of Al_2O_3 - SiO_2 materials

III.3.1.1. Precipitation curves

Figure III.6 shows the precipitation curves of samples N , N - $\text{TMOS}8$, N - $\text{TEOS}8$ and N - $\text{EDAS}8$. All samples presented very similar curves defined by three different precipitation fields.¹ No significant influence of the reactivity of the silicon precursors was observed.

¹: More information about the precipitation fields in part II.3. of Chapter II.

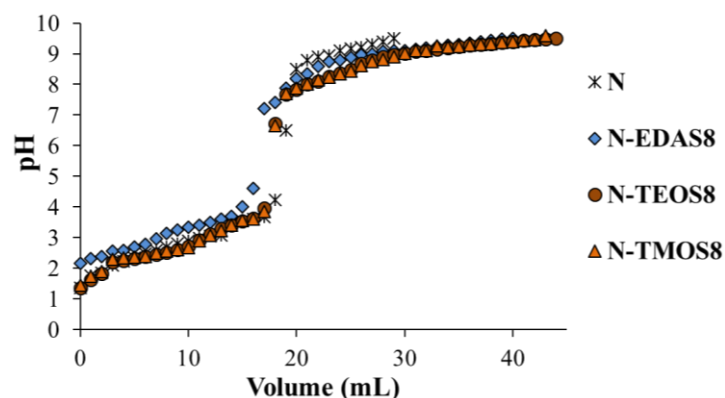


Figure III.6: Precipitation curves for samples *N*, *N-EDAS8*, *N-TMOS8* and *N-TEOS8*.

III.3.1.2. Thermal behaviors

Figure III.7 shows the TG-DSC curves for pure alumina gel (sample *N*) and for alumina gels modified with silicon precursors without a functionalized chain (samples *N-TMOS8* and *N-TEOS8*).

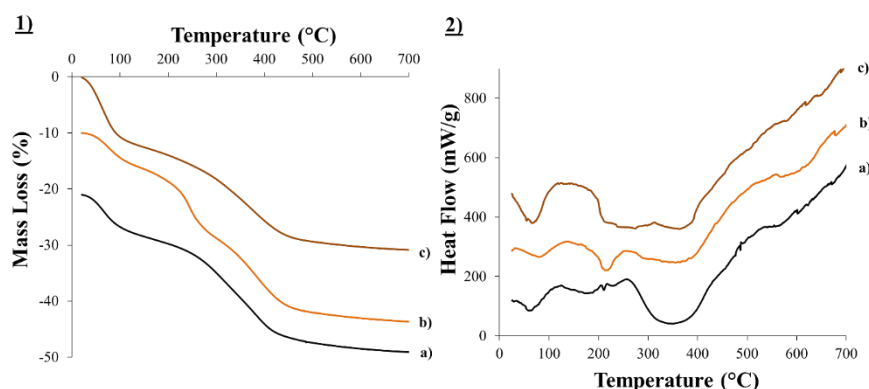


Figure III.7: TG-DSC curves for dried samples made with silicon precursors without a functionalized chain; a. *N*, b. *N-TMOS8* and c. *N-TEOS8*.

In Figure III.7, all samples exhibited a similar behaviour whatever the nature of the silicon precursor used: 1) a first endothermic peak situated at about $T = 100$ °C, which corresponded to the evaporation of water; 2) a second broad peak located between $T = 250$ °C and $T = 450$ °C, which corresponded to the transformation of boehmite into $\gamma\text{-Al}_2\text{O}_3$ ^{[226], [228]}; 3) from $T = 450$ °C to $T = 800$ °C, apparition of a very broad and continuous peak for all the samples, corresponding to the slow evacuation of hydroxyls groups retained in the alumina network^[228].

Figure III.8 shows the TG-DSC curves for pure alumina gel (sample *N*) and for alumina gels modified with silicon precursors containing a functionalized chain (samples *N-APTMS8*, *N-EDAS8*, *N-TOPS8* and *N-TOOS8*).

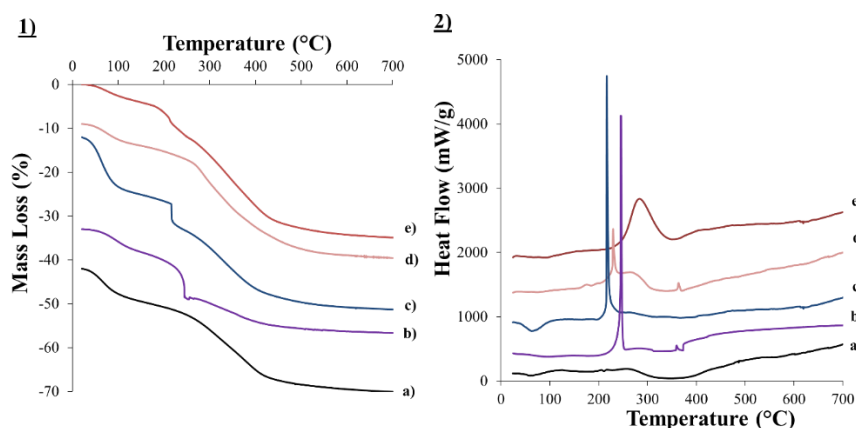


Figure III.8: TG-DSC curves for dried samples made with silicon precursors with a functionalized chain; a. *N*, b. *N-APTMS8*, c. *N-EDAS8*, d. *N-TOPS8*, e. *N-TOOS8*.

The organic compounds of the chains of APTMS ($\text{NH}_2(\text{CH}_2)_3-$) and of EDAS ($\text{NH}_2\text{CH}_2\text{CH}_2\text{NH}(\text{CH}_2)_3-$) presented only one sharp degradation peak located between $T = 210$ °C and $T = 250$ °C (samples *N-APTMS8* and *N-EDAS8*). The degradation of the organic compounds of the alkyl chain of the samples synthesized with TOPS ($\text{CH}_3(\text{CH}_2)_2-$) or with TOOS ($\text{CH}_3(\text{CH}_2)_7-$) were evidenced by broad peaks situated between $T = 200$ and $T = 400$ °C.

III.3.1.3. Compositions of samples

Table III.2 lists the theoretical and actual Al_2O_3 and SiO_2 weight loadings for all calcined samples. It is to notice that the actual SiO_2 and Al_2O_3 loadings were in accordance with the theoretical loadings (error of ± 1 wt. %) for all calcined samples except for samples *N-EDAS16* and *AA-EDAS8*.

Table III.2: Theoretical and actual SiO_2 and Al_2O_3 loadings for calcined $\gamma\text{-Al}_2\text{O}_3$ supports and $\gamma\text{-Al}_2\text{O}_3$ supports modified with a silicon precursor.

Samples	SiO_2		Al_2O_3	
	Theo. (wt. %)	Exp. (wt. %)	Theo. (wt. %)	Exp. (wt. %)
N	0	0	100	100
N-APTMS8	8.3	8.3	91.7	91.7
N-EDAS2	2.1	2.5	97.9	98.0
N-EDAS8	8.3	8.5	91.7	91.5
N-EDAS16	16.7	14.0	83.3	86.0
BA-EDAS8	8.3	8.0	91.7	92.0
AA-EDAS8	8.3	5.5	91.7	94.5
N-TMOS8	8.3	9.0	91.7	91.0
N-TEOS8	8.3	9.0	91.7	91.0
N-TOPS8	8.3	8.2	91.7	91.8
N-TOOS8	8.3	8.1	91.7	91.9

Noteworthy, sample *N-EDAS16* presented a SiO_2 loading of 14.0 wt. % instead of 16.7 wt. % and sample *AA-EDAS8* presented a SiO_2 loading of 5.5 wt. % instead of 8.3 wt. %. One can notice that these samples were prepared twice and showed similar inadequacies. Furthermore, it was noted that, whereas the washing solutions were clear for all the other samples, the washing solutions of samples *N-EDAS16* and *AA-EDAS8* were slightly cloudy.

In the aim of identifying the step where the EDAS loss occurred, additional ICP-AES measurements were performed on samples *N-EDAS16* and *AA-EDAS8*: 1) the composition of the gel was measured after the aging step in order to determine if the SiO₂ loss was due to EDAS evaporation; 2) the composition of the washing solutions was analyzed, in order to determine if the SiO₂ was eliminated during the washing steps. Table III.3 shows the Al/Si ratio of the gels after the aging step, and the concentrations as well as the Al/Si ratio of the sample residues (Al₂O₃ and SiO₂) evacuated in the washing solutions. It is to notice that for all the other samples, the concentrations of residues in the washing solutions were below 10 mg/L, thus confirming that only the samples *N-EDAS16* and *AA-EDAS8* were problematic.

Sample *N-EDAS16* did not present any EDAS loss by evaporation during the aging step since the Al/Si ratio was the same before and after the aging step. In contrary, the washing solutions of sample *N-EDAS16* presented large amounts of Al₂O₃ and SiO₂ (1900 and 410 mg/L respectively). For this sample, the Al/Si ratio of the residues evacuated in the washing solution was lower than the initial Al/Si ratio (4.8 instead of 5.9), which means that the compounds evacuated during the washing steps were slightly richer in SiO₂ than in Al₂O₃.

Table III.3: SiO₂ and Al₂O₃ loadings after the aging step, and in collected washing solutions for samples *N-EDAS-16* and *AA-EDAS-8*.

Samples	Initial Sol	Aged gel	Washing solutions		
	Al/Si Ratio	Al/Si Ratio	SiO ₂ (mg/L)	Al ₂ O ₃ (mg/L)	Al/Si ^a (Washing)
<i>N-EDAS16</i>	5.9	5.9	410	1900	4.8
<i>AA-EDAS8</i>	13.1	16.6	110	90	0.9

^a: Al/Si is equal to the ratio of the concentrations of Al₂O₃ and SiO₂ in washing solutions.

For sample *AA-EDAS8*, a small amount of EDAS was evaporated during the aging step since the Al/Si ratio of the gel highly increased after the aging step (16.6 instead of 13.1). Furthermore, the washing solution of sample *AA-EDAS8* contained 110 mg/L of Al₂O₃ and 90 mg/L of SiO₂, which evidenced the loss of EDAS molecules. The concentration of residues was much lower than for sample *N-EDAS16*. Furthermore, the Al/Si ratio of the compounds evacuated was very different from the Al/Si ratio of the initial sol (0.9 instead of 13.1). So, for sample *AA-EDAS8*, much more SiO₂ than Al₂O₃ was evacuated in the washing solutions.

III.3.1.4. Morphology of the supports

SEM-BSE and SEM-EDX measurements were performed for each sample in order to get an overview of the micro-aspects of the samples and to confirm the homogeneity of composition. It was observed that all samples were homogeneous and presented microscopic morphologies similar to samples *N* and *N-EDAS8* described in Chapter II: the samples consisted of a dense aggregation of micrograins whose sizes were situated between 0.5 and 5 μm.

III.3.2. Effect of EDAS concentration on Al₂O₃-SiO₂ materials

Figure III.9 shows the morphology of the γ -Al₂O₃ crystallites obtained for samples synthesized with different amounts of EDAS (samples *N*, *N-EDAS2*, *N-EDAS8*, *N-EDAS16*). It was observed that when the concentration of EDAS increased, the crystallites of the samples became smaller and more elliptical, leading to a more dense and a more organized structure compared to pure alumina (sample *N*).

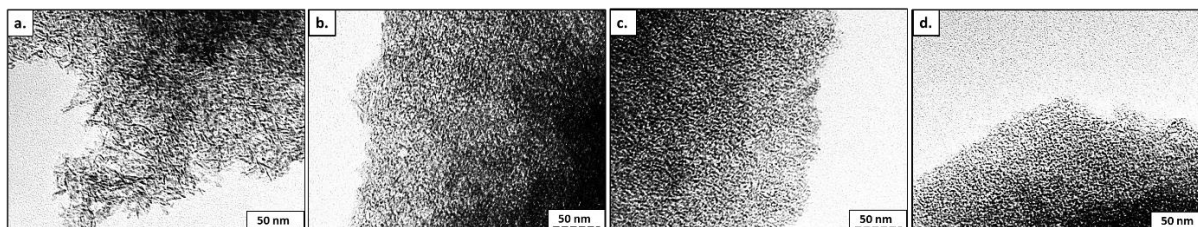


Figure III.9: TEM pictures of calcined samples synthesized with different concentrations of EDAS; a. *N*, b. *N-EDAS2*, c. *N-EDAS8*, d. *N-EDAS16*; 245.000 X.

Similar trends were observed on the nitrogen adsorption-desorption isotherms and the associated mesopore size distributions of the samples (Figure III.10). The increase of the amount of EDAS lead to a narrower and smaller mesopore size distribution. Furthermore, in that case, the total pore volume decreased ($V_{p,N-EDAS2} = 0.5 \text{ cm}^3/\text{g}$ whereas $V_{p,N-EDAS16} = 0.2 \text{ cm}^3/\text{g}$) and the microporous volume slightly increased ($V_{Dubinin,N-EDAS2} = 0.16 \text{ cm}^3/\text{g}$ whereas $V_{Dubinin,N-EDAS16} = 0.18 \text{ cm}^3/\text{g}$) (Table III.4). Despite the fact that the specific surface area was highly increased by the addition of a small amount of EDAS ($S_{BET,N} = 340 \text{ m}^2/\text{g}$ whereas $S_{BET,N-EDAS2} = 490 \text{ m}^2/\text{g}$), samples *N-EDAS8* and *N-EDAS16* reached a maximal S_{BET} value of $530 \text{ m}^2/\text{g}$.

Table III.4: Textural and crystallographic properties of the calcined samples synthesized with different concentrations of EDAS.

Samples	S_{BET} (m ² /g)	V_p (cm ³ /g)	S_{meso} (m ² /g)	$V_{Dubinin}$ (cm ³ /g)	ρ (cm ³ /g)	d_{XRD} (nm)
N	340	0.6	280	0.12	2.97	4.4
N-EDAS2	490	0.5	305	0.16	2.86	3.6
N-EDAS8	530	0.3	225	0.17	2.84	3.3
N-EDAS16	530	0.2	130	0.18	2.71	3.2

S_{BET} : specific surface area; V_p : porous volume; S_{meso} : mesoporous surface area; $V_{Dubinin}$: microporous volume; ρ : apparent density; d_{XRD} : size of γ -Al₂O₃ crystallites determined by XRD.

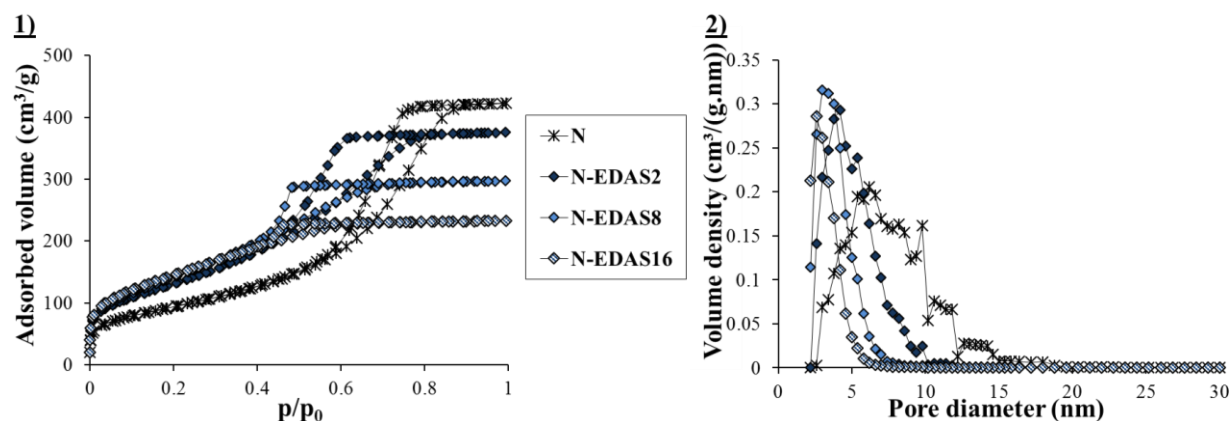


Figure III.10: Nitrogen adsorption-desorption isotherms (left side) and mesopore size distribution (right side) of calcined samples synthesized with different concentrations of EDAS: samples *N*, *N-EDAS2*, *N-EDAS8* and *N-EDAS16*.

It was observed in Figure III.11, that as the amount of EDAS increased, the samples presented smaller crystallite sizes: $d_{XRD,N-EDAS2} = 3.6$ nm, $d_{XRD,N-EDAS8} = 3.3$ nm and $d_{XRD,N-EDAS16} = 3.2$ nm (Table III.4). Following the same trend, when the content of EDAS increased, the Al^V NMR peaks were more visible, which expresses a qualitatively higher incorporation of Si atoms into the alumina bulk (Figure III.11).

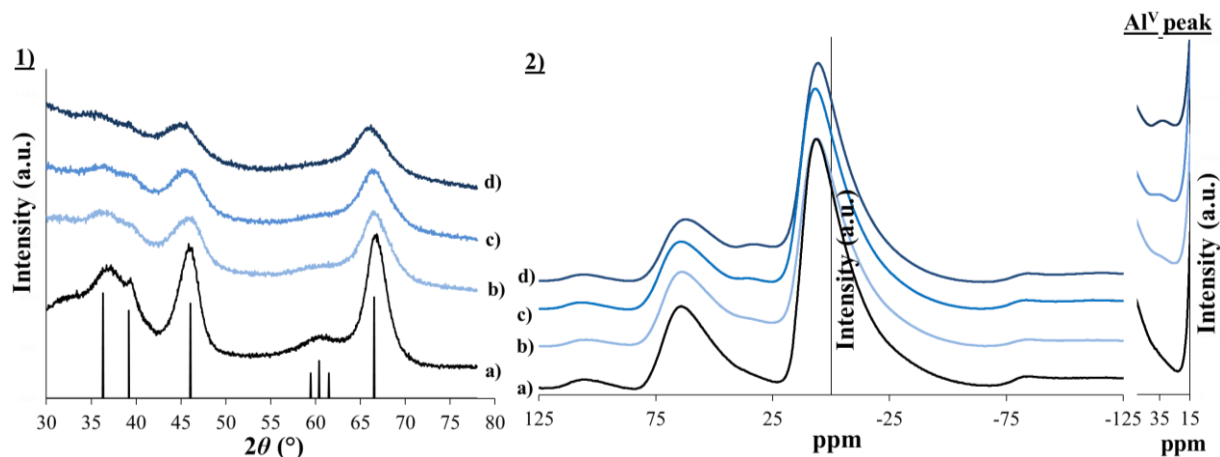


Figure III.11: X-Ray patterns of γ - Al_2O_3 reference rays and calcined samples (left side); and ^{27}Al NMR spectra for calcined samples synthesized with different concentrations of EDAS (right side); a. *N*, b. *N-EDAS2*, c. *N-EDAS8* and d. *N-EDAS16*.

Increasing the amount of EDAS lead to smaller and more spherical γ - Al_2O_3 - SiO_2 crystallites. Based on the results obtained by Alié et al.^[237], it was hypothesized that as the EDAS concentration increased, there was a higher amount of nucleation points, which would result in the formation of smaller γ - Al_2O_3 - SiO_2 crystallites. Therefore, these smaller crystallites formed more compact aggregates with smaller voids, which explains the decrease of the pore volume (V_p) and the narrower mesopore size distribution obtained. Furthermore, the smaller crystallites having a lower volume, this would explain why the microporous volume ($V_{Dubinin}$) and the specific surface area were higher.

However, above a SiO_2 loading equal to 8 wt. % (sample *N-EDAS8*), the increase of the amount of EDAS had no more influence on the textural properties: indeed, samples *N-EDAS8* and *N-EDAS16* showed similar crystallite sizes (3.3 nm and 3.2 nm) and same specific surface areas (530 m²/g) (Table III.4). Furthermore, when the SiO_2 loading was above 14 wt. % (sample *N-EDAS16*), a non-negligible amount of EDAS was evacuated during the washing steps, which led to a high loss of SiO_2 (Tables III.2 and III.3). Since Al_2O_3 was also present in the washing solutions, it was assumed that in the case of sample *N-EDAS16*, only a limited amount of EDAS molecules could be integrated into the bulk of the alumina crystallites. Beyond this critical concentration of EDAS, it was supposed that very small (< 2 nm) and Si-rich nuclei were formed and that, due to their small sizes, these aggregates were more sensible towards colloid forces than to centrifuge forces. As a result, these small crystallites were not retained by the support during the washing steps. This hypothesis was strengthened by the presence of blurred washing solutions for this sample.

In this way, in the next chapters, the amount of EDAS added during the synthesis of supports should not exceed the amount used for the synthesis of sample *N-EDAS8*.

III.3.3. Influences of the addition step of EDAS on $\text{Al}_2\text{O}_3\text{-SiO}_2$ materials

Figure III.12 shows the morphology of the $\gamma\text{-Al}_2\text{O}_3\text{-SiO}_2$ crystallites obtained for samples prepared with different EDAS addition steps: at the same time as aluminum nitrate (sample *N-EDAS8*), before the aging step (sample *BA-EDAS8*) and after the aging step (sample *AA-EDAS8*). It was observed that the shape and the organization of the crystallites of sample *BA-EDAS8* (Figure III.12-c) were similar to sample *N-EDAS8* (Figure III.12-b). In contrary, the organization and the shape of the crystallites of sample *AA-EDAS8* (Figure III.12-d) were more alike sample *N* (Figure III.12-a).

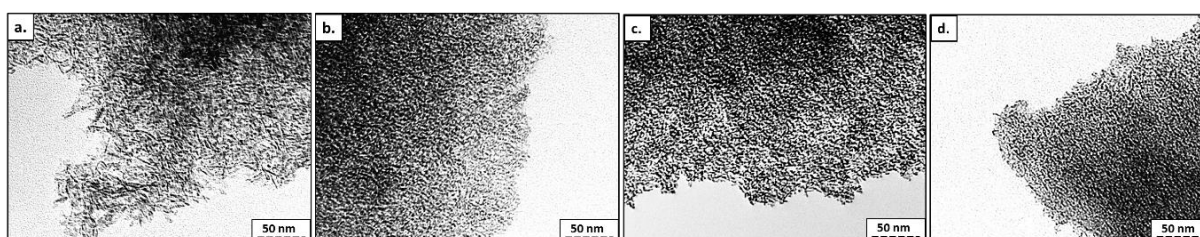


Figure III.12: TEM pictures of calcined samples synthesized with different EDAS addition steps; a. *N*, b. *N-EDAS8*, c. *BA-EDAS8*, d. *AA-EDAS8*; 245.000 X.

Figure III.13 shows the nitrogen-adsorption isotherms and the mesopore size distribution of samples *N*, *N-EDAS8*, *BA-EDAS8* and *AA-EDAS8*. It was observed that the addition step of EDAS had an influence on the final support texture. Adding EDAS just before the agitation step (sample *BA-EDAS8*) led to similar isotherm shapes, pore size distribution and textural values (S_{BET} and V_p) as for sample *N-EDAS8*. However, this was not the case when EDAS was added after the agitation step (sample *AA-EDAS8*). Indeed, with its lower specific surface area value ($S_{BET,AA-EDAS8} = 420 \text{ m}^2/\text{g}$) and its higher pore volume ($V_{p,AA-EDAS8} = 0.4 \text{ cm}^3/\text{g}$), sample *AA-EDAS8* presented intermediate textural properties between sample *N* and sample *N-EDAS8* (Table III.5).

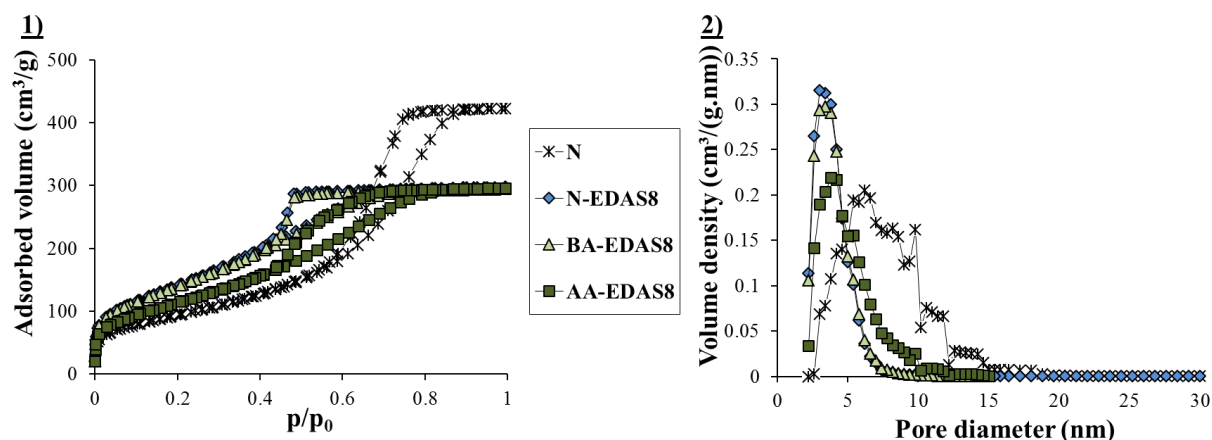


Figure III.13: Nitrogen adsorption-desorption isotherms (left side) and mesopore size distribution (right side) of calcined samples synthesized with different EDAS addition steps: samples *N*, *N-EDAS8*, *BA-EDAS8* and *AA-EDAS8*.

Table III.5: Textural and crystallographic properties of the calcined samples synthesized with different EDAS addition steps.

Samples	S_{BET} (m ² /g)	V_p (cm ³ /g)	S_{meso} (m ² /g)	$V_{Dubinin}$ (cm ³ /g)	ρ (cm ³ /g)	d_{XRD} (nm)
N	340	0.6	280	0.12	2.97	4.4
N-EDAS8	530	0.3	225	0.17	2.84	3.3
BA-EDAS8	520	0.3	220	0.17	2.73	3.5
AA-EDAS8	420	0.4	230	0.14	2.89	4.3

S_{BET} : specific surface area; V_p : porous volume; S_{meso} : mesoporous surface area; $V_{Dubinin}$: microporous volume; ρ : apparent density; d_{XRD} : size of crystallites determined by XRD.

It was observed in Figure III.14 and Table III.5 that, similarly to the textural observations, the addition step of EDAS had an influence on the microstructure of the samples. In this way, when EDAS was added just before the agitation time (sample *BA-EDAS8*), it led to a microstructural profile similar to sample *N-EDAS8* (large X-Ray rays characteristics of small γ -Al₂O₃ crystallites and presence of Al^{IV} NMR peak). On the opposite, when EDAS was added after the agitation time (sample *AA-EDAS8*), it led to a microstructural profile similar to sample *N* (narrow X-Ray rays characteristics of large γ -Al₂O₃ crystallites and no presence of Al^{IV} NMR peak).

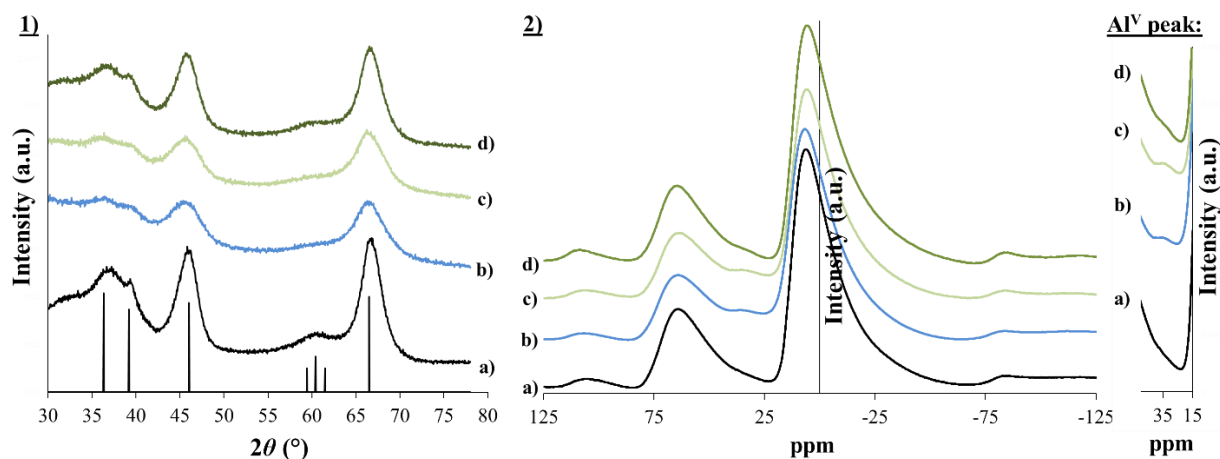


Figure III.14: X-Ray patterns of γ -Al₂O₃ reference rays and calcined samples (left side); and ²⁷Al NMR spectra for calcined samples synthesized with different EDAS addition steps (right side); a. *N*, b. *N-EDAS8*, c. *BA-EDAS8* and d. *AA-EDAS8*.

In light of the sizes, the shapes and the organization of the γ -Al₂O₃-SiO₂ crystallites, and of the textural properties of the materials, it can be noticed that samples synthesized with addition of EDAS either before or just after the precipitation step (samples *N-EDAS8* and *BA-EDAS8*) were very similar. In contrary, sample *AA-EDAS8* showed crystallographic and textural properties very close to pure alumina (sample *N*).

Furthermore, in the opposite of samples *N-EDAS8* and *BA-EDAS8*, sample *AA-EDAS8* presented a significant loss of SiO₂ during both aging and washing steps (Tables III.2 and III.3). Hence, it was assumed that the loss of SiO₂ encountered for sample *AA-EDAS8* was due to an insufficient anchoring of EDAS molecules on aluminum hydroxide nanocrystallites during the agitation step. Consequently, this led to the evacuation of the non-fixed EDAS molecules during the aging and washing steps. This assumption was strengthened by the solid-state ²⁷Al NMR spectra (Figure III.14-d), which did not show any modification of the aluminum atoms environment for sample *AA-EDAS8*, meaning that Si atoms did not incorporate inside the bulk

alumina. In contrary, samples *N-EDAS8* and *BA-EDAS8* presented a high degree of Si incorporation since visible Al^V peaks were present on their NMR spectra (Figure III.14-b and III.14-c). These modifications of the bulk alumina were corroborated by the X-Ray diffraction spectra. Whereas the less defined Al_2O_3 patterns of the X-Ray spectra of samples *N-EDAS8* and *BA-EDAS8* evidenced an alteration of the $\gamma-Al_2O_3$ crystallinity by SiO_2 , in contrary, sample *AA-EDAS8* exhibited an unaltered and well-crystallized $\gamma-Al_2O_3$ pattern (Figure III.14-d).

From these observations, it was concluded that even if the aluminum hydroxide crystallites were formed instantly during the addition of precipitant, a modifying reagent such as EDAS added just after the precipitation step was still able to strongly interact with the bulk alumina structure. This was possible thanks to the structural reorganizations occurring during the agitation step.^{[190], [191]} However, after the long agitation step, the alumina became stable, which explains why EDAS molecules had very limited influence on the bulk structure and could be grafted on the alumina crystallites only up to a SiO_2 loading equal to 5.5 wt. % (sample *AA-EDAS8*, Table III.2).

It can be retained from these results that the synthesis of alumina samples modified with EDAS must be performed always with an addition of EDAS before the precipitation and agitation step (similarly as the synthesis of sample *N-EDAS8*).

III.3.4. Influences of the silicon alkoxide reactivity on $Al_2O_3-SiO_2$ materials

Figure III.15 shows the TEM pictures of pure alumina (sample *N*), of alumina modified with tetramethoxysilane (sample *N-TMOS8*), of alumina modified with tetraethoxysilane (sample *N-TEOS8*) and of alumina modified with EDAS (sample *N-EDAS8*). It was observed that samples *N-TMOS8* and *N-TEOS8* presented similar aspects as sample *N*, *i.e.* platelet-like crystallites assembled in a random way, which is known to be characteristic of $\gamma-Al_2O_3$ supports synthesized by sol-gel methods.^[192] Furthermore, it is to notice that the typical morphology of sample *N-EDAS8* was not visible for the other samples.

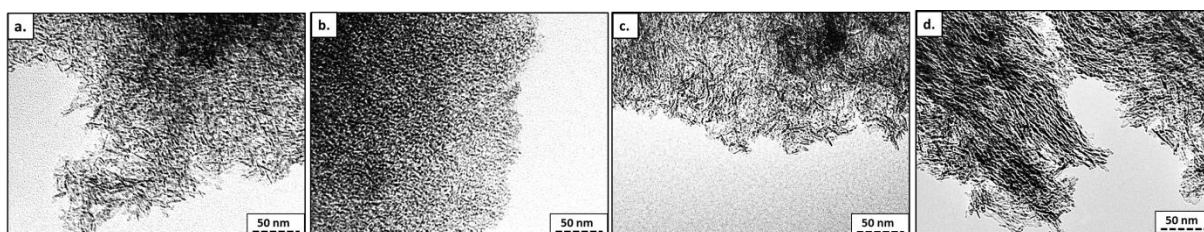


Figure III.15: TEM pictures of calcined samples synthesized with silicon alkoxides containing methoxy- or ethoxy-groups; a. *N*, b. *N-EDAS8*, c. *N-TMOS8*, d. *N-TEOS8*; 245.000 X.

It was observed in Figure III.16 and Table III.6 that, in contrary to the addition of EDAS, the addition of TMOS or TEOS had much less influence on the mesoporosity of the supports. Indeed, in contrary to sample *N-EDAS8* which presented a narrow mesopore size distribution centered on 4 nm, samples *N-TMOS8* and *N-TEOS8* showed a broad pore size distribution very similar to what was obtained for sample *N*. Whereas sample *N-EDAS8* presented peculiar and significant differences in its textural properties, the specific surface area, S_{BET} , microporous

volume, $V_{Dubinin}$, and total pore volume, V_p , values of samples N - $TMOS8$ and N - $TEOS8$ were in contrary very close to the values obtained for sample N (Table III.6).

Table III.6: Textural and crystallographic properties of calcined samples synthesized with silicon alkoxides containing methoxy- or ethoxy- groups.

Samples	S_{BET} (m ² /g)	V_p (cm ³ /g)	S_{meso} (m ² /g)	$V_{Dubinin}$ (cm ³ /g)	ρ (cm ³ /g)	d_{XRD} (nm)
N	340	0.6	280	0.12	2.97	4.4
N-EDAS8	530	0.3	225	0.17	2.84	3.3
N-TMOS8	370	0.5	270	0.14	2.93	3.8
N-TEOS8	340	0.6	240	0.12	2.92	4.3

S_{BET} : specific surface area; V_p : porous volume; S_{meso} : mesoporous surface area; $V_{Dubinin}$: microporous volume; ρ : apparent density; d_{XRD} : size of crystallites determined by XRD.

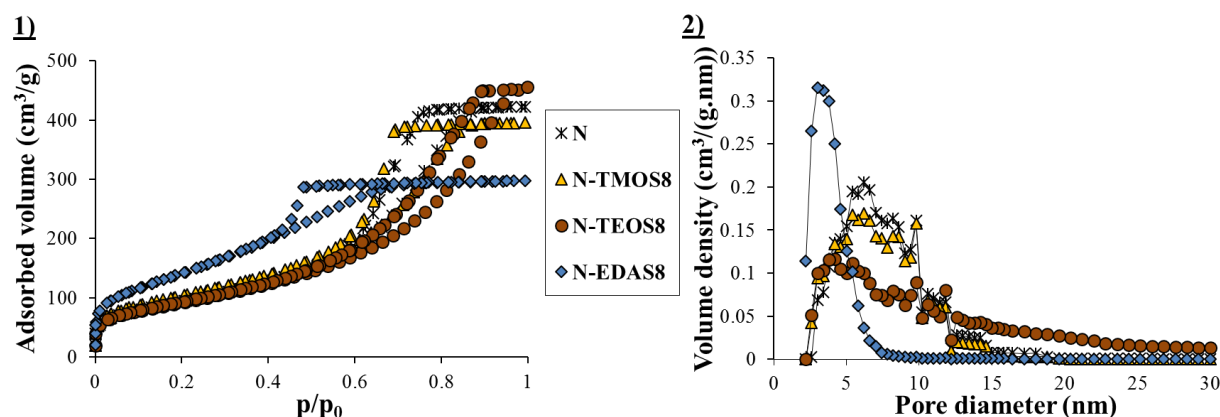


Figure III.16: Nitrogen adsorption-desorption isotherms (left side) and mesopore size distribution (right side) of calcined samples synthesized with silicon alkoxides containing methoxy- or ethoxy- groups; samples N , N - $TMOS8$, N - $TEOS8$ and N - $EDAS8$.

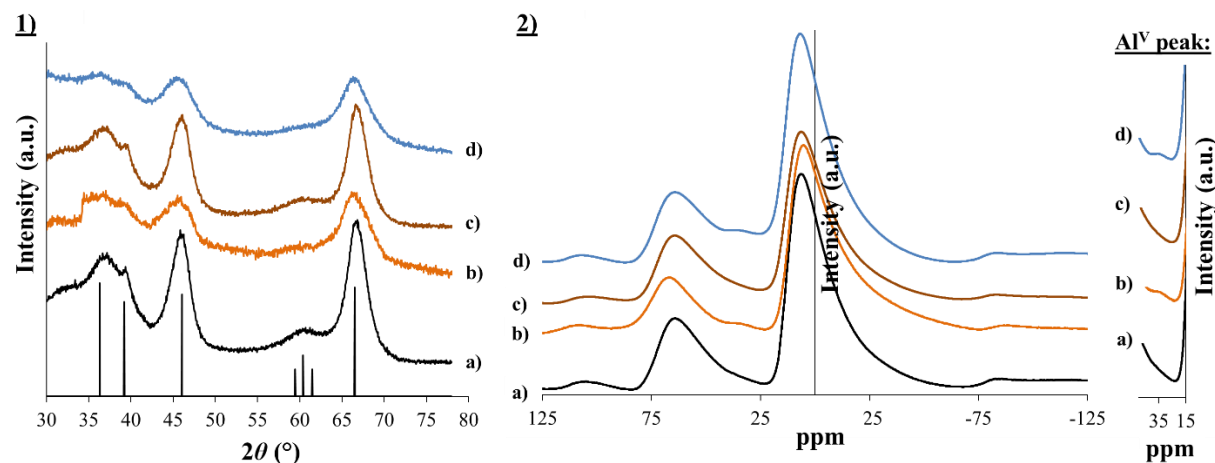


Figure III.17: X-Ray patterns of γ - Al_2O_3 reference rays and calcined samples (Left); and ^{27}Al NMR spectra of calcined samples synthesized with silicon alkoxides with methoxy- or ethoxy- groups (Right): a. N , b. N - $TMOS8$, c. N - $TEOS8$ and d. N - $EDAS8$.

Figure III.17 shows some crystallographic differences between samples N - $TMOS8$ and N - $TEOS8$. In this way, sample N - $TEOS8$ presented a microstructure very close to pure alumina (sample N) with narrow rays characteristic of well crystallized alumina, large γ - Al_2O_3 crystallites ($d_{XRD,N-TEOS8} = 4.3$ nm whereas $d_{XRD,N} = 4.4$ nm, Table III.6) and no Al^V peaks visible on its NMR spectra. In contrary, sample N - $TMOS8$ presented a microstructure very close to sample N - $EDAS8$, i.e. large rays characteristic of more amorphous alumina, small γ - Al_2O_3

crystallites ($d_{XRD,N-TMOS8} = 3.8$ nm whereas $d_{XRD,N-EDAS8} = 3.3$ nm, Table III.6) and Al^v peaks on its NMR spectra.

The degree of modification of the alumina crystallinity by a silicon precursor appeared to be linked to the nature of the silicon precursor used. Indeed, samples *N-EDAS8* and *N-TMOS8* presented important modifications of their crystallinity due to the insertion of Si atoms in their alumina bulk structures. However, this was not the case for sample *N-TEOS8*, which presented X-Ray and NMR spectra similar to pure alumina sample (Figure III.17-c). These observations can be explained by the difference of the reactivity between silicon alkoxides with methoxy groups (-OCH₃), such as TMOS or EDAS, and silicon alkoxides with ethoxy groups (-OCH₂CH₃), such as TEOS. Indeed, the methoxy groups, due to less steric hindrance, are more easily hydrolyzed and therefore more reactive than the ethoxy group.^{[237]–[239]} Hence, the higher reactivity of silicon precursors with methoxy groups allowed a better incorporation of Si atoms during the formation of bulk alumina hydroxide, thus enhancing the modification of the crystallinity of alumina after calcination. However, it is important to note, that if the degree of Si incorporation was low (sample *N-TEOS8*) or high (sample *N-TMOS8*), the shape of the γ -Al₂O₃-SiO₂ crystallites of samples *N-TMOS8* and *N-TEOS8* was nevertheless similar to what was obtained for pure alumina. In this way, the spherical crystallite shape obtained for sample *N-EDAS8* seemed to be caused only by the presence of the functionalized chain of EDAS.

III.3.5. Influences of the length and composition of the silicon alkoxide functional chain on the properties of Al₂O₃-SiO₂ materials

TEM pictures (Figure III.18) revealed different morphologies depending on the kind and the length of the functionalized group in the silicon alkoxides.

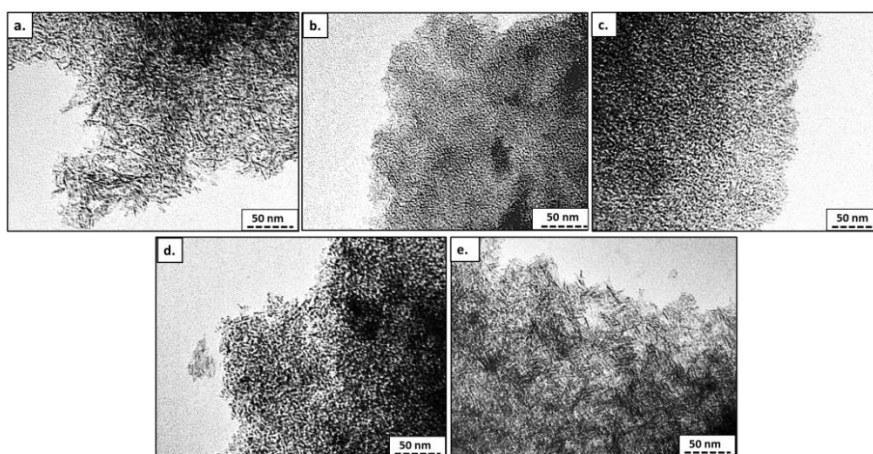


Figure III.18: TEM pictures of calcined samples synthesized with silicon alkoxides functionalized with amino- or alkyl groups; a. *N*, b. *N-APTMS8*, c. *N-EDAS8*, d. *N-TOPSS8*, e. *N-TOOS8*; 245.000 X.

Sample *N-APTMS8*, whose function is an organo-amino chain (NH₂(CH₂)₃-), showed similar morphologies as sample *N-EDAS8*, *i.e.* a well and compacted agglomeration of small and spherical crystallites. However, the crystallites of sample *N-APTMS8* (Figure III.18-b) were smaller than for sample *N-EDAS8* (Figure III.18-c).

Table III.7: Textural and crystallographic properties of calcined samples synthesized with silicon alkoxides functionalized with amino- or alkyl groups.

Samples	S_{BET} (m ² /g)	V_p (cm ³ /g)	S_{meso} (m ² /g)	$V_{Dubinin}$ (cm ³ /g)	ρ (cm ³ /g)	d_{XRD} (nm)
N	340	0.60	280	0.12	2.97	4.4
N-APTMS8	420	0.24	100	0.13	2.67	2.7
N-EDAS8	530	0.31	225	0.17	2.84	3.3
N-TOPS8	425	0.29	170	0.14	2.65	3.0
N-TOOS8	325	0.32	220	0.11	2.88	4.3

S_{BET} : specific surface area; V_p : porous volume; S_{meso} : mesoporous surface area; $V_{Dubinin}$: microporous volume; ρ : apparent density; d_{XRD} : size of crystallites determined by XRD.

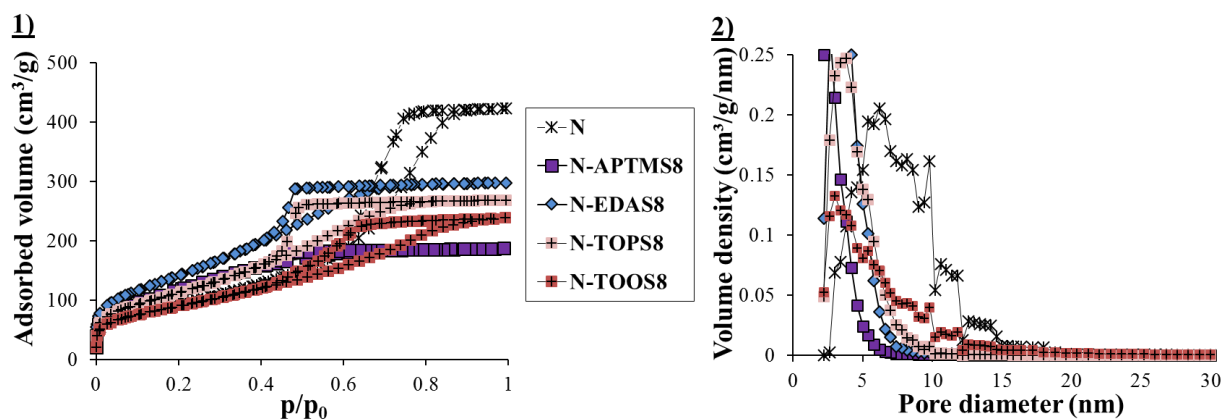


Figure III.19: Nitrogen adsorption-desorption isotherms (left side) and mesopore size distribution (right side) of calcined samples synthesized with silicon alkoxides functionalized with amino- or alkyl groups: samples *N*, *N-APTMS8*, *N-EDAS8*, *N-TOPS8* and *N-TOOS8*.

In Figure III.19, sample *N-APTMS8* presented a narrow pore distribution very similar to sample *N-EDAS8*. However, the distribution of the mesopore sizes was centered on a smaller value: around 3 nm for sample *N-APTMS8* in contrary to 4 nm for sample *N-EDAS8*. It is to notice that, despite the fact that sample *N-APTMS8* presented smaller mesopores, sample *N-EDAS8* presented a higher microporous volume ($V_{Dubinin,N-APTMS8} = 0.13$ cm³/g whereas $V_{Dubinin,N-EDAS8} = 0.17$ cm³/g) and a higher specific surface area ($S_{BET,N-APTMS8} = 420$ m²/g whereas $S_{BET,N-EDAS8} = 530$ m²/g) (Table III.7).

The nitrogen adsorption-desorption isotherms and mesopore size distributions presented in Figure III.19 highlighted the impact of the use of functional chains of different natures (amino groups or alkyl chains). In this way, while sample *N-TOPS8* presented a narrow pore size distribution centered on 4 nm, sample *N-TOOS8* presented in contrary a broader mesopore size distribution. It is also to notice that, when the alkyl chain length increased from sample *N-TOPS8* (propyl) to sample *N-TOOS8* (octyl), S_{BET} decreased (from 425 m²/g to 325 m²/g), the $V_{Dubinin}$ decreased (from 0.14 cm³/g to 0.11 cm³/g), whereas V_p increased (from 0.29 cm³/g to 0.32 cm³/g) (Table III.7).

It was observed in Figure III.20 that the X-Ray diffraction spectrum of sample *N-APTMS8* presented large rays characteristic of small γ -Al₂O₃ crystallites. Furthermore, it is to notice that sample *N-APTMS8* presented smaller crystallite sizes compared to sample *N-EDAS8* ($d_{XRD,N-APTMS8} = 2.7$ nm, whereas $d_{XRD,N-EDAS8} = 3.3$ nm, Table III.7). Similarly to sample *N-EDAS8*, Al^V peaks were visible in the NMR spectra of sample *N-APTMS8* (Figure III.20-b).

The supports modified by a silicon precursor containing an alkyl chain presented different modifications of the γ -Al₂O₃ microstructure depending on the length of the alkyl chain. In this way, sample *N-TOPS8* presented a X-Ray spectrum (Figure III.20-d) with large peaks characteristic of small γ -Al₂O₃ crystallites ($d_{XRD,N-TOPS8} = 3.0$ nm, Table III.7) and a visible Al^V peak was present on its NMR spectrum (Figure III.20-d). In contrary, sample *N-TOOS8* showed a X-Ray spectrum with characteristic rays of well-crystallized γ -Al₂O₃, large crystallites ($d_{XRD,N-TOOS8} = 4.3$ nm, Table III.7) and almost no Al^V peak was visible on its NMR spectrum (Figure III.20-e).

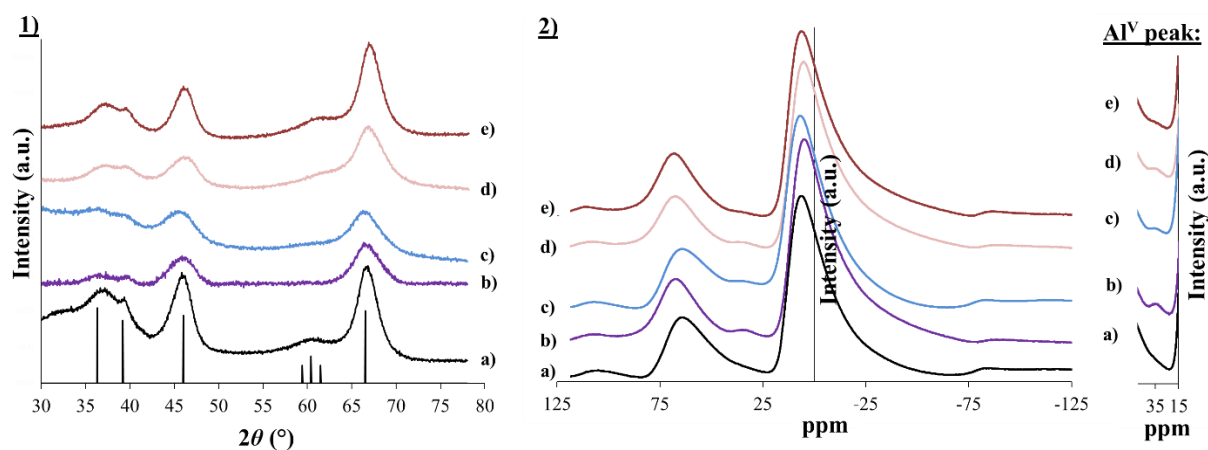


Figure III.20: X-Ray patterns of γ -Al₂O₃ reference rays and calcined samples (left side); and ²⁷Al NMR spectra of calcined samples synthesized with silicon alkoxides functionalized with amino- or alkyl groups (right side): a. *N*, b. *N-APTMS8*, c. *N-EDAS8*, d. *N-TOPS8* and e. *N-TOOS8*.

In view of the results, it appeared that the composition of the functional chain of the silicon alkoxide precursors had significant influences on textural and crystallographic properties of the γ -Al₂O₃ supports. The APTMS molecules modified the γ -Al₂O₃ properties in a similar way as the EDAS molecules: reduction of the crystallite size, narrow and centered mesopore size distribution, integration of Si atoms in the alumina bulk. The functionalized chain of the APTMS being smaller (NH₂(CH₂)₃-) than the EDAS chain (NH₂CH₂CH₂NH(CH₂)₃-), it also explains why sample *N-APTMS8* presented smaller γ -Al₂O₃-SiO₂ crystallites and consequently a mesopore size distribution centered on smaller values.

In contrary, it was observed that the modification of the γ -Al₂O₃ crystallites by a silicon alkoxide functionalized with an alkyl group depended on the chain length of the alkyl group. In this way, TOPS molecule (small alkyl group, CH₃(CH₂)₂-) permitted to modify the textural properties of γ -Al₂O₃-SiO₂ (reduction of crystallite size, narrow and centered mesopore size distribution, integration of Si atoms into the alumina bulk). However, this templating was apparently not optimal since, despite its smaller alkyl chain, the mesopore size distribution of sample *N-TOPS8* was centered at the same value (4 nm) as sample *N-EDAS8*. The results obtained with a silicon alkoxide containing a longer alkyl function (CH₃(CH₂)₇-, sample *N-TOOS8*) confirmed that the γ -Al₂O₃ crystallites templating was strongly influenced by the nature of the chain of the silicon alkoxide. In this way, whereas the function of TOOS molecule is similar in length to the function of EDAS, sample *N-TOOS8* showed very different properties:

broad mesopore size distribution, no reduction of the crystallite size and no visible integration of Si atoms in the alumina bulk.

The influence of the alkyl chain nature on the textural modifications of the γ -Al₂O₃ phase appears to be correlated to the solubility of the silicon alkoxide used: 1) thanks to their amino (H₂N-) and ethylenediamine (NH₂CH₂CH₂NH-) groups, APTMS and EDAS molecules are completely soluble in a water/ethanol medium, which explains their strong influences; 2) TOPS molecules are partially soluble in a water/ethanol medium (small hydrophobic chains counterbalanced by the three methoxy groups), which also explains the textural modifications produced; 3) in contrary, TOOS molecules are almost not soluble in a water/ethanol medium (presence of long hydrophobic chains), which is not adapted for the aqueous precipitation conditions used in this work.

III.3.6. External surface area of the crystallites

Observations of TEM pictures and nitrogen adsorption-desorption measurements led to the hypothesis of the presence of only external voids. In the aim of strengthening this hypothesis, the theoretical external surface area of all crystallites, S_w , was calculated thanks to the Equation III.1:

$$S_w = \frac{6}{\rho \cdot d_{XRD}} \quad (\text{III.1})$$

where ρ is the apparent density determined by helium pycnometry (g/cm³) and d_{XRD} is the crystallite size obtained by X-Ray diffraction (nm).

The comparison between S_{BET} and S_w values allows making hypotheses about the localization of the pores.^[253] In the case of $S_{BET} > S_w$, the mesopores are supposed to be external and the micropores located inside the γ -Al₂O₃ and γ -Al₂O₃-SiO₂ crystallites. On the other hand, in the case of $S_{BET} \leq S_w$, both micro and mesopores are supposed to be external of the crystallites.^[253] The different S_w values are listed in Table III.8.

Table III.8: Actual and theoretical surface areas after calcination obtained from Equation III.1.

Samples	S_{BET} (m ² /g)	S_w (m ² /g)	Samples	S_{BET} (m ² /g)	S_w (m ² /g)	Samples	S_{BET} (m ² /g)	S_w (m ² /g)
N	340	460 ± 20	N-EDAS2	490	580 ± 35	AA-EDAS8	420	480 ± 25
N-TMOS8	370	585 ± 35	N-EDAS8	530	640 ± 40	N-TOPS8	425	755 ± 55
N-TEOS8	340	480 ± 25	N-EDAS16	530	690 ± 45	N-TOOS8	325	485 ± 25
N-APTMS8	420	830 ± 60	BA-EDAS8	520	630 ± 40			

N.B.: The absolute errors (±) were calculated with an estimation of ± 0.01 cm³/g for values of apparent density (ρ) and ± 0.2 nm for the size of crystallites determined by XRD measurements (d_{XRD}).

It was observed that all S_w values were higher than S_{BET} values, consequence of experimental errors caused by the use of the Scherrer equation for the determination of crystallite sizes from XRD measurements. Despite this fact, it is to notice that S_w and S_{BET} values presented similar evolution trends. Hence, it can be assumed that all the micro- and mesoporosity of all samples were only due to voids between nanocrystallites, meaning that the

different pore size distributions could be due to different aggregations of grains between each other.

III.3.7. Evolution of physico-chemical properties of the supports with additional thermal and steaming treatments

The resistance towards sintering and phase transformation as a function of the temperature (at $T = 700, 1000$ or 1200 °C) and of the atmosphere (air or steam) were studied for the following calcined samples: *N*, *N-TMOS8*, *N-TEOS8* and *N-EDAS8*. These different thermal treatments were performed in order to study their stability in conditions similar to the one encountered during catalytic tests.

Table III.9 lists the S_{BET} values (m^2/g) and the surface area losses values, ΔS_{BET} (%), obtained from nitrogen adsorption-desorption isotherms performed on each sample after every calcination or steaming treatment. These results are also presented in two diagrams (Figure III.21).

Table III.9: Specific surface area losses after $t = 6$ h of additional thermal treatment at either $T = 700, 1000$ or 1200 °C; or after $t = 6$ h of steaming treatment at $T = 700$ °C.

Samples	Classic calcination	6 h at 700 °C + 10 vol. %H ₂ O		6 h at 700 °C		6 h at 1000 °C		6 h at 1200 °C	
	S_{BET} (m^2/g)	S_{BET} (m^2/g)	ΔS_{BET} (%)	S_{BET} (m^2/g)	ΔS_{BET} (%)	S_{BET} (m^2/g)	ΔS_{BET} (%)	S_{BET} (m^2/g)	ΔS_{BET} (%)
N	340	165	51	215	37	140	59	10	97
N-TMOS8	370	300	18	320	14	230	38	80	78
N-TEOS8	340	220	35	260	22	145	57	65	81
N-EDAS8	530	410	23	440	17	200	62	70	87

ΔS_{BET} (%) corresponds to the S_{BET} loss in comparison to the S_{BET} (m^2/g) value of classically calcined samples without additional treatments.

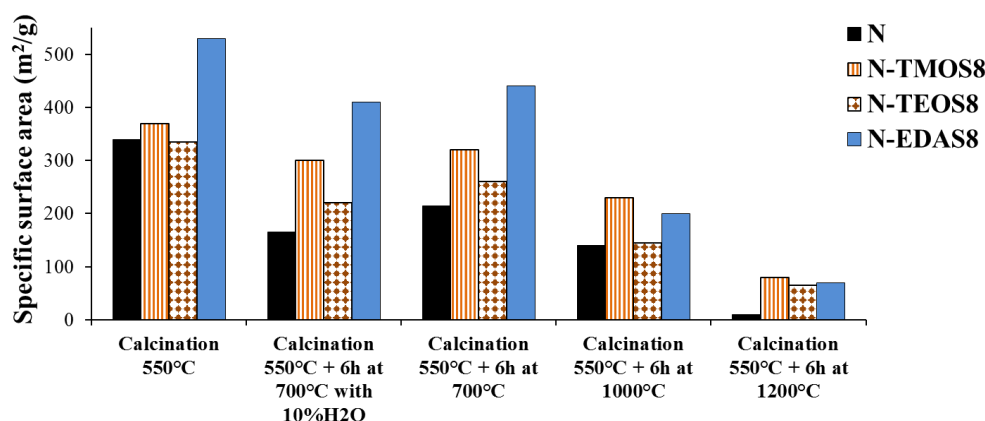


Figure III.21: Specific surface area evolution with different thermal and steaming treatments.

After thermal treatment at $T = 700$ °C, samples *N* and *N-TEOS8* presented the highest specific surface area loss values (respectively 37 and 22 %) in comparison to the ΔS_{BET} of samples *N-TMOS8* and *N-EDAS8* (respectively 14 and 17 %, Table III.9). It is to notice that these values followed the same trends as the ones observed for the samples which had undergone a steaming treatment at $T = 700$ °C. Indeed, after the steaming treatment, samples *N* and *N-TEOS8* presented ΔS_{BET} values of respectively 51 and 35 %, whereas samples *N-TMOS8* and *N-EDAS8* presented ΔS_{BET} values of 18 and 23 % (Table III.9). In this way, the presence of

steam had a higher impact on the specific surface area decay of samples *N* and *N-TEOS8*, compared to samples *N-TMOS8* and *N-EDAS8*.

After the thermal treatment at $T = 1000$ °C, samples *N* and *N-TEOS8* presented same S_{BET} values (~ 140 m²/g), which is in accordance with the usual values obtained in the literature for the calcination of alumina at $T = 1000$ °C.^[260] Samples *N-TMOS8* and *N-EDAS8* exhibited the highest S_{BET} values, with respectively 230 and 200 m²/g.

It is to notice that, after the highest thermal treatment ($T = 1200$ °C), all the silica doped samples presented S_{BET} values seven times higher than pure alumina ($S_{BET,N-EDAS8/N-TMOS8/N-TEOS8} \sim 70$ m²/g whereas to $S_{BET,N} = 10$ m²/g, Table III.9). Figure III.22 shows the X-Ray spectra of samples after $t = 6$ h of thermal treatment at $T = 1200$ °C.

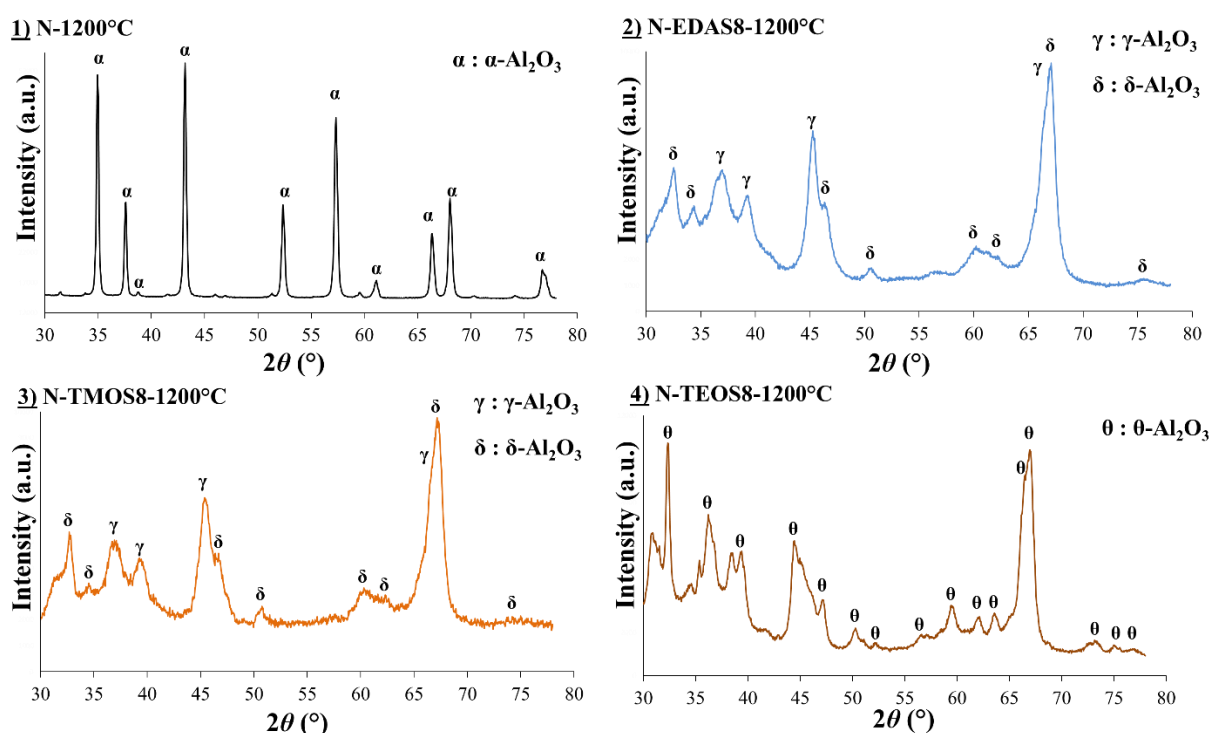


Figure III.22: X-Ray diffraction patterns after $t = 6$ h of thermal treatment at $T = 1200$ °C.

Analysis of the X-Ray diffraction patterns after thermal treatment at $T = 1200$ °C (Figure III.22) showed some modifications of the crystallinity of all the samples. Indeed, for sample *N*, neat rays of α - Al_2O_3 were observed, whereas sample *N-TEOS8* showed a weaker phase transition with θ - Al_2O_3 rays. Samples *N-TMOS8* and *N-EDAS8* presented almost identical rays, *i.e.* a mixture of δ - Al_2O_3 and γ - Al_2O_3 rays. This can be correlated with Figure III.1, which presents the typical phase transformation of γ - Al_2O_3 with the temperature.

The nanostructure of the samples after a thermal treatment at $T = 1200$ °C is presented on TEM pictures below (Figure III.23). Sample *N* presented very dense and very large crystallites (100 nm in diameter) characteristic of α - Al_2O_3 . In comparison, all the samples modified with SiO_2 presented homogeneous crystallites of approximately 10 nm in diameter.

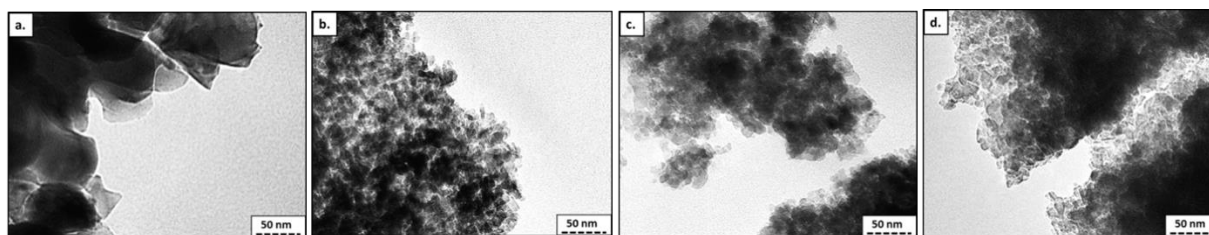


Figure III.23: TEM pictures of samples after $t = 6$ h of thermal treatment at $T = 1200$ °C. 245.000 X; a. N , b. N - $TMOS8$, c. N - $TEOS8$, d. N - $EDAS8$.

These results showed that the type of silicon precursor can have a strong influence on the properties of the supports. Indeed, the samples which presented a high degree of incorporation of Si atoms into the bulk alumina (samples modified with $TMOS$ or $EDAS$) showed the lowest ΔS_{BET} values after calcination at $T = 700$ °C. Furthermore, after a steaming treatment at $T = 700$ °C, samples N - $TMOS8$ and N - $EDAS8$ presented also lower ΔS_{BET} values compared to the samples N - $TEOS8$ and N (Table III.9). According to the literature^{[247], [248], [260]}, doping alumina with SiO_2 increases the resistance against sintering under air or steam atmosphere. Furthermore, the basic HO^- anions formed during the steaming, which cause the collapse of the specific surface area of the support, are known to preferentially attack the Si-O bonds compared to the Al-O bonds.^[261] So, this would explain why the samples which showed a better incorporation of Si inside their bulk alumina (samples N - $EDAS8$ and N - $TMOS8$) were more resistant against sintering than sample N - $TEOS8$.

It was also observed that the reactivity of the silicon alkoxy groups, and hence the incorporation of Si atoms inside the bulk alumina, strongly influenced the phase transformation of alumina sample during an additional calcination at $T = 1200$ °C. Indeed, whereas pure alumina (sample N) presented neat α - Al_2O_3 rays on its XRD spectrum (Figure III.22-1), the alumina supports modified with a high reactive silicon precursor containing methoxy groups (samples N - $TMOS8$ or N - $EDAS8$) showed a mixture of γ - and δ - Al_2O_3 crystalline phases on their XRD spectra (Figures III.22-2 and III.22-3). In contrary, the alumina support modified with a less reactive silicon precursor containing ethoxy groups (sample N - $TEOS8$) presented a less marked phase delay since this support presented θ - Al_2O_3 rays in its XRD spectrum (Figure III.22-4). This effect of Si doping on the delay of the γ - to α - Al_2O_3 phase transition has been reported by several authors.^{[243], [247], [248]} However, though intuitive, no works had yet highlighted the fact that this phase transition delay was correlated to the degree of Si incorporation inside the bulk alumina and to the reactivity of the silicon alkoxide precursor.

III.4. CONCLUSIONS

This chapter evidenced the following items:

- * The formation of small and spherical γ - Al_2O_3 crystallites is directly related to the functionalized chain of $EDAS$. Increasing the amount of $EDAS$ leads to smaller γ - Al_2O_3 crystallites and a narrower mesoporous size distribution. However, the $EDAS$ incorporation inside the alumina crystallites appears to be limited to a maximal value situated around 14 wt.

% of SiO₂. In this way, in the next chapters, the amount of EDAS added during the supports synthesis should not exceed the amount used for the synthesis of sample *N-EDAS8*.

* The tailoring of alumina supports with EDAS is strongly influenced by the addition step of EDAS during the synthesis. Similar properties were obtained when EDAS was added before or just after the precipitation step, whereas almost no modifications of the alumina crystallites appeared when EDAS was added after the aging step. This observation evidenced that, if the properties of the alumina hydroxide can be changed just after the precipitation step, this is no longer possible when the boehmite crystallites are stable after a long agitation step at $T = 85$ °C.

* The tailoring of alumina support through functionalized silicon precursor is directly influenced by the length and the chemical composition of the silicon alkoxide function. Functionalized precursors with a small chain length allowed obtaining small and spherical crystallites, which leads to a narrow mesoporous size distribution. However, the composition and polarity of the functionalized chain must be taken into account in order to perform a correct templating.

* The porosity of the samples seemed to be only due to the presence of voids between the crystallites. The degree of Si incorporation inside the bulk alumina was correlated to the reactivity of the silicon precursor. High reactive silicon precursors containing methoxy groups were more inclined to modify the crystallinity of alumina compared to lower reactive silicon precursors containing ethoxy groups. Though the degree of Si incorporation did not have influences on the shape of the crystallites or on the support mesoporosity, it significantly influenced the crystallography of the samples. Furthermore, a better incorporation of Si atoms inside the bulk alumina allowed affording a higher resistance against sintering at high temperatures and in steam conditions, and also against the γ - to α -Al₂O₃ phase transformation at high temperatures.

Note:

Inspired by the results of this chapter, a study was performed to determine the influences of different silicon precursors (TMOS, TEOS or EDAS) on the catalytic performances of γ -Al₂O₃ supports doped with 10 wt. % of Ni for the reforming of 8000 ppmv of toluene at $T = 650$ °C. This additional study can be found in Annex 6.

Chapter IV

Performances of nickel and iron doped materials used as primary catalysts

- Sol-gel synthesis and characterization of 10 wt. % Fe/ γ -Al₂O₃ and 2 wt. % Ni/ γ -Al₂O₃ catalysts;
- Synthesis by wet impregnation and characterization of olivine doped with either 10 wt. % Fe or 2 wt. % Ni;
- Catalytic performances for the reforming of 8000 ppmv of toluene at either $T = 750\text{ }^{\circ}\text{C}$ or $T = 850\text{ }^{\circ}\text{C}$.

γ -Al₂O₃ supports prepared according to the aqueous precipitation developed in the previous chapters were doped with either 2 wt. % of Ni or 10 wt. % of Fe. In the aim of comparing the performances of the samples with other commonly used catalysts, olivine catalysts doped with either Ni or Fe were also prepared thanks to an impregnation method taken from the literature.

The catalysts were characterized and tested for the reforming of toluene in primary conditions ($T = 750\text{ }^{\circ}\text{C}$ or $T = 850\text{ }^{\circ}\text{C}$). Their catalytic performances, which include their catalytic activities (toluene conversion, methane conversion and benzene selectivity) and their stability against deactivation mechanisms (coking, sintering and phase transformation), were evaluated and compared.

IV.1. INTRODUCTION

The catalysts used to purify the bio-syngas can be either set inside (primary catalysts) or at the outlet (secondary catalysts) of the biomass gasifiers.ⁱ Depending on their location, the catalysts do not operate under the same conditions and do not require the same properties. In the case of primary catalysts, it is mainly expected that the materials are stable at high temperatures ($T = 750\text{-}900\text{ }^{\circ}\text{C}$).^{[39], [100]}

From a catalytic and economic point of view, nickel is known to be the most interesting metallic dopant for reforming applications.^{[3], [9], [146]} Its doping loading usually varies from 1 to 20 wt. %. However, when tested at high temperatures ($T > 800\text{ }^{\circ}\text{C}$), it is generally advised to use low amounts of doping (< 5 wt. % Ni) in order to afford higher interactions with the support, to keep small metallic nanoparticles and to prevent deactivation by sintering.^{[9], [65]} Though being very efficient, nickel-doped materials can be problematic in primary conditions because of the formation of toxic nickel dusts due to catalyst attrition in the case of a fluidized bed. In that case, the presence of hot filters is then required in order to get rid of the toxic dusts.

For these reasons, some studies have focused on the development of iron based materials for primary catalyst applications. Despite showing lower catalytic performances, iron oxides, and especially metallic iron supported on various types of supports (Al₂O₃, olivine, scallop shell...) have proved to be interesting for the reforming of gasification tars.ⁱⁱ However, the low activity of the iron species requires high amounts of dopant, generally situated between 10 and 30 wt. %.^{[39], [64], [100]} The catalytic activity of the iron species being generally increased with their reduction states ($\text{Fe}_2\text{O}_3 < \text{Fe}_3\text{O}_4 < \text{FeO} < \text{Fe}^{(0)}$)^{[51], [129], [130], [262]}, the tests must therefore take place at a sufficiently high temperature in order to favor a partial or complete reduction of the iron species ($T > 750\text{ }^{\circ}\text{C}$).

By its non-toxicity, low cost and high attrition resistance properties, olivine mineral ((Mg,Fe)₂SiO₄) has proved to be a valuable support for primary catalytic use.ⁱⁱⁱ Either doped

ⁱ: More details about primary and secondary catalysts in part I.3.1. of Chapter I.

ⁱⁱ: More details about iron-doped catalysts in part I.4.4.2.3. of Chapter I.

ⁱⁱⁱ: More information about olivine-based catalysts in part I.4.4.2.2. of Chapter I.

with Ni^{[55], [123], [124]} or Fe^{[64], [263], [264]}, this natural mineral has afforded very interesting catalytic performances for the reforming of tars.

Though γ -Al₂O₃ is one of the most used catalytic support, no direct comparison between γ -Al₂O₃ and olivine materials doped with metallic elements and tested in primary conditions has been noticed yet. The results from this chapter were therefore necessary in this project in order to decide to work on the development of primary catalysts or to redirect the study towards the development of secondary catalysts.

IV.2. EXPERIMENTAL

IV.2.1. Catalysts preparation

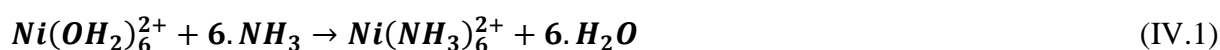
The samples synthesized with alumina contain the prefix “N” and the samples prepared with olivine contain the prefix “Oli”. The prefixes “2Ni” or “10Fe” are related to the nature and the concentration of dopant (2 wt. % of nickel or 10 wt. % of iron). The amounts of olivine, aluminum nitrate, nickel nitrate and iron nitrate used for the synthesis of 10 g of catalyst are given in part V of Annex 2.

IV.2.1.1. Sol-gel synthesis of Ni- and Fe/ γ -Al₂O₃ catalysts

Three alumina-based catalysts were synthesized according to a synthesis procedure similar to the ones described in Chapters II and III. The sols were formed by a slow addition of a NH₄OH solution (30 wt. %, 15 M). After the precipitation, the sols were agitated for $t = 24$ h at $T = 85$ °C, washed two times with water, re-dispersed in water and doped with the metallic salts. The adequate amount of either nickel nitrate hexahydrate (Ni(NO₃)₂.6H₂O) or iron nitrate nonahydrate (Fe(NO₃)₃.9H₂O) was added in order to obtain alumina supports doped with either 2 wt. % of Ni or 10 wt. % of Fe. After $t = 30$ min of stirring, the bottles were opened and the sols were set in an oven for aging ($t = 24$ h, $T = 85$ °C, $P = 700$ mbar). Thereafter, the gels were washed again: once with water in order to evacuate the residual nitrate ions from the metal doping; and once with ethanol in order to maintain a high mesoporosity during the drying step.^{[217], [218]} Finally, the gels were dried ($t = 24$ h, $T = 110$ °C, $P = 900$ mbar) and calcined ($t = 5$ h, $T = 550$ °C, 2 °C/min). It is to notice that the calcination conditions were a little longer (+ 1 h) and at a higher temperature (+ 50 °C) than the ones applied during the synthesis of pure supports in Chapters II and III. These modifications were performed in order to be sure to evacuate all the residual compounds (carbon, nitrates ...) during the calcination process.

- Note about the washing step:

Washing the sols before the addition of metallic salts was an essential step for the nickel-doped alumina support. Indeed, NH⁴⁺ ions can form nickel-ammonium complexes (Equation IV.1), which drastically decrease the loading of nickel in the final materials.



IV.2.1.2. Impregnation of olivine with Ni and Fe

The olivine doping was performed according to the procedure established by Dariusz Swierczynski *et al.*^[55] and Virginie *et al.*^[64]. It is to notice that thanks to a collaboration between the Department of Chemical Engineering-Nanomaterials, Catalysis, Electrochemistry of the University of Liège (ULg-NCE) and the Institut de Chimie et Procédés pour l'Énergie, l'Environnement et la Santé (ICPEES) of the University of Strasbourg, it was possible to get raw olivine from the same batch as in the previously cited works. This olivine support was produced by Magnolithe GmbH (Austria), which improved its mechanical resistance by a calcination of $t = 4$ h at $T = 1600$ °C. The final olivine material is a silicate mineral in which magnesium and iron cations are embedded in the silicate tetrahedral $((\text{Mg}_x\text{Fe}_{1-x})_2\text{SiO}_4)$.^[64]

The olivine doping was performed by wet-impregnation of aqueous solutions of either nickel nitrate hexahydrate ($\text{Ni}(\text{NO}_3)_2 \cdot 6\text{H}_2\text{O}$) or iron nitrate nonahydrate ($\text{Fe}(\text{NO}_3)_3 \cdot 9\text{H}_2\text{O}$). Olivine grains with a diameter comprised between 300 and 700 μm were put inside a glass balloon, with water and the adequate amount of metallic salts. The balloon was fixed to a Rotavap apparatus for the solvent evaporation step ($t = 24$ h, $T = 85$ °C, $P = 300$ mbar) and then set in an oven for further drying ($t = 24$ h, $T = 110$ °C, $P = 900$ mbar). The calcination conditions depended on the nature of the dopant: 1) the olivine doped with nickel was calcined for $t = 5$ h at $T = 550$ °C with a heating rate of 2 °C/min. Due to the low amount of doping (2 wt. % Ni), it was preferred to avoid a too high temperature of calcination in order to prevent the formation of stable and less active Ni-MgO species.^{[142], [265], [266]} It is noteworthy that high calcination temperatures of nickel-olivine materials are generally advised to protect the samples from deactivation by coking when the catalytic tests are performed at low temperatures ($T < 650$ °C)^[55], which is not the case in our current study; 2) the olivine doped with iron was calcined for $t = 4$ h at $T = 1000$ °C with a heating rate of 2 °C/min. According to Virginie *et al.*^[64], calcination of iron-doped olivine at this temperature range allows obtaining more available iron from the olivine structure and preventing the sintering of surface iron oxides by the formation of stable MgFe_2O_4 species.

IV.2.2. Characterization techniques

Composition analysis (ICP–AES), nitrogen adsorption-desorption (BET), X-Ray diffraction (XRD), temperature programmed reduction (TPR), thermogravimetric-differential scanning calorimetry (TG-DSC) and pure reduction (H_2 -Reduction) measurements were performed on samples of this chapter. The $\text{Ni}^{(0)}$ crystallite sizes were calculated by using the Scherrer equation centered on the (2 0 0) ray ($2\theta = 51.8$ °) of the XRD spectra. The $\text{Fe}^{(0)}$ crystallites sizes were calculated by using the Scherrer equation centered on the (1 1 0) ray ($2\theta = 44.8$ °) of the XRD spectra. The crystallites sizes of Fe-Ni alloys were calculated by using the Scherrer equation centered on the (1 1 0) ray of the XRD spectra. Deeper information about the characterizations techniques and variables quoted are provided in part II of Annex 2. X-Ray references cards are given in part VI of Annex 2.

IV.2.3. Catalytic experiments

The catalytic activity of the samples was investigated thanks to an experimental installation reproducing the conditions inside a biomass gasifier. Details about the installation set-up and functioning are given in Annex 3. The catalytic tests were performed with conditions similar to those encountered inside of a steam reforming fluidized bed gasifier of biomass.^[64] The composition of the gas mixture is listed in Table IV.1. For this gas mixture, the (H₂O+CO₂)/C ratio is about 4.7 when only taking toluene as carbon source, and it is about 1.7 when taking toluene+methane as carbon source.

Table IV.1: Syngas mixture used during the catalytic tests.

Gas type	H ₂	CO	CO ₂	H ₂ O	CH ₄	N ₂	Toluene
Concentration	31.5 vol. %	31.5 vol. %	15.2 vol. %	11.0 vol. %	10.0 vol. %	0 vol. %	8000 ppmv (30 g/Nm ³)

The catalytic tests were performed with a *GHSV* of 6000 h⁻¹ (equivalent to a residence time of 0.6 sec), with a catalytic sample mass of 250 mg. The tests were performed for $t = 260$ min (GC injection every 15 min) at the temperatures of $T = 750$ °C and $T = 850$ °C in order to evaluate the catalytic performances of the samples under primary gasifier conditions. It is to notice that no pre-reduction step was undertaken to activate the catalysts.

The toluene conversion, C_{Tolu} , was determined from the Equation IV.2:

$$C_{Tolu} = \frac{C_{rt,Tolu,In} - C_{rt,Tolu,Out}}{C_{rt,Tolu,In}} * 100 \quad (IV.2)$$

where $C_{rt,Tolu,In}$ is the initial toluene concentration (mol/m³) and $C_{rt,Tolu,Out}$ is the toluene concentration at the outlet of the reactor (mol/m³).

The benzene selectivity (S_B) was determined from the Equation IV.3:

$$S_B = \frac{C_{rt,Benz,Out}}{C_{rt,Tolu,In} - C_{rt,Tolu,Out}} * 100 \quad (IV.3)$$

where $C_{rt,Benz,Out}$ is the outlet concentration of benzene (mol/m³), $C_{rt,Tolu,In}$ is the initial toluene concentration (mol/m³) and $C_{rt,Tolu,Out}$ is the toluene concentration at the outlet of the reactor (mol/m³). Theoretically, using the benzene selectivity value implies an equilibrated carbon balance. In this case, the carbon balance error was considered as acceptable (error varied from 1 to 8 %). This was mostly due to the formation of coke caused by the toluene degradation (see calculus in part IV of Annex 2).

The methane conversion, C_{CH_4} , was determined from the Equation IV.4:

$$C_{CH_4} = \frac{C_{rt,CH_4,In} - C_{rt,CH_4,Out}}{C_{rt,CH_4,In}} * 100 \quad (IV.4)$$

where $C_{rt,CH_4,In}$ is the initial methane concentration (mol/m³) and $C_{rt,CH_4,Out}$ is the methane concentration at the outlet of the reactor (mol/m³).

All C_{Tolu} , S_B and C_{CH_4} values were obtained by making an average of the results obtained during the last 10 measurements of each test. In addition to the catalysts and to the pure supports of alumina or olivine, inert pure quartz grains were also tested in order to determine the conversion reached in the absence of a catalyst.

According to the results presented in part III of Annex 2, it was assumed that the samples made of $\gamma\text{-Al}_2\text{O}_3$ (samples N , $N\text{-}2Ni$ and $N\text{-}10Fe$) did not submit neither internal nor external diffusional limitations during the catalytic tests.

IV.2.4. Use of toluene as tar model compound

Though Coll *et al.*^[46] showed that naphthalene is a tar model compound more adequate than toluene (more difficult to convert, higher tendency to form coke), it was however decided to use toluene as a biomass gasification tar model molecule. Indeed, the maximum temperatures reached by the heating-lines of the experimental installation and of the gas chromatograph did not permit to work with naphthalene ($T_{Max,installation} = 200\text{ }^\circ\text{C}$) since the tar dew point of naphthalene is equal to $T_{Naphtha.} = 217\text{ }^\circ\text{C}$. In contrary, the tar dew point of toluene is lower: $T_{Tolu} = 110\text{ }^\circ\text{C}$. Furthermore, the kinetics of degradation of toluene are more simple (generally assumed to be a first law order, $n = 1$)^{[55], [56], [58], [67]}, compared to the degradation of naphthalene (multiple reaction pathways)^[59].

Table IV.2 resumes the possible reactions which can take place during the reforming of toluene. It is to notice that parallel reactions not presented here, such as Boudouard, Water-Gas, Water-Gas shift and methanation, might also take place.ⁱ Figure IV.1 shows the Gibb's free energies for the steam and dry reforming of toluene as a function of the temperature. It is to notice that thermodynamically speaking, the toluene steam reforming reactions (Equations IV.5 and IV.6) are favored when $T < 830\text{ }^\circ\text{C}$ compared to the toluene dry reforming reactions (Equations IV.11 and IV.12). When $T > 830\text{ }^\circ\text{C}$, the dry reforming becomes more favorable than the steam reforming reactions.^[29] The mechanisms of toluene conversion are similar to the general tar conversion:ⁱⁱ first, the dealkylation of the methyl group occurs and leads to the formation of benzene. The methyl group is reformed to CO and H₂. H₂ present at the surface of the catalyst hydrogenates the aromatic ring to form a saturated cyclic ring, which is easily broken down in hydrocarbon fragments. The hydrocarbon fragments are thereafter converted into CO and H₂ via various oxidation steps.^[50]

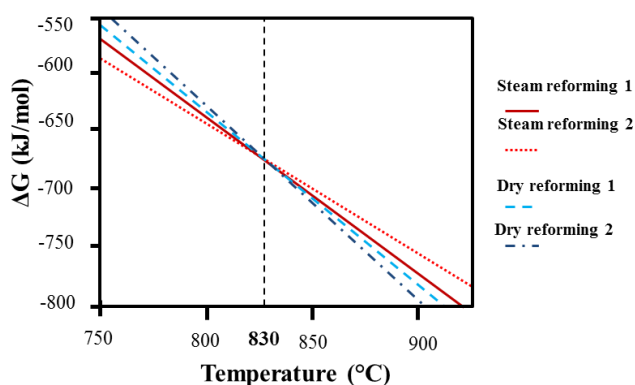
It was shown that even at low conversion of toluene, under the usual reaction conditions, the amounts of the hydrogenation products such as methylcyclohexane, cyclohexane, and their hydrogenolysis products such as alkanes, are always below the detection limits.^[267] So, basically the interactions between toluene and H₂ only lead to the formation of benzene and CH₄. However, it is to remind that benzene, by its high toxicity, is more problematic than toluene. Hence, a low S_B value is a major criterion for a good catalyst.

ⁱ : More details about Boudouard, Water-Gas, Water-Gas shift and methanation reactions in Table I.1.

ⁱⁱ : More information about the general mechanisms of tar reforming in Figure I.7.

Table IV.2: Possible reactions of hydrocarbons in hot gas cleaning conditions, with toluene as model hydrocarbon at $T = 900\text{ }^{\circ}\text{C}$.^[29]

Equations	Heat of reaction (kJ/mol) at 900 °C	Name	Equation n°
$C_7H_8 + 7.H_2O \rightarrow 7.CO + 11.H_2$	+876	Steam reforming 1	IV.5
$C_7H_8 + 14.H_2O \rightarrow 7.CO_2 + 18.H_2$	+647	Steam reforming 2	IV.6
$C_7H_8 + H_2O \rightarrow C_6H_6 + 2.H_2 + CO$	+123	Steam dealkylation 1	IV.7
$C_7H_8 + 2.H_2O \rightarrow C_6H_6 + 3.H_2 + CO_2$	+90	Steam dealkylation 2	IV.8
$C_7H_8 + 10.H_2 \rightarrow 7.CH_4$	-713	Hydrocracking	IV.9
$C_7H_8 + H_2 \rightarrow C_6H_6 + CH_4$	-104	Hydrodealkylation	IV.10
$C_7H_8 + 7.CO_2 \rightarrow 14.CO + 4.H_2$	+1105	Dry reforming 1	IV.11
$C_7H_8 + 11.CO_2 \rightarrow 18.CO + 4.H_2O$	+1236	Dry reforming 2	IV.12
$n.C_7H_8 \rightarrow m.C_xH_y + p.H_2$	n.a.	Thermal cracking	IV.13
$C_7H_8 \rightarrow 7.C + 4.H_2$	-73	Carbon formation	IV.14

Figure IV.1: Gibb's energy of steam and dry reforming of toluene as a function of temperature.^[29]

IV.3. RESULTS AND DISCUSSION

IV.3.1. Characterizations of catalysts

IV.3.1.1. Composition of samples

Table IV.3 lists the theoretical and experimental compositions of the samples obtained by ICP measurements. It is to remind that the ICP measurements are of utmost importance in the case of sol-gel prepared catalysts since a part of the metal doping may be lost during the catalyst preparation, drying, or pretreatment steps.^[268]

Table IV.3: Theoretical and actual compositions of the samples determined by ICP analysis.

Samples	Al ₂ O ₃		SiO ₂		MgO		Ni		Fe	
	Theo. (wt. %)	Exp. (wt. %)	Theo. (wt. %)	Exp. (wt. %)	Theo. (wt. %)	Exp. (wt. %)	Theo. (wt. %)	Exp. (wt. %)	Theo. (wt. %)	Exp. (wt. %)
N	100	100	#	#	#	#	#	#	#	#
N-2Ni	98.0	98.1	#	#	#	#	2.0	1.9	#	#
N-10Fe	90.0	89.5	#	#	#	#	#	#	10.0	10.5
Oli	#	#	#	41.1	#	51.1	#	#	#	7.8
Oli-2Ni	#	#	#	38.9	#	50.9	2.0	2.5	#	7.7
Oli-10Fe	#	#	#	35.6	#	44.2	#	#	17.8	19.6

#: No value expected

It was observed in Table IV.3 that the theoretical and actual compositions of all samples were similar. The high content of Fe (19.6 wt. %) of sample *Oli-10Fe* was caused by the fact that the iron is initially present in raw olivine (7.8 wt. %). So, the true Fe loading of this sample was actually $19.6 - 7.8 = 11.8$ wt. %, which was considered as acceptable for a synthesis by wet impregnation.

IV.3.1.2. Textural and physico-chemical properties of samples

The specific surface area values, S_{BET} , and porous volume values, V_p , of alumina-based catalysts (samples *N*, *N-2Ni* and *N-10Fe*) and of raw olivine (sample *Oli*) are presented in Table IV.4. The doping of alumina with either Ni or Fe slightly reduced the specific surface area values ($S_{BET,N} = 280$ m²/g, whereas $S_{BET,N-2Ni} = 265$ m²/g and $S_{BET,N-10Fe} = 220$ m²/g) but also slightly increased the porous volume values ($V_{p,N} = 0.4$ cm³/g, $V_{p,N-2Ni} = 0.5$ cm³/g and $V_{p,N-10Fe} = 0.7$ cm³/g). The nitrogen adsorption-desorption isotherms and the pore size distributions of these samples were very similar to what was obtained for pure alumina (sample *N*) in Chapters II and III. It was observed that the raw olivine (sample *Oli*) did neither present any micro- nor mesoporosity ($S_{BET,Oli} < 1$ cm²/g and $V_{p,Oli} < 0.01$ cm³/g).

Table IV.4: Specific surface area and pore volume of the samples.

Samples	N	N-2Ni	N-10Fe	Oli
S_{BET} (m ² /g)	280	265	220	< 1
V_p (cm ³ /g)	0.4	0.5	0.7	< 0.01

S_{BET} : specific surface area; V_p : porous volume.

The TPR profiles of samples *Oli*, *Oli-2Ni*, *Oli-10Fe*, *N-2Ni* and *N-10Fe* are shown in Figure IV.2. The TPR profile of sample *Oli* (Figure IV.2-a) showed a weak and broad consumption peak located between $T = 500$ °C and $T = 900$ °C, attributed to the reduction of iron species (α -Fe₂O₃ and MgFe₂O₄) naturally present in the olivine into Fe₃O₄.^{[64], [264]}

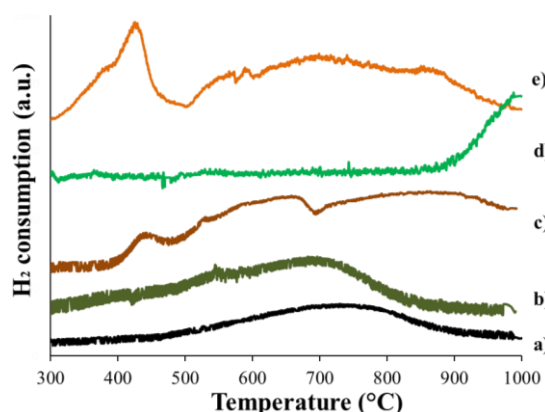


Figure IV.2: TPR profiles for alumina or olivine supports doped with either 2 wt. % Ni or 10 wt. % of Fe; a. *Oli*, b. *Oli-2Ni*, c. *Oli-10Fe*, d. *N-2Ni*, e. *N-10Fe*.

The TPR profile of sample *Oli-2Ni* (Figure IV.2-b) presented a very similar reduction peak as the sample *Oli*, but also a very small peak located at $T = 550$ °C, which was attributed to the reduction of a low amount of bulk nickel oxide (NiO) into metallic nickel. The fact that

the nickel was almost not reduced for this sample is typical and is caused by a strong incorporation of Ni into the magnesium structure (formation of spinel).^[269] It is to notice that the broad peak attributed to the reduction of the Fe species naturally present in olivine was slightly shifted towards lower temperatures ($\Delta T \sim 50$ °C) for sample *Oli-2Ni*. This increase of reducibility is believed to be caused by the presence of metallic nickel Ni⁽⁰⁾ which could promote the reduction of the iron oxide species by “spillover effect”.ⁱ

The TPR profile of sample *Oli-10Fe* (Figure IV.2-c) also presented a broad peak, characteristic of the reduction of iron oxide species from the olivine support. In addition, sample *Oli-10Fe* presented a succession of other peaks caused by the reduction of the additional Fe: the peak situated at $T = 430$ °C was attributed to the reduction of iron oxide present at the olivine surface ($\alpha\text{-Fe}_2\text{O}_3 \rightarrow \text{Fe}_3\text{O}_4$). The second broad peak, situated between $T = 500$ °C and $T = 700$ °C, was attributed to the reduction of various iron oxides present inside the Fe/olivine grain ($\alpha\text{-Fe}_2\text{O}_3$ or MgFe_2O_4). Finally, the last broad peak, situated between $T = 700$ and $T = 1000$ °C, was attributed to a further reduction of iron ($\text{Fe}_3\text{O}_4 \rightarrow \text{FeO}$).^{[64], [264]}

It was observed that the reduction of the nickel for sample *N-2Ni* only started at $T = 880$ °C and was not finished at $T = 1000$ °C (Figure IV.2-d). The very high temperature needed for the reduction of nickel evidenced the presence of very strong interactions between nickel atoms and the alumina support. In that case, Ni²⁺ ions were in a tetrahedral coordination and formed a highly refractory nickel-aluminate (NiAl_2O_4) phase organized in a spinel structure.^{[270]–[272]} Indeed, the percentage of reduced Ni during the TPR measurement was estimated to be only of 20 %.

Sample *N-10Fe* (Figure IV.2-e) presented three characteristic reduction peaks: 1) the first peak, located at $T = 415$ °C, corresponded to the reduction of iron oxide with low interactions with the support ($\alpha\text{-Fe}_2\text{O}_3 \rightarrow \text{Fe}_3\text{O}_4$); 2) the broad reduction peak situated between $T = 500$ °C and $T = 800$ °C, was attributed to the reduction of iron species with strong interactions with alumina ($\text{Fe}_2\text{O}_3/\text{Al}_2\text{O}_3 \rightarrow \text{Fe}_3\text{O}_4/\text{Al}_2\text{O}_3$) and simultaneously to the further reduction of the surface iron oxide species ($\text{Fe}_3\text{O}_4 \rightarrow \text{FeO}$); 3) the slight peak observed at $T = 875$ °C could be due to the conversion of FeO species into metallic Fe⁽⁰⁾.^{[273]–[275]}

X-Ray diffractions (not shown here) were performed on all alumina-based materials after calcination (samples *N*, *N-2Ni* and *N-10Fe*) and no other rays than common $\gamma\text{-Al}_2\text{O}_3$ were observed. In the case of sample *N-2Ni*, the very low loading of Ni could explain the absence of visible NiO rays. In the case of sample *N-10Fe*, the absence of any visible iron oxide rays after calcination indicates a high dispersion of the iron dopant.

Figure IV.3 shows the X-Ray spectra of the alumina-based materials (samples *N*, *N-2Ni* and *N-10Fe*) after TPR measurements.

ⁱ: More details about “spillover effect” in Figure I.12.

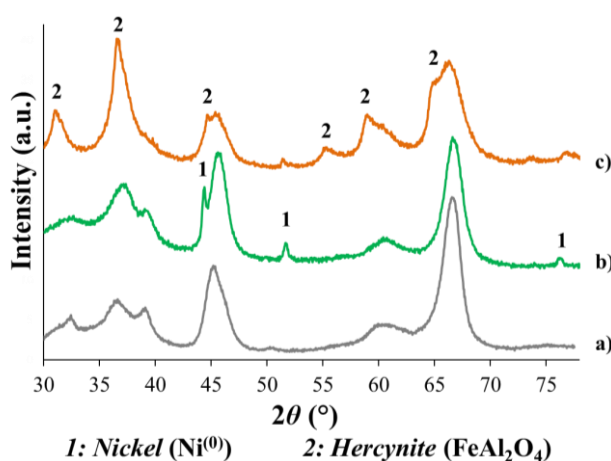


Figure IV.3: X-Ray patterns of alumina-based samples after TPR measurements; a. *N*, b. *N-2Ni*, c. *N-10Fe*.

It was observed that the TPR analysis had no influence on the crystallinity of pure alumina since sample *N* still presented characteristic peaks of $\gamma\text{-Al}_2\text{O}_3$ (Figure IV.3-a). After TPR measurements, sample *N-2Ni* showed characteristic peaks of metallic nickel $\text{Ni}^{(0)}$ (Figure IV.3-b). Sample *N-10Fe* presented several peaks attributed to hercynite (FeAl_2O_4) (Figure IV.3-c). However, it is to notice that no peaks of metallic iron were visible after TPR measurement for sample *N-10Fe*.

Figure IV.4 shows the X-Ray spectra of olivine as received (sample *Oli-C*) or after the TPR measurement (sample *Oli-TPR*).

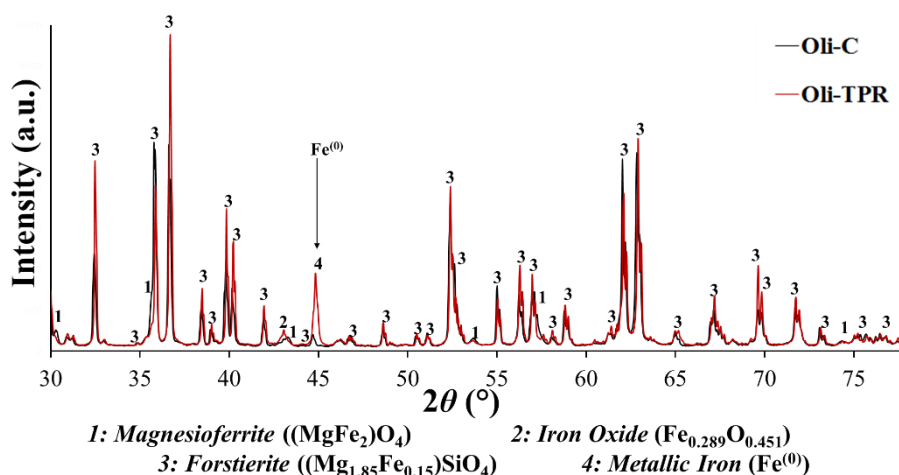


Figure IV.4: X-Ray patterns of olivine sample as received (sample *Oli-C*) and after TPR measurement (sample *Oli-TPR*).

In Figure IV.4, the X-Ray spectrum of sample *Oli-C* presented typical rays of calcined olivine, *i.e.* rays of magnesioferrite ($(\text{MgFe}_2)\text{O}_4$) and forstierite ($(\text{Mg}_{1.85}\text{Fe}_{0.15})\text{SiO}_4$).^{[55], [64], [264]} The reduction during the TPR analysis led to the apparition of an intense ray of metallic iron $\text{Fe}^{(0)}$ located at $2\theta = 44.8^\circ$ in the X-Ray spectrum of sample *Oli-TPR*. A small ray of iron oxide species being partially reduced ($\text{Fe}_{0.289}\text{O}_{0.451}$) was also visible in this spectrum at $2\theta = 43.3^\circ$.

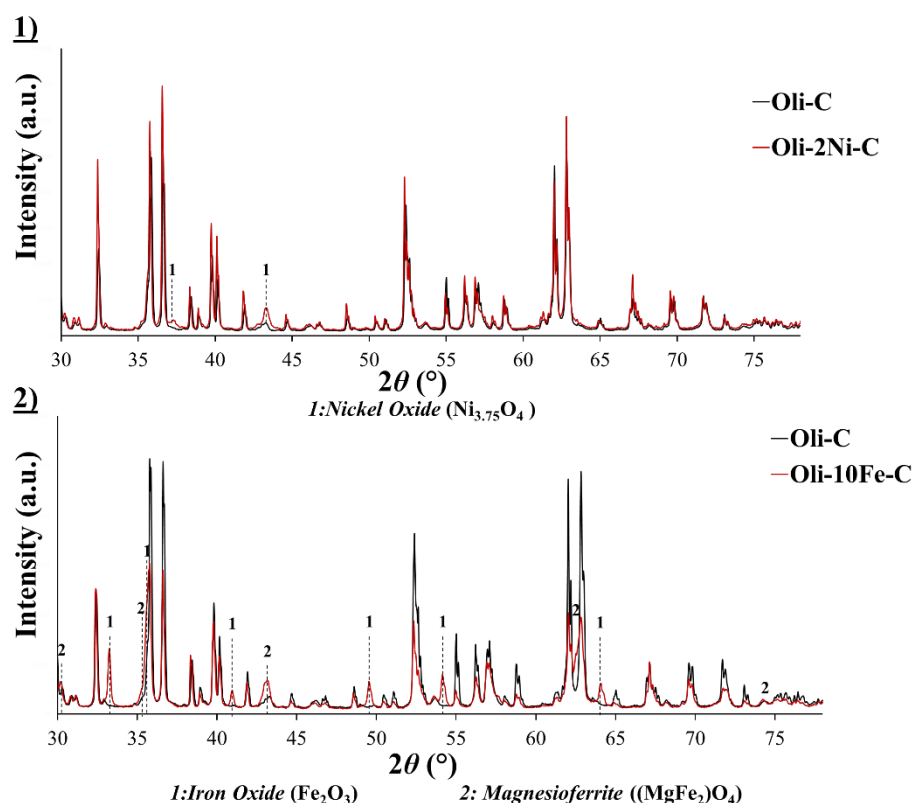


Figure IV.5: X-Ray patterns of calcined samples *Oli-C*, *Oli-2Ni-C* and *Oli-10Fe-C*.

Figure IV.5 shows the X-Ray spectra of the olivine catalysts doped with Ni or Fe after calcination. Both samples presented classic rays of calcined olivine observed in Figure IV.4. In the case of sample *Oli-2Ni-C*, rays of nickel oxide ($\text{Ni}_{3.75}\text{O}_4$) were visible in the spectrum. In the case of sample *Oli-10Fe-C*, rays of iron oxide (Fe_2O_3) and magnesioferrite ($(\text{MgFe}_2)\text{O}_4$) were observed.

Figure IV.6 shows the X-Ray spectra after TPR measurements of raw olivine (sample *Oli-TPR*) or olivine doped with Ni (sample *Oli-2Ni-TPR*).

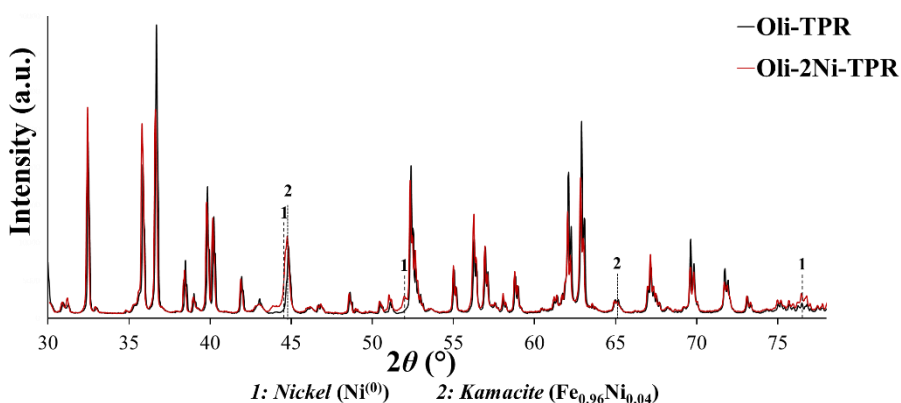
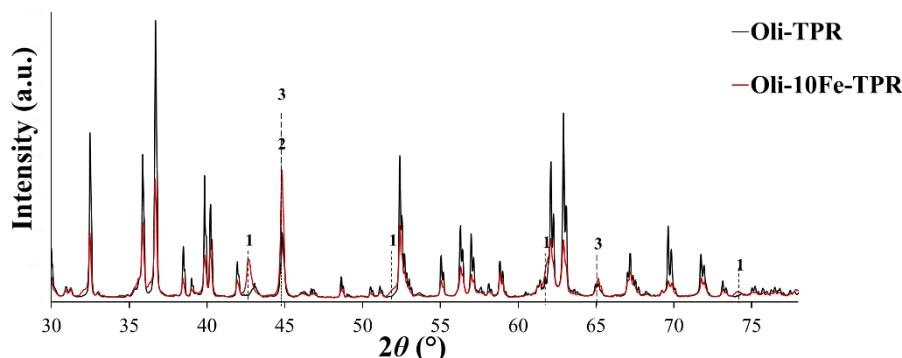


Figure IV.6: X-Ray patterns after TPR of samples *Oli* and *Oli-2Ni*.

In Figure IV.6, the X-Ray spectrum of sample *Oli-2Ni-TPR* showed rays of metallic nickel ($\text{Ni}^{(0)}$) located at $2\theta = 44.6^\circ$ and $2\theta = 51.8^\circ$, and an iron-nickel alloy mostly composed of Fe, called kamacite ($\text{Fe}_{0.96}\text{Ni}_{0.04}$).

Figure IV.7 shows the X-Ray spectra after TPR measurements of pure olivine (sample *Oli-TPR*) and iron-doped olivine (sample *Oli-10Fe-TPR*).



1: Magnesium Iron Oxide ($\text{Mg}_{0.9}\text{Fe}_{0.1}\text{O}$) 2: Iron ($\text{Fe}^{(0)}$) 3: Iron Silicon ($\text{Fe}_{0.9}\text{Si}_{0.1}$)

Figure IV.7: X-Ray patterns after TPR of samples *Oli* and *Oli-10Fe*.

In Figure IV.7, the X-Ray spectrum of sample *Oli-10Fe-TPR* showed three major differences compared to sample *Oli-TPR*: 1) apparition of rays of magnesium iron oxide ($(\text{Mg}_{0.9}\text{Fe}_{0.1})\text{O}$); 2) increase of the intensity of the $\text{Fe}^{(0)}$ rays located at $2\theta = 44.8^\circ$; 3) formation of iron silicon ($\text{Fe}_{0.9}\text{Si}_{0.1}$) whose rays are located at $2\theta = 44.8^\circ$ and $2\theta = 65.1^\circ$.

Table IV.5 shows the sizes of the metallic nanoparticles of all samples after TPR measurements determined from TEM observations and from XRD measurements. It was observed that sample *N-2Ni* showed the lowest values of Ni particle size ($d_{\text{TEM},N-2\text{Ni}} = 30$ nm and $d_{\text{XRD},N-2\text{Ni}} = 23$ nm) and of particle standard deviation ($\sigma_{\text{TEM},N-2\text{Ni}} = 9$ nm). In contrary, samples *Oli*, *Oli-2Ni* and *Oli-10Fe* showed very large Ni and Fe particle sizes (d_{TEM} comprised between 54 nm and 76 nm; d_{XRD} comprised between 29 nm and 43 nm). The high difference between d_{TEM} and d_{XRD} for the olivine-based samples can be explained by their very high standard deviations (σ_{TEM} comprised between 33 nm and 98 nm) and also by the fact that one large metallic particle observed by TEM may be formed from the agglomeration of several crystallites with different crystallographic orientations.¹ Indeed, as depicted in Figure IV.8 for sample *Oli-2Ni*, the olivine-based samples showed very different sizes of metallic ($\text{Fe}^{(0)}$ or $\text{Ni}^{(0)}$) nanoparticles after TPR analysis. Nevertheless, it is to notice that the sizes of metallic particles presented in Table IV.5 were in accordance with the literature. Indeed, Virginie *et al.*^[64] obtained $\text{Fe}^{(0)}$ particles with average size values comprised between 34 nm and 45 nm for 10 wt. % Fe/Olivine catalysts and Swierczynski *et al.*^[55] obtained $\text{Ni}^{(0)}$ particles with average size values of about 20 nm for 3.9 wt. % Ni/Olivine catalysts.

Table IV.5: Metallic particles sizes for alumina or olivine samples doped with 2 wt. % Ni or 10 wt. % Fe after TPR.

Samples	N-2Ni	N-10Fe	Oli	Oli-2Ni	Oli-10Fe
d_{TEM} (nm)	30	No metal NP	54	67	76
σ_{TEM} (nm)	9	No metal NP	33	75	98
d_{XRD} (nm)	23 ¹	No metal NP	43 ²	29 ³	42 ²

d_{TEM} : metallic particles size median; σ_{TEM} : standard deviation; d_{XRD} : metallic crystallites size estimation obtained by XRD.

¹: measured on the (2 0 0) ray of $\text{Ni}^{(0)}$; ²: measured on the (1 1 0) ray of $\text{Fe}^{(0)}$; ³: measured on the (1 1 0) ray of kamacite ($\text{Fe}_{0.96}\text{Ni}_{0.04}$).

¹: More details about differences between d_{TEM} and d_{XRD} values in part II of Annex 2.

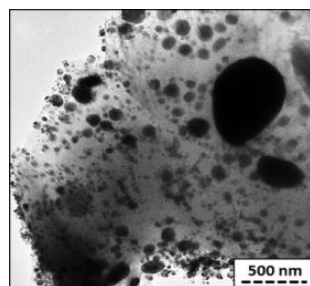


Figure IV.8: TEM picture of sample *Oli-Ni* after TPR, 60.000 X.

The high differences of metallic particle sizes and distributions between the samples made of alumina and of olivine can be explained by two reasons: 1) in opposite to alumina, the olivine support does not show any micro- or mesoporosity (Table IV.4), which is known to play an essential role in the migration and coalescence of the metallic crystallites;^{[9], [65], [152]} 2) the nickel and iron species presented stronger interactions with alumina than with olivine (Figures IV.2 and IV.3). Ni started to be reduced only at high temperatures ($T = 880\text{ }^{\circ}\text{C}$) for sample *N-2Ni*, whereas it started to be reduced at $T = 550\text{ }^{\circ}\text{C}$ for sample *Oli-2Ni*. The metallic nanoparticles being more mobile than the oxide nanoparticles,^{[65], [79]} this would explain why the Ni nanoparticles supported on olivine were larger than the ones supported on alumina.

IV.3.2. Catalytic activity and post-test characterizations

IV.3.2.1. Catalytic performances at $T = 750\text{ }^{\circ}\text{C}$

Figure IV.9 shows the toluene conversion as a function of time for the catalysts doped with Ni or Fe (samples *N-2Ni*, *N-10Fe*, *Oli-2Ni*, *Oli-10Fe*). Figure IV.10 shows the methane conversion and the benzene selectivity of all samples. All catalytic performances (toluene conversion, C_{Tolu} , benzene selectivity, S_B , methane conversion, C_{CH_4} , carbon deposit amount after test) of all samples and quartz are listed in Table IV.6.

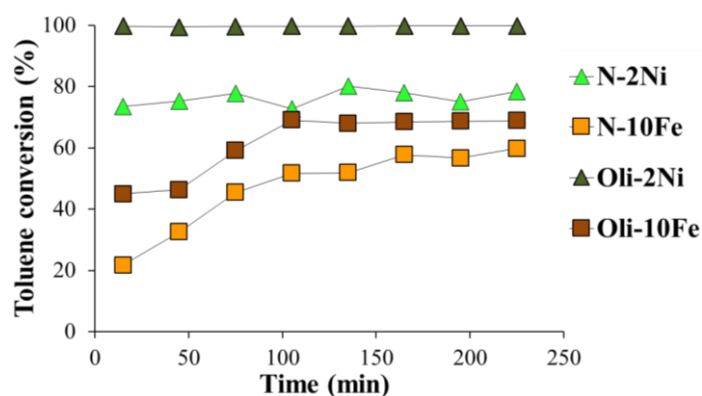


Figure IV.9: Conversion of toluene as a function of time for alumina or olivine samples doped with either 2 wt. % Ni or 10 wt. % Fe tested at $T = 750\text{ }^{\circ}\text{C}$ for the reforming of 8000 ppmv of toluene.

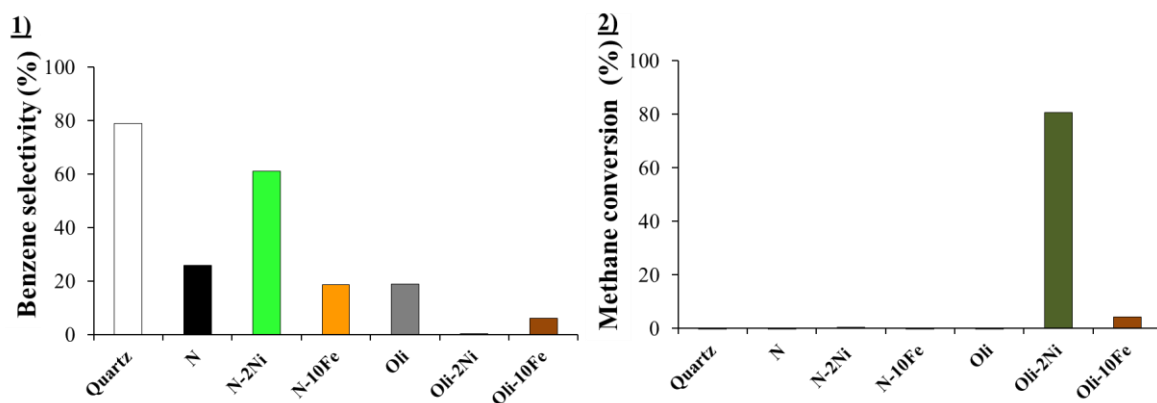


Figure IV.10: Benzene selectivity (left side) and methane conversion (right side) diagrams for alumina or olivine samples doped with either 2 wt. % Ni or 10 wt. % Fe tested at $T = 750$ °C.

Table IV.6: Catalytic performances of alumina or olivine samples doped with either 2 wt. % Ni or 10 wt. % Fe. Test conditions: $T = 750$ °C, 8000 ppmv of toluene, $t = 4$ h, $GHSV = 6000$ h⁻¹.

Samples	C_{Tolu} (%)	S_B (%)	C_{CH_4} (%)	$Coke$ (g _{Carbon} /g _{Cata})
Quartz	5	79	- 3	<0.01
N	18	26	- 3	<0.01
N-2Ni	77	61	0	0.05
N-10Fe	57	19	- 1	0.02
Oli	31	19	- 2	<0.01
Oli-2Ni	99	<0.5	81	<0.01
Oli-10Fe	68	6	4	<0.01

C_{Tolu} : conversion of toluene, S_B : selectivity in benzene; C_{CH_4} : conversion of methane; $Coke$: amount of carbon deposit after 4 h of test determined by TG-DSC.

It was observed in Table IV.6 that at $T = 750$ °C, the raw olivine (sample *Oli*) showed a better catalytic activity than alumina (sample *N*). Indeed, sample *Oli* showed a higher toluene conversion ($C_{Tolu,Oli,750} = 31$ %) compared to sample *N* ($C_{Tolu,N,750} = 18$ %) and to sample *Quartz* ($C_{Quartz,750} = 5$ %). Furthermore, sample *Oli* showed a lower benzene selectivity value ($S_{B,Oli,750} = 19$ %) than sample *N* ($S_{B,N,750} = 26$ %) and sample *Quartz* ($S_{B,Quartz,750} = 79$ %). However, it is to notice that at this temperature, the three samples produced methane (negative conversions values) ($C_{CH_4,Oli,750} = - 2$ %, $C_{CH_4,N,750} = - 3$ % and $C_{CH_4,Quartz,750} = - 3$ %). Since the raw supports showed high values of benzene selectivity and that the supports were free of carbon after the test ($Coke < 0.01$ g_{Carbon}/g_{Cata}), it was assumed that the methane was mostly produced by hydrodealkylation reactions of the toluene molecules (Table IV.2, Equation IV.10).

The better catalytic activity values of samples *N* and *Oli* compared to sample *Quartz* (*i.e.* no catalyst) were attributed to two reasons: 1) the supports were able to adsorb the toluene compounds at their surface, thus favoring their breakdown; 2) the supports favored the adsorption-dissociation of the H₂O and CO₂ molecules necessary for the gasification reactions to take place.¹ This was attributed to the fact that the surface of γ -Al₂O₃ support (sample *N*), or of MgO and FeO_x species (sample *Oli*) can form hydroxyl –OH groups. Furthermore, it was shown by isotope exchange studies that the dissociation of H₂O is favored at the surface of MgO compared to Al₂O₃.^[89] This last observation could explain why the non-porous olivine showed more interesting C_{Tolu} and S_B values than the mesoporous alumina support.

¹: See mechanisms of tar reforming in Figure I.7.

The X-Ray spectra of the alumina-based materials after a catalytic test at $T = 750\text{ }^{\circ}\text{C}$ are presented in Figure IV.11. It was observed after a test at $T = 750\text{ }^{\circ}\text{C}$, that sample *N-2Ni* did neither present any bulk nickel oxide, nor nickel metallic rays (Figure IV.11-a). This fact confirmed the presence of very strong interactions between Ni and the alumina support (formation of spinel).^{[270]–[272], [276]} After a test at $T = 750\text{ }^{\circ}\text{C}$, sample *N-10Fe* showed small rays of hercynite (FeAl_2O_4) (Figure IV.11-b), which revealed strong interactions between the iron species and the alumina support.

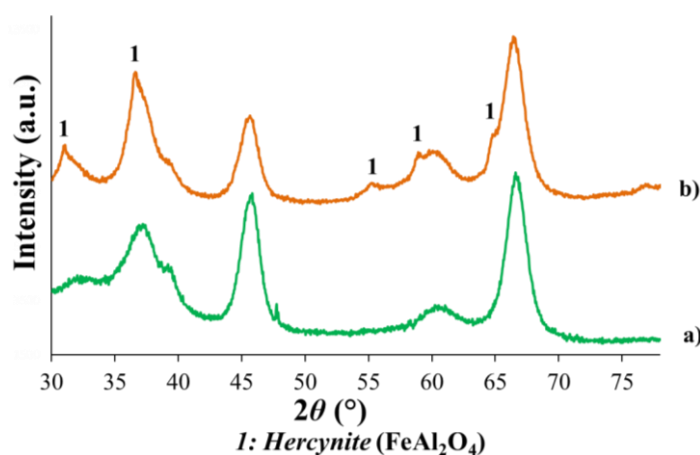


Figure IV.11: X-Ray spectra of samples prepared with alumina and doped with either Ni or Fe after catalytic test at $T = 750\text{ }^{\circ}\text{C}$. a. *N-2Ni-750*, b. *N-10Fe-750*.

In Figure IV.12, after a catalytic test at $T = 750\text{ }^{\circ}\text{C}$, sample *Oli-2Ni-750* presented very small rays of iron oxide partially reduced (FeO) and of kamacite ($\text{Fe}_{0.96}\text{Ni}_{0.04}$). Noteworthy, metallic nickel ($\text{Ni}^{(0)}$) might also be present. However, it is to notice that rays of bulk nickel oxide ($\text{Ni}_{3.75}\text{O}_4$) were still clearly visible.

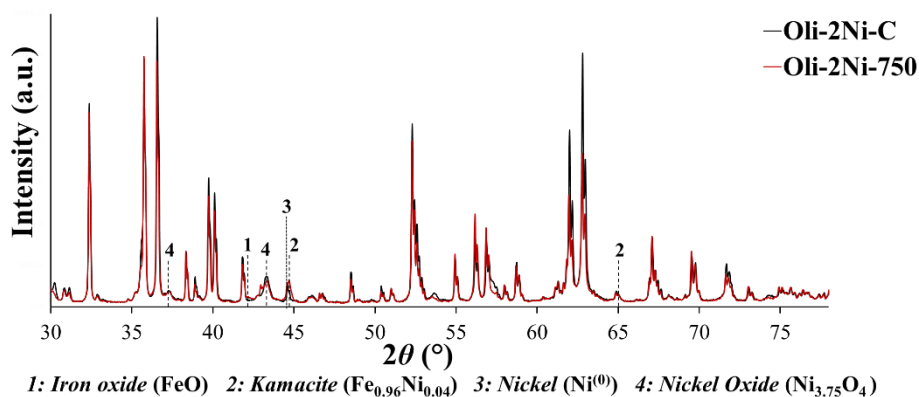


Figure IV.12: X-Ray spectra of sample *Oli-2Ni* after calcination and after catalytic test at $T = 750\text{ }^{\circ}\text{C}$.

In Figure IV.13, after a catalytic test at $T = 750\text{ }^{\circ}\text{C}$, sample *Oli-10Fe-750* presented rays of iron partially reduced (FeO and $\text{Fe}_{0.92}\text{O}$). Noteworthy, the rays of Fe_2O_3 observed after calcination had almost disappeared after a catalytic test at $T = 750\text{ }^{\circ}\text{C}$.

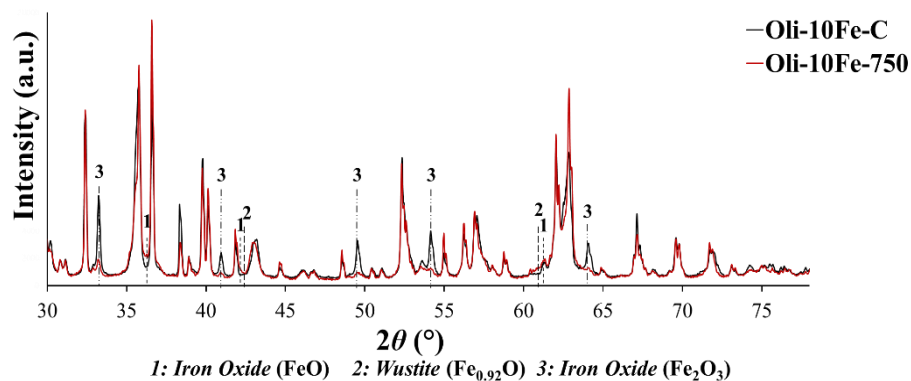


Figure IV.13: X-Ray spectra of sample *Oli-10Fe* after calcination and after catalytic test at $T = 750$ °C.

Figure IV.9 showed that the C_{Tolu} values at $T = 750$ °C stayed similar during the test for both samples *N-2Ni* and *Oli-2Ni*, which suggested that in both cases, the catalysts kept the same active phases and crystallography. During these catalytic tests, sample *Oli-2Ni* showed an almost complete conversion of toluene ($C_{Tolu, Oli-2Ni, 750} = 99$ % whereas $C_{Tolu, N-2Ni, 750} = 77$ %), almost no benzene selectivity ($S_{B, Oli-2Ni, 750} < 0.5$ % whereas $S_{B, N-2Ni, 750} = 61$ %), a much higher methane conversion ($C_{CH_4, Oli-2Ni, 750} = 81$ % whereas $C_{CH_4, N-2Ni, 750} < 0.5$ %) and a much better resistance against coking ($Coke_{Oli-2Ni, 750} < 0.01$ g_{Carbon}/g_{Cata}, whereas $Coke_{N-2Ni, 750} = 0.05$ g_{Carbon}/g_{Cata}) compared to sample *N-2Ni* (Table IV.6). These strong differences of catalytic activity values between samples *N-2Ni* and *Oli-2Ni* were the consequence of different strengths of nickel/support interactions. Indeed, the nickel from sample *N-2Ni* was integrated into a stable and low catalytically active spinel structure ($NiAl_2O_4$) (see TPR, Figure IV.2-d). In contrary, sample *Oli-2Ni* showed more catalytically active species such as oxide partially reduced (FeO), kamacite ($Fe_{0.96}Ni_{0.04}$) and probably metallic nickel ($Ni^{(0)}$). Indeed, such a high methane conversion and low benzene selectivity at $T = 750$ °C observed for sample *Oli-2Ni* necessarily involves the presence of metallic species.^{[55], [65]}

It was observed in Figure IV.9 that the C_{Tolu} values of samples *N-10Fe* and *Oli-10Fe* progressively increased during the catalytic test. This observation suggested that the iron oxide species of both samples were reduced *in situ* during the catalytic test and were progressively more active during the tests. Indeed, the catalytic activity of iron oxide species is generally known to increase with their reduction degree ($Fe_2O_3 < Fe_3O_4 < FeO < Fe^{(0)}$).^{[51], [129], [130], [262]} It was observed that sample *Oli-10Fe* showed a higher toluene conversion value ($C_{Tolu, Oli-10Fe, 750} = 68$ %, whereas $C_{Tolu, N-10Fe, 750} = 57$ %), a lower benzene selectivity value ($S_{B, Oli-10Fe, 750} = 6$ %, whereas $S_{B, N-10Fe, 750} = 19$ %) and a higher methane conversion value ($C_{CH_4, Oli-10Fe, 750} = 4$ %, whereas $C_{CH_4, N-10Fe, 750} = -1$ %) than sample *N-10Fe* (Table IV.6). The better catalytic activity obtained for sample *Oli-10Fe* was mostly attributed to different interactions between iron/alumina and iron/olivine. Indeed, in the case of sample *Oli-10Fe*, the X-Ray spectrum after test (Figure IV.13) revealed the presence of different iron oxide species reduced at different steps (FeO and $Fe_{0.92}O$), which are known to be beneficial for tar reforming reactions.^{[51], [64]} In contrary, the X-Ray spectrum of sample *N-10Fe* (Figure IV.11-b) only showed the presence of iron strongly incorporated into alumina (hercynite, $FeAl_2O_4$), which explains the lower toluene conversion and higher benzene selectivity values obtained for this sample.

IV.3.2.2. Catalytic performances at $T = 850\text{ }^{\circ}\text{C}$

Figure IV.14 shows the toluene conversion as a function of time for the catalysts doped with Ni or Fe (samples *N-2Ni*, *N-10Fe*, *Oli-2Ni* and *Oli-10Fe*). Figure IV.15 shows the methane conversions and the benzene selectivity of all samples. All catalytic performances (toluene conversion, C_{Tolu} , benzene selectivity, S_B , methane conversion, C_{CH_4} , carbon deposit amount after test) are listed in Table IV.7.

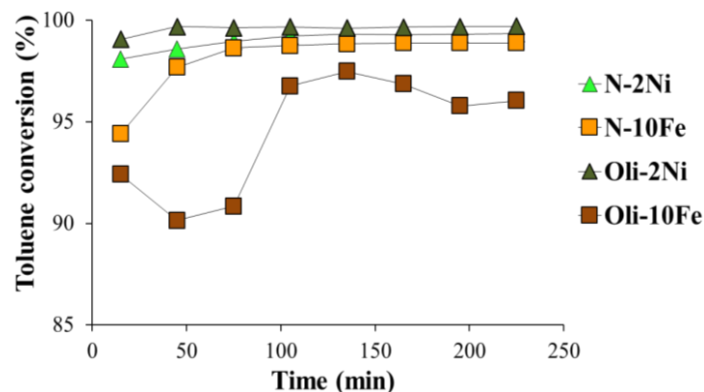


Figure IV.14: Conversion of toluene as a function of time for alumina or olivine samples doped with either 2 wt. % Ni or 10 wt. % Fe tested at $T = 850\text{ }^{\circ}\text{C}$ for the reforming of 8000 ppmv of toluene.

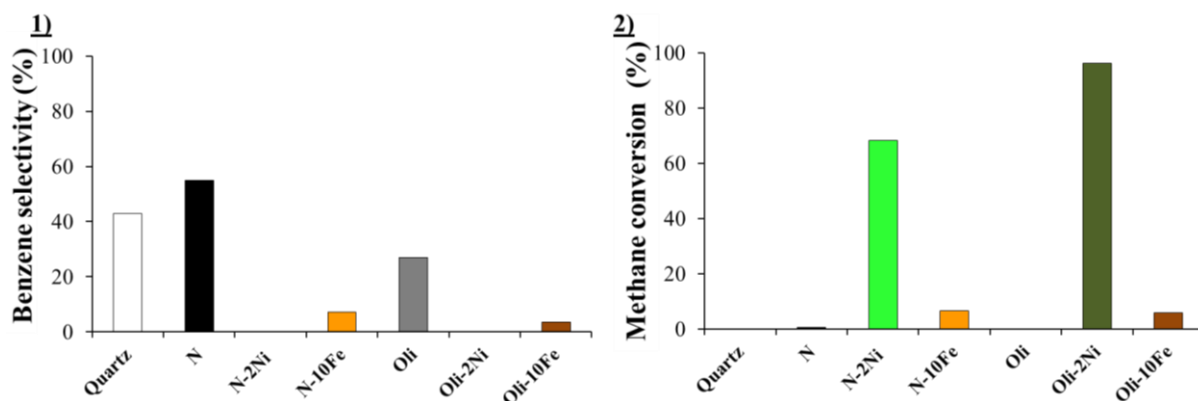


Figure IV.15: Benzene selectivity (left side) and methane conversion (right side) diagrams for alumina or olivine samples doped with either 2 wt. % Ni or 10 wt. % Fe tested at $T = 850\text{ }^{\circ}\text{C}$.

Table IV.7: Catalytic performances of alumina or olivine samples doped with either 2 wt. % Ni or 10 wt. % Fe. Test conditions: $T = 850\text{ }^{\circ}\text{C}$, 8000 ppm of toluene, $t = 4\text{ h}$, $GHSV = 6000\text{ h}^{-1}$.

Samples	C_{Tolu} (%)	S_B (%)	C_{CH_4} (%)	<i>Coke</i> (g _{carbon} /g _{cata.})
Quartz	39	43	0	<0.01
N	76	55	1	0.01
N-2Ni	100	<0.5	68	0.01
N-10Fe	99	7	7	0.01
Oli	72	27	-1	<0.01
Oli-2Ni	100	<0.5	96	<0.01
Oli-10Fe	96	4	6	<0.01

C_{Tolu} : conversion of toluene; S_B : selectivity in benzene; C_{CH_4} : conversion of methane; *Coke*: amount of carbon deposit after 4 h of test determined by TG-DSC.

It was observed in Table IV.7 that at $T = 850\text{ }^{\circ}\text{C}$, samples *N* and *Oli* showed relatively similar toluene conversion values ($C_{Tolu,N,850} = 76\text{ }%$ and $C_{Tolu,Oli,850} = 72\text{ }%$, whereas $C_{Tolu,Quartz,850} = 39\text{ }%$). However, the benzene selectivity value was lower for sample *Oli* compared to sample *N* or sample *Quartz* ($S_{B,Oli,850} = 27\text{ }%$, whereas $S_{B,N,850} = 55\text{ }%$ and $S_{B,Quartz,850}$

= 43 %). Again, it was observed that samples *Quartz*, *Oli* and *N* did not show any methane conversion and were almost free of carbon deposit after test ($Coke \leq 0.01 \text{ g}_{\text{Carbon}}/\text{g}_{\text{Cata}}$).

The X-Ray spectra of the alumina-based materials after a catalytic test are presented in Figure IV.16.

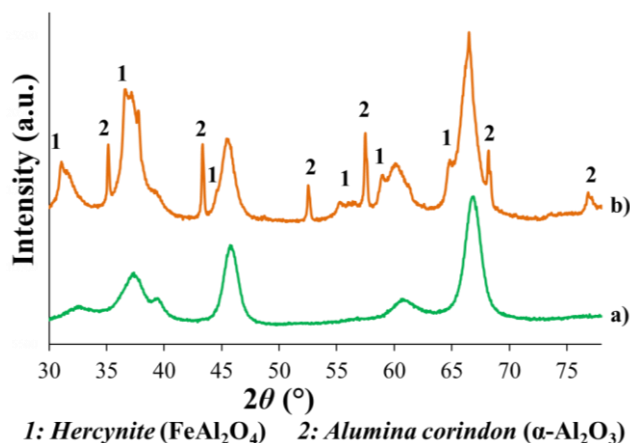


Figure IV.16: X-Ray spectra of samples prepared with alumina and doped with either Ni or Fe after catalytic test at $T = 850 \text{ }^\circ\text{C}$; a. *N-2Ni-850*, b. *N-10Fe-850*.

Sample *N-2Ni* did neither present any bulk nickel, oxide nor nickel metallic rays (Figure IV.16-a). In that case, Ni was so embedded in the spinel structure that it was not being reduced even after a catalytic test at $T = 850 \text{ }^\circ\text{C}$. In the case of sample *N-10Fe* (Figure IV.16-b), the iron species were also integrated into the alumina support since the X-Ray spectrum revealed characteristic rays of hercynite (FeAl_2O_4). The X-Ray spectrum of sample *N-10Fe* also contained intense rays of alumina corindon ($\alpha\text{-Al}_2\text{O}_3$) at $2\theta = 35.1^\circ / 43.4^\circ / 52.5^\circ / 57.4^\circ / 68.2^\circ$ and 76.8° (Figure IV.16-b). This result was unexpected and undesirable. It was caused by a phenomenon highlighted in previous works: during the alumina phase transformation¹, the transitional alumina phases (γ , δ , $\theta\text{-Al}_2\text{O}_3$), organized in a cubic system, are progressively converted into stable hexagonal packing ($\alpha\text{-Al}_2\text{O}_3$).^[277] For the iron oxides, this transformation occurs in a similar way, but the γ - to $\alpha\text{-Fe}_2\text{O}_3$ phase transition happens at much lower temperatures ($T_{\gamma \rightarrow \alpha\text{-Fe}_2\text{O}_3} \sim 350 \text{ }^\circ\text{C}$, while $T_{\gamma \rightarrow \alpha\text{-Al}_2\text{O}_3} \sim 1000 \text{ }^\circ\text{C}$). In the case of strong interactions between Fe and the $\gamma\text{-Al}_2\text{O}_3$ support, $\alpha\text{-Fe}_2\text{O}_3$ can favor the transformation of cubic alumina towards hexagonal packing at lower temperatures.^[277] In the present case, this phenomenon was undesirable since the γ - to $\alpha\text{-Al}_2\text{O}_3$ transformation leads to a disappearance of the advantageous micro- and mesoporosity of the $\gamma\text{-Al}_2\text{O}_3$ phase.

Rays of FeO, kamacite ($\text{Fe}_{0.96}\text{Ni}_{0.04}$) and metallic nickel ($\text{Ni}^{(0)}$) were observed on the X-Ray spectra of sample *Oli-2Ni* after catalytic test at $T = 850 \text{ }^\circ\text{C}$ (Figure IV.17).

¹: More details about the different phase transformation of $\gamma\text{-Al}_2\text{O}_3$ to $\alpha\text{-Al}_2\text{O}_3$ in Figure II.4.

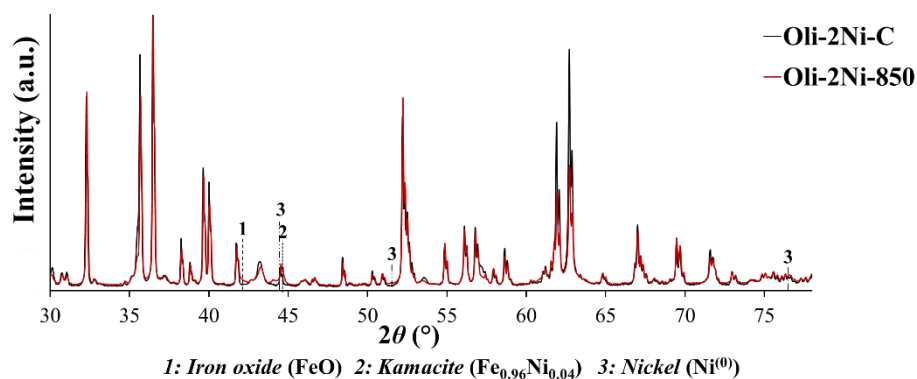


Figure IV.17: X-Ray spectra of sample *Oli-2Ni* after calcination and after catalytic test at $T = 850$ °C.

Rays of metallic iron ($\text{Fe}^{(0)}$) and iron partially reduced (FeO) were observed on the X-Ray spectra of sample *Oli-10Fe* after catalytic test at $T = 850$ °C (Figure IV.18).

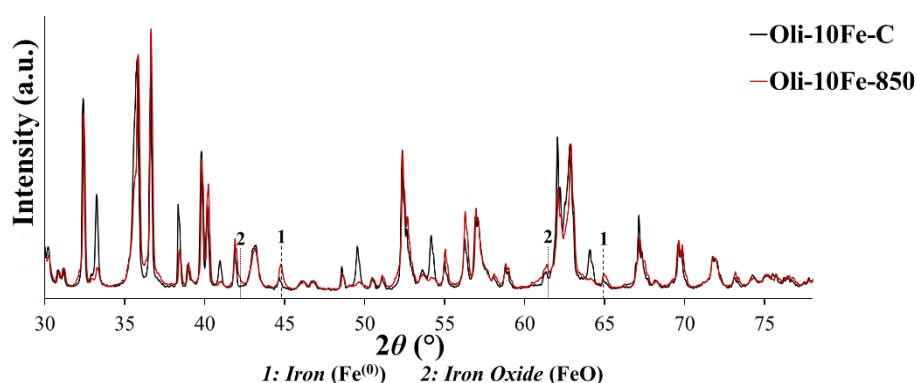


Figure IV.18: X-Ray spectra of sample *Oli-10Fe* after calcination and after catalytic test at $T = 850$ °C.

It was observed in Table IV.7 that both samples *N-2Ni* and *Oli-2Ni* showed complete conversion of toluene ($C_{\text{Tolu},N-2Ni,850} = 100$ % and $C_{\text{Tolu},Oli-2Ni,850} = 100$ %), very low benzene selectivity ($S_{B,N-2Ni,850} < 0.5$ % and $S_{B,Oli-2Ni,850} < 0.5$ %) and were almost free of carbon deposit after test ($\text{Coke} < 0.01$ g_{carbon}/g_{cata}). However, sample *N-2Ni* presented a smaller methane conversion compared to sample *Oli-2Ni* ($C_{\text{CH}_4,N-2Ni,850} = 68$ % whereas $C_{\text{CH}_4,Oli-2Ni,850} = 96$ %). It was assumed that the better catalytic performances of sample *Oli-2Ni* were due to the presence of metallic nickel $\text{Ni}^{(0)}$ (see XRD, Figure IV.17). In the case of sample *N-2Ni*, it seemed that the high temperatures of test permitted to obtain interesting catalytic activity, though Ni was still trapped in the NiAl_2O_4 spinel structure (Figure IV.16-a). The presence of this nickel-aluminate phase explains why sample *N-2Ni* showed a much lower C_{CH_4} value compared to sample *Oli-2Ni*.

During the catalytic test performed at $T = 850$ °C (Figure IV.14), it was observed that the C_{Tolu} values progressively increased for samples *Oli-10Fe* and *N-10Fe* until reaching a value close to 100 %. It was also noticed that both samples showed relatively low benzene selectivity values for iron-doped catalysts ($S_{B,N-10Fe,850} = 7$ % and $S_{B,Oli-10Fe,850} = 4$ %) and that the samples were almost free of carbon deposit after test ($\text{Coke} < 0.01$ g_{carbon}/g_{cata}). However, both samples presented very low methane conversion values compared to the Ni doped samples ($C_{\text{CH}_4,N-10Fe,850} = 7$ % and $C_{\text{CH}_4,Oli-10Fe,850} = 6$ %). In this way, despite the fact that sample *Oli-10Fe* showed metallic iron $\text{Fe}^{(0)}$ during the catalytic test (see XRD, Figure IV.18), its catalytic activity

was however relatively similar to sample *N-10Fe*, which only contained alumina-iron oxides (FeAl_2O_4). Finally, despite the fact that sample *N-10Fe* submitted a phase transformation (γ - to α - Al_2O_3) during the catalytic test, its conversion value of toluene remained stable after $t = 4$ h of test. This could be explained by the fact that, at high temperature of test, the high reaction rates make the presence of specific surface area of the supports much less important.^{[65], [152]}

Among all samples studied in this chapter, it was noticed that whatever the type of support or of dopant, all samples showed very low amounts of carbon deposit after $t = 4$ h of catalytic test at either $T = 750$ °C or $T = 850$ °C. This fact could be explained by several reasons: 1) the tests were performed at high temperatures ($T > 650$ °C), which strongly favors the gasification of the carbon deposit;ⁱ 2) even at $T = 850$ °C, an important fraction of the metals (Ni or Fe) was not fully reduced. It is known that metallic oxides usually show lower reforming activity, but are in contrary much more resistant against carbon deposits.^[65] Furthermore, it was reported that the incorporation of Ni inside NiAl_2O_4 spinel permitted to protect it against sintering and the formation of carbon deposit.^[278]

IV.4. CONCLUSIONS

In this chapter, the characterizations and the catalytic tests of alumina and olivine supports doped with either 2 wt. % of Ni or 10 wt. % Fe were performed.

At $T = 750$ °C, the nickel/olivine sample showed a better catalytic activity (higher toluene conversion and lower benzene selectivity) compared to the nickel/alumina sample. This low activity was attributed to strong interactions between nickel and alumina (formation of a spinel NiAl_2O_4). Similarly, the presence of strong interactions between iron and alumina (formation of hercynite FeAl_2O_4) also explained why the catalyst made of iron/alumina showed a lower toluene conversion and a higher benzene selectivity compared to the iron/olivine sample.

At $T = 850$ °C, the catalysts supported on olivine or alumina showed similar performances. Both nickel-doped supports showed high toluene conversions, low benzene selectivity and were free of carbon deposits. However, due to lower interactions with the support, and better reduction of Ni, the methane conversion of the nickel/olivine sample was higher than the methane conversion of the nickel/alumina sample. At this temperature, iron/alumina and iron/olivine catalysts both showed high toluene conversion, low benzene selectivity, but no methane conversion values.

In conclusion, despite the presence of a lower dispersion of the metallic nanoparticles after reduction and the absence of porosity, the olivine appears to be a more suitable primary catalytic support than alumina. This could be explained by the general notion which states that at high temperatures of test, the high reaction rates make the specific surface area of the support much less important.

ⁱ : More information about formation of carbon deposit in part I.4.3.1. of Chapter I.

In view of the results obtained, it was decided to redirect the future works towards the development of alumina-based materials used as secondary catalysts. Since the reforming ability of Fe as a dopant is only interesting at high temperatures ($T > 750$ °C), and that its presence favored the γ - to α - Al_2O_3 phase transition, it was decided to put aside this element and to focus on the improvement of Ni-based alumina materials. Nevertheless, as Ni and γ - Al_2O_3 formed a stable NiAl_2O_4 spinel, some improvements (higher Ni loading, temperature of calcination ...) must be undertaken for the synthesis of more efficient nickel/alumina catalysts.

Chapter V

Development of Ni-based secondary catalysts supported on γ -Al₂O₃

- Properties of Ni/ γ -Al₂O₃ catalysts synthesized by sol-gel or wet-impregnation methods;
- Influences of the composition of the syngas on the performances of Ni/ γ -Al₂O₃ catalysts;
- Highlight of the phenomenon of “special reduction by toluene”;
- Influences of the loading of nickel on the properties and performances of Ni/ γ -Al₂O₃ catalysts;
- Performances of Ni/ γ -Al₂O₃, pure γ -Al₂O₃ and quartz for the degradation of 24.000 ppmv of toluene at either $T = 650$ °C or at $T = 900 \rightarrow 600$ °C.

This chapter investigates the catalytic performances (catalytic activity and resistance against deactivation) of Ni/ γ -Al₂O₃ catalysts for the reforming of 24.000 ppmv at $T = 650$ °C for $t = 5$ h.

The properties of 10 wt. % Ni/ γ -Al₂O₃ catalysts prepared by wet impregnation or by sol-gel methods were compared. Though the texture and the composition of the samples were identical, it was shown that the preparation method had important influences on the nickel/alumina interactions and consequently on the catalysts performances.

The sol-gel prepared 10 wt. % Ni/ γ -Al₂O₃ catalyst was tested at $T = 650$ °C with different conditions: syngas without CH₄; syngas without toluene; syngas with toluene only for the first $t = 105$ min of test; syngas without neither toluene nor CH₄. The objective was to understand the influence of the syngas composition on the performances of the catalysts.

Ni/ γ -Al₂O₃ catalysts synthesized by sol-gel method with different loadings of Ni (10, 20, 30, 50 wt. %) were characterized and tested for the reforming of toluene. It was shown that the amount of Ni influenced the formation of different types of oxides (NiO, NiO/Al₂O₃ or NiAl₂O₄), and that these species showed a different reducibility, a different catalytic activity and a different resistance against coking mechanisms.

Finally, in order to get a better understanding of the catalysts performances, catalytic tests were performed at $T = 900 \rightarrow 600$ °C with the sol-gel prepared 10 wt. % Ni/ γ -Al₂O₃ catalyst, with pure alumina or with quartz grains.

V.1. INTRODUCTION

It was shown in an additional study presented in Annex 6 that 10 wt. % Ni/ γ -Al₂O₃ catalysts tested for the reforming of 8000 ppmv of toluene at $T = 650$ °C showed very high conversion values, relatively low amounts of carbon deposits and no deactivation after $t = 5$ h of test. Hence, the catalytic tests of this current chapter were performed with a higher amount of toluene (24.000 ppmv) in order to evaluate the performances of the catalysts at a critical concentration of tar.

Due to weaker metal/support interactions, the metallic nanoparticles of impregnated catalysts are generally more inclined to sinter and submit coke deactivation, especially by the formation of filamentous carbon, compared to catalysts prepared by a sol-gel method.^{[183]–[185].}^[279] 10 wt. % Ni/ γ -Al₂O₃ catalysts prepared by sol-gel and wet impregnation methods were therefore tested, in order to confirm this hypothesis and to understand the direct influence of the sol-gel preparation method on the catalytic performances and on the lifetime.

During the first catalytic tests performed in this chapter, several questions appeared:

* whereas the TPR measurements showed that the sol-gel prepared 10 wt. % Ni/ γ -Al₂O₃ catalyst started to be reduced only above $T = 680$ °C, during catalytic tests performed at $T = 650$ °C, this sample was in contrary progressively reduced by the syngas mixture and presented metallic nanoparticles after tests. Hence, it seemed that the composition of the syngas increased

the reducibility of the catalyst and made it catalytically active at lower temperatures than predicted by the TPR performed with H₂. It was shown in a recent study that the presence of several organic compounds could improve the reduction of nickel oxides.^{[280], [281]} *Was the better reducibility observed in the first tests of this chapter caused by the presence of methane or toluene?*

* as described in the part I.4.1.1. of Chapter I, during the reforming mechanisms, the reforming of the toluene molecules at the surface of the metallic active site are in direct competition with the reforming of the CH₄ molecules. Therefore, the presence of methane in the syngas composition could increase the covering of the surface of the metallic Ni particle with CH_x^{*} and C^{*} species. However, the influence of the presence of methane during the reforming of tars is not detailed in the literature. *What were the consequences of the presence of methane in the syngas composition on the formation of carbon deposit and on the conversion of toluene?*

* during the catalytic test, according to the different reactions of toluene conversion,ⁱ the toluene molecules can be either converted into CH₄, or CO and H₂. *What was the fraction of toluene molecules completely converted into syngas (CO+H₂) during catalytic tests performed at T = 650 °C?*

* *what were the influences of parallel reactions such as water-gas shift, water-gas, methanation or Boudouard reactions on the syngas composition during the catalytic tests performed with 10 wt. % Ni/ γ -Al₂O₃?ⁱⁱ*

In order to answer all these questions, catalytic tests were performed at T = 650 °C with a 10 wt. % Ni/ γ -Al₂O₃ catalyst according to five different procedures: 1) with toluene and with methane (standard test); 2) without methane; 3) without toluene; 4) with toluene, but only during the first 105 min of test; 5) without neither toluene nor methane.

It is known that whereas the nickel surface area increases with the nickel loading, the Ni dispersion in contrary decreases when the nickel content increases.^{[65], [276]} For methane steam-reforming with nickel/alumina catalysts, the optimum loading is usually 20 wt. % of Ni for sol-gel prepared catalysts, and 15 wt. % of Ni for impregnated catalysts.^{[9], [65]} In this chapter, sol-gel catalysts were prepared with Ni concentrations varying from 10 wt. % to 50 wt. %. The aim was to understand how the nickel/alumina interactions, the reducibility, the dispersion of the metallic Ni particles, the mesostructure of the support and the catalytic performances evolved with increasing nickel amounts. Furthermore, this study also aimed at confirming if the improvements of the catalysts synthesis performed in Annex 5 permitted to synthesize homogeneous catalysts with high amounts (30-50 wt. %) of metal doping.

Though the catalysts were designed in order to work under secondary catalytic conditions (outlet of the industrial gasifier, T = 500-750 °C), additional catalytic tests were performed at T = 900→600 °C. These tests were performed with a sol-gel prepared 10 wt. % Ni/ γ -Al₂O₃

ⁱ: More information about reactions of toluene conversion in Table IV.2.

ⁱⁱ: More information about parallel reactions in Table I.1.

catalyst, pure alumina and quartz beads in order to dissociate the effects caused by the support and by the metallic active sites during the reforming of toluene and methane. These tests permitted also to estimate the kinetic parameters (E_a and k_0) of the samples for the conversion of toluene in order to compare them to the values obtained in the literature. Finally, it is to notice that catalysts tested at $T = 650$ °C generally submit a pre-reduction step at higher temperature, with H₂ or with *in situ* reduction by the syngas mixture.^{[55], [63], [175], [282]} Hence, these additional catalytic tests permitted also to compare the catalytic performances of a 10 wt. % Ni/ γ -Al₂O₃ catalyst tested at $T = 650$ °C under standard conditions (no pre-reduction) or tested at $T = 650$ °C (with *in situ* previous reduction during the tests performed at $T = 900 \rightarrow 600$ °C).

V.2. EXPERIMENTAL

V.2.1. Synthesis of Ni/ γ -Al₂O₃ catalysts

The catalysts were synthesized according to different preparation methods described below and whose reagent amounts are presented in part V of Annex 2.

V.2.1.1. Ni/ γ -Al₂O₃ catalysts prepared by sol-gel method

The method of preparation of catalysts used in this chapter was inspired by the procedure used in Chapter IV. However, in order to allow a higher loading of metal dopant, the previous method was submitted to some modifications (type of drying solvent, removal of the last washing step) whose details are given in Annex 5. In this way, the sol-gel prepared Ni/ γ -Al₂O₃ catalysts of this chapter were synthesized as follows:

The boehmite sols were prepared according to the standard procedure used for the preparation of sample *N* in Chapter II. The sols were washed two times with water in order to evacuate the NH⁴⁺ ions. Thereafter, the sols were re-dispersed in water, nickel nitrate was added and the sols were stirred for $t = 30$ min. The doped sols were put in an oven for aging ($t = 24$ h, $T = 85$ °C, $P = 700$ mbar) and for drying ($t = 24$ h, $T = 110$ °C, $P = 900$ mbar). The dried gels were calcined for $t = 5$ h at $T = 550$ °C, with a heating rate of 2 °C/min. Samples *N-10Ni*, *N-20Ni*, *N-30Ni* and *N-50Ni* were prepared according to this procedure with loadings of respectively 10, 20, 30 and 50 wt. % of Ni.

V.2.1.2. Ni/ γ -Al₂O₃ catalysts prepared by impregnation method

Sample *IMP-N-10Ni* was prepared by a wet impregnation method. The support consisted of calcined γ -Al₂O₃ synthesized according to the procedure used for the preparation of sample *N* in Chapter II. The support was crushed and sieved in order to get grain sizes comprised between 300 and 700 μ m, which were set in a glass balloon with water and nickel nitrate. The balloon was fixed to a Rotavap apparatus and the water was evaporated under continuous agitation at $T = 85$ °C and $P = 300$ mbar. The dried sample was thereafter calcined with standard calcination procedure ($t = 5$ h at $T = 550$ °C).

V.2.2. Characterization techniques

Composition analysis (ICP–AES), nitrogen adsorption-desorption (BET), microscope analyses (SEM-BSE), X-Ray diffraction (XRD), temperature programmed reduction (TPR), thermogravimetric-differential scanning calorimetry (TG-DSC) and pure reduction (H₂-Reduction) measurements were performed on samples of this chapter. The alumina crystallites sizes were calculated by using the Scherrer equation centered on the (4 0 0) ray γ -Al₂O₃ ($2\theta = 67.0^\circ$) of the XRD spectra. The Ni⁽⁰⁾ crystallites sizes were calculated by using the Scherrer equation centered on the (2 0 0) ray ($2\theta = 51.83^\circ$) of the XRD spectra. Deeper information about the characterization techniques and operating variables are provided in part II of Annex 2. X-Ray references cards are given in part VI of Annex 2.

V.2.3. Catalytic tests

The standard catalytic tests were performed with a toluene concentration of 24.000 ppmv and with a standard gas mixture.ⁱ The mass of the catalyst was set to 300 mg, for a catalytic bed height of $h = 12$ mm, with a gas flowrate of 50 mL/min and consequently a *GHSV* of 5000 h⁻¹ (residence time of 0.72 sec). The standard catalytic tests were performed at $T = 650^\circ\text{C}$, for $t = 300$ min.

The catalytic activity was evaluated thanks to the toluene conversion (C_{Tolu}), the benzene selectivity (S_B) and the methane conversion (C_{CH_4}) whose formulae are reminded in part I of Annex 2. All C_{Tolu} , S_B and C_{CH_4} values were obtained by making an average of the results obtained during the last 10 measurements of the test.

In this chapter, the consumption rate of toluene, r_{Tolu} , in mol_{Tolu}/(g_{Ni}.h), was also compared. For this gas mixture, the (H₂O+ CO₂)/C ratio is about 1.6 when only taking toluene as carbon source, and it is about 1.0 when taking toluene+methane as carbon source. Though these values are low, they are equal or higher to the stoichiometric ratio. Hence, the toluene consumption rate can be expressed with respect only to the toluene concentration and according to a first order ($n = 1$), which leads to:ⁱⁱ

$$-r_{Tolu} = k \cdot C_{rt,Tolu} \quad (\text{V.1})$$

where r_{Tolu} is the consumption rate of toluene (mol_{Tolu}/(g_{Ni}.h)), k is the apparent kinetic constant (m³/(g_{Ni}.h)) and $C_{rt,Tolu}$ is the concentration of toluene (mol_{Tolu}/m³).

Since the reaction rate is assumed to be of first order ($n = 1$), r_{Tolu} can also be expressed as follows^{[283]. [284]}:

$$r_{Tolu} = \left(-\frac{F_{Tolu}}{W} \right) \ln(1 - f_{Tolu}) \quad (\text{V.2})$$

where F_{Tolu} is the molar flowrate of toluene at the reactor inlet (mol_{Tolu}/h), W is the nickel mass inside the reactor (g) and f_{Tolu} is the toluene conversion ($f_{Tolu} = C_{Tolu}/100$).

ⁱ: Composition of standard syngas mixture presented in Table IV.1.

ⁱⁱ: More information about the order of reaction during degradation of tars in part I.4.1.2. of Chapter I.

Some additional catalytic tests were performed at different temperatures ($T = 900 \rightarrow 600$ °C, with $\Delta T = 50$ °C) with the sol-gel prepared 10 wt. % Ni/ $\gamma\text{-Al}_2\text{O}_3$ catalyst (sample *N-10Ni*), pure $\gamma\text{-Al}_2\text{O}_3$ (sample *N* from Chapter II) and inert quartz grains (sample *Quartz*). First, the samples were heated from $T = 25$ °C to $T = 900$ °C under He with a heating rate of 5 °C/min. At $T = 900$ °C, the gas mixture was sent to the catalytic chamber and three GC injections were performed (one every 15 min). Thereafter, the temperature was diminished by 50 °C, three new GC injections were performed and so on, until T reached 600 °C. Hence, for these additional tests, each dot on the graphs corresponds to an average of three GC injections performed every $\Delta T = 50$ °C. The results obtained during these additional tests permitted to calculate the pre-exponential factor, k_0 , and the activation energy, E_a . Since the reaction was assumed to be of first order, the Arrhenius equation was defined as follows:

$$k = k_0 \cdot \exp\left(-\frac{E_a}{RT}\right) \quad (\text{V.3})$$

where k is the apparent kinetic constant ($\text{m}^3/(\text{g}_{\text{Cata}} \cdot \text{h})$), k_0 is the pre-exponential factor ($\text{m}^3/(\text{g}_{\text{Cata}} \cdot \text{h})$), E_a is the activation energy (kJ/mol), R is the gas constant ($8.314 \cdot 10^{-3}$ kJ/(K.mol)) and T is the temperature (K).

However, the determination of the values from Equation V.3 is relatively difficult because of the strong correlation between the two parameters of the exponential equation.^{[285]–[287]} In order to counter this phenomenon, it is common to reconfigure the Arrhenius equation as follows:

$$k = k_{Ref} \cdot \exp\left[-\frac{E_a}{R} \left(\frac{1}{T} - \frac{1}{T_{Ref}}\right)\right] \quad \text{with} \quad k_{Ref} = k_0 \cdot \exp\left(-\frac{E_a}{RT_{Ref}}\right) \quad (\text{V.4})$$

where T_{Ref} (K) is a reference temperature fixed in the middle of the temperature range studied and k_{Ref} is the apparent kinetic constant at T_{Ref} .

In this project, T_{Ref} was set to 1000 K, and both parameters E_a and k_0 were determined thanks to a Nonlinear Parameter Estimation (NLPE) program.

The yield of methane, $Y_{Tolu \rightarrow CH_4}$, which corresponded to the methane produced from the conversion of toluene by hydrocracking ($C_7H_8 + H_2 \rightarrow C_6H_6 + CH_4$) or by hydrodealkylation ($C_7H_8 + 10.H_2 \rightarrow 7.CH_4$) reactions¹ was determined according to Equation V.5:

$$Y_{Tolu \rightarrow CH_4} = \frac{n_{CH_4, Out}}{7 \cdot n_{Tolu, In} - (7 \cdot n_{Tolu, Out} + 6 \cdot n_{Benz, Out})} \quad (\text{V.5})$$

where $n_{Tolu, In}$ is the initial amount of toluene (mol), and $n_{Tolu, Out}$, $n_{Benz, Out}$, $n_{CH_4, Out}$ are respectively the amounts of toluene, benzene and methane at the exit of the reactor (mol). It is to notice that this yield did not take into account the carbon deposit and could only be used as an estimation value.

In order to get a more accurate comparison of the coking tendency of the catalysts, the term *Coke** was introduced. This value corresponds to the amount of carbon formed by gram of toluene converted and is determined by Equation V.6:

¹: More information about reactions of toluene conversion in Table IV.2.

$$Coke^* = \frac{Coke}{r_{Tolu} * \left(\frac{\%Ni}{100}\right) * t * M_{Tolu}} \quad (V.6)$$

where *Coke* is the amount of carbon deposit determined from TG-DSC measurements (g_{Carbon}/g_{Cata}), (%Ni/100) is the gram of nickel by gram of catalyst, determined from ICP-AES measurements, r_{Tolu} is the consumption rate of toluene (mol_{Tolu}/(g_{Ni}.h)), *t* is the time of test (5 h) and M_{Tolu} is the molecular mass weight of toluene (92.1 g/mol).

According to the results presented in part III of Annex 2, it was assumed that all samples did not submit neither internal nor external diffusional limitations during the catalytic tests.

V.3. RESULTS AND DISCUSSION

V.3.1. Composition of Ni/ γ -Al₂O₃ catalysts

Table V.1 shows the theoretical and actual compositions of all samples. It is to notice that the theoretical and actual compositions were similar for all samples.

Table V.1: Theoretical and actual compositions of Ni/ γ -Al₂O₃ catalysts.

Samples	Al ₂ O ₃		Ni	
	Theo. (wt. %)	Exp. (wt. %)	Theo. (wt. %)	Exp. (wt. %)
N-10Ni	90.0	89.5	10.0	10.5
N-20Ni	80.0	79.7	20.0	20.3
N-30Ni	70.0	68.6	30.0	31.4
N-50Ni	50.0	51.2	50.0	48.2
IMP-N-10Ni	90.0	91.1	10.0	8.9

V.3.2. Influences of the catalysts preparation method

V.3.2.1. Properties of Ni/ γ -Al₂O₃ catalysts prepared by impregnation or by sol-gel methods

Table V.2 shows the textural properties after calcination, and the metallic Ni particles sizes after either reduction step or TPR measurements determined by TEM and XRD analyses.

Table V.2: Textural properties after calcination, metallic Ni particles sizes and standard deviations after either reduction or TPR measurements for samples *IMP-N-10Ni* and *N-10Ni*.

Samples	Textural properties			Ni particles size					
				Post-H ₂ Reduction			Post-TPR		
	S_{BET} (m ² /g)	V_p (cm ³ /g)	$V_{Dubinin}$ (cm ³ /g)	d_{TEM} (nm)	σ_{TEM} (nm)	d_{XRD} (nm)	d_{TEM} (nm)	σ_{TEM} (nm)	d_{XRD} (nm)
N-10Ni	240	0.3	0.08	8	2	9	30	9	23
IMP-N-10Ni	210	0.2	0.08	10	3	10	35	15	24

S_{BET} : specific surface area; V_p : porous volume; $V_{Dubinin}$: microporous volume; d_{TEM} : metallic particles size median; σ_{TEM} : standard deviation; d_{XRD} : metallic nickel crystallites size obtained by XRD.

It was observed in Table V.2, that the textural properties of sample *IMP-10Ni* only slightly decreased ($\Delta S_{BET} = -30$ m²/g, $\Delta V_p < 0.1$ cm³/g, $\Delta V_{Dubinin} < 0.01$ cm³/g), probably because of the impregnation with nickel salts and of the second calcination step.

After H₂ reduction step, it was observed that d_{TEM} , σ_{TEM} and d_{XRD} values were relatively similar for samples *N-10Ni* and *IMP-10Ni* (Table V.2). In contrary, after TPR measurement, sample *IMP-N-10Ni* showed a more important standard deviation than sample *N-10Ni* ($\sigma_{TEM,IMP}$).

$N-10Ni = 15$ nm, whereas $\sigma_{TEM,N-10Ni} = 9$ nm) (Table V.2). Figure V.1 presents the distribution of the metallic Ni particle size after H₂ reduction step and after TPR measurement.

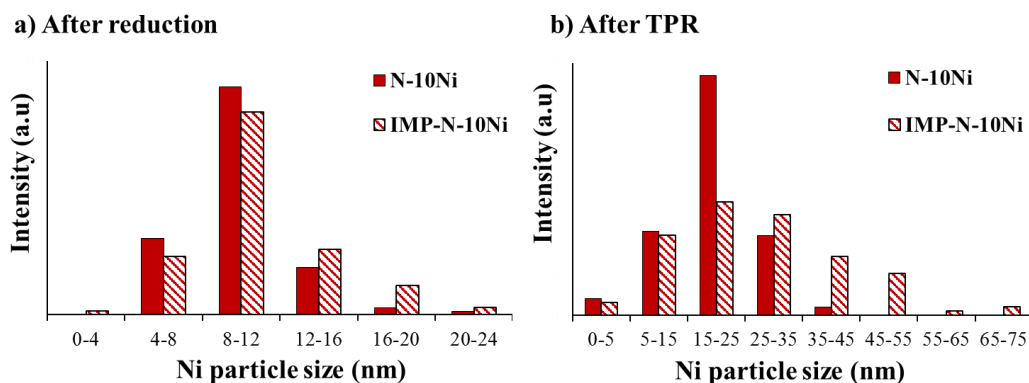


Figure V.1: Metallic Ni particles sizes distributions after H₂ reduction step and after TPR for samples *N-10Ni* and *IMP-N-10Ni*.

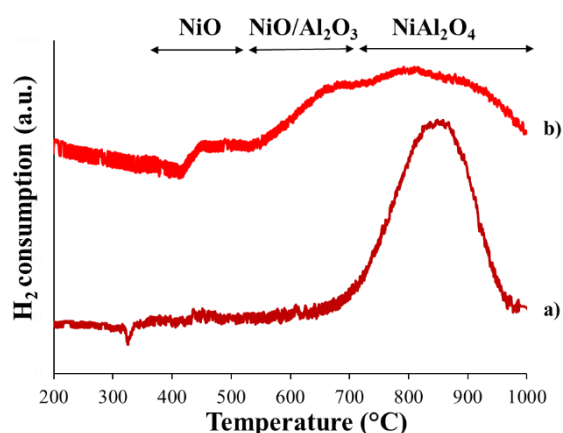


Figure V.2: TPR curves for sol-gel prepared and impregnated samples; a. *N-10Ni*, b. *IMP-N-10Ni*.

Figure V.2 shows the TPR profiles of the samples. In the case of sample *IMP-N-10Ni*, broad and asymmetric H₂ consumption peaks revealed the presence of different interactions between the Ni oxides and the alumina support. Three types of oxides were observed: 1) bulk NiO was present between $T = 400$ °C and $T = 550$ °C. Bulk NiO is known to share very few interactions with the alumina support. Indeed, at this loading of metal (10 wt. %), bulk NiO is more likely encountered for nickel supported on α -Al₂O₃; 2) NiO/Al₂O₃ was present between $T = 550$ °C and $T = 700$ °C. In that case, the Ni²⁺ ions are in octahedral coordination and show relatively strong interactions with the support; 3) NiAl₂O₄ was observed from $T = 700$ °C to $T = 1000$ °C.^{[271], [272], [276]} In that case the Ni²⁺ ions are in tetrahedral coordination and are fully integrated inside a spinel structure of nickel aluminate.^{[276], [288], [289]} The presence of Ni incorporated into γ -Al₂O₃ is evidenced by the fact that the TPR curve did not come back to the baseline at $T = 1000$ °C. Indeed, it was estimated for sample *IMP-N-10Ni*, that only 90 % of the Ni was reduced during the TPR measurement.

In contrary to sample *IMP-N-10Ni*, sample *N-10Ni* presented only a symmetric and narrow consumption peak, which evidenced the exclusive presence of NiAl₂O₄.^{[272], [288], [289]} This observation was in accordance with other studies, in which Ni/ γ -Al₂O₃ materials were prepared by a sol-gel method and with similar nickel doping.^{[278], [279], [290]} In that case, the TPR baseline came back to zero at $T = 1000$ °C and the reduction of Ni was close to 100 %.

Since both samples presented particles with similar initial sizes and dispersions after the H_2 reduction (Figure V.1-a) and showed similar textural properties (Table V.2), it was decided that the different type of Ni oxides observed for sample *IMP-N-10Ni* during the TPR measurement was only a consequence of the preparation method. This assumption was strengthened by the fact that previous studies highlighted that nickel/alumina interactions were greatly influenced by the preparation method.^{[278], [279], [288]}

V.3.2.2. Catalytic performances of Ni/ γ - Al_2O_3 catalysts prepared by impregnation or by sol-gel methods

Figure V.3 shows the evolution of the toluene conversion as a function of time. Table V.3 shows the Ni particles sizes and the catalytic performances of samples *IMP-N-10Ni* and *N-10Ni*.

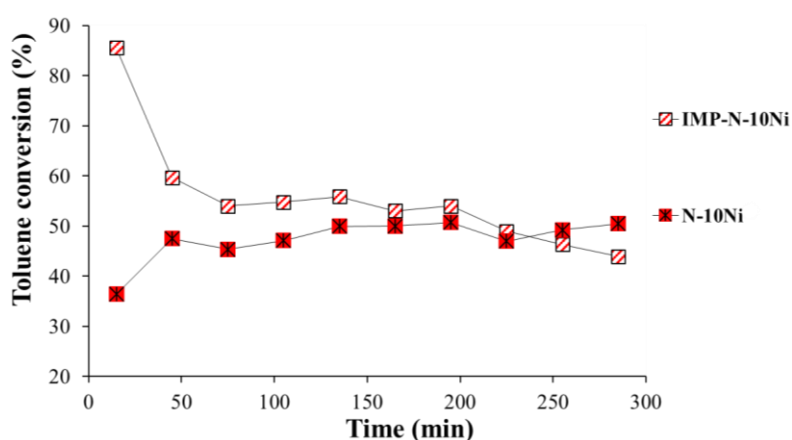


Figure V.3: Toluene conversion as a function of time for samples *IMP-N-10Ni* and *N-10Ni*; 24.000 ppmv of toluene, $T = 650\text{ }^\circ\text{C}$, $t = 300\text{ min}$, $GHSV = 5000\text{ h}^{-1}$.

Table V.3: Ni particles size and catalytic performances of samples prepared by sol-gel or by impregnation methods. Test conditions: $T = 650\text{ }^\circ\text{C}$, $t = 300\text{ min}$, 24.000 ppmv of toluene, $GHSV = 5000\text{ h}^{-1}$.

Samples	Ni particles sizes			Catalytic performances						
	d_{TEM} (nm)	σ_{TEM} (nm)	d_{XRD} (nm)	C_{Tolu} (%)	r_{Tolu} (mol _{Tolu} /(g _{Ni} .h))	C_{CH4} (%)	S_B (%)	Coke (gCarbon/gCata)	Coke* (gCarbon/gTolu)	Fil. carbon
N-10Ni	11	3	12	51	$6.7 \cdot 10^{-2}$	10	15	0.10	$3.1 \cdot 10^{-2}$	+
IMP-N-10Ni	15	7	14	50	$7.6 \cdot 10^{-2}$	13	8	0.28	$8.9 \cdot 10^{-2}$	++

d_{TEM} : particle size median; σ_{TEM} : standard deviation; d_{XRD} : crystallites size estimation obtained by XRD; C_{Tolu} : conversion of toluene; r_{Tolu} : reaction rate of toluene; S_B : selectivity in benzene; C_{CH4} : conversion of methane; Coke: carbon deposit amount after 5 h of test measured by TG-DSC; Coke*: tendency of sample to form carbon deposit.

It was observed in Figure V.3 that sample *IMP-N-10Ni* showed a high C_{Tolu} value at the beginning of the test, but presented a high loss of catalytic activity during the first 75 min ($\Delta C_{Tolu} = -26\%$). After $t = 105\text{ min}$, its toluene conversion was more or less stabilized, but nevertheless progressively decreased until the end of the test. In contrary, sample *N-10Ni* started with a low C_{Tolu} value (38 %) but was progressively activated during the test until it reached a stable C_{Tolu} value (51 %). It is to notice that this sample was not deactivated during the 300 min of test.

It was observed in Table V.3 that sample *IMP-N-10Ni* presented higher catalytic activity values compared to sample *N-10Ni*: a higher toluene reforming rate ($r_{Tolu,IMP-N-10Ni} = 7.6 \cdot 10^{-2}$

mol_{Tolu}/(g_{Ni}.h), whereas $r_{Tolu,N-10Ni} = 6.7 \cdot 10^{-2}$ mol_{Tolu}/(g_{Ni}.h)), a higher methane conversion ($C_{CH_4,IMP-N-10Ni} = 13$ %, whereas $C_{CH_4,N-10Ni} = 10$ %) and a lower benzene selectivity ($S_{B,IMP-N-10Ni} = 8$ %, whereas $S_{B,N-10Ni} = 15$ %). However, sample *IMP-N-10Ni* presented a higher sensibility towards carbon formation than sample *N-10Ni* ($Coke^*_{IMP-N-10Ni} = 8.9 \cdot 10^{-2}$ g_{Carbon}/g_{Tolu}, whereas $Coke^*_{N-10Ni} = 3.1 \cdot 10^{-2}$ g_{Carbon}/g_{Tolu}).

The analysis of the post-test DSC curves presented in Figure V.4 revealed that, whereas the carbon deposit of sample *N-10Ni* was only composed of amorphous carbon (burned at $T < 550$ °C), the carbon deposit of sample *IMP-N-10Ni* was in contrary constituted of both amorphous and filamentous carbon deposits (burned at $T > 550$ °C). TEM observations (not shown here) also confirmed the problematic presence of filamentous carbon for this sample.¹

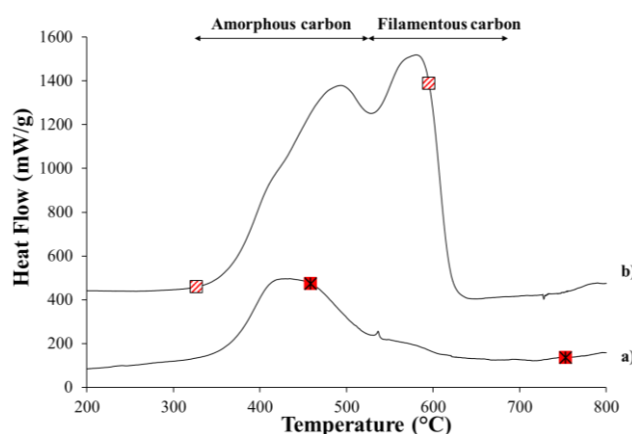


Figure V.4: Post-test DSC curves for sol-gel and impregnated samples; a. *N-10Ni*, b. *IMP-N-10Ni*.

The higher catalytic activity and sensibility towards carbon formation of sample *IMP-N-10Ni* can be explained by the presence of easily reduced bulk nickel oxide (NiO) evidenced during the TPR measurement (Figure V.2-b). Indeed, during the catalytic test performed at $T = 650$ °C, bulk NiO was instantly activated at the beginning of the test. As this type of nickel oxide is known to present the highest catalytic activity but also the lowest interactions with the support, it was quickly deactivated by coking mechanisms.^{[278], [290]} Furthermore, the sintering of NiO was increased by the fact that this type of nickel oxide shows low interactions with the alumina support. This would explain why sample *IMP-N-10Ni* presented larger Ni⁽⁰⁾ particles with a broad distribution of sizes after a catalytic test than sample *N-10Ni* (Table V.2). The growth of filamentous carbon being more favorable for large metallic particles,^{[151], [177], [178]} this would also explain why sample *IMP-N-10Ni* presented filamentous carbon, whereas sample *N-10Ni* only presented amorphous carbon (Figure V.4). Hence, after $t = 105$ min of test, the bulk NiO was assumed to be entirely deactivated by coke and the stable C_{Tolu} of sample *IMP-N-10Ni* was only guaranteed by the nickel which strongly interacted with the support (coming from NiO/Al₂O₃ and NiAl₂O₄).

The stable catalytic activity and low carbon deposit observed for sample *N-10Ni* was attributed to the initial presence of nickel oxide which strongly interacted with the support

¹: More details about the formation and the type of carbon deposit type in Figure I.8.

(NiAl₂O₄). However, at this stage of the study, the behavior of sample *N-10Ni* during the catalytic test was not fully understood. Indeed, despite the fact that the TPR measurement (Figure V.2-a) indicated that the reduction of the NiAl₂O₄ phase of sample *N-10Ni* only started at $T = 680$ °C, this sample was in contrary progressively reduced by the syngas mixture during catalytic tests performed at $T = 650$ °C and presented metallic nanoparticles after catalytic tests (evidenced by XRD and TEM measurements). Hence, it seemed that the composition of the syngas increased the reducibility of the catalyst and made it catalytically active at a lower temperature than predicted. This observation is further discussed in the following part of this chapter.

In this way, for similar initial metallic particles sizes and similar textures, it appeared that the sol-gel prepared 10 wt. % Ni/ γ -Al₂O₃ catalyst, which presented strong and homogeneous metal/support interactions, was better adapted for the reforming of 24.000 ppmv of toluene at $T = 650$ °C. Therefore, this study confirmed the advantageous influence of the use of sol-gel instead of wet impregnation methods for this application.

V.3.3. Influences of the syngas composition

Several catalytic tests were performed in order to understand why sample *N-10Ni* was activated at $T = 650$ °C during the test performed in part V.3.2 of this chapter (Figure V.3) whereas it was reduced only at $T = 680$ °C during H₂-TPR measurement (Figure V.2-a). These tests also permitted to understand the influence of the presence of methane in the syngas mixture, to estimate the fraction of toluene converted to CH₄, or to CO and H₂, and to estimate the influence of the presence of a catalyst on the composition of the syngas mixture by parallel reactions.

The sol-gel prepared 10 wt. % Ni/ γ -Al₂O₃ catalyst was tested for $t = 300$ min at $T = 650$ °C according to the following parameters: 1) standard conditions (sample *N-10Ni*); 2) without methane (sample *N-10Ni-NoCH4*); 3) without toluene (sample *N-10Ni-NoTolu*); 4) with standard conditions, until $t = 105$ min of test, after which the syngas was send without toluene (sample *N-10Ni-Tolustop*); 5) without methane and without toluene (sample *N-10Ni-Nothing*).

Table V.4 shows the composition of the gas mixtures during the catalytic tests. It was observed in Table V.4 that, when the catalytic test was performed without neither methane nor toluene (*N-10Ni-Nothing*), the volumic percentages of CO and H₂O decreased ($\Delta V_{CO} = - 2.0$ %; $\Delta V_{H_2O} = - 1.6$ %) and the volumic percentages of CO₂ and H₂ increased ($\Delta V_{CO_2} = + 2.5$ %; $\Delta V_{H_2} = + 0.7$ %). This effect was mainly attributed to the Water-Gas Shift reactionⁱ ($CO + H_2O \leftrightarrow CO_2 + H_2$) which can occur on Al₂O₃ supports doped with metallic oxides.^{[291], [292]}

ⁱ: More details about Water-Gas Shift, Boudouard and Water-Gas reaction n°3 in Table I.1.

Table V.4: Evolution of the gas composition and catalytic performances of sample *N-10Ni* tested under different atmospheres.

Samples	Gas composition (vol. %)						Catalytic performances	
		CO_2	H_2O	H_2	CH_4	CO		
N-10Ni	Blank	16.2	12.8	29.0	11.2	30.8	$C_{\text{Tolu}} = 51\%$	$\text{Coke} = 0.10 \text{ gCarbon/gCata}$
	Test	15.8	7.3	33.1	10.2	33.6	$C_{\text{CH}_4} = 10\%$	$\text{Sb} = 15\%$
	ΔV	-0.4	-5.5	+4.1	-1.0	+2.8		
N-10Ni-NoCH ₄	Blank	15.7	14.0	30.0	0.0	31.0	$C_{\text{Tolu}} = 54\%$	$\text{Coke} = 0.11 \text{ gCarbon/gCata}$
	Test	15.5	7.0	34.0	0.7	34.3	$C_{\text{CH}_4} = \#$	$\text{Sb} (\%) = 10\%$
	ΔV	-0.2	-7.0	+4.0	+0.7	+3.3		
N-10Ni-ToluStop	Blank	17.6	13.4	29.6	8.0	31.4	$C_{\text{Tolu}} = \#$	$\text{Coke} = 0.04 \text{ gCarbon/gCata}$
	Test	18.9	9.9	33.7	6.0	31.5	$C_{\text{CH}_4} = 25\%$	$\text{Sb} = \#$
	ΔV	+1.3	-3.5	+4.1	-2.0	+0.1		
N-10Ni-NoTolu	Blank	16.9	12.4	29.7	9.4	31.6	$C_{\text{Tolu}} = \#$	$\text{Coke} = 0.02 \text{ gCarbon/gCata}$
	Test	18.3	10.7	30.8	9.1	31.1	$C_{\text{CH}_4} = 3\%$	$\text{Sb} = \#$
	ΔV	+1.4	-1.7	+1.1	-0.3	-0.5		
N-10Ni-Nothing	Blank	16.2	12.6	30.0	0.0	32.2	$C_{\text{Tolu}} = \#$	$\text{Coke} < 0.01 \text{ gCarbon/gCata}$
	Test	18.7	11.0	30.7	<0.1	30.2	$C_{\text{CH}_4} = 0$	$\text{Sb} = \#$
	ΔV	+2.5	-1.6	+0.7	0.0	-2.0		

Test conditions: $T = 650\text{ }^\circ\text{C}$, $t = 300\text{ min}$, 24.000 ppmv of toluene, $\text{GHSV} = 5000\text{ h}^{-1}$; The evolutions of the volume percentages (ΔV) were established by comparing the average of the blank measurements before the test and the average of the 10 last values during the test.

#: No value expected.

N.B.: The carbon balance ratio of the different tests were calculated for each case and commented in part IV of Annex 2.

Figures V.5 and V.6 show the X-Ray diffraction spectra and the DSC curves performed on samples after catalytic tests performed in different atmospheres.

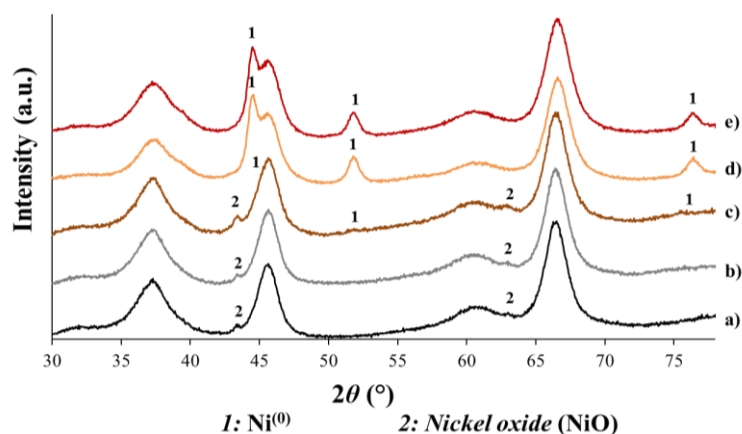


Figure V.5: X-Ray spectra performed after catalytic tests; a. *N-10Ni-Nothing*, b. *N-10Ni-NoTolu*, c. *N-10Ni-ToluStop*, d. *N-10Ni-NoCH₄*, e. *N-10Ni*.

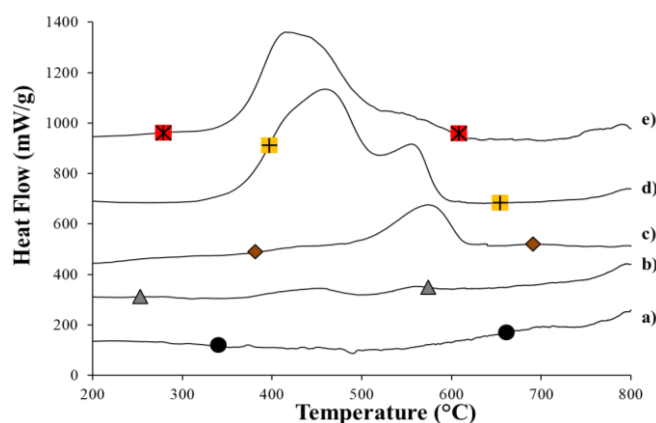


Figure V.6: Post-test DSC curves for the samples tested in different atmospheres; a. *N-10Ni-Nothing*, b. *N-10Ni-NoTolu*, c. *N-10Ni-ToluStop*, d. *N-10Ni-NoCH₄*, e. *N-10Ni*.

It was observed in Table V.4 that the sample tested without methane (sample *N-10Ni-NoCH4*) presented slightly better toluene conversion and lower benzene selectivity values than the standard catalyst *N-10Ni* ($\Delta C_{Tolu} = + 4 \%$; $\Delta S_B = - 5 \%$). However, it was noticed that the absence of methane in the syngas mixture favored the formation of filamentous carbon (Figure V.6-d). Therefore, it was hypothesized that under standard test conditions (toluene+methane, sample *N-10Ni*), the higher covering of the metallic Ni particle by C_{α}^* species, coming from the methane, decreased the adsorption and ring-breaking of the toluene molecules, which would explain the lower C_{Tolu} and S_B values. However, the high covering of the metallic particle by carbon species, coming from methane, might prevent the condensation of large polymeric carbons by the “ensemble control” effect between C_{α}^* and C_{β}^* species, which could explain the absence of filamentous carbon for sample *N-10Ni*.ⁱ

It was observed in Table V.4 that no methanation reactions ($CO+3.H_2 \leftrightarrow CH_4+H_2O$ or $2.CO+2.H_2 \leftrightarrow CH_4+CO_2$)ⁱⁱ occurred during the test of sample *N-10Ni-Nothing*, but that in contrary, sample *N-10Ni-NoCH4* produced methane (+ 0.7 vol. %) during the catalytic test. Hence, it was deduced that this amount of methane was entirely generated from the conversion of toluene molecules. According to Equation V.5, the fraction of toluene converted to methane was estimated to be about 9 %. Since this value was very close to the S_B value (10 %) (Table V.4), it was assumed that most of the methane was produced by hydrodealkylation ($toluene+H_2 \rightarrow benzene+methane$).ⁱⁱⁱ

Interestingly, for both samples *N-10Ni-Nothing* and *N-10Ni-NoTolu*, no Ni⁽⁰⁾ rays, but only NiO rays were observed on the X-Ray spectra after catalytic tests performed at $T = 650 \text{ }^\circ\text{C}$ (Figures V.5-a and V.5-b). However, the small intensity of the NiO rays suggested that a part of nickel atoms might also be incorporated into the γ -Al₂O₃ support in NiAl₂O₄ spinel (not visible by XRD because of γ -Al₂O₃ rays). The absence of Ni⁽⁰⁾ particles for these two samples was also confirmed by TEM measurements (not shown).

Analysis of the X-Ray spectrum of sample *N-10Ni-Tolustop* (Figure V.5-c) revealed similar trends. Indeed, whereas the X-Ray spectrum of sample *N-10Ni* presented only Ni⁽⁰⁾ rays at the end of the catalytic test (Figure V.5-e), the sample *N-10Ni-Tolustop* presented very small rays of Ni⁽⁰⁾ and was mostly composed of NiO (Figure V.5-c). Hence, it appeared that the removal of the toluene from the syngas mixture at $t = 105$ min during the catalytic test led to a re-oxidization of the Ni⁽⁰⁾ particles of sample *N-10Ni* by H₂O and CO₂.

These observations can be correlated with the works of Cheng *et al.*^{[280], [281]}. In this way, it was found that, at temperatures above $T = 450 \text{ }^\circ\text{C}$, the reduction of NiO/ α -Al₂O₃ catalysts was thermodynamically more favorable with several organic compounds (glucose, furfural, acetic acid, ethanol and acetone) than with common reducing agent (CO, H₂). Figure V.7 shows the mechanism of reduction proposed by Cheng *et al.*^{[280], [281]} adapted to this case with toluene.

ⁱ: More information about ensemble effect and formation of filamentous carbon in part I.4.3.1. of Chapter I.

ⁱⁱ: More information about methanation reactions in Table I.1.

ⁱⁱⁱ: More information about reactions of toluene conversion in Table IV.2.

It was decided in the present work to call this phenomenon “special reduction by toluene”. In a first step, the toluene is adsorbed on the nickel oxides and on the alumina support. Thereafter, the toluene molecules are decomposed into carbon (char). The nickel oxides and the char react to form metallic nickel and CO₂. Then CO₂ reacts with the char located at the surface of the support to form CO, which can further reduce the remaining nickel oxides into Ni⁽⁰⁾.

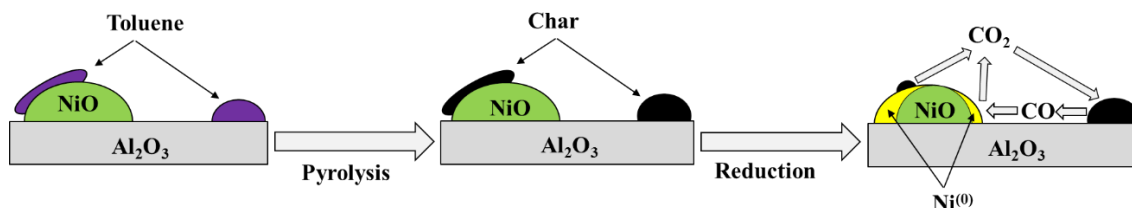


Figure V.7: Mechanism proposed for the phenomenon of “special reduction by toluene” of nickel oxides, inspired by the work of Cheng *et al.*^{[280], [281]}.

Table V.5 shows the Gibb’s free energy values calculated for the reduction of bulk NiO with different compounds. It is to remind that the values presented are only informative since they were calculated for the reduction of bulk NiO, which is very different from the case of nickel oxide nanoparticles supported on γ -Al₂O₃.

Table V.5: Variation of Gibb’s free energy, enthalpy and entropy values for the reduction of bulk NiO with either toluene, CH₄, H₂, CO or C as reducing agent. Values calculated at $T = 650$ °C per mol of NiO reduced.

Equations of reduction	ΔH_{923K} (kJ/mol _{NiO})	ΔS_{923K} (kJ/(mol _{NiO} .K))	ΔG_{923K} (kJ/mol _{NiO})	Eq. n°
$C_7H_8 + 7.NiO \rightarrow 7.Ni + 7.CO + 4.H_2$	140	0.252	- 93	(V.7)
$C_7H_8 + 18.NiO \rightarrow 18.Ni + 7.CO_2 + 4.H_2O$	38	0.105	- 59	(V.8)
$CH_4 + NiO \rightarrow Ni + 2.H_2 + CO$	215	0.331	- 90	(V.9)
$CH_4 + 4.NiO \rightarrow 4.Ni + 2.H_2O + CO_2$	45	0.100	- 47	(V.10)
$H_2 + NiO \rightarrow Ni + H_2O$	- 6	0.038	- 41	(V.11)
$CO + NiO \rightarrow Ni + CO_2$	- 48	0.003	- 51	(V.12)
$C + NiO \rightarrow Ni + CO$	138	0.202	- 48	(V.13)
$C + 2.NiO \rightarrow 2.Ni + CO_2$	45	0.095	- 43	(V.14)

ΔH_{923K} : enthalpy change at $T = 650$ °C; ΔS_{923K} : entropy change at $T = 650$ °C; ΔG_{923K} : Gibb’s free energy change at $T = 650$ °C. Detail of the determination of enthalpy and entropy are presented in part IV of Annex 2.

It is observed in Table V.5 that, when CO and H₂ are used as reducing agents, the exothermic aspect ($\Delta H_{923K} < 0$) of the “NiO+H₂” and “NiO+CO” reactions is the main driving force. In contrary, when C, CH₄ or toluene are used as reducing agents, the reactions of NiO reduction are endothermic ($\Delta H_{923K} > 0$). Hence, for C, CH₄ and toluene, negative ΔG_{923K} values are obtained by an increase of the entropy caused by the production of more gas volumes.^{[280], [281]}

Either considering the formation of CO and H₂ (Equation V.7), or the formation of CO₂ and H₂O (Equation V.8) (Table V.5), the reduction of NiO is thermodynamically more favorable with toluene than with methane or with standard reducing agents (CO, H₂). Furthermore, toluene being more inclined to form carbon deposit than methane, this would increase the reduction of NiO into Ni⁽⁰⁾ by formation of char according to the reduction mechanism proposed in Figure V.7. Finally, this phenomenon is emphasized by the fact that the metallic nuclei, Ni⁽⁰⁾, formed during the reduction of NiO, increase the adsorption-dissociation

of H₂ by “spillover effect”ⁱ and consequently greatly increase the rate of reduction.^[293] Hence, once the reduction is initiated by toluene, and that metallic Ni⁽⁰⁾ is present, the reduction can occur with other reductive molecules (CO and H₂) and leads to the whole reduction of the catalyst. This would explain why sample *N-10Ni* only presented rays of Ni⁽⁰⁾ on its X-Ray spectrum (Figure V.5-e).

During the catalytic test, the atmosphere is reductive ($P_{CO}/P_{CO_2} = 2.1$ and $P_{H_2}/P_{H_2O} = 2.9$)ⁱⁱ. However, in this case, Ni and γ -Al₂O₃ showed very strong interactions: exclusive presence of NiAl₂O₄ and starting of the reduction only at $T = 680$ °C under standard H₂-TPR (Figure V.2-a). Furthermore, during the catalytic tests performed at $T = 650$ °C, the sample *N-10Ni* was tested below its initial theoretical temperature of reduction. So, this would explain why the removal of toluene during the catalytic test at $t = 105$ min led to a re-oxidization of the Ni⁽⁰⁾ particles for sample *N-10Ni-Tolustop* (see XRD, Figure V.5-c).

The low formation of carbon and the good resistance against deactivation by coking observed for sample *N-10Ni* were attributed to the fact that the catalytic tests were performed at the boundary between the oxidation and the reduction of Ni. In this way, it was supposed that during a standard catalytic test (sample *N-10Ni*), as soon as some areas of the Ni⁽⁰⁾ particles were re-oxidized by CO₂ or H₂O, they would be quickly reduced again by the phenomenon of “special reduction by toluene” (Equations V.7 and V.8, Table V.5). Hence, this effect would reduce the formation of carbon deposit.

This hypothesis could explain why, in part V.3.2 of this chapter, the presence of initial bulk NiO caused a severe deactivation of sample *IMP-N-10Ni* during a catalytic test performed at $T = 650$ °C, while sample *N-10Ni* presented a stable activity. Indeed, since the bulk NiO of sample *IMP-N-10Ni* was reduced at low temperature ($T \sim 450$ °C), it was not able to take advantage of the anti-coking properties provided by the phenomenon of “special reduction by toluene”.

V.3.4. Influences of the nickel loading

V.3.4.1. Properties of Ni/ γ -Al₂O₃ catalysts with different Ni loadings

The influence of the nickel loading on properties and catalytic performances of Ni/ γ -Al₂O₃ catalysts was studied for samples *N-10Ni*, *N-20Ni*, *N-30Ni* and *N-50Ni*.

SEM-BSE measurements performed on calcined samples (not shown here) revealed that all samples presented homogenous compositions at microscopic scale. TEM measurements (not shown here) revealed that all samples presented homogenous structure at nanoscopic scale. It was also observed by XRD measurements (not shown here) that all samples presented γ -Al₂O₃ phases.

ⁱ: More details about “spillover effect” in Figure I.12.

ⁱⁱ: Determined from Table IV.1

Figure V.8 presents the nitrogen adsorption-desorption isotherms and the associated pore size distribution of calcined samples.

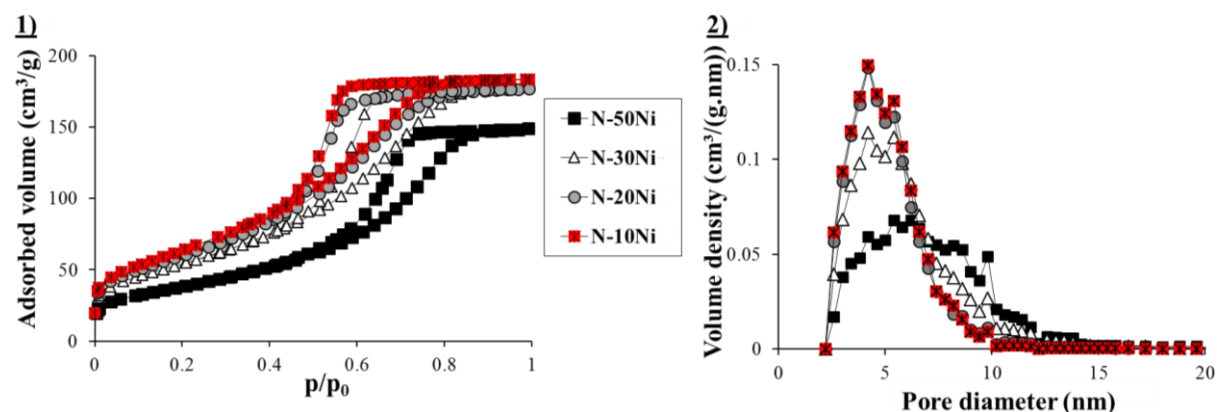


Figure V.8: Nitrogen adsorption-desorption isotherms (left-side) and pore size distribution curves (right-side) for samples synthesized with different Ni loadings.

The textural values (S_{BET} , V_p and $V_{Dubinin}$) of the samples are listed in Table V.6. It was observed that all samples presented a hysteresis, characteristic of mesoporous samples (Figure V.8). Furthermore, all samples were also highly microporous because $V_{Dubinin}$ values were of about $0.08 \text{ cm}^3/\text{g}$, except for sample *N-50Ni* for which $V_{Dubinin}$ was slightly lower ($0.05 \text{ cm}^3/\text{g}$). In that case, the high amount of nickel added closed a part of micropores and small mesopores. Finally, it is also to notice that the nickel loading did not affect the mesopore size distributions of the samples.

Table V.6: Textural properties of the calcined samples and metallic Ni particles sizes after H_2 reduction and after TPR measurements.

Samples	Textural properties			Ni particles sizes					
				Post- H_2 Reduction			Post-TPR		
	S_{BET} (m^2/g)	V_p (cm^3/g)	$V_{Dubinin}$ (cm^3/g)	d_{TEM} (nm)	σ_{TEM} (nm)	d_{XRD} (nm)	d_{TEM} (nm)	σ_{TEM} (nm)	d_{XRD} (nm)
N-10Ni	240	0.3	0.08	8	2	9	30	9	23
N-20Ni	225	0.3	0.08	9	3	10	39	12	25
N-30Ni	200	0.3	0.07	12	5	12	45	28	27
N-50Ni	135	0.2	0.05	17	7	15	50	64	28

S_{BET} : specific surface area; V_p : porous volume; $V_{Dubinin}$: microporous volume, d_{TEM} : metallic particles size median; σ_{TEM} : standard deviation; d_{XRD} : metallic nickel crystallites size estimation obtained by XRD.

Figure V.9 shows the TPR profiles of pure nickel oxide (NiO) and of $\text{Ni}/\gamma\text{-Al}_2\text{O}_3$ catalysts with different nickel loadings. It is to notice that for all samples the reduction was almost complete (between 90 and 100 %) when T reached $1000 \text{ }^\circ\text{C}$. Whereas sample *N-10Ni* presented only one peak of nickel aluminate (NiAl_2O_4), higher loadings of Ni led to the presence of other nickel/alumina oxides. In this way, in addition to a NiAl_2O_4 peak, sample *N-20Ni* also presented a small peak of bulk nickel oxide (NiO) located at $T = 475 \text{ }^\circ\text{C}$. Furthermore, a notable shift of the NiAl_2O_4 peak ($\Delta T = -75 \text{ }^\circ\text{C}$) was also observed for this sample. This important shift was attributed to the presence of easily reduced bulk nickel oxide (NiO). This type of oxide being converted to metallic nickel at low temperature, it can favor the adsorption-dissociation of H_2 molecules by “spillover effect”¹ and improve the reduction of more stable oxide phases like

¹: More information about “spillover effect” in Figure I.12.

$\text{NiO}/\text{Al}_2\text{O}_3$ or NiAl_2O_4 .^{[156], [276], [289]} Higher loadings of Ni (samples *N-30Ni* and *N-50Ni*) led to more intense peaks of bulk nickel (NiO) and to the presence of octahedral nickel ($\text{NiO}/\text{Al}_2\text{O}_3$), associated to a reduction peak shift of NiAl_2O_4 of about $\Delta T \sim -100$ °C.

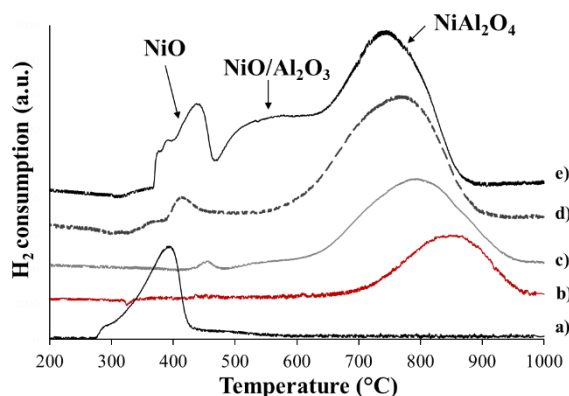


Figure V.9: TPR curves of nickel/alumina samples with different loadings of Ni; a. pure NiO, b. *N-10Ni*, c. *N-20Ni*, d. *N-30Ni*, e. *N-50Ni*.

It was observed in Table V.6 that after the H_2 reduction step, d_{TEM} , d_{XRD} and σ_{TEM} values were relatively similar and remained low for all samples. Indeed, even for sample *N-50Ni* which presented the highest values, σ_{TEM} was only of 7 nm, and d_{TEM} and d_{XRD} values were only of about 16 nm. In this way, even for high loadings of Ni, the samples presented particles of relatively low sizes. In contrary, after TPR measurements, the standard deviation values became very important for samples *N-30Ni* and *N-50Ni* ($\sigma_{\text{TEM},N-30\text{Ni}} = 28$ nm and $\sigma_{\text{TEM},N-50\text{Ni}} = 64$ nm) (Table V.6) and very large nickel particles (up to 200 nm) were observed by TEM measurements. It was also observed that as the nickel content increased, the differences between d_{TEM} and d_{XRD} values became more and more important (sample *N-50Ni* showed the highest difference: $d_{\text{TEM},N-50\text{Ni}} = 50$ nm and $d_{\text{XRD},N-50\text{Ni}} = 28$ nm). These strong differences can be explained by the fact that, during TPR measurement, the Ni particles submitted important sintering and formed large agglomerates constituted of crystallites with different domains as depicted in Figure A2.3 in Annex 2. In addition to the high content of metal, it was assumed that the high sensibility of samples *N-30Ni* and *N-50Ni* towards sintering was also provoked by their high amount of bulk nickel (NiO), which is known to easily sinter because of its low interactions with the support.^{[276], [278], [290]}

V.3.4.2. Catalytic performances of Ni/ γ - Al_2O_3 catalysts with different Ni loadings

The catalytic activity of samples *N-10Ni*, *N-20Ni*, *N-30Ni* and *N-50Ni* were evaluated for the reforming of 24.000 ppmv of toluene for $t = 5$ h at $T = 650$ °C. The toluene conversion values as a function of time are presented in Figure V.10. Table V.7 shows the metallic nickel particles sizes after catalytic tests, and the catalytic performances of the samples. Figure V.11 shows the DSC curves of samples after catalytic tests.

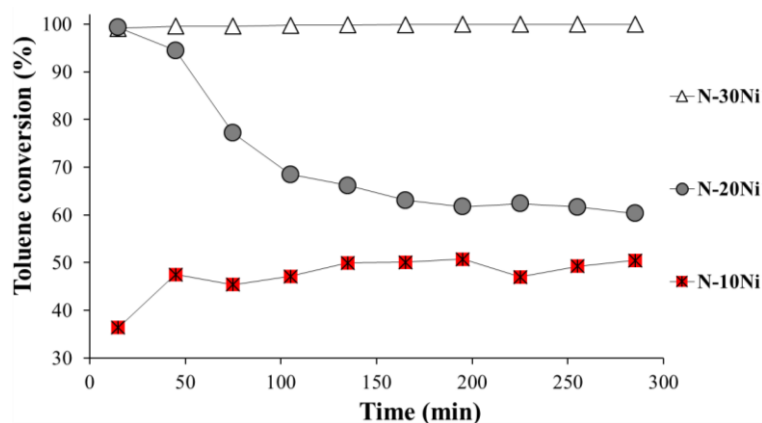


Figure V.10: Toluene conversion as a function of time for samples *N-10Ni*, *N-20Ni* and *N-30Ni*; tests performed at $T = 650^\circ\text{C}$, for $t = 300$ min and with 24.000 ppmv of toluene.

Table V.7: Ni particles sizes and catalytic performances of Ni/ $\gamma\text{-Al}_2\text{O}_3$ catalysts with different nickel loadings. Test conditions: $T = 650^\circ\text{C}$, $t = 300$ min, 24.000 ppmv of toluene, $GHSV = 5000$ h $^{-1}$.

Samples	Ni particles sizes			Catalytic performances						
	d_{TEM} (nm)	σ_{TEM} (nm)	d_{XRD} (nm)	C_{Tolu} (%)	r_{Tolu} (mol _{Tolu} /(g _{Ni} .h))	C_{CH_4} (%)	S_B (%)	$Coke$ (g _{Carbon} /g _{Cata})	$Coke^*$ (g _{Carbon} /g _{Tolu})	<i>Fil. carbon</i>
N-10Ni	11	3	12	51	$6.7 \cdot 10^{-2}$	10	15	0.10	$3.1 \cdot 10^{-2}$	No
N-20Ni	12	8	12	62	$4.7 \cdot 10^{-2}$	7	5	0.71	$1.6 \cdot 10^{-1}$	++
N-30Ni	18	13	14	99	$2.9 \cdot 10^{-1}$	9	0	1.21	$2.0 \cdot 10^{-1}$	+++
The pressure drop increased during the test and reached a stable value of $P = 0.3$ bar at $t = 60$ min.										
N-50Ni	The test was stopped at $t = 15$ min because of too high pressure drop ($P = 1$ bar).									

d_{TEM} : metallic particles size median; σ_{TEM} : standard deviation; d_{XRD} : metallic crystallites size estimation obtained by XRD. C_{Tolu} : conversion of toluene, r_{Tolu} : reaction rate of toluene, S_B : benzene selectivity, C_{CH_4} : methane conversion. $Coke$: carbon deposit amount after 5 h of test measured by TG-DSC, $Coke^*$: tendency of sample to form carbon deposit.

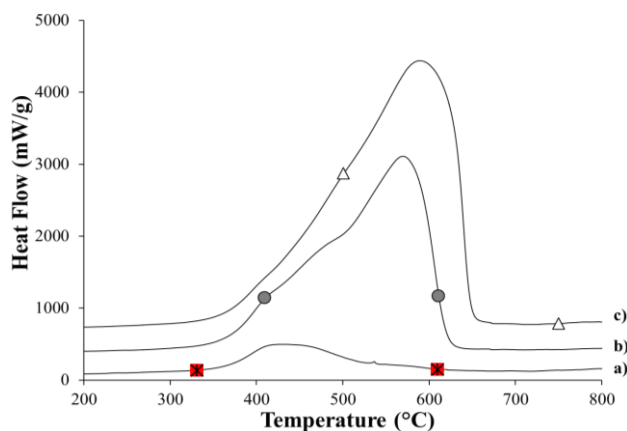


Figure V.11: Post-test DSC curves for Ni/ $\gamma\text{-Al}_2\text{O}_3$ catalysts with different nickel loadings: a. *N-10Ni*, b. *N-20Ni* and c. *N-30Ni*.

In Figure V.10, in contrary to sample *N-10Ni* which showed a progressive activation during the catalytic test, sample *N-20Ni* directly showed a quasi-total toluene conversion ($C_{Tolu} = 99\%$) at the first injection. However, whereas the catalytic activity of sample *N-10Ni* remained stable throughout the test, sample *N-20Ni* showed a drastic loss of its toluene conversion during the first 100 min of test ($\Delta C_{Tolu} \sim -35\%$). Nevertheless, at $t \sim 150$ min of test, the conversion of toluene stabilized ($C_{Tolu} \sim 62\%$). Despite its higher toluene conversion, compared to sample *N-10Ni*, sample *N-20Ni* showed a lower toluene reforming rate ($r_{Tolu, N-20Ni} = 4.7 \cdot 10^{-2}$ mol_{Tolu}/(g_{Ni}.h), whereas $r_{Tolu, N-10Ni} = 6.7 \cdot 10^{-2}$ mol_{Tolu}/(g_{Ni}.h)) and a much higher trend to form carbon deposit ($Coke^*_{N-20Ni} = 1.6 \cdot 10^{-1}$ g_{Carbon}/g_{Tolu}, whereas $Coke^*_{N-10Ni} = 3.1 \cdot 10^{-2}$ g_{Carbon}/g_{Tolu}) (Table V.7). Furthermore, it is to notice that sample *N-20Ni* presented a large

amount of carbon deposit after test ($Coke_{N-20Ni} = 0.71 \text{ g}_{\text{Carbon}}/\text{g}_{\text{Cata}}$) which was both amorphous (burned at $T < 550 \text{ }^\circ\text{C}$) and filamentous (burned at $T > 550 \text{ }^\circ\text{C}$) (Figure V.11-b). The presence of a high amount of filamentous carbon for sample *N-20Ni* was confirmed by TEM measurements (not shown here). Similarly to sample *IMP-N-10Ni* presented in part V.3.2, the deactivation by coking of sample *N-20Ni* was attributed to the presence of bulk nickel (NiO). As this type of nickel oxide is easily reducible ($T \sim 450 \text{ }^\circ\text{C}$), it was quickly activated at the beginning of the catalytic test, which explains the high initial C_{Tolu} value showed by sample *N-20Ni*. However, since NiO was reduced at low temperature, it could not take advantage of the anti-coking influence caused by the mechanism of “special reduction by toluene” described in part V.3.3. This explains why sample *N-20Ni* was quickly deactivated during the test. Hence, it was assumed that, during the catalytic test of sample *N-20Ni* presented in Figure V.10, at $t \sim 150 \text{ min}$, the bulk metallic nickel was totally deactivated and the stable C_{Tolu} observed for the rest of the test was only guaranteed by metallic nickel with strong interactions with the alumina support.

The fact that the toluene conversion of sample *N-30Ni* was nearly equal to 100 % during the catalytic test (Figure V.10) must be interpreted with caution. Indeed, during the test, the pressure drop increased until reaching a stable value of $P = 0.3 \text{ bar}$ at about $t \sim 60 \text{ min}$, which was sustainable for the experimental installation, but could be problematic at higher scale. The sample presented a very high amount of carbon deposit ($Coke_{N-30Ni} = 1.21 \text{ g}_{\text{Carbon}}/\text{g}_{\text{Cata}}$), which was mostly composed of filamentous carbon (Table V.7 and Figure V.11-c). It is also to notice that this sample did not produce any benzene ($S_{B,N-30Ni} = 0 \%$). In view of these observations, it was assumed that the high tendency of sample *N-30Ni* to form filamentous carbon was also caused by the presence of bulk NiO. The total conversion of toluene during the test was explained by the presence of a large amount of nickel, which would compensate the deactivation of one fraction of it during the test. The almost total conversion of toluene could also be partially due to the high coking of the sample, which would consume toluene and benzene to form carbon deposit. It is to notice that the use of this sample is absolutely to be avoided. Indeed, the clogging of the pipe by formation of filamentous carbon can have very serious consequences.

Sample *N-50Ni* also presented a complete conversion of toluene, but the test had to be stopped at $t = 15 \text{ min}$ because of a too high pressure drop ($P = 1 \text{ bar}$). TEM and DSC measurements (not shown here) performed after test revealed that the clogging of the reactor was also provoked by a considerable formation of filamentous carbon, which was assumed to be caused by the initial presence of bulk nickel NiO in large amounts (Figure V.9-e).

Analysis of the metallic Ni particles sizes in Table V.7 revealed that the three catalysts *N-10Ni*, *N-20Ni* and *N-30Ni* did not submit excessive sintering during the catalytic test (compared to value obtained during TPR measurements). The size of the Ni particles being also a crucial factor for the formation of filamentous carbon,ⁱ this observation confirmed the fact that the

ⁱ : More information about the influence of the particle size on the carbon formation in part I.4.4.4. of Chapter I.

sensibility of the Ni/ γ -Al₂O₃ catalysts against coking mechanisms was mostly caused by the initial presence of nickel with low interactions with the support (NiO).

In light of these results, it appeared essential to prevent the formation of bulk NiO for two complementary reasons: 1) its low interactions with the γ -Al₂O₃ support favor the formation of filamentous carbon; 2) by showing a reduction temperature lower than the temperature of catalytic test ($T = 650$ °C), NiO cannot take advantage of the anti-coking phenomenon of “special reduction by toluene”.

In this way, despite the fact that the sol-gel procedure permits to prepare Ni/ γ -Al₂O₃ catalysts with interesting micro- and mesostructure, even at high doping of metals (up to 50 wt. %), it appeared that the 10 wt. % Ni/ γ -Al₂O₃ catalyst was the only one which showed interesting results for the reforming of 24.000 ppmv of toluene at $T = 650$ °C. Indeed, because of the exclusive presence of a NiAl₂O₄ phase, sample *N-10Ni* was able to benefit from the mechanism of “special reduction by toluene” which permits to protect the catalyst from deactivation by coking. In the future, if one would want to design catalysts with a nickel amount higher than 10 wt. %, it should be then essential to perform the calcination steps with longer times and higher temperatures, thus in order to increase the metal/support interactions and to prevent the formation of NiO.^{[278], [294], [295]}

V.3.5. Influences of the temperature on the catalytic performances

Catalytic tests were performed at $T = 900 \rightarrow 600$ °C without a catalyst (sample *Quartz*), with pure alumina (sample *N*) and with the sol-gel prepared 10 wt. % Ni/ γ -Al₂O₃ catalyst (sample *N-10Ni*).

Figure V.12 shows the toluene and the methane conversions as a function of temperature. The catalytic activity values (C_{Tolu} , S_B , C_{CH_4} , H_2/CO , activation energy E_a and pre-exponential factor k_0) and other values obtained by post-test characterizations (amount of carbon deposit, presence of filamentous carbon and sizes of metallic particles) are presented in Table V.8.

In the case of sample *Quartz*, the molecules were assumed to react in gas phase, *i.e.* without the intermediate of a support, which explains why the evolution of the C_{Tolu} values as a function of the temperature presented in Figure V.12 evolved in different ways compared to those of samples *N* and *N-10Ni*. The low C_{Tolu} values associated to negative values of C_{CH_4} and high values of S_B indicated that, for sample *Quartz*, the energy was not sufficient to break the aromatic ring of toluene. As consequence, the toluene molecules were mostly degraded into benzene and methane by hydrodealkylation reaction.¹ The presence of many unsuccessful collisions in the absence of a support was evidenced by the high activation energy and the high pre-exponential factor showed by sample *Quartz* ($E_a = 252$ kJ/mol and $k_0 = 1.4 \cdot 10^{15}$ m³/(g_{Cata}.h)) (Table V.8). Noteworthy, these values calculated for sample *Quartz* were in

¹: More details about hydrodealkylation reaction in Table IV.2.

accordance with the values obtained in the literature for the conversion of toluene without catalysts ($E_{a,literature} \sim 250 \text{ kJ/mol}$ and $k_{0,literature} \sim 3.3 \cdot 10^{13} \text{ m}^3/(\text{g}_{\text{Cata}}\cdot\text{h})$).¹

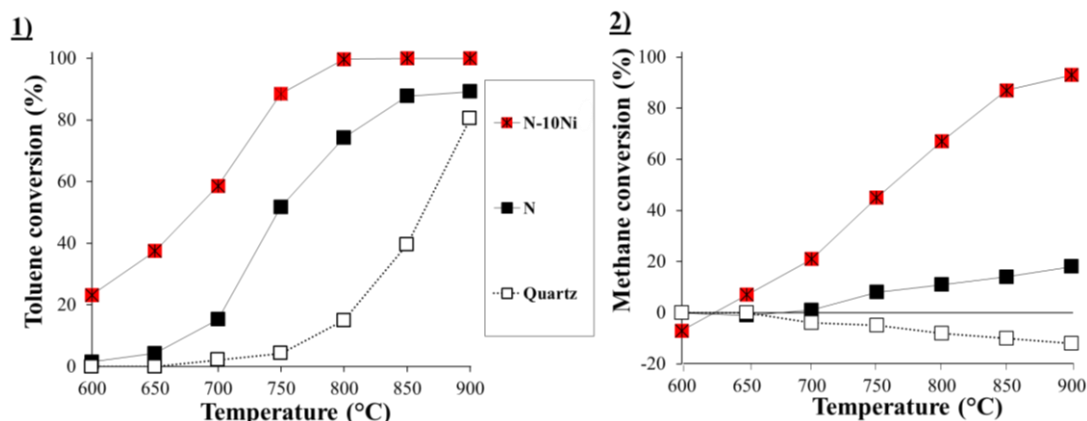


Figure V.12: Toluene conversion (left side) and methane conversion (right side) as a function of temperature for samples *Quartz*, *N* and *N-10Ni*.

Table V.8: Catalytic activity as a function of temperature, kinetic parameters and post-test characterizations for samples *Quartz*, *N* and *N-10Ni*. Toluene concentration: 24.000 ppmv, $T = 900 \rightarrow 600 \text{ }^\circ\text{C}$, $GHSV = 5000 \text{ h}^{-1}$.

Samples	Catalytic activity								Post-test characterizations		
	T (°C)	600	650	700	750	800	850	900			
Quartz	C_{Tolu} (%)	0	0	2	4	15	40	80	<i>Coke</i> = 0 g _{Carbon} /g _{Cata}		
	S_B (%)	0	0	96	71	58	40	24	<i>Filamentous Carbon</i> : No		
	C_{CH4} (%)	0	0	-4	-5	-8	-10	-11			
	H_2/CO	0.98	0.95	0.94	0.93	0.94	0.93	0.94	d_{XRD} = #	d_{TEM} = #	σ_{TEM} = #
	$E_a = 252 \text{ kJ/mol}$		$k_0 = 1.4 \cdot 10^{15} \text{ m}^3/(\text{g}_{\text{Cata}}\cdot\text{h})$								
N	C_{Tolu} (%)	1	4	15	52	74	88	89	<i>Coke</i> = 0.13 g _{Carbon} /g _{Cata}		
	S_B (%)	23	20	13	8	11	12	11	<i>Filamentous Carbon</i> : No		
	C_{CH4} (%)	0	-1	1	8	11	14	18			
	H_2/CO	0.96	0.96	0.97	0.89	0.80	0.79	0.75	d_{XRD} = #	d_{TEM} = #	σ_{TEM} = #
	$E_a = 109 \text{ kJ/mol}$		$k_0 = 6.9 \cdot 10^9 \text{ m}^3/(\text{g}_{\text{Cata}}\cdot\text{h})$								
N-10Ni	C_{Tolu} (%)	23	38	59	88	99	100	100	<i>Coke</i> = 0.36 g _{Carbon} /g _{Cata}		
	S_B (%)	5	2	2	1	1	0	0	<i>Filamentous Carbon</i> : +		
	C_{CH4} (%)	-7	7	21	45	67	87	93			
	H_2/CO	0.96	0.92	0.86	0.81	0.77	0.78	0.77	d_{XRD} = 12 nm	d_{TEM} = 12 nm	σ_{TEM} = 7 nm
	$E_a = 80 \text{ kJ/mol}$		$k_0 = 4.8 \cdot 10^7 \text{ m}^3/(\text{g}_{\text{Cata}}\cdot\text{h})$								

d_{TEM} : metallic particles size median; σ_{TEM} : standard deviation; d_{XRD} : metallic crystallites size estimation obtained by XRD; C_{Tolu} : conversion of toluene; r_{Tolu} : reaction rate of toluene; S_B : selectivity in benzene, C_{CH4} : conversion of methane; *Coke*: carbon deposit amount after test measured by TG-DSC; E_a : activation energy for the destruction of toluene; k_0 : pre-exponential factor for the conversion of toluene.
#: no value expected.

It was observed in Table V.8 that sample *N* showed higher C_{Tolu} values than the ones obtained during the reforming of 8000 ppmv of toluene in Chapter IV ($C_{Tolu,N,750^\circ\text{C},8000\text{ppmv}} = 18 \%$ and $C_{Tolu,N,850^\circ\text{C},8000\text{ppmv}} = 76 \%$ in Chapter IV; whereas $C_{Tolu,N,750^\circ\text{C},24.000\text{ppmv}} = 52 \%$ and $C_{Tolu,N,850^\circ\text{C},24.000\text{ppmv}} = 88 \%$ in Table V.8). Furthermore, whereas sample *N* tested in Chapter IV did not present any carbon deposit, in this case, sample *N* showed a relatively high amount of carbon deposit after test (*Coke* = 0.13 g_{Carbon}/g_{Cata}). It was assumed that the higher concentration of toluene provoked a loss of balance at the surface of the alumina between the formation of carbonaceous compounds from the conversion of toluene (probably by the reaction of cracking: $C_7H_8 \rightarrow 7.C + 4.H_2$) and the gasification reactions of these compounds by oxidative species (O^* ,

¹: Kinetics values obtained in other studies presented in Table I.5.

HO^{*}).ⁱ Hence, it was hypothesized that the higher C_{Tolu} value observed for sample *N* in Table V.8 was caused by the presence of carbon deposit, which would consummate the toluene molecules during its growth.^{[79], [296]}

Figure V.12 highlighted the fundamental role of the support during the reforming of tars. Indeed, it was observed in this graph that the C_{Tolu} values of samples *N* and *N-10Ni* evolved in similar ways as a function of the temperature. This crucial influence of the support was also evidenced by the pre-exponential factor ($k_{0,N} = 6.9 \cdot 10^9 \text{ m}^3/(\text{g}_{\text{Cata}}\cdot\text{h})$) and by the activation energy ($E_{a,N} = 109 \text{ kJ/mol}$) of sample *N*, which were much better compared to sample *Quartz* (Table V.8), and closer to the values obtained for sample *N-10Ni* ($E_{a,N-10Ni} = 80 \text{ kJ/mol}$, $k_{0,N-10Ni} = 4.8 \cdot 10^7 \text{ m}^3/(\text{g}_{\text{Cata}}\cdot\text{h})$). Noteworthy, the activation energy obtained for sample *N-10Ni* was in the same range as what is generally obtained for nickel-based catalysts in the literature ($E_{a,\text{literature}} \sim 70 \text{ kJ/mol}$ and $k_{0,\text{literature}} \sim 1.4 \cdot 10^8 \text{ m}^3/(\text{g}_{\text{Cata}}\cdot\text{h})$).ⁱⁱ

In contrary, it was observed in Figure V.12 and in Table V.8 that the evolution of the C_{CH_4} values was really different between samples *N* and *N-10Ni*. This was explained by the fact that, in the case of toluene reforming, the metallic particles and the support both take part in the mechanism, whereas in the case of methane reforming, the reactions mostly occurred at the surface of the Ni⁽⁰⁾ particles.^[65] It was also observed that the H₂/CO ratio of samples *N* and *N-10Ni* decreased with increasing temperature (from $T = 600 \text{ }^\circ\text{C}$ to $T = 900 \text{ }^\circ\text{C}$, H₂/CO of sample *N*: 0.96→0.75; and H₂/CO of sample *N-10Ni*: 0.96→0.77). This observation was in accordance with Figure IV.1 and Table IV.2 presented in Chapter IV. Indeed, according to Simell *et al.*^[29], with increasing temperature, the dry reforming reactions (which increase the CO production) are thermodynamically more favorable than the steam reforming reactions (which increase the H₂ production).

Analysis of the post-test DSC curves presented in Figure V.13 revealed that the sample *N* was only composed of amorphous carbon deposit (burned at $T < 550 \text{ }^\circ\text{C}$). This observation was coherent since the formation of filamentous carbon is known to occur only on metallic nanoparticles.^{[68], [69]} In contrary, in the case of sample *N-10Ni*, a very broad combustion peak was observed, which suggested the presence of different types of carbon (amorphous and filamentous). This assertion was confirmed by the observation of some filamentous carbon during TEM measurements (Table V.8).

ⁱ: More information about carbon formation reaction and mechanisms of gasification in Figure I.8 and Table IV.2.

ⁱⁱ: Kinetics values obtained in other studies presented in Table I.5.

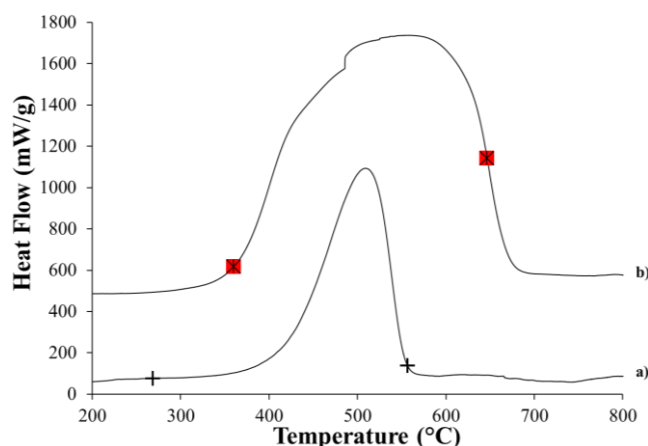


Figure V.13: Post-test DSC curves for samples tested at different temperatures ($T = 900 \rightarrow 600$ °C); a. *N*, b. *N-10Ni*.

One can finally notice in Table V.8 that, during the catalytic tests performed at $T = 900 \rightarrow 600$ °C, when the temperature reached $T = 650$ °C, sample *N-10Ni* showed low toluene reforming ($C_{Tolu} = 38$ %) and low benzene selectivity ($S_B = 2$ %). However, when tested under steady conditions at $T = 650$ °C, the same sample used to present high toluene conversion ($C_{Tolu} = 51$ %) and high benzene selectivity ($S_B = 15$ %) (Table V.7). Apparently, these differences could not have been caused by different Ni particles sizes since sample *N-10Ni* presented relatively similar particles sizes after a catalytic test at $T = 900 \rightarrow 600$ °C or after a steady catalytic test at $T = 650$ °C (Table V.7). This effect could partially be due to a loss of the specific surface area of the support caused by high temperatures. Moreover, it is believed that the difference is mostly due to different states of reduction of Ni between the two samples. Indeed, in the case of a catalytic test performed at $T = 900 \rightarrow 600$ °C, nickel particles were fully reduced when the temperature reached $T = 650$ °C, which explains the low S_B value. However, because of their fully reduced states, the catalyst did not take advantage of the mechanism of “special reduction by toluene”. Therefore, the Ni particles were more inclined to be deactivated by coking, which explains the loss of catalytic activity. In contrary, under steady catalytic tests at $T = 650$ °C, the high S_B value revealed an incomplete reduction of Ni. However, in this situation, the Ni particles were protected from deactivation by coke thanks to the mechanism of “special reduction by toluene”. According to this observation, it seems more interesting to continue the catalytic tests at the border of the Ni/NiO reduction and without any pre-reduction step of the catalyst.

V.5. CONCLUSIONS

This chapter highlighted several essential facts to take into consideration concerning the preparation and the test of Ni/ γ -Al₂O₃ catalysts:

* The properties and catalytic performances of 10 wt. % Ni/ γ -Al₂O₃ catalysts with similar support properties, but either prepared by sol-gel or impregnation method, were compared. It was observed that, whereas the sample prepared by sol-gel method presented only one type of Ni/ γ -Al₂O₃ oxide (NiAl₂O₄), the catalyst prepared by impregnation in contrary showed different nickel oxides (NiO, NiO/Al₂O₃ and NiAl₂O₄). Tested for the reforming of toluene at $T = 650$

°C, the catalyst prepared by impregnation showed a high initial conversion followed by a consequent and progressive deactivation. This behavior confirmed the fact that the presence of bulk nickel (NiO), which shows low interactions with the support and is reduced at lower temperatures than the catalytic tests, should be avoided.

* The stable catalytic activity and relatively low carbon deposit observed for the sol-gel prepared 10 wt. % Ni/ γ -Al₂O₃ catalyst was explained by the fact that, during catalytic tests performed at $T = 650$ °C, the sample was tested at the boundary between the reduction and oxidation of Ni. The calculation of the Gibb's free energy values at this temperature showed that, from a thermodynamic point of view, the toluene is a more effective reducing agent than CO or H₂. Indeed, without toluene in the syngas mixture, the catalysts did not show Ni⁽⁰⁾ particles after catalytic test, but instead NiO rays on XRD. Furthermore, it was observed that, if toluene was withdrawn from the syngas mixture during the catalytic test, the sample was progressively re-oxidized by CO₂ and H₂O.

* As the Ni loading increased (from 10 wt. % to 50 wt. %), the nickel oxide with strong interactions (NiAl₂O₄) was progressively joined by nickel oxide with low interactions (NiO/Al₂O₃) and bulk nickel oxide (NiO). It was observed that, when the Ni loading was equal or above 20 wt. %, bulk nickel (NiO) was present. This led to a high initial conversion of toluene, but also to a progressive loss of the catalytic activity throughout the catalytic test. In addition to low metal/support interactions, the high sensibility of the bulk nickel towards coking was also attributed to the fact that NiO was reduced at a lower temperature ($T \sim 450$ °C) than the catalytic test ($T = 650$ °C), and hence did not take advantage of the anti-coking effect brought by the phenomenon of "special reduction by toluene". It was shown that the sol-gel method developed throughout this work permitted to synthesize Ni/ γ -Al₂O₃ catalysts with high amounts of metal which kept high textural properties. However, it is to notice that, if future studies aim at designing catalysts with more than 10 wt. % of Ni, calcination steps with longer time and/or at higher temperatures should be performed in order to form NiO/Al₂O₃ or NiAl₂O₄ rather than NiO.

* The catalytic tests performed at $T = 900 \rightarrow 600$ °C permitted to confirm that the kinetic values obtained (k_0 and E_a) were similar to those encountered in the literature. Furthermore, these tests permitted to understand that, whereas the methane reforming was mostly influenced by the metallic particles, the toluene reforming was in contrary influenced by both particles and support. Finally, these tests tend to confirm the fact that it seems more judicious to perform the catalytic test at $T = 650$ °C without a pre-reduction step, in order to take advantage of the anti-coking effect brought by the mechanism of "special reduction by toluene".

Chapter VI

Influences of the support texture on the performances of 10 wt. % Ni/ γ -Al₂O₃ catalysts

- Development of an aqueous sol-gel method allowing the modification of Ni/ γ -Al₂O₃ catalysts with a surfactant (stearic acid);
- Influences of the surfactant addition on the textural properties of the supports;
- Consequences of the texture on the reducibility of Ni particles and on their sizes;
- Impacts of the texture on the catalytic performances of 10 wt.% Ni/ γ -Al₂O₃ catalysts.

In this chapter, Ni/ γ -Al₂O₃ catalysts modified with a surfactant (stearic acid) during their synthesis are studied. The influence of the addition step of the surfactant (before the precipitation or after a long agitation step) and the influence of the composition of the solution media (water/ethanol or only ethanol) on the textural properties of the catalysts are evaluated. Thereafter, the sample which showed the most interesting textural properties is further characterized and tested for the reforming of toluene.

VI.1. INTRODUCTION

The texture of catalysts synthesized by the sol-gel process can be tailored via the addition of surfactants. Surfactants are interesting molecules as their dual hydrophilic/hydrophobic character leads to the formation of a locally organized structure (micelles, cylinders ...) that may assemble into larger structures called lyotropic phases (hexagonal structure, lamellar structure, micellar cubic ...).^{[297], [298]} The lyotropic phases may act as soft template during the gelation of a sol, *i.e.* they prevent gelation where they are located and leave corresponding voids upon removal by heat treatment. Hence, tailoring the gel porosity at the mesoscale becomes possible and has been reported for alumina in previous studies.^{[299], [300]} Nevertheless, it was observed that the surfactants do not systematically lead to uniform and regular pore shapes by formation of micelles (for example honeycomb structure). Indeed, it was shown that the surfactant may also be adsorbed onto charged alumina crystallite surfaces, which results in structures without a direct link to the theoretical micelle shapes.^[301] The two more common types of surfactants used for the tailoring of alumina are linear carboxylic acids, such as stearic acid, lauric acid or caproic acid,^{[221], [299], [302]} or block copolymers, such as Pluronic P123[®] or Pluronic F127[®].^{[300], [303], [304]}

In this chapter, it was decided to study the influence of stearic acid. The stearic/Al molar ratio was set in reference to the work of Kim *et al.*^[299] who performed the synthesis of γ -Al₂O₃ supports in similar conditions as the synthesis procedure used in this work (water solvent, *pH* = 8-12, agitation at *T* = 80 °C). However, it is to notice that, in the quoted work, Al-tri-*Sec*-butoxide was used as aluminum source. In contrary, in the present work, in order to develop a common and easy aqueous sol-gel method for the synthesis of surfactant modified Ni/ γ -Al₂O₃ catalysts, Al(NO₃)₃ was used as aluminum source.

Finally, the sample which showed the most interesting textural properties was tested for the reforming of 24.000 ppmv of toluene at *T* = 650 °C.

VI.2. EXPERIMENTAL

VI.2.1. Synthesis of Ni/ γ -Al₂O₃ catalysts modified with stearic acid

All the amounts of reagents used for the synthesis of these catalysts are listed in part V of Annex 2. In order to match with the procedures applied by Kim *et al.*^[299], the amount of stearic acid used was set to a “surfactant/Al” molar ratio equal to 0.2. Figure VI.1 depicts the different methods used to prepare the samples. In the case of samples prepared by the method “PS”, the

stearic acid was added at the same time as the other reagents (Figure VI.1-a). The solution was stirred for $t = 30$ min and the precipitation was performed with NH₄OH. After the washing steps, the sol was dispersed in a media of water/ethanol (volumic ratio = 2.8), doped with nickel nitrate, stirred for $t = 30$ min and put in oven for drying. This method was used for the preparation of sample *N-10Ni-PS*. The method “PS-eth” was similar, except that instead of using a water/ethanol media in the initial solution, pure ethanol was used (Figure VI.1-b). This method was used for the preparation of sample *N-10Ni-PS-eth*.

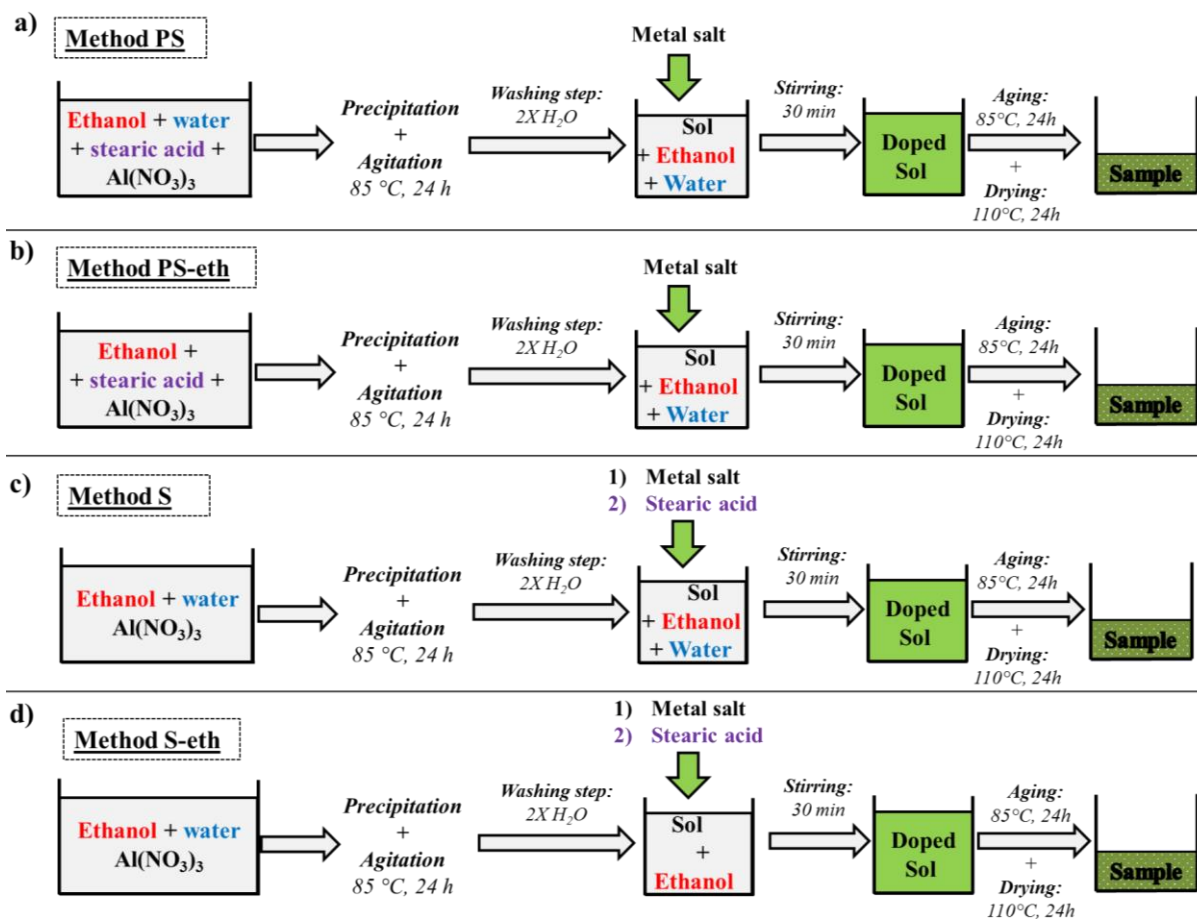


Figure VI.1: Synthesis methods for the preparation of Ni/ γ -Al₂O₃ catalysts modified with stearic acid.

In the case of samples prepared by the method “S” (Figure VI.1-c), the boehmite sol was prepared according to the standard procedure used for the preparation of sample *N* in Chapter II. After being washed, the sol was redispersed in the water/ethanol medium (volumic ratio = 2.8). First, nickel nitrate was added, followed by the stearic acid. The sol was stirred for $t = 30$ min and put in oven for drying. This method was used for the preparation of sample *N-10Ni-S*. The method “S-eth” was similar, except that instead of using a water/ethanol medium in the dispersed solution, pure ethanol was used (Figure VI.1-d). This method was used for the preparation of sample *N-10Ni-S-eth*.

VI.2.2. Characterization techniques

Composition analysis (ICP–AES), nitrogen adsorption-desorption (BET), microscope analyses (SEM-BSE), temperature programmed reduction (TPR), thermogravimetric-

differential scanning calorimetry (TG-DSC), helium pycnometry (Pycno-He), mercury porosimetry (Poro-Hg) and X-Ray diffraction (XRD) measurements were performed on the samples of this chapter. The alumina crystallites sizes were calculated by using the Scherrer equation centered on the (4 0 0) ray of γ -Al₂O₃ ($2\theta = 67.0^\circ$) of the XRD spectra. The Ni⁽⁰⁾ crystallites sizes were calculated by using the Scherrer equation centered on the (2 0 0) ray ($2\theta = 51.8^\circ$) of the XRD spectra. Deeper information about the characterizations techniques and variables quoted are provided in part II of Annex 2. X-Ray references cards are given in part VI of Annex 2.

VI.2.3. Catalytic tests

The samples were tested at $T = 650^\circ\text{C}$, for $t = 300$ min, with a standard gas mixture¹ and with a toluene concentration of 24.000 ppmv. The mass of the catalyst was set to 300 mg, for a catalytic bed height of $h = 12$ mm, with a gas flowrate of 50 mL/min and consequently a $GHSV$ of 5000 h⁻¹ (residence time of 0.72 sec).

The catalytic activity values were evaluated thanks to the toluene conversion (C_{Tolu}), the benzene selectivity (S_B), the methane conversion (C_{CH4}), the toluene reforming rate (r_{Tolu}) and the trend to form carbon deposit ($Coke^*$) whose formulae are reminded in part I of Annex 2. All the C_{Tolu} , S_B and C_{CH4} values were obtained by making an average of the results obtained during the last 10 measurements of each test.

According to the results presented in part III of Annex 2, it was assumed that all samples did not submit neither internal nor external diffusional limitations during the catalytic tests.

VI.3. RESULTS AND DISCUSSION

VI.3.1. Compositions of samples

Sample $N-10Ni$ used in this study is the same as in Chapter V. Table VI.1 shows the theoretical and actual compositions of the samples. It is to notice that all samples presented similar theoretical and actual compositions.

Table VI.1: Composition of Ni/ γ -Al₂O₃ catalysts.

Samples	Al ₂ O ₃		Ni	
	Theo. (wt. %)	Exp. (wt. %)	Theo. (wt. %)	Exp. (wt. %)
N-10Ni	90.0	89.5	10.0	10.5
N-10Ni-S	90.0	90.2	10.0	9.8
N-10Ni-PS	90.0	88.7	10.0	11.3
N-10Ni-S-eth	90.0	89.6	10.0	10.4
N-10Ni-PS-eth	90.0	89.2	10.0	11.1

VI.3.2. Influences of the synthesis method on 10 wt. % Ni/ γ -Al₂O₃ catalysts tailored with stearic acid

In Figure VI.2, TEM pictures showed that all samples $N-10Ni-S$, $N-10Ni-S-eth$, $N-10Ni-PS$, $N-10Ni-PS-eth$ had similar texture at nanoscale and that the addition of the surfactant did

¹: See Table IV.1

not cause any visible modifications of the alumina crystallites sizes, of their morphology or of the arrangement of the aggregates.

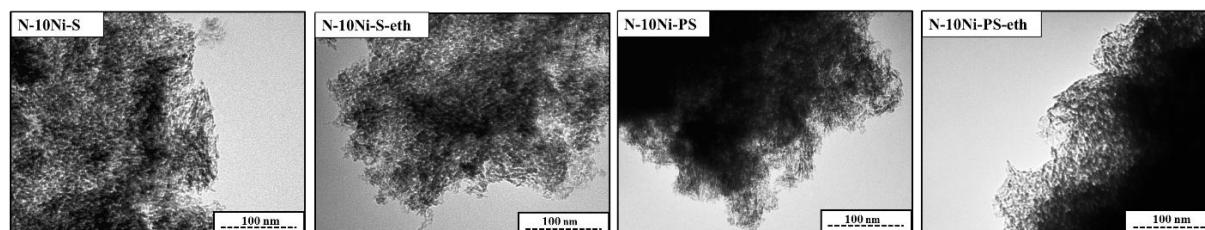


Figure VI.2: TEM observations of calcined Ni/ γ -Al₂O₃ catalysts modified with stearic acid. 130.000 X.

The nitrogen adsorption-desorption isotherms and the associated mesopore size distribution of the samples are presented in Figure VI.3. The textural properties (S_{BET} , V_p and $V_{Dubinin}$) and the sizes of the alumina crystallites obtained by X-Ray diffraction (d_{XRD,Al_2O_3}) are presented in Table VI.2.

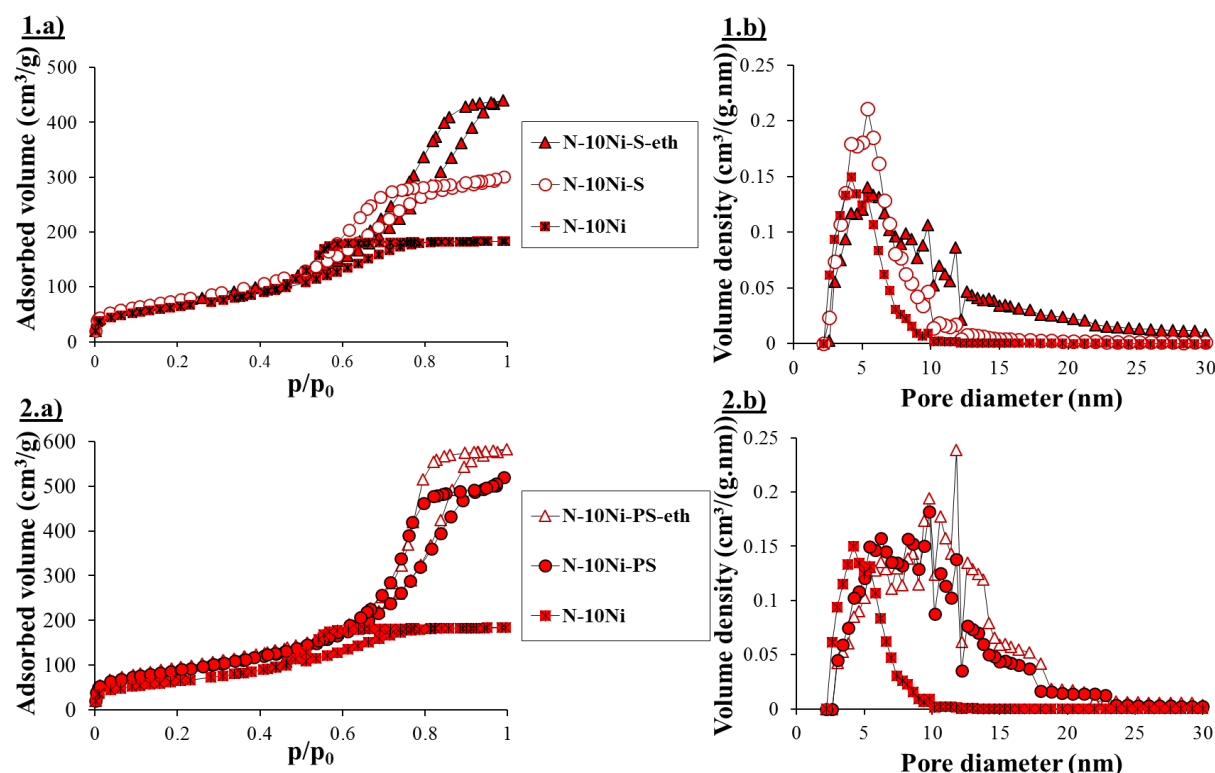


Figure VI.3: Nitrogen adsorption-desorption isotherms and mesopore size distribution for Ni/ γ -Al₂O₃ catalysts synthesized with stearic acid.

Table VI.2: Textural properties and γ -Al₂O₃ crystallites sizes. Ni⁽⁰⁾ particles sizes and their distribution obtained after reduction and TPR measurements for nickel/alumina samples modified with stearic acid.

Samples	Textural properties			Ni particles sizes						
				After Reduction				After TPR		
	S_{BET} (m ² /g)	V_p (cm ³ /g)	$V_{Dubinin}$ (cm ³ /g)	d_{TEM} (nm)	σ_{TEM} (nm)	d_{XRD} (nm)	d_{XRD,Al_2O_3} (nm)	d_{TEM} (nm)	σ_{TEM} (nm)	d_{XRD} (nm)
N-10Ni	240	0.3	0.08	8	2	9	5.4	30	9	23
N-10Ni-S	280	0.5	0.10	7	2	10	5.6	28	12	21
N-10Ni-PS	315	0.8	0.12	5	1	6	5.6	16	6	16
N-10Ni-S-eth	275	0.7	0.09	8	2	8	5.4	28	14	24
N-10Ni-PS-eth	330	0.9	0.12	7	1	7	5.5	24	6	19

S_{BET} : specific surface area; V_p : porous volume; $V_{Dubinin}$: microporous volume, d_{TEM} : metallic particles size median; σ_{TEM} : standard deviation; d_{XRD} : metallic nickel crystallites size estimation made by XRD on the Ni (2 0 0) ray; d_{XRD,Al_2O_3} : γ -Al₂O₃ crystallites size determined by XRD on the (4 4 0) ray.

It was observed in Table VI.2 that the sizes of the γ -Al₂O₃ crystallites (d_{XRD,Al_2O_3}) were similar for all samples. This observation is in accordance with the TEM observations, for which the addition of stearic acid did not influence the morphology and size of the γ -Al₂O₃ crystallites.

Table VI.2 revealed that the textural properties (S_{BET} , V_p and $V_{Dubinin}$) increased for all samples synthesized with stearic acid. For both solvent media (pure ethanol or water/ethanol), the addition of the surfactant before the precipitation step (method “PS”) allowed a deeper modification of the textural properties of the samples compared to an addition of the surfactant after the agitation step (method “S”). In this way, in comparison to reference sample *N-10Ni*, sample *N-10Ni-PS* showed a higher increase of its textural properties ($\Delta S_{BET} = + 75 \text{ m}^2/\text{g}$, $\Delta V_p = + 0.5 \text{ cm}^3/\text{g}$, $\Delta V_{Dubinin} = + 0.04 \text{ cm}^3/\text{g}$) compared to sample *N-10Ni-S* ($\Delta S_{BET} = + 40 \text{ m}^2/\text{g}$, $\Delta V_p = + 0.2 \text{ cm}^3/\text{g}$, $\Delta V_{Dubinin} = + 0.02 \text{ cm}^3/\text{g}$). Similar trends were observed when comparing the textural values between samples *N-10Ni*, *N-10Ni-S-eth* and *N-10Ni-PS-eth*.

Since no regular structuration of the alumina support was observed by TEM measurements and that d_{XRD,Al_2O_3} values were similar for all samples, it was assumed that the stearic acid molecules were more inclined to be adsorbed on the surface of the boehmite crystallites rather than forming separated micelles.^[301] In this way, in the case of the addition of the surfactant before the precipitation step (samples *N-10Ni-PS* and *N-10Ni-PS-eth*), the alumina hydroxide crystallites were fully covered by the stearic acid molecules as soon as they began to form. During the drying step, the presence of these molecules prevented a compact aggregation of the crystallites, which resulted in an increase of the micro- and mesoporosity of the samples after calcination. In contrary, when the surfactant was added after the agitation time (samples *N-10Ni-S* and *N-10Ni-S-eth*), it was assumed that the boehmite crystallites were already partially agglomerated. Consequently, the chains of stearic acid molecules had more difficulties to cover the surface of the boehmite crystallites, which resulted in a lower modification of the textural properties of the samples. Figure VI.4 illustrates this interpretation.

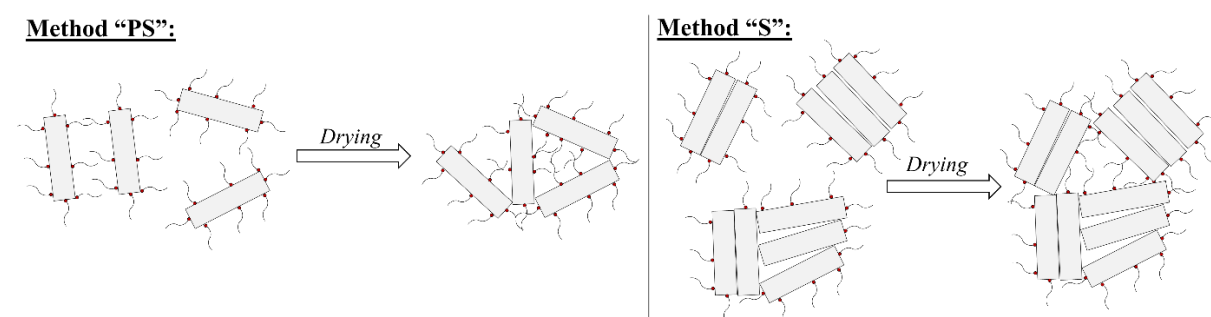


Figure VI.4: Proposed mechanism explaining the differences between samples prepared by method “PS” or by method “S”.

It was observed in Table VI.2 that the use of pure ethanol instead of water/ethanol as solvent medium led to samples with similar $V_{Dubinin}$ and S_{BET} values. Nevertheless, the porous volume at saturation pressure of nitrogen, V_p , was higher when pure ethanol was used as solvent. Despite the total volume of solvent being established in both cases to totally dissolve the stearic acid, the variations of V_p values could be a consequence of a different dispersion of the surfactant molecules. Indeed, the solubility of stearic acid is clearly higher in ethanol than in

water ($solubility_{Ethanol,25^{\circ}C} = 3.16 \text{ g}_{Surfactant}/\text{g}_{Ethanol}$ whereas $solubility_{H_2O,25^{\circ}C} = 0.034 \text{ g}_{Surfactant}/\text{g}_{H_2O}$).^[305] Hence, a higher solubility did not apparently influence the covering of the alumina crystallites (no higher $V_{Dubinin}$), but could have favored the formation of micelles, which would explain the increase of V_p .

Based on the data presented in Table VI.2, Figure VI.5 plots the metallic nickel particles sizes (calculated by doing an average of d_{TEM} and d_{XRD} values) for all samples as a function of their microporous volumes, $V_{Dubinin}$. It was observed that the samples with the highest microporous volumes (samples *N-10Ni-PS* and *N-10Ni-PS-eth*) presented the lowest initial metallic particles sizes (Figure VI.5-a) and the lowest trend to sinter (Figure VI.5-b). This observation confirmed the fact that the sintering of the metallic Ni particles occurred via a mechanism of crystallite migration, and that they were strongly affected by the support microposity.^{[65], [152], [253]}

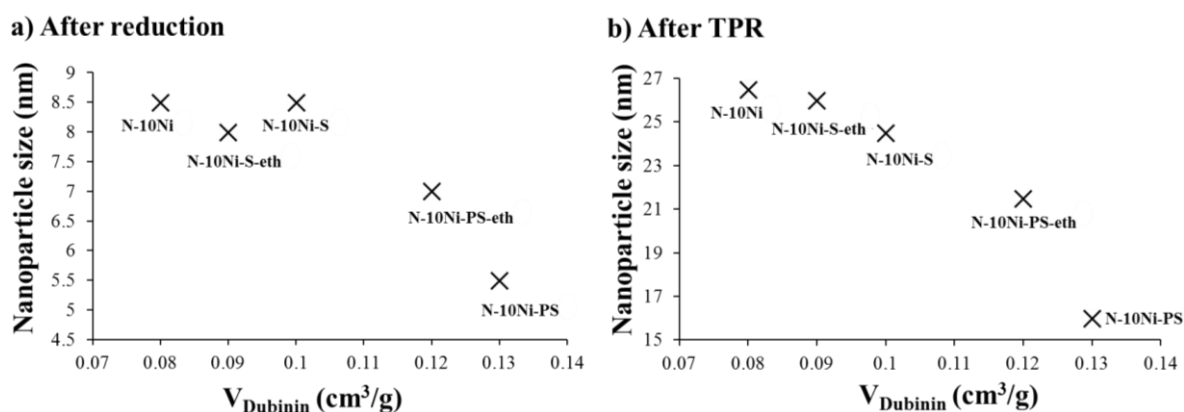


Figure VI.5: Sizes of the metallic Ni particles as a function of microporous volume for 10 wt. % Ni/ γ -Al₂O₃ samples modified with stearic acid after H₂ reduction or after TPR measurement. The metallic Ni particles sizes were obtained by making an average of the d_{XRD} and d_{TEM} values.

Figure VI.6 shows the TPR profiles of the Ni/ γ -Al₂O₃ samples modified with stearic acid:

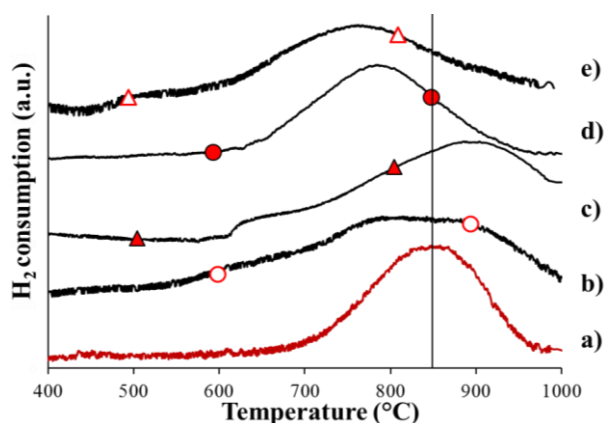


Figure VI.6: TPR profiles of 10 wt. % Ni/ γ -Al₂O₃ catalysts synthesized with stearic acid; a. *N-10Ni*, b. *N-10Ni-S*, c. *N-10Ni-S-eth*, d. *N-10Ni-PS*, e. *N-10Ni-PS-eth*.

It is observed in Figure VI.6, that, though being composed of Ni and of γ -Al₂O₃ in similar ratios and prepared with the same operating variables, the samples presented different reduction profiles. This was probably because of their different initial nickel oxide particles sizes. Indeed, in the most common cases, the smaller the particles are, the more reducible they are.^{[65], [152], [253]}

However, this assertion is not necessary true for metal-supported γ -Al₂O₃ catalysts, especially when they are synthesized by the sol-gel process. Indeed, smaller nickel oxide particles could also led to stronger interactions with the γ -Al₂O₃ support, and consequently delay the reduction of nickel oxide.^{[290], [306]}

In Figure VI.6-b, it was observed for sample *N-10Ni-S* that the maximal reduction peak value was not changed ($T \sim 850$ °C), but that the peak was broadened ($T = 600$ - 1000 °C). By comparison to sample *N-10Ni*, sample *N-10Ni-S* showed a more important microporous volume (Table VI.2), which could led to smaller initial nickel oxide particles and explains the shift of the H₂ consumption peak towards lower temperatures ($T = 600$ - 700 °C). The broadening of the H₂ consumption peak towards higher temperatures ($T = 900$ - 1000 °C) could in contrary be a consequence of larger initial nickel oxide particles, since sample *N-10Ni-S* also presented a high standard deviation after TPR ($\sigma_{TEM, N-10Ni-S} = 12$ nm) (Table VI.2).

For sample *N-10Ni-S-eth* (Figure VI.6-c), the reduction peak was broadened and shifted towards higher temperatures ($\Delta T_{N-10Ni-S-eth} = + 60$ °C). The broadening of the peak can be explained by the initial presence of nickel oxide particles with different sizes since this sample showed the highest TEM standard deviation after TPR ($\sigma_{TEM, N-10Ni-S-eth} = 14$ nm). The shift of the H₂ reduction peak towards higher reduction temperatures could also be evidenced by the presence of larger initial nickel oxide particles. Indeed, after TPR the Ni⁽⁰⁾ were large ($d_{TEM, N-10Ni-S-eth} = 28$ nm and $d_{XRD, N-10Ni-S-eth} = 24$ nm) (Table VI.2). Since sample *N-10Ni-S-eth* showed a higher porous volume, V_p , than samples *N-10Ni* and *N-10Ni-S*, it was deduced that the presence of a higher V_p would favor the formation of larger initial nickel oxides particles and would also favor the formation of larger metallic particles by sintering.

It was observed in Figures VI.6-d and VI.6-e that samples *N-10Ni-PS* and *N-10Ni-PS-eth* showed centered reduction peaks which were shifted towards lower temperatures ($T \sim 780$ °C). Both samples showed the highest $V_{Dubinin}$ and V_p values and lowest metallic Ni particles sizes with small standard deviation ($\sigma_{TEM} = 6$ nm) after TPR (Table VI.2). It was noticed that both samples had similar values of $V_{Dubinin}$. However, sample *N-10Ni-PS-eth*, which presented a higher V_p value, showed larger metallic particle sizes after TPR than sample *N-10Ni-PS* (for sample *N-10Ni-PS-eth*: $d_{TEM} = 16$ nm and $d_{XRD} = 16$ nm; whereas for sample *N-10Ni-PS-eth*: $d_{TEM} = 24$ nm and $d_{XRD} = 19$ nm) (Table VI.2).

In view of these results, the following assumptions were strengthened: 1) the samples which showed smaller initial nickel oxide particles were easier to reduce; 2) an increase of the microporosity of the alumina support permits to prevent the sintering of the metallic particles at high temperatures; 3) an increase of the mesoporous volume of the alumina support without an adequate microporous volume favors the formation of larger metallic particles with broad distribution of sizes.

VI.3.3. Further characterizations and catalytic performances of the most promising Ni/ γ -Al₂O₃ sample synthesized with stearic acid

Sample *N-10Ni-PS-eth* was selected for further characterizations and a catalytic test. This sample was chosen because it showed the highest V_p value, a high $V_{Dubinin}$ value, and a symmetric H₂ consumption peak which was shifted towards lower temperatures during TPR measurement.

VI.3.3.1. Textural properties of sample *N-10Ni-PS-eth*

Figures VI.7 shows the microscopic aspect of sample *N-10Ni-PS-eth* at different scales (400 X and 2000 X). Sample *N-10Ni-PS-eth* was formed of microscopic grains whose shapes and sizes were similar to pure γ -Al₂O₃ supports (sample *N*, Chapter II). However, it is to notice that, whereas samples *N* and *N-10Ni* presented a close compaction of their grains and hence a relatively smooth surface, in the case of sample *N-10Ni-PS-eth*, the grains were expanded and the microscopic surface was extremely rough.

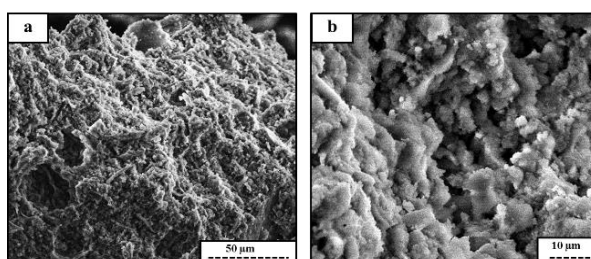


Figure VI.7: SEM pictures of sample *N-10Ni-PS-eth*; a. 400 X, b. 2000 X.

Figures VI.8 shows the mercury porosimetry curves for samples *N-10Ni-PS-eth* and *N-10Ni*. In contrary to sample *N-10Ni* which showed no macroporosity, it was observed that sample *N-10Ni-PS-eth* was macroporous with pore sizes comprised between 1 and 10 μ m and a macroporous volume, V_{Hg} , equal to 0.9 cm³/g (Table VI.3).

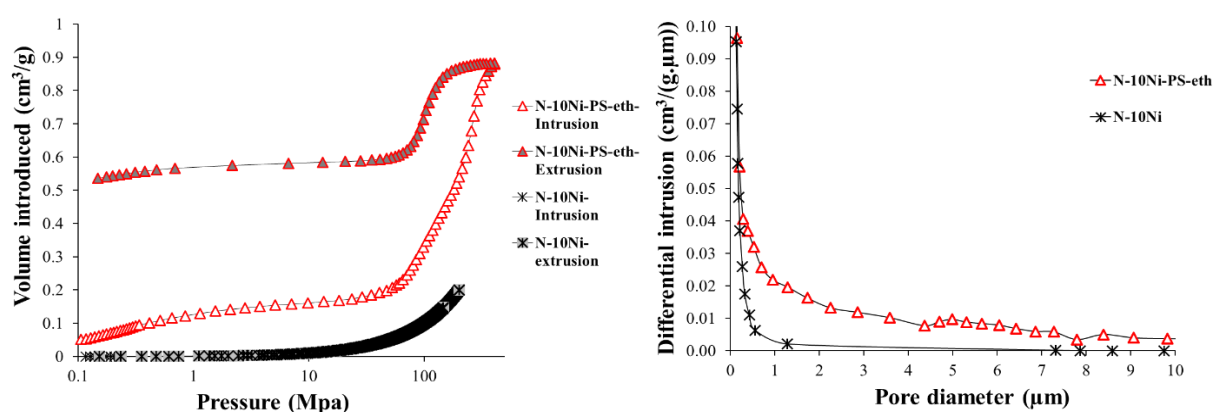


Figure VI.8: Mercury porosimetry curves (left side) and macropore size distribution determined from mercury porosimetry measurements (right side) for samples *N-10Ni-PS-eth* and *N-10Ni*.

Table VI.3: Macroporous volume and density values.

Samples	V_{Hg} (cm ³ /g)	ρ (g/cm ³)	ρ_{Eff} (g/cm ³)
N-10Ni	< 0.1	3.0	0.7
N-10Ni-PS-eth	0.9	3.1	0.2

V_{Hg} : macroporous volume determined by mercury porosimetry measurements; ρ : apparent density determined by helium pycnometry; ρ_{Eff} : effective density determined by the density of the catalysts bed and a close-packing of 0.74.

It was observed in Table VI.3 that the apparent density value measured by He pycnometry, ρ , of sample *N-10Ni-PS-eth* was very close to the value of sample *N-10Ni*. The effective density value, ρ_{Eff} , which corresponds to the mass of pellets inside the catalyst bed divided by the volume of catalytic bed with close-packing of 0.74, was in contrary very different between the two samples: 0.7 g/cm³ for sample *N-10Ni* and 0.2 g/cm³ for sample *N-10Ni-PS-eth*.ⁱ

VI.3.3.2. Catalytic performances of sample *N-10Ni-PS-eth*

Since the effective density, ρ_{Eff} , of sample *N-10Ni-PS-eth* was smaller than for the reference catalyst *N-10Ni* (Table VI.3), the catalytic bed volume and the gas flowrate were kept at standard values, but the mass of the catalyst was set to 100 mg instead of 300 mg. Figure VI.9 shows the conversion of toluene as a function of time for both samples. It is to remind that since the masses between samples *N-10Ni-PS-eth* and *N-10Ni* were different, the rigorous comparison of the catalyst activity must only be performed according to their r_{Tolu} values presented in Table VI.4.

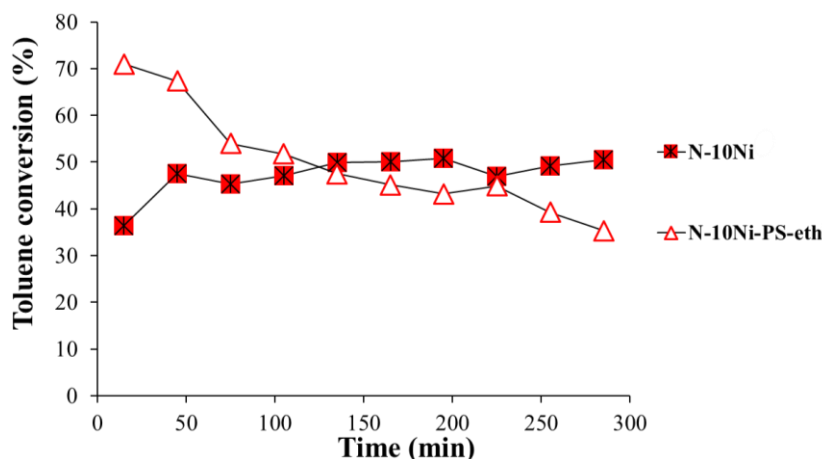


Figure VI.9: Toluene conversion as a function of time for samples *N-10Ni* and *N-10Ni-PS-eth*.

It was observed in Figure VI.9 that sample *N-10Ni-PS-eth* presented a high conversion of toluene at its first injection ($C_{Tolu} = 71\%$). This was attributed to small initial nickel oxide particles which were easily reduced (see TPR, Figure VI.6-e). However, sample *N-10Ni-PS-eth* presented an important and continuous loss of its catalytic activity during the test (between $t = 0$ min and $t = 300$ min: $\Delta C_{Tolu} \sim -35\%$).

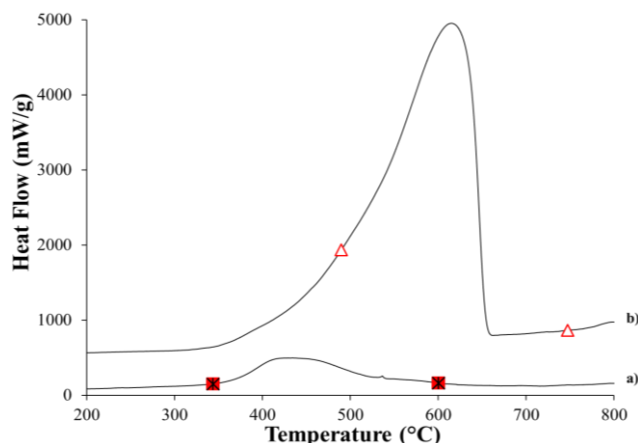
Table VI.4 shows the metallic Ni particles sizes after test, and the catalytic performances of the samples. The DSC curves obtained for the samples after test are presented in Figure VI.10.

ⁱ: Definitions of apparent and effective densities given in part II of Annex 2.

Table VI.4: Catalytic performances for samples *N-10Ni* and *N-10Ni-PS-eth*. Test conditions: $T = 650$ °C, $t = 300$ min, 24.000 ppmv of toluene, $GHSV = 5000$ h⁻¹.

Samples	Ni particles sizes			Catalytic performances					
	d_{TEM} (nm)	σ_{TEM} (nm)	d_{XRD} (nm)	C_{Tolu} (%)	r_{Tolu} (mol _{Tolu} /(gNi.h))	S_B (%)	<i>Coke</i> (g _{Carbon} /g _{Cata})	<i>Coke*</i> (g _{Carbon} /g _{Tolu})	<i>Fil. carbon</i>
N-10Ni	11	3	12	51	$6.7 \cdot 10^{-2}$	15	0.10	$3.1 \cdot 10^{-2}$	+
N-10Ni-PS-eth	15	7	13	42	$1.4 \cdot 10^{-1}$	12	1.35	$2.0 \cdot 10^{-1}$	+++

d_{TEM} : metallic particles size median; σ_{TEM} : standard deviation; d_{XRD} : metallic crystallites size estimation obtained by XRD. C_{Tolu} : conversion of toluene, r_{Tolu} : reaction rate of toluene, S_B : benzene selectivity. *Coke*: carbon deposit amount after 5 h of test measured by TG-DSC, *Coke**: tendency of sample to form carbon deposit.

Figure VI.10: Post-test DSC curves for sample modified with a surfactant; a. *N-10Ni*, b. *N-10Ni-PS-eth*.

It was observed in Table VI.4 that sample *N-10Ni-PS-eth* showed a high increase of r_{tolu} value compared to the standard sample *N-10Ni*. However, sample *N-10Ni-PS-eth* presented a very high amount of carbon deposit after test ($Coke_{N-10Ni-PS-eth} = 1.35$ g_{Carbon}/g_{Cata}), which was mostly constituted of filamentous carbon (Figures VI.10-b). Furthermore, though the r_{Tolu} value was multiplied by 2 between samples *N-10Ni* and *N-10Ni-PS-eth*, the *Coke** value was in contrary multiplied by 6.

The catalytic behavior of sample *N-10Ni-PS-eth* was similar to the results obtained in Chapter V for samples *N-20Ni* and *IMP-N-10Ni*, for which NiO, reducible at lower temperature than the catalytic test, did not take advantage of the mechanism of “special reduction by toluene”, and as consequence was deactivated during the catalytic test. However, the fact that sample *N-10Ni-PS-eth* showed much more sensibility towards coking than the samples *N-20Ni* and *IMP-N-10Ni* suggested that other parameters emphasized the formation of carbon.

It is to remind that the reforming of toluene on Ni/Al₂O₃ occurs according to several reactions which take place simultaneously, and which can be summarized as follows:¹

1) in a first step, toluene is adsorbed on the surface of the metallic particle and cracked into $C_xH_y^* + C^* + H^*$ species. $r_{Tolu,ads.+crack.}$ is the rate of adsorption and cracking of the toluene molecules;

2) in parallel, H₂O and CO₂ molecules are adsorbed on the surface and dissociated into reactive species (O*, HO*, H*);

¹: Mechanisms of tar reforming on heterogeneous catalysts presented in Figure I.7.

3) the reactive oxidant species (O^* , HO^*) react with the carbonaceous compounds (coming from the cracking of toluene) to form CO and H₂ by gasification reactions. $r_{gasification}$ is the rate of gasification of the carbonaceous compounds into CO and H₂.

The cracking of toluene occurs quickly. In contrary, the mechanism of carbon removal, which includes the dissociation of the H₂O or CO₂ molecules on the surface of the support, and the diffusion of the oxidant species (O^* , HO^*) from the support surface to the metallic particle, requires a long contact time.^{[65], [307]} In this way, it was shown in Annex 6 and in the publication of Da Silva *et al.*^[307], that an increase of the GHSV (equal to a lower residence time) could lead to a loss of balance between the cracking of toluene and the gasification reactions at the surface of the nanoparticle (in other terms, $r_{Tolu,ads.+crack.}$ was higher than $r_{gasification}$).

It is shown in part III of Annex 2, that neither external nor internal diffusional limitations were observed for both samples, which means that they both worked under chemical regime.^{[308], [309]} Nevertheless, sample *N-10Ni-PS-eth* presented a more open structure (larger meso- and macropores) than sample *N-10Ni*. As a consequence, it was assumed that the diffusion of the gaseous reagents was better for sample *N-10Ni-PS-eth* compared to sample *N-10Ni*. This better diffusion could explain the very high r_{Tolu} value observed for sample *N-10Ni-PS-eth* during the catalytic test. In return, this better diffusion might have destabilized the balance between the cracking ($r_{Tolu,ads.+crack.}$) and the gasification reactions ($r_{gasification}$) at the surface of the Ni⁽⁰⁾ particles, thus explaining why sample *N-10Ni-PS-eth* presented very large amounts of carbon deposit compared to sample *N-10Ni* (Table VI.4). Figure VI.11 gives an overview of the two different cases.

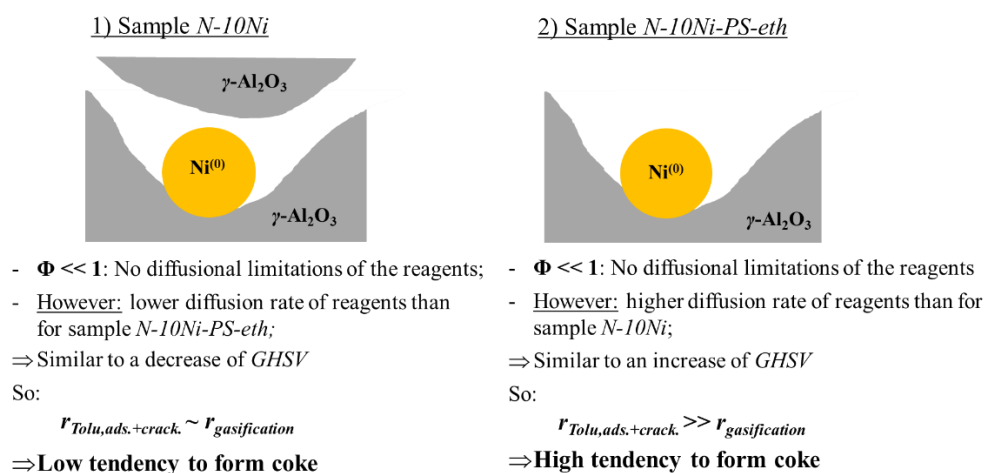


Figure VI.11: Influences of the morphology on the catalytic activity and coking between samples *N-10Ni* and *N-10Ni-PS-eth*.

Finally, it was also hypothesized that the presence of a broad and large distribution of meso- and macropore sizes for sample *N-10Ni-PS-eth* could have favored the growth of filamentous carbon.

VI.4. CONCLUSIONS

This chapter highlighted that the sol-gel preparation method developed throughout this project can efficiently modify the textural properties of 10 wt. % Ni/ γ -Al₂O₃ catalysts thanks to the addition of a common surfactant. It was shown that the step of addition of the surfactant (before precipitation vs. after long agitation) and the composition of the solvent medium (water/ethanol vs. pure ethanol) had a consequent influence on the texture modification of the samples. In this way, because of a better initial dispersion of the surfactant molecules and a good covering of the boehmite particles as soon as they were formed, the sample prepared with addition of stearic acid before the precipitation step and inside a pure ethanol medium showed the highest increase of micro- and mesoporosity.

The modification of the textural properties also proved to influence the size of the Ni particles, and thus the reducibility of the 10 wt. % Ni/ γ -Al₂O₃ catalysts. In this way, the samples with high microporosity showed lower and more uniform initial nickel oxide particles, which were easier to reduce. Furthermore, the high $V_{Dubinin}$ afforded a better resistance to the samples against sintering at high temperatures ($T \sim 1000$ °C). In contrary, the samples which showed higher mesoporous values and no adequate microporous values, presented a broader distribution of Ni⁽⁰⁾ particles sizes and broader TPR reduction profiles.

SEM and mercury porosimetry measurements confirmed that the addition of the surfactant modified the macroporosity of the catalyst. The modification of the textural properties proved to be a powerful tool in order to greatly increase the reaction rate of the conversion of toluene. However, it was observed that the catalyst modified with the surfactant showed a progressive deactivation during the catalytic tests and large amounts of carbon deposit after the test. This high trend towards the formation of carbon was in part attributed to the presence of nickel oxides easily reduced, which did not take advantage of the anti-coking effect brought by the mechanism of “special reduction by toluene”. It was also hypothesized that the large macropores did not permit to restrict the formation of filamentous carbon. Moreover, the high formation of carbon was also attributed to the high diffusion capacity of the catalyst modified with the surfactant, which was assumed to destabilize the ratio between the amount of tar cracked and the amount of carbonaceous compounds gasified by O* and HO* radicals. However, more studies need to be performed in order to get a better understanding of the influence of the texture on the catalytic performances of Ni/ γ -Al₂O₃ catalysts during the reforming of toluene.

Chapter VII

Enhancement of the catalytic performances and lifetime of nickel/alumina catalysts via addition and combination of dopants

- Properties and catalytic performances of 10 wt. % Ni/ γ -Al₂O₃ samples doped with 2 wt. % of Cu, Co, Fe, Mn or Mo;
- Influences of Mn or Mo loadings on the properties and catalytic performances of 10 wt. % Ni/ γ -Al₂O₃ catalysts;
- Properties and catalytic performances of 10 wt. % Ni/ γ -Al₂O₃ catalysts doped with 1.5 wt. % of Ca, Mg, K or Ce;
- Influences of Ca or K loadings on the properties and catalytic performances of 10 wt. % Ni/ γ -Al₂O₃ catalysts;
- Synergistic effects by the doping of 10 wt. % Ni/ γ -Al₂O₃ catalysts with two different metals or two different oxides;
- Performances of the most promising catalysts during catalytic tests performed at $T = 900 \rightarrow 600$ °C.

It was shown in Chapter I that the catalytic performances (catalytic activity and resistance against deactivation) of Ni/Al₂O₃ catalysts used for the reforming of tars can be improved thanks to the addition of various elements. However, the diverse methods used for the preparation of the catalysts and the numerous conditions of catalytic tests existing in the literature made the comparison of the influences afforded by these elements very difficult. Therefore, the objective of this chapter is to perform a vast screening in order to highlight some interesting combinations of elements.

A first step of this chapter consists in the characterization and test of catalysts at $T = 650$ °C for the reforming of 24.000 ppmv of toluene. 10 wt. % Ni/ γ -Al₂O₃ catalysts were doped with either 2 wt. % of metal (Cu, Co, Fe, Mn or Mo), 1.5 wt. % of alkali (Mg, Ca, K) or 1.5 wt. % of a rare earth (Ce). Looking for synergistic influences, it was also decided to study 10 wt. % Ni/ γ -Al₂O₃ catalysts doped with 2 wt. % of two different metals or with 1.5 wt. % of two different oxides. In view of the result obtained, it was also decided to dope 10 wt. % Ni/ γ -Al₂O₃ catalysts with 4 wt. % of the most promising metals (Mn and Mo) or with 3 wt. % of the most promising oxides (Ca and K).

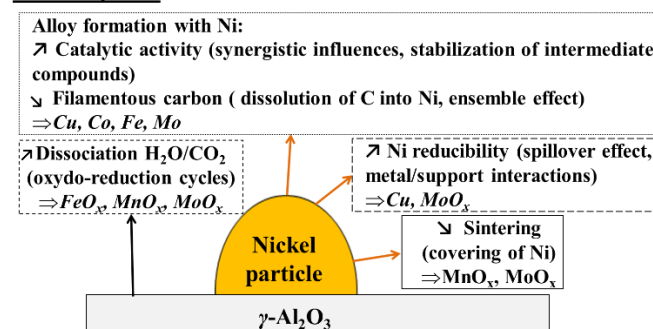
The catalysts, which showed the most interesting performances during the catalytic tests performed at $T = 650$ °C were selected for further catalytic tests under different temperatures ($T = 900 \rightarrow 600$ °C). These tests permitted to estimate the kinetic parameters for the reforming of toluene and the resistance of the catalysts against deactivation phenomena (coking, sintering, phase transition). Hence, it was highlighted that catalysts which showed very interesting performances when tested at $T = 650$ °C, did not necessarily show interesting performances when tested at $T = 900 \rightarrow 600$ °C.

VII.1. INTRODUCTION

As exhaustively described in Chapter I, the addition of elements interacting with the metallic active site, the catalytic support or both, is a common and easy way to improve the catalytic performances of a material. The reviews of Chan & Tanksale^[3], Anis & Zainal^[39] and Yung *et al.*^[100] give an overview of the numerous studies for the development of tar reforming catalysts. Among them, nickel and alumina, promoted thanks to different metals or oxides, appear as the most interesting types of catalysts. In the case of reforming catalysts, the two major criteria of a dopant lie in its ability to increase the catalytic conversion and to decrease the coking of the catalyst. Furthermore, other properties are usually targeted such as better selectivity, enhancement of the H₂/CO ratio, improvement of the conversion of CH₄ and prevention of the formation of filamentous carbon. Obviously, the doping of the catalyst must not alter the standard properties such as the crystallinity or the specific surface area of the support. Nevertheless, the variability of the synthesis procedures (impregnation vs. sol-gel, conditions of calcination) and the numerous conditions of catalytic tests applied among the studies (type of tar, concentration of tar, H₂O/C ratio, CO₂/C ratio, temperature, GHSV, gas mix, duration of test) make the comparison of the results very difficult.

For several reasons detailed in Chapter I and reminded in Figure VII.1, the use of bimetallic nickel/alumina as reforming catalysts has shown to afford very good performances in terms of catalytic activity and/or catalyst lifetime.^{[3], [66], [121], [166], [172], [310]–[312]} Many studies highlighted the beneficial effect of noble metal additions (Pt, Ru, Rh or Ir) on nickel-based catalysts used for the reforming of tars.^{[161], [165], [174], [313], [314]} However, the high prices of these elements make them economically inadequate for the development of catalysts intended for the purification of biomass gasifier tars. On the other hand, the association of Ni with more affordable metals such as Cu, Co, Fe, Mn or Mo have also proved to be beneficial for reforming applications.ⁱ In the search of new trends and new properties, trimetallic catalysts (Ni + metal n°1 + metal n°2) are also studied in this chapter. The literature about such catalysts is almost nonexistent, and some properties exhibited by these catalysts remain unclear. However, basic characterization techniques (TPR, XRD and TEM), and meticulous comparison with literature cases, permitted to evidence some trends.

Metal dopants:



Oxide dopants:

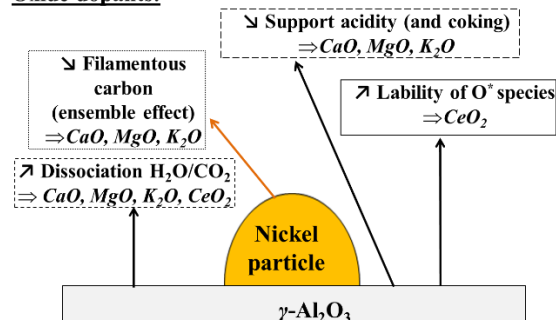


Figure VII.1: Overview of the possible influences of the doping elements on nickel/alumina catalysts.

As the gasification rates of the carbonaceous compounds located at the surface of the metallic nickel particle strongly depend on the support properties, it was also decided to prepare samples with the three more common alkali oxides dopants (CaO, MgO or K₂O) and with cerium oxide (CeO₂), which is believed to be one of the oxide dopant affording the highest anti-coking properties.ⁱⁱ The doping of nickel/alumina reforming catalysts with two different oxides has been the subject of recent studies: K+Ca^{[111], [145]}, Ca+Mg^[111], Mg+K^{[111], [315]}, Mg+Ce^[313], K+Ce^[316], Ca+Ce^[282]. The beneficial association of these oxides was mainly attributed to a better ability of the alkali doped supports to adsorb and dissociate the H₂O and CO₂ molecules. Moreover, Nandini *et al.*^[316] and Ashok *et al.*^[282] agreed on the fact that the combination of alkali and CeO_x species permitted to increase the dissociation rate of the H₂O and CO₂ molecules adsorbed on alkali thanks to an increase of the migration of O* species on the surface of the support caused by CeO_x.

i: More details about nickel/alumina catalysts doped with noble metals, or more available elements such as Cu, Mn, Mo, Co or Fe in part I.4.4.3. of Chapter I.

ii: More details about alumina promoted catalysts in part I.4.4.2.4. of Chapter I.

VII.2. EXPERIMENTAL

VII.2.1. Synthesis of doped Ni/ γ -Al₂O₃ catalysts

The amounts of reagents used for the synthesis of 10 g of each sample are shown in part V of Annex 2.

The catalysts were prepared according to the sol-gel aqueous method used in Chapters V and VI. The alumina hydroxide sol was prepared and washed two times with water, then Ni(NO₃)₂ was added, followed by the addition of further dopants. Most of the doping were performed with nitrate salts of formulae M(NO₃)_x.nH₂O, where M is Cu, Co, Fe, Mn, Ca, Mg or K. For Mo, the doping was performed with molybdic acid salt (MoO₃·H₂O). After the addition of salts, the sol was stirred for $t = 30$ min and put into an oven for classic drying steps: $t = 24$ h at $T = 85$ °C under $P = 700$ mbar, and then $t = 24$ h at $T = 110$ °C under $P = 900$ mbar. Finally, the dried samples were calcined under air for $t = 5$ h at $T = 550$ °C with a heating rate of 2 °C/min.

Six samples, used as reference materials, but not tested as catalysts, were prepared with γ -Al₂O₃ and 2 wt. % of metal (Ni, Cu, Co, Fe, Mn, Mo) or with 1.5 wt. % of Ce. The complete study of these reference samples is detailed in part II of Annex 4.

Simple doped catalysts were composed of γ -Al₂O₃, 10 wt. % of Ni and either 2 wt. % of metal (Cu, Co, Fe, Mn, Mo) or 1.5 wt. % of elements which were in the form of oxide (Ca, Ce, K, Mg).

Influence of the element loading was studied with catalysts composed of γ -Al₂O₃, 10 wt. % of Ni and either 4 wt. % of the best metals (Mn and Mo) or 3 wt. % of the best oxides (Ca, K).

Double doped catalysts were composed of γ -Al₂O₃, 10 wt. % of Ni and either 2 wt. % of two different metal dopants (Cu, Co, Fe, Mn, Mo) or 1.5 wt. % of two different oxides (Ca, Ce, K, Mg).

In order to guarantee the homogenous repartition of the elements into the samples, microscope elemental measurements (SEM-BSE and SEM-EDX) were performed for each composition. These controls revealed that the doping method was not adapted for the 10 wt. % Ni/ γ -Al₂O₃ catalysts doped with 1.5 wt. % of Ce or doped with two different oxides. Description and interpretation of the presence of microscopic heterogeneity for these samples are given in part I of Annex 4. Hence, for these samples, the doped sols were dried in a Rotavapor[®] instrument. For these catalysts, the prefix “®” is added to the name of the samples.

VII.2.2. Characterization techniques

Composition analysis (ICP–AES), nitrogen adsorption-desorption (BET), microscopic analyses and observations (SEM-GSE, SEM-BSE, SEM-EDX), transmission electron microscope observations (TEM), X-Ray diffraction (XRD), temperature programmed reduction

(TPR) and thermogravimetric-differential scanning calorimetry (TG-DSC) measurements were performed. The Ni⁽⁰⁾ particles sizes were calculated by using the Scherrer equation centered on the Ni ray (2 0 0) ($2\theta = 51.83^\circ$). The size of the crystallites of the Ni-M alloys (M = Cu, Fe, Co, Mn or Mo) were determined by using the Scherrer equation centered on the Ni-M ray (2 0 0). The Mo⁽⁰⁾ particles sizes were calculated on the Mo ray (2 1 1) ray ($2\theta = 73.70^\circ$). The Cu⁽⁰⁾ particles sizes were calculated on the Cu ray (2 0 0) ray ($2\theta = 50.48^\circ$). Deeper information about the characterization techniques and variables quoted are provided in part II of Annex 2. X-Ray references cards are given in part VI of Annex 2.

- Note about the determination of Ni-M alloy by X-Ray diffraction:

The composition of the Ni-M alloys presented in this chapter were determined from the EVA software coupled to the XRD device. Though these data are very interesting from a qualitative point of view, one must keep in mind that such a level of precision is not possible by only using XRD characterization. Furthermore, it is to notice that XRD characterization does not inform about the homogeneity of the Ni-M crystallite (for example, the surface composition of alloy is often different from the bulk composition). These remarks are particularly important in the case of trimetallic catalysts (Ni + metal n°1 + metal n°2).

VII.2.3. Catalytic experiments

The catalytic tests were performed with similar conditions as presented in Chapter VI: $T = 650^\circ\text{C}$, $t = 300$ min, with a toluene concentration of 24.000 ppmv and a standard gas mixture. The $GHSV$ value was set at 5000 h^{-1} (equivalent to a residence time of 0.72 sec) for a mass of the catalyst equal to 300 mg.

The catalytic activity values of the materials were evaluated thanks to the toluene conversion (C_{Tolu}), the benzene selectivity (S_B), the methane conversion (C_{CH4}) and to the consumption rate of toluene (r_{tolu}) whose formulae are reminded in part I of Annex 2. All the C_{Tolu} , S_B and C_{CH4} values were obtained by making an average of the results obtained during the last 10 measurements of each test.

Additional tests were performed for the most promising materials at different temperatures ($T = 900 \rightarrow 600^\circ\text{C}$ with $\Delta T = 50^\circ\text{C}$). First, the samples were heated from $T = 25^\circ\text{C}$ to $T = 900^\circ\text{C}$ under He with a heating rate of $5^\circ\text{C}/\text{min}$. At $T = 900^\circ\text{C}$, the gas mixture was sent to the catalytic chamber and three GC injections were performed (one every 15 min). Thereafter, the temperature was diminished by 50°C , three new GC injections were performed and so on until T reached 600°C . Hence, for these additional tests, each dot on the graphs corresponded to an average of three GC injections performed every $\Delta T = 50^\circ\text{C}$. Similarly as in Chapter V, these tests allow estimating the pre-exponential factor, k_0 , and the activation energy, E_a , of the samples.

VII.3. RESULTS AND DISCUSSION

VII.3.1. γ -Al₂O₃ supports doped as reference materials

γ -Al₂O₃ supports doped with 2 wt. % of metal (Ni, Cu, Co, Fe, Mn, Mo) or with 1.5 wt. % of cerium were prepared by the sol-gel method. Interpretation of the TPR and X-Ray diffractions measurements performed on these samples are detailed in part II of Annex 4 and permitted to get a better understanding of the behavior of most of the 10 wt. % Ni/ γ -Al₂O₃ doped catalysts studied in this chapter.

VII.3.2. Catalysts doped with 2 wt. % of metal or 1.5 wt. % of oxide

VII.3.2.1. Composition and textural properties

Table VII.1 shows the composition of 10 wt. % Ni/ γ -Al₂O₃ catalysts prepared with 2 wt. % of metal or with 1.5 wt. % of oxide. It was observed that theoretical and actual loadings were similar for all samples.

Table VII.1: Theoretical and actual compositions of 10 wt. % Ni/ γ -Al₂O₃ catalysts doped with 2 wt. % of metal or with 1.5 wt. % of oxide.

Samples	Theoretical composition (wt. %)	Actual composition (wt. %)
Metal : 2 wt. %		
N-10Ni-2Mo	88.0 Al ₂ O ₃ / 10.0 Ni / 2.0 Mo	89.1 Al ₂ O ₃ / 9.0 Ni / 1.9 Mo
N-10Ni-2Mn	88.0 Al ₂ O ₃ / 10.0 Ni / 2.0 Mn	89.6 Al ₂ O ₃ / 9.7 Ni / 1.8 Mn
N-10Ni-2Cu	88.0 Al ₂ O ₃ / 10.0 Ni / 2.0 Cu	89.4 Al ₂ O ₃ / 9.3 Ni / 2.3 Cu
N-10Ni-2Co	88.0 Al ₂ O ₃ / 10.0 Ni / 2.0 Co	88.4 Al ₂ O ₃ / 9.7 Ni / 1.9 Co
N-10Ni-2Fe	88.0 Al ₂ O ₃ / 10.0 Ni / 2.0 Fe	88.0 Al ₂ O ₃ / 9.6 Ni / 2.4 Fe
Oxide: 1.5 wt. %		
N-10Ni-1.5Ca	88.5 Al ₂ O ₃ / 10.0 Ni / 1.5 Ca	87.5 Al ₂ O ₃ / 11.1 Ni / 1.5 Ca
N-10Ni-1.5K	88.5 Al ₂ O ₃ / 10.0 Ni / 1.5 K	88.0 Al ₂ O ₃ / 10.4 Ni / 1.6 K
N-10Ni-1.5Mg	88.5 Al ₂ O ₃ / 10.0 Ni / 1.5 Mg	87.9 Al ₂ O ₃ / 10.8 Ni / 1.3 Mg
N-10Ni-1.5Ce [®]	88.5 Al ₂ O ₃ / 10.0 Ni / 1.5 Ce	87.7 Al ₂ O ₃ / 10.6 Ni / 1.7 Ce

Table VII.2 shows the textural properties (S_{BET} , V_p and $V_{Dubinin}$) of sample N-10Ni and of the Ni/ γ -Al₂O₃ samples doped with 2 wt. % of metal or with 1.5 wt. % of oxide.

Table VII.2: Textural properties of samples.

Samples	S_{BET} (m ² /g)	V_p (cm ³ /g)	$V_{Dubinin}$ (cm ³ /g)	Samples	S_{BET} (m ² /g)	V_p (cm ³ /g)	$V_{Dubinin}$ (cm ³ /g)
N-10Ni	240	0.3	0.08	N-10Ni-1.5Ca	240	0.3	0.08
N-10Ni-2Mo	260	0.3	0.09	N-10Ni-1.5K	235	0.3	0.08
N-10Ni-2Mn	255	0.3	0.08	N-10Ni-1.5Mg	230	0.3	0.08
N-10Ni-2Cu	240	0.3	0.08	N-10Ni-1.5Ce [®]	245	0.3	0.08
N-10Ni-2Co	235	0.3	0.08				
N-10Ni-2Fe	240	0.3	0.08				

S_{BET} : specific surface area; V_p : porous volume; $V_{Dubinin}$: microporous volume.

It is observed in Table VII.2 that all the samples were micro- and mesoporous. Furthermore, at these loadings, the element doping had no visible influence on the textural properties of the samples. Consequently, it was assumed that the textural properties were

relatively similar for all samples of this chapter and that the differences of performances exhibited were only attributed to the different dopants.

VII.3.2.2. Doping with 2 wt. % of metal

VII.3.2.2.1. Properties of Ni/ γ -Al₂O₃ catalysts doped with 2 wt. % of metal

Figure VII.2 presents the reduction profiles and the X-Ray spectra after TPR for samples *N-10Ni-2Mo*, *N-10Ni-2Mn*, *N-10Ni-2Cu*, *N-10Ni-2Co* and *N-10Ni-2Fe*. Table VII.3 presents the metallic particles sizes and the eventual presence of Ni-M alloys (M = Cu, Fe, Co, Mn or Mo) determined after TPR measurement by TEM and X-Ray analyses.

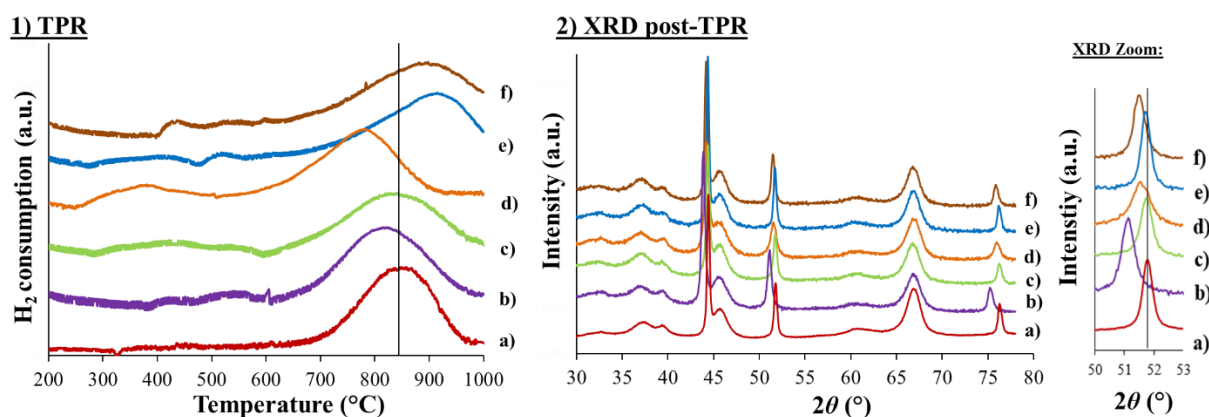


Figure VII.2: TPR profiles (left side), X-Ray spectra (right side) and XRD zooms ($50^\circ < 2\theta < 53^\circ$) for 10 wt. % Ni/ γ -Al₂O₃ catalysts doped with 2 wt. % metal; a. *N-10Ni*, b. *N-10Ni-2Mo*, c. *N-10Ni-2Mn*, d. *N-10Ni-2Cu*, e. *N-10Ni-2Co*, f. *N-10Ni-2Fe*.

Table VII.3: Metallic particles sizes and X-Ray observations after TPR measurements for 10 wt. % Ni/ γ -Al₂O₃ catalysts doped with 2 wt. % metal.

Samples	Particles sizes			Ni-Metal (2 0 0) ray (°)	Reference (2 0 0) ray of pure doping metal (°)	Possible phases
	d_{TEM} (nm)	σ_{TEM} (nm)	d_{XRD} (nm)			
N-10Ni	30	9	23	51.83	Ni = 51.83	
N-10Ni-2Mo	28	7	20	51.11	Mo = 44.95	Possibility of Ni _{0.90} Mo _{0.10} alloy / No rays of molybdenum oxide or Mo ⁽⁰⁾ visible
N-10Ni-2Mn	27	8	23	51.80	Mn = 52.38	No rays of manganese oxide visible
N-10Ni-2Cu	16	4	15	51.56	Cu = 50.43	Possibility of Ni _{0.76} Cu _{0.24} alloy / No rays of Cu ⁽⁰⁾ visible
N-10Ni-2Co	35	10	26	51.76	Co = 51.59	Possibility of Ni _{0.75} Co _{0.25} alloy / No rays of cobalt oxide visible
N-10Ni-2Fe	29	9	23	51.53	Fe = 50.52	Possibility of Ni _{0.82} Fe _{0.18} alloy / No rays of iron oxide or Fe ⁽⁰⁾ visible

d_{TEM} : metallic particles size median; σ_{TEM} : standard deviation; d_{XRD} : metallic crystallites size obtained by XRD.

N.B.: Ni⁽⁰⁾ and all Ni-M alloys observed were all organized in a cubic system (see crystallographic reference in part VI of Annex 2).

The TPR profile of sample *N-10Ni-2Mo* (Figure VII.2-b) showed three reduction peaks: one peak located at about $T = 430^\circ\text{C}$, attributed to the reduction step of Mo oxides with low interactions with the support ($\text{MoO}_3 \rightarrow \text{MoO}_2$); a second peak located at about $T = 550^\circ\text{C}$, attributed to the reduction of Mo oxides with high interactions with the support ($\text{MoO}_3/\gamma\text{-Al}_2\text{O}_3 \rightarrow \text{MoO}_2/\gamma\text{-Al}_2\text{O}_3$),ⁱ and a large peak from $T = 625^\circ\text{C}$ to $T = 975^\circ\text{C}$, characteristic of the

ⁱ: More details about the reduction of Mo supported on γ -Al₂O₃ samples in part II of Annex 4.

reduction of NiAl_2O_4 . Compared to sample *N-10Ni*, this last peak was shifted towards lower temperatures ($\Delta T = - 50$ °C). The better reduction of nickel oxide caused by addition of molybdenum has been notably described by Brito & Laine.^[317] The authors highlighted the fact that when calcined at low temperatures ($T = 400\text{-}600$ °C), NiO and MoO_x oxides supported on $\gamma\text{-Al}_2\text{O}_3$ were accelerating the reduction of each other phase. Youn *et al.*^[171] explained this phenomenon by the fact that the formation of a Ni-MoO_x phase prevents Ni to form NiAl_2O_4 spinel, which is difficult to reduce. In the present case, the X-Ray spectrum obtained after TPR (Figure VII.2-b, Table VII.3) showed an important shift of the Ni (2 0 0) diffraction ray towards the Mo (2 0 0) ray, which indicated the possible presence of a nickel-molybdenum alloy ($\text{Ni}_{0.90}\text{Mo}_{0.10}$).

The TPR profile of sample *N-10Ni-2Mn* (Figure VII.2-c) presented two reduction peaks located at $T = 400$ °C and $T = 575$ °C, which were respectively attributed to the $\text{MnO}_2 \rightarrow \text{Mn}_2\text{O}_3$ and $\text{Mn}_2\text{O} \rightarrow \text{MnO}$ reduction steps.ⁱ This sample showed a slight shift of the nickel oxide reduction step towards lower temperatures ($\Delta T = - 20$ °C) compared to sample *N-10Ni*. Indeed, it is also asserted that Ni-MnO_x interactions prevent the formation of hardly reducible NiAl_2O_4 spinel, which consequently favor the reduction of Ni.^[176] Nevertheless, the X-Ray spectrum after TPR of sample *N-10Ni-2Mn* did not evidence the formation of any Ni-Mn alloy.

The TPR profile of sample *N-10Ni-2Cu* (Figure VII.2-d) showed at first a broad peak with low intensity located between $T = 300$ °C and $T = 500$ °C, which was attributed to the reduction of copper oxides in $\text{Cu}^{(0)}$ metallic nanoparticles.ⁱⁱ It is to notice that for this sample, the reduction step of NiAl_2O_4 was significantly shifted towards lower temperatures ($\Delta T = - 60$ °C). This enhancement of the Ni reducibility due to Cu addition is well-known in the literature^{[167], [168], [318]}. It is attributed to the early presence of metallic copper nanoparticles, which favor the adsorption and activation of H_2 molecules by spillover effect.ⁱⁱⁱ The formation of $\text{Ni}_{0.76}\text{Cu}_{0.24}$ alloy was suggested on the X-Ray spectrum by the absence of $\text{Cu}^{(0)}$ rays and by the shift of the Ni (2 0 0) ray towards the diffraction angle of $\text{Cu}^{(0)}$ (2 0 0) (Figure VII.2-d, Table VII.3). Indeed, by their similar crystalline organization and their close atomic radius, Ni and Cu are known to easily form homogeneous solid solutions.^{[167], [168], [318]} Furthermore, from both X-Ray and TEM measurements, a noticeable decrease of the sizes of the metallic Ni-Cu particles after TPR was seen (for *N-10Ni-2Cu*: $d_{\text{TEM}} = 16$ nm and $d_{\text{XRD}} = 15$ nm; whereas for *N-10Ni*: $d_{\text{TEM}} = 30$ nm and $d_{\text{XRD}} = 23$ nm) (Table VII.3). The presence of smaller Ni-Cu particles by addition of Cu is apparently characteristic.^[167] However, no interpretations were given to explain this phenomenon.

The TPR profile of sample *N-10Ni-2Co* (Figure VII.2-e) presented two peaks at about $T = 400$ °C and $T = 550$ °C, which were respectively attributed to the reduction of cobalt oxides with low and high interactions with the alumina support.^{iv} It is to notice that the addition of Co

ⁱ: More details about the reduction of Mn supported on $\gamma\text{-Al}_2\text{O}_3$ samples in part II of Annex 4.

ⁱⁱ: More details about the reduction of Cu supported on $\gamma\text{-Al}_2\text{O}_3$ samples in part II of Annex 4.

ⁱⁱⁱ: More details about "spillover effect" in Figure I.12.

^{iv}: More details about the reduction of Co supported on $\gamma\text{-Al}_2\text{O}_3$ samples in part II of Annex 4.

broadened the reduction step of Ni and shifted the reduction peak of Ni towards higher temperatures ($\Delta T = + 100$ °C) compared to sample *N-10Ni*. This delay of the Ni reduction caused by Co has also been noticed by Sengupta *et al.*^[319]. Bortolozzi *et al.*^[320] highlighted by Raman spectroscopy that the addition of a small amount of Co to Ni/Al₂O₃ materials could lead to the formation of a stable Ni(Co)O solid solution, thus increasing the reduction temperature of Ni. In the present case, the shift of the Ni (2 0 0) ray towards lower diffraction angle observed in the X-Ray spectrum suggested the presence of Ni_{0.75}Co_{0.25} alloy after TPR measurement (Figure VII.2-e, Table VII.3).

The TPR profile of sample *N-10Ni-Fe* (Figure VII.2-f) presented at first a small reduction peak located at $T = 450$ °C, attributed to the Fe₂O₃→Fe₃O₄ reduction step, and a broad H₂ consumption peak, from $T = 500$ °C to $T = 1000$ °C, attributed to the further reduction of iron oxide species with different interactions with the support.ⁱ Noteworthy, the reduction step of the NiAl₂O₄ phase of this sample was shifted towards higher temperatures ($\Delta T = + 75$ °C). Indeed, the iron oxide species being reduced at higher temperatures, it is asserted that strong Ni/Fe_yO_x interactions led to a harder reducibility of the nickel oxides.^{[169], [312]} The presence of Ni_{0.82}Fe_{0.18} alloy after TPR measurement was evidenced by the shift of the Ni (2 0 0) diffraction ray in the X-Ray spectrum (Figure VII.2-f, Table VII.3). Indeed, Ni and Fe easily form solid solutions.^{[66], [169], [312]} One can also notice that after TPR measurement, whereas the sample made of only 2 wt. % Fe/ γ -Al₂O₃ (sample *N-2Fe*, part II of Annex 4) presented α -Al₂O₃ rays and that the sample made of 10 wt. % Fe/ γ -Al₂O₃ (sample *N-10Fe*, Chapter IV) presented hercynite rays (FeAl₂O₄), none of these rays were present for sample *N-10Ni-2Fe*. The absence of an alteration of the γ -Al₂O₃ phase confirmed that instead of interacting with the support, the Fe species in sample *N-10Ni-2Fe* were more inclined to form strong interactions with Ni.

VII.3.2.2.2. Catalytic performances of Ni/ γ -Al₂O₃ catalysts doped with 2 wt. % of metal

The catalytic performances of all 10 wt. % Ni/ γ -Al₂O₃ catalysts doped with 2 wt. % of metal were measured. Figure VII.3 shows the toluene conversion, C_{Tolu} , as a function of time and the toluene reforming rate, r_{Tolu} , as a function of the amount of carbon deposit. Figure VII.4 shows the benzene selectivity, S_B , and the methane conversion, C_{CH_4} . The metallic particles sizes, the nature of the metallic phases present after the catalytic test as well as the catalytic performances of the samples are presented in Table VII.4. Figure VII.5 shows the DSC curves performed on samples after catalytic tests.

ⁱ : More details about the reduction of Fe supported on γ -Al₂O₃ samples in part II of Annex 4.

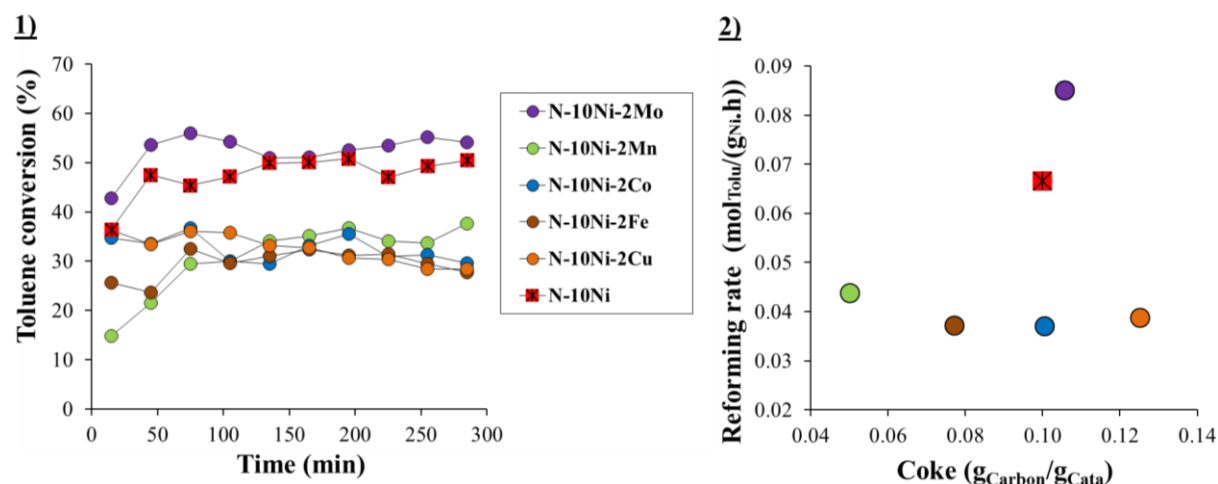


Figure VII.3: Toluene conversion as a function of time (left side) and toluene reforming rate as a function of carbon deposit amount (right side) for 10 wt. % Ni/ γ -Al₂O₃ catalysts doped with 2 wt. % metal.

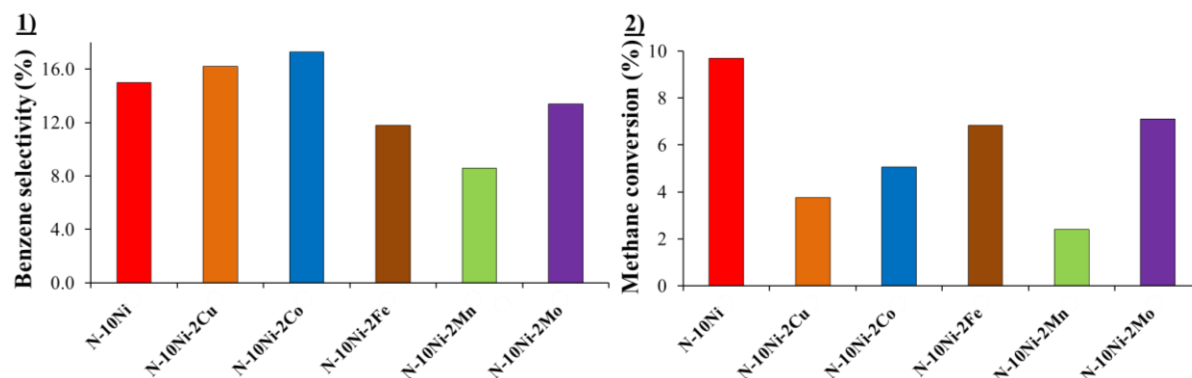


Figure VII.4: Benzene selectivity (left side) and methane conversion (right side) diagrams for 10 wt. % Ni/ γ -Al₂O₃ catalysts doped with 2 wt. % metal.

Table VII.4: Metallic particles sizes, metal alloy phases and catalytic performances for 10 wt. % Ni/ γ -Al₂O₃ catalysts doped with 2 wt. % metal. Test conditions: $T = 650$ °C, $t = 300$ min, 24.000 ppmv of toluene, $GHSV = 5000$ h⁻¹.

Samples	Particules sizes			Possible metal phase	Catalytic performances					
	d_{TEM} (nm)	σ_{TEM} (nm)	d_{XRD} (nm)		C_{Tolu} (%)	r_{tolu} (molTolu/(gNi.h))	S_B (%)	C_{CH4} (%)	Coke (gCarbon/gCata)	Fil. carbon
N-10Ni	12	4	12	Ni	51	$6.7 \cdot 10^{-2}$	15	10	0.10	No
N-10Ni-2Mo	12	6	11	Ni _{0.97} Mo _{0.03}	54	$8.5 \cdot 10^{-2}$	13	7	0.11	No
N-10Ni-2Mn	10	2	14	Ni	35	$4.4 \cdot 10^{-2}$	9	2	0.05	No
N-10Ni-2Cu	8	4	8	Ni _{0.75} Cu _{0.25}	31	$3.9 \cdot 10^{-2}$	16	4	0.13	No
N-10Ni-2Co	15	11	13	Ni _{0.8} Co _{0.2}	31	$3.7 \cdot 10^{-2}$	17	5	0.10	+
N-10Ni-2Fe	14	5	17	Ni _{0.82} Fe _{0.18}	30	$3.7 \cdot 10^{-2}$	12	7	0.08	+

d_{TEM} : metallic particles size median; σ_{TEM} : standard deviation; d_{XRD} : metallic crystallites size estimation obtained by XRD; C_{Tolu} : conversion of toluene; r_{tolu} : reaction rate of toluene; S_B : selectivity in benzene, C_{CH4} : conversion of methane; Coke: carbon deposit amount after 5 h of test measured by TG-DSC.

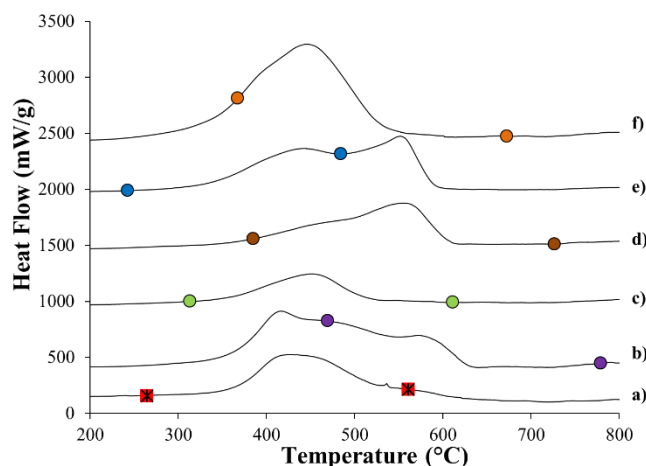


Figure VII.5: Post-test DSC curves for 10 wt. % Ni/ γ -Al₂O₃ catalysts doped with 2 wt. % metal; a. *N-10Ni*, b. *N-10Ni-2Mo*, c. *N-10Ni-2Mn*, d. *N-10Ni-2Fe*, e. *N-10Ni-2Co*, f. *N-10Ni-2Cu*.

In view of the results presented, it appeared that the doping of the catalysts with copper led to the worst results. In this way, sample *N-10Ni-2Cu* showed a low r_{Tolu} value ($3.9 \cdot 10^{-2}$ mol_{Tolu}/(g_{Ni}.h)), a low C_{CH_4} value (4 %) and the largest amount of carbon deposit (0.13 g_{Carbon}/g_{Cata}) (Table VII.4). However, the TG-DSC curve (Figure VII.5-f) and TEM observations (not shown here) showed that the carbon deposit of this sample was exclusively constituted of amorphous carbon. This fact can be explained by the formation of a Ni-Cu alloy phase confirmed by XRD after test (Table VII.4). Indeed, it is known that the dissolution of carbon inside a Ni-Cu alloy is more difficult than inside pure Ni particles, which consequently results in a prevention of filamentous carbon formation.^[158] However, whereas in the case of methane reforming, the spacing of Ni atoms by Cu atoms prevents the formation of C-C bonds and reduces the amount of carbon deposit by “ensemble control”,ⁱ this phenomenon does not seem to be relevant in the case of the reforming of toluene. Hence, the progressive deactivation of sample *N-10Ni-2Cu* throughout the test (Figure VII.3) was assumed to be caused by the formation of a high amount of amorphous carbon, which covered and deactivated the surface of the Ni-Cu particles. Finally, the low CH_4 value observed for sample *N-10Ni-2Cu* (Table VII.4, Figure VII.4) has to be correlated to the work of Kratzer *et al.*^[321], which showed by DFT calculations, that the activation energy of methane chemisorption on a nickel atom in the Ni (1 1 1) surface is significantly smaller if the neighbour atom is an atom of Cu instead of Ni.

The catalysts doped with iron (sample *N-10Ni-2Fe*) or with cobalt (sample *N-10Ni-2Co*) showed similar trends. In this way, their C_{Tolu} and C_{CH_4} values were lower (Figure VII.3, Table VII.4) compared to sample *N-10Ni*, which was assumed to be caused by an insufficient reduction of the metallic active sites (see TPR, Figures VII.2-e and VII.2-f). Both samples were more inclined to form filamentous carbon (Figures VII.5-d and VII.5-e, Table VII.4). These observations can be explained by the fact that Co/Fe elements are commonly used to modify Ni-based catalysts in order to produce carbon nanotubes at industrial scale.^{[322], [323]}

ⁱ: more information about “ensemble control” in Figure I.12.

In the case of manganese addition (sample *N-10Ni-2Mn*), the catalyst showed lower C_{Tolu} and C_{CH_4} values (Figures VII.3 and VII.4, Table VII.4), but this was balanced by a very low amount of carbon deposit ($0.05 \text{ g}_{\text{Carbon}}/\text{g}_{\text{Cata}}$). DSC curves (Figures VII.5-c) and TEM observations revealed that the carbon deposit of this sample was only constituted of amorphous carbon. These results were in accordance with the literature and were attributed to the migration of the MnO_x species to the surface of the metallic nickel particles.^{[143], [176], [316], [324]} By their location at the surface of the metallic nickel particles, the MnO_x species can partially decrease the catalytic activity because of the blockage of active sites. However, they can provide high anti-coking effects. Indeed, it is asserted that the moderate basicity of the manganese oxide species improves the adsorption of the H_2O and CO_2 molecules,^[324] and that the redox properties of the MnO_x species favor their dissociation, and also the migration of the O^* species^{[176], [316], [324]}. This higher rate to form oxidative species led to a better oxidation of the intermediate compounds and of the carbonaceous deposits, which explained the low S_B value and the low carbon deposit obtained for sample *N-10Ni-2Mn*. Furthermore, in the case of methane reforming, Seok *et al.*^[324] suggested that the covering of the particle by MnO_x species divided the surface of $\text{Ni}^{(0)}$ particle into different patches, which were large enough to perform the CH_4 reforming, but too small to permit the formation of carbon deposit thanks to “ensemble control” effect.

The catalysts doped with 2 wt. % of molybdenum showed the more interesting results. Indeed, sample *N-10Ni-2Mo* showed a higher r_{Tolu} and a relatively good C_{CH_4} value (7 %) for an acceptable amount of carbon deposit ($Coke = 0.11 \text{ g}_{\text{Carbon}}/\text{g}_{\text{Cata}}$) compared to sample *N-10Ni* (Figures VII.3 and VII.4, Table VII.4). Similarly to Mn, the MoO_x species are also known to be able to surround and cover the $\text{Ni}^{(0)}$ particles of the catalyst. These MoO_x species are generally in different oxidation states (Mo^{n+} with $4 < n < 6$)^[325], which is believed to increase the redox cycles of the Ni- MoO_x compounds and to favor the dissociation reactions of H_2O and of CO_2 .^{[171], [172], [311]} Moreover, Maluf *et al.*^[173] also obtained higher methane reforming activity for Ni/ Al_2O_3 materials doped with Mo. Since the authors observed that the addition of Mo decreased the surface metallic area, but increased the specific activity of the active sites, they concluded that the higher reforming activity was caused by a transfer of electrons from the MoO_x species to the nickel atoms, leading to an increase of the electron density of the Ni atoms. Though the influence of MoO_x species is relatively well detailed, there is a lack of literature about the effect of the formation of Ni-Mo alloys.

VII.3.2.3. Doping with 1.5 wt. % of oxide

VII.3.2.3.1. Properties of Ni/ γ - Al_2O_3 catalysts doped with 1.5 wt. % of oxide

Figure VII.6 shows the TPR profile of 10 wt. % Ni/ γ - Al_2O_3 catalysts doped with 1.5 wt. % of oxide (samples *N-10Ni-1.5Ca*, *N-10Ni-1.5Mg*, *N-10Ni-1.5K* and *N-10Ni-1.5Ce*). The metallic nickel particles sizes obtained by TEM and XRD measurements are presented in Table VII.5.

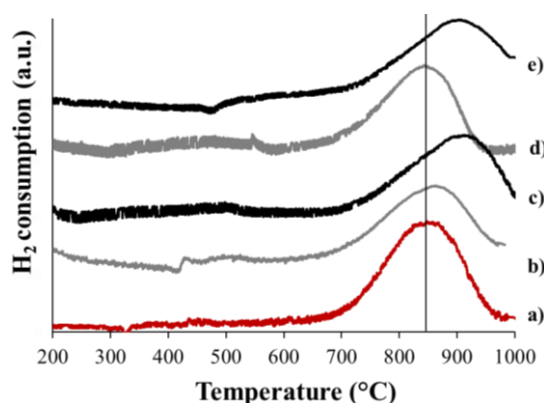


Figure VII.6: H₂-TPR curves for 10 wt. % Ni/γ-Al₂O₃ catalysts doped with 1.5 wt. % of oxide; a. N-10Ni, b. N-10Ni-1.5Ca, c. N-10Ni-1.5Mg, d. N-10Ni-1.5K, e. N-10Ni-1.5Ce®.

Table VII.5: Ni particles sizes and X-Ray observations for 10 wt. % Ni/γ-Al₂O₃ catalysts doped with 1.5 wt. % of oxide.

Samples	d_{TEM} (nm)	σ_{TEM} (nm)	d_{XRD} (nm)
N-10Ni	30	9	23
N-10Ni-1.5Ca	36	10	26
N-10Ni-1.5K	38	11	27
N-10Ni-1.5Mg	34	11	25
N-10Ni-1.5Ce®	44	12	28

d_{TEM} : metallic particles size median; σ_{TEM} : standard deviation; d_{XRD} : metallic crystallites size estimation obtained by XRD.

The TPR profile of sample N-10Ni-1.5Ca (Figure VII.6-b) showed a peak with low intensity located at about $T = 500$ °C, which could be attributed to nickel oxide with low interactions with the support. Indeed, it was shown by Elias *et al.*^[326] that the strong affinity of CaO with Al₂O₃ can partially decrease the interactions between Ni and γ-Al₂O₃. However, it is to notice that the main reduction peak of Ni of sample N-10Ni-1.5Ca stayed at the same temperature.

The sample doped with potassium (sample N-10Ni-1.5K) also showed a TPR profile with a peak of low intensity located at about $T = 500$ °C (Figure VII.6-d). This phenomenon is based on the same principle as for sample N-10Ni-1.5Ca and was recorded by Hu *et al.*^[327]. However, it was noticed that for sample N-10Ni-1.5K, the main reduction step of Ni was also not changed.

It was observed in the TPR profile of sample N-10Ni-1.5Mg (Figure VII.6-c) that the addition of magnesium shifted the reduction step of Ni towards higher temperatures ($\Delta T = + 65$ °C) compared to sample N-10Ni. This influence of MgO on the nickel reduction has been well established in the literature^{[313], [328], [329]}. According to Wang *et al.*^[122], “because MgO has a lattice parameter and bond distance close to those of NiO, MgO and NiO can form a solid solution resulting in its lowered reducibility”. However, contrary to the results seen in some previous studies^{[313], [330]}, the sample N-10Ni-1.5Mg did not show smaller metallic nickel particles after TPR ($d_{XRD} = 25$ nm and $d_{TEM} = 34$ nm) (Table VII.5).

Sample N-10Ni-1.5Ce® presented a TPR profile (Figures VII.6-e) with a broad peak of low intensity located between $T = 450$ °C and $T = 700$ °C, which was attributed to the CeO₂→Ce₂O₃ reduction step.¹ It was also observed that the main reduction peak of Ni was

¹: More details about the reduction of Ce supported on γ-Al₂O₃ samples in part II of Annex 4.

shifted towards higher temperatures ($\Delta T = + 60$ °C) compared to sample *N-10Ni*. Despite the common agreement on the fact that the interactions between Ni and CeO_x are strong, the consequence of CeO₂ on the reducibility of Ni supported on γ -Al₂O₃ varies among the publications. Some authors found that the addition of cerium decreased the temperature needed for the reduction of Ni.^{[135], [150]} This was attributed to the fact that Ni-CeO_x interactions might prevent the formation of NiAl₂O₄ spinel, which is difficult to reduce. In contrary, Liu *et al.*^[331] found that the addition of Ce made the reduction of Ni oxides more difficult. The author attributed the delay of the reduction to the presence of CeO_x species on the surface of Ni. It was also noticed that, whereas the addition of CeO₂ apparently permits to reduce the sintering rate of the Ni⁽⁰⁾ particles^{[150], [331], [332]}, in the present case, sample *N-10Ni-1.5Ce* presented large metallic particles sizes after TPR ($d_{XRD} = 28$ nm and $d_{TEM} = 44$ nm) (Table VII.5). Nevertheless, it is capital to keep in mind that the catalysts studied in the aforementioned studies were all prepared by impregnation methods, which generally provide very different metal/support interactions compared to sol-gel preparation methods.

It was observed that NH₃-TPD measurements (Figures VII.7) and their corresponding volumes of NH₃ desorbed (Table VII.6) led to very close results for all 10 wt. % Ni/ γ -Al₂O₃ catalysts doped with 1.5 wt. % of oxide. The presence of similar acido-basicity properties was attributed to the low amount of alkali and to the relatively low calcination temperature ($T = 550$ °C), which was insufficient to enable the formation of strong interactions between the alkali and the γ -Al₂O₃ support during the preparation of catalysts.^{[333]–[335]}

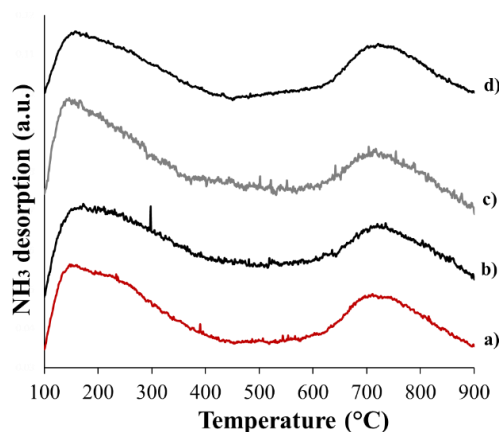


Figure VII.7: NH₃-TPD curves for 10 wt. % Ni/ γ -Al₂O₃ catalysts doped with 1.5 wt. % of alkali; a. *N-10Ni*, b. *N-10Ni-1.5Ca*, c. *N-10Ni-1.5Mg*, d. *N-10Ni-1.5K*.

Table VII.6: Amounts of NH₃ desorbed determined by TPD-NH₃ measurements.

Samples	Weak acid sites (mmol _{NH3} /g)	Strong acid sites (mmol _{NH3} /g)	Total acidity (mmol _{NH3} /g)
N-10Ni	0.27	0.20	0.47
N-10Ni-1.5Ca	0.27	0.23	0.50
N-10Ni-1.5Mg	0.31	0.19	0.50
N-10Ni-1.5K	0.23	0.24	0.47

VII.3.2.3.2. Catalytic performances of Ni/ γ -Al₂O₃ catalysts doped with 1.5 wt. % of oxide

The catalytic performances of all 10 wt. % Ni/ γ -Al₂O₃ catalysts doped with 1.5 wt. % of oxide were measured. Figure VII.8 shows the toluene conversion, C_{Tolu} , as a function of time

and the toluene reforming rate, r_{Tolu} , as a function of the amount of carbon deposit. Figure VII.9 shows the benzene selectivity, S_B , and the methane conversion, C_{CH_4} . Figure VII.10 shows the DSC curves performed on samples after catalytic tests. The metallic particles sizes, the type of metallic phase present after tests as well as the catalytic performances of the samples are resumed in Table VII.7.

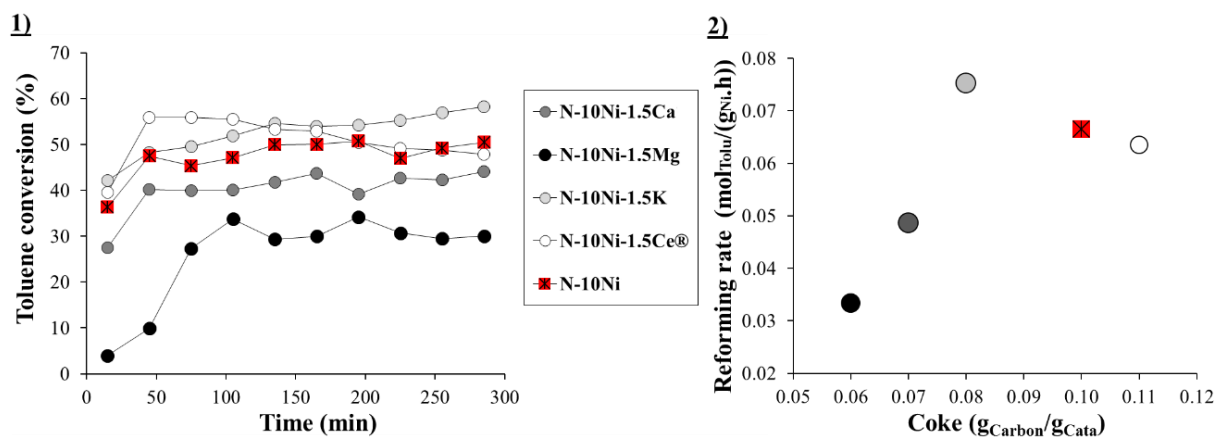


Figure VII.8: Toluene conversion as a function of time (left side) and toluene reforming rate as a function of carbon deposit amount (right side) for 10 wt. % Ni/ γ -Al₂O₃ catalysts doped with 1.5 wt. % of oxide.

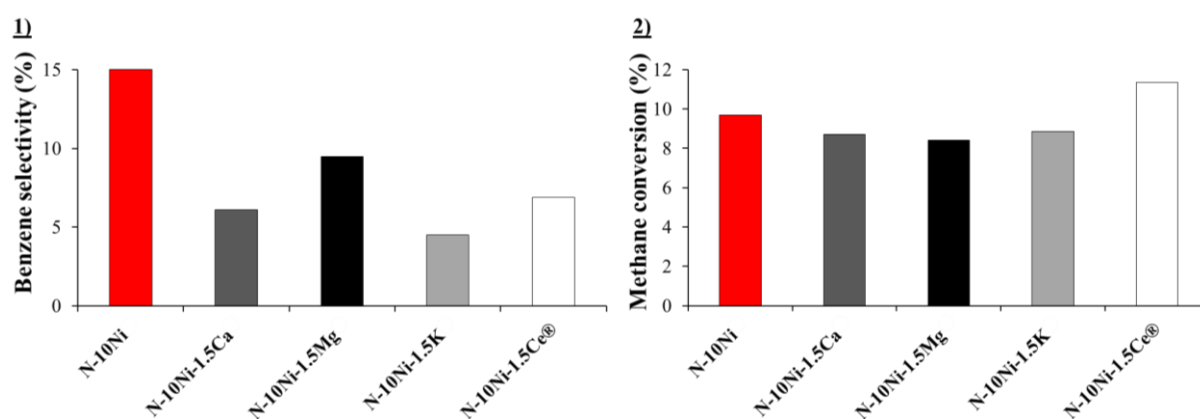


Figure VII.9: Benzene selectivity (left side) and methane conversion (right side) diagrams for 10 wt. % Ni/ γ -Al₂O₃ catalysts doped with 1.5 wt. % of oxide.

Table VII.7: Ni particles sizes and catalytic performances for 10 wt. % Ni/ γ -Al₂O₃ catalysts doped with 1.5 wt. % of oxide. Test conditions: $T = 650$ °C, $t = 300$ min, 24.000 ppmv of toluene, $GHSV = 5000$ h⁻¹.

Samples	Ni particles sizes			Catalytic performances					
	d_{TEM} (nm)	σ_{TEM} (nm)	d_{XRD} (nm)	C_{Tolu} (%)	r_{Tolu} (mol _{Tolu} /(gNi.h))	C_{CH_4} (%)	S_B (%)	Coke (gCarbon/gCata)	Fil. carbon
N-10Ni	11	3	12	51	$6.7 \cdot 10^{-2}$	10	15	0.10	No
N-10Ni-1.5Ca	11	5	10	42	$4.9 \cdot 10^{-2}$	9	6	0.07	No
N-10Ni-1.5K	12	4	12	55	$7.2 \cdot 10^{-2}$	9	4	0.08	No
N-10Ni-1.5Mg	11	7	12	31	$3.3 \cdot 10^{-2}$	8	9	0.06	+
N-10Ni-1.5Ce®	8	2	12	50	$6.4 \cdot 10^{-2}$	11	7	0.11	+

d_{TEM} : metallic particles size median; σ_{TEM} : standard deviation; d_{XRD} : metallic crystallites size estimation obtained by XRD; C_{Tolu} : conversion of toluene; r_{Tolu} : reaction rate of toluene; S_B : selectivity in benzene, C_{CH_4} : conversion of methane; Coke: carbon deposit amount after 5 h of test measured by TG-DSC.

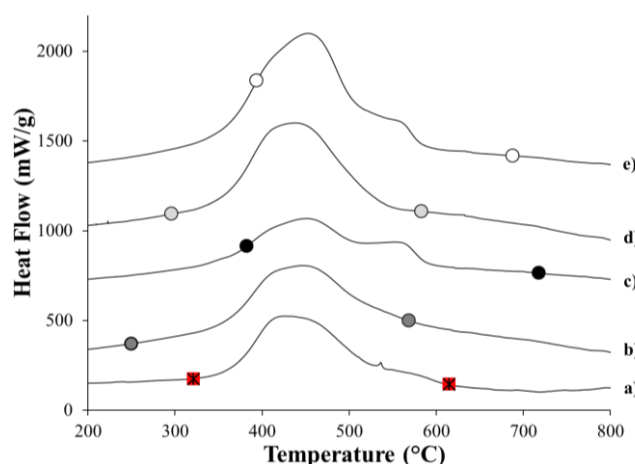


Figure VII.10: Post-test DSC curves for 10 wt. % Ni/ γ -Al₂O₃ catalysts doped with 1.5 wt. % of oxide; a. *N-10Ni*, b. *N-10Ni-1.5Ca*, c. *N-10Ni-1.5Mg*, d. *N-10Ni-1.5K*, e. *N-10Ni-1.5Ce*®.

The materials doped with an alkali (samples *N-10Ni-1.5Ca*, *N-10Ni-1.5Mg* and *N-10Ni-1.5K*) showed much lower S_B values (4-9 %, instead of 15 % for sample *N-10Ni*) and lower amounts of carbon deposit after test (*Coke* of 0.06-0.08 g_{Carbon}/g_{Cata}, instead of 0.10 g_{Carbon}/g_{Cata} for sample *N-10Ni*) (Table VII.7). Furthermore, it is to notice that samples *N-10Ni-1.5Ca* and *N-10Ni-1.5K* did not show any filamentous carbon after catalytic test (Figures VII.10-b and VII.10-d). Since the TPD-NH₃ measurements (Figure VII.7 and Table VII.6) revealed that the alkali addition did not have a strong influence on the acido-basicity of the alumina supports, it was assumed that the better anti-coking properties showed by the alkali-doped samples were mostly due to their better ability to adsorb and dissociate the H₂O and CO₂ molecules.¹ In this way, the higher presence of oxidative species (O* and HO*) favored the gasification of the carbonaceous compounds produced during the cracking of the toluene and prevented these molecules to react with each other and to form stable filamentous carbon.^{[3], [110], [111]}

Figure VII.8 revealed that sample *N-10Ni-1.5Mg* presented a very low C_{Tolu} value at the beginning of the catalytic test, and that this sample needed more time to be activated during the test. Furthermore, even at the end of the test, this sample showed low C_{Tolu} values (at $t = 300$ min, for *N-10Ni-1.5Mg* $C_{Tolu} = 31$ %, whereas $C_{Tolu} = 51$ % for *N-10Ni*). Hence, in that case, too strong NiO-MgO interactions (see TPR, Figure VII.6-c) were detrimental for the catalytic activity.

It was observed that sample *N-10Ni-1.5Ca* showed slightly lower C_{Tolu} and C_{CH_4} values (Table VII.7) compared to sample *N-10Ni*. It was hypothesized that these lower conversions were caused by the covering of the Ni⁽⁰⁾ particles by CaO. Indeed, it was shown that during catalytic tests, alkali oxides can migrate and cover the surface of the Ni⁽⁰⁾ particles. This covering can have beneficial influences since it favors the adsorption-dissociation of H₂O and CO₂ molecules, and therefore increases the direct oxidation of the carbonaceous species cracked.^{[65], [118], [336], [337]} However, it was shown for the steam and dry reforming of CH₄, that the presence of alkali at the surface of Ni⁽⁰⁾ could also block the access to some active sites and greatly decrease the catalytic activity of the materials. This effect depended on different

¹ : More information about the ability of alkali toward the adsorption-dissociation of H₂O and CO₂ species in part I.4.4.2.2. of Chapter I.

parameters such as the synthesis method^{[338], [339]} or the amount of doping^[139]. Furthermore, it was also shown that alkali element could modify the electronic environment of the Ni atoms and hence increase the energetic barrier needed for the CH₄ dissociation.^{[65], [340]}

Despite a slight decrease of the C_{CH_4} value, the addition of potassium had beneficial influences on the catalytic performances of sample *N-10Ni-1.5K* compared to sample *N-10Ni*: lower S_B value (4 %) (Table VII.7), higher r_{Tolu} value ($7.2 \cdot 10^{-2} \text{ mol}_{Tolu}/(\text{g}_{Ni} \cdot \text{h})$) and low amount of carbon deposit after test ($Coke = 0.08 \text{ g}_{Carbon}/\text{g}_{Cata}$) (Table VII.7). It is to notice that no clear explanations was found in the literature to explain the different activities between K and Ca doped materials. It could probably be due to different rates of adsorption-dissociation of H₂O and CO₂ molecules between CaO and K₂O.

Despite the fact that the addition of cerium in the composition of reforming catalysts is more and more encouraged in the literature^{[146]–[149]}, sample *N-10Ni-1.5Ce®* did not show exceptional performances. Indeed, sample *N-10Ni-1.5Ce®* showed similar catalytic activity and similar coking values as sample *N-10Ni* (Table VII.7). The low influences of the Ce doping could be attributed to inadequate interactions between the $\gamma\text{-Al}_2\text{O}_3$ support and the Ce oxide species. Indeed, in contrary to the present aqueous sol-gel synthesis used, in most previous studies, the supports were prepared by the doping of commercial $\gamma\text{-Al}_2\text{O}_3$ support with Ce by incipient wetness methods.^{[134], [150], [151], [341]} In these studies, the calcination temperature varies from $T = 450 \text{ }^\circ\text{C}$ to $T = 1200 \text{ }^\circ\text{C}$. This strong influence of the preparation method on the properties of Ni/CeO₂/Al₂O₃ catalysts was notably highlighted by Tomishige *et al.*^[342], who showed that catalysts prepared by co-impregnation method exhibited much higher performances than the same materials prepared by sequential impregnation. In the present case, it was assumed that the calcination temperature was not enough high to create sufficient interactions between the Ce oxide species and alumina, and to form the anti-coking AlCeO_x phases.

VII.3.3. Double doping and synergistic effects

VII.3.3.1. Catalysts doped with two different metals

VII.3.3.1.1. General trends

10 wt. % Ni/ $\gamma\text{-Al}_2\text{O}_3$ catalysts doped with 2 wt. % of one metal and 2 wt. % of a second metal (Metal = Cu, Co, Mn, Mo or Fe) were synthesized, characterized and tested for the reforming of 24.000 ppmv of toluene at $T = 650 \text{ }^\circ\text{C}$. Figure VII.11 gives an overview of the reforming rate of toluene, r_{Tolu} , as a function of the amount of carbon deposit after test for all samples. Figure VII.12 gives an overview of the benzene selectivity, S_B , and methane conversion, C_{CH_4} , for all catalysts.

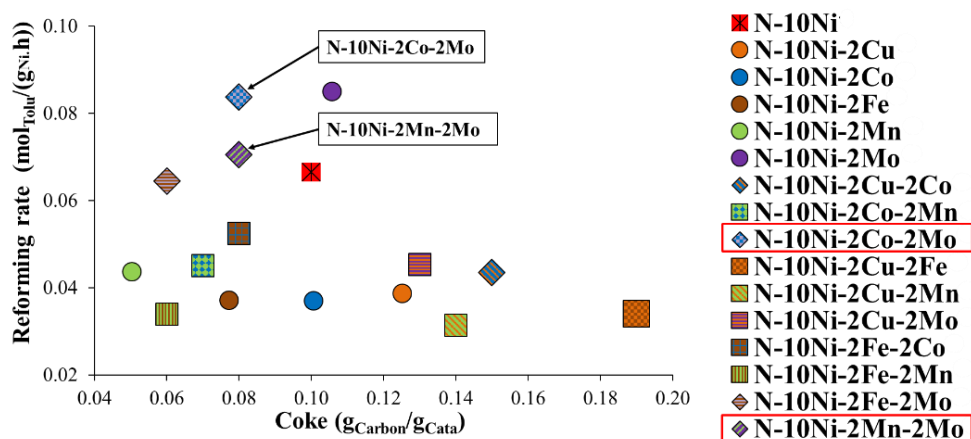


Figure VII.11: Toluene reforming rate as a function of carbon deposit for 10 wt. % Ni/ γ -Al₂O₃ catalysts doped twice with 2 wt. % of different metals.

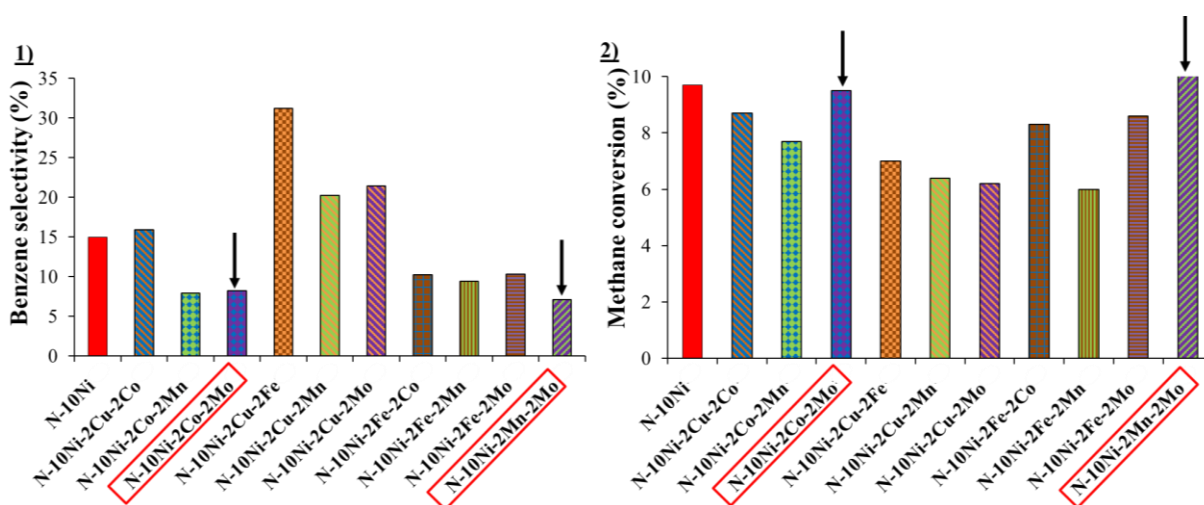


Figure VII.12: Benzene selectivity (left side) and methane conversion (right side) diagrams for 10 wt. % Ni/ γ -Al₂O₃ catalysts doped with 2 wt. % of two different metals.

It appeared that the samples *N-10Ni-2Co-2Mo* and *N-10Ni-2Mn-2Mo* showed the best catalytic performances. Hence, the properties and catalytic performances of these two best catalysts are presented in the following parts.

VII.3.3.1.2. Properties of samples doped with Co+Mo or Mn+Mo

It is shown in Table VII.8 that, for samples *N-10Ni-2Co-2Mo* and *N-10Ni-2Mn-2Mo*, the theoretical and actual compositions are similar.

Table VII.8: Theoretical and actual compositions of 10 wt. % Ni/ γ -Al₂O₃ catalysts doped twice with 2 wt. % of metals

Samples	Theoretical composition (wt. %)	Actual composition (wt. %)
N-10Ni-2Mn-2Mo	86.0 Al ₂ O ₃ / 10.0 Ni / 2.0 Mn / 2.0 Mo	85.3 Al ₂ O ₃ / 10.9 Ni / 1.7 Mn / 2.1 Mo
N-10Ni-2Co-2Mo	86.0 Al ₂ O ₃ / 10.0 Ni / 2.0 Co / 2.0 Mo	86.0 Al ₂ O ₃ / 10.2 Ni / 1.8 Co / 2.0 Mo

Figure VII.13 shows the TPR profiles and the post-TPR X-Ray spectra of samples *N-10Ni-2Co-2Mo* and *N-10Ni-2Mn-2Mo*. For a better comparison, the results of samples *N-10Ni*, *N-10Ni-2Mn*, *N-10Ni-2Mo* and *N-10Ni-2Co* were also added to the graphs. Table VII.9 shows

the metallic particles sizes and their compositions after TPR determined by TEM and XRD measurements.

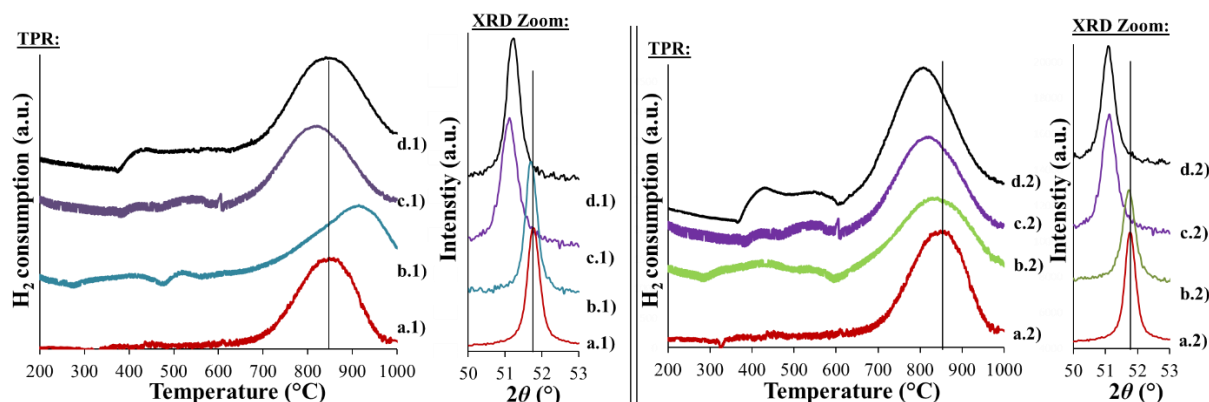


Figure VII.13: TPR profiles and post-TPR X-Ray spectra. Left side: a.1. *N-10Ni*, b.1. *N-10Ni-2Co*, c.1. *N-10Ni-2Mo*, d.1. *N-10Ni-2Co-2Mo*; Right side: a.2. *N-10Ni*, b.2. *N-10Ni-2Mn*, c.2. *N-10Ni-2Mo*, d.2. *N-10Ni-2Mn-2Mo*.

Table VII.9: Metallic particles sizes and X-Ray observations for nickel-alumina doped with two different metal dopants.

Samples	d_{TEM} (nm)	σ_{TEM} (nm)	d_{XRD} (nm)	Ni-Metal (2 0 0) ray (°)	Possible phases
N-10Ni	30	9	23	51.83	#
N-10Ni-2Mn-2Mo	25	5	21	51.11	Possibility of Ni _{0.9} Mo _{0.1} phase
N-10Ni-2Co-2Mo	41	9	25	51.30	Possibility of Ni _{0.91} Mo _{0.09} phase

d_{TEM} : metallic particles size median; σ_{TEM} : standard deviation; d_{XRD} : metallic crystallites size estimation obtained by XRD.

#: no value expected.

Sample *N-10Ni-2Co-2Mo* showed a broad H₂ consumption peak located between $T = 400$ °C and $T = 700$ °C attributed to the reduction of Co and Mo oxide species (Figure VII.13-d.1). Whereas the Ni reduction step of sample *N-10Ni-Co* was shifted towards higher temperatures ($\Delta T = + 100$ °C, Figure VII.13-b.1), and the reduction step of Ni of sample *N-10Ni-2Mo* was shifted towards lower temperatures ($\Delta T = - 50$ °C, Figure VII.13-c.1), for sample *N-10Ni-2Co-2Mo*, the reduction step of Ni was only slightly shifted towards lower temperatures ($\Delta T_{Ni} = - 15$ °C, Figure VII.13-d.1). This observation indicated that during their reduction step, the Ni oxide species were influenced by both Co and Mo. The analysis of the X-Ray spectrum after TPR suggests the presence of a Ni_{0.91}Mo_{0.01} phase, but no Ni-Co phase was visible (Table VII.9).

The reduction profile of sample *N-10Ni-2Mn-2Mo* (Figure VII.13-d.2) showed a simultaneous reduction of the MnO_x and MoO_x species, located respectively at $T = 425$ °C and $T = 550$ °C. It is to notice that sample *N-10Ni-2Mn-2Mo* showed a shift of the reduction step of nickel towards lower temperatures ($\Delta T = - 50$ °C) similar to the one observed for sample *N-10Ni-2Mo* (Figure VII.13-c.2). The analysis of the X-Ray spectrum after TPR suggests the presence of a Ni_{0.9}Mo_{0.1} alloy. The association of Mn and Mo apparently permitted to decrease the sintering of the metallic particles since sample *N-10Ni-2Mn-2Mo* showed low d_{XRD} and d_{TEM} values (21 and 25 nm) and σ_{TEM} value (5 nm) (Table VII.9).

VII.3.3.1.3. Catalytic performances of samples doped with Co+Mo or Mn+Mo

Figure VII.14 shows the toluene conversion, C_{Tolu} , as a function of time and the toluene reforming rate, r_{Tolu} , as a function of the amount of carbon deposit for samples *N-10Ni-2Co-2Mo*, *N-10Ni-2Mn-2Mo*, the simple doped catalysts (samples *N-10Ni-2Co*, *N-10Ni-2Mo* and *N-10Ni-2Mn*) and sample *N-10Ni*. Figure VII.15 shows the DSC curves after catalytic tests. The metallic particles sizes, the type of metallic phase present after test and the catalytic performances of the samples are presented in Table VII.10.

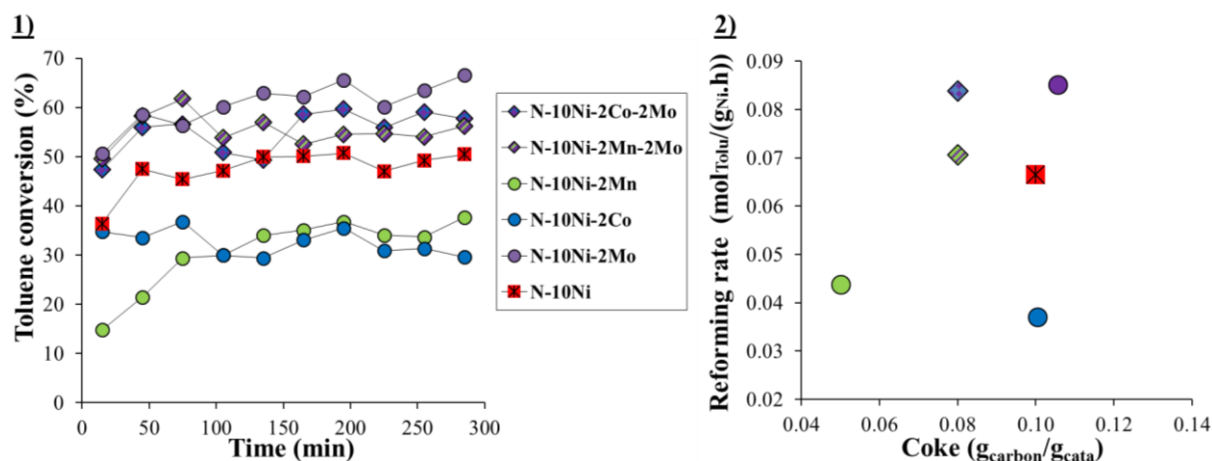


Figure VII.14: Toluene conversion as a function of time (left side) and toluene reforming rate as a function of carbon deposit amount (right side) for samples *N-10Ni-2Co-2Mo*, *N-10Ni-2Mn-2Mo*, *N-10Ni-2Mn*, *N-10Ni-2Mo*, *N-10Ni-2Co*, *N-10Ni*.

Table VII.10: Metallic particles sizes, metal alloy phases and catalytic performances for samples *N-10Ni*, *N-10Ni-2Mn-2Mo* and *N-10Ni-2Co-2Mo*. Test conditions: $T = 650$ °C, $t = 300$ min, 24.000 ppmv of toluene, $GHSV = 5000$ h⁻¹.

Samples	Particules sizes			Possible metal phases	Catalytic performances					
	d_{TEM} (nm)	σ_{TEM} (nm)	d_{XRD} (nm)		C_{Tolu} (%)	r_{Tolu} (mol _{Tolu} /(g _{Ni} .h))	S_B (%)	C_{CH4} (%)	Coke (g _{Carbon} /g _{Cata})	Fil. carbon
N-10Ni	11	3	12	Ni	51	$6.7 \cdot 10^{-2}$	15	10	0.10	No
N-10Ni-2Mn-2Mo	11	3	11	Ni _{0.97} Mo _{0.03}	54	$7.1 \cdot 10^{-2}$	7	10	0.08	No
N-10Ni-2Co-2Mo	12	4	11	Ni _{0.97} Mo _{0.03} Ni _{0.2} Co _{0.8}	58	$8.4 \cdot 10^{-2}$	8	9	0.08	+

d_{TEM} : metallic particles size median; σ_{TEM} : standard deviation; d_{XRD} : metallic crystallites size estimation obtained by XRD; C_{Tolu} : conversion of toluene; r_{Tolu} : reaction rate of toluene; S_B : selectivity in benzene; C_{CH4} : conversion of methane; Coke: carbon deposit amount after 5 h of test measured by TG-DSC.

The high r_{Tolu} value ($8.4 \cdot 10^{-2}$ mol_{Tolu}/(g_{Ni}.h)) observed for sample *N-10Ni-2Co-2Mo* compared to sample *N-10Ni-2Co*, and the presence of a Ni-Mo alloy after test (Table VII.10) indicated that the activity of this sample was mostly attributed to the addition of Mo. However, whereas samples *N-10Ni-2Co* and *N-10Ni-2Mo* presented high S_B values (13-17 %, Table VII.10), sample *N-10Ni-2Co-2Mo* did in contrary present a lower S_B value (8 %, Table VII.10). The observation of the post-test DSC curve of sample *N-10Ni-2Co-2Mo* in Figure VII.15-c also revealed a synergistic effect between Co and Mo. Indeed, whereas samples *N-10Ni-2Mo* and *N-10Ni-2Co* presented both amorphous and filamentous carbon deposits (Figures VII.5-b and VII.5-e), the carbon deposit of sample *N-10Ni-2Co-2Mo* was in contrary entirely constituted of amorphous type. Furthermore, it is to notice that for similar or even higher r_{Tolu} values, sample *N-10Ni-2Co-2Mo* presented lower amount of coke after test (0.08 g_{Carbon}/g_{Cata}, Table VII.10)

compared to samples *N-10Ni-2Co* and *N-10Ni-2Mo* (respectively 0.10 g_{Carbon}/g_{Cata} and 0.11 g_{Carbon}/g_{Cata}, Table VII.4).

In the case of sample *N-10Ni-2Mn-2Mo*, the high r_{Tolu} value ($7.4 \cdot 10^{-2}$ mol_{Tolu}/(g_{Ni}.h)) and the possible presence of a Ni-Mo alloy after test (Table VII.10) also indicated that the activity of the samples was mostly attributed to the addition of Mo. However, the combination of Mn and Mo permitted in this case to avoid the formation of filamentous carbon (Figure VII.15-b) and to decrease the formation of carbon for sample *N-10Ni-2Mn-2Mo* ($Coke = 0.08$ g_{Carbon}/g_{Cata}).

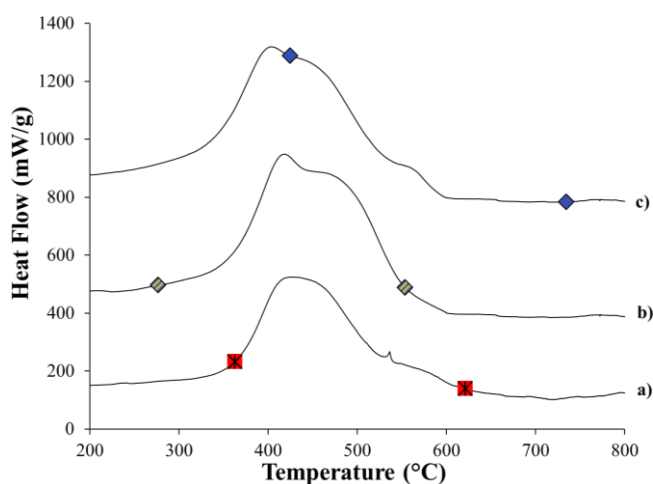


Figure VII.15: Post-test DSC curves for double metals doped catalysts; a. *N-10Ni*, b. *N-10Ni-2Mn-2Mo*, c. *N-10Ni-2Co-2Mo*.

VII.3.3.2. Catalysts doped with two oxides

VII.3.3.2.1. General trends

10 wt. % Ni/ γ -Al₂O₃ catalysts doped with 1.5 wt. % of one oxide and 1.5 wt. % of a second oxide (Oxide = Ce, Ca, Mg or K) were synthesized, characterized and tested for the reforming of 24.000 ppmv of toluene at $T = 650$ °C. Figure VII.16 gives an overview of the reforming rate of toluene, r_{Tolu} , as a function of the amount of carbon deposit after test for all samples. Figure VII.17 gives an overview of the benzene selectivity, S_B , and methane conversion, C_{CH_4} , for all catalysts.

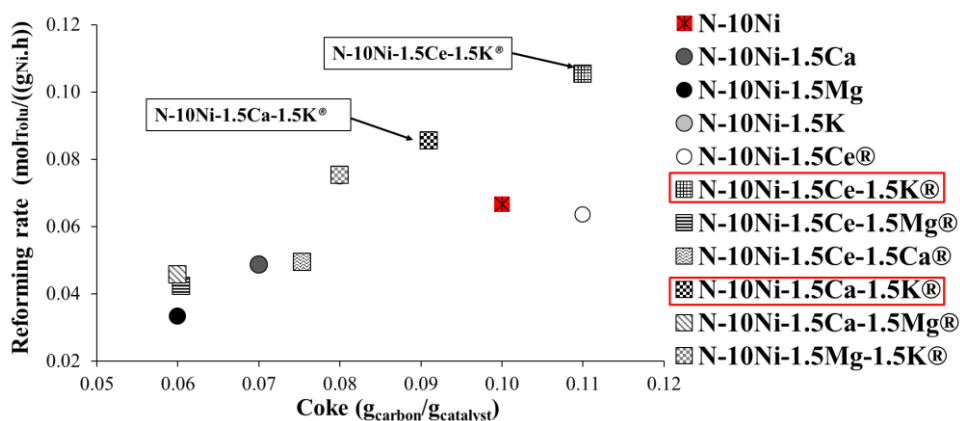


Figure VII.16: Toluene reforming rate as a function of carbon deposit for 10 wt. % Ni/ γ -Al₂O₃ catalysts doped twice with 1.5 wt. % of different oxides. *N.B.*: The mark of sample *N-10Ni-1.5Mg-1.5K* covers the mark of sample *N-10Ni-1.5K*.

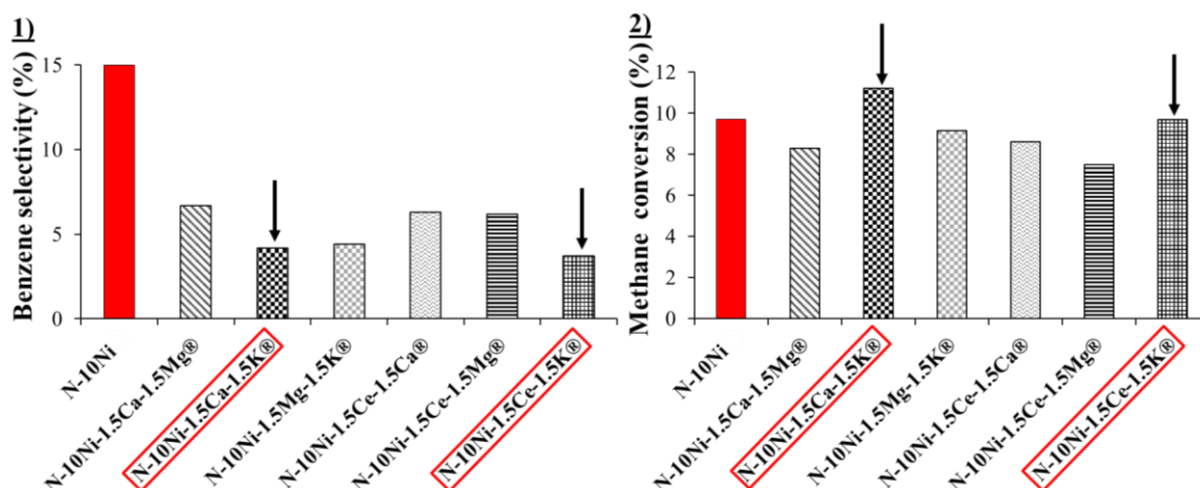


Figure VII.17: Benzene selectivity (left side) and methane conversion (right side) diagrams for 10 wt. % Ni/ γ -Al₂O₃ catalysts doped with 1.5 wt. % of two different oxides.

It appeared that the samples *N-10Ni-1.5Ca-1.5K*® and *N-10Ni-1.5Ce-1.5K*® showed the best catalytic performances. Hence, the properties and catalytic performances of these two best catalysts are presented in the following parts.

VII.3.3.2.2. Properties of samples doped with Ca+K or Ce+K

It is shown in Table VII.11 that, for samples *N-10Ni-1.5Ca-1.5K*® and *N-10Ni-1.5Ce-1.5K*®, the theoretical and actual compositions are similar.

Table VII.11: Theoretical and actual compositions of 10 wt. % Ni/ γ -Al₂O₃ catalysts doped twice with 1.5 wt. % of oxides.

Samples	Theoretical composition (wt. %)	Actual composition (wt. %)
<i>N-10Ni-1.5Ca-1.5K</i> ®	87.0 Al ₂ O ₃ / 10.0 Ni / 1.5 Ca / 1.5 K	85.8 Al ₂ O ₃ / 11.0 Ni / 1.5 Ca / 1.7 K
<i>N-10Ni-1.5Ce-1.5K</i> ®	87.0 Al ₂ O ₃ / 10.0 Ni / 1.5 Ce / 1.5 K	85.5 Al ₂ O ₃ / 11.1 Ni / 1.7 Ce / 1.7 K

Figure VII.18 shows the TPR profiles of samples *N-10Ni-1.5Ca-1.5K*® and *N-10Ni-1.5Ce-1.5K*®. For a better comparison, the curves of samples *N-10Ni-1.5Ca*, *N-10Ni-1.5K*, *N-10Ni-1.5Ce*® and *N-10Ni* were added.

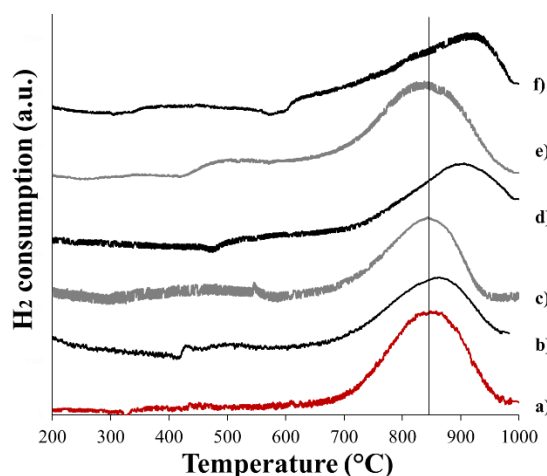


Figure VII.18: TPR profiles of samples doped with 1.5 wt. % of oxide or with two oxides; a. *N-10Ni*, b. *N-10Ni-1.5Ca*, c. *N-10Ni-1.5K*, d. *N-10Ni-1.5Ce*®, e. *N-10Ni-1.5Ca-1.5K*®, f. *N-10Ni-1.5Ce-1.5K*®.

Similarly as for samples *N-10Ni-1.5Ca* and *N-10Ni-1.5K*, sample *N-10Ni-1.5Ca-1.5K*[®] showed a small and broad peak located between $T = 450$ °C and $T = 625$ °C (Figure VII.18-e), attributed to the presence of Ca and K which reduce the interactions between Ni and γ - Al_2O_3 .^{[326], [327]} In that case also, sample *N-10Ni-1.5Ca-1.5K*[®] did not show a shift of the Ni reduction peak.

In the case of sample *N-10Ni-1.5Ce-1.5K*[®], similarly as for sample *N-10Ni-1.5K*, a peak of very small intensity was also observed between $T = 400$ °C and $T = 600$ °C (Figure VII.18-f). Furthermore, the peak of Ni reduction at $T = 850$ °C was broadened and shifted towards higher temperatures, which highlighted the presence of strong Ni-CeO_x interactions.

It was observed in Table VII.12 that samples *N-10Ni-1.5Ca-1.5K*[®] and *N-10Ni-1.5Ce-1.5K*[®] presented similar particles sizes compared to the sizes obtained for samples doped only with one oxide (Table VII.5).

Table VII.12: Ni particles sizes for nickel/alumina samples doped with two different oxides.

Samples	d_{TEM} (nm)	σ_{TEM} (nm)	d_{XRD} (nm)
N-10Ni	30	9	23
N-10Ni-1.5Ca-1.5K [®]	33	11	27
N-10Ni-1.5Ce-1.5K [®]	33	10	25

d_{TEM} : metallic particles size median; σ_{TEM} : standard deviation; d_{XRD} : metallic crystallites size estimation obtained by XRD.

VII.3.3.2.3. Catalytic performances of samples doped with Ca+K or Ce+K

Figure VII.19 shows the toluene conversion, C_{Tolu} , as a function of time and the toluene reforming rate, r_{Tolu} , as a function of the amount of carbon deposit for samples *N-10Ni-1.5Ca-1.5K*[®], *N-10Ni-1.5Ce-1.5K*[®], the simple doped catalysts (samples *N-10Ni-1.5Ce*, *N-10Ni-1.5Ca* and *N-10Ni-1.5K*) and sample *N-10Ni*. Figure VII.20 shows the DSC curves after catalytic tests. The Ni⁽⁰⁾ particles sizes and the catalytic performances of the samples are shown in Table VII.13.

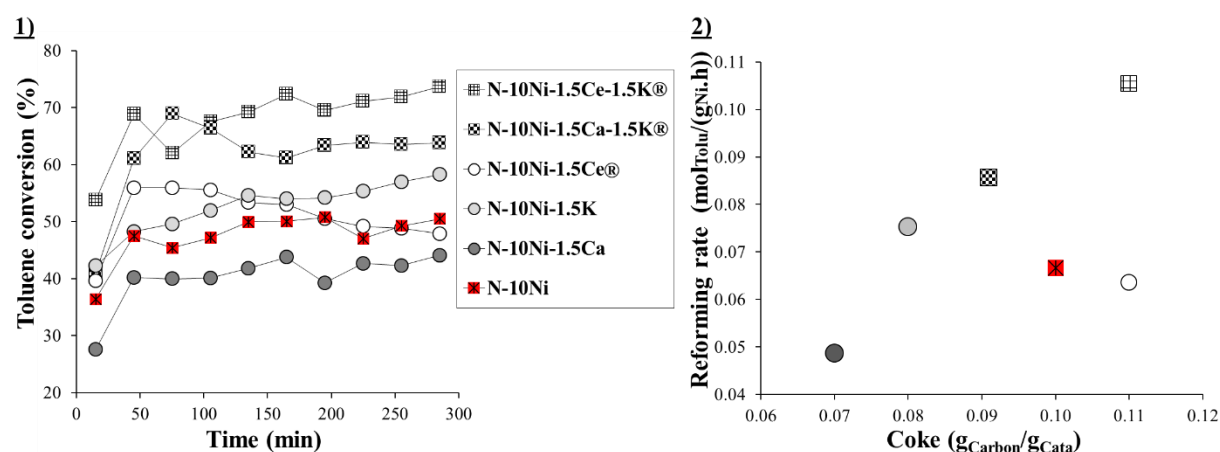
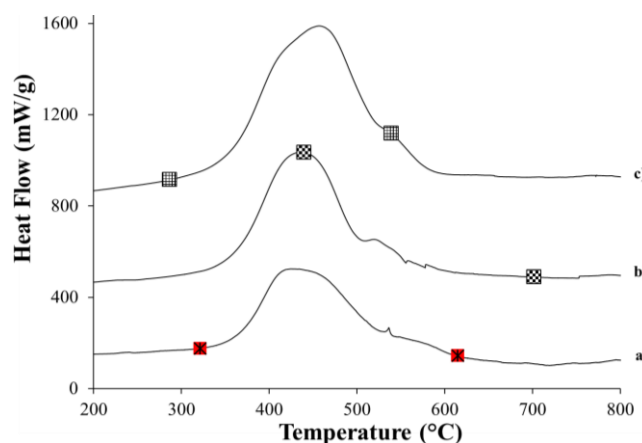


Figure VII.19: Toluene conversion as a function of time (left side) and toluene reforming rate as a function of carbon deposit amount (right side) for samples *N-10Ni-1.5Ca-1.5K*[®], *N-10Ni-1.5Ce-1.5K*[®], *N-10Ni-1.5Ca*, *N-10Ni-1.5K*, *N-10Ni-1.5Ce*[®], *N-10Ni*.

Table VII.13: Ni particles sizes and catalytic performances of nickel/alumina samples doped with two different oxides. Test conditions: $T = 650\text{ }^{\circ}\text{C}$, $t = 300\text{ min}$, 24,000 ppmv of toluene, $GHSV = 5000\text{ h}^{-1}$.

Samples	Ni particles sizes			Catalytic performances					
	d_{TEM} (nm)	σ_{TEM} (nm)	d_{XRD} (nm)	C_{Tolu} (%)	r_{Tolu} (mol _{Tolu} /(g _{Ni} .h))	C_{CH4} (%)	S_B (%)	$Coke$ (g _{Carbon} /g _{Cata})	Fil. carbon
N-10Ni	11	3	12	51	$6.7 \cdot 10^{-2}$	10	15	0.10	No
N-10Ni-1.5Ca-1.5K [®]	10	9	12	61	$8.6 \cdot 10^{-2}$	11	4	0.09	No
N-10Ni-1.5Ce-1.5K [®]	9	3	11	70	$1.1 \cdot 10^{-1}$	10	4	0.11	No

d_{TEM} : metallic particles size median; σ_{TEM} : standard deviation; d_{XRD} : metallic crystallites size estimation obtained by XRD; C_{Tolu} : conversion of toluene; r_{Tolu} : reaction rate of toluene; S_B : selectivity in benzene, C_{CH4} : conversion of methane; $Coke$: carbon deposit amount after 5 h of test measured by TG-DSC.

Figure VII.20: Post-test DSC curves for double oxides doped catalysts; a. *N-10Ni*, b. *N-10Ni-1.5Ca-1.5K[®]*, c. *N-10Ni-1.5Ce-1.5K[®]*.

In Figure VII.19 and Table VII.13, sample *N-10Ni-1.5Ca-1.5K[®]* evidenced that under these conditions of test, the combination of Ca and K led to a catalyst with a slightly higher amount of carbon deposit ($Coke = 0.09\text{ g}_{Carbon}/\text{g}_{Cata}$), but which showed a better r_{Tolu} value ($8.6 \cdot 10^{-2}\text{ mol}_{Tolu}/(\text{g}_{Ni} \cdot \text{h})$) compared to the samples *N-10Ni-1.5Ca* and *N-10Ni-1.5K*. A synergistic influence between Ca and K could increase the adsorption-dissociation of H_2O and CO_2 molecules.^{[111], [145]} Furthermore, the better catalytic activity observed for sample *N-10Ni-1.5Ca-1.5K[®]* could also be attributed to the increase of reducibility of the nickel oxide caused by the presence of alkali (see TPR, Figure VII.18-e). Finally, it is to notice that similarly as for samples *N-10Ni-1.5Ca* and *N-10Ni-1.5K*, the carbon deposit of sample *N-10Ni-1.5Ca-1.5K[®]* was only constituted of amorphous carbon.

Though the association of Ce and K did not show the anti-coking effect expected, sample *N-10Ni-1.5Ce-1.5K[®]* showed a higher catalytic activity compared to samples *N-10Ni-1.5Ce* or *N-10Ni-1.5K*. Indeed, it can be seen in Figure VII.19 and Table VII.13 that sample *N-10Ni-1.5Ce-1.5K[®]* showed the highest r_{Tolu} value of all the samples of this chapter ($1.1 \cdot 10^{-1}\text{ mol}_{Tolu}/(\text{g}_{Ni} \cdot \text{h})$) for an acceptable amount of carbon deposit ($Coke = 0.11\text{ g}_{Carbon}/\text{g}_{Cata}$).

VII.3.4. Influences of dopant loadings

In view of the results obtained in the upper parts of this chapter, it was decided to study 10 wt. % Ni/ $\gamma\text{-Al}_2\text{O}_3$ catalysts doped with a higher loading (4 wt. %) of Mn or Mo as metals, or with a higher loading (3 wt. %) of Ca or K. Table VII.14 shows the theoretical and actual compositions of these samples.

Table VII.14: Theoretical and actual compositions of 10 wt. % Ni/ γ -Al₂O₃ catalysts doped with 4 wt. % of metals or doped twice with 3 wt. % of oxide dopant.

Samples	Theoretical composition (wt. %)	Actual composition (wt. %)
Metal dopant : 4 wt. %		
N-10Ni-4Mo	86.0 Al ₂ O ₃ / 10.0 Ni / 4.0 Mo	86.5 Al ₂ O ₃ / 9.4 Ni / 4.1 Mo
N-10Ni-4Mn	86.0 Al ₂ O ₃ / 10.0 Ni / 4.0 Mn	86.2 Al ₂ O ₃ / 10.1 Ni / 3.7 Mn
Oxide dopant: 3 wt. %		
N-10Ni-3Ca	87.0 Al ₂ O ₃ / 10.0 Ni / 3.0 Ca	86.8 Al ₂ O ₃ / 10.0 Ni / 3.2 Ca
N-10Ni-3K	87.0 Al ₂ O ₃ / 10.0 Ni / 3.0 K	85.7 Al ₂ O ₃ / 10.9 Ni / 3.4 K

VII.3.4.1. Catalysts doped with Mn or Mo

VII.3.4.1.1. Properties of 10 wt. % Ni/ γ -Al₂O₃ catalysts doped with 4 wt. % of Mn or Mo

Figure VII.21 shows the influence of Mo and Mn loadings (0, 2 or 4 wt. %) on the reduction of 10 wt. % Ni/ γ -Al₂O₃ catalysts. The metallic particles sizes and compositions after TPR measurements determined by XRD and TEM analyses are presented in Table VII.15.

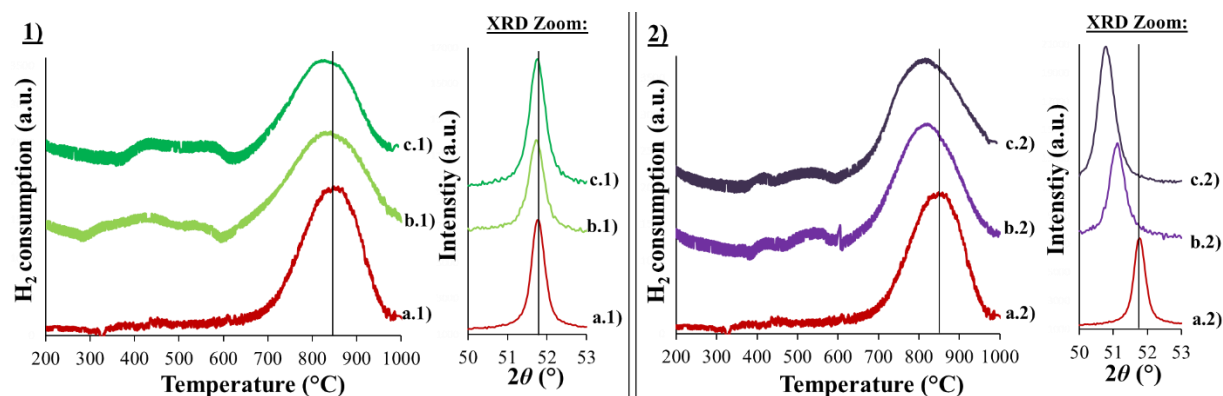


Figure VII.21: TPR measurements and XRD zoom ($50^\circ < 2\theta < 53^\circ$) for 10 wt. % Ni/ γ -Al₂O₃ catalysts doped with different amounts of manganese or molybdenum. On the left side: a. *N-10Ni*; b. *N-10Ni-2Mn*; c. *N-10Ni-4Mn*. On the right side: a. *N-10Ni*; b. *N-10Ni-2Mo*; c. *N-10Ni-4Mo*.

Table VII.15: Metallic particles sizes and X-Ray observations after TPR measurements for 10 wt. % Ni/ γ -Al₂O₃ catalysts doped with different amounts of Mn or Mo.

Samples	Particles sizes			Ni-Metal (2 0 0) ray (°)	Reference (2 0 0) ray of pure doping metal (°)	Possible phases
	d_{TEM} (nm)	σ_{TEM} (nm)	d_{XRD} (nm)			
N-10Ni	30	9	23	51.83	Ni = 51.83	
N-10Ni-2Mo	29	7	20	51.11	Mo = 44.95	Possibility of Ni _{0.90} Mo _{0.10} alloy / No rays of molybdenum oxide or Mo ⁽⁰⁾ visible
N-10Ni-4Mo	22	7	17	50.73	Mo = 44.95	Possibility of Ni _{0.83} Mo _{0.17} alloy / No rays of molybdenum oxide or Mo ⁽⁰⁾ visible
N-10Ni-2Mn	27	8	23	51.80	Mn = 52.38	No rays of manganese oxide visible
N-10Ni-4Mn	26	8	21	51.80	Mn = 52.38	No rays of manganese oxide visible

d_{TEM} : metallic particles size median; σ_{TEM} : standard deviation; d_{XRD} : metallic crystallites size estimation obtained by XRD.

It was observed in Figures VII.21-b.1 and VII.21-c.1 that the increase of Mn content from 2 wt. % to 4 wt. % did not have strong consequence on the reduction of the sample. Furthermore, similarly as for sample *N-10Ni-2Mn*, the X-Ray spectrum after TPR measurement did not

permit to confirm the formation of any Ni-Mn alloy or to reveal the presence of MnAl_2O_x phases for sample *N-10Ni-4Mn*.

The increase of the loading of Mo up to 4 wt. % led to a catalyst with a similar reducibility as sample *N-10Ni-2Mo* (Figures VII.21-b.2 and VII.21-c.2), but which presented a Ni-Mo alloy richer in molybdenum ($\text{Ni}_{0.83}\text{Mo}_{0.17}$) and with smaller metallic nanoparticles after TPR measurement ($d_{\text{TEM}} = 22$ nm, $\sigma_{\text{TEM}} = 7$ nm and $d_{\text{XRD}} = 17$ nm). This observation was in accordance with the literature and confirmed the fact that MoO_x species served as a barrier for preventing the growth of $\text{Ni}^{(0)}$ particles.^{[171], [172]}

VII.3.4.1.2. Catalytic performances of 10 wt. % Ni/ γ - Al_2O_3 catalysts doped with 4 wt. % of Mn or Mo

Figures VII.22 shows the toluene conversion, C_{Tolu} , as a function of time and the toluene reforming rate, r_{Tolu} , as a function of the carbon deposit for the samples prepared with different loadings of Mo or Mn. Figures VII.23 shows the DSC curves performed on samples after catalytic test. The metallic particles sizes and compositions after test determined by TEM and XRD measurements as well as the catalytic performances are listed in Table VII.16.

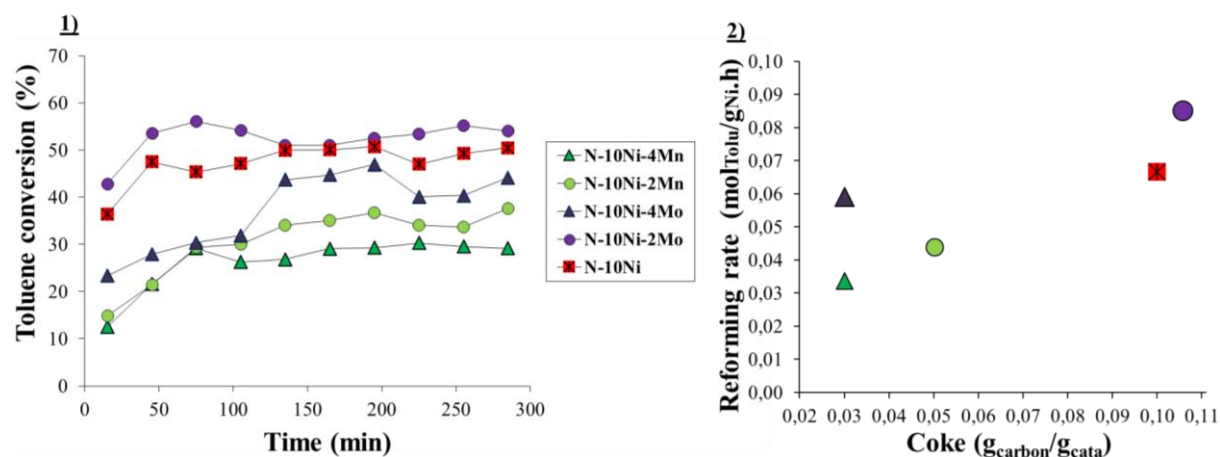


Figure VII.22: Toluene conversion as a function of time (left side) and toluene reforming rate as a function of carbon deposit (right side) for 10 wt. % Ni/ γ - Al_2O_3 catalysts doped with different loadings of Mn or Mo.

It was observed that the increase of the loading of Mo up to 4 wt. % decreased the catalytic activity. Indeed, sample *N-10Ni-4Mo* presented a lower r_{Tolu} value ($5.9 \cdot 10^{-2}$ mol_{Tolu}/(g_{Ni}.h)), a higher S_B value (21 %) and a lower C_{CH_4} value (5 %) compared to sample *N-10Ni-2Mo* (Table VII.16). This was attributed to a large covering of the surface of the $\text{Ni}^{(0)}$ particles by MoO_x species, which in high amounts are known to block the sites necessary for the reforming reactions.^{[172], [173]} Furthermore, it was observed in Figure VII.22 that the progressive activation of the catalyst took more time and that no steady conversion value was reached at $t = 300$ min. Since the TPR of the sample did not evidence a delay of the Ni reduction, it was also assumed that the high covering of the Ni particles by MoO_x species made the reduction more difficult, as it was observed in previous works.^{[171], [172]} Nevertheless, in accordance with the literature, this high covering was highly efficient to protect sample *N-10Ni-4Mo* from coking ($\text{Coke} = 0.03$ g_{Carbon}/g_{Cata}) and from the formation of filamentous carbon (Figure VII.23-e).

Table VII.16: Metallic particles sizes, metal alloy phases and catalytic performances of 10 wt. % Ni/ γ -Al₂O₃ catalysts doped with different loadings of Mn or Mo. Test conditions: $T = 650$ °C, $t = 300$ min, 24.000 ppmv of toluene, $GHSV = 5000$ h⁻¹.

Samples	Particules sizes			Possible metal phase	Catalytic performances					
	d_{TEM} (nm)	σ_{TEM} (nm)	d_{XRD} (nm)		C_{Tolu} (%)	r_{tolu} (mol _{tolu} /(gNi·h))	C_{CH4} (%)	S_B (%)	Coke (g _{Carbon} /g _{Cata})	Fil. carbon
N-10Ni	11	3	12	Ni	51	$6.7 \cdot 10^{-2}$	10	15	0.10	No
N-10Ni-2Mo	12	6	11	Ni _{0.97} Mo _{0.03}	54	$8.5 \cdot 10^{-2}$	7	13	0.11	No
N-10Ni-4Mo	13	7	14	Ni _{0.97} Mo _{0.03}	43	$5.9 \cdot 10^{-2}$	5	21	0.03	No
N-10Ni-2Mn	10	2	14	Ni	35	$4.4 \cdot 10^{-2}$	2	9	0.05	No
N-10Ni-4Mn	12	4	15	Ni	29	$3.4 \cdot 10^{-2}$	5	9	0.03	No

d_{TEM} : metallic particles size median; σ_{TEM} : standard deviation; d_{XRD} : metallic crystallites size estimation obtained by XRD; C_{Tolu} : conversion of toluene; r_{tolu} : reaction rate of toluene; S_B : selectivity in benzene; C_{CH4} : conversion of methane; Coke: carbon deposit amount after 5 h of test measured by TG-DSC.

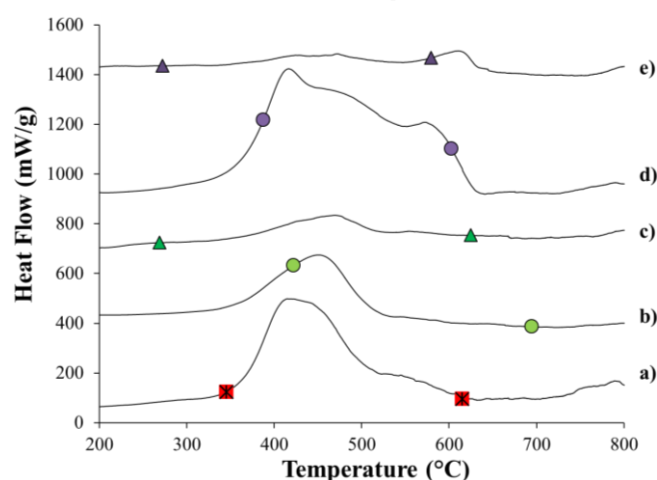


Figure VII.23: Post-test DSC curves for Ni/ γ -Al₂O₃ catalysts doped with different loadings of Mn or Mo; a. *N-10Ni*, b. *N-10Ni-2Mn*, c. *N-10Ni-4Mn*, d. *N-10Ni-2Mo*, e. *N-10Ni-4Mo*.

The catalytic performance of the 10 wt. % Ni/ γ -Al₂O₃ catalyst doped with a higher loading of Mn (sample *N-10Ni-4Mn*) was affected in a similar way as for the Mo doping. This was also assumed to be caused by a large covering of the Ni⁽⁰⁾ particles by MnO_x species.^{[143], [176], [316], [324]} Indeed, it can be observed in Table VII.16 that sample *N-10Ni-4Mn* also presented a lower r_{Tolu} value and difficulties to be activated during the catalytic test. Furthermore, sample *N-10Ni-4Mn* also presented a remarkably low amount of carbon deposit after test (0.03 g_{Carbon}/g_{Cata}), which was only constituted of amorphous carbon (Figure VII.23-c).

Hence, it appeared that despite their low catalytic activity, the samples doped with 4 wt. % of either Mo or Mn might be appropriated for long term-tests at $T = 650$ °C thanks to their remarkable anti-coking performances.

VII.3.4.2. Catalyst doped with Ca or K

VII.3.4.2.1. Properties of 10 wt. % Ni/ γ -Al₂O₃ catalysts doped with 3 wt. % of Ca or K

Figure VII.24 shows the TPR profiles of the samples doped with different loadings of Ca or K. The metallic nickel particles sizes after TPR measurements determined by TEM and XRD analyses are presented in Table VII.17.

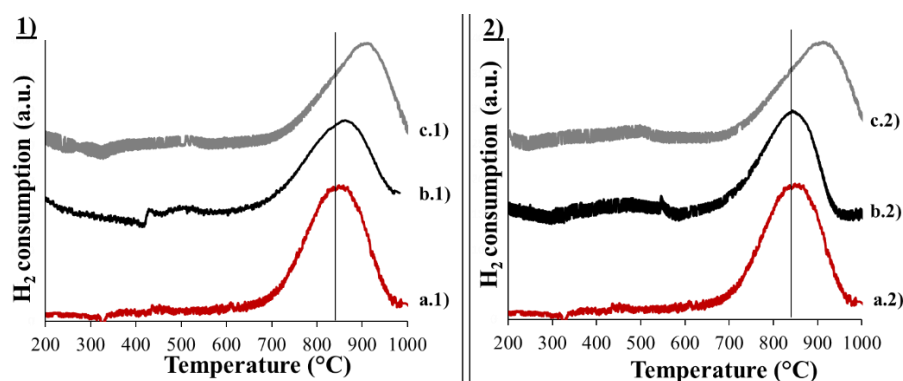


Figure VII.24: TPR profiles for 10 wt. % Ni/ γ -Al₂O₃ catalysts doped with different loadings of Ca or K. On the left side: a.1. *N-10Ni*; b.1. *N-10Ni-1.5Ca*; c.1. *N-10Ni-3Ca*; On the right side: a.2. *N-10Ni*; b.2. *N-10Ni-1.5K*; c.2. *N-10Ni-3K*.

Table VII.17: Ni particles sizes for 10 wt. % Ni/ γ -Al₂O₃ catalysts doped with different loadings of Ca or K.

Samples	d_{TEM} (nm)	σ_{TEM} (nm)	d_{XRD} (nm)
N-10Ni	30	9	23
N-10Ni-1.5Ca	36	10	26
N-10Ni-3Ca	35	11	26
N-10Ni-1.5K	38	11	27
N-10Ni-3K	37	10	27

d_{TEM} : metallic particles size median; σ_{TEM} : standard deviation; d_{XRD} : metallic crystallites size estimation obtained by XRD.

Similarly to sample *N-10Ni-1.5Ca*, sample *N-10Ni-3Ca* showed a small peak of H₂ consumption located at about $T = 500$ °C (Figure VII.24-c.1). However, the higher doping of Ca shifted the main peak of Ni reduction towards a higher temperature ($\Delta T = + 60$ °C). Indeed, when added in important amounts, CaO can cover the NiO particles and therefore decrease their reducibility.^[139] It is also to notice that after TPR measurements, sample *N-10Ni-3Ca* presented similar metallic Ni particles sizes as sample *N-10Ni-1.5Ca* (Table VII.17).

The TPR profile of sample *N-10Ni-3K* also presented a small H₂ consumption peak located about $T = 500$ °C. Similarly to sample doped with Ca, the addition of 3 wt. % of K also led to a shift of the Ni reduction peak towards a higher temperature ($\Delta T = + 65$ °C) (Figure VII.24-c.2), probably for the same reason explained for sample *N-10Ni-3Ca*. It is also to notice that sample *N-10Ni-3K* presented relatively similar metallic Ni particles sizes as sample *N-10Ni-3Ca* after TPR measurement (Table VII.17).

VII.3.4.2.2. Catalytic performances of 10 wt. % Ni/ γ -Al₂O₃ catalysts doped with 3 wt. % of Ca or K

Figure VII.25 shows the toluene conversion, C_{Tolu} , as a function of the time and the toluene reforming rate, r_{Tolu} , as a function of the carbon deposit for the samples prepared with different loadings of Ca or K. Figure VII.26 shows the DSC curves performed on samples after catalytic tests. The metallic Ni particles sizes after test determined by TEM and XRD measurements, as well as the catalytic performances are listed in Table VII.18.

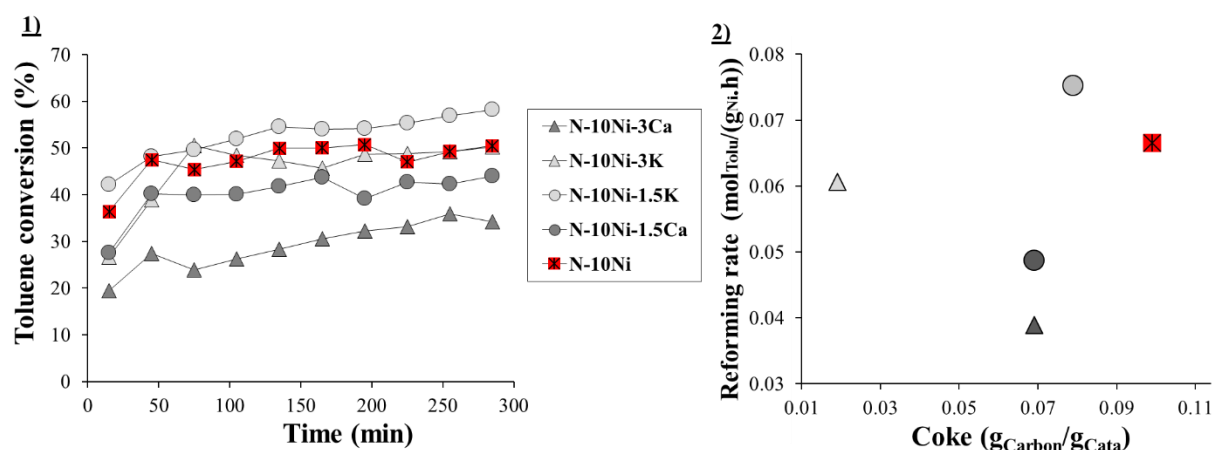


Figure VII.25: Toluene conversion as a function of time (left side) and toluene reforming rate as a function of carbon deposit amount (right side) for 10 wt. % Ni/ γ -Al₂O₃ catalysts doped with different loadings of Ca or K.

Table VII.18: Ni particles sizes and catalytic performances for 10 wt. % Ni/ γ -Al₂O₃ catalysts doped with different loadings of Ca or K. Test conditions: $T = 650$ °C, $t = 300$ min, 24.000 ppmv of toluene, $GHSV = 5000$ h⁻¹.

Samples	Particules sizes			Catalytic performances					
	d_{TEM} (nm)	σ_{TEM} (nm)	d_{XRD} (nm)	C_{Tolu} (%)	r_{Tolu} (molTolu/(gNi.h))	C_{CH4} (%)	S_B (%)	Coke (gCarbon/gCata)	Fil. carbon
N-10Ni	11	3	12	51	$6.7 \cdot 10^{-2}$	10	15	0.10	No
N-10Ni-1.5Ca	11	5	10	42	$4.9 \cdot 10^{-2}$	9	6	0.07	No
N-10Ni-3Ca	15	17	19	33	$3.9 \cdot 10^{-2}$	3	7	0.07	+
N-10Ni-1.5K	12	4	12	55	$7.5 \cdot 10^{-2}$	9	5	0.08	No
N-10Ni-3K	14	13	17	48	$6.1 \cdot 10^{-2}$	7	6	0.02	No

d_{TEM} : metallic particles size median; σ_{TEM} : standard deviation; d_{XRD} : metallic crystallites size estimation obtained by XRD; C_{Tolu} : conversion of toluene; r_{Tolu} : reaction rate of toluene; S_B : selectivity in benzene; C_{CH4} : conversion of methane; Coke: carbon deposit amount after 5 h of test measured by TG-DSC.

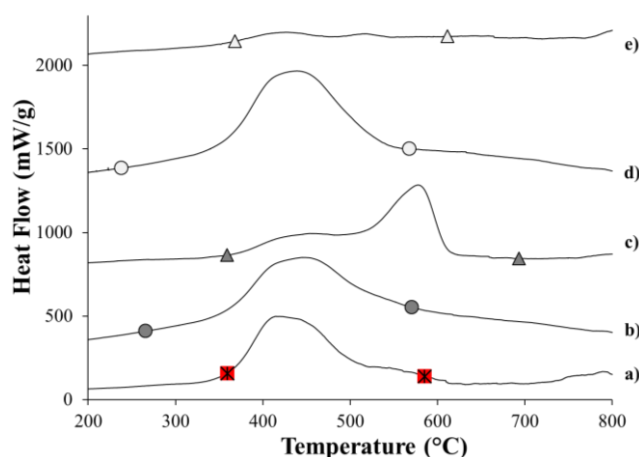


Figure VII.26: Post-test DSC curves for 10 wt. % Ni/ γ -Al₂O₃ catalysts doped with different loadings of Ca or K; a. *N-10Ni*, b. *N-10Ni-1.5Ca*, c. *N-10Ni-3Ca*, d. *N-10Ni-1.5K*, e. *N-10Ni-3K*.

Sample *N-10Ni-3Ca* presented a lower r_{Tolu} value ($3.9 \cdot 10^{-2}$ molTolu/(gNi.h)) and a lower C_{CH4} value (3 %) compared to sample *N-10Ni-1.5Ca* (Table VII.18). These lower catalytic activity values were attributed to the lower reducibility of sample *N-10Ni-3Ca* (see TPR, Figure VII.24-c.1) and probably also to the blockage of Ni⁽⁰⁾ active sites by the large amount of CaO. Despite a lower catalytic activity, sample *N-10Ni-3Ca* presented the same amount of carbon deposit as sample *N-10Ni-1.5Ca* (0.07 gCarbon/gCata). Furthermore, whereas sample *N-10Ni-1.5Ca* presented carbon deposit only constituted of amorphous carbon, the increase of the loading of Ca up to 3 wt. % led to the formation of filamentous carbon (Figure VII.26-c). In this way, whereas after TPR measurements, samples *N-10Ni-1.5Ca* and *N-10Ni-3Ca* presented

similar Ni particles sizes (Table VII.17), after catalytic test, sample *N-10Ni-3Ca* presented in contrary larger Ni particles ($d_{XRD} = 19$ nm and $d_{TEM} = 15$ nm) with a broad size distribution ($\sigma_{TEM} = 17$ nm) (Table VII.18). This presence of larger Ni particles could explain the growth of filamentous carbon.¹ Indeed, it has been shown in previous studies that the alkali can increase the sintering rate of Ni particles.^{[65], [106], [343]} It was suggested that the higher loading of doping, and the formation of more mobile $\text{Ca}(\text{OH})_2$ and CaCO_3 ^[344] species during the catalytic test favored the sintering of the Ni particles. This would explain why sample *N-10Ni-3Ca* showed different properties compared to sample *N-10Ni-1.5Ca*.

Sample *N-10Ni-3K* also presented lower r_{Tolu} and C_{CH_4} values. The reason was once more attributed to a large covering of the $\text{Ni}^{(0)}$ particles by potassium oxide.^{[338], [340], [345]} However, in this case, the catalytic activity was only slightly decreased by a few percent, whereas in previous studies concerning methane reforming, the catalytic activity was strongly decreased because of the presence of K.^[346] It was assumed that the high covering of the metallic Ni particle by K_2O permitted in contrary to efficiently prevent the catalyst from the formation of carbon deposit ($Coke = 0.02$ g_{Carbon}/g_{Cata}). It was also noticed that, as for sample *N-10Ni-3Ca*, sample *N-10Ni-3K* was more sensible towards sintering during the catalytic test ($d_{XRD} = 17$ nm, $d_{TEM} = 13$ nm and $\sigma_{TEM} = 14$ nm) (Table VII.18), due to a higher loading of K. However, it seemed that the high anti-coking ability of K permitted to counter this drawback since no filamentous carbon was observed after the test for sample *N-10Ni-3K* (Figure VII.26-e).

Hence, catalysts with a higher loading of alkali (Ca or K) presented lower catalytic activity, but had metallic nickel particles more inclined to sinter. However, the good anti-coking performance of K_2O countered the drawbacks caused by the presence of larger Ni particles and allowed keeping a sample almost free of carbon after $t = 5$ h of catalytic test at $T = 650$ °C.

VII.3.5. Catalytic performances of the most promising catalysts at different temperatures

In order to get more information on the performances of the most promising catalysts at different temperatures, catalytic tests were performed at different temperatures $T = 900 \rightarrow 600$ °C, with a toluene concentration of 24.000 ppmv. Since the tests were performed at $T = 900 \rightarrow 600$ °C, several phenomena (reduction of the metals, sintering, alumina phase transformation, formation of metallic alloy, and higher sensibility against coking for $T < 650$ °C) were expected to occur.

VII.3.5.1. Evolution of the performances of the best Ni/ γ - Al_2O_3 catalysts promoted with metal dopants

Taking into account the catalytic activity for toluene reforming and the resistance against coking, it appeared from the results obtained in the previous parts of this chapter that samples *N-10Ni-2Co-2Mo*, *N-10Ni-2Mn-2Mo* and *N-10Ni-4Mo* were the most adequate for the

¹: See influences between filamentous carbon and metallic particles sizes in part I.4.4.4. of Chapter I.

reforming of 24.000 ppmv of toluene at $T = 650\text{ }^{\circ}\text{C}$. Therefore, these samples were tested at $T = 900 \rightarrow 600\text{ }^{\circ}\text{C}$. In order to get a better understanding of the influence of each element, the following simple doped catalysts were also studied: samples $N-10Ni-2Co$, $N-10Ni-2Mn$ and $N-10Ni-2Mo$. Figures VII.27 and VII.28 respectively show the toluene and the methane conversions, C_{Tolu} and C_{CH_4} , as a function of the temperature. Figure VII.29 presents the post-test DSC curves. Catalytic activity values (C_{Tolu} , S_B , C_{CH_4} , E_a , k_0) and additional post-test characterizations (carbon deposit amount, presence of filamentous carbon, size of metallic particles) are presented in Table VII.19.

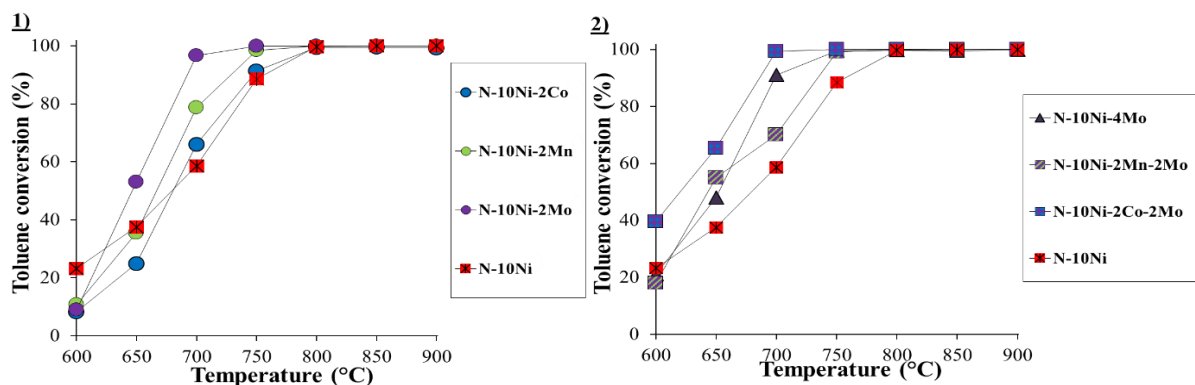


Figure VII.27: Toluene conversion as a function of temperature for the most promising Ni/ γ -Al₂O₃ catalysts doped with metals.

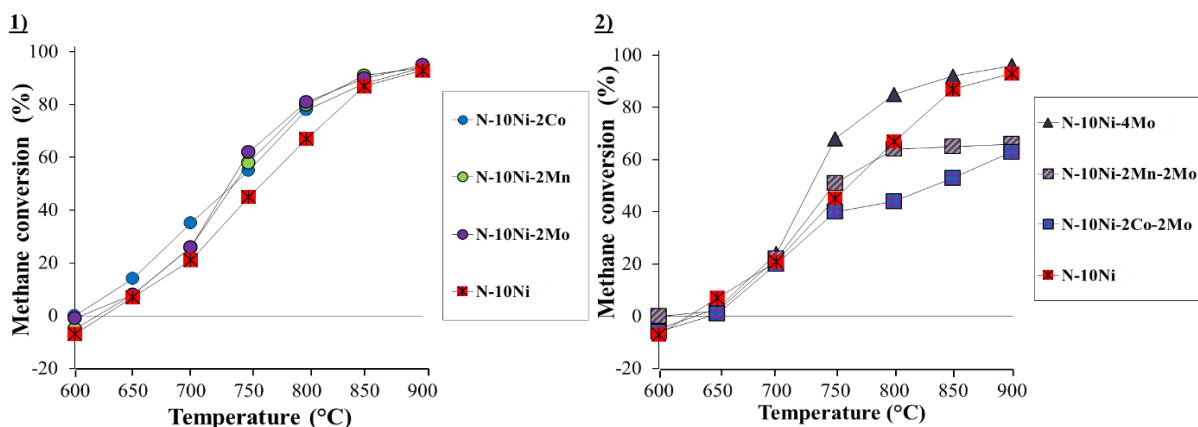


Figure VII.28: Methane conversion as a function of temperature for the most promising Ni/ γ -Al₂O₃ catalysts doped with metals.

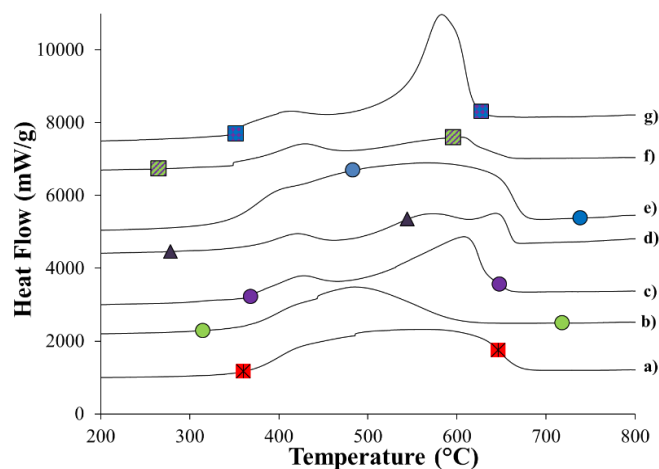


Figure VII.29: DSC curves performed on samples tested at $T = 900 \rightarrow 600\text{ }^{\circ}\text{C}$ for the most promising Ni/ γ -Al₂O₃ catalysts doped with metals; a. $N-10Ni$, b. $N-10Ni-2Mn$, c. $N-10Ni-2Mo$, d. $N-10Ni-4Mo$, e. $N-10Ni-2Co$, f. $N-10Ni-2Mn-2Mo$, g. $N-10Ni-2Co-2Mo$.

Table VII.19: Catalytic activity as a function of the temperature and post-test characterizations for the most promising Ni/ γ -Al₂O₃ catalysts doped with metals. Toluene concentration: 24.000 ppmv, $T = 900 \rightarrow 600$ °C, $GHSV = 5000 \text{ h}^{-1}$.

Samples	Catalytic activity								Post-test characterizations		
	T (°C)	600	650	700	750	800	850	900			
N-10Ni	C_{Tolu} (%)	23	38	59	88	99	100	100	$Coke = 0.36 \text{ g}_{Carbon}/\text{g}_{Cata}$		$Fil. carbon: +$
	S_B (%)	5	2	2	1	1	0	0			
	C_{CH_4} (%)	-7	7	21	45	67	87	93	$d_{XRD} = 12 \text{ nm}$	$d_{TEM} = 12 \text{ nm}$	$\sigma_{TEM} = 7 \text{ nm}$
	$E_a = 80 \text{ kJ/mol}$				$k_0 = 4.8 \cdot 10^7 \text{ m}^3/(\text{g}_{Cata} \cdot \text{h})$						
N-10Ni-2Mn	C_{Tolu} (%)	11	35	79	98	99	100	100	$Coke = 0.20 \text{ g}_{Carbon}/\text{g}_{Cata}$		$Fil. carbon: ++$
	S_B (%)	12	7	2	0	0	0	0	$d_{XRD} = 12 \text{ nm}$	$d_{TEM} = 13 \text{ nm}$	$\sigma_{TEM} = 5 \text{ nm}$
	C_{CH_4} (%)	-5	8	26	58	80	91	94	Possible phase: No evidence of Ni-Mn alloy		
	$E_a = 73 \text{ kJ/mol}$				$k_0 = 1.1 \cdot 10^8 \text{ m}^3/(\text{g}_{Cata} \cdot \text{h})$						
N-10Ni-2Mo	C_{Tolu} (%)	9	53	97	100	100	100	100	$Coke = 0.24 \text{ g}_{Carbon}/\text{g}_{Cata}$		$Fil. carbon: ++$
	S_B (%)	27	8	1	0	0	0	0	$d_{XRD} = 13 \text{ nm}$	$d_{TEM} = 14 \text{ nm}$	$\sigma_{TEM} = 5 \text{ nm}$
	C_{CH_4} (%)	-1	8	26	62	81	90	95	Possible phase: Ni _{0.91} Mo _{0.09}		
	$E_a = 52 \text{ kJ/mol}$				$k_0 = 1.3 \cdot 10^7 \text{ m}^3/(\text{g}_{Cata} \cdot \text{h})$						
N-10Ni-4Mo	C_{Tolu} (%)	21	48	91	100	100	100	100	$Coke = 0.20 \text{ g}_{Carbon}/\text{g}_{Cata}$		$Fil. carbon: ++$
	S_B (%)	12	10	3	0	0	0	0	$d_{XRD} = 12 \text{ nm}$	$d_{TEM} = 15 \text{ nm}$	$\sigma_{TEM} = 3 \text{ nm}$
	C_{CH_4} (%)	-5	3	24	68	85	92	96	Possible phases: Ni _{0.97} Mo _{0.03} , Ni _{0.91} Mo _{0.09} and molybdenum carbide MoC _{0.64}		
	$E_a = 48 \text{ kJ/mol}$				$k_0 = 5.4 \cdot 10^6 \text{ m}^3/(\text{g}_{Cata} \cdot \text{h})$						
N-10Ni-2Co	C_{Tolu} (%)	8	25	66	91	99	100	100	$Coke = 0.73 \text{ g}_{Carbon}/\text{g}_{Cata}$		$Fil. carbon: +++$
	S_B (%)	21	11	5	2	0	0	0	$d_{XRD} = 14 \text{ nm}$	$d_{TEM} = 18 \text{ nm}$	$\sigma_{TEM} = 17 \text{ nm}$
	C_{CH_4} (%)	0	14	35	53	78	88	94	Possible phase: Ni _{0.8} Co _{0.2}		
	$E_a = 58 \text{ kJ/mol}$				$k_0 = 1.2 \cdot 10^7 \text{ m}^3/(\text{g}_{Cata} \cdot \text{h})$						
N-10Ni-2Mn-2Mo	C_{Tolu} (%)	18	55	70	99	100	100	100	$Coke = 0.11 \text{ g}_{Carbon}/\text{g}_{Cata}$		$Fil. carbon: +$
	S_B (%)	12	2	1	1	0	0	0	$d_{XRD} = 17 \text{ nm}$	$d_{TEM} = 22 \text{ nm}$	$\sigma_{TEM} = 10 \text{ nm}$
	C_{CH_4} (%)	0	2	22	51	64	65	66	Possible phase: Ni _{0.91} Mo _{0.09}		
	$E_a = 74 \text{ kJ/mol}$				$k_0 = 1.3 \cdot 10^8 \text{ m}^3/(\text{g}_{Cata} \cdot \text{h})$						
N-10Ni-2Co-2Mo	C_{Tolu} (%)	39	65	99	100	100	100	100	$Coke = 0.27 \text{ g}_{Carbon}/\text{g}_{Cata}$		$Fil. carbon: +++$
	S_B (%)	3	1	1	1	1	0	0	$d_{XRD} = 19 \text{ nm}$	$d_{TEM} = 30 \text{ nm}$	$\sigma_{TEM} = 17 \text{ nm}$
	C_{CH_4} (%)	-6	1	20	40	44	53	63	Possible phases: Ni _{0.65} Co _{0.35} and Ni _{0.97} Mo _{0.03}		
	$E_a = 46 \text{ kJ/mol}$				$k_0 = 7.3 \cdot 10^6 \text{ m}^3/(\text{g}_{Cata} \cdot \text{h})$						

d_{TEM} : metallic particles size median; σ_{TEM} : standard deviation; d_{XRD} : metallic crystallites size estimation obtained by XRD; C_{Tolu} : conversion of toluene; S_B : selectivity in benzene; C_{CH_4} : conversion of methane; $Coke$: carbon deposit amount after test measured by TG-DSC; E_a : activation energy for the conversion of toluene; k_0 : pre-exponential factor for the conversion of toluene.

- Catalysts doped with one metal

It was observed that all catalysts doped with 2 wt. % of metal (samples *N-10Ni-2Mn*, *N-10Ni-2Mo* and *N-10Ni-2Co*) showed significantly lower C_{Tolu} values than the reference sample *N-10Ni* when the temperature of test reached $T = 600$ °C (Figure VII.27 and Table VII.19). In the case of sample *N-10Ni-2Co*, the loss of activity was attributed to the deactivation by oxidation since Co is thermodynamically more inclined to be reoxidized than Ni.^[293]

The E_a value of sample *N-10Ni-2Mn*, was slightly better compared to the reference sample *N-10Ni* (73 kJ/mol against 80 kJ/mol). The presence of a low amount (0.20 g_{Carbon}/g_{Cata}) of carbon deposit after test, which was strictly amorphous (Figure VII.29-b and Table VII.19), confirmed the fact that Mn is an effective anti-coking element whatever the temperature of test.

Among all the catalysts tested, sample *N-10Ni-2Co* showed the worst performances. Indeed, though this catalyst showed high C_{CH_4} and C_{Tolu} values for temperatures above $T = 650$ °C, it was observed that the addition of cobalt considerably favored the formation of a large amount of both amorphous and filamentous carbon deposits ($Coke = 0.73 \text{ g}_{Carbon}/\text{g}_{Cata}$) (Figure

VII.29-e and Table VII.19). More than being due to the element Co, this large amount of carbon could be also the consequence of the presence of large metallic particles sizes ($d_{TEM} = 18$ nm and $d_{XRD} = 14$ nm) with a broad distribution of sizes ($\sigma_{TEM} = 17$ nm) observed after test for sample *N-10Ni-2Co* (Table VII.19).

Sample *N-10Ni-2Mo* presented the best catalytic performances compared to samples *N-10Ni-2Mn*, *N-10Ni-2Co* and *N-10Ni*: best kinetics parameters ($E_a = 52$ kJ/mol and $k_0 = 1.3 \cdot 10^7$ m³/(g_{Cata}.h)) associated to a relatively low carbon deposition (*Coke* = 0.24 g_{Carbon}/g_{Cata}). These higher performances might be due to the formation of a Ni-Mo alloy (Ni_{0.91}Mo_{0.09}), suggested by post-test XRD measurements (Table VII.19). Nevertheless, it was noticed that, during the catalytic test, both amorphous and filamentous carbon were formed on the catalyst (Figure VII.29-c).

Though containing a higher loading of Mo, sample *N-10Ni-4Mo* showed a similar activity as sample *N-10Ni-2Mo* (Table VII.19). Furthermore, whereas sample *N-10Ni-4Mo* used to show a very high anti-coking capacity when tested under static conditions at $T = 650$ °C (Figure VII.23-e), after a catalytic test at $T = 900 \rightarrow 600$ °C, sample *N-10Ni-4Mo* showed an amount of carbon deposit relatively similar to the other samples (*Coke* = 0.20 g_{Carbon}/g_{Cata}) (Table VII.19). X-Ray measurements after test revealed that, though containing a higher amount of Mo, this sample did not show a higher incorporation of Mo inside Ni compared to sample *N-10Ni-2Mo* (Table VII.19). Furthermore, the post-test DSC (Figure VII.29-d) and XRD measurements revealed that sample *N-10Ni-4Mo* contained a molybdenum carbide phase (MoC_{0.64}), which could be problematic since this phase is very difficult to regenerate.¹ Therefore, it was assumed that the higher content of Mo, associated to the higher temperatures of test, increased the reduction of the MoO_x species, which made them more sensible to the incorporation of carbon atoms in their lattice structure. This test highlighted the fact that a high doping of Mo might be an asset to protect the catalyst from coking. However, the conditions of tests must be wisely chosen in order to prevent the formation of Mo carbides.

- Catalysts doped with two metals

In the case of sample *N-10Ni-2Mn-2Mo*, the catalyst was influenced by the simultaneous presence of Mn and Mo. Indeed, whereas sample *N-10Ni-2Mo* showed better kinetic parameters ($E_a = 52$ kJ/mol, $k_0 = 1.3 \cdot 10^7$ m³/(g_{Cata}.h)), sample *N-10Ni-2Mn-2Mo* showed kinetic values close to those encountered for sample *N-10Ni-2Mn* (for sample *N-10Ni-2Mn-2Mo*: $E_a = 74$ kJ/mol and $k_0 = 1.3 \cdot 10^8$ m³/(g_{Cata}.h); when for sample *N-10Ni-2Mn*: $E_a = 73$ kJ/mol and $k_0 = 1.1 \cdot 10^8$ m³/(g_{Cata}.h)) (Table VII.19). However, the X-Ray analysis after test suggested the formation of a Ni-Mo alloy (Ni_{0.91}Mo_{0.09}) (Table VII.19) and the DSC curve of sample *N-10Ni-2Mn-2Mo* revealed that the carbon deposit was of similar constitution as for sample *N-10Ni-2Mo* (Figure VII.29-f). Moreover, the DSC curve also revealed the synergistic anti-coking effect provided by the combination of Mn and Mo. Indeed, sample *N-10Ni-2Mn-2Mo* presented

¹: More details about metal carbides and regeneration in part I.4.3. of Chapter I.

the lowest amount of carbon deposit of all the catalysts tested ($Coke = 0.11 \text{ g}_{\text{Carbon}}/\text{g}_{\text{Cata}}$). Finally, it was also observed that for $T > 800 \text{ }^\circ\text{C}$, in contrary to the simple doped catalysts, the C_{CH_4} value of sample $N-10Ni-2Mn-2Mo$ was restricted to a maximum of 65 %. This phenomenon strengthened the hypothesis that MnO_x and MoO_x covered the $Ni^{(0)}$ particles. Indeed, it is known that the high covering of the $Ni^{(0)}$ particle by MnO_x and MoO_x species can partially block the active sites necessary for the reforming of methane.^[173]

Sample $N-10Ni-2Co-2Mo$ showed the highest C_{Tolu} value, and consequently the more interesting kinetic parameters ($E_a = 46 \text{ kJ/mol}$ and $k_0 = 7.3 \cdot 10^6 \text{ m}^3/(\text{g}_{\text{Cata}}\cdot\text{h})$) of all metal-doped materials (Figure VII.27 and Table VII.19). Noteworthy, this sample also showed the lowest methane conversion (Figure VII.28 and Table VII.19), thus confirming the fact that the active sites and mechanisms involved in the reforming of toluene are different from those involved for the reforming of methane. The post-test DSC curve (Figure VII.29-g) revealed that the aspect of the carbon deposit of sample $N-10Ni-2Co-2Mo$ was similar to what was obtained for the sample $N-10Ni-2Mo$ (presence of both amorphous and filamentous types of carbon). The presence of Co seemed to favor the production of the two types of carbon (Figure VII.29-g). Here also, the presence of cobalt seemed to have favored the growth of the Ni-M metallic particles ($d_{XRD} = 19 \text{ nm}$, $d_{TEM} = 30 \text{ nm}$, $\sigma_{TEM} = 18 \text{ nm}$) (Table VII.19), which could explain the higher amount of carbon deposit observed for sample $N-10Ni-2Co-2Mo$ ($Coke_{N-10Ni-2Co-2Mo} = 0.27 \text{ g}_{\text{Carbon}}/\text{g}_{\text{Cata}}$).

Hence, the Mn+Mo association provides the most beneficial performances and it seems more advantageous in terms of catalytic activity and lifetime to use 2 wt. % of two different metals, rather than 4 wt. % of one type of metal.

VII.3.5.2. Evolution of the performances of the best $Ni/\gamma\text{-Al}_2\text{O}_3$ catalysts promoted with oxide dopants

Samples $N-10Ni-3K$, $N-10Ni-1.5Ca-1.5K$ ®, $N-10Ni-1.5Ce-1.5K$ ® were chosen for their high catalytic activity for toluene reforming and good resistance against coking. In order to get a better understanding of the influence of each element, the following simple doped catalysts were also studied: samples $N-10Ni-1.5Ca$, $N-10Ni-1.5K$ and $N-10Ni-1.5Ce$ ®.

Figures VII.30 and VII.31 respectively show the toluene and the methane conversions, C_{Tolu} and C_{CH_4} , as a function of the temperature

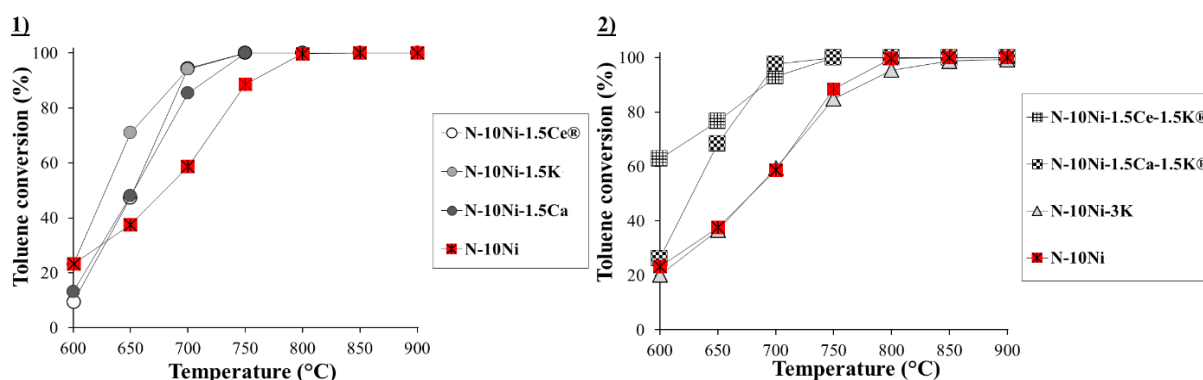


Figure VII.30: Toluene conversion as a function of temperature for the best $Ni/\gamma\text{-Al}_2\text{O}_3$ catalysts doped with oxides.

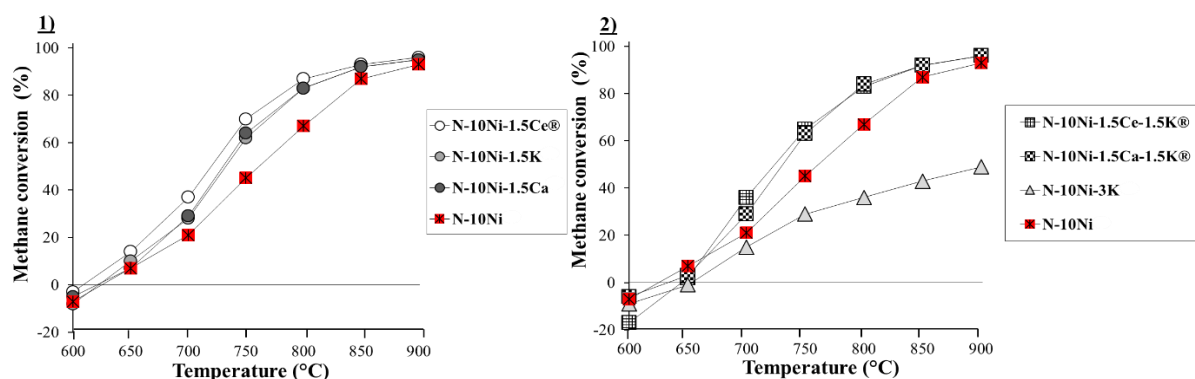


Figure VII.31: Methane conversion as a function of temperature for the best Ni/ γ -Al₂O₃ catalysts doped with oxides.

Catalytic activity values (C_{Tolu} , S_B , C_{CH_4} , E_a and k_0) and additional post-test characterizations (amount of carbon deposit, presence of filamentous carbon, and size of the metallic nanoparticles) are presented in Table VII.20. Figure VII.32 presents the post-test DSC curves.

Table VII.20: Catalytic activity as a function of the temperature and post-test characterizations for the best Ni/ γ -Al₂O₃ catalysts doped with oxides. Toluene concentration: 24.000 ppmv, $T = 900 \rightarrow 600$ °C, $GHSV = 5000$ h⁻¹.

Samples	Catalytic activity								Characterizations post-test		
	T (°C)	600	650	700	750	800	850	900			
N-10Ni	C_{Tolu} (%)	23	38	59	88	99	100	100	$Coke = 0.36$ g _{Carbon} /g _{Cata}		$Fil. carbon: +$
	S_B (%)	5	2	2	1	1	0	0			
	C_{CH_4} (%)	-7	7	21	45	67	87	93			
	$E_a = 80$ kJ/mol				$k_0 = 4.8 \cdot 10^7$ m ³ /(g _{Cata} .h)				$d_{XRD} = 12$ nm	$d_{TEM} = 12$ nm	$\sigma_{TEM} = 7$ nm
N-10Ni-1.5Ca	C_{Tolu} (%)	13	48	85	100	100	100	100	$Coke = 0.17$ g _{Carbon} /g _{Cata}		$Fil. carbon: +$
	S_B (%)	11	4	1	0	0	0	0			
	C_{CH_4} (%)	-5	7	29	64	83	92	95			
	$E_a = 55$ kJ/mol				$k_0 = 1.9 \cdot 10^7$ m ³ /(g _{Cata} .h)				$d_{XRD} = 11$ nm	$d_{TEM} = 12$ nm	$\sigma_{TEM} = 4$ nm
N-10Ni-1.5K	C_{Tolu} (%)	21	71	94	100	100	100	100	$Coke = 0.15$ g _{Carbon} /g _{Cata}		$Fil. carbon: +$
	S_B (%)	9	2	1	0	0	0	0			
	C_{CH_4} (%)	-8	10	28	62	83	92	95			
	$E_a = 50$ kJ/mol				$k_0 = 7.5 \cdot 10^6$ m ³ /(g _{Cata} .h)				$d_{XRD} = 12$ nm	$d_{TEM} = 13$ nm	$\sigma_{TEM} = 5$ nm
N-10Ni-3K	C_{Tolu} (%)	20	37	60	85	95	99	100	$Coke = 0.18$ g _{Carbon} /g _{Cata}		$Fil. carbon: ++$
	S_B (%)	4	5	4	6	2	1	1			
	C_{CH_4} (%)	-9	-1	15	29	36	43	49			
	$E_a = 70$ kJ/mol				$k_0 = 3.6 \cdot 10^7$ m ³ /(g _{Cata} .h)				$d_{XRD} = 27$ nm	$d_{TEM} = 22$ nm	$\sigma_{TEM} = 47$ nm
N-10Ni-1.5Ce®	C_{Tolu} (%)	9	47	94	100	100	100	100	$Coke = 0.25$ g _{Carbon} /g _{Cata}		$Fil. carbon: +$
	S_B (%)	15	5	1	0	0	0	0			
	C_{CH_4} (%)	-3	14	37	70	87	93	96			
	$E_a = 53$ kJ/mol				$k_0 = 1.5 \cdot 10^7$ m ³ /(g _{Cata} .h)				$d_{XRD} = 12$ nm	$d_{TEM} = 12$ nm	$\sigma_{TEM} = 5$ nm
N-10Ni-1.5Ca-1.5K®	C_{Tolu} (%)	26	68	98	100	100	100	100	$Coke = 0.14$ g _{Carbon} /g _{Cata}		$Fil. carbon: +$
	S_B (%)	8	2	0	0	0	0	0			
	C_{CH_4} (%)	-6	3	29	63	84	92	96			
	$E_a = 49$ kJ/mol				$k_0 = 9.9 \cdot 10^6$ m ³ /(g _{Cata} .h)				$d_{XRD} = 12$ nm	$d_{TEM} = 11$ nm	$\sigma_{TEM} = 3$ nm
N-10Ni-1.5Ce-1.5K®	C_{Tolu} (%)	63	77	93	100	100	100	100	$Coke = 0.32$ g _{Carbon} /g _{Cata}		$Fil. carbon: ++$
	S_B (%)	2	0	1	0	0	0	0			
	C_{CH_4} (%)	-17	2	36	65	83	92	96			
	$E_a = 54$ kJ/mol				$k_0 = 1.7 \cdot 10^7$ m ³ /(g _{Cata} .h)				$d_{XRD} = 12$ nm	$d_{TEM} = 12$ nm	$\sigma_{TEM} = 11$ nm

d_{TEM} : metallic particles size median; σ_{TEM} : standard deviation; d_{XRD} : metallic crystallites size estimation obtained by XRD; C_{Tolu} : conversion of toluene; S_B : selectivity in benzene; C_{CH_4} : conversion of methane; $Coke$: carbon deposit amount after test measured by TG-DSC; E_a : activation energy for the destruction of toluene; k_0 : pre-exponential factor for the destruction of toluene.

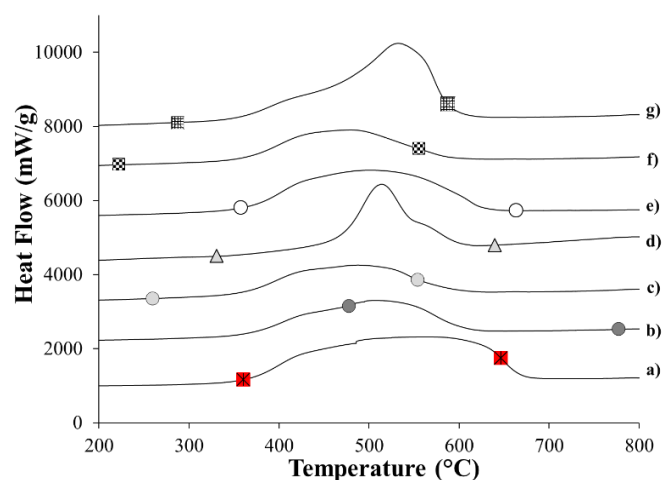


Figure VII.32: DSC curves performed on samples tested at $T = 900 \rightarrow 600$ °C for the most promising Ni/ γ -Al₂O₃ catalysts doped with oxides; a. *N-10Ni*, b. *N-10Ni-1.5Ca*, c. *N-10Ni-1.5K*, d. *N-10Ni-3K*, e. *N-10Ni-1.5Ce*®, f. *N-10Ni-1.5Ca-1.5K*®, g. *N-10Ni-1.5Ce-1.5K*®.

As a general observation, it is to notice that all the samples doped with oxides presented higher catalytic activities (better E_a and k_0 values, higher C_{Tolu} and C_{CH_4} values) and lower carbon deposit amounts compared to the reference sample *N-10Ni* (Figures VII.30 and VII.31, Table VII.20).

- Catalysts doped with one oxide

It was observed in Table VII.20 that all catalysts doped with 1.5 wt. % of oxide presented similar E_a values (~ 55 kJ/mol). However, it is to notice that samples *N-10Ni-1.5Ca* and *N-10Ni-1.5K* presented less amounts of carbon deposit ($Coke \sim 0.16$ g_{Carbon}/g_{Cata}) than sample *N-10Ni-1.5Ce*® ($Coke \sim 0.25$ g_{Carbon}/g_{Cata}). This observation confirmed that, in the synthesis conditions of this work, Ce did not permit to reach the high anti-coking properties that were expected during the literature review.¹ Noteworthy, sample *N-10Ni-1.5Ce*® presented the highest C_{CH_4} value of all samples (Figure VII.31 and Table VII.20).

Though sample *N-10Ni-1.5K* showed the highest catalytic performances among the catalysts doped with 1.5 wt. % of oxides, the increase of the loading of K (sample *N-10Ni-3K*) led in contrary to disadvantageous effects during the catalytic tests performed at $T = 900 \rightarrow 600$ °C. Indeed, compared to sample *N-10Ni-1.5K*, sample *N-10Ni-3K* showed a higher activation energy ($E_a = 70$ kJ/mol). Furthermore, sample *N-10Ni-3K* also presented the lowest C_{CH_4} values of all samples of this study (Figure VII.31 and Table VII.20). These poor results were attributed to a large covering of the Ni⁽⁰⁾ particles by potassium oxide, which is known to block the access to the metallic active sites^{[339], [340], [346]} and to increase the energy barrier for the dissociation of CH₄ by modification of the electronic environment of Ni⁽⁰⁾^[340]. It is also to notice that, when tested at $T = 900 \rightarrow 600$ °C, sample *N-10Ni-3K* did not show such exceptional anti-coking properties as when tested under steady conditions at $T = 650$ °C. In this way, sample *N-10Ni-3K* showed an amount of carbon deposit similar to the other samples ($Coke \sim 0.18$ g_{Carbon}/g_{Cata}) and presented a high formation of filamentous carbon (Table VII.20 and Figure VII.32-d). This

¹: More details about Ce element used as anti-coking dopant in part I.4.4.2.4. of Chapter I.

trend to form filamentous carbon was once more attributed to the presence of large metallic nickel particles with a broad size distribution ($d_{XRD} = 27$ nm, $d_{TEM} = 22$ nm and $\sigma_{TEM} = 47$ nm) (Table VII.20), whose sintering was favored by a high amount of potassium. Noteworthy, from the TEM measurements performed on sample *N-10Ni-3K* after the catalytic test, metallic Ni⁽⁰⁾ particles as large as 200 nm were observed among others with more standard sizes (~ 20 nm). Hence, in that case, the anti-coking ability of K was not sufficient to counter the formation of filamentous carbon favored by large metallic nickel particles.

- *Catalysts doped with two oxides*

Sample *N-10Ni-1.5Ca-1.5K*® appeared as the most interesting sample among all the catalysts doped with oxides (Table VII.20, Figure VII.32-f). Indeed, it showed a high reforming activity ($E_a = 49$ kJ/mol and $k_0 = 9.9 \cdot 10^6$ m³/(g_{Cata}.h)), relatively small nickel particles sizes with a narrow distribution of sizes after catalytic test ($d_{XRD} = 12$ nm, $d_{TEM} = 11$ nm and $\sigma_{TEM} = 3$ nm), a good C_{CH_4} value and a low amount of carbon deposit which was only constituted of amorphous carbon ($Coke = 0.14$ g_{Carbon}/g_{Cata}).

In contrary, sample *N-10Ni-1.5Ce-1.5K*® showed more questionable results. On one hand, this material showed a high reforming activity ($E_a = 54$ kJ/mol and $k_0 = 1.7 \cdot 10^7$ m³/(g_{Cata}.h)), small Ni⁽⁰⁾ particles sizes after test ($d_{XRD} = 12$ nm and $d_{TEM} = 12$ nm), and a relatively good C_{CH_4} value. On the other hand, this sample showed more broad size distribution of the Ni⁽⁰⁾ particles sizes ($\sigma_{TEM} = 11$ nm) and a high amount of carbon deposit after test ($Coke = 0.32$ g_{Carbon}/g_{Cata}), which contained a large part of filamentous carbon (Table VII.20 and Figure VII.32-g). The high amount of carbon deposit encountered for this sample could be in part due to the presence of large Ni⁽⁰⁾ particles and to the high activity of this sample at low temperatures. Indeed, when the temperature of test was equal to $T = 600$ °C, sample *N-10Ni-1.5Ce-1.5K*® showed a remarkably high C_{Tolu} value (63 %), a low S_B value (2 %) but also a high production of methane ($C_{CH_4} = - 17$ %). It was noticed that, in contrary to all the other samples which presented high H₂/CO ratios ($H_2/CO = 1.14-1.18$) at $T = 600$ °C, sample *N-10Ni-1.5Ce-1.5K*® was the only one which presented a low H₂/CO ratio ($H_2/CO = 1.01$). Consequently, it was assumed that an amount of H₂ molecules were consumed to perform the hydrocracking of toluene into methane ($C_7H_8 + 10.H_2 \rightarrow 7.CH_4$).ⁱ

Hence, the combination Ca+K showed the most beneficial performances. Furthermore, this part showed that Ni/ γ -Al₂O₃ catalysts with interesting catalytic activity and high anti-coking properties can be developed without the use of Ce. It was also highlighted that it seems more advantageous in terms of catalytic activity and lifetime to use 1.5 wt. % of two different oxides, rather than 3 wt. % of one type of oxide.

ⁱ : More details about reaction of hydrocracking of toluene in Table IV.2.

VII.4. CONCLUSIONS

The vast screening performed in this chapter permitted to determine which elements were the most interesting for the doping of 10 wt. % Ni/ γ -Al₂O₃ catalysts.

It appeared that Ni/ γ -Al₂O₃ catalysts doped with 2 wt. % of copper showed the worst catalytic performances. Indeed, the sample showed a progressive deactivation during the catalytic tests caused by the formation of high amounts of amorphous carbon. As the formation of Ni-Cu alloys was suggested by XRD measurement, and that the samples presented a high benzene selectivity, it was assumed that the deactivation by coking was caused by a lower ability of the Ni-Cu alloy to break aromatic rings. However, the presence of a Ni-Cu alloy prevented the dissolution of C atoms inside the metallic particles, and avoided the formation of filamentous carbon.

The addition of Co or Fe had similar influences on the properties of the Ni/ γ -Al₂O₃ catalysts. In this way, both elements caused a more difficult reduction of Ni because of strong interactions between Ni-FeO_x and Ni(O)Co species, which led to low catalytic activity values during catalytic tests performed at $T = 650$ °C. It was also observed that Co or Fe favored the production of filamentous carbon. Finally, the poor catalytic performances observed for the 10 wt. % Ni/ γ -Al₂O₃ catalyst doped with 2 wt. % of Co when tested for $T = 900 \rightarrow 600$ °C confirmed the fact that Co is a metal dopant to avoid.

Though they showed slightly lower activities, all Ni/ γ -Al₂O₃ catalysts doped with 2 wt. % of Mn showed interesting anti-coking properties and no formation of filamentous carbon during the two different types of catalytic tests ($T = 650$ °C or $T = 900 \rightarrow 600$ °C). The beneficial influence of an addition of Mn was attributed to the good ability of the MnO_x species to increase the adsorption-dissociation of H₂O and CO₂ molecules, which led to a better gasification of the carbonaceous deposits at the surface of the Ni⁽⁰⁾ particles. It was observed that a higher loading of Mn (4 wt. %) prevented an efficient activation of Ni during the catalytic test, probably due to a large covering of Ni⁽⁰⁾ particles by MnO_x species. Despite its low activity, the sample doped with 4 wt. % of Mn presented a remarkably low amount of carbon deposit after a test at $T = 650$ °C.

Mo proved to be the most interesting simple metal dopant. Indeed, when tested at $T = 650$ °C, the Ni/ γ -Al₂O₃ catalyst doped with 2 wt. % of Mo showed the highest toluene reforming activity, for an acceptable amount of carbon deposit. This better activity was attributed to: 1) a better reduction of Ni evidenced by TPR measurement; 2) an increase of the adsorption-dissociation of H₂O and CO₂ molecules by the MoO_x species; 3) an increase of oxygen ionic conductivity of Ni caused by electronic interactions between Mo and Ni, which increase the gasification rate of the CH_x species to CO and H₂. It was noticed that the sample doped with 2 wt. % of Mo also showed a high activity for a relatively low amount of carbon deposit when tested at $T = 900 \rightarrow 600$ °C. Nevertheless, during this test, this sample formed filamentous carbon. It was observed that a higher amount of Mo (4 wt. %) decreased the catalytic activity during the standard test at $T = 650$ °C, probably because of a large covering of Ni⁽⁰⁾ particles by

MoO_x. However, in that case, this sample presented a very low amount of carbon deposit after test. When tested at higher temperatures ($T = 900 \rightarrow 600$ °C), the sample doped with 4 wt. % of Mo showed relatively interesting catalytic activity, but not such exceptional coking resistance. Furthermore, after this test, X-Ray analyses and TG-DSC measurements revealed the presence of molybdenum carbide (MoC_{0.64}) for this sample. The reasons for the formation of this undesirable metal carbide phase were attributed to lower interactions between the MoO_x species and the alumina support because of a high loading of Mo, associated to a better reduction of the MoO_x species, also caused by the high loading, combined to the high temperature of test.

Among all 10 wt. % Ni/ γ -Al₂O₃ catalysts doped with 2 wt. % of two different metals, the samples which combined Mn+Mo or Co+Mo showed the most interesting catalytic performances at $T = 650$ °C. Both samples showed high toluene reforming activity and low amounts of carbon deposit. When tested at $T = 900 \rightarrow 600$ °C, the catalyst doped with Co+Mo showed the highest catalytic activity, but also a high amount of carbon deposit, which was mostly composed of filamentous carbon. This high sensibility against coking was attributed to the presence of Co, which favored the growth of large metallic particles. In contrary, the sample doped with Mn+Mo showed a relatively good activity, associated to a very low amount of carbon deposit after test.

NH₃-TPD measurements highlighted that the addition of 1.5 wt. % of alkali (Ca, K or Mg) did not influence the acido-basicity properties of 10 wt. % Ni/ γ -Al₂O₃ catalysts. It was assumed that no sufficient interactions were formed between the oxides and the alumina support during the preparation of the catalysts. In this way, the influence of doping with alkali was assumed to be directly caused by the presence of these oxides and not to a modification of the acido-basicity of the support.

All samples doped with 1.5 wt. % of oxide (Ca, K, Mg or Ce) presented a decrease of benzene selectivity and of the amount of carbon deposit. These results were attributed to a better degradation of the intermediate compounds of toluene and of the carbonaceous compounds because of a higher amount of H₂O and CO₂ molecules adsorbed on these oxides.

The addition of Mg led to strong Ni/MgO interactions which decreased the catalytic activity of the catalysts at $T = 650$ °C.

The catalyst doped with 1.5 wt. % of cerium did not show the remarkable anti-coking properties that were expected at $T = 650$ °C. This was attributed to the synthesis method, whose calcination temperature was believed to be insufficient to form AlCeO_x phase.

The addition of 1.5 wt. % of Ca led to a slightly lower catalytic activity at $T = 650$ °C, but to a better resistance against the coking. The anti-coking ability brought by the addition of 1.5 wt. % of Ca was also beneficial when the catalyst was tested at $T = 900 \rightarrow 600$ °C. However, when the loading of Ca increased up to 3 wt. %, the sample showed a harder Ni reducibility, which led to a lower catalytic activity during the test at $T = 650$ °C. Furthermore, because of this large amount of Ca, the sintering of the Ni⁽⁰⁾ particles was favored during the catalytic test, which resulted in an increase of the formation of filamentous carbon.

The potassium appeared to be the most interesting alkali dopant. Indeed, when tested at $T = 650\text{ }^{\circ}\text{C}$ or at $T = 900\rightarrow 600\text{ }^{\circ}\text{C}$, the catalyst doped with 1.5 wt. % of K showed a very good toluene reforming activity associated to a low amount of carbon deposit. At higher doping (3 wt. %), the sample showed a slight decrease of its catalytic activity and a low methane conversion during the catalytic test at $T = 650\text{ }^{\circ}\text{C}$. Once more, this was attributed to the covering of the $\text{Ni}^{(0)}$ particles by K_2O . It was also noticed that the high amount of alkali increased the sintering of the $\text{Ni}^{(0)}$ particles and led to the formation of large metallic particles with a broad distribution of sizes. However, despite the presence of large $\text{Ni}^{(0)}$ particles, the sample doped with 3 wt. % of K showed almost no carbon deposit after a catalytic test at $T = 650\text{ }^{\circ}\text{C}$. In contrary, this became a problem when tested at $T = 900\rightarrow 600\text{ }^{\circ}\text{C}$ since these large metallic nickel particles (up to 200 nm) favored the formation of filamentous carbon.

Among the different compositions of $\text{Ni}/\gamma\text{-Al}_2\text{O}_3$ catalysts doped with two different types of oxides, the catalysts doped either with K+Ce, or K+Ca showed the most interesting performances. When tested at $T = 650\text{ }^{\circ}\text{C}$ or at $T = 900\rightarrow 600\text{ }^{\circ}\text{C}$, the sample doped with K+Ce showed the highest toluene reforming rates among all catalysts of this chapter, especially at low temperatures ($T = 600, 650\text{ }^{\circ}\text{C}$). However, it was assumed that at these temperatures, the gasification rates of the carbonaceous compounds were insufficient to balance the high rate of toluene cracking, which resulted in large amounts of carbon deposits. In contrary, when tested at $T = 650\text{ }^{\circ}\text{C}$ or at $T = 900\rightarrow 600\text{ }^{\circ}\text{C}$, the sample doped with Ca+K showed interesting toluene and methane conversions, associated to a relatively low amount of carbon deposit exclusively formed of amorphous type. Furthermore, in spite of its high loading of alkali, this catalyst still presented $\text{Ni}^{(0)}$ particles with a narrow distribution of size. Therefore, it was shown that catalysts with very interesting catalytic activity and good anti-coking performances can be obtained only thanks to the combination of classic alkali dopant (Ca and K) and without the use of the expensive ceria element.

For equal loadings, it seems more advantageous from a catalytic activity and catalyst lifetime point of view, to dope the catalysts with two types of elements (2 X 2 wt. % of metals or 2 X 1.5 wt. % of oxide dopants), than with only type of element (4 wt. % of metal or 3 wt. % of oxide dopant).

As a final remark, it is to notice that there is a major lack of knowledge and too many vague hypotheses in the literature to clearly explain the good performances of many of the dopants studied in this chapter. In this way, now that some interesting compositions have been highlighted, it would be relevant to get a better understanding of the behavior of the catalysts (especially the samples containing two different dopants) thanks to further characterizations such as XPS/LEIS spectroscopy, STEM+EDX, SSITKA^[347], Infrared spectroscopy, EXAFS spectroscopy, steam and CO_2 adsorption comparisons by micro-calorimetry^[89] or analysis with a TAP reactor^[348].

Chapter VIII

Catalytic performances of the most promising Ni/ γ -Al₂O₃ catalysts during long-term tests and in presence of H₂S

- Comparison of the performances of the most promising Ni/ γ -Al₂O₃ catalysts of this project with a commercial steam reforming catalyst;

- Long-term catalytic tests;

- Catalytic tests performed in the presence of H₂S.

The aims of this chapter are to evaluate the performances of the catalysts during long-term tests or in presence of H₂S. The catalytic tests are performed at $T = 650$ °C with a standard syngas mixture and with 24.000 ppmv of toluene.

Long-term catalytic tests are performed for $t = 30$ h with the most promising catalysts of Chapter VII (samples *N-10Ni*, *N-10Ni-2Mn-2Mo*, *N-10Ni-1.5Ca-1.5K*® and *N-10Ni-1.5Ce-1.5K*®) and with a commercial steam reforming catalyst (sample *Hifuel*).

The influence of the presence of H₂S on the catalytic performance of *N-10Ni* is evaluated thanks to two different tests: the catalytic test is interrupted by pulses of H₂S (200 ppmv) or the catalytic test is performed with a continuous presence of H₂S (40 ppmv).

VIII.1. INTRODUCTION

The catalytic performances (catalytic activity and resistance against deactivation) of a reforming catalyst are mostly determined during its first 5 h of test, which explains the rarity of studies presenting catalysts tested in long-term conditions. However, the common omission of this type of test is problematic since it tends to widen the gap between the literature results and the industrial needs. Indeed, rather than the catalytic activity, the stability of the catalyst is usually the first criterion needed in industrial applications.^{[9], [39], [349]} This can be explained by the fact that, during their use, the catalysts are threatened by various phenomena (coke, sintering, phase transformation ...).ⁱ

Most of the studies also omit to test the catalysts in presence of H₂S. This lack of information is also generally an obstacle for the use of the catalysts at larger scale. Indeed, H₂S is intrinsically present in the syngas mixture (between 20 and 200 ppmv).ⁱⁱ Though the final syngas is usually purified of H₂S via adsorbers, due to their temperatures of application, the catalysts (primary and secondary) must always be situated before these clean-up steps.ⁱⁱⁱ Hence, the resistance against H₂S is a crucial criterion, especially for secondary catalysts working at low temperatures ($T = 500$ - 700 °C). Indeed, the sensitivity of the reforming catalysts to chemisorb sulfur compounds is known to increase when the temperature decreases.^{iv} A good example to illustrate the decisive challenge of developing catalysts resistant to H₂S lies in the study made by Gallego *et al.*^[350]. The author developed LaNiO₃ perovskite catalysts for the dry reforming of methane which exhibited very good long-term results (100 h without carbon deactivation). However, only a small amount of H₂S (25 ppm) was sufficient to entirely deactivate the catalyst in 5 h of test. In this chapter, the influence of the presence of H₂S was evaluated with the reference 10 wt. % Ni/ γ -Al₂O₃ catalyst synthesized by sol-gel process. Two types of tests were performed: pulse of 200 ppmv of H₂S, or continuous presence of 40 ppmv of H₂S.

ⁱ : More information about the deactivation of the catalysts in part I.4.3. of Chapter I.

ⁱⁱ : Amount of H₂S generally present in the syngas showed in Table I.4.

ⁱⁱⁱ : More details about the processes implied in the fabrication and purification of bio-syngas in part I.3.1. of Chapter I.

^{iv} : More details about deactivation by sulphidic compounds in part I.4.3.2. of Chapter I.

Table VIII.1 resumes the global reactions which can happen on a metallic active site during catalytic tests in presence of H₂S and during regeneration with H₂O, H₂ or O₂.

Table VIII.1: Global reactions happening between a metallic active site (M), H₂S and H₂, H₂O or O₂.

Equation	Name of reaction	Equation n°
$MO_x + x.H_2S \rightarrow MS_x + x.H_2O$	Reduction and poisoning	VIII.1
$M + x.H_2S \rightarrow MS_x + x.H_2$	Poisoning	VIII.2
$MS_x + x.H_2O \rightarrow MO_x + x.H_2S$	Regeneration by H ₂ O	VIII.3
$MS_x + x.H_2 \rightarrow M + x.H_2S$	Regeneration by H ₂	VIII.4
$MS_x + \left(\frac{3x}{2}.O_2\right) \rightarrow MO_x + x.SO_2$	Regeneration by O ₂	VIII.5

VIII.2. EXPERIMENTAL

VIII.2.1 Ni-based catalysts selected

Samples *N-10Ni*, *N-10Ni-2Mn-2Mo*, *N-10Ni-1.5Ce-1.5K®* and *N-10Ni-1.5Ca-1.5K®* were chosen for long-term catalytic tests. It is to notice that these catalysts are identical to those studied in Chapter VII.

In this chapter, the catalytic performances of a commercial nickel-based steam reforming catalyst (called *Hifuel® R110*), produced by the company Johnson Matthey, were investigated. This catalyst is mostly used in natural gas, in liquefied petroleum gas and in methane steam reforming applications.^[351] It has also been used in some cases for the reforming of toluene.^[26] For a simpler nomenclature, this sample is called *Hifuel* in this chapter.

VIII.2.2 Characterization techniques

Composition analysis (ICP–AES), nitrogen adsorption-desorption (BET), mercury porosimetry (Poro-Hg), X-Ray diffraction (XRD), temperature programmed reduction (TPR) and thermogravimetric-differential scanning calorimetry (TG-DSC) measurements were performed on the samples of this chapter. The Ni⁽⁰⁾ crystallites sizes were calculated by using the Scherrer equation centered on the (2 0 0) ray ($2\theta = 51.83^\circ$) of the XRD spectra. Further information about the characterization techniques and operating variables are provided in part II of Annex 2. X-Ray references cards are given in part VI of Annex 2.

VIII.2.3. Catalytic tests

The catalytic activities were evaluated thanks to the toluene conversion (C_{Tolu}), the benzene selectivity (S_B), the methane conversion (C_{CH_4}) and the toluene reforming rate (r_{Tolu}) whose formulae are reminded in part I of Annex 2. All C_{Tolu} , S_B and C_{CH_4} values were obtained by making an average of the results obtained during the last 10 measurements of each test.

Three types of tests were performed:

- Long-term tests

Long-term tests were performed with catalytic conditions similar to those used in previous chapters. The samples were tested at $T = 650$ °C, with a standard gas mixture¹ and with a toluene concentration of 24.000 ppmv. The mass of catalyst was set to 300 mg, for a catalytic bed height of $h = 12$ mm, with a gas flowrate of 50 mL/min and consequently a $GHSV$ of 5000 h⁻¹ (residence time of 0.72 sec). The tests were performed for $t = 30$ h, with a GC injection every 30 min.

- Test performed with pulse feed of H₂S

The test conditions (mass of catalyst, gas composition, temperature and gas flowrate) were similar as during a standard test. However, the catalytic test was interrupted twice, at $t = 90$ min and $t = 195$ min, to perform the procedure of pulse of H₂S as follows:

- 1) bypass of the syngas mixture and purge of the reactor for $t = 5$ min with 30 mL/min of He;
- 2) injection of a continuous flow of N₂/H₂S mixture with 30 mL/min (200 ppmv of H₂S) for $t = 5$ min;
- 3) purge of the reactor for $t = 5$ min with 30 mL/min of He and reinjection of the syngas mixture.

- Test performed with continuous feed of H₂S

In this case, the gas flowrate was composed of 40 mL/min of standard syngas and 10 mL/min of N₂/H₂S mixture (200 ppmv of H₂S), which led to a global concentration of 40 ppmv of H₂S. The mass of catalyst was set to 240 mg, in order to keep a $GHSV$ of 5000 h⁻¹, when taking into account exclusively the syngas mixture as incoming gas. The catalytic tests started without H₂S (injection of syngas mixture + pure N₂). At $t = 90$ min, the pure N₂ was replaced by the mixture of N₂/H₂S until the end of the test.

VIII.3. RESULTS AND DISCUSSION

VIII.3.1. Characterization of the commercial catalyst

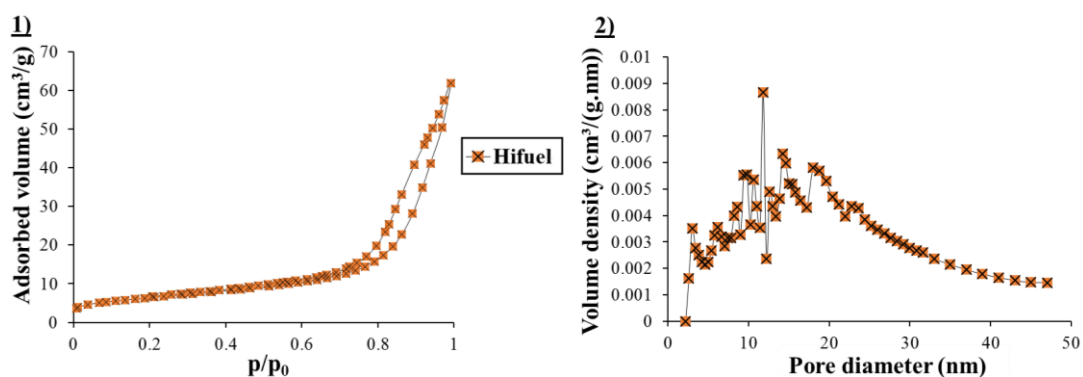
Table VIII.2 shows the actual composition of the commercial steam reforming catalyst (sample *Hifuel*). This sample was mainly composed of Al₂O₃, Ni and CaO.

Table VIII.2: Composition of commercial catalyst *Hifuel* in wt. %.

Sample	Al ₂ O ₃	Ni	CaO	SiO ₂	MgO	Na ₂ O
Hifuel	67.4	16.0	16.3	0.1	0.1	0.1

Nitrogen adsorption-desorption (Figure VIII.1) and mercury porosimetry (not shown here) measurements were performed in order to characterize the textural properties of sample *Hifuel*. The textural values obtained by the nitrogen adsorption-desorption measurement (S_{BET} , V_p and $V_{Dubinin}$) and the macroporous volume (V_{Hg}) obtained by mercury porosimetry are presented in Table VIII.3.

¹: See Table IV.1, Chapter IV

Figure VIII.1: Nitrogen adsorption-desorption isotherm and mesopore size distribution of sample *Hifuel*.Table VIII.3: Textural properties obtained for nitrogen-adsorption and mercury porosimetry measurements for sample *Hifuel*.

Sample	S_{BET} (m ² /g)	V_{Hg} (cm ³ /g)	V_p (cm ³ /g)	$V_{Dubinin}$ (cm ³ /g)
Hifuel	20	0.2	0.08	0.008

S_{BET} : specific surface area; V_p : porous volume; $V_{Dubinin}$: microporous volume; V_{Hg} : macroporous volume.

It was observed in Figure VIII.1 and Table VIII.3 that, at low p/p_0 values, sample *Hifuel* presented a very low adsorbed volume. Indeed, the microporous volume of this sample was very low ($V_{Dubinin} = 0.008$ cm³/g). Furthermore this sample showed a very low specific surface area ($S_{BET} = 20$ m²/g) and a low porous volume ($V_p = 0.08$ cm³/g). At higher pressure ($p/p_0 > 0.8$), sample *Hifuel* presented a slight hysteresis loop, characteristic of the presence of large mesopores.^[229] Indeed, the mesopore size distribution (Figure VIII.1) showed a large distribution of mesopore sizes varying from 2 to 50 nm. However, the mercury porosimetry measurement revealed that the sample could be considered as not macroporous (V_{Hg} of only 0.2 cm³/g).

A X-Ray diffraction was performed on sample *Hifuel* as received. The X-Ray spectrum (not shown here) revealed that the catalyst was composed of four phases: 1) corindon alumina, *i.e.* α -Al₂O₃, which explains why the sample presents a low micro- and mesoporous texture; 2) grossite, *i.e.* CaAl₄O₇, which is obtained by calcination of CaO and Al₂O₃ at high temperatures ($T \sim 1000$ °C)^[333]; 3) bulk nickel oxide, NiO; 4) spinels of nickel aluminate (NiAl₂O₄). After TPR measurement (Figure VIII.2), the NiO rays disappeared and intense rays of Ni⁽⁰⁾ were visible at $2\theta = 44.4^\circ$, 51.8° and 76.3° . Nevertheless, the X-Ray spectrum of sample *Hifuel* presented very similar rays of α -Al₂O₃ and CaAl₄O₇ as received.

The TPR profile presented in Figure VIII.2 evidenced that sample *Hifuel* contained the three different types of nickel oxides: bulk NiO (reduction at $T \sim 450$ °C), NiO/Al₂O₃ (reduction at $T \sim 625$ °C) and NiAl₂O₄ (reduction at $T \sim 775$ °C).^{[276], [289], [352]} Table VIII.4 shows the Ni particles sizes after reduction and after TPR measurements determined by TEM and XRD analyses.

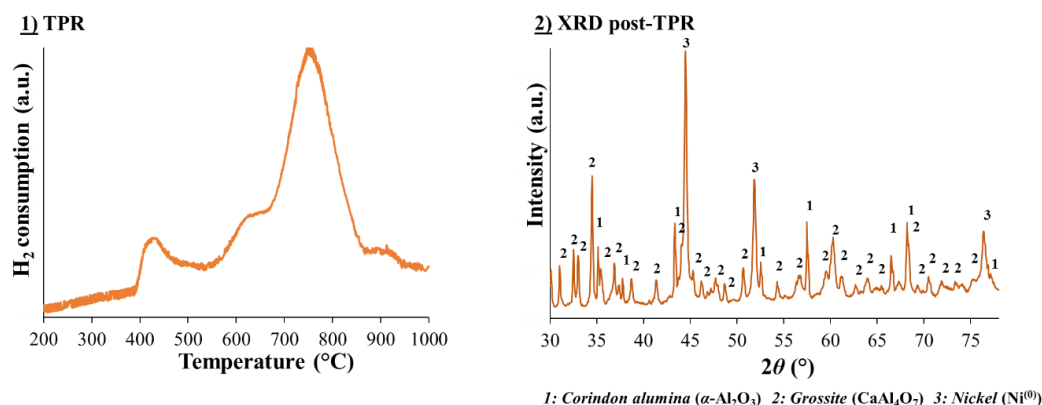
Figure VIII.2: TPR profile (left side) and post-TPR XRD spectrum (right side) of sample *Hifuel*.

Table VIII.4: Ni particles sizes after reduction and after TPR measurements.

Sample	After reduction			After TPR		
	d_{TEM} (nm)	σ_{TEM} (nm)	d_{XRD} (nm)	d_{TEM} (nm)	σ_{TEM} (nm)	d_{XRD} (nm)
Hifuel	26	15	23	32	26	34

d_{TEM} : metallic particles size median; σ_{TEM} : standard deviation; d_{XRD} : metallic nickel crystallites size estimation obtained by XRD.

It can be observed in Table VIII.4 that, after H₂ reduction step, sample *Hifuel* presented large Ni particles sizes ($d_{TEM} = 26$ nm and $d_{XRD} = 23$ nm) with a broad distribution of size ($\sigma_{TEM} = 15$ nm). After TPR measurement, the Ni particles became larger ($d_{TEM} = 32$ nm and $d_{XRD} = 34$ nm), with a very high σ_{TEM} value (26 nm). It was asserted that the large particles sizes and sensibility against sintering observed for sample *Hifuel* were caused by two simultaneous facts: 1) a low microporous texture, which did not prevent the migration of the metallic particles; 2) the presence of a high amount of bulk NiO, which is known to easily sinter because of its low interactions with the alumina support.

VIII.3.2. Long-term tests

Figure VIII.3 shows the toluene conversion, C_{Tolu} , as a function of time for samples *N-10Ni*, *N-10Ni-2Mn-2Mo*, *N-10Ni-1.5Ca-1.5K®*, *N-10Ni-1.5Ce-1.5K®* and *Hifuel*. Figure VIII.4 shows the DSC measurements performed on the samples after catalytic tests. The metallic particles sizes, the type of metallic phase present after tests and the catalytic performances of the samples are resumed in Table VIII.5.

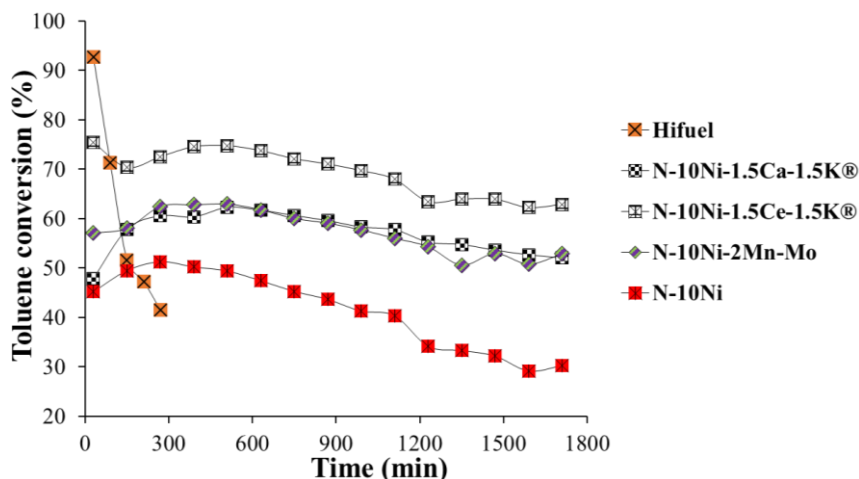
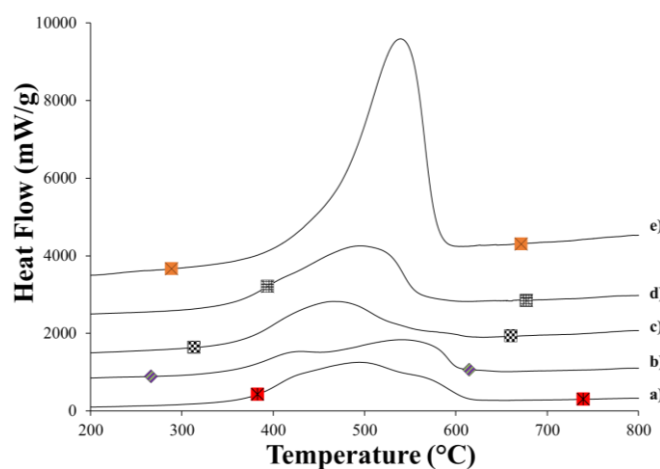


Figure VIII.3: Toluene conversion as a function of time for long-term tests.

Table VIII.5: Metallic particles sizes, metal alloy phases and catalytic performances of catalysts during long-term tests. Test conditions: $T = 650\text{ }^{\circ}\text{C}$, $t = 30\text{ h}$, 24.000 ppmv of toluene, $GHSV = 5000\text{ h}^{-1}$.

Samples	Particules size			Metal phase	Catalytic performances				
	d_{TEM} (nm)	σ_{TEM} (nm)	d_{XRD} (nm)		C_{Tolu} (%)	C_{CH_4} (%)	S_B (%)	Coke (g _{Carbon} /g _{Cata})	Fil. carbon
N-10Ni	12	4	12	Ni	50 → 30	12 → 14	12 → 7	0.20	+
N-10Ni-2Mn-2Mo	12	2	10	Ni _{0.97} Mo _{0.03}	59 → 52	11 → 10	7 → 7	0.19	+
N-10Ni-1.5Ca-1.5K®	12	5	12	Ni	59 → 53	10 → 14	5 → 4	0.19	+
N-10Ni-1.5Ce-1.5K®	16	7	12	Ni	72 → 63	13 → 8	4 → 3	0.28	+
Hifuel	30	16	25	Ni	90 → 42	-3 → -3	10 → 58	0.96	+++
	Note: Test with <i>Hifuel</i> stopped at $t = 300\text{ min}$ because of too high pressure ($P = 1\text{ bar}$)								

d_{TEM} : metallic particles size median; σ_{TEM} : standard deviation; d_{XRD} : metallic crystallites size estimation obtained by XRD; C_{Tolu} : conversion of toluene; S_B : selectivity of benzene, C_{CH_4} : conversion of methane; *Coke*: carbon deposit amount after 5 h of test measured by TG-DSC. For all samples excepted *Hifuel*, the catalytic activity values (C_{Tolu} , S_B , C_{CH_4}) were determined by making an average of the values between $t = 60\text{--}300\text{ min}$, and between $t = 1500\text{--}1740\text{ min}$. For sample *Hifuel*, the values were obtained by doing the average of the 5 first injections and of the 5 last injections.

Figure VIII.4: DSC curves after long-term catalytic tests; a. *N-10Ni*, b. *N-10Ni-2Mn-2Mo*, c. *N-10Ni-1.5Ca-1.5K®*, d. *N-10Ni-1.5Ce-1.5K®*, e. *Hifuel* (stopped at $t = 300\text{ min}$).

Observations of Figure VIII.3 and Table VIII.5 revealed that sample *N-10Ni* showed a slow deactivation during the catalytic test ($\Delta C_{Tolu} = -20\%$). However, it was noticed that, for similar test conditions, the catalyst showed very similar properties after $t = 30\text{ h}$ of catalytic test compared to after $t = 5\text{ h}$ of test (see Chapter VII). Indeed, after a long-term test, sample *N-10Ni* showed small Ni⁽⁰⁾ particles sizes (d_{TEM} and d_{XRD} of 12 nm) with a narrow distribution of size ($\sigma_{TEM} = 4\text{ nm}$), and its amount of carbon deposit was only multiplied by 2 (after $t = 30\text{ h}$ of test: *Coke* = 0.20 g_{Carbon}/g_{Cata}; whereas after $t = 5\text{ h}$ of test: *Coke* = 0.10 g_{Carbon}/g_{Cata}).ⁱ Furthermore, Figure VIII.4-a evidenced that, similarly as after $t = 5\text{ h}$ of catalytic test, the carbon deposit of sample *N-10Ni* was mostly composed of amorphous carbon (burned at $T < 550\text{ }^{\circ}\text{C}$). It was also noticed that the X-Ray spectrum (not shown here) obtained after a long-term test did not show any alteration of the γ -Al₂O₃ phase. These observations were very positive. Indeed, since the crystallinity and the metallic dispersion of this sample were correct, and that sample *N-10Ni* only presented amorphous carbon after $t = 30\text{ h}$ of catalytic test, regeneration steps (by injection of air or H₂O) could be planned in the future in order to reactivate the catalyst.ⁱⁱ

ⁱ : *Coke* value after $t = 5\text{ h}$ of catalytic test at $T = 650\text{ }^{\circ}\text{C}$ in Table VII.4.

ⁱⁱ : More details about operations of regeneration in part I.4.3. of Chapter I.

In the case of samples *N-10Ni-2Mn-2Mo*, *N-10Ni-1.5Ca-1.5K®* and *N-10Ni-1.5Ce-1.5K®*, it appeared that the doping of 10 wt. % Ni/ γ -Al₂O₃ catalysts effectively reduced the loss of catalytic activity ($\Delta C_{Tolu} < -9\%$, whereas $\Delta C_{Tolu} = -20\%$ for sample *N-10Ni*). Furthermore, all samples presented low amounts of carbon deposits (*Coke* = 0.19 g_{Carbon}/g_{Cata} for samples *N-10Ni-2Mn-2Mo* and *N-10Ni-1.5Ca-1.5K®*, and *Coke* = 0.28 g_{Carbon}/g_{Cata} for sample *N-10Ni-1.5Ce-1.5K®*) and kept relatively low Ni⁽⁰⁾ particles sizes (Table VIII.5). Since these samples mostly presented amorphous carbon deposits, they are also good candidates for future catalytic tests performed with a regeneration step.

It was observed in Figure VIII.3 that sample *Hifuel* showed a very high initial C_{Tolu} , followed by a quick and intense deactivation ($\Delta C_{Tolu} = -50\%$ after $t = 300$ min). The formation of coke for this sample was so important that it increased the pressure drop inside the reactor and obliged us to stop the test at $t = 300$ min. DSC (Figure VIII.4-e) and TEM measurements (not shown) performed after test evidenced that nearly the entire carbon deposit was of filamentous type. These results have to be correlated to what was obtained for the Ni/ γ -Al₂O₃ catalysts studied in Chapter V (samples *IMP-N-10Ni*, *N-30Ni* and *N-50Ni*) and in Chapter VI (*N-10Ni-PS-eth*). Hence, the strong deactivation observed for sample *Hifuel* was attributed to a combination of detrimental influences. First, sample *Hifuel* presented large amounts of bulk NiO. This type of nickel oxide being reduced at low temperatures ($T \sim 450$ °C), it was not able to take advantage of the anti-coking effect brought by the mechanism of “special reduction by toluene”.ⁱ Furthermore, because of its high catalytic activity and its low interactions with the support, NiO was quickly deactivated. Its low interactions with the support also make it more inclined to form large Ni⁽⁰⁾ particles by sintering, which would also favor the formation of filamentous carbon. It was assumed that this last effect was reinforced by the fact that sample *Hifuel* showed a very low micro- and mesoporous texture (Table VIII.3). Though the high amount of CaO might increase the rate of adsorption-dissociation of the H₂O and CO₂ molecules, the very low specific surface area showed by sample *Hifuel* ($S_{BET} = 20$ m²/g, Table VIII.3) reduced the surface available for these reactions to take place. Finally, the presence of large mesopores (evidenced in Figure VIII.1) could have favored the formation of coke for two reasons hypothesized in Chapter VI: 1) the increase of the diffusion of the reactants through the catalyst might have reinforced the disequilibrium between the reaction rates of toluene cracking and those of gasification; 2) the presence of very large pores might not have prevented the formation of filamentous carbon.ⁱⁱ

Hence, despite the catalyst *Hifuel* having shown interesting performances for the steam reforming of various compounds (glycerol, ethanol, methane ...) [351], and also of toluene (noteworthy in less intense conditions: only 5000 ppmv of toluene and a high H₂O/C ratio equal to 2) [26], it appears that this catalyst must be proscribed for tar reforming applications. Though the tests performed in all the chapters of this work used a concentration of toluene much higher than in common conditions (usually, tar concentration between 1000-10.000 ppmv), it is

ⁱ : More information about mechanism of “special reduction by toluene” in Chapter V.

ⁱⁱ : More details about the influences of macroporous texture on the catalytic performances for sample *N-10Ni-PS-eth* in Chapter VI.

assumed that if sample *Hifuel* cannot be resistant against deactivation by coking in presence of toluene, it would probably be also deactivated in presence of high deactivating tars such as naphthalene or pyrene.^[46]

VIII.3.3. Catalytic performances in sulphidic conditions

Figure VIII.5 shows the two types of tests performed to determine the performance of sample *N-10Ni* in sulphidic environments: a standard reforming test interrupted with pulses of 200 ppmv of H₂S (sample *N-10Ni-Pulse-H2S*) or a standard catalytic test with injection of 40 ppmv of H₂S (sample *N-10Ni-Cont-H2S*). The evolution of the catalytic performances during the tests, and the sizes of the metallic nickel particles determined by XRD and TEM measurements after catalytic tests are presented in Table VIII.6. Figure VIII.6 shows the DSC curves obtained after catalytic tests.

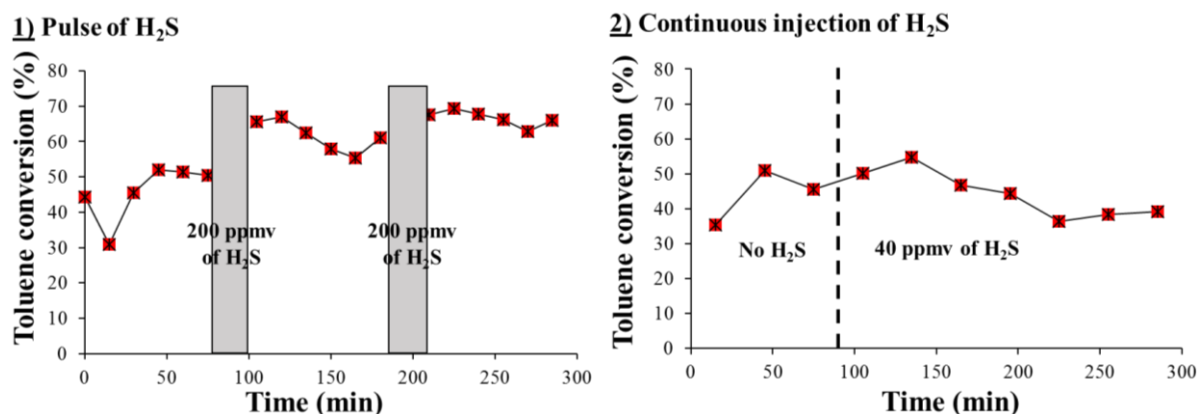


Figure VIII.5: Toluene conversion as a function of time in sulphidic environments. On the left side: pulses of 200 ppmv of H₂S; on the right side: continuous presence of 40 ppmv of H₂S.

Table VIII.6: Ni particles sizes and catalytic performances of sample *N-10Ni* tested with pulses of 200 ppmv of H₂S or with continuous injection of 40 ppmv of H₂S. Test conditions: $T = 650\text{ }^{\circ}\text{C}$, $t = 5\text{ h}$, 24.000 ppmv of toluene, $GHSV = 5000\text{ h}^{-1}$.

Samples	Ni particles sizes			Catalytic performances				
	d_{TEM} (nm)	σ_{TEM} (nm)	d_{XRD} (nm)	C_{Tolu} (%)	C_{CH4} (%)	S_B (%)	Coke (gCarbon/gCata)	Fil. carbon
<i>N-10Ni</i> (classic test)	11	3	12	51	10	15	0.10	No
<i>N-10Ni-Pulse-H2S</i>	12	6	11	49→63	7→10	17→7	0.14	+
<i>N-10Ni-Conti-H2S</i>	14	8	12	48→37	7→1	12→10	0.11	+

d_{TEM} : metallic particles size median; σ_{TEM} : standard deviation; d_{XRD} : metallic crystallites size estimation obtained by XRD; C_{Tolu} : conversion of toluene; S_B : selectivity in benzene; C_{CH4} : conversion of methane; *Coke*: carbon deposit amount after 5 h of test measured by TG-DSC. The catalytic activity values (C_{Tolu} , S_B , C_{CH4}) were determined by making an average of the values obtained during the 5 first injections and during the 5 last injections.

X-Ray measurements were performed after both catalytic tests (not shown here). For both tests, the spectra only presented rays of γ -Al₂O₃ and of Ni⁽⁰⁾, and no nickel sulfide rays (such as NiS or Ni₃S₂) were observed. It was assumed that either these species were not present, because of regeneration reactions (Equations VIII.3 and VIII.4), or that these species only covered the Ni⁽⁰⁾ particles, and hence were in insufficient amounts to be detected by X-Ray diffraction.

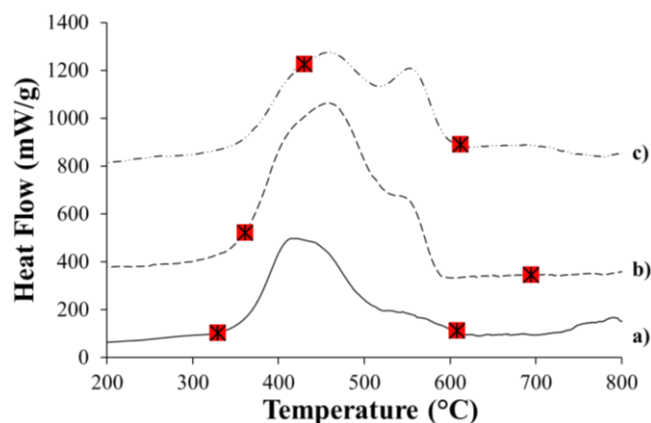


Figure VIII.6: DSC curves after catalytic tests performed in presence of H₂S: a. *N-10Ni* (classic test), b. *N-10Ni-Pulse-H2S*, c. *N-10Ni-Conti-H2S*.

It is observed for sample *N-10Ni-Pulse-H2S* (Figure VIII.5), that after the first pulse of H₂S, the conversion of toluene was considerably increased ($\Delta C_{Tolu, before. 1st. H_2S. pulse / after. 1st. H_2S. pulse} = + 15 \%$). This observation suggests that the injection of a mixture of H₂S (200 ppmv)/He increased the reduction of the catalysts via the Equation VIII.1 and that, once the syngas was reinjected, the NiS species were regenerated by the H₂ and H₂O compounds via Equations VIII.3 and VIII.4. This hypothesis lies in the fact that sample *N-10Ni-Pulse-H2S* presented a high C_{CH_4} value at the end of the test (10 %, Table VIII.6), and that the conversion of methane is usually more affected by sulphide deactivation than the conversion of tars.^[65] Furthermore, the higher C_{Tolu} value and the lower S_B value of sample *N-10Ni-Pulse-H2S* suggested that more nickel was catalytically active.

It was noticed that sample *N-10Ni-Pulse-H2S* presented similar d_{TEM} and d_{XRD} values as during a classic catalytic test (Table VIII.6). This observation is interesting, since Ni-S compounds are more inclined to sinter than pure Ni⁽⁰⁾.^{[79], [81]} However, sample *N-10Ni-Pulse-H2S* presented a broader metallic particle size ($\sigma_{TEM} = 6$ nm) compared to what was observed during a classic test ($\sigma_{TEM} = 3$ nm for sample *N-10Ni*). The presence of some larger Ni⁽⁰⁾ particles, evidenced by the higher σ_{TEM} value, could explain why a small part of filamentous carbon was observed in the DSC curve of sample *N-10Ni-Pulse-H2S* (Figure VIII.6-b).ⁱ

In the case of sample *N-10Ni-Conti-H2S* (Figure VIII.5), it was observed that the addition of 40 ppmv of H₂S led to a slight increase of the C_{Tolu} value during the first $t = 45$ min of tests. Here also, it was assumed that the addition of H₂S increased the reduction of Ni. However, from $t = 135$ min to the end of the test, the C_{Tolu} value slightly decreased ($\Delta C_{Tolu, before H_2S / end of test} = - 11 \%$). This influence was more visible for the methane conversion since the C_{CH_4} value dropped to 1 % at the end of the test. These observations suggested that a partial deactivation of the surface of the Ni⁽⁰⁾ particles occurs by the formation of Ni-S compounds. Furthermore, though d_{TEM} and d_{XRD} values remained small, sample *N-10Ni-Conti-H2S* showed a broad distribution of metallic particles sizes ($\sigma_{TEM} = 8$ nm, Table VIII.6), which led to a higher formation of filamentous carbon evidenced in the DSC curve (Figure VIII.6-c). In that case, the fact that the

ⁱ: Relations between metallic particles sizes and formation of carbon detailed in part I.4.4.4. of Chapter I.

sample was more inclined to sinter was attributed to the formation of Ni-S compounds, whose Tamman's temperatures are lower than pure Ni⁽⁰⁾. [79], [81]

Hence, in that case, instead of protecting the Ni⁽⁰⁾ particles from coking by “ensemble control” effect,ⁱ the presence of H₂S did in contrary favor the formation of filamentous carbon. This difference could be explained by the fact that most of the studies highlighted this phenomenon for methane reforming^{[65], [87]}, which occurs according to slightly different mechanisms than those involved during the reforming of tars.

Finally, it was noticed that the loss of catalytic activity for the reforming of toluene was relatively small for sample *N-10Ni-Conti-H2S* compared to what can be observed in the literature for this amount of H₂S and at this temperature.ⁱⁱ The following hypotheses were set to explain the very good resistance against deactivation by H₂S: 1) the Ni particles having strong interactions with the γ -Al₂O₃ support (NiAl₂O₄ evidenced by TPR in Figure V.2), it would facilitate the migration of the O* and HO* species from the support to the Ni⁽⁰⁾ particles. This would increase the reaction of regeneration of the deactivated sites Ni-S (Equations VIII.3 and VIII.4); 2) this effect could be emphasized by the fact that the catalyst was tested at the boundary between the oxidation and the reduction of Ni.

VIII.4. CONCLUSIONS

This chapter permitted to evaluate the catalytic performances of the most promising Ni/ γ -Al₂O₃ catalysts developed throughout this project in more severe conditions (long-term tests or presence of H₂S) and to compare their performances with a commercial nickel-based steam reforming catalyst for the reforming of 24.000 ppmv of toluene.

It was observed that the sol-gel prepared 10 wt. % Ni/ γ -Al₂O₃ catalyst presented a low but progressive deactivation throughout the 30 h of test. However, the post-test characterizations revealed that this sample kept very small Ni⁽⁰⁾ particles with a narrow size distribution, did not show any alteration of the crystallinity of the γ -Al₂O₃ support and only presented amorphous carbon. These observations were positive since they opened the way for future catalytic tests performed with regeneration steps.

All 10 wt. % Ni/ γ -Al₂O₃ catalysts doped with Mn+Mo, Ca+K or Ce+K showed better resistance against deactivation than pure 10 wt. % Ni/ γ -Al₂O₃ catalyst. Furthermore, as these samples also kept interesting properties after $t = 30$ h of catalytic tests, they are also potential candidates for regeneration steps.

It was hypothesized that the slow deactivation observed for all Ni/ γ -Al₂O₃ catalysts, tested in long-term conditions, might be the consequence of an insufficient temperature of calcination. Indeed, since the calcination was performed at $T = 550$ °C and that the catalytic test was performed at $T = 650$ °C, a part of Ni could progressively be incorporated inside the γ -Al₂O₃ lattice (to form catalytically inactive NiAl₂O₄ spinel), which would explain a progressive

ⁱ : More details about “ensemble control” effect due to H₂S presence in Figure I.9.

ⁱⁱ: More details of studies in presence of H₂S in part I.4.3.2.1. of Chapter I.

deactivation of the catalytic activity. This hypothesis was strengthened by the fact that the catalysts did not seem to be deactivated neither by the formation of carbon deposit, nor by the sintering of the metallic particles. This assumption would also explain why the deactivation was lower for doped catalysts. Indeed, it was shown in previous studies that the presence of dopants (Mn, Mo, Ca or K) can reduce the tendency of Ni to be incorporated into a NiAl₂O₄ spinel.

The strong and quick deactivation observed for sample *Hifuel* confirmed the importance of designing catalysts with metal/support interactions adapted to the conditions of test, in order to take advantage of the anti-coking effect brought by the “mechanism of special reduction by toluene” described in Chapter V.

The 10 wt. % Ni/ γ -Al₂O₃ catalyst revealed to be only slightly affected by the presence of H₂S in the syngas mixture. This was attributed to two facts: 1) the Ni particles having strong interactions with the γ -Al₂O₃ support, it would facilitate the migration of the O* and HO* species from the support to the Ni⁽⁰⁾ particles, and increase the reaction of regeneration of the deactivated sites Ni-S; 2) this effect could be emphasized by the fact that the catalyst was tested at the boundary between the oxidation and the reduction of Ni.

General conclusions and perspectives

This work is an essential step in the advancement of the research pursued at the *Department of Chemical Engineering – Nanomaterials, Catalysis, Electrochemistry* for the development of aqueous sol-gel methods for the synthesis of alumina-based catalysts and for the use of catalysts during the gasification of biomass.

Processes of biomass gasification and of catalytic purification of the bio-syngas were presented. Furthermore, it was shown how the conditions of gasification (nature of the feedstock, temperature, water concentration, pressure, contact time ...) strongly influence the final properties of the bio-syngas and the performances of the catalysts. Moreover, the mechanisms involved during the catalytic conversion of tars and how the catalysts can be deactivated during these catalytic tests are detailed. Finally, a large inventory of the types of catalysts used for the reforming of tars was performed, which represents a source of inspiration for the development of future catalysts.

The development of a simple and convenient sol-gel method for the preparation of alumina-based catalysts is one major achievement of this thesis. In this way, an aqueous sol-gel method using simple and non-toxic reagents ($\text{Al}(\text{NO}_3)_3$, NH_4OH and H_2O) was performed. Indeed, it has been shown that under adequate conditions of synthesis (*pH*, long agitation step and temperature of calcination), the use of $\text{Al}(\text{NO}_3)_3$ leads to reproducible $\gamma\text{-Al}_2\text{O}_3$ supports with higher porous textural values and similar crystallography as when *Al-sec*-butoxide was used.

The sol-gel process developed in this work also allowed the modification of $\gamma\text{-Al}_2\text{O}_3$ via silicon alkoxide precursors. The first modification of $\gamma\text{-Al}_2\text{O}_3$ was performed with a functionalized silicon precursor, 3-(2-aminoethylamino)propyltrimethoxysilane, called EDAS. It was shown that $\gamma\text{-Al}_2\text{O}_3$ supports presented platelet-like crystallites with sizes of about 4.4 nm and a broad mesopore size distribution (from 2 to 30 nm). In contrary, the addition of EDAS leads to $\gamma\text{-Al}_2\text{O}_3\text{-SiO}_2$ crystallites of smaller sizes (about 3.3 nm) and with spherical shapes, which leads to a distribution of mesopore sizes centered on 4 nm. It was shown that an increase of the amount of EDAS leads to smaller $\gamma\text{-Al}_2\text{O}_3\text{-SiO}_2$ crystallites and to a shift of the mesopore sizes distribution towards lower values. However, the incorporation of EDAS inside the alumina crystallites was limited to a maximal value situated around 14 wt. % of SiO_2 . The addition of EDAS before or just after the precipitation step leads to $\gamma\text{-Al}_2\text{O}_3\text{-SiO}_2$ supports with similar properties, whereas the addition of EDAS after a long time of agitation leads to $\gamma\text{-Al}_2\text{O}_3\text{-SiO}_2$ supports whose properties were more similar to pure $\gamma\text{-Al}_2\text{O}_3$. It was deduced that the modification of the crystallites of boehmite ($\gamma\text{-AlOOH}$) mainly occurs during the step of dissolution-reorganization of $[\text{Al}(\text{OH})_3]_n$ clusters which takes place during the agitation of the

sols. γ - Al_2O_3 supports were also synthesized with non-functionalized silicon precursors of different reactivity (tetramethoxysilane, TMOS; or tetraethoxysilane, TEOS), with a functionalized silicon precursor constituted of three methoxy groups as for EDAS, but with a smaller functionalized chain length (3-aminopropyltrimethoxysilane, APTMS), or with silicon precursors constituted of three methoxy groups as for EDAS, but with different alkyl chain lengths (trimethoxypropylsilane, TOPS; or trimethoxyoctylsilane, TOOS). These studies permitted to highlight that the reactivity of the silicon precursor, caused by the presence of methoxy or ethoxy groups, influences the crystallography of the γ - Al_2O_3 - SiO_2 supports. In this way, supports synthesized with silicon precursors containing methoxy groups showed a high incorporation of Si atoms into the bulk alumina. This modification permitted to increase the resistance of the support against sintering at high temperatures ($T = 700$ - 1200 °C) and under steam conditions ($T = 700$ °C, 10 vol. % H_2O). Furthermore, a better incorporation of Si atoms inside the bulk alumina also permitted to delay the phase transition of γ - Al_2O_3 into α - Al_2O_3 which occurs at high temperatures ($T > 1000$ °C). In contrary, it was shown that the modification of the shape of the alumina crystallites, which leads to samples with different pore sizes distributions, was only caused by the presence of a functional chain in the silicon precursors. In this way, a γ - Al_2O_3 support modified with APTMS showed smaller spherical crystallites and consequently a narrow mesopore sizes distribution shifted towards lower values (3 nm) compared to a γ - Al_2O_3 support modified with EDAS. Hence, the synthesis of boehmite functionalized with a silicon precursor can be performed thanks to a simple aqueous sol-gel method, which could be a useful alternative to classic grafting methods, which require toxic organic solvents and strictly anhydrous conditions.

In the case of the reforming of 8000 ppmv of toluene under primary catalytic conditions ($T = 750$ - 850 °C), it appeared that the catalysts made of olivine were more performant than those constituted of γ - Al_2O_3 for similar amounts of metal doping (2 wt. % Ni or 10 wt. % Fe). For the catalysts made of γ - Al_2O_3 , the low loading of Ni leads to the formation of a NiAl_2O_4 spinel, which prevented the formation of $\text{Ni}^{(0)}$ nanoparticles, and the doping with Fe favored the phase transition of γ - Al_2O_3 into α - Al_2O_3 . The olivine being a more interesting primary catalyst by its price and its catalytic performances, it seemed more interesting to focus on the development of catalysts tested in secondary conditions.

The aqueous sol-gel method developed during this work proved to be efficient for the synthesis of homogeneous Ni/ γ - Al_2O_3 catalysts which kept high specific surface area and pore volume values with Ni loadings up to 50 wt. %. In the case of 10 wt. % Ni/ γ - Al_2O_3 catalysts, the sol-gel method only leads to the formation of NiAl_2O_4 , whereas the impregnation method leads to the formation of nickel oxides which showed different interactions with the support (NiO , $\text{NiO}/\text{Al}_2\text{O}_3$ and NiAl_2O_4). Though the reduction of the catalysts entirely composed of NiAl_2O_4 only started at $T = 680$ °C during TPR measurements performed with H_2 , in contrary, this sample was reduced during the catalytic reforming of 24.000 ppmv of toluene at $T = 650$ °C. It was calculated that under these conditions of test, toluene is a better reducing agent than H_2 or CO , and that the reduction of nickel located inside the NiAl_2O_4 spinel by the toluene

enables its conversion to syngas with a very little formation of coke. This phenomenon was called “special reduction by toluene”. However, this phenomenon did not prevent the formation of coke if the catalyst also showed bulk NiO (reduced at low temperatures $T \sim 450$ °C). In this case, a quick deactivation of the catalyst by formation of carbon deposit appeared. The catalytic tests performed at $T = 900 \rightarrow 600$ °C permitted to confirm that the kinetic values obtained were similar to those encountered in the literature ($E_a = 252$ kJ/mol for quartz grains, 110 kJ/mol for pure γ -Al₂O₃ support and 80 kJ/mol for the 10 wt. % Ni/ γ -Al₂O₃ catalyst). These tests also showed that, whereas the methane reforming was mostly influenced by the presence of metallic particles, the toluene reforming was in contrary influenced by both the metallic particles and the support. According to these tests, it seemed more interesting to continue the catalytic test at $T = 650$ °C without a pre-reduction step, thus in order to take advantage of the anti-coking effect brought by the phenomenon of “special reduction by toluene”.

While most of surfactant-assisted synthesis methods follows organic sol-gel routes, it was shown that Ni/ γ -Al₂O₃ catalysts could be tailored during the aqueous sol-gel synthesis via the addition of a common surfactant (stearic acid). The use of stearic acid with different conditions (step of addition, solvents) permitted to synthesize 10 wt. % Ni/ γ -Al₂O₃ catalysts with identical compositions, but with different micro-, meso- and macroporosity. These samples highlighted the influences of the textural properties on the reducibility of the catalysts and on the size of the Ni⁽⁰⁾ particles. In this way, 10 wt. % Ni/ γ -Al₂O₃ catalysts with higher microporosity were reduced at lower temperatures and presented smaller Ni⁽⁰⁾ particles with narrow distribution of sizes. Furthermore, a high microporosity of the samples decreased the sintering rate of the Ni⁽⁰⁾ particles, especially at high temperatures ($T \sim 1000$ °C). In contrary, it was shown that an increase of the mesoporous volume without an increase of the microporous volume leads to catalysts which showed broader Ni reduction peaks and Ni⁽⁰⁾ particles with broader distribution of sizes.

When tested for the reforming of 24.000 ppmv of toluene at $T = 650$ °C, compared to a standard catalyst, a Ni/ γ -Al₂O₃ catalyst modified with stearic acid showed a reaction rate for toluene reforming multiplied by 2, but a tendency to form carbon deposit multiplied by 6. The higher catalytic activity was attributed to a better diffusion of the gaseous reagents inside the porosity of the catalyst. It was hypothesized that the much higher sensibility towards deactivation by coking may be the consequence of a combination of several facts: 1) a better diffusion of the reagents, which favored the reaction of toluene cracking to the detriment of the gasification of the carbonaceous compounds; 2) the reduction of Ni at lower temperatures, which avoided to take advantage of the anti-coking effect brought by the phenomenon of “special reduction by toluene”; 3) the presence of large pores, which did not prevent the growth of filamentous carbon.

The vast screening performed with 10 % Ni/ γ -Al₂O₃ catalysts doped with metals (Cu, Mn, Fe, Mo or Mn) or oxides (CaO, K₂O, MgO or CeO₂) permitted to select the dopants the most adequate in order to increase the catalytic activity and the resistance against coking. Among the simple doping (2 wt. % of metal or 1.5 wt. % of oxide), it appeared that Mn, Mo, Ca and K are

the most interesting elements. According to the literature, all these elements favor the mechanisms of adsorption-dissociation of H₂O and CO₂ molecules, which leads to a better gasification of the carbonaceous deposits at the surface of the Ni⁽⁰⁾ particles. Tested at $T = 650$ °C, the catalysts doped with higher loadings (4 wt. % of Mn or Mo / 3 wt. % of Ca or K) showed lower catalytic activity, but very good resistance against coking. This was attributed to the high covering of the Ni⁽⁰⁾ particles by the dopant oxides. In contrary, when tested at $T = 900 \rightarrow 600$ °C, these samples did not show such interesting anti-coking properties. Worse, the high loading of K increased the sintering of Ni⁽⁰⁾ particles, which leads to the formation of filamentous carbon, while the high loading of Mo leads to the formation of molybdenum carbide. In contrary, when tested at $T = 650$ °C or at $T = 900 \rightarrow 600$ °C, 10 % Ni/ γ -Al₂O₃ catalysts doped with two elements (Co+Mo, Mn+Mo, Ca+K or Ce+K) showed a high catalytic activity and a high resistance against coking.

Tested during long-term catalytic tests ($t = 30$ h), the 10 wt. % Ni/ γ -Al₂O₃ catalyst showed a slow deactivation which was more important compared to 10 wt. % Ni/ γ -Al₂O₃ doped with Mn+Mo, Ca+K or Ce+K. The fact that all the catalysts presented low amounts of carbon deposit and small metallic particles sizes after test, suggested that the slow deactivation observed might be due to a progressive incorporation of Ni inside the γ -Al₂O₃ lattice (to form catalytically inactive NiAl₂O₄ spinel). This hypothesis is strengthened by the fact that the presence of dopants (Mn, Mo, Ca or K) is known to reduce the tendency of Ni to be incorporated into a NiAl₂O₄ spinel.

A 10 wt. % Ni/ γ -Al₂O₃ catalyst was tested in presence of H₂S during the toluene reforming test. It was shown that 10 wt. % Ni/ γ -Al₂O₃ catalysts were only slightly deactivated (loss of toluene conversion of 10 % after 2 h) by the presence of 40 ppmv of H₂S. This good resistance was attributed to the fact that the catalysts initially presented only Ni particles with strong interactions with the γ -Al₂O₃ support (NiAl₂O₄). The strong interactions with the support could facilitate the migration of the O* and HO* species from the support to the Ni⁽⁰⁾ particles, and increase the reaction of regeneration of the Ni-S deactivated sites. It was also assumed that the presence of H₂S slightly influenced the conversion of toluene because the catalysts were tested at the boundary between the oxidation and the reduction of Ni.

Hence, the most promising catalysts might be suitable for industrial applications.

PERSPECTIVES

In line of the results obtained during this thesis and in the aim of developing suitable catalysts for the reforming of tars at the exit of the biomass gasifiers, several points could be investigated:

* It was shown in Chapter V that the high resistance against deactivation by coking of 10 wt. % Ni/ γ -Al₂O₃ catalysts was mostly attributed to the phenomenon of “special reduction by toluene”. However, excepted the works of Cheng *et al.*^{[280], [281]}, no other studies mentioned this phenomenon. Hence, further investigations are of utmost importance in order to get a better understanding and to optimize the advantageous effects brought by this phenomenon;

* It appeared that the addition of Mn, Mo, Ca and K permitted to increase the catalytic activity and to reduce the coking of 10 wt. % Ni/ γ -Al₂O₃ catalysts. Starting from these four elements, it could be interesting to look for new synergistic combinations such as: one metal + one oxide, one metal + two oxides, two metals + one oxide, two metals + two oxides. It would be also essential to get a finer comprehension of the influences of these elements thanks to other characterization techniques (X-Ray Photo-electron Spectroscopy (XPS), Low Energy Ion Spectroscopy (LEIS), STEM associated to EDX, Steady State Isotopic Transient Kinetics Analysis (SSTIKA), H₂O and CO₂ adsorption microcalorimetry ...);

* After a long-term test ($t = 30$ h), the most promising Ni/ γ -Al₂O₃ catalysts still presented low metallic particles, γ -Al₂O₃ phase and a low amount of carbon which was only composed of amorphous carbon. These reasons make us believe that a regeneration step (with H₂O or air) could allow the recovering of the catalytic performances without the destruction of the structure of the catalysts. Indeed, the development of catalysts easily regenerated is a crucial step for their utilization at larger scale;

* Given that the calcination of the Ni/ γ -Al₂O₃ catalysts studied in this thesis was performed at $T = 550$ °C, while the catalytic test was performed at $T = 650$ °C, it would be adequate, in order to increase the stability, to study Ni/ γ -Al₂O₃ catalysts with a temperature of calcination equal or superior to $T = 650$ °C. However, the calcination procedure and the loading of Ni should be meticulously chosen in order to only form a NiAl₂O₄ phase and to continue to take advantage of the anti-coking advantage brought by the phenomenon of “special reduction by toluene”;

* Though the catalytic activity of 10 wt. % Ni/ γ -Al₂O₃ was relatively stable in presence of H₂S, the decisive aspect of the development of catalysts resistant against deactivation by sulphidation necessitates more investigations on the subject. Hence, catalytic tests should be performed with a continuous presence of higher concentrations of H₂S and for longer times. Furthermore, it could be interesting to test if the dopants improve the resistance of the Ni/ γ -Al₂O₃ catalysts towards H₂S poisoning;

* In order to test the catalysts in conditions as close as possible to the real conditions encountered at the exit of a biomass gasifier, it would be necessary to perform the catalytic tests

with other aromatic compounds than toluene (naphthalene, pyrene ...). Furthermore, it could be also interesting to evaluate the performances of catalysts poisoned with typical fly-ashes elements (Cl, Zn, Na ...);

* It was shown in Annex 6 that 10 wt. % Ni/ γ -Al₂O₃ catalysts modified with EDAS slightly favored the dispersion of Ni⁽⁰⁾ particles compared to a classic 10 wt. % Ni/ γ -Al₂O₃ catalyst. This was mainly due to the fact that Ni supported on γ -Al₂O₃ requires high temperatures of reduction, which lowers the initially better dispersion of metallic particles. However, it could be interesting to study the influence of the addition of EDAS on the properties and catalytic performances of 10 wt. % Ni/ γ -Al₂O₃ doped with one or two metals. Indeed, it is suspected that the addition of EDAS could modify the formation of Ni-based alloys;

* As detailed in Chapter VI, the texture also plays a crucial role on the catalytic performances of Ni/ γ -Al₂O₃ catalysts. Hence, it would be interesting to study how other types of surfactant (Pluronic[®], Brij[®] ...) can tailor the texture of the catalysts. The final objective would be a Ni/ γ -Al₂O₃ catalyst which would show a high reaction rate of toluene (thanks to an open texture) and which would be at the same time resistant against coking (e.g. thanks to adequate doping or calcinations);

* In order to use the reforming catalysts inside reactors with high dimensions, it would be interesting to develop an efficient method for the coating of Ni/ γ -Al₂O₃ catalysts on monolithic supports. This subject, introduced in Annex 7, is also a crucial step for the use of the catalysts in real conditions.

Annexes

Annex 1:

Additional information relative to Chapter I

Annex 2:

Formulae, characterization techniques, calculations, amount of reagents and X-Ray references

Annex 3:

Experimental installation used for catalytic tests

Annex 4:

Additional information relative to Chapter VII

Annex 5:

Complementary study about the optimization of operating variables for the synthesis of γ -Al₂O₃ based catalysts

Annex 6:

Complementary study about 10 wt. % Ni/ γ -Al₂O₃ catalysts modified with different silicon precursors

Annex 7:

Complementary study about the coating of honeycomb cordierite support with Ni/boehmite gels

Annex 1: Additional information relative to Chapter I

I. COMPLEMENTARY INFORMATION TO PART I.2

I.1. Figures

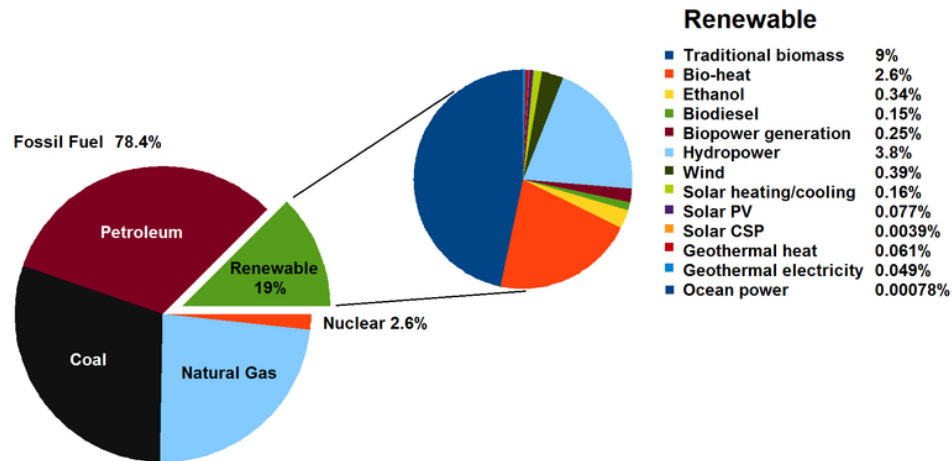


Figure A1.1: Total global energy consumption by source in 2013.^[353]

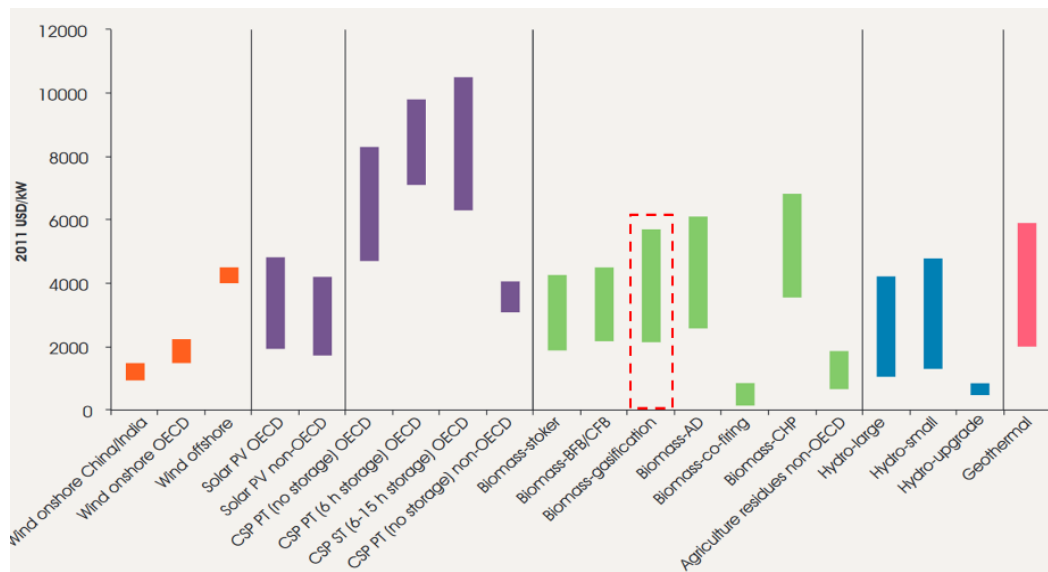


Figure A1.2: Typical cost ranges for renewable power generation technologies.^[354]

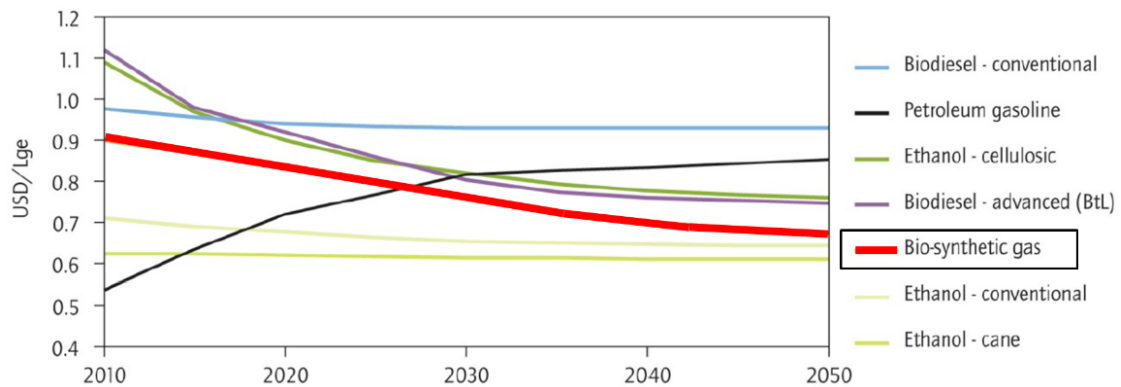


Figure A1.3: Projected costs of biofuels compared to petroleum gasoline, 2010-2050^[15]. *N.B.*: Lge stands for litres of gasoline equivalent.

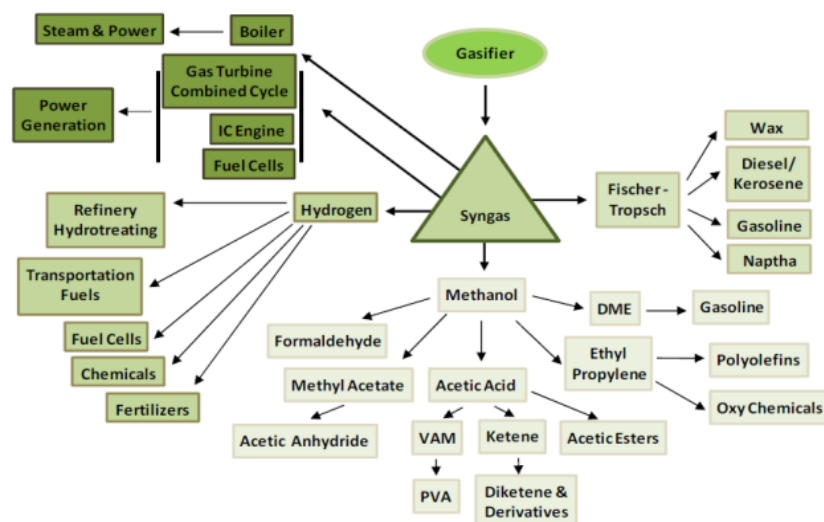


Figure A1.4: Gasification output pathways^[1]. *N.B.*: DME stands for dimethyl ether, VAM stands for vinyl acetate monomer and PVA stands for polyvinyl acetate.

I.2. Physico-chemical transformations

Three main technologies of physicochemical transformations can be distinguished: oil extraction, fermentation and anaerobic digestion.

The oil extraction from plants is made through mechanical processes.^[2] A typical example is the colza oil extraction which can then be converted into biodiesel via transesterification reactions using an alcohol (usually methanol or ethanol).^[355] In the case of fermentation, the starch and the cellulose are converted into primary alcohols thanks to bacteria. The alcohols are then extracted via distillation processes.^{[356], [357]} The anaerobic digestion, also called “bio-methanization”, differs from the classic fermentation since the process takes place without oxygen. The gaseous product obtained is therefore called “biogas” which is a mixture of methane, CH₄ (50 to 75 %), and carbonic gas, CO₂ (25 to 50 %). The biogas can be used as a substitute for natural gas after purification.^[358] This is currently the most developed industrialized bio-energy technology since in the year of 2011, 8000 Bio-Methanizer installations were in function in the E.U..^[14]

I.3. Other thermo-chemical transformations than gasification

Combustion processes

Combustion is the most obvious and the oldest method to create energy from biomass. During combustion, material is burned in the presence of oxygen and converted into CO₂ and H₂O while releasing energy. By definition, combustion reactions are always exothermic. During these processes, three main steps occur: drying, pyrolysis and combustion. During the drying step, the humidity of the samples is released using temperatures between $T = 120$ °C and $T = 200$ °C. At temperatures up to $T = 600$ °C, pyrolysis and reduction steps decompose the organic matter into carbonaceous residues and volatile compounds. Finally, between $T = 700$ °C and $T = 1400$ °C, the combustion steps consist in the oxidation of the combustible gas and the carbonaceous residues into CO₂ and H₂O.^{[10], [17]}

Pyrolysis processes

Pyrolysis is rperformed at high temperatures ($T = 400$ - 700 °C) without the use of oxygen. Thus, the biomass is converted into char, liquids (bio-oils) and gas.^[11] The obtained products strongly depend on the process operating parameters (temperature and time). One major advantage of these methods is the storage and carrying capacity in case of solid and liquid products. From a technical point of view, these processes can be considered as mature and are currently being developed at an industrial scale.^{[359], [360]}

The first stage of the pyrolysis consists in a pre-pyrolysis step ($T = 120\text{-}200\text{ }^{\circ}\text{C}$) during which the biomass undergoes internal rearrangements such as the breaking of chemical bonds, appearance of free radicals, formation of carbonyls groups, water evaporation and production of CO and CO₂. The pyrolysis step can be divided into two paths: 1) the “slow pyrolysis” is used to create solid chars, which can be used for household purposes (cooking, heating), raw carbon for the chemistry field and as active charcoal for adsorption uses. The “slow pyrolysis” operating parameters are characterized by a low temperature ($T = 400\text{ }^{\circ}\text{C}$) and high residence times (hours or days); 2) the “fast pyrolysis” or “flash-pyrolysis”, is characterized by higher operating temperatures ($T = 450\text{-}550\text{ }^{\circ}\text{C}$) and very short residence times (seconds).^[11] These operating parameters lead to the production of bio-oils. These bio-oils, usually showing a high calorific power (15-20 MJ/kg), are generally mixed with classic fuel for “liquid combustible” purposes.^[360] Other valorizations of these bio-oils become growingly interesting: the bio-oils can be washed with water in order to separate the water soluble and non-soluble compounds. The molecules present in the washing solutions (mainly acetic acid and acetone) are then converted into syngas via classic steam reforming processes, whereas the non-soluble phases, mainly composed of phenolic compounds, are used as raw materials for the synthesis of phenolic resins.^{[359], [360]}

II. COMPLEMENTARY INFORMATION TO PART I.3

II.1. Types of biomass gasifiers

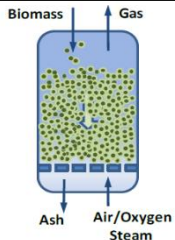
Updraft fixed bed		<p>Biomass is fed at the top of the gasifier. Air/oxygen/steam is injected countercurrently. Some of the resulting chars falls and burns to provide heat. The gas rich in methane and tars leaves at the top of the gasifier and the ash falls from the grate at the bottom.^{[11], [19], [36], [42]}</p> <p>⇒ Not attractive because of their high tar levels ($> 100\text{ g/m}^3$).</p> <p>Ex.: Harboøre (Denemark)^c,^[422]</p>
--------------------------	--	---

Table A1.1: Updraft fixed bed. *p*: pilot installation; *c*: commercial installation.

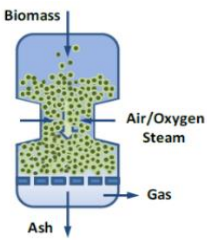
Downdraft fixed bed		<p>Biomass is fed at the top of the gasifier. Air/oxygen/steam is injected on the top or on sides, hence biomass and gases move in the same direction. The gases pass through a flaming pyrolysis step and a charcoal bed. This leads to a low tar amount ($< 5\text{ g/m}^3$) and almost no secondary tar.^{[11], [19], [42]}</p> <p>⇒ - : Only for small scale application ($< 2\text{ MWh}$).</p> <p>⇒ + : Good Syngas quality / Simple processing.</p> <p>Ex.: Xylowatt[®] (Belgium)^c,^[423], Carmarthen^c (U.K.).^[424]</p>
----------------------------	---	--

Table A1.2: Downdraft fixed bed. *p*: pilot installation; *c*: commercial installation.

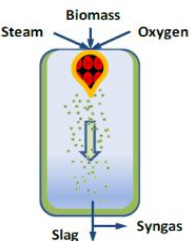
Entrained flow		<p>Powdered biomass is fed at the top of the gasifier with oxygen/steam. Turbulent flame at the top burns the biomass at high temperatures ($T \sim 1300\text{ }^{\circ}\text{C}$). Ashes and slags are collected at the bottom.</p> <p>⇒ - : Biomass must be finely milled / Injection of pure oxygen.</p> <p>⇒ + : Able to process high quantity by day / High quality syngas.^{[9], [11], [19]}</p> <p>Ex.: Köpling (Sweden)^c,^[425], ECN (Netherlands) gasifier^p,^[426]</p>
-----------------------	---	--

Table A1.3: Entrained flow bed. *p*: pilot installation; *c*: commercial installation.^[19]

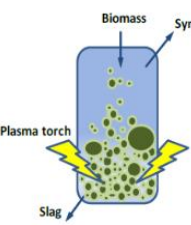
Plasma reactor		<p>Untreated biomass is fed at the top, coming into contact with electric generated plasma at atmospheric pressure and high temperature ($T = 1500\text{-}5000\text{ }^{\circ}\text{C}$)</p> <p>Biomass is converted to syngas and ashes are transformed into inert slags.</p> <p>⇒ - : Various technical problems during functioning / High costs / More R&D needed.</p> <p>⇒ + : No biomass pretreatments / High Syngas quality.^{[11], [19]}</p> <p>Ex.: Madison, Pennsylvania (USA)^p.^[19]</p>
-----------------------	---	--

Table A1.4: Plasma reactor. *p*: pilot installation; *c*: commercial installation.

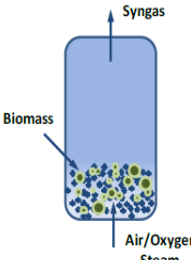
Bubbling fluidized bed		<p>Fine bed of inert material (ex.: sand) at the bottom is agitated with air/oxygen/steam. Biomass is fed from the sides, mixed and combusted at temperatures below $T = 900\text{ }^{\circ}\text{C}$ to avoid ashes melting. Syngas is evacuated at the top.^{[9], [11], [19]}</p> <p>⇒ - : Biomass must be finely milled / Injection of pure oxygen.</p> <p>⇒ + : Able to process high quantity by day / Very high quality syngas.</p> <p>Ex.: Gothenburg (Sweden)^{c [425]}, Skive (Denemark)^{p [19]}</p>
------------------------	---	--

Table A1.5: Bubbling fluidized bed. *p*: pilot installation; *c*: commercial installation.

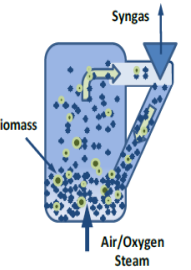
Circulating fluidized bed		<p>Fine bed of inert material (ex.: sand, olivine) is suspended throughout the reactor with air/oxygen/steam. Biomass is fed from the sides and burns to provide heat or reacts to form Syngas. The mixture of syngas and particles is separated using a cyclone at the top. Temperatures are below $900\text{ }^{\circ}\text{C}$ to avoid ashes melting.^{[9], [11], [19]}</p> <p>⇒ - : Heat transfer less efficient than in bubbling reactor / Equipment erosion due to attrition.</p> <p>⇒ + : Adapted for large installations (up to 100 MWh).</p> <p>Ex.: Varnamo (Sweden)^{c [427]}, ECN (Netherlands)^{p [426]}, VTT (Finland)^{c [19]}</p>
---------------------------	---	---

Table A1.6: Circulating fluidized bed. *p*: pilot installation; *c*: commercial installation.

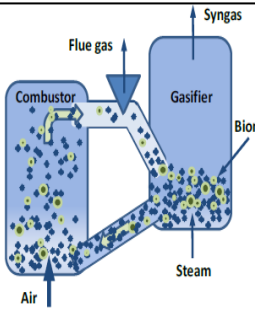
Dual fluidized bed		<p>The system has two chambers: a gasifier and a combustor. Biomass is fed in the gasification chamber and converted into nitrogen-free syngas and char using steam. The char is burnt in air in the combustion chamber and provides heat to the inert particle bed (sand, olivine). The particles are fed back to the gasification chamber, providing the heat. A cyclone remove the flue gas (N_2) whereas the syngas is evacuated upward the gasifier. Temperature are below $900\text{ }^{\circ}\text{C}$ to avoid ashes melting.^{[9], [11], [19]}</p> <p>⇒ - : Equipment erosion due to attrition.</p> <p>⇒ + : Adapted for high installation (up to 100 MWh) / Nitrogen-free Syngas with high LHV</p> <p>Ex.: Gussing (Austria)^{c [428]}</p>
--------------------	--	---

Table A1.7: Dual fluidized bed. *p*: pilot installation; *c*: commercial installation.

II.2. Influences of experimental parameters on the final bio-syngas composition

Influences of feedstock

Couto *et al.*^[37] evaluated the gasification of biomass residues of different origins (rice husk, nut shell, vine pruning, eucalyptus and pine) and concluded that the biomass feedstock does not have a strong influence on the final syngas composition. Paradoxically, Hanaoka *et al.*^[361] showed that the air-steam gasification of the main woody biomass compounds (cellulose, xylan and lignin) do not show the same ability to be converted and do not lead to the same final syngas composition. Cellulose was the easiest convertible compound compared to xylan and lignin, with a conversion reaching 98, 92 and 53 % respectively. However, the H_2/CO ratio was the highest for xylan and lignin (1.3 and 1.2), whereas cellulose was showing the lowest ratio (0.8). Barneto *et al.*^[362] observed that the composting of biomass increased the lignin content in the compost, which increased the H_2 production up to 20%. Pinto *et al.*^{[23], [24]} studied the co-gasification of mixtures of different feedstock (pine wastes, coal and polyethylene). According to the authors, the addition of coal or polyethylene did not cause any technical problems. The addition of PE apparently favored the formation of gaseous hydrocarbons and tars whereas the addition of coal leads to the release of higher NH_3 contents. In both cases, the association of coal or PE with biomass permitted to decrease the concentration of hydrocarbons (- 63 %), to increase production of H_2 (+ 70 %) and therefore to produce a syngas with a higher LHV.

Based on similar technologies, the gasification of raw plastic wastes is a field becoming growingly interesting since it would constitute an appropriate method to take advantage of undesirable plastic wastes. However, this subject needs to be studied more thoroughly before commercialization.^{[20]-[22]}

Influences of the temperature

Many studies showed that a temperature increase tends to decrease the global tar amount at the gasifier outlet.^{[6], [24], [363], [364]} Nevertheless, at high operating temperatures, the remaining tars are essentially heavy polyaromatic hydrocarbons which are very difficult to reduce.^[365] Indeed, compounds containing oxygen such as phenol exist in significant amounts only at temperatures below $T = 800$ °C, whereas the destruction of aromatic hydrocarbons occurs only above $T = 850$ °C.^[363] Furthermore, one can notice that a decrease of up to 40 % of tar formation was reported when the temperature was raised from $T = 700$ °C to $T = 900$ °C.^[366]

Narvaez *et al.*^[6] studied the effect of temperature ($T = 700$ - 850 °C) in a bubbling fluidized bed on the final syngas. They reported that when the temperature increased from $T = 700$ to $T = 850$ °C, the H_2 concentration increased from 5 to 10 %, the CO concentration increased from 12 to 18 % and the CO_2 concentration decreased from 16 to 14 %. It was also reported that the LHV of the produced gas was slightly increased thanks to the increase of the H_2 and CO content. Moghtaderi *et al.*^[367] confirmed that the gasification below $T = 600$ °C was absolutely useless, since below that temperature, the CH_4 production is much more favored than the generation of H_2 .

More generally, it has been proved that the reaction of coke with water and CO_2 is thermodynamically more favorable at higher temperatures, producing CO and H_2 .^[127] However, a too high temperature may have a negative effect on the H_2 yield due to the inversion of the Water-Gas shift reaction at $T > 850$ °C, thus decreasing the final syngas heating value.^[37] Therefore, the internal maximum temperature for a fluidized bed gasifier seems to be situated around $T = 850$ °C. It is to notice that the complete conversion of tars into gas without any catalysts would require operating temperatures up to $T = 1100$ °C.^[42]

Gasifying reactants

Two major operating ratios have to be taken into account for a defined biomass flow rate: the equivalence ratio (Equation A1.1) for the air gasification applications and the steam to biomass ratio (Equation A1.2) for the steam gasification applications.

$$ER = \frac{\left(\frac{Air_{kg}}{Dry\ Biomass_{kg}} \right)_{Actual}}{\left(\frac{Air_{kg}}{Dry\ Biomass_{kg}} \right)_{Stoichiometric}} \quad (A1.1)$$

The equivalence ratio (ER) (Equation A1.1) is defined as the actual air to biomass weight ratio divided by the stoichiometric air to biomass weight ratio needed for complete combustion.^[6] A high degree of combustion occurs at high ER which supplies more air into the gasifier and improves the burning of char and tars to produce CO_2 instead of combustible gases such as CO, H_2 , CH_4 and C_nH_m . A too high ER value results in a lower concentration of H_2 , CO and higher CO_2 , thus decreasing the LHV of the gas.^[5] However, studies have shown that a too small ER is also unfavorable for biomass gasification because the combustion reactions are not favored, thus decreasing the heat which is needed for other endothermic reactions.^[368] Narvaez *et al.*^[6] showed that the amount of tars can be divided by 3 when increasing the ER from 0.25 to 0.50, however, the LHV of the gas was decreased from 6 to 4 MJ.m³. Therefore, an ER optimum value in biomass gasification ranges from 0.2–0.4.^{[5], [6]} When the produced gas is burnt in downstream furnaces, tar compounds are not a serious problem and the gas should have a high heating value. Therefore, the gasifier can be operated at a minimum ER of about 0.2. In case of temperatures lower than $T = 850$ °C, the tar yield is high and the ER should be increased to about 0.3–0.4 to compensate such negative effects.^{[5], [6]}

$$S. B. = \frac{Steam_{(kg/h)}}{Dry\ Biomass_{(kg/h)}} \quad (A1.2)$$

The steam to biomass ratio (SB) (Equation A1.2) is defined as the flow rate of the steam fed into the gasifier divided by the biomass flow rate. It is one of the most important process parameters involved in steam gasification.^[369] Raising the SB ratio increases H₂ and CO₂ yields and decreases the CO and CH₄ yields, thus, raising the LHV value of the exit gas. These results can be explained as a consequence of the reactions involved in this process, mainly Water-Gas shift and steam reforming of tars and methane.^{[7], [8]}

More than allowing a significant tar reduction, addition of water also strongly modifies the tar composition. Indeed, raising the SB ratio is known to decrease the formation of high aromatic compounds and to increase the formation of phenolic compounds.^[370] This is a huge advantage since these compounds are much easier to reform with catalysts.^[42] In this way, Narvaez *et al.*^[6] showed that a strong decrease of the tar content (from 20 to 5 g/m³) can be obtained when the SB ratio is increased from 1.6 to 2.2 at $T = 800$ °C.

All optimum SB ratios advised in literature are situated between 1.3 and 4.^{[6], [8], [9]} In the case of a SB > 4, the LHV and carbon conversion are decreased due to the low reaction temperature caused by the addition of steam. According to some economic evaluations, the best SB ratio tends to be situated around 2.5.^[9]

Influences of gasifying pressure

According to the review carried out by Couto *et al.*^[37], pressurized gasification operations usually create more problems than they solve. Indeed, in that case biomass feeding becomes more complex and very costly, and requires a high inert gas for purging. Although equipment sizes are much smaller, pressurized gasification systems can cost up to four times more than atmospheric systems.^[37] These processes become only relevant in case of large installations (30-50 MWh), in which the exiting gas does not need to be compressed for further combustion in turbines.^[37] Increasing the pressure leads to similar gas compositions, and LHVs. Although the total amount of tars decreases, raising the pressure favors the formation of stable PAH compounds.^[371]

Influences of gasification time

According to Delgado *et al.*^[119], the residence time has a little influence on the tar yield, but it significantly influences the tar composition. Indeed, it was found that increasing the contact time results in less O₂ containing compounds, less 1- and 2- ring compounds but more 3- and 4- ring compounds in the total tar fraction. A study conducted by the Energy research Centre of the Netherlands concludes that increasing the gas residence time in a hot zone has similar effects as raising the temperature.^[365]

III. COMPLEMENTARY INFORMATION TO PART I.4

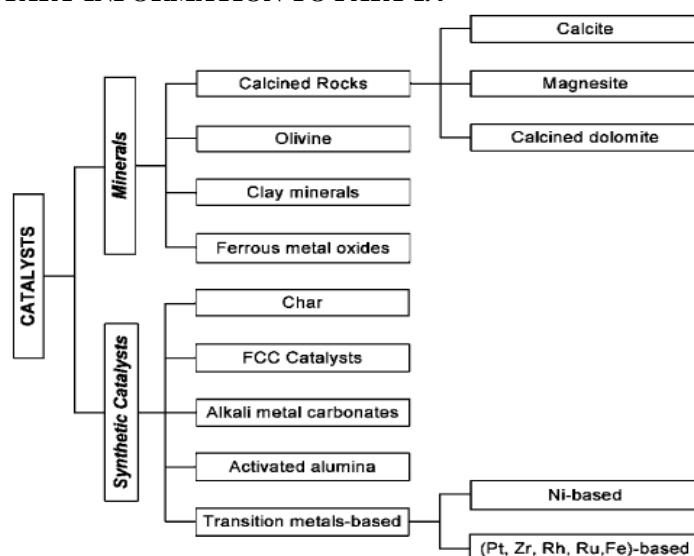


Figure A1.5: Classification and types of catalysts used for tar elimination.^[47]

Annex 2: Formulae, characterization techniques, calculations, amount of reagents and X-Ray references

I. FORMULAE

Toluene conversion:

$$C_{Tolu} = \frac{C_{rt,Tolu,In} - C_{rt,Tolu,Out}}{C_{rt,Tolu,In}} * 100 \quad (A2.1)$$

where $C_{rt,Tolu,In}$ is the initial toluene concentration (mol/m³) and $C_{rt,Tolu,Out}$ is the toluene concentration at the outlet of the reactor (mol/m³).

Benzene selectivity:

$$S_B = \frac{C_{rt,Benz,Out}}{C_{rt,Tolu,In} - C_{rt,Tolu,Out}} * 100 \quad (A2.2)$$

where $C_{rt,Benz,Out}$ is the outlet concentration of benzene (mol/m³), $C_{rt,Tolu,In}$ is the initial toluene concentration (mol/m³) and $C_{rt,Tolu,Out}$ is the toluene concentration at the outlet of the reactor (mol/m³).

Methane conversion:

$$C_{CH4} = \frac{C_{rt,CH4,In} - C_{rt,CH4,Out}}{C_{rt,CH4,In}} * 100 \quad (A2.3)$$

where $C_{rt,CH4,In}$ is the initial methane concentration (mol/m³) and $C_{rt,CH4,Out}$ is the methane concentration at the outlet of the reactor (mol/m³).

Toluene reaction rate:

Since the reaction rate was assumed to be of first order ($n = 1$), r_{Tolu} (mol_{Tolu}/(g_{Ni}.h)) can be expressed as follows^{[283], [284]}:

$$r_{Tolu} = \left(-\frac{F_{Tolu}}{W} \right) \ln(1 - f_{Tolu}) \quad (A2.4)$$

where F_{Tolu} is the molar flowrate of toluene at the reactor inlet (mol_{Tolu}/h), W is the nickel mass inside the reactor (g) and f_{Tolu} is the toluene conversion ($f_{Tolu} = C_{Tolu}/100$).

Yield of methane:

$$Y_{Tolu \rightarrow CH4} = \frac{n_{CH4,Out}}{7 * n_{Tolu,In} - (7 * n_{Tolu,Out} + 6 * n_{Benz,Out})} \quad (A2.5)$$

where $n_{Tolu,In}$ is the initial amount of toluene (mol), and $n_{Tolu,Out}$, $n_{Benz,Out}$, $n_{CH4,Out}$ are respectively the amount of toluene, benzene and methane at the exit of the reactor (mol). It is to notice that this yield did not take into account the carbon deposit and could only be used as an estimation value.

Tendency to form coke:

$$Coke^* = \frac{Coke}{r_{Tolu} * \left(\frac{\%Ni}{100} \right) * t * M_{Tolu}} \quad (A2.6)$$

where $Coke$ is the amount of carbon deposit determined from TG-DSC measurements (g_{Carbon}/g_{Cata}), ($\%Ni/100$) is the gramm of nickel by gramm of catalyst, determined from ICP-AES measurements, r_{Tolu} is the consumption rate of toluene (mol_{Tolu}/(g_{Ni}.h)), t is the time of test (h) and M_{Tolu} is the molecular mass weight of toluene (92.1 g_{Tolu}/mol_{Tolu}).

II. CHARACTERIZATION TECHNIQUES

Inductively Coupled Plasma Atomic Emission Spectroscopy (ICP-AES)

ICP-AES were performed on ICAP 6500 THERMO Scientific device by CELABOR. Before, gel samples were crushed to a powder below 100 μ m and dissolved in hydrofluoric acid, lithium tetraborate or aqua regia. Element loadings were obtained by comparison with standard solutions in the same medium.

Dynamic Light Scattering (DLS)

The Dynamic Light Scattering Apparatus used in this work was a Viscotek 802 DLS instrument. The sols were diluted 30X in MilliQ water and put 5 min on ultra-sound in order to eliminate the presence of air bubbles. Dynamic light scattering (DLS) is a technique, which allows to obtain the particle hydrodynamic size distribution of a liquid dispersion from the nanometer to the micrometer range.

Viscosimeter (Visco.)

Viscosity measurements were performed on a DV-2+ Pro Brookfield viscometer at 10, 20, 50 and 100 rpm on a S61 or S62 spindle to ensure that the measured torque was superior to 10 %. Solutions were poured in a 100 mL graduated cylinder to allow immersion of the spindle to the required level. To avoid border effect, the spindle was also placed at the center of the graduated cylinder.

The measurement consists in the rotation of a spindle at a fixed speed in a fluid and the measurement of the amount of torque required to maintain the speed as viscous forces impede the rotation. It translates into torsion of a spring inside the apparatus, proportional to the fluid viscosity. Apparent viscosity (shear stress divided by shear rate, expressed as mPa.s or centipoise, cP) was then recorded.

Point of Zero Charge (PZC)

PZC measurements were performed by powder addition method by adding crushed cordierite or 1 mL of sample *N-10Ni* sol to 10 mL flasks filled with deionized water, with a *pH* adjusted between *pH* 1 and 12 with NaOH and HCl. The flasks were stirred for $t = 2$ h and the *pH* was measured.

As the hydroxyl surface groups of the powder protonate and deprotonate, the number of protons within the solution decreased or increased and the final *pH* changed. The hydroxyl surface groups of the powder assumed the role of a buffer and providing that sufficient surface groups were available, the solution reached equilibrium. On a plot of initial *pH* versus final *pH*, a plateau value is observed and corresponds to the PZC point.

pH measurements

pH measurements were done using a Consort P901 device, calibrated once a day before use. The *pH* probe was kept in a KCl solution and thoroughly washed with tap water prior to every measurement.

Transmission Electron Microscopy (TEM)

Transmission electron microscopy analyses were performed on a CM10-PW6020 Philips Electron Microscope. First, crushed samples were dispersed in absolute ethanol. Then a drop of the dispersion was placed on a copper grid (Formvar/Carbon 200 Mesh Cu from Agar Scientific). For a higher quality of the pictures, the vacuum lines were cooled with liquid N₂ $t = 30$ min before the measurements.

TEM measurements permitted to get information about the nanostructure of the supports, the type of carbon deposits and the dispersion of the metallic nanoparticles. The metallic particle size median (d_{TEM}) and the standard deviation (σ_{TEM}) were obtained from 100 measurements made on 5 different grains. The basic advantage of the median in describing data compared to a simple average is that it is not skewed so much by extremely large or small values of particle sizes, and so it may give a better idea

of a 'typical' value.^{[372], [373]} Figure A2.1 illustrates the different between the mean and the median value for two distributions of values with a different standard deviations σ .

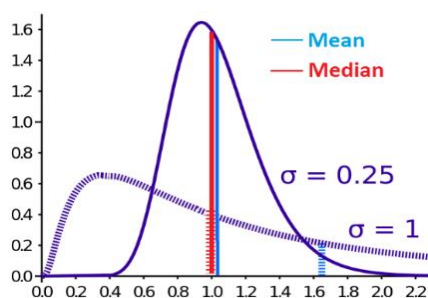


Figure A2.1: Comparison of mean and median of two log-normal distributions with different standard deviation.

Scanning Electron Microscopy (SEM)

Scanning Electron Microscopy measurements were performed with a FEI ESEM-FEG XL3 device. Pictures made with secondary Electron (SEM-GSE) detectors permitted to get a basic information about the surface of the samples. Pictures made with Backscattered Electron (SEM-BSE) detectors permitted to get a view of the surface of the samples, with different contrasts depending on the elemental composition. Energy Dispersive X-ray analyses (SEM-EDX) were also performed with the same apparatus in order to determine the elemental composition of a defined a surface (400x300 μm) and to build up element mapping pictures. The measurements were performed at an acceleration voltage of 15 keV, set on the Spot 4 and with a vacuum of 0.4 Torr. No previous metallization of the samples was necessary.

Mercury porosimetry (Poro-Hg)

Mercury porosimetry measurements were performed on monoliths samples crushed between 300 and 700 μm using a Poremaster60 instrument from Quantachrome with pressures going from 1 to 60000 Psi. The measurements permitted to determine the macroporous volume (V_{Hg} , cm^3/g), to plot the curves of volume introduced as a function of the pressure and to plot the macropore size distribution.

Nitrogen-adsorption-desorption measurements (BET)

Nitrogen adsorption-desorption isotherms were measured at $T = -196$ °C on a Micromeritics ASAP 2010 instrument after $t = 12$ h of outgassing at $T = 300$ °C and $P = 10^{-5}$ Pa.

The total specific surface area (S_{BET} , m^2/g) and mesoporous surface area (S_{meso} , m^2/g) were determined by the Brunauer-Emmet-Teller (BET) theory on the part of the nitrogen adsorption curves for p/p_0 values from 0.05 to 0.3. The Dubinin volume ($V_{Dubinin}$, cm^3/g) corresponds to the sample microporous volume and was calculated using the Dubinin-Raduskevitch model^[229]. The pore volume at saturation pressure (V_p , cm^3/g) and the pore size distributions were determined by a home-made informatic programs which applied the Broekhoff de Boer theory (BdB) to the adsorption profile-branch of the nitrogen isotherms. The pore volume density is defined by the pore volume (cm^3/g) as a function of the pore size (nm).

Helium pycnometry (Pycno-He)

Apparent density (ρ , g/cm^3) was measured by using helium pycnometry with a Micromeritics AccuPyc 1330 at $T = 25$ °C. The density was determined from an average of six consecutive measurements. According to IUPAC recommendations for the characterization of porous solids, the apparent density of an object is defined as the density of that object including closed pores.^[231] The effective density or true density, ρ_{Eff} , in g/cm^3 , is defined as the density of an object excluding pores. The ρ_{Eff} values were calculated by dividing the mass of the catalyst bed by the catalytic bed volume inside the quartz tube ($\text{Ø} = 8$ mm, $h = 12$ mm), for sieved grains (average Ø of 500 μm) and assuming that the

grains were sphere-like and closed-packed at the highest ratio (0.74). Figure A2.2 depicts the apparent density, ρ , and the effective density, ρ_{Eff} .

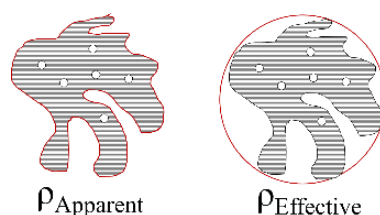


Figure A2.2: Scheme of effective and apparent density.

²⁷Al Nuclear Magnetic Resonance (²⁷Al NMR)

All solid-state NMR experiments were performed with a Bruker Avance I spectrometer at an operating ¹H Larmor frequency of 400.13 MHz, using a Bruker 4 mm HXY probe in double resonance mode at a spinning frequency of 10 kHz. ²⁷Al one-pulse experiments were acquired using a pulse length of duration 2.5 μ s. A total of 1024 co-added transients were acquired for each spectrum, using a recycle delay of 1 s. All spectra were referenced to AlCl₃ at 0 ppm. The ²⁷Al NMR measurements permitted to give information about the crystallography of γ -Al₂O₃ materials and γ -Al₂O₃ materials modified with SiO₂. Chapter III gives an explanation about how to interpret the ²⁷Al NMR spectra.

Reduction with hydrogen (H₂ reduction)

H₂ reduction steps were performed by putting 1 g of catalyst inside a cylindrical quartz tube inserted inside a metallic reactor, which was itself placed inside a tubular oven. The reactor was first purged with helium at room temperature ($t = 15$ min, 50 mL/min), then a hydrogen flux was sent to the sample (50 mL/min) and the temperature was increased (from $T = 25^\circ\text{C}$ to $T = 750^\circ\text{C}$ with a heating rate of $5^\circ\text{C}/\text{min}$). After $t = 1$ h at $T = 750^\circ\text{C}$, the heating was stopped and the reactor was purged with helium (50 mL/min).

Temperature Programmed Reduction (TPR)

Temperature Programmed Reduction measurements were performed with a TPD/R/O 1100 device from CE instruments. An amount of 0.2 g of catalyst was put in a tube quartz. Samples were heated from $T = 25^\circ\text{C}$ to $T = 1000^\circ\text{C}$ with a heating rate of $2^\circ\text{C}/\text{min}$ and under a flow of 20 mL/min of a gas mixture (5 % vol. H₂/95 % vol. N₂). The measurement of the H₂ consumption thanks to a TCD device situated inside the instrument permitted to give information about the reduction of the metallic species (Ni, Fe ...) present in the samples.

Temperature Programmed Desorption (TPD-NH₃)

The surface acidity measurements were obtained on a Temperature Programmed Desorption (TPD) performed on a AutoChem II 2920 instrument from Micromeritics. The measurements were performed according to the following steps: first, the samples were heated from $T = 25^\circ\text{C}$ to $T = 600^\circ\text{C}$ with a heating rate of $10^\circ\text{C}/\text{min}$ and under an air flow of 50 mL/min. These conditions were maintained for 1 h at $T = 600^\circ\text{C}$. Then, the samples were purged with a He flow of 50 mL/min and the heating was stopped until the temperature reached $T = 100^\circ\text{C}$. At $T = 100^\circ\text{C}$, an ammonia gas mixture (5 % vol. NH₃/95 % vol. He) was injected with a flow-rate of 50 mL/min during 1 h. Thereafter, the sample was purged once more with 50 mL/min of He for 30 min. Finally, a slow heating rate was applied ($2^\circ\text{C}/\text{min}$, $T = 100$ - 600°C) under He (50 mL/min). The TPD-NH₃ curves were determined from this last operating step. The amount of ammonia by gram of catalysts (V_{NH_3} , mmol_{NH₃}/g) desorbed during the TPD-NH₃ measurements were determined by comparing the area under the peaks with a calibration performed on the instrument.}

Thermogravimetric-Differential Scanning Calorimetry (TG-DSC)

TG-DSC measurements were performed on a Sensys Setaram instrument. 0.05 g of the samples were crushed and introduced into an alumina crucible. The samples were heated from $T = 25\text{ }^{\circ}\text{C}$ to $T = 800\text{ }^{\circ}\text{C}$ with a heating rate of $2\text{ }^{\circ}\text{C}/\text{min}$ under air (20 mL/min).

The TG curves permitted to determine the mass loss with increasing temperature, due for example as the evacuation of water during the boehmite to $\gamma\text{-Al}_2\text{O}_3$ phase transformation, and to determine the amount of carbon deposit (*Coke*, $\text{g}_{\text{Carbon}}/\text{g}_{\text{Cata}}$) on a sample after a catalytic test. The DSC curves permitted to show some phase transition (for example boehmite to $\gamma\text{-Al}_2\text{O}_3$) and to get a better view of the nature of carbon deposit after the catalytic tests.

X-Ray Diffraction (XRD)

X-ray diffraction measurements were performed on a Bruker D8 Twin-Twin diffractometer (Cu- $K\alpha$ Radiation). The samples were crushed, and the measurements were performed between $2\theta = 30$ and $2\theta = 80$ degrees with a step time of 18 s and a step size of 0.04 s. The determination of the crystalline phases and of the crystallite sizes were performed thanks to the Eva software. The crystallite sizes (d_{XRD} , nm) were estimated using the Scherrer equation^[374] showed below:

$$\tau = \frac{K\lambda}{\beta \cdot \cos\theta} \quad (\text{A2.7})$$

where τ is the mean size of the ordered (crystalline) domains, which may be smaller or equal to the grain size; K is a dimensionless shape factor, with a value close to unity; λ is the X-ray wavelength; β is the line broadening at half the maximum intensity (FWHM), after subtracting the instrumental line broadening, in radians. This quantity is also sometimes denoted as $\Delta(2\theta)$; θ is the Bragg angle.

Note about large differences observed between d_{TEM} and d_{XRD} values

Though d_{TEM} presents a median value and d_{XRD} presents a mean value, it happens sometimes that $d_{\text{TEM}} > d_{\text{XRD}}$. This phenomenon is usually observed after high temperature treatments (which includes sintering of the nanoparticle) and is explained by the fact that, in that case, the particles are constituted of clusters of single-crystals which different domains (Figure A2.3)^{[375]–[377]}.

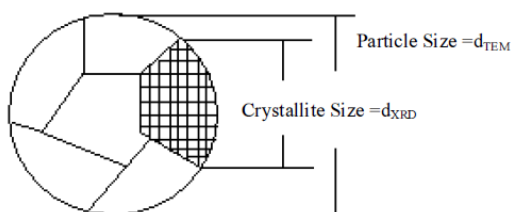


Figure A2.3: Illustration showing the difference of particle size obtained by TEM or XRD.^[375]

III. ESTIMATION OF DIFFUSIONAL LIMITATIONS

The diffusion of the reactants throughout the pores of a catalyst is an important fact to take in consideration since the reaction rate and the activation energy observed may be greatly skewed in the case of diffusional limitations and may need calculus adjustments.^{[308], [309]} Figure A2.4 shows the two type of diffusion ranges. External diffusion concerns the diffusion from the gas phase to the surface of the catalyst pellet. Internal diffusion concerns the diffusion of the reactants throughout the internal pores of the catalyst. The Weisz modulus number, which is the ratio between the reaction rate and the diffusion rate, permit to confirm if the catalysts are in chemical or diffusion range.^{[308], [309]}

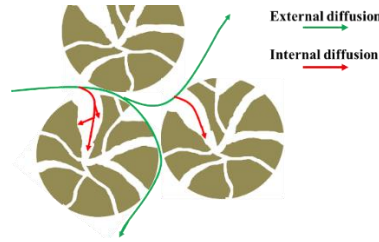


Figure A2.4: External and internal diffusion ranges.

In the aim of highlighting the presence of diffusional limitations, sample *N-10Ni* of Chapter V was tested under several conditions: 1) in order to detect internal diffusional limitations, some tests were performed with standard conditions, but with different grain sizes ranges (100–200 μm , 200–300 μm and 300–700 μm); 2) in order to detect external diffusional limitations, some tests were performed with two different catalytic bed heights ($h = 6 \text{ mm}$ and $h = 24 \text{ mm}$), but with flowrates adjusted in order to keep in both case a *GHSV* equal to 5000 h^{-1} . All catalytic tests were performed at $T = 650 \text{ }^\circ\text{C}$ and with 24.000 ppmv of toluene.

External limitations

The samples tested with different catalytic bed heights (samples *N-10Ni-V_{1/2}*, *N-10Ni* and *N-10Ni-V_{X2}*) presented relatively similar toluene reforming rates ($r_{Tolu} \sim 6.5 \cdot 10^{-2} \text{ mol}_{Tolu}/(\text{g}_{Ni}\cdot\text{h})$) and similar amount of carbon deposits (*Coke* $\sim 0.09 \text{ g}_{Carbon}/\text{g}_{Cata}$) (Table A2.1). Hence, it was assumed that under the standard conditions of catalytic test, the catalysts did not submit any external diffusional limitations.^{[308], [309]}

Table A2.1: Toluene reforming and amount of carbon deposit after test for sample *N-10Ni* tested with different catalytic bed heights. Test conditions: $T = 650 \text{ }^\circ\text{C}$, $t = 5 \text{ h}$, 24.000 ppmv of toluene, *GHSV* = 5000 h^{-1} .

Samples	C_{Tolu} (%)	r_{Tolu} ($\text{mol}_{Tolu}/(\text{g}_{Ni}\cdot\text{h})$)	<i>Coke</i> ($\text{g}_{Carbon}/\text{g}_{Cata}$)	<i>Coke</i> * ($\text{g}_{Carbon}/\text{g}_{Tolu}$)
N-10Ni	51	$6.7 \cdot 10^{-2}$	0.10	$3.1 \cdot 10^{-2}$
N-10Ni-V _{1/2}	50	$6.5 \cdot 10^{-2}$	0.09	$2.9 \cdot 10^{-2}$
N-10Ni-V _{X2}	49	$6.3 \cdot 10^{-2}$	0.09	$2.9 \cdot 10^{-2}$

Internal limitations

The samples tested with different grains sizes of catalyst (samples *N-10Ni*, *N-10Ni-100-200* and *N-10Ni-200-300*) presented relatively similar toluene reforming rates ($r_{Tolu} \sim 7.1 \cdot 10^{-2} \text{ mol}_{Tolu}/(\text{g}_{Ni}\cdot\text{h})$) and similar amount of carbon deposits (*Coke* $\sim 0.10 \text{ g}_{Carbon}/\text{g}_{Cata}$) (Table A2.2). Hence, it was assumed that under the standard conditions of catalytic test, the catalysts did not submit internal diffusional limitations.^{[308], [309]}

Table A2.2: Toluene reforming and amount of carbon deposit after test for sample *N-10Ni* tested with different grain sizes. Test conditions: $T = 650 \text{ }^\circ\text{C}$, $t = 5 \text{ h}$, 24.000 ppmv of toluene, *GHSV* = 5000 h^{-1} .

Samples	C_{Tolu} (%)	r_{Tolu} ($\text{mol}_{Tolu}/(\text{g}_{Ni}\cdot\text{h})$)	<i>Coke</i> ($\text{g}_{Carbon}/\text{g}_{Cata}$)	<i>Coke</i> * ($\text{g}_{Carbon}/\text{g}_{Tolu}$)
N-10Ni	51	$6.7 \cdot 10^{-2}$	0.10	$3.1 \cdot 10^{-2}$
N-10Ni-100-200	54	$7.3 \cdot 10^{-2}$	0.10	$2.9 \cdot 10^{-2}$
N-10Ni-200-300	53	$7.1 \cdot 10^{-2}$	0.10	$2.9 \cdot 10^{-2}$

r_{Tolu} : reaction rate of toluene; *Coke*: carbon deposit amount after 5 h of test measured by TG-DSC; *Coke**: tendency of sample to form carbon deposit. *N.B.*: the reference sample *N-10Ni* was tested with grains sizes comprised between 300 and 700 μm .

Weisz Modulus values

The Weisz modulus values were determined from the results obtained during the catalytic tests of samples *N-10Ni* (Chapter V) and *N-10Ni-PS-eth* (Chapter VI).

The Weisz modulus, Φ , is given by the following formula:

$$\Phi = \frac{r \cdot \rho_{Eff} \cdot L_a^2}{D_e \cdot C_s} \quad (\text{A2.8})$$

where r is the apparent specific reaction rate ($\text{mol}_{\text{Tolu}}/(\text{g}_{\text{cata}}\cdot\text{h})$), ρ_{Eff} is the effective density of the catalyst ($\text{g}_{\text{cata}}/\text{m}^3$), L_a is the characteristic dimension of the aggregate of particles, equal to $d_a/6$ (m) (considering spherical particles of diameter d_a in m), C_s is the pollutant concentration at the external surface of the catalyst ($\text{mol}_{\text{Tolu}}/\text{m}^3$), D_e is the effective diffusivity through the aggregate porosity (m^2/h).

The effective diffusivity is defined by:

$$D_e = \frac{\varepsilon \cdot D_m}{\tau} \quad (\text{A2.9})$$

where ε is the void fraction of the catalyst; τ is the tortuosity of the catalyst, set to 1.36 according to a study on mesoporous $\gamma\text{-Al}_2\text{O}_3$ ^[378]; D_m is the molecular diffusivity (m^2/h), set to $5.76 \times 10^{-2} \text{ m}^2/\text{h}$ according to a study performed on syngas at $T = 500 \text{ }^\circ\text{C}$ ^[379].

The void fraction of the catalyst, ε , can be defined as:

$$\varepsilon = \frac{V_V}{\left(\frac{1}{\rho_{\text{Eff}}}\right)} \quad (\text{A2.10})$$

where V_V is the total pore volume and ρ_{Eff} is the effective density determined by the density of the catalysts bed and a close-packing of 0.74.

In the case of samples with macro-, meso- and micropores: $V_v = V_{H_g} + V_{p,7nm} + V_{\text{Dubinin}}$

In the case of samples with meso- and micropores: $V_v = V_p + V_{\text{Dubinin}}$

where V_{H_g} is the macroporous volume determined by mercury porosimetry, V_p is the porous volume determined by nitrogen adsorption-desorption and calculated from 2 to 50 nm by Broekhoff-De-Boer method, $V_{p,7nm}$ is the porous volume determined by nitrogen adsorption-desorption and calculated from 2 to 7 nm by Broekhoff-De-Boer method, V_{Dubinin} is the microporous volume determined by nitrogen adsorption-desorption and calculated by using the Dubinin–Raduskevitch model, ρ_{Eff} is the effective density determined by the density of the catalysts bed and a close-packing of 0.74.

For sample *N-10Ni*, $V_p + V_{\text{Dubinin}} = 0.3 + 0.08 = 0.38 \text{ cm}^3/\text{g}$ and $\rho_{\text{Eff}} = 0.7 \text{ g/cm}^3$, $\varepsilon_{N-10Ni} = 0.26$, so $D_{e,N-10Ni} = 1.1 \cdot 10^{-2} \text{ m}^2/\text{h}$.

For sample *N-10Ni-PS-eth*, $V_{H_g} + V_{p,7nm} + V_{\text{Dubinin}} = 0.9 + 0.2 + 0.12 = 1.22 \text{ cm}^3/\text{g}$ and $\rho_{\text{Eff}} = 0.2 \text{ g/cm}^3$, $\varepsilon_{N-10Ni-PS-eth} = 0.24$, so: $D_{e,N-10Ni-PS-eth} = 1.1 \cdot 10^{-2} \text{ m}^2/\text{h}$.

It is to remind that:

$$r_{\text{Tolu}} = \left(-\frac{F_{\text{Tolu}}}{W}\right) \ln(1 - f_{\text{Tolu}}) \quad (\text{A2.11})$$

The number of moles of toluene for 1000 ppmv of toluene in 1 m^3 of gas:

$$n = \frac{P \cdot V}{R \cdot T} = \frac{(101325 \cdot 1 \cdot 10^{-3})}{(8.314 \cdot 298)} = 4.09 \cdot 10^{-2} \text{ mol} \quad (\text{A2.12})$$

Then the concentration of toluene, $C_{rt,\text{Tolu}}$, for 24.000 ppmv is:

$$C_{rt,\text{Tolu}} = 9.81 \cdot 10^{-1} \text{ mol}_{\text{Tolu}}/\text{m}^3 \quad (\text{A2.13})$$

The total flowrate was fixed to 50 mL/min, which corresponds to:

$$Q = 3.0 \cdot 10^{-3} \text{ m}^3/\text{h} \quad (\text{A2.14})$$

Hence, the molar flowrate of toluene at the reactor inlet becomes:

$$F_{\text{Tolu}} = Q \cdot C_{rt,\text{Tolu}} = 2.9 \cdot 10^{-3} \text{ mol}_{\text{Tolu}}/\text{h} \quad (\text{A2.15})$$

Converting the density from g/cm^3 to g/m^3 leads to: $\rho_{\text{Eff}, N-10Ni} = 7.0 \cdot 10^5 \text{ g/m}^3$ and $\rho_{\text{Eff}, N-10Ni-PS-eth} = 2.0 \cdot 10^5 \text{ g/m}^3$

In the present case, no external diffusional limitations were present, so C_s was considered equal to $C_{rt,\text{Tolu}}$. Table A2.3 shows the Weisz modulus values for sample *N-10Ni* and for sample *N-10Ni-PS-eth* with grain sizes of 300/700 μm .

Table A2.3: Weisz modulus calculations for samples *N-10Ni* of Chapter V and *N-10Ni-PS-eth* of Chapter VI.

Samples	C_{Tolu} (%)	r_{Tolu} (mol _{Tolu} /g _{cata} ·h)	ρ_{eff} (g/m ³)	De (m ² /h)	$L_a^2 = (d_p/6)^2$ (m ²)	C_s (mol _{Tolu} /m ³)	Φ (Weisz modulus)
N-10Ni	51	$7.0 \cdot 10^{-3}$	$7.0 \cdot 10^5$	$1.1 \cdot 10^{-2}$	$6.9 \cdot 10^{-9}$	$9.8 \cdot 10^{-1}$	$3.2 \cdot 10^{-3}$
N-10Ni-PS-eth	42	$1.6 \cdot 10^{-2}$	$2.0 \cdot 10^5$	$1.6 \cdot 10^{-2}$	$6.9 \cdot 10^{-9}$	$9.8 \cdot 10^{-1}$	$2.1 \cdot 10^{-3}$

ρ_{eff} : effective density determined by the density of the catalysts bed and a close-packing of 0.74.

N.B.: in that case, the r_{Tolu} values are function of the mass of catalyst, and not the mass of Ni as usually used in this work.

Hence, for both samples *N-10Ni* and *N-10Ni-PS-eth*, the diffusion rate of the reagents inside the catalysts were higher than the reaction rate, which means that the catalysts worked under chemical regime.

IV. OTHER CALCULATIONS

Carbon ratio balance for catalytic tests made with different syngas compositions in Chapter V

The carbon ratio balance were measured by comparison of the amount of carbon which enter inside the reactor and the amount of carbon at the outlet of the reactor as defined as follows:

$$Difference(mol) = (7 * n_{Tolu,In} + n_{CO,In} + n_{CO2,In} + n_{CH4,In}) - (7 * n_{Tolu,Out} + 6 * n_{Benz,Out} + n_{CO,Out} + n_{CO2,Out} + n_{CH4,Out}) \quad (A2.16)$$

where $n_{Tolu,In}$, $n_{CO,In}$, $n_{CO2,In}$ and $n_{CH4,In}$ are the molar amount of toluene, CO, CO₂ and CH₄ which enter inside the reactor (mol); and $n_{Tolu,Out}$, $n_{CO,Out}$, $n_{CO2,Out}$, $n_{CH4,Out}$ and $n_{Benz,Out}$ are the molar amount of toluene, CO, CO₂, CH₄ and benzene which go outside the reactor (mol).

With the same data, it is also possible to estimate the percentage of error:

$$Error(\%) = \left| \frac{(7 * n_{Tolu,In} + n_{CO,In} + n_{CO2,In} + n_{CH4,In}) - (7 * n_{Tolu,Out} + 6 * n_{Benz,Out} + n_{CO,Out} + n_{CO2,Out} + n_{CH4,Out})}{(7 * n_{Tolu,In} + n_{CO,In} + n_{CO2,In} + n_{CH4,In})} \right| * 100 \quad (A2.17)$$

Table A2.4: Difference of carbon balance and error percentage for samples *N-10Ni*, *N-10Ni-NoCH4*, *N-10Ni-NoTolu* and *N-10Ni-Nothing* during the catalytic tests performed in Chapter V.

	N-10Ni	N-10Ni-NoCH4	N-10Ni-NoTolu	N-10Ni-Nothing
Difference (mol)	$1.4 \cdot 10^{-4}$	$8.9 \cdot 10^{-5}$	$-1.1 \cdot 10^{-5}$	$-8.7 \cdot 10^{-6}$
Error (%)	8.8	6.9	1.0	0.9

It was observed that samples *N-10Ni* and *N-10Ni-NoCH4* presented relatively high error percentage (8.8 % and 6.9 %). In contrary, the samples tested without toluene (samples *N-10Ni-NoTolu* and *N-10Ni-Nothing*) presented very low percentages of error. This indicated that the high values observed for samples *N-10Ni* and *N-10Ni-NoCH4* were caused by high carbon deposits due to toluene reforming and confirmed that the GC measurements were correct.

Determination of enthalpy and entropy values at $T = 923 K$

Table A2.5 shows the enthalpy and entropy values at $T = 923 K$:

Table A2.5: Enthalpy and entropy values determined at $T = 923 K$.

Compounds	ΔH_{298K}^0 (kJ/mol)	ΔH_{923K} (kJ/mol)	S_{298K}^0 (kJ/(mol.K))	S_{923K} (kJ/(mol.K))	C_p (kJ/(mol.K))
Toluene (gas)	50.0	115.0	0.320	0.437	0.1040
Ni ⁽⁰⁾ (solid)	0.0	24.3	0.030	0.074	0.0389
NiO (solid)	-240.0	-212.3	0.038	0.088	0.0443
CO (gas)	-110.0	-93.0	0.198	0.231	0.0274
CO ₂ (gas)	-393.0	-377.4	0.214	0.242	0.0250
H ₂ (gas)	0.0	22.0	0.130	0.170	0.036
H ₂ O (gas)	-242.0	-221.0	0.189	0.222	0.032
C (solid)	0.0	5.3	0.006	0.015	0.0085
CH ₄ (gas)	-74.5	-52.2	0.186	0.225	0.0357

The enthalpy and entropy values were determined from the references values obtained in the website of National Institute of Standards and Technology and by applying the following equations:

$$\Delta H_{923K} = \Delta H_{298K}^0 + C_p * (923 - 298) \quad (\text{A2.18})$$

$$\Delta S_{923K} = \Delta S_{298K}^0 + C_p * \ln(923/298) \quad (\text{A2.19})$$

V. AMOUNTS OF REAGENTS USED FOR THE PREPARATION OF THE SAMPLES

Samples of Chapter II

Table A2.6: Synthesis of γ -Al₂O₃ supports and γ -Al₂O₃ supports modified with EDAS, prepared with either aluminum nitrate or aluminum-*sec*-butoxide. Reagent amounts for the synthesis of 10 g of calcined supports.

Samples	Al- <i>Sec</i> -butoxide (mol)	Al(NO ₃) ₃ (mol)	EDAS (mol)	Water (mL)	Ethanol (mL)
A	1.96.10 ⁻¹	0	0	170	60
A-EDAS8	1.80.10 ⁻¹	0	1.37.10 ⁻²	170	60
N	0	1.96.10 ⁻¹	0	170	60
N-EDAS8	0	1.80.10 ⁻¹	1.37.10 ⁻²	170	60

Samples of Chapter III

Table A2.7: Synthesis of γ -Al₂O₃ materials and γ -Al₂O₃ materials modified with different silicon alkoxyde precursors. Reagent amounts for the synthesis of 10 g of calcined supports.

Samples	Al(NO ₃) ₃ (mol)	APTMS (mol)	EDAS (mol)	TMOS (mol)	TEOS (mol)	TOPS (mol)	TOOS (mol)	Water (mL)	Ethanol (mL)
N	1.96.10 ⁻¹	0	0	0	0	0	0	170	60
N-APTMS8	1.80.10 ⁻¹	1.37.10 ⁻²	0	0	0	0	0	170	60
N-EDAS2	1.88.10 ⁻¹	0	3.44.10 ⁻³	0	0	0	0	170	60
N-EDAS8	1.80.10 ⁻¹	0	1.37.10 ⁻²	0	0	0	0	170	60
N-EDAS16	1.63.10 ⁻¹	0	2.75.10 ⁻²	0	0	0	0	170	60
BA-EDAS8	1.80.10 ⁻¹	0	1.37.10 ⁻²	0	0	0	0	170	60
AA-EDAS8	1.80.10 ⁻¹	0	1.37.10 ⁻²	0	0	0	0	170	60
N-TMOS8	1.80.10 ⁻¹	0	0	1.37.10 ⁻²	0	0	0	170	60
N-TEOS8	1.80.10 ⁻¹	0	0	0	1.37.10 ⁻²	0	0	170	60
N-TOPS8	1.80.10 ⁻¹	0	0	0	0	1.37.10 ⁻²	0	170	60
N-TOOS8	1.80.10 ⁻¹	0	0	0	0	0	1.37.10 ⁻²	170	60

Samples of Chapter IV

Table A2.8: Synthesis of 2 wt. % Ni/ γ -Al₂O₃, 2 wt. % Ni/Olivine, 10 wt. % Fe/ γ -Al₂O₃ and 10 wt. % Fe/Olivine catalysts. Reagents amounts for the synthesis of 10 g of calcined catalyst.

Samples	Olivine (g)	Al(NO ₃) ₃ (mol)	Ni(NO ₃) ₂ (mol)	Fe(NO ₃) ₃ (mol)	Water (mL)	Ethanol (mL)
N-2Ni	0	1.92.10 ⁻¹	3.4.10 ⁻³	0	170	60
N-10Fe	0	1.76.10 ⁻¹	0	1.79.10 ⁻²	170	60
Oli-2Ni	9.8	0	3.4.10 ⁻³	0	100	0
Oli-10Fe	9.0	0	0	1.8.10 ⁻²	100	0

Samples of Chapter V

Table A2.9: Ni/ γ -Al₂O₃ catalysts with different loadings of Ni, or prepared by impregnation method with calcined sample *N* as supports. Reagents amounts for the synthesis of 10 g of calcined catalyst.

Samples	Sample N (g)	Al(NO ₃) ₃ (mol)	Ni(NO ₃) ₂ (mol)	Water (mL)	Ethanol (mL)
N-10Ni	0	1.76.10 ⁻¹	1.70.10 ⁻²	170	60
N-20Ni	0	1.57.10 ⁻¹	3.40.10 ⁻²	170	60
N-30Ni	0	1.37.10 ⁻¹	5.11.10 ⁻²	170	60
N-50Ni	0	9.80.10 ⁻²	8.52.10 ⁻²	170	60
IMP-N-10Ni	9.0	0	1.70.10 ⁻²	100	0

Samples of Chapter VITable A2.10: 10 wt. % Ni/ γ -Al₂O₃ catalysts prepared with stearic acid as surfactant. Reagents amounts for the synthesis of 10 g of calcined catalyst.

Samples	Al(NO ₃) ₃ (mol)	Ni(NO ₃) ₃ (mol)	Stearic acid (mol)	Water (mL)		Ethanol (mL)	
				1	2	1	2
N-10Ni	1.76.10 ⁻¹	1.70.10 ⁻²	0	170	170	60	60
N-10Ni-S	1.76.10 ⁻¹	1.70.10 ⁻²	3.50.10 ⁻²	170	170	60	60
N-10Ni-S-eth	1.76.10 ⁻¹	1.70.10 ⁻²	3.50.10 ⁻²	170	0	60	230
N-10Ni-PS	1.76.10 ⁻¹	1.70.10 ⁻²	3.50.10 ⁻²	170	170	60	60
N-10Ni-PS-eth	1.76.10 ⁻¹	1.70.10 ⁻²	3.50.10 ⁻²	0	170	230	60

1: Solvent amount in initial mixture; 2: Solvent amount in redispersed sol.

Samples of Chapter VIITable A2.11: Synthesis of γ -Al₂O₃ reference samples doped with 2 wt. % of metal or 1.5 wt. % of Ce. Reagents amounts for the syntheses of 10 g of calcined catalyst.

Samples	Al(NO ₃) ₃ (mol)	Dopants (mol)	Water (mL)	Ethanol (mL)
N-2Mo	1.92.10 ⁻¹	2.08 .10 ⁻³ H ₂ MoO ₃	170	60
N-2Mn	1.92.10 ⁻¹	3.64 .10 ⁻³ Mn(NO ₃) ₃	170	60
N-2Cu	1.92.10 ⁻¹	3.15 .10 ⁻³ Cu(NO ₃) ₃	170	60
N-2Co	1.92.10 ⁻¹	3.40 .10 ⁻³ Co(NO ₃) ₃	170	60
N-2Fe	1.92.10 ⁻¹	3.58 .10 ⁻³ Fe(NO ₃) ₃	170	60
N-1.5Ce	1.95.10 ⁻¹	1.07 .10 ⁻³ Ce(NO ₃) ₃	170	60

Table A2.12: Synthesis of 10 wt. % Ni/ γ -Al₂O₃ catalysts doped with 2 wt. % of metal or 1.5 wt. % of oxide. Reagents amounts for the syntheses of 10 g of calcined catalyst.

Samples	Al(NO ₃) ₃ (mol)	Ni(NO ₃) ₃ (mol)	Dopants (mol)	Water (mL)	Ethanol (mL)
N-10Ni-2Mo	1.73.10 ⁻¹	1.70.10 ⁻²	2.08.10 ⁻³ H ₂ MoO ₃	170	60
N-10Ni-2Mn	1.73.10 ⁻¹	1.70.10 ⁻²	3.64.10 ⁻³ Mn(NO ₃) ₃	170	60
N-10Ni-2Cu	1.73.10 ⁻¹	1.70.10 ⁻²	3.15.10 ⁻³ Cu(NO ₃) ₃	170	60
N-10Ni-2Co	1.73.10 ⁻¹	1.70.10 ⁻²	3.40.10 ⁻³ Co(NO ₃) ₃	170	60
N-10Ni-2Fe	1.73.10 ⁻¹	1.70.10 ⁻²	3.58.10 ⁻³ Fe(NO ₃) ₃	170	60
N-10Ni-1.5Ca	1.75.10 ⁻¹	1.70.10 ⁻²	3.74.10 ⁻³ Ca(NO ₃) ₃	170	60
N-10Ni-1.5Mg	1.75.10 ⁻¹	1.70.10 ⁻²	6.17.10 ⁻³ Mg(NO ₃) ₃	170	60
N-10Ni-1.5K	1.75.10 ⁻¹	1.70.10 ⁻²	3.85.10 ⁻³ K(NO ₃) ₃	170	60
N-10Ni-1.5Ce	1.75.10 ⁻¹	1.70.10 ⁻²	1.07.10 ⁻³ Ce(NO ₃) ₃	170	60

Table A2.13: Synthesis of 10 wt. % Ni/ γ -Al₂O₃ catalysts doped 4 wt. % of Mn or Mo, or doped with 3 wt. % of Ca or K. Reagents amounts for the synthesis of 10 g of calcined catalyst.

Samples	Al(NO ₃) ₃ (mol)	Ni(NO ₃) ₃ (mol)	Dopants (mol)	Water (mL)	Ethanol (mL)
N-10Ni-4Mn	1.69.10 ⁻¹	1.70.10 ⁻²	7.28 .10 ⁻³ Mn(NO ₃) ₃	170	60
N-10Ni-4Mo	1.69.10 ⁻¹	1.70.10 ⁻²	4.17 .10 ⁻³ H ₂ MoO ₃	170	60
N-10Ni-3Ca	1.72.10 ⁻¹	1.70.10 ⁻²	7.48 .10 ⁻³ Ca(NO ₃) ₃	170	60
N-10Ni-3K	1.72.10 ⁻¹	1.70.10 ⁻²	7.70 .10 ⁻³ K(NO ₃) ₃	170	60

Table A2.14: Synthesis of 10 wt. % Ni/ γ -Al₂O₃ catalysts doped twice with 2 wt. % of two different metals or 1.5 wt. % of two different oxides. Reagents amounts for the synthesis of 10 g of calcined catalyst.

Samples	Al(NO ₃) ₃ (mol)	Ni(NO ₃) ₃ (mol)	Dopants (mol)	Water (mL)	Ethanol (mL)
N-10Ni-2Mn-2Mo	1.69.10 ⁻¹	1.70.10 ⁻²	2.08.10 ⁻³ H ₂ MoO ₃ + 3.64.10 ⁻³ Mn(NO ₃) ₃	170	60
N-10Ni-2Cu-2Mo	1.69.10 ⁻¹	1.70.10 ⁻²	2.08.10 ⁻³ H ₂ MoO ₃ + 3.15.10 ⁻³ Cu(NO ₃) ₃	170	60
N-10Ni-2Co-2Mo	1.69.10 ⁻¹	1.70.10 ⁻²	2.08.10 ⁻³ H ₂ MoO ₃ + 3.40.10 ⁻³ Co(NO ₃) ₃	170	60
N-10Ni-2Fe-2Mo	1.69.10 ⁻¹	1.70.10 ⁻²	2.08.10 ⁻³ H ₂ MoO ₃ + 3.58.10 ⁻³ Fe(NO ₃) ₃	170	60
N-10Ni-2Cu-2Mn	1.69.10 ⁻¹	1.70.10 ⁻²	3.64.10 ⁻³ Mn(NO ₃) ₃ + 3.15.10 ⁻³ Cu(NO ₃) ₃	170	60
N-10Ni-2Co-2Mn	1.69.10 ⁻¹	1.70.10 ⁻²	3.64.10 ⁻³ Mn(NO ₃) ₃ + 3.40.10 ⁻³ Co(NO ₃) ₃	170	60
N-10Ni-2Fe-2Mn	1.69.10 ⁻¹	1.70.10 ⁻²	3.64.10 ⁻³ Mn(NO ₃) ₃ + 3.58.10 ⁻³ Fe(NO ₃) ₃	170	60
N-10Ni-2Cu-2Co	1.69.10 ⁻¹	1.70.10 ⁻²	3.15.10 ⁻³ Cu(NO ₃) ₃ + 3.40.10 ⁻³ Co(NO ₃) ₃	170	60
N-10Ni-2Cu-2Fe	1.69.10 ⁻¹	1.70.10 ⁻²	3.15.10 ⁻³ Cu(NO ₃) ₃ + 3.58.10 ⁻³ Fe(NO ₃) ₃	170	60
N-10Ni-2Co-2Fe	1.69.10 ⁻¹	1.70.10 ⁻²	3.40.10 ⁻³ Co(NO ₃) ₃ + 3.58.10 ⁻³ Fe(NO ₃) ₃	170	60
N-10Ni-1.5Ca-1.5Mg	1.72.10 ⁻¹	1.70.10 ⁻²	3.74.10 ⁻³ Ca(NO ₃) ₃ + 6.17.10 ⁻³ Mg(NO ₃) ₃	170	60
N-10Ni-1.5Ca-1.5K	1.72.10 ⁻¹	1.70.10 ⁻²	3.74.10 ⁻³ Ca(NO ₃) ₃ + 3.85.10 ⁻³ K(NO ₃) ₃	170	60
N-10Ni-1.5Mg-1.5K	1.72.10 ⁻¹	1.70.10 ⁻²	6.17.10 ⁻³ Mg(NO ₃) ₃ + 3.85.10 ⁻³ K(NO ₃) ₃	170	60
N-10Ni-1.5Ce-1.5Ca	1.72.10 ⁻¹	1.70.10 ⁻²	1.07.10 ⁻³ Ce(NO ₃) ₃ + 3.74.10 ⁻³ Ca(NO ₃) ₃	170	60
N-10Ni-1.5Ce-1.5Mg	1.72.10 ⁻¹	1.70.10 ⁻²	1.07.10 ⁻³ Ce(NO ₃) ₃ + 6.17.10 ⁻³ Mg(NO ₃) ₃	170	60
N-10Ni-1.5Ce-1.5K	1.72.10 ⁻¹	1.70.10 ⁻²	1.07.10 ⁻³ Ce(NO ₃) ₃ + 3.85.10 ⁻³ K(NO ₃) ₃	170	60

Samples of Annex 6Table A2.15: Synthesis of 10 wt. % Ni/ γ -Al₂O₃ catalysts modified with EDAS, TMOS or TEOS. Reagents amounts for the synthesis of 10 g of calcined catalyst.

Samples	Al(NO ₃) ₃ (mol)	EDAS (mol)	TMOS (mol)	TEOS (mol)	Ni(NO ₃) ₃ (mol)
N-10Ni	1.76.10 ⁻¹	0	0	0	1.70.10 ⁻²
N-EDAS8-10Ni	1.60.10 ⁻¹	1.36.10 ⁻²	0	0	1.70.10 ⁻²
N-TMOS8-10Ni	1.60.10 ⁻¹	0	1.36.10 ⁻²	0	1.70.10 ⁻²
N-TEOS8-10Ni	1.60.10 ⁻¹	0	0	1.36.10 ⁻²	1.70.10 ⁻²

VI. REFERENCES OF COMPOUNDS DETERMINED BY X-RAY DIFFRACTIONReferences of Chapter II

- γ -Al₂O₃: Alumina Gamma, Cubic System, PDF Card 00-010-0425

References of Chapter III

- γ -Al₂O₃: Alumina Gamma, Cubic System, PDF Card 00-010-0425
- α -Al₂O₃: Alumina Corindon, Hexagonal System, PDF Card 01-075-1865
- θ -Al₂O₃: Alumina Theta, Cubic System, PDF Card 00-009-0440
- δ -Al₂O₃: Alumina Delta, Cubic System, PDF Card 00-016-0394

References of Chapter IV

- γ -Al₂O₃: Alumina Gamma, Cubic System, PDF Card 00-010-0425
- α -Al₂O₃: Alumina Corindon, Hexagonal System, PDF Card 04-004-2852
- Ni⁽⁰⁾: Metallic nickel, Cubic System, PDF Card 00-001-1258
- Ni_{3.75}O₄: Nickel Oxide, Monoclinic System, PDF Card 04-007-0510
- Fe_{0.96}O_{0.04}: Kamacite, Cubic System, PDF Card 04-008-08470
- FeAl₂O₄: Hercynite, Cubic System, PDF Card 00-007-0068
- (MgFe₂)O₄: Magnesioferrite, Cubic system, PDF Card 01-073-1720
- (Mg_{1.85}Fe_{0.15})SiO₄: Forstierite, Orthorhombic system, PDF Card 01-080-1639
- Fe⁽⁰⁾: Metallic iron, Cubic System, PDF Card 00-003-1050
- FeO: Iron Oxide, Cubic System, PDF Card 04-002-3667
- Fe_{0.92}O: Wustite, Cubic System, PDF Card 01-074-1880
- Fe₂O₃: Iron Oxide, Rhombohedral system, PDF Card 04-006-6579

References of Chapter V

- γ -Al₂O₃: Alumina Gamma, Cubic System, PDF Card 00-010-0425
- Ni⁽⁰⁾: Metallic nickel, Cubic System, PDF Card 00-001-1258
- NiO: Nickel Oxide, Cubic System, PDF Card 01-089-3080

References of Chapter VI

- γ -Al₂O₃: Alumina Gamma, Cubic System, PDF Card 00-010-0425
- Ni⁽⁰⁾: Metallic nickel, Cubic System, PDF Card 00-001-1258

References of Chapter VII and of Annex 4

- Ni⁽⁰⁾: Metallic nickel, Cubic System, PDF Card 00-001-1258
- Mo⁽⁰⁾: Metallic Molybdenum; Cubic System, PDF Card 01-088-2331
- Cu⁽⁰⁾: Metallic Copper, Cubic system, PDF Card 00-004-0836
- α -Al₂O₃: Alumina Corindon, Hexagonal System, PDF Card 04-004-2852
- γ -Al₂O₃: Alumina Gamma, Cubic System, PDF Card 00-010-0425
- Ni_{0.83}Mo_{0.17}: Nickel Molybdenum, Cubic System, PDF Card 04-018-1300
- Ni_{0.90}Mo_{0.10}: Nickel Molybdenum, Cubic System, PDF Card 01-077-2966
- Ni_{0.91}Mo_{0.09}: Nickel Molybdenum, Cubic System, PDF Card 04-003-2240
- Ni_{0.97}Mo_{0.03}: Nickel Molybdenum, Cubic System, PDF Card 04-011-9055
- Ni_{0.19}Cu_{0.81}: Nickel Copper, Cubic System, PDF Card 00-047-1406
- Ni_{0.4}Cu_{0.6}: Nickel Copper, Cubic System, PDF Card 01-077-7711
- Ni_{0.75}Cu_{0.25}: Nickel Copper, Cubic System, PDF Card 04-004-4502
- Ni_{0.76}Cu_{0.24}: Nickel Copper, Cubic System, PDF Card 04-003-2249
- Ni_{0.4}Co_{0.6}: Nickel Cobalt, Cubic System, PDF Card 01-077-7711
- Ni_{0.65}Co_{0.35}: Nickel Cobalt, Cubic System, PDF Card 04-002-1075
- Ni_{0.8}Co_{0.2}: Nickel Cobalt, Cubic System, PDF Card 04-004-4780
- Ni_{0.75}Co_{0.25}: Nickel Cobalt, Cubic System, PDF Card 04-003-2246

- Ni_{0.75}Fe_{0.25}: Awaruite, Cubic System, PDF Card 04-004-6754
- Ni_{0.82}Fe_{0.18}: Nickel Iron, Cubic System, PDF Card 04-003-2245

References of Chapter VIII

- Ni⁽⁰⁾: Metallic nickel, Cubic System, PDF Card 00-001-1258
- α -Al₂O₃: Corindon alumina, Rhombohedrique hexagonal axes, PDF 00-043-1484
- CaAl₄O₇: Grossite, Monoclinic System, PDF 04-007-8975
- NiO: Nickel Oxide, Cubic System, PDF Card 01-089-3080
- NiAl₂O₄: Nickel Aluminum Oxide, Cubic System, PDF Card 01-081-0710

References of Annex 5

- γ -Al₂O₃: Alumina Gamma, Cubic System, PDF Card 00-010-0425
- Ni⁽⁰⁾: Metallic nickel, Cubic System, PDF Card 00-001-1258

References of Annex 6

- γ -Al₂O₃: Alumina Gamma, Cubic System, PDF Card 00-010-0425
- Ni⁽⁰⁾: Metallic nickel, Cubic System, PDF Card 00-001-1258

Annex 3: Experimental installation used for catalytic tests

The design and build up of the experimental installation was inspired by the works of Felix *et al.*^[380], Sato *et al.*^[57], Tao *et al.*^[128], and by the experimental installation used by the Institut de Chimie et Procédés pour l’Energie, l’Environnement et la Santé (ICPEES) of the University of Strasbourg (France).

I. PLANS OF THE INSTALLATION

The catalytic tests were performed thanks to an experimental installation whose schemes are represented in Figures A3.1 and A3.2, and whose pictures are showed in Figures A3.3. In order to prevent corrosion, the tubing was made of inox 316 stainless steel. Each gas line was composed by a filter (2 μm), an electro-valve, a security pressure valve, a mass flow controller and a check valve. Security lines are linked to the security pressure valves, which in case of over pressure (> 15 bars), open and send the gas to the ventilation.

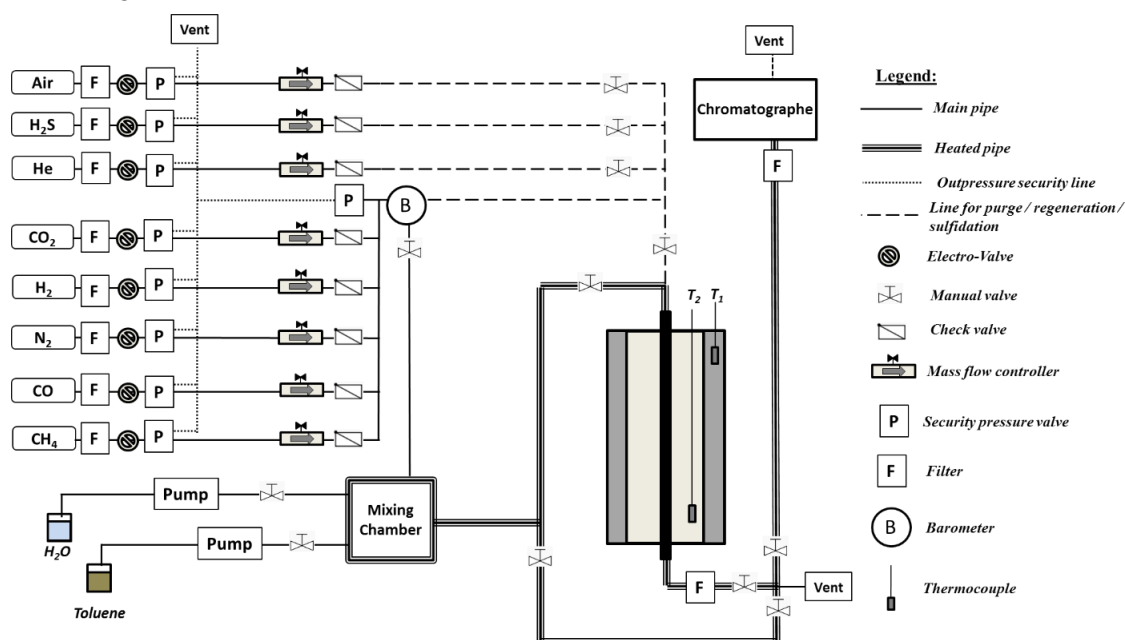


Figure A3.1: Scheme of the experimental installation.

Liquid deionized water was injected thanks to a peristaltic pump (ISMATEC, Multi channels). Due to incompatibility between toluene and the polymer tubes of the peristaltic pump, the liquid toluene was injected by a syringe pump (KDSscientific, Legato) and a toluene-resistant syringe made of glass and PTFE. The different gases and liquids were injected and heated in a home-made mixing chamber. It is to notice that at first a mixing chamber full of glass beads was used. However, the reproducibility of the toluene concentration measurements was then inadequate (more than 20 % of difference between two injections) whatever the diameter of the beads used ($\varnothing = 2, 3, 5$ mm). A home-made mixing chamber consisting of a muddle of metallic channels made by Jadition enterprise and allowed a higher flux mixture and a good reproducibility (less than 5 % of difference between two injections). The mixing chamber and all the downstream tubes were heated at $T = 180$ °C in order to prevent any water/toluene condensation. At the exit of the mixing chamber, the gas mixture was directed either toward the reactor or toward the bypass line. Figures A3.2 shows the reactor inside setting. In order to get more information about the thermal distribution inside the reactor, the temperature profile curves inside the quartz tube were measured for different temperatures ($T = 400, 500, 600, 700, 800$ °C) with a N_2 flux of 50 mL/min.

According to the temperature gradient measurements, the catalyst bed was settled between 250 and 400 mm from the reactor bottom.

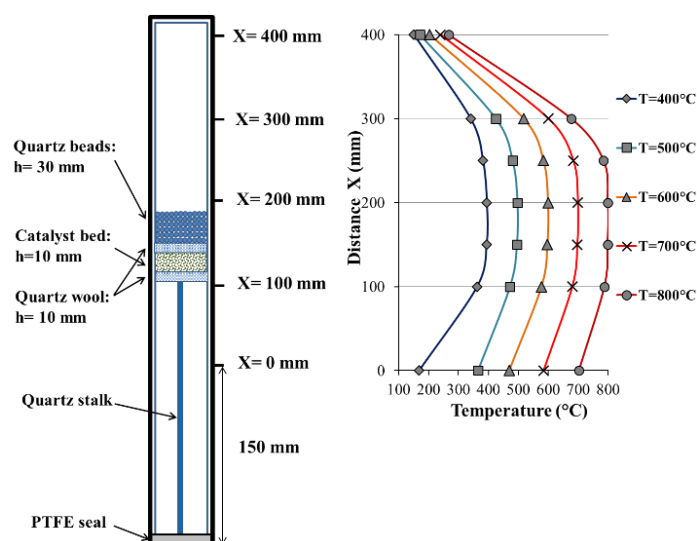


Figure A3.2: Catalytic reactor set-up and thermal gradient inside the reactors. The thermal gradient measurements were performed with a N_2 flux of 50 mL/min.

The metallic reactor was made of inox 316 with $\frac{1}{2}$ inch diameter. A quartz tube ($\varnothing = 8$ mm) containing the catalyst bed was set inside the metallic reactor, thus avoiding the contact of the gas mixture and the metallic reactor. The catalyst bed was maintained by two quartz wool layers and a quartz stalk in order to prevent any bed motion. Before entering in contact with the catalyst bed, the flow had to pass through a small bed a quartz beads ($\varnothing = 2$ mm). This quartz bed was set in order to insure a proper heating of the flow. Indeed, it is known that a difference of temperature between the gas flow and the catalyst bed strongly favors the coking of the catalyst.^[65] A PTFE seal was set between the inox reactor and the quartz tube at the bottom of the reactor.

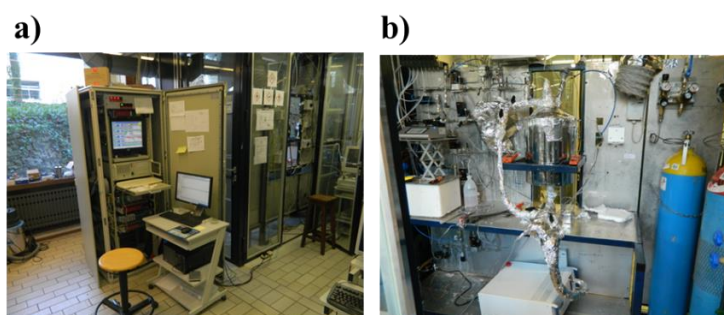


Figure A3.3: Installation view from the entrance (left side) and from inside the testing chamber (right side).

II. INFORMATIC SYSTEM

Most of the instruments of the installation (heating resistances, flowmeters, electro-valves, thermocouples, pressure captor, fixed-detectors) were controlled by an informatic system. The connections between a common computer and the instruments were made thanks to electronic Input/Output modules. The left side of Figure A3.4 shows the command control of the computer screen. Icons were created for the command of the installation apparatus. The right side of Figure A3.4 shows three informatic codes created: 1) the “RAMPE” code aims at controlling the oven. One can set different parameters such as the heating rate or temperature dwell; 2) the “ARRET URGENCE” code was created in need of an emergency stop. When pressing the button, the oven, all the gas electrovalves and all the flowmeters are stopped. Then a N_2 flux is sent to purge the lines; 3) the “CO/H₂S” code is linked to the CO and H₂S fixed detectors. If the CO or H₂S concentration exceeded a threshold of 50 ppmv, a signal is sent to the associated modules and therefore to the computer. Simultaneously, the oven and all the gas electrovalves and flowmeters are stopped, and a N_2 flux is sent to purge the lines.

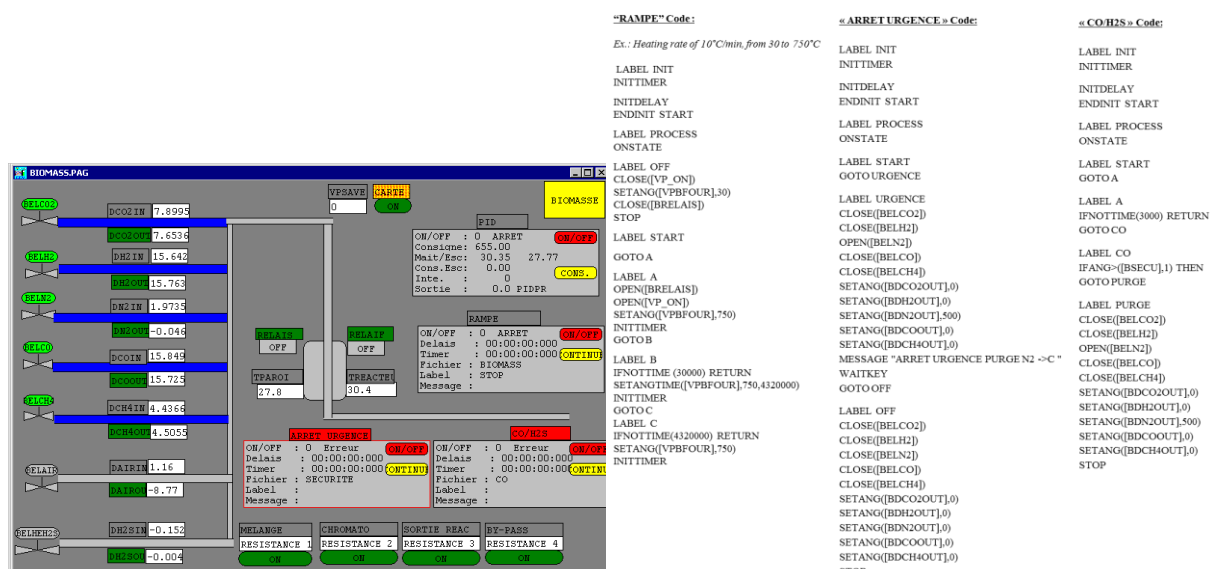


Figure A3.4: On the left side: Command screen on the computer. On the right side: "RAMPE", "ARRET URGENCE" and "CO/H2S" program code.

III. SECURITY PROCEDURES

Though the installation had run for more than 1000 h without any problems, several security procedures were set during the assembly and were systematically applied during the tests in order to prevent any accident:

- A security pushing button was set at the entrance of the installation. Pushing this button turns off the electricity steam of all the installation and electronic devices.
- Two fixed detectors (CO and H₂S) were linked to the informatic system by modules and set a purging procedure in case of gas detection according to the "CO/H2S" program. Furthermore, a screen box situated before the entrance informs about the actual CO and H₂S concentrations inside the laboratory. In case of gas detection, this external box triggers an alarm.
- When running tests, three portable detectors (CO, H₂-CH₄ and O₂) were activated.
- In order to prevent the breathing of quartz wool dusts during the tests setting, a dust-mask was systematically used. When reloading the syringe with toluene, an aromatic gas mask was used in order to prevent the breathing of toluene. Furthermore, an external training taught by firemen and supported by the University of Liege was done in order to learn the functioning of a self-contained breathing apparatus. This apparatus permits to operate in an asphyxiating/toxic atmosphere and could be used in case of a high CO or H₂S leak.
- The screen button named "ARRET URGENCE" was created. Clicking on this button stops the gas entry and flush the installation with N₂.

IV. INFORMATION RELATIVE TO THE CHROMATOGRAPH APPARATUS

The gas mixture was analyzed by gas chromatography (GC Compact, Interscience) with different detectors and columns: 1) a FID detector to quantify the organic compounds (CH₄, toluene, benzene) with an analytic column (RTX1); 2) a TCD detector for the other gas (CO₂, CO, H₂, N₂) containing a backflush line with two analytic columns (Molsieve 5A and Porapak). It was also possible to quantify H₂O with the TCD detector. For both detectors, He was used as carrier gas. All the tubing is made with Sulfinert coating, which affords its resistance toward sulfur compounds and was heated at $T = 160$ °C in order to prevent H₂O/toluene condensation.

V. REPRODUCIBILITY OF THE MEASUREMENTS

The reproducibility between two injections of the syngas mixture were of about ± 500 ppmv in the case of the presence of 8000 ppmv of toluene, and of about ± 0.5 vol. % for the other compounds (water and gases).

Annex 4: Additional information relative to Chapter VII

I. HETEROGENEOUS GELS AND PREPARATION METHOD ®

In order to guarantee the homogenous repartition of the elements among the samples, elementary microscope measurements (SEM-BSE and SEM-EDX) were performed for each sample. These analyses revealed that the doping method was not adapted in the case of a doping with 1.5 wt. % of Ce or in the case of two doping with 1.5 wt. % of two different oxides. In these cases, the dried gels and the calcined samples were composed of two phases which presented different morphological aspects and compositions (Figure A4.1). It was assumed that in the presence of Ce or two different alkali dopants, the dopant ions would be adsorbed at the surface of Al_2O_3 crystallites and would favor their flocculation. As results, a biphasic sol was progressively formed during the aging step: an alumina rich gel at the bottom of the vessel and a nickel rich solution at the top. As the drying steps went by, the upper solutions formed nickel rich crusts at the top of the gels.

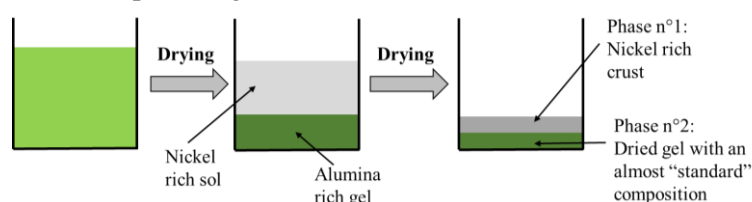


Figure A4.1: Scheme resuming the formation of biphasic gels.

These catalysts were therefore synthesized a second time with a different method in order to encounter the problem of heterogeneity. Instead of simply putting the vessel into an oven for a classic drying operation, the doped alumina hydroxide solutions were introduced in a glass balloon which was attached to a RotaVapor® instrument. This modification allowed drying the solutions with a constant and homogeneous agitation. In that case, the prefix “®” was added to the name of the samples. In that case, elementary microscope (SEM-BSE and SEM-EDX) measurements were performed and validated the formation of homogenous materials.

II. CHARACTERIZATION OF ALUMINA SUPPORT DOPED WITH 2 WT. % OF METAL OR 1.5 WT. % OF CERIUM

TPR measurements followed by X-Ray analyses were performed for the samples made of $\gamma\text{-Al}_2\text{O}_3$ doped with 2 wt. % of metal (samples *N-2Ni*, *N-2Mo*, *N-2Mn*, *N-2Cu*, *N-2Co*, *N-2Fe*) or doped with 1.5 wt. % of cerium (sample *N-1.5Ce*) (Figure A4.2). The results enabled to study separately the evolution of the reducible species reduction during TPR measurements and their influence on the behavior of the different 10 wt. % $\text{Ni}/\gamma\text{-Al}_2\text{O}_3$ catalysts doped in the Chapter VII. Table A4.1 shows the metallic particles sizes of samples from TEM and XRD observations after TPR measurements.

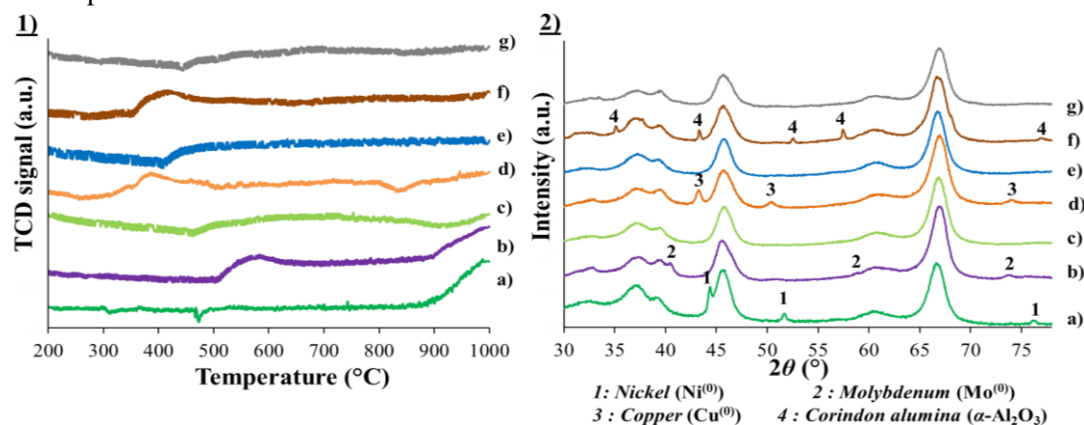


Figure A4.2: TPR profiles (left side) and X-Ray spectra (right side) for $\gamma\text{-Al}_2\text{O}_3$ doped with 2 wt. % of metal or 1.5 wt. % of Ce; a. *N-2Ni*, b. *N-2Mo*, c. *N-2Mn*, d. *N-2Cu*, e. *N-2Co*, f. *N-2Fe*, g. *N-1.5Ce*.

Table A4.1: Metallic particles sizes and X-Ray observations after TPR measurements for γ -Al₂O₃ supports doped with 2 wt. % of metal or with 1.5 wt. % of Ce.

Samples	Particles sizes			Comments
	d_{TEM} (nm)	σ_{TEM} (nm)	d_{XRD} (nm)	
N-2Ni	30	9	23	Presence of Ni ⁽⁰⁾ rays visible at $2\theta = 44.4^\circ / 51.8^\circ / 71.7^\circ$
N-2Mo	14	4	17 ¹	Raw Mo ⁽⁰⁾ rays visible at $2\theta = 40.49^\circ / 58.64^\circ / 73.68^\circ$; No evidence of Mo oxide
N-2Mn	#	#	#	No evidence of Mn metal rays; No evidence of Mn oxide rays
N-2Cu	17	12	13 ²	Raw Cu ⁽⁰⁾ rays visible at $2\theta = 43.25^\circ / 50.48^\circ / 74.10^\circ$
N-2Co	#	#	#	No evidence of Co metal rays / No evidence of Co oxide rays
N-2Fe	#	#	#	No evidence of Fe or FeO rays; No evidence of Fe ₂ O ₃ rays; Presence of α -Al ₂ O ₃ rays
N-1.5Ce	#	#	#	No rays of cerium oxide visible; No rays of cerium-aluminate visible

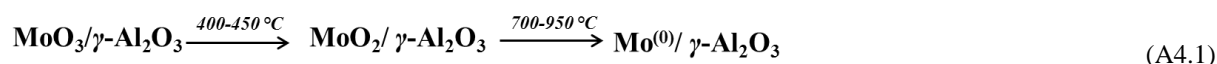
d_{TEM} : metallic particles size median; σ_{TEM} : standard deviation; d_{XRD} : metallic crystallites size.

1: measured on the (2 1 1) ray of Mo⁽⁰⁾ at $2\theta = 73.70^\circ$;

2: measured on the (2 0 0) ray of Cu⁽⁰⁾ at $2\theta = 50.48^\circ$.

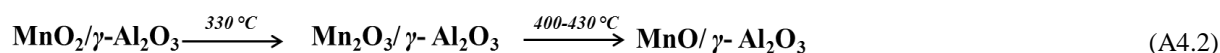
#: not available;

Mo/ γ -Al₂O₃: Molybdenum oxides supported on γ -Al₂O₃ are reduced according to the following steps^{[172], [381], [382]}:



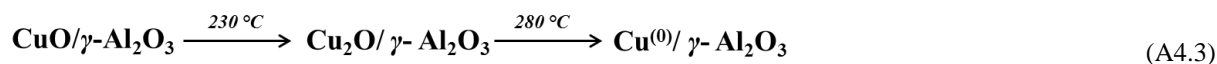
Sample *N-2Mo* showed a similar reduction profile in Figure A4.2-b: 1) a first peak located around $T = 550^\circ\text{C}$, which was attributed to the reduction of MoO₃ to MoO₂; 2) a second peak beginning at $T = 900^\circ\text{C}$ and not finished at $T = 1000^\circ\text{C}$, which was attributed to the reduction of MoO₂ to Mo⁽⁰⁾. Small metallic Mo⁽⁰⁾ particles ($d_{TEM} = 14$ nm and $d_{XRD} = 17$ nm), with a low standard deviation ($\sigma_{TEM} = 4$ nm) (Table A4.1) were obtained after TPR measurement.

Mn/ γ -Al₂O₃: Manganese oxides supported on γ -Al₂O₃ are reduced according to the following steps^{[176], [383]}:



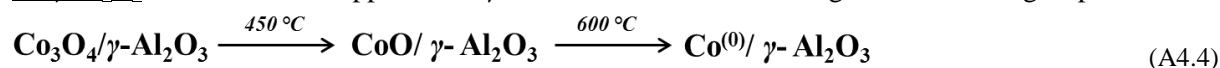
In the present case, the reduction of the Mn oxides seemed harder since the TPR profile of the sample *N-2Mn* (Figure A4.2-c) only showed a broad H₂ consumption peak comprised between $T = 480^\circ\text{C}$ and $T = 910^\circ\text{C}$. It is also to notice that the intensity of the diffraction rays of the Mn oxides were too low to be visible on the X-Ray spectrum after TPR measurement.

Cu/ γ -Al₂O₃: Copper oxides supported on γ -Al₂O₃ are reduced according to the following steps^[168]:



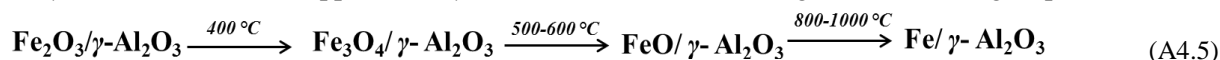
In this work, sample *N-2Cu* showed a first reduction peak at $T = 380^\circ\text{C}$ followed by a small second peak located at $T = 450^\circ\text{C}$ (Figure A4.2-d). After TPR measurement, the sample showed small metallic Cu⁽⁰⁾ particles ($d_{TEM} = 17$ nm and $d_{XRD} = 13$ nm), but with a large distribution of sizes ($\sigma_{TEM} = 12$ nm) (Table A4.1).

Co/ γ -Al₂O₃: Cobalt oxides supported on γ -Al₂O₃ are reduced according to the following steps^{[319], [320]}:



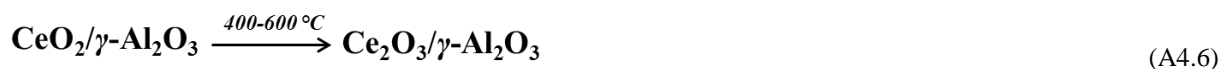
TPR profile of sample *N-2Co* (Figure A4.2-e) only showed a broad H₂ consumption peak with low intensity situated from $T = 450^\circ\text{C}$ to $T = 1000^\circ\text{C}$, which was attributed to Co oxide species with strong interactions with alumina and with different degrees of metal/support interactions. It is to notice that no metallic cobalt was observed after the TPR measurements.

Fe/ γ -Al₂O₃: Iron oxides supported on γ -Al₂O₃ are reduced according to the following steps^{[273], [274]}:



In the case of sample *N-2Fe*, the TPR profile only showed a visible reduction peak at $T = 450\text{ }^\circ\text{C}$ attributed to the reduction of Fe₂O₃ in Fe₃O₄ (Figure A4.2-f). Furthermore, similarly to a phenomenon deeply detailed in the Chapter IV, the presence of iron caused the apparition of α -Al₂O₃ rays.

CeO₂/ γ -Al₂O₃: Cerium oxides supported on γ -Al₂O₃ are reduced according to the following step^{[161], [331]}:



In accordance with the literature^{[161], [331]}, the TPR profile of sample *N-1.5Ce* (Figure A4.2-g) showed a small and broad H₂ consumption peak located between $T = 450\text{ }^\circ\text{C}$ and $T = 800\text{ }^\circ\text{C}$. However, the X-Ray analysis performed after TPR was not able to detect any CeO_x or AlCeO_x phases, probably due to too small rays intensities.

It was observed for all samples that the temperature needed for the reduction of the metal oxides were higher than those registered in the literature. These differences were attributed to two reasons: 1) the presence of a low metal doping (2 wt. %), which is known to favor formation of strong metal/support interactions^[253]; 2) the preparation of the samples by sol-gel methods, which are also known to lead to stronger metal/support interactions compared to classic impregnation methods^{[279], [290]}.

Annex 5: Complementary study about the optimization of operating variables for the synthesis of γ -Al₂O₃ based catalysts

In this study, the sol-gel procedures for the synthesis of γ -Al₂O₃ supports used in Chapters II and III, and the synthesis of Ni/ γ -Al₂O₃ catalysts used in Chapter IV and Annex 6 are optimized. In a first part, the influence of the *pH* of the precipitant on the final properties of pure γ -Al₂O₃ supports or γ -Al₂O₃ supports modified with EDAS molecules is investigated. Thereafter, the influence of different operating conditions used during the drying of the gels is studied. Finally, a new procedure for the development of Ni/ γ -Al₂O₃ catalysts with more than 10 wt. % of metal doping is established. The properties of Ni/ γ -Al₂O₃ materials developed with this new procedure are compared to the materials prepared by the classic method.

I. INTRODUCTION

Though the influence of the type of precipitant (NaOH, NH₄OH, KOH ...) [106], [384] or of the *pH* of the final solution [191], [198], [199], [385] have been the subject of different studies, no work was found in the literature about the influence of the concentration of precipitant during the synthesis of alumina. In this way, in this study, pure γ -Al₂O₃ and γ -Al₂O₃ modified with EDAS molecules were synthesized with a classic NH₄OH solution (15 M, 30 wt. %) or with a diluted NH₄OH solution (5 M, 10 wt. %).

The drying conditions are known to have a significant influence on the final morphology of the materials. When the liquid evaporates from the porous gel, the pore walls are subjected to a stress equal to the capillary pressure. This stress can cause a shrinkage of the gel and a collapse of the pore walls. [186] Furthermore, in the case of heterogeneity of evaporation, the gels can be exposed to pressure gradients between the wet and dry parts or the pores, which can result in the formation of cracks. The capillary pressure, defined by the Young-Laplace equation, is showed in Equation A5.1. [186], [386]

$$P = \frac{2\gamma_{LV}\cos\theta}{r} \quad (\text{A5.1})$$

where P is the capillary pressure (Pa), γ_{LV} is the liquid-vapor interfacial tension (N/m), θ is the contact angle (°) and r is the pore radius (m).

The drying of gels with liquids having a low surface tension is interesting to reduce the tension of the liquid supported by the solid phase and thus avoid the collapse of the pore. This effect has been confirmed by several authors, who highlighted the beneficial influence of washing steps performed with ethanol instead of water on the pore structure of γ -Al₂O₃ materials during the drying steps. [217], [387] It is for this reason that the gels were always washed and dried with ethanol during the syntheses performed in Chapters II, III, IV and in Annex 6. The aim of this chapter is therefore to understand the influence and to check the relevance of this washing step with ethanol. In this way, a part of this study aimed at determining the properties of pure γ -Al₂O₃ supports and EDAS-modified γ -Al₂O₃ supports dried with three common solvents: water, ethanol and acetone. Furthermore, the vapor pressure of the liquids is also known to play a significant role during the drying of the gels. Indeed, the rate of evaporation is proportional to the difference between the vapor pressure and the ambient vapor pressure (Equation A5.2) [186]:

$$V_E = k(p_v - p_a) \quad (\text{A5.2})$$

where V_E is the rate of evaporation (g/(cm².min)), k is a constant that depends on different operating parameters (draft rate, design of the drying chamber), p_v is the vapor pressure of the liquid (Pa) and p_a is the ambient vapor pressure (Pa).

Table A5.1 lists the different vapor pressures and the surface tensions of the solvents. It is to notice that, at $T = 20$ °C, the surface tension values of ethanol and acetone are relatively similar ($\gamma_{LV,Acetone/Ethanol} \sim 22$ -24. 10⁻³ N/m) and are significantly lower compared to the value of water ($\gamma_{LV,H2O} \sim 73$. 10⁻³ N/m). At $T = 110$ °C, the vapor pressure, p_v , of the solvents follows this range: acetone > ethanol > water.

Table A5.1: Physical properties of the solvents used during the drying step.^[388]

Solvent	Boiling point (°C)	Surface tension of the solvent against air at $T = 20$ °C (10 ⁻³ N/m)	Vapor pressure of liquid at $T = 110$ °C (kPa)
Water	100	72.8	143.0
Ethanol	79	22.3	320.0
Acetone	56	23.7	506.6

The initial procedure of synthesis of Ni/ γ -Al₂O₃ catalysts (Chapter IV and Annex 6) used to be performed according to the following steps: 1) preparation of the alumina sol; 2) washing of the sol with water; 3) re-dispersion of the sol in water; 4) addition of the nickel nitrate; 5) washing of the sol, at first with water, and then with ethanol; 6) drying and calcination. These procedures were efficient for the synthesis of catalysts with 2 and 10 wt. % of metal doping. However, it was found that these procedures did not allow to load the alumina materials with more than 13 wt. % of Ni: beyond this amount of doping, the surface of the boehmite nanocrystallites were saturated by adsorbed nickel ions. Hence, any further doping lead to the evacuation of the excess nickel ions during the washing steps.

In order to encounter this limitation, it was decided to skip the washing step of the doped sols (step 5) and to directly dry the doped sols. It was thought that this adjustment of the initial synthesis procedure could have several consequences on the properties of the materials for two main reasons: 1) instead of drying a gel, it was then a sol, which was dried; 2) the absence of a final washing led to the presence of residual nitrate ions (NO₃⁻) coming from nickel nitrate doping. Therefore, it was necessary to control that the presence of residual NO₃⁻ ions did not provoke a degradation of the γ -Al₂O₃ structure/crystallography, and that it did not lower the dispersion of the Ni nanoparticles.

II. EXPERIMENTAL

II.1. Variations of the operating conditions

Table A5.2 shows the different operating variables applied for the synthesis of pure γ -Al₂O₃ and of γ -Al₂O₃ modified with EDAS.

Table A5.2: Samples nomenclature in function of their synthesis conditions.

Samples	NH ₄ OH concentration	Drying solvent	Gel drying conditions
<i>Reference materials</i>			
N	30 wt. % (15 M)	ethanol	110 °C, 900 mbar
N-EDAS8	30 wt. % (15 M)	ethanol	110 °C, 900 mbar
<i>Influences of base concentration</i>			
N-10%	10 wt. % (5 M)	ethanol	110 °C, 900 mbar
N-EDAS8-10%	10 wt. % (5 M)	ethanol	110 °C, 900 mbar
<i>Influences of drying solvent</i>			
N-H2O	30 wt. % (15 M)	water	110 °C, 900 mbar
N-Acetone	30 wt. % (15 M)	acetone	110 °C, 900 mbar
N-EDAS8-H2O	30 wt. % (15 M)	water	110 °C, 900 mbar
N-EDAS8-Acetone	30 wt. % (15 M)	acetone	110 °C, 900 mbar
<i>Influences of drying solvent + drying pressure</i>			
N-H2O-P700	30 wt. % (15 M)	water	110 °C, 700 mbar
N-P700	30 wt. % (15 M)	ethanol	110 °C, 700 mbar
N-Acetone-P700	30 wt. % (15 M)	acetone	110 °C, 700 mbar
N-EDAS8-H2O-P700	30 wt. % (15 M)	water	110 °C, 700 mbar
N-EDAS8-P700	30 wt. % (15 M)	ethanol	110 °C, 700 mbar
N-EDAS8-Acetone-P700	30 wt. % (15 M)	acetone	110 °C, 700 mbar

Samples *N-10%* and *N-EDAS8-10%* were synthesized with identical procedures as for the preparation of sample *N* and sample *N-EDAS8* described in Chapter III, except that the NH₄OH solution was in that case at a lower concentration (10 wt. % instead of 30 wt. %).

For the preparation of the samples where the influences of the drying solvent and of the drying steps were studied, one batch of alumina hydroxide sol and one batch of EDAS-modified hydroxide sol were prepared according to the synthesis procedures of sample *N* and sample *N-EDAS8*. These two batches were divided in 6 parts (*i.e.* 12 sols preparations). Half of these sols went under aging step ($t = 24$ h at $T = 85$ °C, $P = 700$ mbar), followed by two washing steps with water, and a last washing step with either water, ethanol or acetone. After centrifugation, the gels were dried under classic conditions ($t = 24$ h at $T = 110$ °C, $P = 900$ mbar). This was the case for samples *N*, *N-H₂O*, *N-Acetone*, *N-EDAS8*, *N-EDAS8-H₂O* and *N-EDAS8-Acetone*. The other half of these sols went under aging step ($t = 24$ h at $T = 85$ °C, $P = 700$ mbar), followed by two washing steps with water and a last washing step with either water, ethanol or acetone. Thereafter, the centrifuged gels were dried at lower pressure ($t = 24$ h at $T = 110$ °C, $P = 700$ mbar). This was the case for samples *N-P700*, *N-H₂O-P700*, *N-Acetone-P700*, *N-EDAS8-P700*, *N-EDAS8-H₂O-P700* and *N-EDAS8-Acetone-P700*.

II.2. Modification of the metal doping procedure

The initial procedure used for the preparation of Ni/ γ -Al₂O₃ (described in Chapter IV and Annex 6) was modified for both samples *N-10Ni** and *N-EDAS8-10Ni**. The boehmite sols were prepared in a similar way and were washed two times with water in order to evacuate the NH₄⁺ ions. Thereafter, the sols were re-dispersed in water, nickel nitrate was added and the sols were stirred for 30 min. The doped sols were put in an oven for aging ($t = 24$ h, $T = 85$ °C, $P = 700$ mbar) and for drying ($t = 24$ h, $T = 110$ °C, $P = 900$ mbar). The dried gels were calcined for $t = 5$ h at $T = 550$ °C, with a heating rate of 2 °C/min. Figure A5.1 gives an insight of the differences between the initial method and the new method.

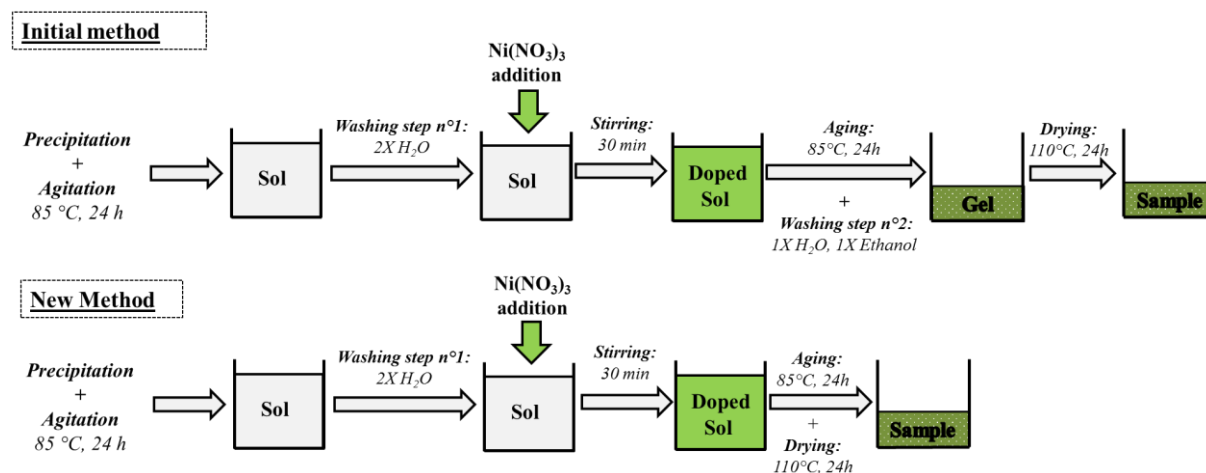


Figure A5.1: Classic method and new procedure established for the preparation of Ni/ γ -Al₂O₃ catalysts.

II.3. Characterization techniques

Composition analysis, (ICP-AES), nitrogen adsorption-desorption (BET), X-Ray diffraction (XRD), temperature programmed reduction (TPR), pure reduction of the samples (H₂-Reduction), and transmission electron microscopy (TEM) measurements were performed on the samples of this study. The γ -Al₂O₃ crystallite size (d_{XRD,Al_2O_3} , nm) were estimated from Scherrer equation applied on the ray located at $2\theta = 66.9$ °, which corresponds to the (4 4 0) planar direction. The Ni⁽⁰⁾ particle sizes ($d_{XRD,Ni}$, nm), were calculated by using the Scherrer equation centered on the Ni ray (2 0 0) ($2\theta = 51.83$ °). Deeper information about the characterizations techniques and variables quoted are provided in part II of Annex 2.

III. RESULTS AND DISCUSSION

III.1. Influences of the operating conditions

III.1.1. Concentration of base

Figure A5.2 shows the precipitation curves of the supports made of pure γ -Al₂O₃ and of γ -Al₂O₃ modified with EDAS for NH₄OH concentrations of 10 wt. % (5 M) and of 30 wt. % (15 M).

It was noticed that the precipitation range II was not affected by the change of base concentration ($\Delta V_{I-III, 10\text{wt.}\%} = 9$ mL and $V_{I-III, 30\text{wt.}\%} = 10$ mL). This suggests that the transformation of mononuclear Al species and of small aluminum hydroxides species (Al₂-Al₁₂) into large polymeric Al species (Al₁₃-Al₅₄)^{[222]–[224]} was apparently not influenced by the concentration of base precipitant.

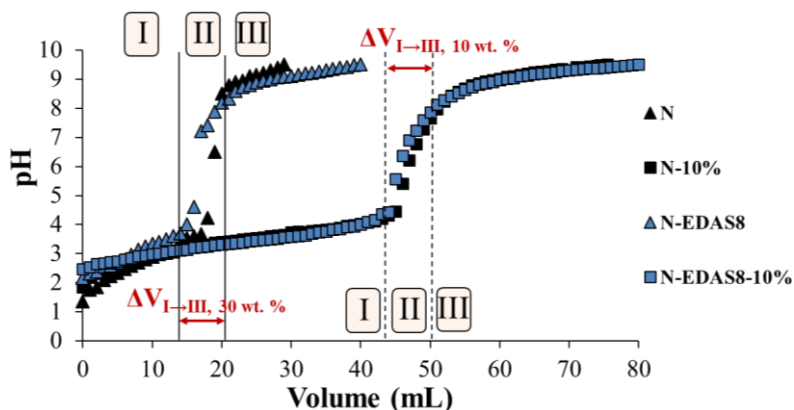


Figure A5.2: Precipitation curves of samples *N*, *N-10%*, *N-EDAS8* and *N-EDAS8-10%*.

Table A5.3 shows the textural and crystallographic properties of samples *N*, *N-10%*, *N-EDAS8* and *N-EDAS8-10%*. It was observed that the concentration of base precipitant had almost no influence on the morphology of the samples. Furthermore, it is to notice that X-Ray diffraction patterns (not shown here) were identical between samples *N* and *N-10%*, and between samples *N-EDAS8* and *N-EDAS8-10%*.

Table A5.3: Textural and crystallographic properties of the samples precipitated with different concentrations of NH₄OH.

Samples	S_{BET} (m ² /g)	V_p (cm ³ /g)	S_{meso} (m ² /g)	$V_{Dubinin}$ (cm ³ /g)	d_{XRD, Al_2O_3} (nm)	ρ (cm ³ /g)
N-10%	255	0.39	205	0.087	4.5	3.07
N	280	0.40	220	0.087	4.3	3.05
N-EDAS8-10%	470	0.16	125	0.136	3.4	2.79
N-EDAS8	450	0.18	135	0.134	3.3	2.71

S_{BET} : specific surface area; V_p : porous volume; S_{meso} : mesoporous surface area; $V_{Dubinin}$: microporous volume; ρ : apparent density; d_{XRD, Al_2O_3} : alumina crystallites size estimation by XRD.

III.1.2. Drying solvent and drying pressure

Table A5.4 presents the textural and crystallographic properties of calcined supports whose gels were dried with different solvents, at lower drying pressure; and with simultaneous different solvent and at lower drying pressure. It is to notice that in each case, the drying conditions had no influence on the crystallite sizes of the samples.

When dried at $P = 900$ mbar, calcined supports of pure alumina obtained from the gels dried with ethanol (sample *N*), water (sample *N-H₂O*), or acetone (sample *N-Acetone*) presented almost identical morphological and crystalline properties. Hence, it was assumed that in these cases, once the shrinkage of the gel reached its maximum, the arrangements of the γ -Al₂O₃ particles were therefore stiff enough to withstand the capillary pressures of each of solvents.^[186]

In the case of supports made of alumina modified with EDAS and dried at $P = 900$ mbar, the type of solvent had also very few influences on the textural properties of the supports. Similarly to the case of pure alumina, the arrangements of the alumina particles of samples *N-EDAS8*, *N-EDAS8-H₂O* and *N-EDAS8-Acetone* were therefore stiff enough to withstand the capillary pressures of each solvent.^[186]

Table A5.4: Textural and crystallographic properties of the calcined samples synthesized with different operating conditions.

Samples	S_{BET} (m^2/g)	V_p (cm^3/g)	S_{meso} (m^2/g)	$V_{Dubinin}$ (cm^3/g)	d_{XRD,Al_2O_3} (nm)	ρ (cm^3/g)
<i>Drying solvent</i>						
N	280	0.4	215	0.09	4.4	3.14
N-H ₂ O	280	0.4	220	0.09	4.3	3.05
N-Acetone	280	0.4	215	0.09	4.3	3.09
N-EDAS8	450	0.2	125	0.13	3.4	2.79
N-EDAS8-H ₂ O	450	0.2	135	0.13	3.3	2.71
N-EDAS8-Acetone	455	0.2	110	0.13	3.2	2.79
<i>Drying solvent + Drying pressure</i>						
N-P700	255	0.4	200	0.08	4.4	3.06
N-H ₂ O-P700	260	0.4	195	0.08	4.3	3.08
N-Acetone-P700	240	0.3	175	0.08	4.4	3.06
N-EDAS8-P700	340	0.1	50	0.11	3.2	2.87
N-EDAS8-H ₂ O-P700	380	0.1	60	0.12	3.3	2.78
N-EDAS8-Acetone-P700	340	0.1	55	0.10	3.3	2.83

S_{BET} : specific surface area; V_p : porous volume; S_{meso} : mesoporous surface area; $V_{Dubinin}$: microporous volume; ρ : apparent density; d_{XRD,Al_2O_3} : alumina crystallites size estimation by XRD.

Figure A5.3 shows the nitrogen adsorption-desorption isotherms and the mesopore size distribution of calcined samples made of pure alumina and dried at $P = 700$ mbar. It was observed that the isotherms of samples *N*, *N-P700*, *N-H₂O-P700* and *N-Acetone-P700* were very similar and characteristic of mesoporous samples. Nevertheless, it is to notice that sample *N-Acetone-P700* showed lower V_p value ($0.3 \text{ cm}^3/\text{g}$ instead of $0.4 \text{ cm}^3/\text{g}$ for the other samples, Table A5.4).

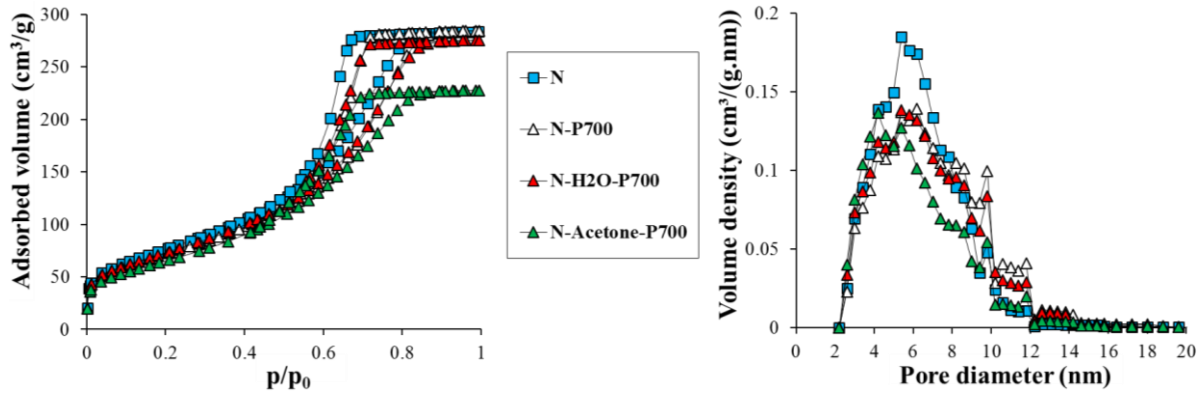


Figure A5.3: Nitrogen adsorption-desorption isotherms (left side) and their related mesopore size distribution (right side) for calcined samples *N*, *N-P700*, *N-H₂O-P700* and *N-Acetone-P700*.

It can be observed in Table A5.4 that the gels dried at $P = 700$ mbar with ethanol (sample *N-P700*) and with water (sample *N-H₂O-P700*) presented similar textural properties losses ($\Delta S_{BET} \sim -20 \text{ m}^2/\text{g}$, $\Delta S_{meso} \sim 20 \text{ m}^2/\text{g}$, $\Delta V_p \sim 0 \text{ cm}^3/\text{g}$ and $\Delta V_{Dubinin} \sim 0.003 \text{ cm}^3/\text{g}$). In contrary, the gel dried with acetone (sample *N-Acetone-P700*) was greatly affected by the drying step at lower pressure ($\Delta S_{BET, N-Acetone}$ vs. *N-Acetone-P700* = $-40 \text{ m}^2/\text{g}$, $\Delta S_{meso, N-Acetone}$ vs. *N-Acetone-P700* = $-40 \text{ m}^2/\text{g}$, $\Delta V_p, N-Acetone}$ vs. *N-Acetone-P700* = $-0.1 \text{ cm}^3/\text{g}$ and $\Delta V_{Dubinin, N-Acetone}$ vs. *N-Acetone-P700* = $-0.01 \text{ cm}^3/\text{g}$) (Table A5.4). These differences seem to be correlated to the partial pressures, p_v , of the solvents (Table A5.1). Therefore, it was assumed that the high partial pressure of acetone, associated to the lower drying pressure led to a very high evaporation rate of this solvent (Equation A5.2). Due to this higher evaporation rate, the γ - Al_2O_3 particles of sample *N-Acetone-P700* were not able to agglomerate in sufficiently stiff arrangements, which led to a partial collapse of the mesoporosity of the sample.^[186]

Figure A5.4 shows the nitrogen adsorption-desorption isotherms and the mesopore size distributions of calcined supports made of alumina modified with EDAS and dried at $P = 700$ mbar. It was observed that the reduction of the drying pressure from $P = 900$ mbar to $P = 700$ mbar provoked an almost total disappearance of the mesoporosity of the samples, leading to strictly microporous materials with pore diameters lower than 5 nm.

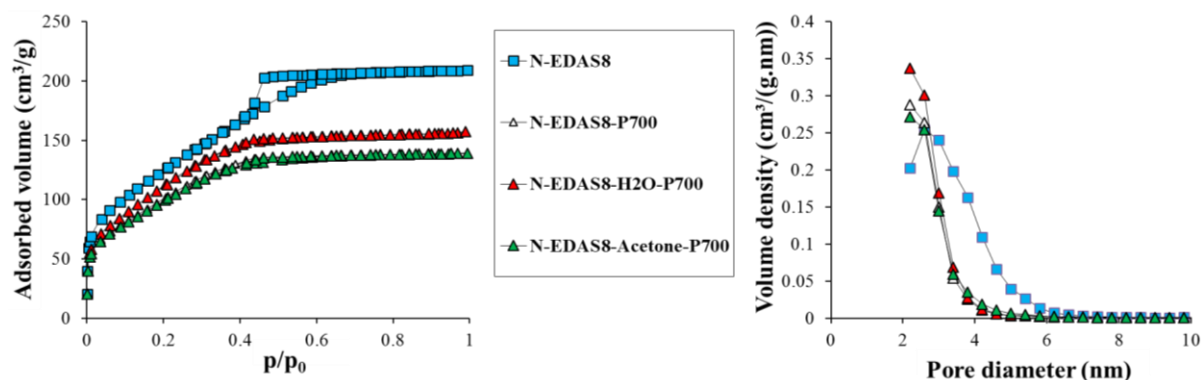


Figure A5.4: Nitrogen adsorption-desorption isotherms (left side) and their related mesopore size distribution (right side) for calcined samples *N-EDAS8*, *N-EDAS8-P700*, *N-EDAS8-H2O-P700* and *N-EDAS8-Acetone-P700*.

It was observed in Table A5.4 that samples *N-EDAS8-P700*, *N-EDAS8-H2O-P700* and *N-EDAS8-Acetone-P700* presented high losses of their mesoporous surface areas ($\Delta S_{meso} \sim 80 \text{ m}^2/\text{g}$) and a drastic diminution of their total pore volumes (V_p divided by a factor of about two). However, the microporosity of the samples was less affected ($\Delta V_{Dubinin} \sim -0.03 \text{ cm}^3/\text{g}$), which explained why the samples still presented relatively high specific surface area values ($S_{BET} \sim 340\text{-}380 \text{ m}^2/\text{g}$) (Table A5. A5.4). It is to notice that the samples dried with ethanol (sample *N-EDAS8-P700*) and with acetone (sample *N-EDAS8-Acetone-P700*) were the most affected by the lowering of the drying pressure. The trends observed were similar to the results obtained for the pure alumina samples but more marked in that case. It was assumed that the spherical shape of the EDAS-modified alumina crystallites, associated to a bad arrangement of the particles caused by the high evaporation rate led to a higher shrinkage of the gels, and therefore a total disappearance of the mesoporosity of the samples.^[186]

III.2. Impact of the new synthesis method on the properties of Ni/ γ - Al_2O_3 catalysts

Table A5.5 shows the compositions of samples *N-10Ni** and *N-EDAS8-10Ni** determined by ICP-AES measurements. Both samples presented similar theoretical and actual values, meaning that the residual nitrates ions did not cause any element evacuation during the calcination step.

Table A5.5: Samples composition determined by ICP measurements.

Samples	Composition					
	Al_2O_3		SiO_2		Ni	
	Theo. (wt. %)	Exp. (wt. %)	Theo. (wt. %)	Exp. (wt. %)	Theo. (wt. %)	Exp. (wt. %)
N-10Ni*	90.0	89.5	0	0	10.0	10.5
N-EDAS8-10Ni*	81.8	81.5	8.2	8.4	10.0	10.1

Figure A5.5 shows the nitrogen adsorption-desorption isotherms and the mesopore size distributions of calcined samples. It was observed that the samples prepared by the new method (samples *N-10Ni** and *N-EDAS8-10Ni**) also presented isotherms characteristic of mesoporous materials and similar pore diameters distribution as previous samples (samples *N-10Ni* and *N-EDAS8-10Ni*).

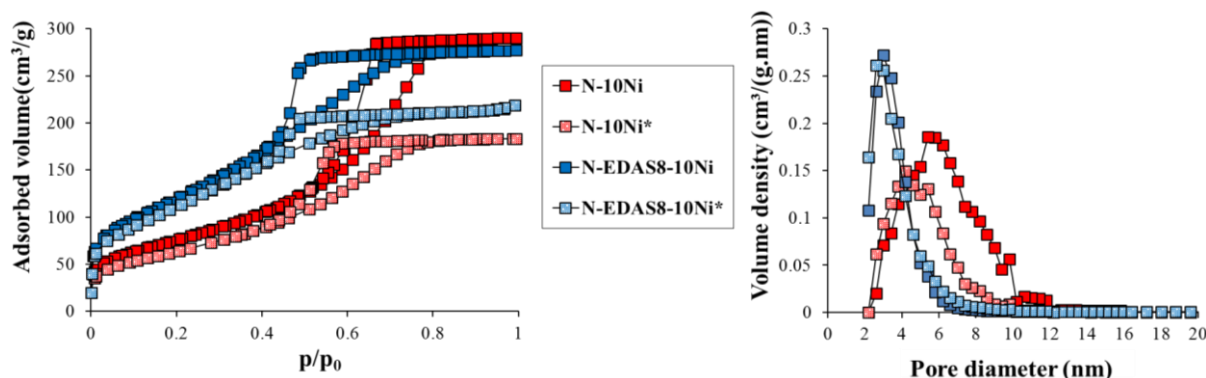


Figure A5.5: Nitrogen adsorption-desorption isotherms (left side) and mesopore size distribution (right side) for samples *N-10Ni*, *N-10Ni**, *N-EDAS8-10Ni* and *N-EDAS8-10Ni**.

Table A5.6 presents the textural properties after calcination and the metallic nickel particles sizes after reduction step (H₂, $t = 1$ h, $T = 750$ °C) for the samples prepared by the classic and the new method.

Table A5.6: Textural properties of the calcined samples and Ni particles sizes after H₂ reduction.

Samples	Textural properties			Ni particles sizes after H ₂ reduction		
	S_{BET} (m ² /g)	V_p (cm ³ /g)	$V_{Dubinin}$ (cm ³ /g)	d_{TEM} (nm)	σ_{TEM} (nm)	d_{XRD} (nm)
N-10Ni	280	0.40	0.09	8.3	3	9.7
N-10Ni*	240	0.24	0.08	9.4	2	9.5
N-EDAS8-10Ni	450	0.31	0.14	5.4	2	7.0
N-EDAS8-10Ni*	420	0.22	0.13	5.9	2	7.1

S_{BET} : specific surface area; V_p : porous volume; $V_{Dubinin}$: microporous volume ; d_{TEM} : Ni particles size median; σ_{TEM} : standard deviation of Ni particles sizes; d_{XRD} : Ni crystallites size average obtained by XRD.

It was observed in Table A5.6 that the modification of the preparation method led to a small decrease of the textural properties of the catalysts prepared by the new method (samples *N-10Ni** and *N-EDAS8-Ni**) compared to those prepared by the previous method: $\Delta S_{BET} \sim 30$ -40 m²/g, $\Delta V_p \sim 0.10$ -0.21 cm³/g and $\Delta V_{Dubinin} \sim 0.01$ cm³/g. This decrease of textural properties was attributed to the presence of residual NO₃⁻ ions coming from the nickel nitrate hexahydrate doping. Two explanations were considered: 1) the thermal degradation of the nitric acid (HNO₃) into NO₂, O₂ and H₂O is an endothermic reaction ($\Delta H_{r,298K} = + 46$ kJ/mol).^[389] Its degradation during the calcination of the dried gels could have lead to the presence of hot and cold spots. These thermal heterogeneities during calcination are known to provoke a collapse of the materials mesostructure^{[220], [221]}; 2) in the dried gel, there is still presence of NH₄⁺ ions which can be adsorbed at the surface of the boehmite crystallites. The thermal degradation of ammonium nitrate (NH₄NO₃) into N₂, H₂O and O₂ being highly reactive and exothermic ($\Delta H_{r,298K}^0 = - 154$ kJ/mol), it could also have lead to thermal heterogeneities during calcination, which would have provoke a collapse of the materials mesostructure.

Observation of the d_{XRD} , d_{TEM} and σ_{TEM} values presented in Table A5.6 revealed that the new method of preparation did not seem to affect the size and distribution of the Ni⁽⁰⁾ particles after H₂ reduction step. It was therefore concluded that the new preparation method permitted to obtained catalysts with almost unchanged properties.

IV. CONCLUSIONS

Different paths were studied in order to optimize the preparation method of the supports and catalysts. The following observations and interpretations were made:

* Changing the NH₄OH concentration from 30 wt. % to 10 wt. % had no influence on the textural and crystalline properties of supports made of γ -Al₂O₃ and of γ -Al₂O₃ modified with EDAS.

* The type of solvent (water, ethanol, acetone) used during the drying of gels made of alumina hydroxide or of alumina hydroxide modified with EDAS had almost no influence on the final textural properties of the supports. However, it was observed that a lower drying pressure strongly decreased the mesoporosity of the materials. This effect was attributed to a high evaporation rate of the solvents, which prevented the correct arrangement of the particles during the gel shrinkage and led to a decrease of the mesoporous structure of the support. Indeed, the sample prepared with acetone was the most affected by the lowest drying pressure because acetone is the solvent which shows the higher partial pressure.

* The impact of a new method for the synthesis of Ni/ γ -Al₂O₃ catalysts was studied. It was observed that the catalysts prepared by the new method were slightly less mesoporous than the materials prepared by a classic method. However, no influences on the size and distribution of the Ni particles after a reduction step were observed. In light of these conclusions, it can be said that the new method open the way for the synthesis of Ni/ γ -Al₂O₃ catalysts with higher amounts of metal loading than 10 wt. %.

Annex 6: Complementary study about 10 wt. % Ni/ γ - Al_2O_3 catalysts modified with different silicon precursors

Taking into account the results from Chapter IV, it was decided to focus on the development of Ni/ γ - Al_2O_3 catalysts with a higher loading of nickel (Ni = 10 wt. %) for the reforming of toluene under secondary catalytic conditions.

It was observed in Chapter III that the addition of a silicon alkoxide precursor during the sol-gel synthesis of γ - Al_2O_3 had a strong influence on the final properties of the support. Furthermore, the modification of γ - Al_2O_3 properties (texture, crystallinity ...) was strongly influenced by the nature of the silicon precursor (reactivity of alkoxy groups, functionalization).

In line with these results, this study investigates the synthesis, the characterization and the catalytic test of 10 wt. % Ni/ γ - Al_2O_3 catalysts modified with different silicon alkoxydes. Samples were synthesized with tetramethoxysilane (TMOS) and tetraethoxysilane (TEOS) in order to understand the influence of the reactivity of the silicon precursor. The use of EDAS is also investigated in order to understand the influence of a precursor containing an organo-amino function. The catalytic activity and stability of the catalysts are evaluated for the reforming of 8000 ppmv of toluene at $T = 650\text{ }^\circ\text{C}$ for $t = 5$ h and with the classic syngas mixture.

I. INTRODUCTION

Though zeolites materials are widely used for many different heterogeneous catalytic applications, these supports have proved to be unfitted for steam reforming application. This is mainly due to the large presence of Brönsted acid sites, which stabilize the carbon intermediates (carbonium ions) responsible of carbon deposit.ⁱ

A comparison of the catalytic performances of nickel supported on γ - Al_2O_3 and SiO_2 for the reforming of toluene and naphthalene at temperatures similar to those encountered inside the reactor ($T = 730\text{-}850\text{ }^\circ\text{C}$) was made by Srinakruang *et al.*^[390]. The authors showed that Ni/ γ - Al_2O_3 catalysts allowed a higher catalytic activity compared to Ni/ SiO_2 materials. The higher catalytic activity was notably attributed to the higher metal-support interactions of Ni/ γ - Al_2O_3 materials. Indeed, the strong interactions between Ni and γ - Al_2O_3 are known to prevent the sintering of the nickel nanoparticles and afford a higher catalytic activity.^{[9], [65], [278]} Furthermore, it is suspected that the simultaneous presence of metallic Ni⁽⁰⁾ particles and unreduced spinel NiAl_2O_4 could favor a higher catalytic activity and a lower coking.^[278]

Chapter III highlighted that the more reactive the silicon precursor was, the more important the Si atoms were incorporated inside the bulk alumina. These modifications permitted notably to delay the γ - to α - Al_2O_3 phase transition, and to improve the resistance of the catalysts support against sintering and steaming. In line with these results, it would be interesting to evaluate the influence of the degree of Si incorporation into the bulk alumina for the catalytic performances (catalytic activity + coking resistance) of the Ni/ γ - Al_2O_3 catalysts modified with SiO_2 synthesized in this study.

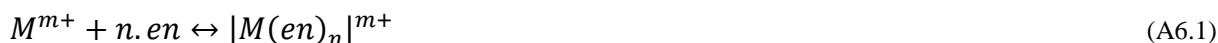
For several reasons the size of the metallic nanoparticles plays a major role for the catalytic activity and stability of a reforming catalyst.ⁱⁱ Therefore, in the aim of obtaining finely dispersed metallic nanoparticles on the γ - Al_2O_3 supports, the influence of a silicon precursor with a chelating function (EDAS) was studied. The ethylenediamine ($\text{NH}_2\text{-(CH}_2\text{)}_2\text{-NH-}$) groups contained in the functional chain of EDAS molecules are able to form a chelate with a metallic cation,ⁱⁱⁱ increasing the dispersion of the metallic nanoparticles into the support (SiO_2 , TiO_2 ...) and consequently the catalytic activity of these

ⁱ : See part I.4.4.2.3. of Chapter I.

ⁱⁱ : More information about the influence of particles size in part I.4.4.4. of Chapter I.

ⁱⁱⁱ : See Figure II.6.

samples.^{[212], [391]} Equation A6.1 presents the formation of a complex between one ethylenediamine group and a metal ion:



where M is the metal, $m+$ is the electronic charge of the ion and en is the ethylenediamine group. In the case of a complex formation between one ethylenediamine group and one Ni²⁺ ion at room temperature, the constant of formation and the enthalpy of formation are both high ($\text{Log}(K) = 7.5$ and $\Delta H_{f,298\text{K}} = -37.7$ kJ/mol).^[392]

It is to notice that the use of Al₂O₃ supports modified with chelating silicon precursors has been already studied in the literature.^[393] However, the functionalization of γ -Al₂O₃ has always been performed by grafting methods,ⁱ which are very different from the cogelation procedure used in this work.

It has been shown in Chapter III that γ -Al₂O₃ samples modified with EDAS presented smaller and spherical shaped crystallites. As a result, these samples were micro- and mesoporous with a narrow pore size distribution. Since the textural properties of the support is known to have a strong influence on the sintering of the metallic nanoparticles, the average size and the standard deviation of the metallic nanoparticle sizes of all the samples were compared after different treatments (pure H₂ reduction, TPR, catalytic test).

II. EXPERIMENTAL

II.1. Preparation of Ni/ γ -Al₂O₃ catalysts modified with EDAS, TMOS or TEOS

Samples *N-10Ni*, *N-TMOS8-10Ni*, *N-TEOS8-10Ni* and *N-EDAS8-10Ni* were prepared according to preparation method similar to the one used in Chapter IV. Silicon precursors (TMOS, TEOS or EDAS) were added before the precipitation step. After the precipitation, the sols were agitated for $t = 24$ h at $T = 85$ °C, washed two times with water, re-dispersed in water and doped with nickel nitrate. After $t = 30$ min of stirring, the bottles were opened and the sols were set in an oven for aging ($t = 24$ h, $T = 85$ °C, $P = 700$ mbar). Thereafter, the gels were washed again (once with water and once with ethanol), dried ($t = 24$ h, $T = 110$ °C, $P = 900$ mbar) and calcined ($t = 5$ h, $T = 550$ °C, 2 °C/min). The type and amounts of reagents (aluminum nitrate, EDAS, TMOS and TEOS) used for the synthesis of 10 g of catalyst are listed in part V of Annex 2.

II.2 Characterization techniques

Compositions analyses (ICP–AES), nitrogen adsorption-desorption isotherms (BET), X-Ray analysis (XRD), temperature programmed reduction (TPR), transmission electron microscopy (TEM), thermogravimetric-differential scanning calorimetry (TG-DSC), pure reduction (H₂-Reduction), temperature programmed desorption (TPD-NH₃) measurements were performed on the samples of this study. The Ni⁽⁰⁾ particle sizes, were calculated by using the Scherrer equation centered on the Ni ray (2 0 0) ($2\theta = 51.83$ °). Deeper information about the characterizations techniques and variables quoted are provided in part II of Annex 2.

II.3. Catalytic experiments

The catalytic tests were performed at $T = 650$ °C, for $t = 300$ min, with a toluene concentration of 8000 ppmv. A standard syngas mixture was used (Table IV.1, Chapter IV). Two *GHSV* conditions were used: 1) *GHSV* n°1 was set at 6000 h⁻¹ (equivalent to a residence time of 0.6 sec), for a mass of catalytic sample mass of 250 mg; 2) *GHSV* n°2 was set at 24.000 h⁻¹ (equivalent to a residence time of 0.15 sec), for a mass of catalytic sample of 62.5 mg. The catalytic performances of the samples were determined thanks to the toluene conversion (C_{Tolu}), benzene selectivity (S_B), methane conversion (C_{CH4}), reaction

ⁱ: More information about grafting methods in part II.1.3. of Chapter II.

rate of toluene (r_{Tolu}) and tendency to form carbon (*Coke**). These formulae are reminded in part I in Annex 2.

III. RESULTS AND DISCUSSION

III.1. Compositions

Table A6.1 shows the composition of the samples determined by ICP-AES measurements. It was observed that the theoretical and actual values were similar.

Table A6.1: Theoretical and experimental compositions of the samples determined by ICP-AES measurements.

Samples	Al ₂ O ₃		SiO ₂		Ni	
	Theo. (wt. %)	Exp. (wt. %)	Theo. (wt. %)	Exp. (wt. %)	Theo. (wt. %)	Exp. (wt. %)
N-10Ni	90	90.9	0	0	10	9.1
N-EDAS8-10Ni	81.8	81.8	8.2	8.6	10	9.6
N-TMOS8-10Ni	81.8	82.2	8.2	7.5	10	10.3
N-TEOS8-10Ni	81.8	81.6	8.2	8.8	10	9.6

III.2. Textural and physico-chemical properties of 10 wt. % Ni/ γ -Al₂O₃ catalysts modified with a silicon precursor

Figure A6.1 shows the nitrogen adsorption-desorption isotherms and their associated mesopore size distributions for all calcined samples. The values of the specific surface area, S_{BET} , the pore volume, V_p , and the microporous volume, $V_{Dubinin}$, values are listed in Table A6.2.

Table A6.2: Textural properties of calcined samples.

Samples	S_{BET} (m ² /g)	V_p (cm ³ /g)	$V_{Dubinin}$ (cm ³ /g)
N-10Ni	280	0.4	0.09
N-EDAS8-10Ni	450	0.3	0.14
N-TMOS8-10Ni	335	0.5	0.11
N-TEOS8-10Ni	390	0.8	0.13

S_{BET} : specific surface area; V_p : porous volume; $V_{Dubinin}$: microporous volume.

It can be observed in Table A6.2 that the textural properties of all samples were very similar to the results obtained for the characterization of γ -Al₂O₃ samples modified with the same silicon alkoxides, but without Ni (Chapter III). Therefore, the doping of 10 wt. % of Ni during the synthesis procedure did not affected greatly the micro- and mesoporosity of the supports.

In this way, sample *N-EDAS8-10Ni* still presented a narrow mesopore size distribution centered on 4 nm, the highest specific surface area ($S_{BET} = 450$ m²/g), the highest microporous volume ($V_{Dubinin} = 0.14$ cm³/g) and the lowest pore volume ($V_{p,N-EDAS8-10Ni} = 0.3$ cm³/g). Similarly to the pure γ -Al₂O₃ studied in Chapter III, samples *N-10Ni*, *N-TMOS-10Ni* and *N-TEOS8-10Ni* presented lower S_{BET} and $V_{Dubinin}$ values, but a broader mesopore size distributions comprised between 2 and 20 nm.

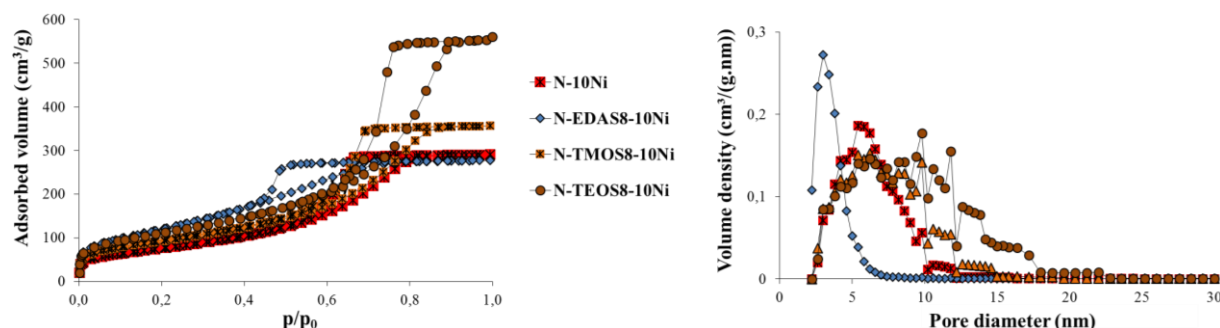


Figure A6.1: Nitrogen adsorption-desorption curves (left side) and their associated mesopore size distribution (right side) for calcined samples *N-10Ni*, *N-EDAS8-10Ni*, *N-TMOS8-10Ni* and *N-TEOS8-10Ni*.

Figure A6.2 presents the NH₃-TPD curves performed on calcined samples. For each sample, a first desorption peak corresponding to weak acid sites was observed between $T = 100$ and $T = 400$ °C, followed by a second peak characteristic of stronger acid sites.^[394] It was highlighted in Chapter III that the modification of γ -Al₂O₃ with different silicon precursors (EDAS, TMOS, TEOS ...) led to

modifications of the alumina crystallinity and to different degree of Si incorporation into the bulk alumina. Nevertheless, in Figure A6.2 and Table A6.3, all samples presented similar TPD-NH₃ profiles and similar amounts of NH₃ desorbed (~ 0.5 mmol_{NH₃}/g). The similar results obtained for all the samples may be due to the low amount of SiO₂ loadings. Noteworthy, this value was in the order of magnitude of what is usually obtained for alumina and alumino-silicate materials.^{[394], [395]}

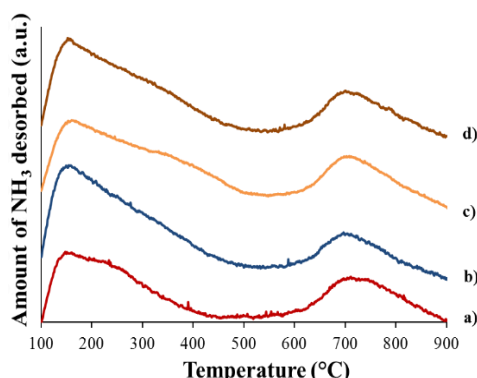


Figure A6.2: Acidity measurement by NH₃-TPD measurements of calcined samples; a. *N-10Ni*, b. *N-EDAS8-10Ni*, c. *N-TMOS8-10Ni*, d. *N-TEOS8-10Ni*.

Table A6.3: Quantity of NH₃ desorbed during the TPD-NH₃ measurements.

	N-10Ni	N-EDAS8-10Ni	N-TMOS8-10Ni	N-TEOS8-10Ni
Weak acid sites (mmol _{NH₃} /g)	0.28	0.36	0.34	0.36
Strong acid sites (mmol _{NH₃} /g)	0.20	0.16	0.18	0.16
Total acidity (mmol _{NH₃} /g)	0.48	0.52	0.52	0.52

Figure A6.3 presents the TPR profiles of calcined samples. The TPR profile of sample *N-10Ni* showed a large peak from $T = 700$ °C to $T = 950$ °C, with a maximum set at $T = 850$ °C, characteristic of nickel oxide with strong interactions with the support (NiAl₂O₄).^{[272], [288], [289]} It was observed that the reduction profiles of samples *N-TMOS8-10Ni*, *N-TEOS8-10Ni* and *N-EDAS8-10Ni* were influenced by the nature of the silicon precursor used. In the case of a strong incorporation of Si atoms inside the bulk alumina (samples *N-TMOS8-10Ni* and *N-EDAS8-10Ni*), the reduction of NiAl₂O₄ was highly shifted toward lower temperatures ($\Delta T = -75$ °C or -50 °C). In contrary, when the incorporation of Si atoms inside the bulk alumina was less important (sample *N-TEOS8-10Ni*), the shift of the Ni reduction was less important ($\Delta T = -25$ °C). This can be explained by the fact that NiO supported on SiO₂ is reduced at lower temperature ($T = 400$ - 600 °C) compared to when supported on γ -Al₂O₃.^{[396], [397]} Consequently, a better incorporation of Si inside the bulk alumina could help to shift the reduction peaks toward lower temperatures.

The better reduction observed for sample *N-EDAS8-10Ni* compared to sample *N-TMOS8-10Ni* was explained by the fact that sample *N-EDAS8-10Ni* presented lower Ni particles (Table A6.4). Indeed, it has been highlighted in Chapter VI that the smaller the particles were, the more reducible they were.

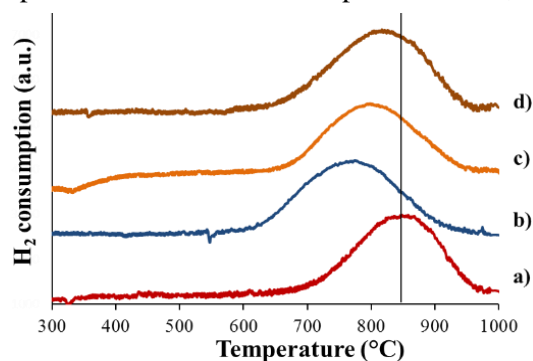


Figure A6.3: TPR curves of calcined samples; a. *N-10Ni*, b. *N-EDAS8-10Ni*, c. *N-TMOS8-10Ni*, d. *N-TEOS8-10Ni*.

X-Ray diffraction (not shown here) were performed on calcined samples and only presented γ -Al₂O₃ rays, but no visible rays of NiO or NiAl₂O₄. This was assumed to be characteristic of a very fine dispersion of the nickel oxides on the γ -Al₂O₃ and γ -Al₂O₃-SiO₂ supports. Figure A6.4 shows the X-Ray diffraction patterns of the samples after H₂ reduction step and after TPR measurements. In both case, all X-Ray patterns presented characteristic rays of γ -Al₂O₃ and of metallic nickel.

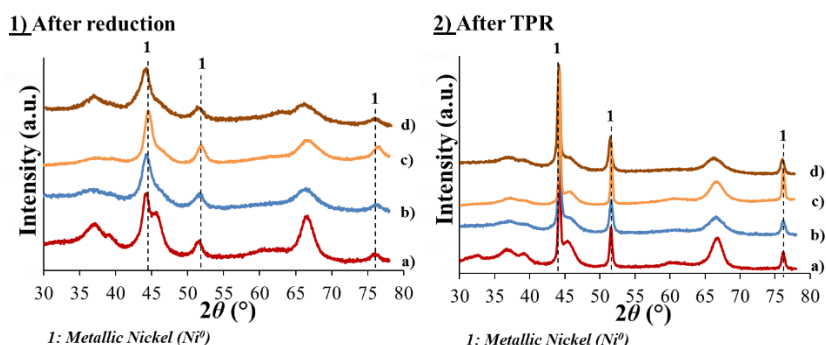


Figure A6.4: X-Ray diffraction patterns of samples after H₂ reduction and after TPR measurements; a. *N-10Ni*, b. *N-EDAS8-10Ni*, c. *N-TMOS8-10Ni*, d. *N-TEOS8-10Ni*.

Table A6.4 shows the Ni⁽⁰⁾ particles size medians and their standard deviation for all samples after H₂ reduction ($t = 1$ h, $T = 750$ °C) and after TPR measurements. For a better view, Figure A6.5 presents the data from Table A6.4 in diagrams.

Table A6.4: Ni particles sizes after H₂ reduction and after TPR measurement.

Samples	After H ₂ Reduction			After TPR		
	d_{XRD} (nm)	σ_{TEM} (nm)	d_{TEM} (nm)	d_{XRD} (nm)	σ_{TEM} (nm)	d_{TEM} (nm)
N-10Ni	10	3	8	24	10	32
N-EDAS8-10Ni	7	2	5	16	8	23
N-TMOS8-10Ni	8	3	9	30	11	42
N-TEOS8-10Ni	8	3	9	20	9	28

d_{TEM} : metallic particles size median; σ_{TEM} : standard deviation; d_{XRD} : metallic crystallites size estimation obtained by XRD.

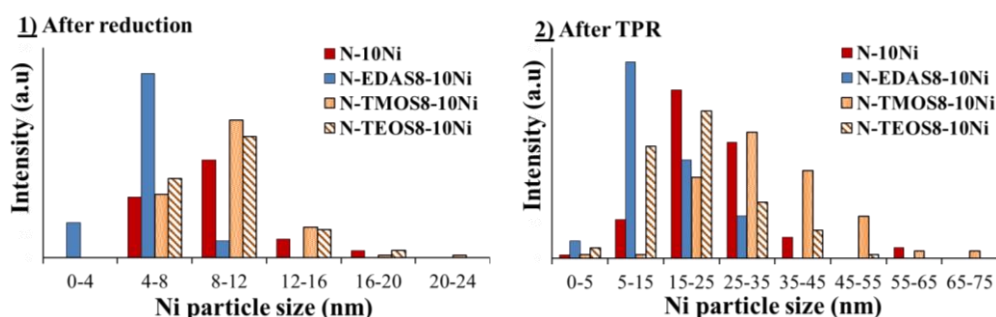


Figure A6.5: Nickel particles sizes distributions after H₂ reduction step (left side) and after TPR measurements (right side) for samples *N-10Ni*, *N-EDAS8-10Ni*, *N-TMOS8-10Ni* and *N-TEOS8-10Ni*.

After H₂ reduction, sample *N-EDAS8-10Ni* showed the lowest Ni particle size ($d_{XRD} = 7$ nm and $d_{TEM} = 5$ nm), the lowest standard deviation value ($\sigma_{TEM} = 2$ nm) and a narrow Ni particle size distribution (Figure A6.5). The Ni⁽⁰⁾ particles sizes obtained for samples *N-10Ni*, *N-TMOS8-10Ni* and *N-TEOS8-10Ni* were slightly higher compared to sample *N-EDAS8-10Ni*.

So, thanks to the formation of complexes with the Ni²⁺ ions, the ethylenediamine groups of the chains of the EDAS molecules allowed obtaining smaller and more uniform nickel metallic nanoparticles. It is however to notice that the interesting influence of EDAS on the dispersion of the metallic nanoparticles was less important than expected. This was attributed to two reasons: 1) in previous works which used the EDAS as complexing molecule, the EDAS/metal ratio was usually equal to 4 in order to afford an efficient dispersion of the metal active species.^{[211], [212], [398]} Unfortunately, it was not possible in this work to use such a high ratio. Indeed, Chapter III highlighted the impossibility to add more than 14 wt. % of SiO₂ from EDAS during the synthesis of γ -Al₂O₃. Consequently, sample

N-EDAS8-10Ni was synthesized in order to contain 8.2 wt. % of SiO₂ after calcination, and hence the EDAS/Ni ratio was in that case only equal to 1; 2) EDAS molecules proved to be very efficient for the dispersion of different metals (Pd^[211], Pd and Ag^[212], Pd and Cu^[212], Cu^[212]; Ni and Cu^[398]) supported on SiO₂. However, in those studies, the samples presented low metal/support interactions, which allowed to form metallic nanoparticles at low temperatures ($T \sim 350$ °C). In the present case, the Ni/ γ -Al₂O₃ and Ni/ γ -Al₂O₃-SiO₂ materials presented very strong metal/support interactions and required very high temperature to be reduced ($T > 650$ °C). Because of these high temperatures, the sintering of the Ni nanoparticles was more important, which explains why the differences of particle sizes between samples *N-10Ni*, *N-TMOS8-10Ni*, *N-TEOS8-10Ni* and *N-EDAS8-10Ni* were not very different after a reduction step.

Interestingly, after TPR measurement, sample *N-EDAS8-10Ni* presented also the lowest metallic nickel nanoparticle sizes ($d_{XRD} = 16$ nm and $d_{TEM} = 23$ nm) and the lowest standard deviation ($\sigma_{TEM} = 8$ nm) (Table A6.4). In contrary, sample *N-TMOS8-10Ni* showed the largest nanoparticle sizes ($d_{XRD} = 30$ nm and $d_{TEM} = 42$ nm) and the highest standard deviation value ($\sigma_{TEM} = 11$ nm).

Due to the lower metal/support interactions, Ni/SiO₂ materials are usually more affected by sintering than Ni/ γ -Al₂O₃ materials.^{[396], [397], [399]} Since samples *N-TMOS8-10Ni* and *N-EDAS8-10Ni* shared very similar support crystallinity, the lower Ni particle sizes observed for sample *N-EDAS8-10Ni* after TPR could only be a consequence of its support morphology (higher microporous volume, smaller and narrow mesopore size distribution) (Table A6.2, Figure A6.1). Finally, one can notice that several TEM observations obtained for all samples depicted metallic nanoparticles about to coalesce (Figure A6.6). The sintering by crystallite migration mechanisms being strongly influenced by the support morphology, this would explain the better Ni particles dispersion obtained for sample *N-EDAS8-10Ni*.

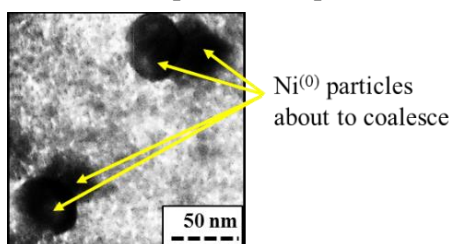


Figure A6.6: Illustration of the sintering of Ni⁽⁰⁾ particles. TEM picture taken on sample *N-TMOS8-10Ni* after TPR measurement. Magnification: 245.000X.

III.3 Catalytic performances of 10 wt. % Ni/ γ -Al₂O₃ catalysts modified with a silicon precursor

Figure A6.7 shows the toluene conversions, C_{Tolu} , as a function of time for both space ratios. Table A6.5 lists the catalytic performances of all samples at both $GHSV$ values. For all samples, C_{Tolu} increased during the first 60 min of test due to the *in situ* reduction of the nickel active sites. After about $t = 60$ min, for all samples, C_{Tolu} reached a stable level until the end of the catalytic test.

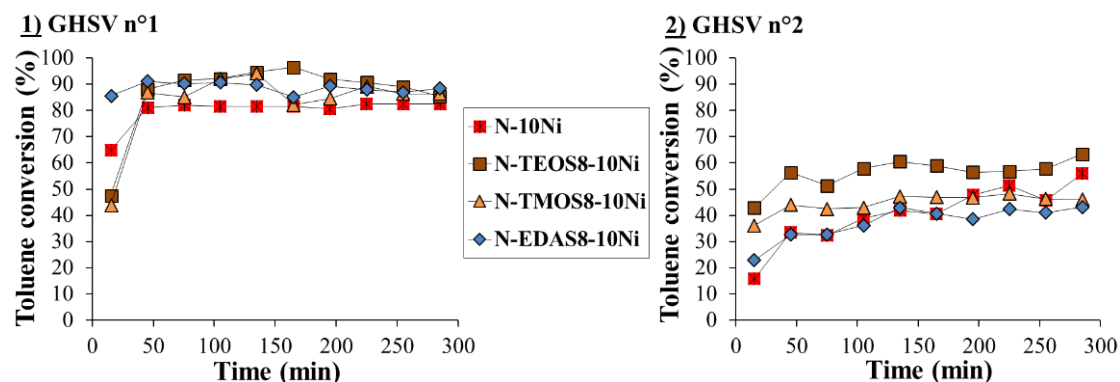


Figure A6.7: Toluene conversion as a function of time at $T = 650$ °C with 8000 ppmv of toluene with $GHSV$ $n^{\circ}1$ of 6000 h⁻¹ (left side) or with $GHSV$ $n^{\circ}2$ of 24.000 h⁻¹ (right side).

Table A6.5: Catalytic performances of samples for the reforming of 8000 ppm toluene and methane at $T = 650$ °C, for $t = 5$ h and with two different space volume ratio ($GHSV$ $n^{\circ}1 = 6000$ h⁻¹ and $GHSV$ $n^{\circ}2 = 24.000$ h⁻¹).

Samples / GHSV	C_{Tolu} (%)		r_{Tolu} (mol _{Tolu} /(g _{Ni} .h))		S_B (%)		C_{CH4} (%)		Coke (g _{Carbon} /g _{Cata})		Coke* (g _{Carbon} /g _{Tolu})	
	1	2	1	2	1	2	1	2	1	2	1	2
N	2	#	#	#	15	#	< 0.5	#	0.04	#	#	#
N-10Ni	82	47	8.3 .10 ⁻²	3.1 .10 ⁻²	< 0.5	4	15	9	0.30	0.24	8.6 .10 ⁻²	1.9 .10 ⁻²
N-EDAS8-10Ni	86	41	8.1 .10 ⁻²	2.2 .10 ⁻²	1	3	13	3	0.13	0.10	3.6 .10 ⁻²	1.0 .10 ⁻¹
N-TMOS8-10Ni	87	47	7.8 .10 ⁻²	2.4 .10 ⁻²	2	4	11	5	0.15	0.12	4.0 .10 ⁻²	1.1 .10 ⁻¹
N-TEOS8-10Ni	94	58	1.2 .10 ⁻¹	3.6 .10 ⁻²	4	8	15	8	0.61	0.55	1.1 .10 ⁻¹	3.5 .10 ⁻¹

$GHSV$ $n^{\circ}1$: 6000 h⁻¹; $n^{\circ}2$: 24.000 h⁻¹; C_{Tolu} : conversion of toluene; r_{Tolu} : reaction rate of toluene; S_B : selectivity in benzene, C_{CH4} : conversion of methane, Coke: carbon deposit amount after 5 h of test measured by TG-DSC; Coke*: tendency to form coke. #: samples not tested

Table A6.6 shows the Ni particle sizes and standard deviation measured for samples tested with $GHSV$ $n^{\circ}1$ of 6000 h⁻¹. It was observed that sample *N-EDAS8-10Ni* showed the lowest Ni particle size ($d_{XRD} = 10$ nm and $d_{TEM} = 12$ nm) and the lowest standard deviation ($\sigma_{TEM} = 3$ nm). The particle sizes and standards deviation of the three other samples were relatively similar ($d_{XRD} \sim 13$ -14 nm, $d_{TEM} \sim 6$ -8 nm and $\sigma_{TEM} \sim 6$ -8 nm).

Table A6.6: Ni particles sizes and standard deviation after catalytic test at $T = 650$ °C for $t = 5$ h and with a $GHSV$ of 6000 h⁻¹.

Samples	d_{XRD} (nm)	σ_{TEM} (nm)	d_{TEM} (nm)
N-10Ni	13	6	14
N-EDAS8-10Ni	10	3	12
N-TMOS8-10Ni	14	6	16
N-TEOS8-10Ni	13	8	16

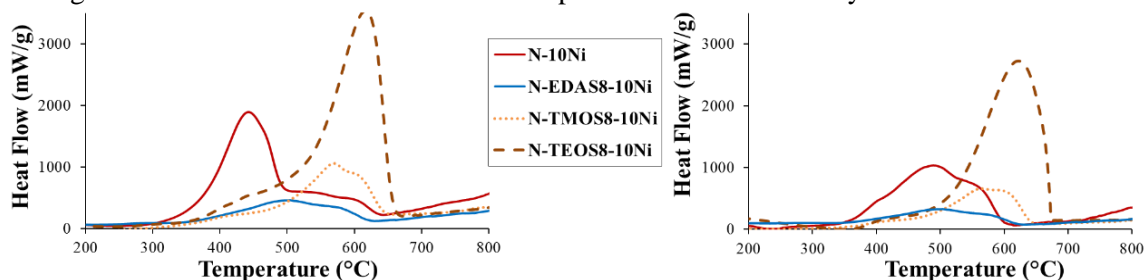
d_{TEM} : metallic particles size median; σ_{TEM} : standard deviation; d_{XRD} : metallic crystallites size estimation obtained by XRD.

At $GHSV$ $n^{\circ}1$ of 6000 h⁻¹, sample *N* (pure alumina) showed very low C_{Tolu} value (2 %), very high S_B value (15 %) and no methane conversion. In contrary, all catalysts (samples *N-10Ni*, *N-TMOS8-10Ni*, *N-TEOS8-10Ni* and *N-EDAS8-10Ni*) presented high C_{Tolu} values comprised between 80 and 95 %, low S_B values (< 4 %) and C_{CH4} values comprised between 11 and 15 % (Table A6.5).

Table A6.5 shows that, at $GHSV$ $n^{\circ}1$ of 6000 h⁻¹, sample *N-TEOS8-10Ni* showed the highest toluene reaction rate ($r_{Tolu} = 1.2 \cdot 10^{-1}$ mol_{Tolu}/(g_{Ni}.h)) and high methane conversion ($C_{CH4} = 15$ %), however this sample also showed the highest benzene selectivity ($S_B = 4$ %). Samples *N-TMOS8-10Ni* and *N-EDAS8-10Ni* showed similar catalytic performances: toluene reactions rates relatively similar to those of sample *N-10Ni*, relatively low benzene selectivity ($S_B \sim 1$ -2 %) and the lowest methane conversion values ($C_{CH4} \sim 11$ -13 %).

It was noticed that an increase of the $GHSV$ value from 6000 h⁻¹ to 24.000 h⁻¹ decreased the catalytic activity of all samples because of a lower time for the reactants and intermediate products to react together. Globally, r_{Tolu} was divided by a factor of about 3, S_B was increased by a factor of about 2 and C_{CH4} was divided by a factor of about 2-3 (around 2 for samples *N-10Ni* and *N-TEOS8-10Ni*, and around 3 for samples *N-TMOS8-10Ni* and *N-EDAS8-10Ni*). It was observed that the sample *N-EDAS8-10Ni* was the most affected by the increase of $GHSV$ (r_{Tolu} was divided by 3.7 and C_{CH4} was divided by 3.8) (Table A6.5). This sensitivity toward $GHSV$ was assumed to be caused by the very narrow mesopore size distribution of this sample, which could had caused some diffusional limitations of the reagents at high $GHSV$.

Figure A6.8 shows the DSC measurements performed after the catalytic tests:

Figure A6.8: Curves of DSC measurements performed on samples after catalytic tests at $T = 650$ °C, $t = 5$ h and with 8000 ppm of toluene with $GHSV$ $n^{\circ}1$ of 6000 h⁻¹ (left side) or with $GHSV$ $n^{\circ}2$ of 24.000 h⁻¹ (right side).

The TEM pictures presented in Figure A6.9 depict the two major types of carbon (amorphous and filamentous) deposit which were observed on the samples after catalytic tests.

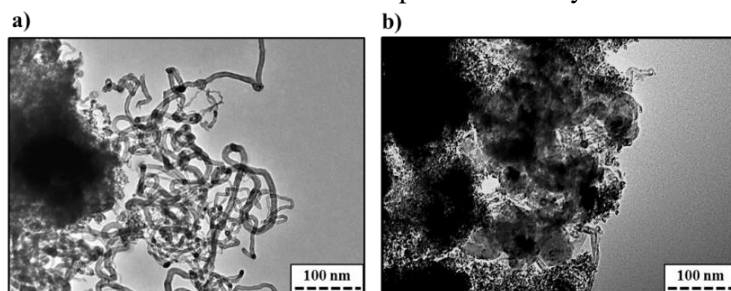


Figure A6.9: Illustrations of the two main types of carbon deposit observed after catalytic test: a. filamentous carbon, b. amorphous carbon. Magnification: 80.000 X.

It was observed in Figure A6.8 that, for GHSV n°1 of 6000 h⁻¹, the carbon deposit of sample *N-10Ni* was mainly constituted of amorphous carbon (burned at $T < 550$ °C) and a small part of filamentous carbon (burned at $T > 550$ °C).^{[68], [69]} However, this sample showed a high tendency to form carbon deposit ($Coke^*_{N-10Ni} = 8.6 \cdot 10^{-2}$ g_{Carbon}/g_{Tolu}) (Table A6.5). In comparison, samples *N-TMOS8-10Ni* and *N-EDAS8-10Ni* were less inclined to form carbon deposit ($Coke^*_{N-EDAS8-10Ni} = 3.6 \cdot 10^{-2}$ g_{Carbon}/g_{Tolu} and $Coke^*_{N-TMOS8-10Ni} = 4.0 \cdot 10^{-2}$ g_{Carbon}/g_{Tolu}) and presented the lowest *Coke* values after test. It is to notice that sample *N-EDAS8-10Ni* had a carbon deposit made of comparable proportions of amorphous and filamentous carbon, and that, sample *N-TMOS8-10Ni* showed in contrary a more important amount of filamentous than amorphous carbon (Figure A6.8). Sample *N-TEOS8-10Ni* presented the highest tendency to form carbon deposit ($Coke^*_{N-TEOS8-10Ni} = 1.1 \cdot 10^{-1}$ g_{Carbon}/g_{Tolu}) and the largest amount of carbon deposit after test ($Coke_{N-TEOS8-10Ni} = 0.61$ g_{Carbon}/g_{Cata}). Furthermore, TG-DSC (Figure A6.8) and TEM measurements revealed that the carbon deposit of this sample was mostly of filamentous nature.

These results can be correlated to the work of Srinakruang *et al.*^[390], which found out that after $t = 6$ h of steam reforming of a tar mix (toluene + naphthalene) at $T = 770$ °C, the Ni/SiO₂ catalysts showed a carbon deposit amount four times higher than the Ni/ γ -Al₂O₃ catalysts. Furthermore, TG-DSC measurements performed after the catalytic tests revealed that the carbon deposits were more amorphous for the Ni/ γ -Al₂O₃ catalysts ($T_{combustion} = 400-750$ °C) and more filamentous for the Ni/SiO₂ catalysts ($T_{combustion} = 540-750$ °C).

Hence, in these conditions of test, a better incorporation of the Si atoms inside the bulk alumina, provoked by a highly reactive silicon precursors (TMOS and EDAS), resulted in catalysts with slightly lower catalytic activity than the standard Ni/ γ -Al₂O₃ catalyst, but which presented a more marked resistance against coking. The fact that sample *N-TMOS8-10Ni* presented a slightly higher amount of carbon deposit, which was more filamentous-like than sample *N-EDAS8-10Ni* is assumed to two reasons: 1) presence of lower Ni particle sizes for sample *N-EDAS8-10Ni*. Indeed larger metallic nanoparticle sizes favors the coking and the formation of filamentous carbon; 2) lower activity of sample *N-EDAS8-10Ni*, which was attributed to the possible presence of more difficult diffusion of the reactants inside the small and narrow pores of the support (Figure A6.1).

In contrary, the modification of the γ -Al₂O₃ support with a low reactive silicon precursor (TEOS) led to catalysts with slightly better toluene and methane conversions, but with higher benzene selectivity and which were more sensible toward coking. It is assumed that, in that case, SiO₂ was not fully integrated inside the bulk alumina and led to a higher amount and more stable carbon deposit as in the case of Ni/SiO₂ catalysts.^[390]

It was observed for all samples, that an increase of GHSV decreased the catalytic activity, but led to similar amount and type of carbon deposit after test (Table A6.5, Figure A6.8). Consequently, the tendency to form coke increased at higher GHSV (*Coke** values about 2 times higher when GHSV goes from 6000 h⁻¹ to 24.000 h⁻¹). This observation was important to notice since usually an increase of GHSV allows a lower carbon deposit due to the lower catalytic activity and to the lower time for the carbon

atoms to transform into stable species.^{[9], [65], [68]} Nevertheless, the results of the present study can be compared to the work of da Silva *et al.*^[307], who performed the steam reforming of ethanol at $T = 500$ °C. The authors highlighted that during reforming reactions, the relation between the space ratio and the amount of carbon deposit was absolutely not linear and not predictable. In this way, the authors found out that the amount of carbon deposit increased with *GHSV* until reaching a maximum value. Further increase of *GHSV* led to a decrease of the carbon deposit amount, and finally to a standard value. According to the authors, the cracking of the ethanol molecule occurs quickly, but the mechanism of carbon removal which includes the diffusion of the oxidant species (O^* , HO^*) from the support surface to the metallic particle requires long contact time. In the present case, it appeared that the two *GHSV* were situated in the range where the carbon deposit rate reached a standard value, which explains why a modification of the space time modified the catalysts conversions but had little effect on the coking. In view of these results, it seemed more interesting to perform the next catalytic tests at *GHSV* of 6000 h⁻¹ instead of 24.000 h⁻¹.

V. CONCLUSIONS

This study compared the catalytic performances of 10 wt. % Ni/ γ -Al₂O₃ materials modified with different type of silicon precursors (TMOS, TEOS and EDAS) for the reforming of 8000 ppmv of toluene at $T = 650$ °C.

By the formation of EDAS/Ni²⁺ complexes during the synthesis, alumina modified with EDAS allowed obtaining a better initial dispersion of the metallic Ni particles. However, the low EDAS/Ni ratio and the strong Ni/support interactions tempered the beneficial influence of EDAS on the dispersion of the metallic active sites. On the other hand, the EDAS modified catalyst showed the best resistance against the sintering of Ni particles. This was attributed to the high microporous volume and the narrow mesoporous distribution of the support which would decrease the migration of the metallic Ni crystallites.

The catalytic tests revealed that the reactivity of the silicon precursor played a major role on the conversion of toluene. For alumina supports modified with a silicon precursor with a low reactivity such as TEOS, the poor integration of the Si atoms inside the bulk alumina led to slightly higher catalytic activities, but also to a high formation of filamentous carbon. This was explained by the fact that Ni/SiO₂ catalysts are known to be more sensible against coking than Ni/ γ -Al₂O₃ catalysts. The opposite effect was observed for the samples modified with a highly reactive silicon precursor, such as TMOS or EDAS, which showed slightly lower catalytic activities, but also better resistances against coking than pure Ni/ γ -Al₂O₃ catalysts. No clear interpretation was however found to explain why the better incorporation of Si led to better resistance against the formation of carbon deposit.

Finally, it was observed for all samples that a higher *GHSV* led to a lower catalytic activity, but also to higher tendency to form carbon deposit. This was assumed to be caused by the fact that, whereas the cracking of the toluene at the surface of the Ni particles is relatively quick, the dissociation of the H₂O and CO₂ molecules, and the migration of their oxidative species (O^* and HO^*) from the support to the carbonaceous compounds situated at the surface of the Ni particles requires a longer contact time. In this way, it seemed more appropriate to keep a *GHSV* of about 6000 h⁻¹ for the future catalytic tests.

Annex 7: Complementary study about the coating of honeycomb cordierite support with Ni/boehmite gels

This study presents the development of a method for the washcoating of Ni/boehmite gels (prepared by in our laboratory by sol-gel process) onto the surface of a ceramic monolith. Indeed, from economic and technical point of views, it is common to use secondary catalysts made of an inert ceramic support coated with an active phase. The development of an effective washcoating method in the lab would therefore allow the use of the catalysts designed throughout this project at larger scale.

An experimental assembly was made in order to apply the coating on the surfaces of a commercial honeycomb monolith made of cordierite. It was observed that the simple deposition of the Ni/boehmite gel led to a coating with many defects (cracks, coating-free areas and big aggregates). Hence, the influences of the composition of the coating solutions (type of solvent, concentration, acidity, slurry and sol+slurry) and of the procedures variables (withdrawal speed, number of impregnation, blowdown step and impregnation with a syringe) are investigated in order to optimize the quality of the deposited film.

I. INTRODUCTION

I.1. Monolithic reactors

Ceramic monolithic supports can be either foam-shaped or divided into channels of different shapes (square, triangular or hexagonal). The use of monolithic reactors have different advantages/disadvantages in comparison to packed-bed reactors, whose catalytic phase spatial arrangement does not exhibit any geometrical regularity or symmetry. Among these particularities, one can retain: 1) the low-pressure drop, associated with a laminar flow of the reaction mixture within the straight channels of the monolith; 2) the almost impossibility to plug the channels. However, fouling can occur by impaction of dust particles or by coking against the channels walls; 3) the easiness of scaling-up; 4) the absence of attrition of the active phase; 5) the high surface-to-volume ratio.^{[400]–[402]}

The ceramic monoliths used in catalysis are classified according to the porous properties of the constitutive material and of the method of incorporation of the active phase (Figure A7.1).^[403]

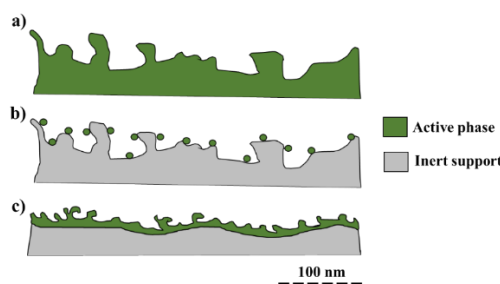


Figure A7.1: types of monolith as a function of the method of deposition of the active phase and of the porous properties of the monolith constitutive material. (a) “integral” (b) “high-surface” (c) “low-surface”.

“Integral” monoliths (Figure A7.1-a) are partially or entirely made out of the active phase. They are usually formed from a paste, which is either molded or extruded, and then fired at high temperature ($T > 1000$ °C).^[403] “High-surface” monoliths (Figure A7.1-b) show a well-designed porous structure (specific surface of a few hundreds of m^2/g), over which precursors of the active phases (usually salts) can be directly deposited by impregnation techniques. However, these supports show low mechanical strengths.^[404] “Low-surface” monoliths” (Figure A7.1-c) show a low specific surface (< 10 m^2/g), but present higher mechanical strength. The purpose of the low-surface monolith is to be a support for the deposition of a high surface coating. The coating material can either be a commercial high-surface catalyst or a highly porous support phase, such as mesoporous γ -alumina or colloidal boehmite.^{[405], [406]}

The active phase can be either contained inside the coating phase, or impregnated thereafter on the high-surface area layer.

In this study, it was decided to use “low-surface” monoliths. Indeed, the design of “integral” Ni/ γ -Al₂O₃ monoliths made of Ni/boehmite gels is theoretically conceivable, but required expensive and specialized tools, such as mold or extruder, which are not available in the laboratory. In the case of “high-surface” monoliths, no supplementary advantage appeared since the Ni/boehmite coating would completely prevent the access to the porosity of the primary support. Furthermore, “low-surface” monoliths have a higher mechanical strength than “high-surface” monoliths.

It was decided to work with a commercial cylinder of cordierite with square-shaped cross-section (Figure A7.2). Cordierite material (2Al₂O₃·2MgO·5SiO₂) is commonly used as monolith support in the catalysts field. In the present case, this material was interesting because of its ability to withstand the conditions at the exit of a biomass gasifier (high temperature, presence of steam), of its mechanical resistances and of its very low thermal expansion.^[407] Monoliths of this type are described by a small set of measurements (length H , inner width l of a channel and channel wall thickness t) (Figure A7.2) from which can be determined the three variables shown in Table A7.1.

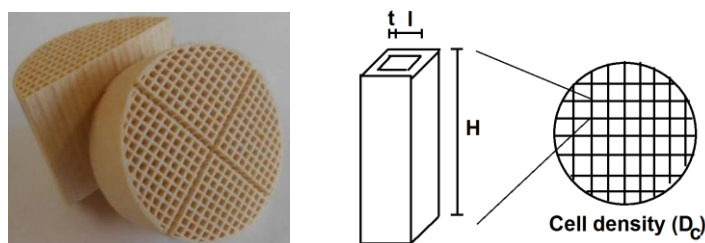


Figure A7.2: Cordierite monolith used in this work and schematic view of a channel and a monolith section.

Table A7.1: Main variables defining a monolith with square-shaped-cross-section.^[407]

Name	Cell density (in cpsi, with 1 cpsi = 0.155 cells/cm ²)	Surface-to-Volume ratio	Open Frontal Area
Equation	(A7.1) $D_c = \frac{1}{(l+t)^2}$	(A7.2) $\frac{A}{V} = 4D_c^{1/2}$	(A7.3) $OFA = \frac{l^2}{(l+t)^2}$

It is to notice that the optimal cell density takes into account both matter and heat transfer.^[408] However, this issue is not studied in this work. The Open Frontal Area (OFA) is the clear cross-section surface available for the flow of the reaction mixture. It is relatively constant. It is to notice that the pressure drop decreases with the OFA.^[400] Hence, it must be kept as close as possible to 1, in order to maintain a pressure drop as low as possible. Application of a coating, however, may slightly lower the OFA.

I.2. Principles of monolith coating

The coating precursor phase is either a powder slurry or a sol that undergoes gelation in the channels of the monolith.^[406] The premises of monolith coating were established by Taylor^[409] for the coating of cylindrical capillaries, extending the work of Fairbrothers & Stubbs^[410] to a greater range of experimental conditions. The method developed by the authors, known as gas-fluid displacement, consisted in sending a gas flux into a previously filled glass capillary. As the bubble of gas crosses the capillary at a given speed, it drives out a fraction of the liquid and leaves the remaining as a film. A few decades later, Kolb & Cerro^[411] devised a similar method to coat porous square-channeled monoliths. The coating was performed in 3 steps: filling of the channels by dip, removal of the liquid with a blowdown step and drying (Figure A7.3). The blowdown step allows the formation of a film whilst pre-drying it, thus preventing the appearance and growth of instabilities in the liquid coating film.^[412]

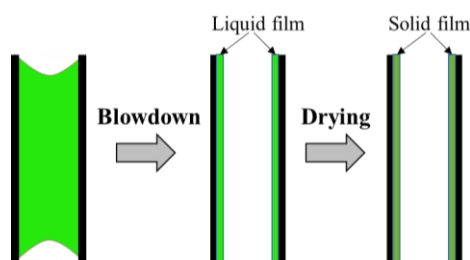


Figure A7.3: Coating process used by Kolb^[412].

The thickness and quality of the deposited layer depends of two simultaneous mechanisms: 1) the mechanism of “filter-cake formation”, which consists in the selective absorption of the solvent by capillary suction into the porous monolith walls, leaving behind a concentrated layer of particles that may gel if the concentration of particles exceeds a critical value.^[405] Its name “filter” comes from the fact that the support acts the same way as a classical filter used to recover a solid from a colloidal solution; 2) the mechanism of “viscous adhesion”, which is defined by the remaining of a liquid film on the monolith walls after the blowdown step. The film thickness depends on the purging gas velocity and on the viscosity of the coating solution.^{[405], [412]}

In this work, the blowdown step could not be carried out in a practical and reproducible way due to the lack of an adequate equipment to homogeneously blow the air (air knife). Indeed, the experimental assembly was a first prototype. Hence, for most samples, the channels of the monolith were dried while still filled by the coating solution. The drying was supposed to occur in analogy with the drying mechanism of capillaries filled with solvent and closed at one of their extremity.^[413] Hence, it was believed that the formation of a homogeneous coating would occur according to a mechanism of receding menisci, followed by a spread of the central drops to the extremities of the channel, in which the evaporation rates were assumed to be higher (Figure A7.4).

In order to make a comparison with the literature, a blowdown step was nevertheless carried out manually, using a plastic tube connected to a nitrogen gas cylinder.

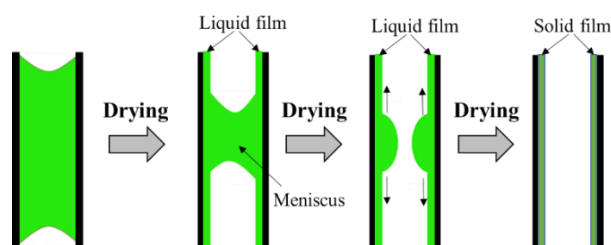


Figure A7.4: Proposed mechanism of film formation upon filled channels drying.

Once a solid film is deposited, it must adhere strongly enough to the monolith walls to prevent spalling during operation. Coating adhesion is mainly the result of anchoring and interlocking of the washcoated gel with the support surface irregularities and porosity. In comparison, chemical affinity between the support and the coating apparently is asserted to play a little role.^[414]

II. EXPERIMENTAL

II.1. Characterization techniques

In this study electronic microscopy analysis (SEM-BSE), nitrogen adsorption-desorption (BET), mercury porosimetry (Poro-HG), dynamic viscosity (Visco), dynamic light scattering (DLS) and point of zero charge (PZC) measurements were performed. Details about characterizations techniques and variables quoted are provided in part II of Annex 2.

II.2. Properties of monolithic support

The cylinder cordierite monolith was furnished by the CTI SAS enterprise. Its cell density was of 400 cpsi (62 cells/cm²). The diameter of the cylinder was determined of 25.5 mm ± 1mm. The channels

were square-shaped with an inner width of 1 mm and the cordierite walls thickness was roughly of 0.275 mm. The cylinder was sliced in different parts of 0.96 cm for the impregnations. Hence, the Surface-to-Volume ratio of the monoliths was of 31.5 for an OFA of 61 %.

Nitrogen adsorption-desorption measurements (not shown) revealed that the support did not present any micro/mesoporosity ($V_{Dubinin} < 0.001 \text{ cm}^3/\text{g}$; $V_p < 0.1 \text{ cm}^3/\text{g}$) and had a very low specific surface area ($S_{BET} < 1 \text{ m}^2/\text{g}$). Figure A7.5 shows a SEM-BSE picture of cordierite support. It can be observed that the support was macroporous with a wide pore size distribution, from a few μm to a tens of μm .

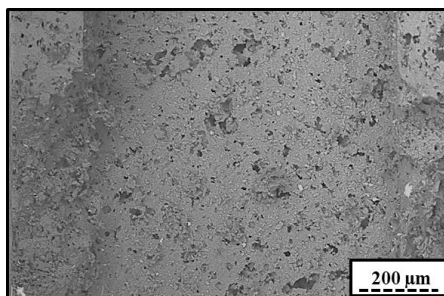


Figure A7.5: Cordierite channel surface (front view). SEM-BSE 100 X.

Figure A7.6 shows the intrusion-extrusion of Hg as a function of pressure and the macropore size distribution for cordierite sample.

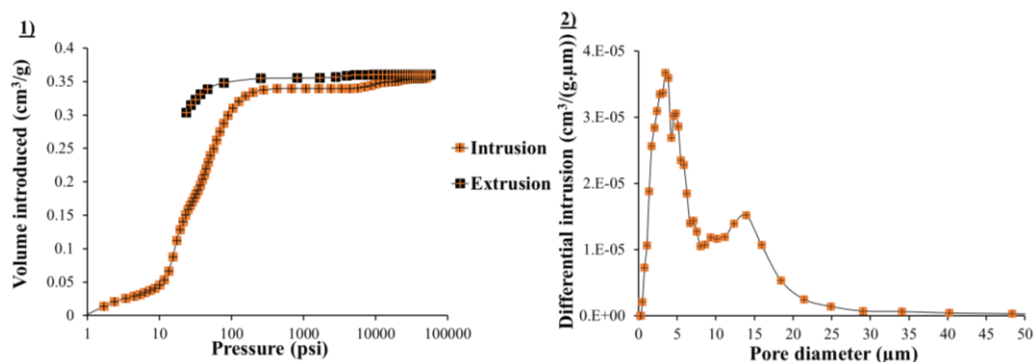


Figure A7.6: Mercury porosimetry curve for the cordierite sample; a. mercury volume introduced as a function of the pressure, b. macropore size distribution.

It is observed in Figure A7.6 that most of the macropore sizes of the cordierite are comprised between 1 and 20 μm . The macroporous volume, $V_{Hg,Cordierite}$, was relatively small ($0.30 \text{ cm}^3/\text{g}$).

II.3. Coating apparatus

Figure A7.7 shows the experimental apparatus used for the preparation of cordierite supports coated with Ni/boehmite sols.

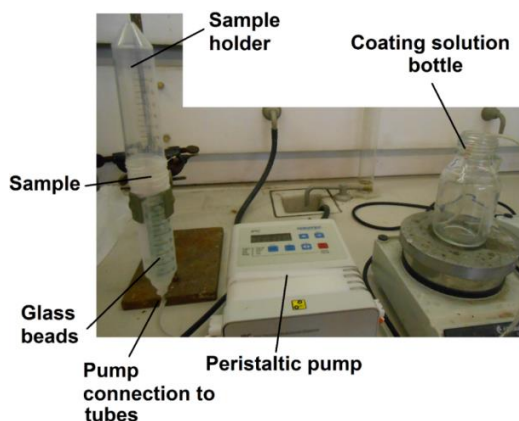


Figure A7.7: Coating apparatus used for the coating of cordierite supports with Ni/boehmite gels.

The coating apparatus consisted of two joined plastic tubes of a diameter slightly larger than the cordierite samples, so that the cordierite cylinders could be made to fit by surrounding their outer border with Parafilm®. The coating solution was sent in the tubes via an ISMATEC IPC peristaltic pump and rise at 0.6 cm/min up until the monolith was completely covered. The pump was then stopped and after $t = 2$ min, the liquid was pumped back to the coating solution bottle. Clean glass beads were added to the bottom tube in order to reduce the dead volume and speed up the process. Finally, the monolith sample was carefully removed and dried from its top and bottom face at $T = 85$ °C and $P = 700$ mbar for $t = 24$ h.

II.4. Properties of coating solutions

II.4.1. Properties of standard Ni/boehmite sol

The Ni/boehmite sols were prepared according to the method used in Chapter V for the preparation of sample *N-10Ni*.

Figure A7.8 presents the particle size distribution of the standard sol of Ni/boehmite (sample *Imp-Ref*). It was observed that the major part of the boehmite grains sizes were either about 250 or 1500 nm.

PZC measurements were carried out using the powder addition method to highlight potential electrostatic interactions between the *Imp-Ref* coating solution and the cordierite monolith. The PZC of cordierite was around 9.8, whereas it was around 8.1 for the Ni/boehmite sol (Figure A7.9). For information the *pH* of a freshly prepared Ni/boehmite sol was equal to 6.7. Hence, the particles of boehmite were positively charged and were therefore theoretically able to be adsorbed on the basic surface of cordierite.

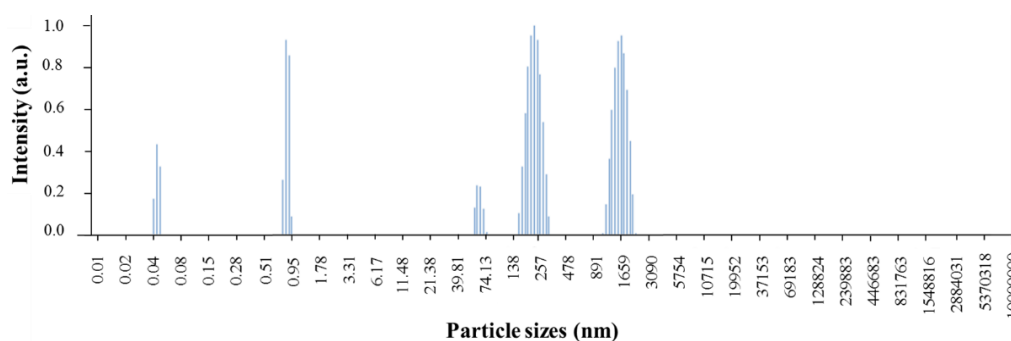


Figure A7.8: Particle size distribution of a standard Ni/boehmite sol (sample *Imp-Ref*). The measurement was performed by APTIS/Greenmat laboratory.

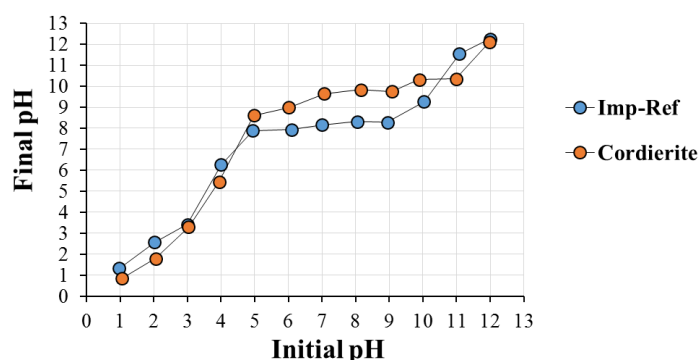


Figure A7.9: PZC measurements performed on cordierite and the standard Ni/boehmite sol (sample *Imp-Ref*).

II.4.2. Properties of different Ni/boehmite sols

The composition of the standard Ni/boehmite sol (sample *Imp-Ref*) was modified according to different parameters. Table A7.2 presents the different parameters investigated, their corresponding samples names, and the viscosity of the sols measured at 10 rpm. It is to notice that, in the case of sample *Imp-2C*, the sol was paste-like and unsuitable for coating.

Table A7.2: Modifications of the coating solutions and corresponding viscosity.

Samples	Modified parameter	Coating solution viscosity (in cP); at 10 rpm and $T = 25\text{ }^{\circ}\text{C}$
Imp-Ref	-	630
Imp-0.5C	Solution concentration (x0.5)	80
Imp-2C	Solution concentration (x2)	(too high to be measured)
Imp-HNO3	Solution pH (1.8)	1490
Imp-Acetone	Solution solvent (acetone)	710
Imp-Ethanol	Solution solvent (ethanol)	1100
Imp-Slurry	Coating with a slurry composed of calcined Ni/ γ -Al ₂ O ₃ , crushed below 45 μm and dispersed in water.	~ 1
Imp-Sol/Slurry	Slurry/sol 50/50 % vol. mixture	200

Figure A7.10 shows the viscosity of the different sols measured with rotating spindles and at different rotation speeds (10, 20, 50 and 100 rpm).

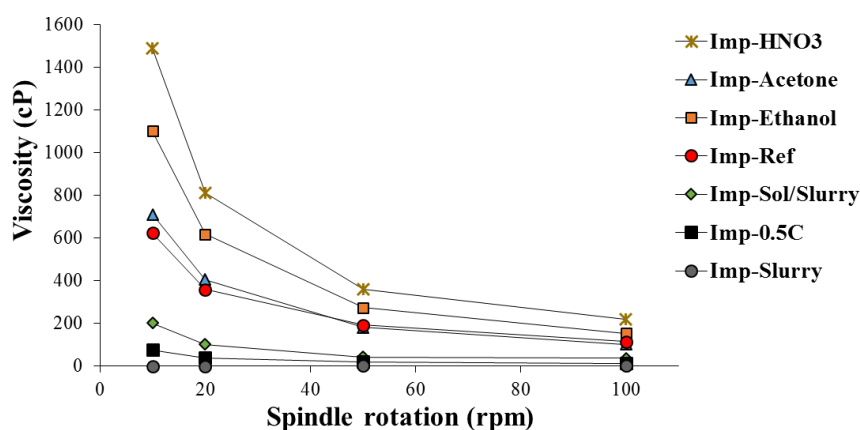
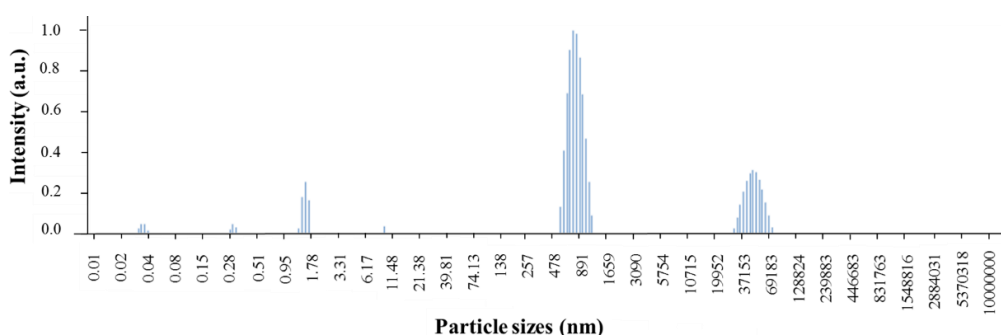


Figure A7.10: Viscosity of the coating solutions at 10, 20, 50 and 100 rpm.

It is observed in Figure A7.10 that, excepted for sample *Imp-Slurry*, all the sols showed shear-thinning (*i.e.* non-Newtonian) behaviors, meaning that their viscosity values decreases under increasing shear strain. For example, the viscosity of sample *Imp-Ref* was measured to be equal to 630 cP at 10 rpm, but decreased to 110 cP when the rotation speed was set at 100 rpm. This rheological property can be explained by the interactions between the particles, which can form micron and submicron-sized agglomerates, evidenced by DLS measurement (Figure A7.8). These agglomerates are destroyed upon stirring, but reassembles as soon as stirring strength is decreased.^{[415], [416]}

In the case of sample *Imp-Slurry*, DLS measurement (Figure A7.11) showed that the slurry was mostly composed of grains of either about 800 nm or 5 μm . This information was important since it has been shown in the literature that coatings performed with slurry and slurry/boehmite sols should be performed with calcined alumina particles whose diameters are of 5 μm maximum.^[417] The very low viscosity (magnitude of the viscosity of water, ~ 1 cP) observed for this sample (Figure A7.10, Table A7.2) was attributed to the very few interactions existing between the calcined γ -Al₂O₃ particles of the slurry.^[405]

Figure A7.11: Particle size distribution of Ni/ γ -Al₂O₃ slurry sol (sample *Imp-Slurry*). The measurement was performed by APTIS/Greenmat laboratory.

The addition of nitric acid, down to a pH of 1.8, for the coating solution of sample *Imp-HNO₃*, resulted in an increase of viscosity compared to sample *Imp-Ref* (Figure A7.10 and Table A7.2). Figure A7.12 shows the typical behavior of the viscosity of a boehmite solution as a function of pH .^[228] At high acidic or basic pH (case of sample *Imp-HNO₃*), the viscosity is increased due to the presence of strong, long-range particle-particle repulsions.^{[228], [416]} Then, when the pH is moderately acidic or basic, the viscosity goes through minima because of lower repulsion forces between the particles (case of sample *Imp-Ref*). As the pH of the boehmite sol come closer to the isoelectric point (typically a pH of 8-9, in the present case 8.1), the suspended particles are no more repulsed and flocculate, which greatly increase the viscosity of the sol.^[416]

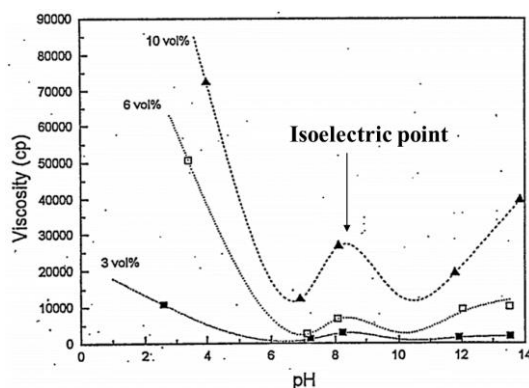


Figure A7.12: General evolutions of the viscosity of boehmite sols versus pH for different loadings of solid.^[416]

It was observed in Figure A7.10 that the viscosities changed with the nature of solvent in this increasing order: *Imp-Ref* < *Imp-Acetone* < *Imp-Ethanol*. This was attributed to two reasons: 1) the dielectric constant values of ethanol and acetone are much lower than water ($\epsilon_{Water,25^\circ C} = 80.1 > \epsilon_{Ethanol,25^\circ C} = 25.1 > \epsilon_{Acetone,25^\circ C} = 20.3$).^[418] This could result in greater repulsion between particles of similar charges and consequently an increase of the viscosity^[419]; 2) the absolute viscosity value of the solvents are as follow: $\mu_{Ethanol,25^\circ C} = 1.09 \text{ cP} > \mu_{Water,25^\circ C} = 0.89 \text{ cP} > \mu_{Acetone,25^\circ C} = 0.30 \text{ cP}$ ^[418]. Which would explain why, among the three solutions, the sample *Imp-Ethanol* showed the highest viscosity.

In accordance with the literature^[416], it was observed that the evolution of the viscosity of the sol with the concentration of Ni/boehmite was non-linear (Figure A7.10, Table A7.2). In the case where the gel concentration was multiplied by 2 (sample *Imp-2C*), the sol was far too viscous to enable to measure its viscosity or to coat in on the monolith. In contrary, when the Ni/boehmite concentration was divided by 2 (sample *Imp-0.5C*), the sol was much less viscous (viscosity divided by 8 at 10 rpm) (Figure A7.10, Table A7.2).

It is to notice that the presence of slurry particles increased the viscosity of the sol. Indeed, for a similar concentration of boehmite, sample *Imp-Sol/Slurry* presented a viscosity of 200 cP at 10 rpm instead of 80 cP for sample *Imp-0.5C*.

II.3. Coating procedures

Table A7.3 presents the different coating procedures investigated and the corresponding names of the samples.

Table A7.3: Modifications of the coating procedures.

Samples	Modified parameter
Imp-Ref	-
Imp-0.5V	Withdrawal speed (x0.5)
Imp-2V	Withdrawal speed (x2)
2Imp	Number of impregnations (2)
Imp-Syringe	Channels filled with a syringe
Imp-Blow	Blowdown step

Prior to coating, the monoliths were cleaned in diluted nitric acid (1 M) for $t = 30$ min, followed by thorough washing with water and acetone, and a drying step at $T = 120$ °C for $t = 2$ h. The solid content of the coating solutions was equal to 5 g of calcined 10 wt. % Ni/ γ -Al₂O₃ per 100 mL, excepted for the sol of the sample *Imp-0.5C*, for which the amount of solid content was set to 2.5 g. In the case of sample *2Imp*, the support was impregnated, dried for $t = 2$ h, and then submitted a second impregnation.

III. RESULTS AND DISCUSSION

III.1. Control of the coatings masses

Figure A7.13 reminds the typical geometrical variables used to definite a honeycomb channel inside a monolith.

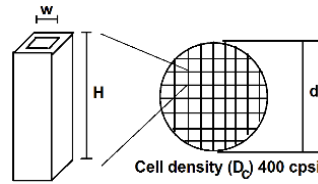


Figure A7.13: Schematic representation of a channel and monolith section seen from the top.

In order to control that the amount deposited was equal to the amount expected, the samples were weighted before the coating and after the drying steps. The theoretical mass load after calcination, m_{th} , was calculated for each sample with Equation A7.4. It corresponds to the total amount of solid that should be found in the monolith after drying, considering that the whole channels volume was filled by the coating solution.

$$m_{th} = V_{ch} \cdot D_c \cdot A_{monolith} \cdot C_{sol,wt}. \quad (A7.4)$$

Where m_{th} is the theoretical mass load, V_{ch} is the whole channels volume, D_c is the cell density, $A_{monolith}$ is the monolith of cross section area and $C_{sol,wt}$ is the concentration of the coating solution.

Replacing $V_{channel}$ by $H \cdot W^2$ and $A_{section}$ by $\pi \cdot (d/2)^2$, Equation A7.4 becomes:

$$m_{th} = H \cdot W^2 \cdot C_{sol,wt} \cdot D_c \cdot \pi \cdot \frac{d^2}{4} \quad (A7.5)$$

$C_{alumina,wt.}$ was set to 0.05 g/mL. H , W and d were respectively equal to 0.96 cm, 0.1 cm and 2.55 cm. D_c was equal to 62 cells/cm².

$$m_{th,calcined.sample} = 0.96 \cdot (0.1)^2 \cdot 0.05 \cdot 62 \cdot \pi \cdot \frac{(2.55)^2}{4} = 0.15 \text{ g} \quad (A7.6)$$

According to TG-DSC measurements performed in the laboratory, the mass loss during transformation of boehmite to γ -Al₂O₃ is of 75 %. Hence, the theoretical mass of boehmite obtained after coating and drying is:

$$m_{th,boehmite} = \frac{1}{0.75} \cdot m_{th,calcined.sample} = 0.20 \text{ g} \quad (A7.7)$$

It was observed in Figure A7.14 that most of the coated monoliths presented large differences between their theoretical and actual loadings after drying. These high differences revealed a technical problem occurring during the impregnation. For instance, sample *Imp-Ref* presented a coating mass of about 70 % of the theoretical load. When impregnated a second time (sample *2Imp*), the sample presented a higher mass (123 %), but this value was still below the theoretical mass gain value (in case of twice doping: 200 %).

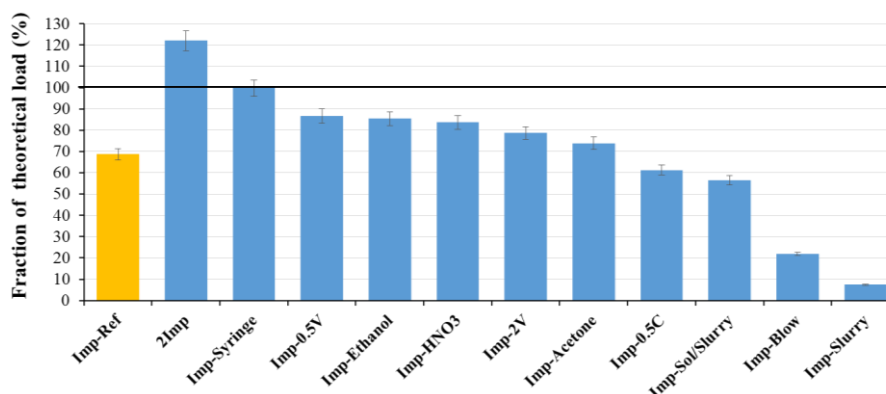


Figure A7.14: Diagram showing the actual load of coating compared to the theoretical load of coating. The error intervals were estimated by taking into account the uncertainty about the monoliths diameters.

It was suspected that the high viscosity of the coating solutions avoided their uniform penetration through the channels of the monolith. Indeed, it was observed that the coating solutions penetrated at first the sample only by a few channels, whilst the others may have been only partially filled. Aside from inhomogeneous filling of the channels by the coating solutions, the difference between actual and theoretical coating mass deposited was also attributed to the presence of air bubbles trapped by the coating solution during the sol rise through the monolith channels. Evidences confirming this effect are presented in the next section.

It is to notice that the change of the withdrawal speed (samples *Imp-0.5V* and *Imp-2V*) did not had a visible influence of the mass of coating deposit.

Since ethanol and acetone are showing lower tension surface values compared to water ($\gamma_{Ethanol} \sim 0.022$ N/m and $\gamma_{Acetone} \sim 0.024$ N/m, whereas $\gamma_{Water} \sim 0.073$ N/m)^[388], one could have expected that it would have promoted the capillary filling of the channels. However, as these samples were also showing high viscosity values (Figure A7.10, Table A7.2), it could explain why these samples also showed too low mass deposits (Figure A7.14).

The very low mass deposit observed for sample *Imp-Blow* is attributed to the fact that the nitrogen flux caused the evacuation of a part of the sol out of the channels (Figure A7.14).

In the case of samples *Imp-0.5C* and *Imp-Slurry*, it was assumed that the coating solutions had a too low viscosity to remain totally inside the channels when solutions were withdrawn. As a result, only a liquid film, whose thickness is a function of the coating solution viscosity, was deposited when the coating solution was withdrawn. Furthermore, as the particles of the slurry had very low interactions between each other, this would explain why sample *Imp-Slurry* showed the lowest mass gain value (8 %).

The correct mass deposit (99 % of mass gain) obtained for the sample prepared by an individual filling of each channel with a syringe (sample *Imp-Syringe*) tends to confirm the assumption that the mass deficits were principally caused by an incomplete filling of the channels.

III.2. Defects in the coatings

SEM measurements were performed on each dried sample in order to get an overview of the aspects of the coatings. Three main types of defect were observed: coating-free areas, large aggregates and cracks. Table A7.4 lists the observations made on the samples coated varying the solution properties and the coating procedure parameters.

Table A7.4: Coated samples, related coating method and observed defects on dried coatings.

Samples	Modified parameters	Coating solution viscosity at 10rpm (cP)	Coating-free areas	Cracks	Aggregates
Imp-Ref	-	630	Yes	Yes	Yes
Imp-0.5V	Withdrawal speed (x0.5)	630	Yes	Yes	Yes
Imp-2V	Withdrawal speed (x2)	630	Yes	Yes	Yes
Imp-0.5C	Solution concentration (x0.5)	80	Little	Almost none	Few
Imp-2C	Solution concentration (x2)	Impregnation not possible, solution too much viscous			
Imp-HNO3	Solution pH (1.8)	1490	Little	Almost none	Few
Imp-Acetone	Solution solvent (acetone)	710	Yes	Yes	Yes
Imp-Ethanol	Solution solvent (ethanol)	1100	Yes	Yes	Yes
2Imp	Number of impregnations (x2)	630	Yes	Yes	Yes
Imp-Syringe	Channels filled with a syringe	630	Yes	Yes	Yes
Imp-Blow	Blowdown step	630	Yes	No	No
Imp-Slurry	Particles slurry instead of boehmite sol	~1	Almost exclusively (scattered particles)	No	No
Imp-Sol/Slurry	Slurry/sol 50/50 % vol. mixture	200	Almost none	Little	Few

It is to notice that all the coatings prepared at different withdrawal speed (samples *Imp-0.5V* and *Imp-2V*), with different solvents (samples *Imp-Ethanol* and *Imp-Acetone*), with a second impregnation (sample *2Imp*) or with a filling of the channels by a syringe (sample *Imp-Syringe*) presented the typical defects observed for a standard impregnation (sample *Imp-Ref*), that is to say: coating-free areas, cracks and large aggregates.

The transformation of boehmite into $\gamma\text{-Al}_2\text{O}_3$ is known to be topotactic (no variation of volume).^{[200], [201]} Hence, the formation of a homogeneous Ni/boehmite gel coating free of defects appears as the most critical step. This assumption was confirmed by the fact that SEM observations (not shown here) performed on a calcined coating of Ni/ $\gamma\text{-Al}_2\text{O}_3$ prepared according to the standard impregnation method (sample *Imp-Ref*) presented similar aspects and same defects as what was observed for the dried samples. For this reason, only the aspects of dried samples were described in the following parts.

III.2.1. Coating-free areas and large aggregates

Coating-free areas were observed for almost all the samples (Table A7.4). In the case of sample *Imp-Slurry*, instead of a film, only isolated micron-sized slurry particles were present on the channel walls (Figure A7.15).

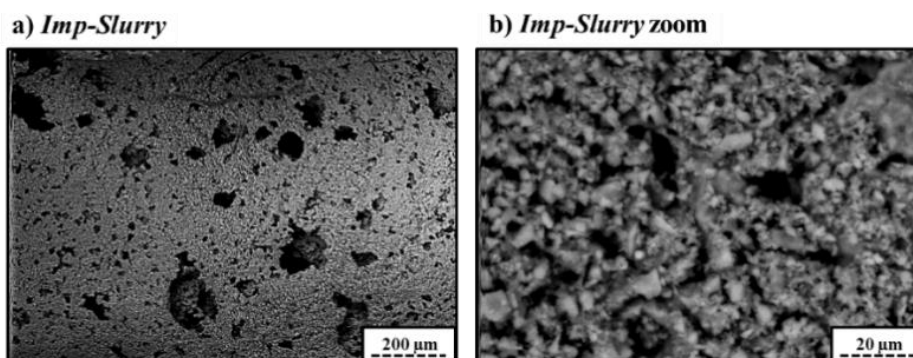


Figure A7.15: Picture of sample *Imp-Slurry*: a. magnification of 100 X, b. magnification of 1000 X.

Figure A7.16 gives an overview of the three main aspects and reasons leading to the presence of coating-free areas.

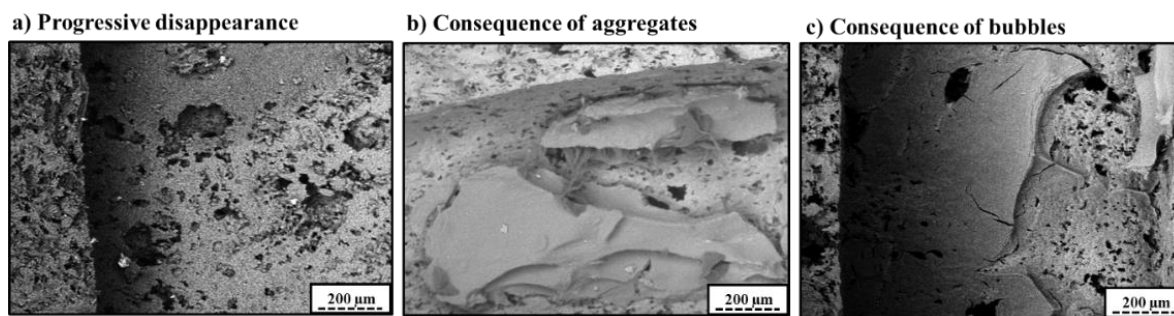


Figure A7.16: Illustrations of the three main type coating-free areas encountered.

The presence of “progressive disappearance” (Figure A7.16-a) of the coating in some areas was a consequence of an inhomogeneous repartition of the coating. According to the surface of monolith available and to the theoretical mass deposited (determined in part III.1. of this annex), the thickness of a homogeneous coating was expected to be of at most $4.2\ \mu\text{m}$ for a standard impregnation. In reality, in some areas, the coating was thicker than the theoretical value of $4.2\ \mu\text{m}$. Hence, in some other areas, it was thinner than $4.2\ \mu\text{m}$, sometimes to such an extent that there was no coating anymore. The “progressive disappearance” generally occurred in a gradual transition from thick to thin and, finally, to no coating. This behavior could be attributed to an uneven drying which tended to draw the coating solution to places where the evaporation was the fastest, usually the outer rims.^{[406], [408]} Indeed, it was observed during SEM measurements that these coating-free areas were usually present at the center of the channels.

Figure A7.16-b shows a typical example of a coating-free area caused by the formation of large aggregates. The formation of these large aggregates is believed to be caused by an insufficient anchoring of the gelating sol within the porosity of the cordierite support.^[414] In this way, during the drying step, the shrinking gels are broken apart from the support and compacted into huge agglomerates.

Figure A7.16-c shows a typical aspect of a circular coating-free area caused by the presence of bubbles. Indeed, during the impregnation, bubbles could be either remained within the cordierite porosity or directly into the coating solution.

Sample *Imp-Blown* confirmed the positive influence of a blowdown step on the formation of homogeneous coating (Table A7.4). In that case the flux permitted to prevent the formation of large aggregates and to eliminate the presence of bubbles. However, coating-free areas of “progressive disappearance” type were observed, caused by a too high experimental blowing pressure. Noteworthy, in some places where the coating film was homogenous, darker spots were visible during SEM-BSE measurements (Figure A7.17-a). These darker spots were actually pores of cordierite filled with the Ni/boehmite gel. This fact was positive since a good anchoring of the gels within the support porosity is known to prevent the shrinkage of the gels and its associated undesirable consequences.

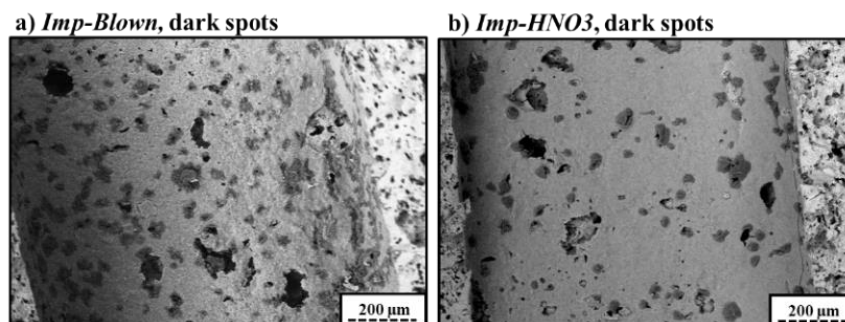


Figure A7.17: Homogeneous coatings with presence of dark spots: a. sample *Imp-Blown*, b. sample *Imp-HNO3*.

These darker spots were also observed for the solution acidified by nitric acid (sample *Imp-HNO3*). Whereas this sample was the one presenting the highest viscosity value (Table A7.2), it presented a homogeneous coating, almost free of cracks and almost free of large agglomerates. This

good aspect of the coating was attributed to the presence of strong repulsions between positively charged boehmite particles at a strongly acidic pH (Figure A7.9), which would permit to retain a good dispersion of the particles and to prevent the aggregation of the coating in large aggregates.^{[228], [405]}

III.2.2. Cracks

Cracks are thought to result from shrinkage-induced stresses in the gelating sol, mostly caused by non-uniform drying rates through the coating. Once the stresses reach a critical value, cracks appear.^{[405], [420]} However, it is known that for a given support and a given coating material, below a critical thickness, the coating can withstand the residual stresses and consequently the formation of cracks is prevented.^[186] For the coating of cordierite monoliths, the critical value of the calcined Al_2O_3 film thickness is about $10\ \mu m$.^[405] Since in this work the theoretical Al_2O_3 thickness value was equal to $4.2\ \mu m$ for a standard impregnation, it is assumed that a better homogeneity of the coating homogeneity would theoretically result in a coating free of crack.

The most visible influence of the influence of the critical thickness value was observed for sample *Imp-0.5C* (Figure A7.18), where a reduction of the concentration of the coating solution decreased the thickness of the coating and led to a film which was almost free of cracks. However, it is to notice, as depicted in Figure A7.18, that the sample still presented some heterogeneity in the repartition of its coating.

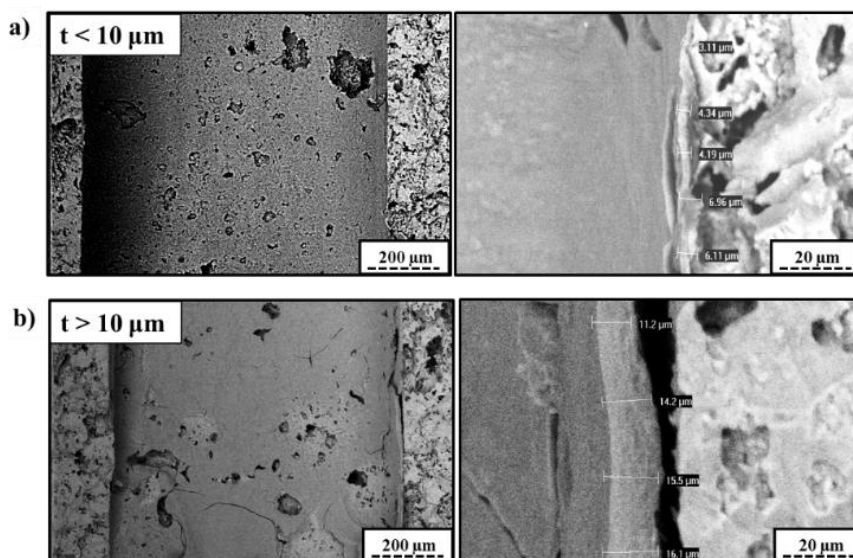


Figure A7.18: Influence of the coating thickness on the appearance of cracks for sample *Imp-0.5C* after drying step; a. thickness below the critical value, b. thickness above the critical value.

The support impregnated with a mixture of sol and slurry (sample *Imp-Sol/Slurry*) presented a composite-like aspect with a homogeneous distribution of the slurry grains dispersed within the gelated sol matrix (Figure A7.19).

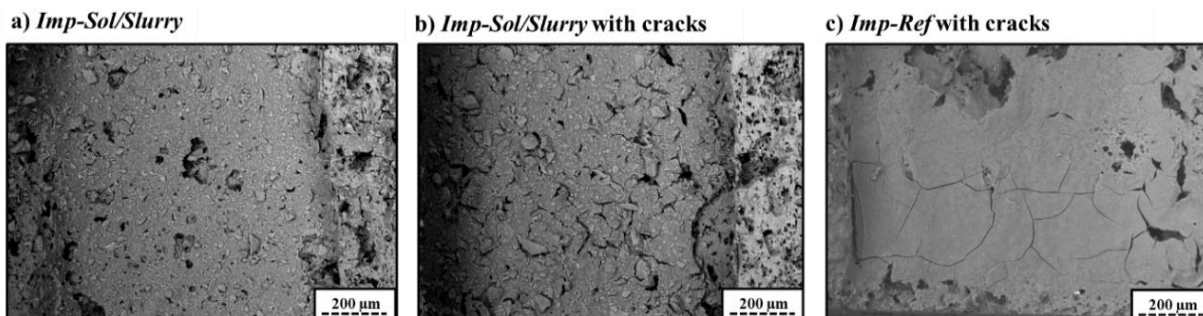


Figure A7.19: Pictures of dried coatings; a. *Imp-Sol/Slurry*, b. cracks on sample *Imp-Sol/Slurry* coating, c. cracks on sample *Imp-Ref* coating.

The coating of sample *Imp-Sol/Slurry* presented almost no cracks, and the few ones had smaller lengths compared to those observed in a standard sample. This beneficial association of the colloidal boehmite and the slurry of alumina particles (whose diameters are $< 5 \mu\text{m}$) was also evidenced by Agrafiotis & Tsetsekou.^[405] In the present case, it was assumed that the interactions at the interface between the slurry particles and the gelating sol helped the coating to resist the capillary pressure-induced shrinkage and resulting stresses during drying. Furthermore, it is assumed that the presence of slurry grains slowed down the propagation of cracks as the energy would be dissipated by the change of directions needed to bypass the slurry grains.^[421]

IV. CONCLUSIONS

This study permitted to set the basis for the development of an efficient method for the washcoating of cordierite monolith with an aqueous sol of Ni/boehmite.

The presence of high mass losses of coating for almost all the samples was the first technical problem. From visual observations and since the sample prepared by an individual filling of the channels with a syringe did not present this mass loss, it was deduced that the mass losses resulted from an imperfect penetration of the sols through the channels of the support. A small pressurization or depressurization applied on the solution during the coating step could be a simple and efficient way to favor the penetration of the solutions through the support channels.

Furthermore, it appears necessary to improve the coating assembly prototype in order to apply a blowdown step with an adjustable flowrate. Indeed, the sample prepared with a manual blowdown presented a good quality of coating (no cracks, no aggregates), but the too high nitrogen flux caused a high mass loss and coating-free areas.

No influences on the coatings quality were observed at different withdrawal speed, with different solvents (water, ethanol or acetone), with a second impregnation or by filling of the channels by a syringe.

The *pH* of the sol appeared to play a role even more important than the viscosity. Indeed, despite having the highest viscosity, the sol acidified with nitric acid showed a coating which was almost free of cracks or of large aggregates. This was attributed to the presence of strong repulsions between positively charged boehmite particles at a strongly acidic *pH*, which permit to retain a good dispersion of the particles and to prevent the aggregation of the coating in large aggregates. One way of investigation would therefore be to determine the optimal *pH* for the deposition of the coating.

The presence of a mix of a slurry of calcined alumina particles and of colloidal boehmite appeared also as an interesting path to follow. The beneficial influence of a slurry was attributed to a better resistance of the coating against the stresses induced during drying, and a deviation of the cracks in the gels by slurry grains. It would be however interesting to determine the influence of the slurry/boehmite ratio on the property of the coating.

One other path of investigation, which has already been performed in the literature, would be to mix the coating solutions with surfactants. Indeed, it has been shown in the literature that organic molecules, such as poly-vinyl-alcohol (PVA), permitted to get a fine control of the solution viscosity and allow a more homogenous rate of evaporation, thus preventing the formation of cracks. Hence, it would be interesting to see if the use of a surfactant such as the stearic acid used in Chapter VII could also permit a better repartition of the coating and a better resistance against the apparition of cracks.

Once the development of a method allowing the deposit of a coating with a homogeneous and defect-free aspect will be available, it will be necessary to check the adherence of the coating on the support (by ultrasonic methods and by a flux of steam at high temperature) and to confirm that the quality remains the same after a calcination step. Only then the performances as secondary catalysts of the coated monoliths could be investigated in lab first, and then possibly at larger scale.

REFERENCES

- [1] Gershman, Brickner & Bratton Inc., “*Gasification of non-recycled plastics from municipal solid waste in the United States*”, G.B.B. report, (2013).
- [2] J. Viterbo, “*La biomasse, une énergie en plein essor*”, La Recherche, (2011), n° 454, p. 85–91.
- [3] F.L. Chan and A. Tanksale, “*Review of recent developments in Ni-based catalysts for biomass gasification*”, *Renew. Sustain. Energy Rev.*, (2014), vol. 38, p. 428–438.
- [4] M. Qiu, Y. Li, T. Wang, Q. Zhang, C. Wang, X. Zhang, C. Wu, L. Ma and K. Li, “*Upgrading biomass fuel gas by reforming over Ni–MgO/ γ -Al₂O₃ cordierite monolithic catalysts in the lab-scale reactor and pilot-scale multi-tube reformer*”, *Appl. Energy*, (2012), vol. 90, p. 3–10
- [5] Z.A.B.Z. Alauddin, P. Lahijani, M. Mohammadi and A.R. Mohamed, “*Gasification of lignocellulosic biomass in fluidized beds for renewable energy development: A review*”, *Renew. Sustain. Energy Rev.*, (2010), vol. 14, p. 2852–2862.
- [6] I. Narvaez, A. Orio and M.P. Aznar, “*Biomass gasification with air in an atmospheric bubbling Fluidized bed. Effect of six operational variables on the quality of the produced raw gas*”, *Ind. Eng. Chem. Res.*, (1996), vol. 35, n°. 7, p. 2110–2120.
- [7] P.A. Simell and J.B. Bredenberg, “*Catalytic purification of tarry fuel gas*”, *Fuel*, (1990), vol. 69, p. 1219–1225.
- [8] M.L. Salvador, J. Arauzo and R. Bilbao, “*Catalytic steam gasification of pine sawdust . Effect of catalyst weight/biomass flow rate and steam/biomass ratios on gas production and composition*”, *Energy and Fuels*, (1999), vol. 13, n°4, p. 851–859.
- [9] S. Albertazzi, F. Basile, J. Brandin, J. Einvall, E. Gustafsson, C. Hulteberg, M. Sanati and F. Trifiro, “*Clean Hydrogen-rich Synthesis Gas*”, CHRISGAS report, (2004).
- [10] A. Kumar, D.D. Jones and M.A. Hanna, “*Thermochemical Biomass Gasification: A Review of the Current Status of the Technology*”, *Energies*, (2009), vol. 2, p. 556–581.
- [11] L. Zhang, C. Xu, and P. Champagne, “*Overview of recent advances in thermo-chemical conversion of biomass*”, *Energy Convers. Manag.*, (2010), vol. 51, p. 969–982.
- [12] “*Total world energy consumption by source 2013*”, Wikipédia. From: REN21 Renewables 2014 Global Status Report.
- [13] European Renewable Energy Council, “*Renewable energy in europe, market trends and technologies*”, E.R.E.C. report, (2010).
- [14] International Renewable Energy Agency, “*Renewable energy technologies: cost analysis series. Biomass for power generation*”, I.R.E.N.A. report, (2012), vol. 1, n°1/5.
- [15] A. Brown, S. Muller, and Z. Dobrotková, “*Renewable energy: market and prospect by technology*”, I.E.A report, (2011).
- [16] International Renewable Energy Agency, “*Renewable power generation costs in 2012: An overview*”, I.R.E.N.A. report, (2013).
- [17] P. Basu, “*Biomass gasification and pyrolysis*”, Elsevier, Burlington, USA, (2010).
- [18] J. Wertz, “*Le bioraffinage ou valorisation optimale de la biomasse pétrole brut biomasse*”, Valbiom report, 2010.
- [19] E4tech, “*Review of technologies for gasification of biomass and wastes*”, E4Tech report, (2009).
- [20] A. Brems, R. Dewil, J. Baeyens and R. Zhang, “*Gasification of plastic waste as waste-to-energy or waste-to-syngas recovery route.*” *Nat. Sci.*, (2013), vol. 5, n°. 6, p. 695–704.
- [21] The Environment and Industry Council Association, Canadian Plastics Industry, “*The gasification of residual plastics derived from municipal recycling facilities*”, (2004).
- [22] J. Leppalahti and T. Koljonen, “*Nitrogen evolution from coal, peat and wood during gasification: Literature review*” *Fuel Process. Technol.*, (1995), vol. 43, p. 1–45.
- [23] F. Pinto, H. Lopes, R.N. André, I. Gulyurtlu and I. Cabrita, “*Effect of catalysts in the quality of syngas and by-products obtained by co-gasification of coal and wastes. 1. Tars and nitrogen compounds abatement*”, *Fuel*, (2007), vol. 86, p. 2052–2063.
- [24] F. Pinto, C. Franco, R.N. André, C. Tavares, M. Dias, I. Gulyurtlu and I. Cabrita, “*Effect of experimental conditions on co-gasification of coal, biomass and plastics wastes with air/steam mixtures in a fluidized bed system*”, *Fuel*, (2003), vol. 82, p. 1967–1976.
- [25] A. Gómez-Barea and B. Leckner, “*Modeling of biomass gasification in fluidized bed.*” *Prog. Energy Combust. Sci.*, (2010), vol. 36, p. 444–509,.
- [26] L.S. Marin, “*Treatment of biomass-derived synthesis gas using commercial steam reforming catalysts and biochar*”, PhD Thesis, Oklahoma State University, (2011).
- [27] C. Picard, “*Thermochimie: exercices corrigés*”, De Boeck, Bruxelles, (1998).
- [28] A. E. Van Diepen and J.A. Moulijn, “*Effect of Process Conditions on Thermodynamics of Gasification*”, Springer-Verlag Berling Heidelberg, (1998).

- [29] P.A. Simell, J. O. Hepola and A.O.I. Krause, “Effects of gasification gas components on tar and ammonia decomposition over hot gas cleanup catalysts”, *Fuel*, (1997), vol. 76, n°. 12, p. 1117–1127.
- [30] M. Balat, M. Balat, E. Kirtay and H. Balat, “Main routes for the thermo-conversion of biomass into fuels and chemicals. Part 2: Gasification systems”, *Energy Convers. Manag.*, (2009), vol. 50, p. 3158–3168.
- [31] G. Sridhar, P.J. Paul and H. S. Mukunda, “Biomass derived producer gas as a reciprocating engine fuel - An experimental analysis”, *Biomass and Bioenergy*, (2001), vol. 21, p. 61–72.
- [32] P. Huang, H. Ju, S. Tan, H. Wang, and T.Zhao, “The future of methanol fuel: An analysis on the feasibility of methanol as an alternative fuel”, *The Franke Institute for Humanities report*, (2015).
- [33] S. Faberi and L. Paolucci, “Methanol: a future transport fuel based on hydrogen and carbon dioxide”, *European Parliamentary Research Service report*, (2014).
- [34] M. Asadullah, “Barriers of commercial power generation using biomass gasification gas: A review”, *Renew. Sustain. Energy Rev.*, (2014), vol. 29, p. 201–215.
- [35] L. Devi, K. J. Ptasinski and F.J.J.G. Janssen, “A review of the primary measures for tar elimination in biomass gasification processes”, *Biomass and Bioenergy*, (2003), vol. 24, p. 125–140.
- [36] M.D. Brown, E. Baker and L. K. Mudge, “Environmental design considerations for thermochemical biomass energy”, *Biomass*, (1986), vol. 11, p. 255–270.
- [37] N. Couto, A. Rouboa, V. Silva, E. Monteiro and K. Bouziane, “Influence of the Biomass Gasification Processes on the Final Composition of Syngas”, *Energy Procedia*, (2013), vol. 36, p. 596–606.
- [38] P. Simell, E. Kurkela, P. Ståhlberg and J. Hepola, “Catalytic hot gas cleaning of gasification gas”, *Catal. Today*, (1996), vol. 27, p. 55–62.
- [39] S. Anis and Z.A. Zainal, “Tar reduction in biomass producer gas via mechanical, catalytic and thermal methods: A review”, *Renew. Sustain. Energy Rev.*, (2011), vol. 15, p. 2355–2377.
- [40] D. Vamvuka, C. Arvanitidis and D. Zachariadis, “Flue Gas Desulfurization at High Temperatures: A Review”, *Environ. Eng. Sci.*, (2004), vol. 21, n°. 4, p. 525–547.
- [41] European Biomass Industry Association Website: <http://www.eubia.org/>
- [42] T.A. Milne, R.J. Evans and N. Abatzoglou, “Biomass gasifier ‘tars’: Their nature, formation, and conversion”, *U.S.A National Renewable Energy Laboratory report*, (1998).
- [43] D.C. Elliott, “Relation of reaction time and temperature to chemical composition of pyrolysis oils”, *ACS symposium series 376: pyrolysis oils from biomass*, (1988), p. 55–65.
- [44] U. Wolfesberger-Schwabl, I. Aigner and H. Hofbauer, “Mechanism of tar generation during fluidized bed gasification and low temperature pyrolysis”, *Ind. Eng. Chem. Res.*, (2012), vol. 51, pp. 13001–13007.
- [45] C. Li and K. Suzuki, “Tar property, analysis, reforming mechanism and model for biomass gasification—An overview”, *Renew. Sustain. Energy Rev.*, (2009), vol. 13, p. 594–604.
- [46] R. Coll, J. Salvado, X. Farriol and D. Montané, “Steam reforming model compounds of biomass gasification tars: conversion at different operating conditions and tendency towards coke formation”, *Fuel Process. Technol.*, (2001), vol. 74, p. 19–31.
- [47] Z. Abu El-Rub, E.A. Bramer and G. Brem, “Review of catalysts for tar elimination in biomass gasification processes”. *Ind. Eng. Chem. Res.*, (2004), vol. 43, p. 6911–6919.
- [48] J. Kiel, S. Van Paasen, J. Neeft, L. Devi, K.J. Ptasinki, F.J.J.G. Janssen, R. Meijer, R.H. Berends, H.M.G. Temmink, G. Brem, N. Padban and E.A. Bramer, “Primary measures to reduce tar formation in fluidised-bed biomass gasifiers”, *Energy research Centre of the Netherlands report*, (2004).
- [49] W. Torres, S.S. Pansare and J.G. Goodwin, “Hot gas removal of tars, ammonia, and hydrogen sulfide from biomass gasification gas”, *Catal. Rev.*, (2007), vol. 49, p. 407–456.
- [50] L. Garcia, R. French, S. Czernik and E. Chornet, “Catalytic steam reforming of bio-oils for the production of hydrogen: effects of catalyst composition”, *Appl. Catal. A Gen.*, (2000), vol. 201, pp. 225–239.
- [51] G. Guan, G. Chen, Y. Kasai, E.W.C. Lim, X. Hao, M. Kaewpanha, A. Abuliti, C. Fushimi and A. Tsutsumi, “Catalytic steam reforming of biomass tar over iron- or nickel-based catalyst supported on calcined scallop shell”, *Appl. Catal. B Environ.*, (2012), vol. 115–116, p. 159–168.
- [52] D. Duprez, “Selective steam reforming of aromatic compounds on metal catalysts”, *Appl. Catal. A Gen.*, (1992), vol. 82, p. 111–157.
- [53] N. Bion, F. Epron and D. Duprez, “Bioethanol reforming for H₂ production. A comparison with hydrocarbon reforming”, *Catalysis*, (2010), vol. 22, p. 1–55.
- [54] M. Ito, T. Tagawa and S. Goto, “Suppression of carbonaceous depositions on nickel catalyst for the carbon dioxide reforming of methane”, *Appl. Catal. A Gen.*, (1999), vol. 177, p. 15–23.
- [55] D. Świerczyński, S. Libs, C. Courson and A. Kiennemann, “Steam reforming of tar from a biomass gasification process over Ni/olivine catalyst using toluene as a model compound”, *Appl. Catal. B Environ.*, (2007), vol. 74, p. 211–222.
- [56] D. Fuentes-Cano, A. Gómez-Barea, S. Nilsson and P. Ollero, “Decomposition kinetics of model tar compounds over chars with different internal structure to model hot tar removal in biomass gasification”, *Chem. Eng. J.*, (2013), vol.

- 228, p. 1223–1233.
- [57] K. Sato and K. Fujimoto, “Development of new nickel based catalyst for tar reforming with superior resistance to sulfur poisoning and coking in biomass gasification”, *Catal. Commun.*, (2007), vol. 8, p. 1697–1701.
- [58] I. Narvaez, J. Corella and A. Orío, “Fresh tar (from a biomass gasifier) elimination over a commercial steam-reforming catalyst. Kinetics and effect of different variables operation”, *Ind. Eng. Chem. Res.*, (1997), vol. 36, p. 317–327.
- [59] L. Devi, K.J. Ptasiniski and F.J.J.G. Janssen, “Decomposition of naphthalene as a biomass tar over pretreated olivine: effect of gas composition, kinetic approach, and reaction Scheme”, (2005), *Ind. Eng. Chem. Res.*, p. 9096–9104.
- [60] B. Dou, W. Pan, J. Ren, B. Chen, J. Hwang and T.U. Yu, “Removal of tar component over cracking catalysts from high temperature fuel gas”, *Energy Convers. Manag.*, (2008), vol. 49, p. 2247–2253.
- [61] P. Aznar, M. A. Caballero, J. Gil, J. A. Martín and J. Corella, “Commercial steam reforming catalysts to improve biomass gasification with steam-oxygen mixtures. 2. Catalytic tar”, *Ind. Eng. Chem. Res.*, (1998), vol. 37, p. 2668–2680.
- [62] C.M. Kinoshita, Y. Wang and J. Zhou, “Effect of reformer conditions on catalytic reforming of biomass-gasification tars”, *Ind. Eng. Chem. Res.*, (1995), vol. 34, p. 2949–2954.
- [63] F. Ferella, J. Stoehr, I. De Michelis and A. Hornung, “Zirconia and alumina based catalysts for steam reforming of naphthalene”, *Fuel*, (2013), vol. 105, p. 614–629.
- [64] M. Virginie, C. Courson, D. Niznansky, N. Chaoui and A. Kiennemann, “Characterization and reactivity in toluene reforming of a Fe/olivine catalyst designed for gas cleanup in biomass gasification” *Appl. Catal. B Environ.*, (2010), vol. 101, no. 1–2, p. 90–100.
- [65] J. Rostrup-Nielsen, “Catalytic Steam Reforming”, p. 1–117. Chapter 1 from: J. R. Anderson *et al.*, “Catalysis”, Springer-Verlag, Berlin, Heidelberg, vol. 5, (1984).
- [66] N. Laosiripojana, W. Sutthisripok, S. Charojrochkul and S. Assabumrungrat, “Development of Ni–Fe bimetallic based catalysts for biomass tar cracking/reforming: Effects of catalyst support and co-fed reactants on tar conversion characteristics”, *Fuel Process. Technol.*, (2014), vol. 127, p. 26–32
- [67] C. Li, D. Hirabayashi and K. Suzuki, “Development of new nickel based catalyst for biomass tar steam reforming producing H₂-rich syngas”, *Fuel Process. Technol.*, (2009), vol. 90, p. 790–796.
- [68] D.L. Trimm, “Coke formation and minimisation during steam reforming reactions”, *Catal. Today*, (1997), vol. 37, p. 233–238.
- [69] J. Rostrup-Nielsen and D. Trimm, “Mechanisms of carbon formation on nickel containing catalysts”, *J. Catal.*, (1977), vol. 48, p. 155–165.
- [70] T. Mendiara, J.M. Johansen, R. Utrilla, P. Geraldo, A. D. Jensen and P. Glarborg, “Evaluation of different oxygen carriers for biomass tar reforming (I): Carbon deposition in experiments with toluene”, *Fuel*, vol. 90, p. 1049–1060, (2011).
- [71] C. Wu and P.T. Williams, “Investigation of coke formation on Ni-Mg-Al catalyst for hydrogen production from the catalytic steam pyrolysis-gasification of polypropylene”, *Appl. Catal. B Environ.*, (2010), vol. 96, p. 198–207.
- [72] F.M. Josuinkas, C.P.B. Quitete, N.F.P. Ribeiro and M.M.V.M. Souza, “Steam reforming of model gasification tar compounds over nickel catalysts prepared from hydrotalcite precursors”, *Fuel Process. Technol.*, (2014), vol. 121, p. 76–82.
- [73] J.Z. Luo, Z.L. Yu, C.F. Ng and C.T. Au, “CO₂/CH₄ reforming over Ni–La₂O₃/5A: An investigation on carbon deposition and reaction steps,” *J. Catal.*, (2000), vol. 194, p. 198–210.
- [74] P. Azadi and R. Farnood, “Review of heterogeneous catalysts for sub- and supercritical water gasification of biomass and wastes”, *Int. J. Hydrogen Energy*, (2011), vol. 36, p. 9529–9541
- [75] R.L. Bain, D.C. Dayton, D.L. Carpenter, S. R. Czernik, C.J. Feik, R.J. French, K.A. Magrini-bair and S.D. Phillips, “Evaluation of catalyst deactivation during catalytic steam reforming of biomass-derived syngas”, *Ind. Eng. Chem. Res.*, (2005), vol. 44, p. 7945–7956.
- [76] T. Furusawa, K. Saito, Y. Kori, Y. Miura, M. Sato and N. Suzuki, “Steam reforming of naphthalene/benzene with various types of Pt- and Ni-based catalysts for hydrogen production”, *Fuel*, (2013), vol. 103, p. 111–121.
- [77] F. Moseley, R.W. Stephens, K.D. Stewart and J. Wood, “The poisoning of a steam hydrocarbon gasification catalyst”, *J. Catal.*, (1972), vol. 24, p. 18–39.
- [78] B.L. Augusto, L.O.O. Costa, F.B. Noronha, R.C. Colman and L.V. Mattos, “Ethanol reforming over Ni/CeGd catalysts with low Ni content”, *Int. J. Hydrogen Energy*, (2012), vol. 37, p. 12258–12270.
- [79] M. Argyle and C. Bartholomew, “Heterogeneous Catalyst Deactivation and Regeneration: A Review”, *Catalysts*, (2015), vol. 5, p. 145–269.
- [80] D.C. McCulloch, “Catalytic hydrotreating in pre-toluene refining”, *Applied Industrial Catalysis*; Leach, B.E., Ed., NY, USA, (1983), p. 69–121.
- [81] P. Forzatti and L. Lietti, “Catalyst deactivation”, *Catal. Today*, (1999), vol. 52, p. 165–181.
- [82] J.A. Rodríguez and J. Hrbek, “Interaction of sulfur with well-defined metal and oxide surfaces: Unraveling the mysteries behind catalyst poisoning and desulfurization”, *Acc. Chem. Res.*, (1999), vol. 32, n°9, p. 719–728.

- [83] N. Macleod, J.R. Fryer, D. Stirling and G. Webb, "Deactivation of bi- and multimetallic reforming catalysts: Influence of alloy formation on catalyst activity", *Catal. Today*, (1998), vol. 46, p. 37–54.
- [84] W.J.W. Bakker, J.C.P. Van Rossen, J.P. Janssens and J.A. Moulijn, "Hot gas cleaning, sulfiding mechanisms in absorption of H_2S by solids", Springer-Verlag Berlin Heidelberg, NATO ASI Series, vol. G 42, (1998).
- [85] J. Rodriguez, E. Romeo, J.L.G. Fierro, J. Santamaria and A. Monzon, "Deactivation by coking and poisoning of spinel-type Ni catalysts", *Catal. Today*, (1997), vol. 37, p. 255–265.
- [86] S. Albertazzi, F. Basile, J. Brandin, J. Einvall, G. Fornasari, C. Hulteberg, M. Sanati, F. Trifiro and A. Vaccari, "Effect of fly ash and H_2S on a Ni-based catalyst for the upgrading of a biomass-generated gas", *Biomass and Bioenergy*, (2008), vol. 32, p. 345–353.
- [87] J. Rostrup-Nielsen, "Sulfur-passivated nickel catalysts for carbon-free steam reforming of methane", *J. Catal.*, (1984), vol. 85, p. 31–43.
- [88] U. Olsbye, "Hydrocarbon processing: Catalytic Combustion and Partial Oxidation to Syngas". Chapter 8 from: "Handbook of Advanced Methods and Processes in Oxidation Catalysis. From Laboratory to Industry", Duprez & F. Cavani, Ed. Imperial College Press, (2014).
- [89] I. Alstrup, B.S. Clausen, C. Olsen, R.H.H. Smits and J.R. Rostrup-Nielsen, "Promotion of Steam Reforming Catalysts", *Stud. Surf. Sci. and Cata.*, (1998), vol. 119., p. 5-14.
- [90] S. Sinquefeld and T. Fan, "Sulfur and alkali tolerant catalyst", US Patent, (2007), n°: 2007/0169412 A1.
- [91] H. Topsoe, "In situ characterization of catalysts", *Stud. Surf. Sci. and Cata.*, (2000), vol. 130, p. 1-21.
- [92] P.R. Westmoreland and D.P. Harrison, "Evaluation of candidate solids for high-temperature desulfurization of low-Btu gases", *Environ. Sci. Technol.*, (1976), vol. 10, n°. 7, p. 659–661.
- [93] C.K. Ryu, M.W. Ryoo, I.S. Ryu and S.K. Kang, "Catalytic combustion of methane over supported bimetallic Pd catalysts: Effects of Ru or Rh addition", *Catal. Today*, (1999), vol. 47, p. 141–147.
- [94] D. Pérez-Martínez, S.A. Giraldo and A. Centeno, "Effects of the H_2S partial pressure on the performance of bimetallic noble-metal molybdenum catalysts in simultaneous hydrogenation and hydrodesulfurization reactions", *Appl. Catal. A Gen.*, (2006), vol. 315, p. 35–43.
- [95] S. Albertazzi, F. Basile, J. Brandin, J. Einvall, G. Fornasari, C. Hulteberg and M. Sanati, "Effect of fly ash and H_2S on a Ni-based catalyst for the upgrading of a biomass-generated gas", (2008), vol. 32, pp. 345–353.
- [96] J.A. Moulijn, A.E. Van Diepen and F. Kapteijn, "Catalyst deactivation : is it predictable? What to do?", *Appl. Catal. A Gen.*, (2001), vol. 212, p. 3–16.
- [97] T.L. Roussière, "Catalytic reforming of methane in the presence of CO_2 and H_2O at high pressure", PhD Thesis, Karlsruhe Institut für Technologie, (2013).
- [98] B. Novakovic, Z. Vukovic and N. Jovanovic, "The stability of porous alumina catalyst support against sintering", *Adv. Sci. Technol. Sinter.*, (1999), p. 347–352.
- [99] J. Sehested, J.A.P. Gelten, I.N. Remediakis, H. Benggaard and J.K. Nørskov, "Sintering of nickel steam-reforming catalysts: effects of temperature and steam and hydrogen pressures", *J. Catal.*, (2004), vol. 223, p. 432–443.
- [100] M.M. Yung, W.S. Jablonski and K.A. Magrini-Bair, "Review of Catalytic Conditioning of Biomass-Derived Syngas", *Energy & Fuels*, (2009), vol. 23, p. 1874–1887.
- [101] J.N. Kuhn, Z. Zhao, L.G. Felix, R.B. Slimane, C.W. Choi and U.S. Ozkan, "Olivine catalysts for methane- and tar-steam reforming", *Appl. Catal. B Environ.*, (2008), vol. 81, p. 14–26.
- [102] Y. Shen and K. Yoshikawa, "Recent progresses in catalytic tar elimination during biomass gasification or pyrolysis—A review", *Renew. Sustain. Energy Rev.*, (2013), vol. 21, p. 371–392.
- [103] C. Xu, J. Donald, E. Byambajav and Y. Ohtsuka, "Recent advances in catalysts for hot-gas removal of tar and NH_3 from biomass gasification", *Fuel*, (2010), vol. 89, p. 1784–1795.
- [104] J. T. Richardson, "Principles of catalyst development", Springer, Houston, Texas, (1989).
- [105] G. Guan, X. Hao and A. Abudula, "Heterogeneous catalysts from natural sources for tar removal : A mini review", *J. Adv. Catal. Sci. Technol.*, (2014), vol. 1, p. 20–28.
- [106] Y.S. Jung, W.L. Yoon, Y.S. Seo and Y.W. Rhee, "The effect of precipitants on Ni- Al_2O_3 catalysts prepared by a co-precipitation method for internal reforming in molten carbonate fuel cells", *Catal. Commun.*, (2012), vol. 26, p. 103–111.
- [107] H. Tian, S. Li, L. Zeng, H. Ma and J. Gong, "Assembly of ordered mesoporous alumina-supported nickel nanoparticles with high temperature stability for CO methanation", *Sci. China Mater.*, (2015), vol. 58, n°. 1, p. 9–15.
- [108] C. Xu, S. Hamilton and M. Ghosh, "Hydro-treatment of Athabasca vacuum tower bottoms in supercritical toluene with microporous activated carbons and metal-carbon composite", *Fuel*, (2009), vol. 88, p. 2097–2105.
- [109] Z.A. El-Rub, E.A. Bramer and G. Brem, "Experimental comparison of biomass chars with other catalysts for tar reduction", *Fuel*, (2008), vol. 87, p. 2243–2252.
- [110] L. Xu, H. Song and L. Chou, "Ordered mesoporous MgO- Al_2O_3 composite oxides supported Ni based catalysts for CO_2 reforming of CH_4 : Effects of basic modifier and mesopore structure", *Int. J. Hydrogen Energy*, (2013), vol. 38, p. 7307–7325.

- [111] A. Zhenissova, F. Micheli, L. Rossi, S. Stendardo, P.U. Foscolo and K. Gallucci, “Experimental evaluation of Mg- and Ca-based synthetic sorbents for CO₂ capture”, Chem. Eng. Res. Des., (2014), vol. 92, p. 727–740.
- [112] M.C. Paganini, M. Chiesa, P. Martino and E. Giamello, *EPR study of the surface basicity of calcium oxide. I. The CaO-NO chemistry*” J. Phys. Chem. B, (2002), vol. 106, p. 12531–12536.
- [113] G. Pacchioni, J. J. M. Ricart and F. Illas, “Ab initio cluster model calculations on the chemisorption of CO₂ and SO₂ probe molecules on MgO and CaO (1 0 0) surfaces. A theoretical measure of oxide basicity”, J. Am. Chem. Soc., (1994), vol. 116, p. 10152–10158.
- [114] G. Sciences, “Carbonation, hydration, and melting relations in the system MgO-H₂O-CO₂, at pressures up to 100 kbar”, Am. Mineral., (1979), vol. 64, p. 32–40.
- [115] I. Zamboni, C. Courson, D. Niznansky and A. Kiennemann, “Simultaneous catalytic H₂ production and CO₂ capture in steam reforming of toluene as tar model compound from biomass gasification”, Appl. Catal. B Environ., (2014), vol. 145, p. 63–72.
- [116] W. Brice and L. Chang, “Subsolidus phase relations in Aragonite-type Carbonates. III. The systems MgCO₃-CaCO₃-BaCO₃, MgCO₃-CaCO₃-SrCO₃ and MgCO₃-SrCO₃-BaCO₃”, (1973), Am. Mineral., vol. 58, p. 979–985.
- [117] L. Di Felice, C. Courson, P.U. Foscolo and A. Kiennemann, “Iron and nickel doped alkaline-earth catalysts for biomass gasification with simultaneous tar reformation and CO₂ capture”, Int. J. Hydrogen Energy, (2011), vol. 36, p. 5296–5310.
- [118] B. Acharya, A. Dutta and P. Basu, “An investigation into steam gasification of biomass for hydrogen enriched gas production in presence of CaO”, Int. J. Hydrogen Energy, (2010), vol. 35, p. 1582–1589.
- [119] J. Delgado, M. P. Aznar and J. Corella, “Biomass gasification with steam in fluidized bed: effectiveness of CaO, MgO, and CaO-MgO for hot raw gas cleaning”, Ind. Eng. Chem. Res., (1997), vol. 36, p. 1535–1543.
- [120] C. Li, D. Hirabayashi and K. Suzuki, “Steam reforming of biomass tar producing H₂-rich gases over Ni/MgO_x/CaO_{1-x} catalyst”, Bioresour. Technol., (2010), vol. 101, p. S97–S100.
- [121] M. Zhao, X. Yang, T.L. Church and A.T. Harris, “Interaction between a bimetallic Ni-Co catalyst and micrometer-sized CaO for enhanced H₂ production during cellulose decomposition”, Int. J. Hydrogen Energy, (2011), vol. 36, p. 421–431.
- [122] S. Wang and G.Q.M. Lu, “CO₂ reforming of methane on Ni catalysts: Effects of the support phase and preparation technique”, Appl. Catal. B Environ., (1998), vol. 16, p. 269–277.
- [123] J.N. Kuhn, Z. Zhao, A. Senefeld-Naber, L.G. Felix, R.B. Slimane, C.W. Choi and U.S. Ozkan, “Ni-olivine catalysts prepared by thermal impregnation: Structure, steam reforming activity, and stability”, Appl. Catal. A Gen., (2008), vol. 341, p. 43–49.
- [124] Z. Zhao, N. Lakshminarayanan, J.N. Kuhn, A. Senefeld-Naber, L.G. Felix, R.B. Slimane, C.W. Choi, and U. S. Ozkan, “Optimization of thermally impregnated Ni-olivine catalysts for tar removal”, Appl. Catal. A Gen., (2009), vol. 363, p. 64–72.
- [125] R.Q. Long, S.M. Monfort, G.B. Arkenberg, P.H. Matter and S.L. Swartz, “Sulfur tolerant magnesium nickel silicate catalyst for reforming of biomass gasification products to syngas”, Catalysts, (2012), vol. 2, p. 264–280.
- [126] M. Stöcker, H.G. Karge, J.C. Jansen and J.W. Weitkamp, “Advance in zeolite science and applications”, Elsevier, (1994).
- [127] P.R. Buchireddy, R.M. Bricka, J. Rodriguez and W. Holmes, “Biomass gasification: catalytic removal of tars over zeolites and nickel supported zeolites”, Energy & Fuels, (2010), vol. 24, p. 2707–2715.
- [128] J. Tao, L. Zhao, C. Dong, Q. Lu, X. Du, and E. Dahlquist, “Catalytic steam reforming of toluene as a model compound of biomass gasification tar using Ni-CeO₂/SBA-15 catalysts”, Energies, (2013), vol. 6, p. 3284–3296.
- [129] T. Nordgreen, V. Nemanova, K. Engvall and K. Sjöström, “Iron-based materials as tar depletion catalysts in biomass gasification: Dependency on oxygen potential”, Fuel, (2012), vol. 95, p. 71–78.
- [130] Y. Richardson, J. Blin, and A. Julbe, “A short overview on purification and conditioning of syngas produced by biomass gasification: Catalytic strategies, process intensification and new concepts”, Prog. Energy Combust. Sci., (2012), vol. 38, p. 765–781.
- [131] M. Uddin, H. Tsuda, S. Wu and E. Sasaoka, “Catalytic decomposition of biomass tars with iron oxide catalysts”, Fuel, vol. 87, p. 451–459, 2008.
- [132] Z. Huang, F. He, Y. Feng, K. Zhao, A. Zheng, S. Chang, G. Wei, Z. Zhao, and H. Li, “Characteristics of biomass gasification using chemical looping with iron ore as an oxygen carrier”, Energy & Fuels, (2013), vol. 38, p. 14568–14575.
- [133] Z. Min, M. Asadullah, P. Yimsiri, S. Zhang, H. Wu and C.Z. Li, “Catalytic reforming of tar during gasification. Part I. Steam reforming of biomass tar using ilmenite as a catalyst”, Fuel, (2011), vol. 90, p. 1847–1854.
- [134] Z.R. Ismagilov, M.A. Kerzhentsev, V.A. Sazonov, L.T. Tsykoza, N.V. Shikina, V.V. Kuznetsov, V.A. Ushakov, S.V. Mishanin, N.G. Kozhukhar, G. Russo and O. Deutschmann, “Study of catalysts for catalytic burners for fuel cell power plant reformers”, Korean J. Chem Eng., (2003), vol. 20, p. 461–467.
- [135] T. Miyazawa, T. Kimura, J. Nishikawa, S. Kado, K. Kunitomi and K. Tomishige, “Catalytic performance of supported Ni catalysts in partial oxidation and steam reforming of tar derived from the pyrolysis of wood biomass”, Catal. Today,

- (2006), vol. 115, p. 254–262.
- [136] D. Mazza, A. Delmastro and S. Ronchetti, “Co, Ni, Cu aluminates supported on mullite precursors via a solid state reaction”, *J. Eur. Ceram. Soc.*, (2000), vol. 20, p. 699–706.
- [137] S. Nwamaka-Ude, “The synthesis and crystal chemistry of $\text{Ca}_{12}\text{Al}_{14}\text{O}_{33}$ doped with Fe_2O_3 ”, Master’s Thesis, University of Tennessee, (2010).
- [138] C. Li, D. Hirabayashi and K. Suzuki, “A crucial role of O_2^- and O_2^{2-} on mayenite structure for biomass tar steam reforming over $\text{Ni}/\text{Ca}_{12}\text{Al}_{14}\text{O}_{33}$ ”, *Appl. Catal. B Environ.*, (2009), vol. 88, p. 351–360.
- [139] K. Engelen, D. J. Draelants and G. V. Baron, “Improvement of sulphur resistance of a nickel-modified catalytic filter for tar removal from biomass gasification gas”, *Proceedings 5th International Symposium on Gas Cleaning at High Temperature*, CD Edition, (2003).
- [140] S. Zhou, Y. Zhou, Y. Zhang, X. Sheng, Z. Zhang and J. Kong, “Synthesis of core-shell-structured $\text{SBA-15}/\text{MgAl}_2\text{O}_4$ with enhanced catalytic performance of propane dehydrogenation”, *J. Mater. Sci.*, (2014), vol. 49, p. 1170–1178.
- [141] J. Li, T. Ikegami, J. Lee, T. Mori and Y. Yajima, “Synthesis of Mg-Al spinel powder via precipitation using ammonium bicarbonate as the precipitant”, *J. Eur. Ceram. Soc.*, (2001), vol. 21, pp. 139–148.
- [142] Q. Li, S. Ji, J. Hu and S. Jiang, “Catalytic steam reforming of rice straw biomass to hydrogen-rich syngas over Ni-based catalysts”, *Chinese J. Catal.*, (2013), vol. 34, p. 1462–1468.
- [143] S. Seok, S.H. Choi, E.D. Park, S.H. Han and J.S. Lee, “Mn-promoted $\text{Ni}/\text{Al}_2\text{O}_3$ catalysts for stable carbon dioxide reforming of methane”, *J. Catal.*, (2002), vol. 209, p. 6–15.
- [144] M.E. Gálvez, S. Ascaso, P. Stelmachowski, P. Legutko, A. Kotarba, R. Moliner and M.J. Lázaro, “Influence of the surface potassium species in Fe-K/ Al_2O_3 catalysts on the soot oxidation activity in the presence of NO_x ”, *Appl. Catal. B Environ.*, (2014), vol. 152–153, p. 88–98.
- [145] Z. Hou, X. Zheng and T. Yashima, “High coke-resistance of K-Ca promoted Ni/ α - Al_2O_3 catalyst for CH_4 reforming with CO_2 ”, *React. Kinet. Catal. Lett.*, (2005), vol. 84, n°. 2, p. 229–235.
- [146] D. Li, Y. Nakagawa and K. Tomishige, “Development of Ni-based catalysts for steam reforming of tar derived from biomass pyrolysis”, *Chinese J. Catal.*, (2012), vol. 33, n°. 4, p. 583–594.
- [147] J.S. Chang, D.Y. Hong, X. Li and S.E. Park, “Thermogravimetric analyses and catalytic behaviors of zirconia-supported nickel catalysts for carbon dioxide reforming of methane”, *Catal. Today*, (2006), vol. 115, p. 186–190.
- [148] H.S. Roh, H. S. Potdar and K.W. Jun, “Carbon dioxide reforming of methane over co-precipitated Ni-CeO₂, Ni-ZrO₂ and Ni-Ce-ZrO₂ catalysts”, (2004), *Catal. Today*, vol. 93–95, p. 39–44.
- [149] H.J. Park, S.H. Park, J.M. Sohn, J. Park, J.K. Jeon, S.S. Kim and Y.K. Park, “Steam reforming of biomass gasification tar using benzene as a model compound over various Ni supported metal oxide catalysts”, *Bioresour. Technol.*, (2010), vol. 101, p. S101–S103.
- [150] S. Wang and G.Q.M. Lu, “Role of CeO₂ in Ni/CeO₂- Al_2O_3 catalysts for carbon dioxide reforming of methane”, *Appl. Catal. B Environ.*, (1998), vol. 19, p. 267–277.
- [151] C.P.B. Quitete, R.C.P. Bittencourt and M.M.V.M. Souza, “Steam reforming of tar using toluene as a model compound with nickel catalysts supported on hexaaluminates”, *Appl. Catal. A Gen.*, (2014), vol. 478, p. 234–240.
- [152] I. Chorenorff and J.W. Niemantsverdriet, “Concepts of modern catalysis and kinetics”, WILEY-VCH Verlag GmbH & Co, Weinheim, (2003).
- [153] J.L.C. Fajín, M.N.D.S. Cordeiro and J.R.B. Gomes, “Water dissociation on bimetallic surfaces: General trends”, *J. Phys. Chem. C*, (2012), vol. 116, p. 10120–10128.
- [154] T.K. Shashkova, M.R. Kantserova and S.N. Orlik, “Sulfur resistance and stability of yttrium-stabilized binary Co-Cu and Ni-Cu composites with zirconium dioxide in the oxidative conversion of methane”, *Theor. Expe. Chem.*, (2009), vol. 45, n°. 5, p. 306–311.
- [155] S.M. Hashemnejad and M. Parvari, “Deactivation and regeneration of Nickel-based catalysts for steam-Methane reforming”, *Chinese J. Catal.*, (2011), vol. 32, p. 273–279.
- [156] J. Conradie, J. Gracia, J.W. Niemantsverdriet, “Energetic driving force of H spillover between Rhodium and Titania surfaces: A DFT view”, *J. Phys. Chem. C*, (2012), vol. 116, p. 25362–25367.
- [157] W.C. Conner and J.L. Falconer, “Spillover in heterogeneous catalysis”, *Chem. Rev.*, (1995), vol. 95, p. 759–788.
- [158] I. Alstrup, M.T. Tavares, C.A. Bernardo, O. Sorensen and J.R. Rostrup-Nielsen, “Carbon formation on nickel and nickel-copper alloy catalysts”, *Mater. Corros.*, (1998), vol. 49, pp. 367–372.
- [159] G. Jones, J.G. Jakobsen, S.S. Shim, J. Kleis, M.P. Andersson, J. Rossmeisl, F. Abild-Pedersen, T. Bligaard, S. Helveg, B. Hinnemann, J.R. Rostrup-Nielsen, I. Chorkendorff, J. Sehested and J. K. Nørskov, “First principles calculations and experimental insight into methane steam reforming over transition metal catalysts”, *J. Catal.*, (2008), vol. 259, p. 147–160.
- [160] J. Rostrup-Nielsen and J.H.B. Hansen, “CO₂-reforming of methane over transition metals”, *Journal of Catalysis*, (1993), vol. 144, p. 38–49.
- [161] J. Nishikawa, K. Nakamura, M. Asadullah, T. Miyazawa, K. Kunimori and K. Tomishige, “Catalytic performance of Ni/CeO₂/ Al_2O_3 modified with noble metals in steam gasification of biomass”, *Catal. Today*, (2008), vol. 131, p. 146–

- 155.
- [162] T. Miyazawa, T. Kimura, J. Nishikawa, K. Kunimori and K. Tomishige, “Catalytic properties of Rh/CeO₂/SiO₂ for synthesis gas production from biomass by catalytic partial oxidation of tar”, *Sci. Technol. Adv. Mater.*, (2005), vol. 6, p. 604–614.
- [163] M. Asadullah, T. Miyazawa, S. Ito, K. Kunimori, S. Koyama and K. Tomishige, “A comparison of Rh/CeO₂/SiO₂ catalysts with steam reforming catalysts, dolomite and inert materials as bed materials in low throughput fluidized bed gasification systems”, *Biomass and Bioenergy*, (2004), vol. 26, pp. 269–279.
- [164] M. Asadullah, K. Tomishige and K. Fujimoto, “A novel catalytic process for cellulose gasification to synthesis gas”, *Catal. Commun.*, (2001), vol. 2, p. 63–68.
- [165] V.L. Dagle, R. Dagle, L. Kovarik, A. Genc, Y.G. Wang, M. Bowden, H. Wan, M. Flake, V.A. Glezakou, D.L. King and R. Rousseau, “Steam reforming of hydrocarbons from biomass-derived syngas over MgAl₂O₄-supported transition metals and bimetallic IrNi catalysts”, *Appl. Catal. B Environ.*, (2016), vol. 184, p. 142–152.
- [166] L. Wang, D. Li, M. Koike, H. Watanabe, Y. Xu, Y. Nakagawa, and K. Tomishige, “Catalytic performance and characterization of Ni–Co catalysts for the steam reforming of biomass tar to synthesis gas”, *Fuel*, (2013), vol. 112, p. 654–661.
- [167] W. Juszczuk, J.C. Colmenares, A. Śrębowata and Z. Karpinski, “The effect of copper and gold on the catalytic behavior of nickel/alumina catalysts in hydrogen-assisted dechlorination of 1,2-dichloroethane”, *Catal. Today*, (2011), vol. 169, p. 186–191.
- [168] B.C. Miranda, R.J. Chimentão, J. Szanyi, A.H. Braga, J.B.O. Santos, F. Gispert-Guirado, J. Llorca, and F. Medina, “Influence of copper on nickel-based catalysts in the conversion of glycerol”, *Appl. Catal. B Environ.*, (2015), vol. 166–167, p. 166–180.
- [169] J. Ashok and S. Kawi, “Nickel–Iron alloy supported over Iron–Alumina catalysts for steam reforming of biomass tar model compound”, *ACS Catal.*, (2014), vol. 4, p. 289–301.
- [170] J. Hepola and P. Simell, “Sulphur poisoning of nickel-based hot gas cleaning catalysts in synthetic gasification gas. I. Effect of different process parameters”, *Appl. Catal. B Environ.*, (1997), vol. 14, p. 287–303.
- [171] M.H. Youn, J.G. Seo, P. Kim and I.K. Song, “Role and effect of molybdenum on the performance of Ni-Mo/γ-Al₂O₃ catalysts in the hydrogen production by auto-thermal reforming of ethanol”, *J. Mol. Catal. A Chem.*, (2007), vol. 261, p. 276–281.
- [172] Z.O. Malaibari, E. Croiset, A. Amin and W. Epling, “Effect of interactions between Ni and Mo on catalytic properties of a bimetallic Ni-Mo/Al₂O₃ propane reforming catalyst”, *Appl. Catal. A Gen.*, (2015), vol. 490, p. 80–92.
- [173] S.S. Maluf and E.M. Assaf, “Ni catalysts with Mo promoter for methane steam reforming”, *Fuel*, (2009), vol. 88, p. 1547–1553.
- [174] P. Chaiprasert and T. Vitidsant, “Effects of promoters on biomass gasification using nickel/dolomite catalyst”, *Korean J. Chem. Eng.*, (2010), vol. 26, n^o. 6, p. 1545–1549.
- [175] G. Oh, S.Y. Park, M.W. Seo, Y.K. Kim, H.W. Ra, J.G. Lee and S.J. Yoon, “Ni/Ru-Mn/Al₂O₃ catalysts for steam reforming of toluene as model biomass tar”, *Renew. Energy*, (2016), vol. 86, p. 841–847.
- [176] M. Koike, C. Ishikawa, D. Li, L. Wang, Y. Nakagawa and K. Tomishige, “Catalytic performance of manganese-promoted nickel catalysts for the steam reforming of tar from biomass pyrolysis to synthesis gas”, *Fuel*, (2013), vol. 103, p. 122–129.
- [177] E. Baker and L. Mudge, “Catalysis in Biomass Gasification”, Pacific Northwest Laboratory, Richland, Washington, (1984).
- [178] J.A. Lercher, J.H. Bitter, W. Hally, W. Niessen and K. Seshan, “Design of stable catalysts for methane-carbon dioxide reforming”, *Stud. Surf. Sci. Catal.*, (1996), vol. 101, p. 463–472.
- [179] S. Xu, R. Zhao and X. Wang, “Highly coking resistant and stable Ni/Al₂O₃ catalysts prepared by W/O microemulsion for partial oxidation of methane”, *Fuel Process. Technol.*, (2004), vol. 86, p. 123–133.
- [180] J.H. Kim, D.J. Suh, T.J. Park and K.L. Kim, “Effect of metal particle size on coking during CO₂ reforming of CH₄ over Ni–alumina aerogel catalysts”, *Appl. Catal. A Gen.*, (2000), vol. 197, p. 191–200.
- [181] A. Mohsenzadeh, K. Bolton and T. Richards, “DFT study of the adsorption and dissociation of water on Ni(111), Ni(110) and Ni(100) surfaces”, *Surf. Sci.*, (2014), vol. 627, p. 1–10.
- [182] D.W. Goodman, “Structure-reactivity relationships for alkane dissociation and hydrogenolysis using crystal kinetics”, *Catal. Today*, (1992), vol. 12, p. 189–199.
- [183] W.S. Xia, Y.H. Hou, G. Chang, W.Z. Weng, G.B. Han and H.L. Wan, “Partial oxidation of methane into syngas (H₂ + CO) over effective high-dispersed Ni/SiO₂ catalysts synthesized by a sol–gel method”, *Int. J. Hydrogen Energy*, (2012), vol. 37, p. 8343–8353.
- [184] Y. Zhang, G. Xiong, S. Sheng and W. Yang, “Deactivation studies over NiO/γ-Al₂O₃ catalysts for partial oxidation of methane to syngas”, *Catal. Today*, (2000), vol. 63, p. 517–522.
- [185] L. Zhang, X. Wang, B. Tan and U.S. Ozkan, “Effect of preparation method on structural characteristics and propane steam reforming performance of Ni–Al₂O₃ catalysts”, *J. Mol. Catal. A Chem.*, (2009), vol. 297, p. 26–34.

- [186] C. Brinker and G. Scherer, "Sol-gel science: the physics and chemistry of sol-gel processing", Academic press, San Diego, CA, (1990).
- [187] P.K. Sharma, V.V. Varadan and V.K. Varadan, "A critical role of pH in the colloidal synthesis and phase transformation of nano size α - Al_2O_3 with high surface area", (2003), vol. 23, p. 659–666.
- [188] B.J.J. Zelinski and D.R. Uhlmann, "Gel technology in ceramics", J. Phys. Chem. Solids, (1984), vol. 45, n^o. 10, p. 1069–1090.
- [189] A. Elnahrawy and A. Ali, "Influence of reaction conditions on sol-gel process producing SiO_2 and SiO_2 - P_2O_5 gel and glass", New J. Glas. Ceram., (2014), vol. 4, p. 42–47.
- [190] J.P. Jolivet, "De la solution à l'oxyde", Savoirs actuels, Paris, (1994).
- [191] J. Livage, "Sol-gel synthesis of heterogeneous catalysts from aqueous solutions", Catal. Today, (1998), vol. 41, p. 3–19.
- [192] A. Rajaeiyan and M.M. Bagheri-Mohagheghi, "Comparison of sol-gel and co-precipitation methods on the structural properties and phase transformation of γ and α - Al_2O_3 nanoparticles", Adv. Manuf., (2013), vol. 1, p. 176–182.
- [193] R. Demichelis, B. Civalleri, Y. Noel, A. Meyer and R. Dovesi, "Structure and stability of aluminium trihydroxides bayerite and gibbsite: A quantum mechanical ab initio study with the CRYSTAL06 code", Chem. Phys. Lett., (2008), vol. 465, p. 220–225.
- [194] K. Okada, T. Nagashima, Y. Kameshima and A. Yasumori, "Effect of crystallite size of boehmite on sinterability of alumina ceramics", (2003), vol. 29, p. 533–537.
- [195] D. Panias, P. Asimidis and I. Paspaliaris, "Solubility of boehmite in concentrated sodium hydroxide solutions: model development and assessment", Hydrometallurgy, (2001), vol. 59, p. 15–29.
- [196] K. Wefers and C. Misra, "Oxides and Hydroxides of Aluminum", Alcoa Technical Paper, (1987), n^o. 19, pp. 1–92.
- [197] P.S. Santos, H.S. Santos, and S.P. Toledo, "Standard transition aluminas. Electron microscopy studies", Mater. Res., (2000), vol. 3, n^o. 4, p. 104–114.
- [198] K. Okada, T. Nagashima, Y. Kameshima, A. Yasumori and T. Tsukada, "Relationship between formation conditions, properties, and crystallite size of boehmite", J. Colloid Interface Sci., (2002), vol. 253, p. 308–314.
- [199] H.W. Lee, B.K. Park, M.Y. Tian and J.M. Lee, "Relationship between properties of pseudo-boehmite and its synthetic conditions", J. Ind. Eng. Chem., (2006), vol. 12, n^o2, p. 295–300.
- [200] P. Raybaud, M. Digne, P. Sautet, P. Euzen and H. Toulhoat, "Use of DFT to achieve a rational understanding of acid-basic properties of gamma-alumina surfaces", J. Catal., (2004), vol. 226, p. 54–68.
- [201] P. Alphonse and M. Courty, "Structure and thermal behavior of nanocrystalline boehmite", Thermochim. Acta, (2005), vol. 425, p. 75–89.
- [202] C.J. Brinker, "Hydrolysis and condensation of silicates: Effects on structure", J. Non. Cryst. Solids, (1988), vol. 100, p. 31–50.
- [203] D.A. Donatti and D.R. Vollet, "Study of the hydrolysis of TEOS-TMOS mixtures under ultrasound stimulation", J. Non. Cryst. Solids, (1996), vol. 204, p. 301–304.
- [204] F. Mirjalili, L. Chuah, H. Mohamad and A. Fakhru, "Effect of stirring time on synthesized of ultra fine α - Al_2O_3 powder by a simple sol-gel process", J. Ceram. Process. Res., (2011), vol. 12, p. 738–741.
- [205] F. Akhlaghian, J. Tow, A. Mohajeri and A. Zamaniyan, "Comparison of sol-gel methods for washcoating metallic substrates", Chem. Chem. Eng., (2010), vol. 17, n^o. 2, p. 191–197.
- [206] E. van Steen, M. Claeys and L.H. Callanan, "Recent advances in the science and technology of zeolites and related materials", Cape Town, South Africa, Elsevier, (2004).
- [207] J.E. Blendell and C.A. Handwerker, "Effect of chemical composition on sintering of ceramics", J. Cryst. Growth, (1986), vol. 75, pp. 138–160.
- [208] R. Narayan and P. Colombo, "Advances in Bioceramics and Porous Ceramics II: Ceramic Engineering and Science Proceedings", Vol. 30, Issue 6, Willey, (2009).
- [209] V. Mandic, E. Tkalcec and S. Kurajica, "The influence of La_2O_3 on sol-gel derived mullite densification behavior", Minerals to materials conference, (2008), p. 1-8.
- [210] W. Wang, D. Weng and X.D. Wu, "Preparation and thermal stability of zirconia-doped mullite fibers via sol-gel method", Prog. Nat. Sci. Mater. Int., (2011), vol. 21, p. 117–121.
- [211] B. Heinrichs, G. Beketov, S. Lambert, J. W. Geus and J.P. Pirard, "Immobilizing metal nanoparticles in porous silica through sol-gel process", Sci. Bases Prep. Heterog. Catal., (2006), vol. 4, p. 521–528.
- [212] S. Lambert, F. Ferauche, A. Bresseur, J.P. Pirard and B. Heinrichs, "Pd-Ag/ SiO_2 and Pd-Cu/ SiO_2 cogelled xerogel catalysts for selective hydrodechlorination of 1,2-dichloroethane into ethylene", Catal. Today, (2005), vol. 100, p. 283–289.
- [213] S. Lambert, C. Cellier, E. M. Gaigneaux, J.P. Pirard and B. Heinrichs, "Ag/ SiO_2 , Cu/ SiO_2 and Pd/ SiO_2 cogelled xerogel catalysts for benzene combustion: Relationships between operating synthesis variables and catalytic activity", Catal. Commun., (2007), vol. 8, p. 1244–1248.

- [214] J.L. Hardin, N.A. Oyler, E.D. Steinle and G.A. Meints, "Spectroscopic analysis of interactions between alkylated silanes and alumina nanoporous membranes", *J. Colloid Interface Sci.*, (2010), vol. 342, p. 614–619.
- [215] V.G.P. Sripathi, B.L. Mojat, A. Nijmeijer and N. E. Benes, "Vapor phase versus liquid phase grafting of meso-porous alumina", *Microporous Mesoporous Mater.*, (2013), vol. 172, p. 1–6.
- [216] S. Yang, P. Yuan, H. He, Z. Qin, Q. Zhou, J. Zhu and D. Liu, "Effect of reaction temperature on grafting of γ -aminopropyl triethoxysilane (APTES) onto kaolinite", *Appl. Clay Sci.*, (2012), vol. 62–63, p. 8–14.
- [217] J. Nair, P. Nair, J.G. Van Ommen, J.R.H. Ross, A.J. Burggraaf and F. Mizukami, "Influence of peptization and ethanol washing on the pore-structure evolution of sol-gel-derived alumina catalyst supports", *J. Am. Ceram. Soc.*, (1998), vol. 81, n°. 10, pp. 2709–2712.
- [218] J. Del Angel, A.F. Aguilera, I.R. Galindo, M. Martínez and T.Viveros, "Synthesis and characterization of alumina-zirconia powders obtained by sol-gel method: effect of solvent and water addition rate", *Mater. Sci. Appl.*, (2012), vol. 3, p. 650–657.
- [219] R.B. Bagwell and G.L. Messing, "Critical factors in the production of sol-gel derived porous alumina", *Key Eng. Mater.*, (1996), vol. 115, p. 45–64.
- [220] J. Aguado, J.M. Escola and M.C. Castro, "Influence of the thermal treatment upon the textural properties of sol-gel mesoporous γ -alumina synthesized with cationic surfactants", *Microporous Mesoporous Mater.*, (2010), vol. 128, p. 48–55.
- [221] J. Čejka, "Organized mesoporous alumina: synthesis, structure and potential in catalysis", *Appl. Catal. A Gen.*, (2003), vol. 254, p. 327–338.
- [222] S. Bi, C. Wang, Q. Cao and C. Zhang, "Studies on the mechanism of hydrolysis and polymerization of aluminum salts in aqueous solution: Correlations between the 'Core-links' model and 'Cage-like' Keggin- Al_{13} model", *Coord. Chem. Rev.*, (2004), vol. 248, p. 441–455.
- [223] R.E. Mesmer and C.F. Baes, "Acidity measurements at elevated temperatures. V. Aluminum ion hydrolysis", *Inorg. Chem.*, (1971), vol. 10, n°. 10, p. 2290–2296.
- [224] J.H. Patterson and S.Y. Tyree, "A light scattering study of the hydrolytic polymerization of aluminum", *J. Colloid Interface Sci.*, (1973), vol. 43, n°. 10, p. 389–398.
- [225] M. Fournier, C. Ostiguy, J. Lesage and H. Van Tra, "Méthode pour l'évaluation simultanée de différentes amines en milieu de travail", rapport IRST, (2007).
- [226] J. A. Wang, X. Bokhimi, A. Morales, O. Novaro, T. Lopez and R. Gomez, "Aluminum local environment and defects in the crystalline structure of sol-gel alumina catalyst", *J. Phys. Chem. B*, (1999), vol. 103, p. 299–303.
- [227] P. Alphonse and M. Courty, "Surface and porosity of nanocrystalline boehmite xerogels", *J. Colloid Interface Sci.*, (2005), vol. 290, n°. 1, p. 208–219.
- [228] S. Ananthakumar, V. Raja and K.G.K. Warriar, "Effect of nanoparticulate boehmite sol as a dispersant for slurry compaction of alumina ceramics", *Mater. Lett.*, (2000), vol. 43, p. 174–179.
- [229] A.J. Lecloux, "Texture of catalysts", *Catal. Sci. Technol.*, vol. 2, p. 171, Ed. R. Anderson and M. Boudart, Springer, Berlin, (1981).
- [230] K.S.W. Sing, D.H. Everett, R.A.W. Haul, L. Moscou, R.A. Pierotti, J. Rouquérol and T. Siemieniewska, "Reporting physisorption data for gas-solid systems with special reference to the determination of surface area and porosity", *Pure Appl. Chem.*, (1985), vol. 57, n°. 4, p. 603–619.
- [231] J. Rouquérol, D. Avnir, C. W. Fairbridge, D.H. Everett, N. Pernicone, J.D. Ramsay, K. Sing and K.K. Unger, "Recommendations for the characterization of porous solids", *Pure Appl. Chem.*, (1994), vol. 66, no. 8, pp. 1739–1758.
- [232] S.Sakka, "Handbook of sol-gel science and technology. 3. Application of sol-gel technology", Springer Science & Business Media, Vol.3, (2005).
- [233] N. Özer, J.P. Cronin and A.P. Tomsia, "Preparation of amorphous Al_2O_3 films by the sol-gel process", Conference on Solar Optical Materials XV, Denver, Colorado, (1999), vol. 3789, p. 77–83.
- [234] E. Reale, A. Leyva, A. Corma, C. Martínez, H. García and F. Rey, "A fluoride-catalyzed sol-gel route to catalytically active non-ordered mesoporous silica materials in the absence of surfactants", *J. Mater. Chem.*, (2005), vol. 15, p. 1742–1754.
- [235] K. Sinko, N. Hüsing, G. Goerigk and H. Peterlik, "Nanostructure of gel-derived aluminosilicate materials", *Langmuir*, (2008), vol. 24, p. 949–956.
- [236] K. Ma, C. Mendoza, M. Hanson, U. Werner-Zwanziger, J. Zwanziger and U. Wiesner, "Control of ultrasmall sub-10 nm ligand-functionalized fluorescent core-shell silica nanoparticle growth in water", *Chem. Mater.*, (2015), vol. 27, p. 4119–4133.
- [237] C. Alié and J.P. Pirard, "Preparation of low-density xerogels from mixtures of TEOS with substituted alkoxyxilanes. I. ^{17}O NMR study of the hydrolysis–condensation process", *J. Non. Cryst. Solids*, (2003), vol. 320, p. 21–30.
- [238] M.P.J. Peeters, T.N.M. Bernards and M.J. Van Bommel, " ^{17}O -NMR of sol-gel processes of TEOS and TMOS", *J. Sol-Gel Sci. Technol.*, (1998), vol. 13, p. 71–74.

- [239] M. Niederberger and N. Pinna, *"Metal oxide nanoparticles in organic solvents"*, Springer, London, (2009).
- [240] U. Schubert and N. Husing, *"Synthesis of Inorganic Materials"*, Wiley-CH, Weinheim, (2005).
- [241] J. Yu, J. Shi, Q. Yuan, Z. Yang and Y. Chen, *"Effect of composition on the sintering and microstructure of diphasic mullite gels"*, *Ceram. Int.*, (2000), vol. 26, p. 255–263.
- [242] L.L. Pérez, V. Zarubina, A. Mayoral and I. Melián-Cabrera, *"Silica promoted self-assembled mesoporous aluminas. Impact of the silica precursor on the structural, textural and acidic properties"*, *Catal. Today*, (2015), vol. 250, p. 115–122.
- [243] K. Kosuge and A. Ogata, *"Effect of SiO₂ addition on thermal stability of mesoporous γ -alumina composed of nanocrystallites"*, *Microporous Mesoporous Mater.*, (2010), vol. 135, p. 60–66.
- [244] L.S. Cividanes, T.M.B. Campos, L.A. Rodrigues, D.D. Brunelli and G.P. Thim, *"Review of mullite synthesis routes by sol-gel method"*, *J. Sol-Gel Sci. Technol.*, (2010), vol. 55, p. 111–125.
- [245] B.E. Yoldas and D.P. Partlow, *"Formation of mullite and other alumina-based ceramics via hydrolytic polycondensation of alkoxides and resultant ultra- and microstructural effects"*, *J. Mater. Sci.*, (1988), vol. 23, p. 1895–1900.
- [246] B. Yoldas, *"Thermal stabilization of an active alumina and effect of dopants on the surface area"*, *J. Mater. Sci.*, (1976), vol. 11, p. 465–470.
- [247] B. Beguin, E. Garbowski and M. Primet, *"Stabilization of alumina toward thermal sintering by silicon addition"*, *J. Catal.*, (1991), vol. 127, p. 595–604.
- [248] L. Johnson, *"Surface Area stability of aluminas"*, *J. Catal.*, (1990), vol. 123, p. 245–259.
- [249] G. Chase, M. Espe, *"Metal oxide fibers and nanofibers, method for making same, and uses thereof"*, European Patent Application, n° EP 2 267 199 A2, (2010).
- [250] O. Rahmanpour, A. Shariati, M. Reza and K. Nikou, *"New method for synthesis nano size γ -Al₂O₃ catalyst for dehydration of methanol to dimethyl ether"*, *Int. J. Chem. Eng. Appl.*, (2012), vol. 3, n° 2, p. 2–5.
- [251] C.D. Keith and A.P. Hael, *"Process for preparing alumina catalyst compositions"*, USA Patent, n° 498.084, (1959).
- [252] *"Space Group Diagrams and Tables"*, Birkbeck College, University of London. Available: <http://img.chem.ucl.ac.uk/sgp/large/sgp.htm>
- [253] G. Ertl, H. Knozinger and J. Weitkamp, *"Handbook of heterogeneous catalysis"*, (1997), vol. 3, Wiley, Weinheim.
- [254] B.C. Lippens and J.H. De Boer, *"Study of phase transformations during calcination of aluminum hydroxides by selected area electron diffraction"*, *Acta Cryst.*, (1964), vol. 17, p. 1312–1321.
- [255] L.A. O'Dell, S.L.P. Savin, A.V. Chadwick and M.E. Smith, *"A ²⁷Al MAS NMR study of a sol-gel produced alumina: Identification of the NMR parameters of the θ -Al₂O₃ transition alumina phase"*, *Solid State Nucl. Magn. Reson.*, (2007), vol. 31, p. 169–173.
- [256] S. Davis and G. Gutiérrez, *"Structural, elastic, vibrational and electronic properties of amorphous Al₂O₃ from ab initio calculations"*, *J. Phys. Condens. Matter*, (2011), vol. 23, p. 1–84.
- [257] J.F. Shackelford and R.H. Doremus, *"Ceramic and glass materials: structure, properties and processing"*, New-York, Springer, (2008).
- [258] C. Pecharroman, I. Sobrados, J.E. Iglesias, T. Gonzalez-Carreno and J. Sanz, *"Thermal evolution of transitional aluminas followed by NMR and IR spectroscopies"*, *J. Phys. Chem. B*, (1999), vol. 103, p. 6160–6170.
- [259] M. Schmücker and H. Schneider, *"New evidence for tetrahedral triclusters in aluminosilicate glasses"*, *Journal of Non-Crystalline Solids*, (2002), vol. 311, p. 211–215.
- [260] L. Lopez Perez, S. Perdriau, B.J. Kooi, H.J. Heeres and I. Melia-Cabrera, *"Stabilization of self-Assembled alumina mesophases"*, *Chem. Mater.*, (2013), vol. 25, p. 848–855.
- [261] M. Xu and R. J. Madon, *"Refining: Improved residuum cracking"*, Engelhard Corporation. Available: www.digitalrefining.com/article/1000098
- [262] T. Nordgreen, T. Liliedahl and K. Sjoström, *"Metallic iron as a tar breakdown catalyst related to atmospheric, fluidised bed gasification of biomass"* *Fuel*, (2006), vol. 85, p. 689–694.
- [263] M. Virginie, J. Adánez, C. Courson, L.F. de Diego, F. García-Labiano, D. Niznansky, A. Kiennemann, P. Gayán, and A. Abad, *"Effect of Fe-olivine on the tar content during biomass gasification in a dual fluidized bed"*, *Appl. Catal. B Environ.*, (2012), vol. 121–122, p. 214–222.
- [264] M. Virginie, *"Elaboration et développement d'un catalyseur Fe/olivine pour le vaporéformage de molécules modèles de goudrons formés lors de la gazéification de la biomasse"*, PhD Thesis, Université de Strasbourg, (2011).
- [265] S. Hu, M. Xue, H. Chen and J. Shen, *"The effect of surface acidic and basic properties on the hydrogenation of aromatic rings over the supported nickel catalysts"*, *Chem. Eng. J.*, (2010), vol. 162, p. 371–379.
- [266] K. Meng, Y. Qi, L. U. Wen, F. A. N. Zheyong, F.E.I. Jinhua and Z. Xiaoming, *"Effect of calcination temperature on characteristics and performance of Ni/MgO Catalyst for CO₂ reforming of toluene"*, *Chinese J. Catal.*, (2012), vol. 33, p. 1508–1516.
- [267] M. Koike, Y. Hisada, L. Wang, D. Li, H. Watanabe, Y. Nakagawa and K. Tomishige, *"High catalytic activity of Co-*

- Fe/α-Al₂O₃ in the steam reforming of toluene in the presence of hydrogen*”, Appl. Catal. B Environ., (2013), vol. 140–141, p. 652–662.
- [268] C.K. Lambert and R.D. Gonzalez, “The importance of measuring the metal content of supported metal catalysts prepared by the sol-gel method”, Appl. Catal. A Gen., (1998), vol. 172, p. 233–239.
- [269] L. Di Felice, “Synthesis, characterization and reactivity of combined catalysts and sorbents for biomass gasification and simultaneous CO₂ capture process”, PhD thesis, Université de Strasbourg, (2009).
- [270] J. Parmentier and S. Vilminot, “Influence of transition metal oxides on sol-gel mullite crystallization”, Journal of Alloys and Compounds, (1998), vol. 264, p. 136–141.
- [271] A. Mattos, S. Probst, J. Afonso and M. Schmal, “Hydrogenation of 2-Ethyl-hexen-2-al on Ni/Al₂O₃ Catalysts”, J. Braz. Chem. Soc., (2004), vol. 15, n° 5, p. 760–766.
- [272] B.W. Hoffer, A. Dick van Langeveld, J.P. Janssens, R.L.C. Bonne, C.M. Lok and J.A. Moulijn, “Stability of highly dispersed Ni/Al₂O₃ catalysts: Effects of pretreatment”, (2000), J. Catal., vol. 192, p. 432–440.
- [273] J.Y. Park, Y.J. Lee, P.K. Khanna, K.W. Jun, J.W. Bae and Y.H. Kim, “Alumina-supported iron oxide nanoparticles as Fischer–Tropsch catalysts: Effect of particle size of iron oxide”, J. Mol. Catal. A Chem., (2010), vol. 323, p. 84–90.
- [274] D.S. Xue, Y.L. Huang, Y. Ma, P.H. Zhou, Z.P. Niu, F.S. Li, R. Job and W.R. Fahrner, “Magnetic properties of pure Fe-Al₂O₃ nanocomposites”, J. Mater. Sci. Lett., (2003), vol. 22, p. 1817–1820.
- [275] S. Tasfy, N. Zabidi and D. Subbarao, “Comparison of synthesis techniques for supported iron nanocatalysts”, J. Appl. Sci., (2011), vol. 11, no. 7, p. 1150–1156.
- [276] C.H. Bartholomew and R.J. Farrauto, “Chemistry of nickel-alumina catalysts”, J. Catal., (1976), vol. 45, p. 41–53.
- [277] G.C. Bye and G.T. Simpkin, “Influence of Cr and Fe on formation of α-Al₂O₃ from γ-Al₂O₃”, J. Am. Ceram. Soc., (1974), vol. 57, n° 8, p. 367–371.
- [278] Y. Chen and J. Ren, “Conversion of methane and carbon dioxide into synthesis gas over alumina-supported nickel catalysts. Effect of Ni-Al₂O₃ interactions”, Catal. Letters, (1994), vol. 29, p. 39–48.
- [279] G. Li, L. Hu and J.M. Hill, “Comparison of reducibility and stability of alumina-supported Ni catalysts prepared by impregnation and co-precipitation”, Appl. Catal. A Gen., (2006), vol. 301, p. 16–24.
- [280] F. Cheng, V. Dupont and M.V. Twigg, “Temperature-programmed reduction of nickel steam reforming catalyst with glucose”, Applied Catal. A, Gen., (2016), vol. 527, p. 1–8.
- [281] F. Cheng, “Bio-compounds as reducing agents of reforming catalyst and their subsequent steam reforming performance”, PhD Thesis, University of Leeds, (2014).
- [282] J. Ashok and S. Kawi, “Steam reforming of toluene as a biomass tar model compound over CeO₂ promoted Ni/CaO-Al₂O₃ catalytic systems”, Int. J. Hydrogen Energy, (2013), vol. 38, p. 13938–13949.
- [283] S. Lambert, C. Cellier, F. Ferauche, E. M. Gaigneaux and B. Heinrichs, “On the structure-sensitivity of 2-butanol dehydrogenation over Cu/SiO₂ cogelled xerogel catalysts”, Catal. Commun., (2007), vol. 8, p. 2032–2036.
- [284] S. Mani, J.R. Kastner and A. Juneja, “Catalytic decomposition of toluene using a biomass derived catalyst”, Fuel Process. Technol., (2013), vol. 114, p. 118–125.
- [285] D. M. Himmelbau, “Process analysis by statistical methods”, Wiley, New York, (1970).
- [286] J. Villiermaux, “Génie de la réaction chimique-Conception et Fonctionnement des réacteurs”, Lavoisier. Paris, (1993).
- [287] B. Yonathan., Nonlinear Parameter Estimation and Programming (NLPE), I.B.M. Contributed Program Library 360 D, (1967).
- [288] P.K. De Bokx, W.B.A. Wassenberg and J.W. Geus, “Interaction of nickel ions with a γ-Al₂O₃ support during deposition from aqueous solution”, J. Catal., (1987), vol. 104, p. 86–98.
- [289] M. Zangouei, A.Z. Moghaddam and M. Arasteh, “The influence of nickel loading on reducibility of NiO/Al₂O₃ catalysts synthesized by sol-gel method”, Chem. Eng. Res. Bull., (2010), vol. 14, p. 97–102.
- [290] Z. Hao, Q. Zhu, Z. Jiang, B. Hou and H. Li, “Characterization of aerogel Ni/Al₂O₃ catalysts and investigation on their stability for CH₄-CO₂ reforming in a fluidized bed”, Fuel Process. Technol., (2009), vol. 90, p. 113–121.
- [291] C. Karakaya, R. Otterstätter, L. Maier and O. Deutschmann, “Kinetics of the water-gas shift reaction over Rh/Al₂O₃ catalysts”, Appl. Catal. A Gen., (2014), vol. 470, p. 31–44.
- [292] T. Shishido, M. Yamamoto, D. Li, Y. Tian, H. Morioka, M. Honda, T. Sano and K. Takehira, “Water-gas shift reaction over Cu/ZnO and Cu/ZnO/Al₂O₃ catalysts prepared by homogeneous precipitation”, Appl. Catal. A Gen., (2006), vol. 303, p. 62–71.
- [293] N.W. Hurst, S.J. Gentry, A. Jones and B.D. McNicol, “Temperature programmed reduction”, Catal. Rev. Sci. Eng., (1982), vol. 24, n° 2, p. 233–309.
- [294] L. Zhou, L. Li, N. Wei, J. Li and J.M. Basset, “Effect of NiAl₂O₄ formation on Ni/Al₂O₃ stability during dry reforming of methane”, Chem. Cat. Chem., (2015), vol. 7, p. 2508–2516.
- [295] J. Chen, Q. Ma, T.E. Rufford, Y. Li and Z. Zhu, “Influence of calcination temperatures of Feitknecht compound precursor on the structure of Ni-Al₂O₃ catalyst and the corresponding catalytic activity in methane decomposition to hydrogen and carbon nanofibers”, Appl. Catal. A Gen., (2009), vol. 362, p. 1–7.

- [296] J. Corella, M.A. Caballero, M.P. Aznar and C. Brage, "Two advanced models for the kinetics of the variation of the tar composition in its catalytic elimination in biomass gasification", *Ind. Eng. Chem. Res.*, (2003), vol. 42, n°. 13, p. 3001–3011.
- [297] J.P. Hill, L.K. Shrestha, S. Ishihara, Q. Ji and K. Ariga, "Self-assembly: From amphiphiles to chromophores and beyond", *Molecules*, (2014), vol. 19, p. 8589–8609.
- [298] S.L. Burkett and M.E. Davis, "Mechanism of structure direction in the synthesis of Si-ZSM-5: An investigation by intermolecular ^1H - ^{29}Si CP MAS NMR", *J. Phys. Chem.*, (1994), vol. 98, p. 4647–4653.
- [299] Y. Kim, B. Lee and J. Yi, "Synthesis of mesoporous γ -alumina through pre- and post-hydrolysis methods", *Korean J. Chem. Eng.*, (2002), vol. 19, no. 5, p. 908–910.
- [300] L. Wan, H. Fu, K. Shi and X. Tian, "Simple synthesis of mesoporous alumina thin films", *Mater. Lett.*, (2008), vol. 62, p. 1525–1527.
- [301] H.Y. Zhu, J.D. Riches and J.C. Barry, " γ -Alumina nanofibers prepared from aluminum hydrate with poly(ethylene oxide) surfactant", *Chem. Mater.*, (2002), vol. 14, p. 2086–2093.
- [302] P. Kim, Y. Kim, H. Kim, I. K. Song and J. Yi, "Synthesis and characterization of mesoporous alumina with nickel incorporated for use in the partial oxidation of methane into synthesis gas", *Appl. Catal. A Gen.*, (2004), vol. 272, p. 157–166.
- [303] P.F. Fulvio, R.I. Brosey and M. Jaroniec, "Synthesis of mesoporous alumina from boehmite in the presence of triblock copolymer", *Appl. Mater. Interfaces*, (2010), vol. 2, n°. 2, p. 588–593.
- [304] R. Bleta, P. Alphonse, L. Pin, M. Gressier and M.J. Menu, "An efficient route to aqueous phase synthesis of nanocrystalline γ - Al_2O_3 with high porosity: From stable boehmite colloids to large pore mesoporous alumina", *J. Colloid Interface Sci.*, (2012), vol. 367, p. 120–128.
- [305] Properties of stearic acid. Available: <http://chemister.ru/Database/properties-en.php?dbid=1&id=4852>
- [306] J. Guo, H. Lou, H. Zhao, D. Chai and X. Zheng, "Dry reforming of methane over nickel catalysts supported on magnesium aluminate spinels", *Appl. Catal. A Gen.*, (2004), vol. 273, p. 75–82.
- [307] A.M. Da Silva, L.O.O. Da Costa, K.R. Souza, L.V. Mattos and F.B. Noronha, "The effect of space time on Co/CeO₂ catalyst deactivation during oxidative steam reforming of ethanol", *Catal. Commun.*, (2010), vol. 11, p. 736–740.
- [308] J.L. Houzelot, "Reacteurs chimiques polyphasés", *Techniques de l'Ingénieur*, (1980).
- [309] C.N. Satterfield, "Mass transfer in heterogeneous catalysis", M.I.T. Press, Cambridge, (1970).
- [310] H. Wu, V. La Parola, G. Pantaleo, F. Puleo, A. Venezia and L. Liotta, "Ni-based catalysts for low temperature methane steam reforming: Recent results on Ni-Au and comparison with other bi-metallic systems", *Catalysts*, (2013), vol. 3, p. 563–583.
- [311] T. Borowiecki, A. Golebiowski and B. Stasinska, "Effects of small MoO₃ additions on the properties of nickel catalysts for the steam reforming of hydrocarbons", *Appl. Catal. A Gen.*, (1997), vol. 153, p. 141–156.
- [312] D. Tian, Z. Liu, D. Li, H. Shi, W. Pan and Y. Cheng, "Bimetallic Ni-Fe total-methanation catalyst for the production of substitute natural gas under high pressure", *Fuel*, (2013), vol. 104, p. 224–229.
- [313] K. Nakamura, T. Miyazawa, T. Sakurai, T. Miyao, S. Naito, N. Begum, K. Kunimori and K. Tomishige, "Promoting effect of MgO addition to Pt/Ni/CeO₂/Al₂O₃ in the steam gasification of biomass", *Appl. Catal. B Environ.*, (2009), vol. 86, p. 36–44.
- [314] F. Morales-Cano, L.F. Lundegaard, R.R. Tiruvalam, H. Falsig and M.S. Skjøth-Rasmussen, "Improving the sintering resistance of Ni/Al₂O₃ steam-reforming catalysts by promotion with noble metals", *Appl. Catal. A Gen.*, (2015), vol. 498, p. 117–125.
- [315] M.M. Yung and J.N. Kuhn, "Deactivation mechanisms of Ni-based tar reforming catalysts as monitored by X-ray absorption spectroscopy", *Langmuir*, (2010), vol. 26, n°. 21, p. 16589–16594.
- [316] A. Nandini, K.K. Pant and S.C. Dhingra, "K-, CeO₂-, and Mn-promoted Ni/Al₂O₃ catalysts for stable CO₂ reforming of methane", *Appl. Catal. A Gen.*, (2005), vol. 290, p. 166–174.
- [317] J.L. Brito and J. Laine, "Reducibility of Ni-Mo/Al₂O₃ Catalysts: A TPR study", *Journal of Catalysis*, (1993), vol. 139, p. 540–550.
- [318] A. Roman and B. Delmon, "Promoter and carrier effects in the reduction of NiO-SiO₂", *J. Catal.*, (1973), vol. 30, p. 333–342.
- [319] S. Sengupta, K. Ray and G. Deo, "Effects of modifying Ni/Al₂O₃ catalyst with cobalt on the reforming of CH₄ with CO₂ and cracking of CH₄ reactions", *Int. J. Hydrogen Energy*, (2014), vol. 39, p. 11462–11472.
- [320] J.P. Bortolozzi, L.B. Gutierrez and M.A. Ulla, "Synthesis of Ni/Al₂O₃ and Ni-Co/Al₂O₃ coatings onto AISI 314 foams and their catalytic application for the oxidative dehydrogenation of ethane", *Appl. Catal. A Gen.*, (2013), vol. 452, p. 179–188.
- [321] P. Kratzer, B. Hammer and J. Norskov, "A theoretical study of CH₄ dissociation on pure and gold-alloyed Ni(111) surfaces", *J. Chem. Phys.*, (1996), vol. 105, n° 13, p. 5595–5604.
- [322] K.A. Shah and B.A. Tali, "Synthesis of carbon nanotubes by catalytic chemical vapour deposition: A review on carbon sources, catalysts and substrates", *Mater. Sci. Semicond. Process.*, (2016), vol. 41, p. 67–82.

- [323] L.M. Hoyos-Palacio, A.G. García, J.F. Pérez-Robles, J. González and H.V. Martínez-Tejada, “Catalytic effect of Fe, Ni, Co and Mo on the CNTs production”, *Mater. Sci. Eng.*, (2014), vol. 59, p. 1–8.
- [324] S.H. Seok, S.H. Han and J.S. Lee, “The role of MnO in Ni/MnO-Al₂O₃ catalysts for carbon dioxide reforming of methane”, *Appl. Catal. A Gen.*, (2001), vol. 215, p. 31–38.
- [325] T. Borowiecki, R. Dziembaj, M. Drozdek, G. Giecko, M. Pańczyk and Z. Piwowarska, “Studies of the model Ni-Mo/alumina catalysts in the n-butane hydrogenolysis reaction”, *Appl. Catal. A Gen.*, (2003), vol. 247, p. 17–25.
- [326] K.F.M. Elias, A.F. Lucrédio and E.M. Assaf, “Effect of CaO addition on acid properties of Ni–Ca/Al₂O₃ catalysts applied to ethanol steam reforming”, *Int. J. Hydrogen Energy*, (2013), vol. 38, p. 4407–4417.
- [327] X. Hu and G. Lu, “Inhibition of methane formation in steam reforming reactions through modification of Ni catalyst and the reactants”, *Green Chem.*, (2009), vol. 11, p. 724–732.
- [328] L. Garcia, R. French, S. Czernik and E. Chornet, “Catalytic steam reforming of bio-oils for the production of hydrogen: effects of catalyst composition”, *Appl. Catal. A Gen.*, (2000), vol. 201, p. 225–239.
- [329] C. Wang, T. Wang, L. Ma, Y. Gao and C. Wu, “Steam reforming of biomass raw fuel gas over NiO–MgO solid solution cordierite monolith catalyst”, *Energy Convers. Manag.*, (2010), vol. 51, p. 446–451.
- [330] V.R. Choudhary, B.S. Uphade and A.S. Mamman, “Oxidative conversion of methane to syngas over nickel supported on commercial low surface area porous catalyst carriers precoated with alkaline and rare earth oxides”, (1997), vol. 172, p. 281–293.
- [331] Q. Liu, J. Gao, M. Zhang, H. Li, F. Gu, G. Xu, Z. Zhong and F. Su, “Highly active and stable Ni/γ-Al₂O₃ catalysts selectively deposited with CeO₂ for CO methanation”, *RSC Adv.*, (2014), vol. 4, p. 16094–16103.
- [332] K. Tapia-Parada, G. Valverde-Aguilar, A. Mantilla, M.A. Valenzuela and E. Hernández, “Synthesis and characterization of Ni/Ce–SiO₂ and Co/Ce–TiO₂ catalysts for methane decomposition”, *Fuel*, (2013), vol. 110, p. 70–75.
- [333] M. Puchalska, E. Zych, M. Sobczyk, A. Watras and P. Deren, “Effect of charge compensation on up-conversion and UV excited luminescence of Eu³⁺ in Yb³⁺-Eu³⁺ doped calcium aluminate CaAl₄O₇”, *Mater. Chem. Phys.*, (2014), vol. 147, p. 304–310.
- [334] J.G. Li, T. Ikegami, J.H. Lee, T. Mori and Y. Yajima, “A wet-chemical process yielding reactive magnesium aluminate spinel (MgAl₂O₄) powder”, *Ceram. Int.*, (2001), vol. 27, p. 481–489.
- [335] A.P. De Kroon, G.W. Schafer, and F. Aldinger, “Crystallography of potassium aluminate K₂O·Al₂O₃”, *Journal of Alloys and Compounds*, (2001), vol. 314, p. 147–153.
- [336] R. Hadden, J. Howe and K.C. Waugh, “Hydrocarbon steam reforming catalysts- alkali induced resistance to carbon formation”, *Catal. Deactiv.*, (1991), p. 177–184.
- [337] L. Xu, H. Song and L. Chou, “One-pot synthesis of ordered mesoporous NiO–CaO–Al₂O₃ composite oxides for catalyzing CO₂ reforming of CH₄”, *ACS Catal.*, (2012), vol. 2, p. 1331–1342.
- [338] A. Golebiowski, K. Stolecki, U. Prokop, A. Kusmierowska, A. Denis and C. Sikorska, “Influence of potassium on the properties of steam reforming catalysts”, *React. Kinet. Catal. Lett.*, (2004), vol. 82, n°. 1, p. 179–189.
- [339] H. M. Swaan, V. C. H. Kroll, G. A. Martin and C. Mirodatos, “Deactivation of supported nickel catalysts during the reforming of methane by carbon dioxide”, *Catal. Today*, (1994), vol. 21, p. 571–578.
- [340] T. Osaki and T. Mori, “Role of potassium in carbon-free CO₂ reforming of methane on K-promoted Ni/Al₂O₃ Catalysts”, *J. Catal.*, (2001), vol. 204, p. 89–97.
- [341] W. Chen, G. Zhao, Q. Xue, L. Chen and Y. Lu, “High carbon-resistance Ni/CeAlO₃-Al₂O₃ catalyst for CH₄/CO₂ reforming”, *Appl. Catal. B Environ.*, (2013), vol. 136–137, p. 260–268.
- [342] K. Tomishige, T. Kimura, J. Nishikawa, T. Miyazawa and K. Kunimori, “Promoting effect of the interaction between Ni and CeO₂ on steam gasification of biomass”, *Catal. Commun.*, (2007), vol. 8, p. 1074–1079.
- [343] M. Matsumura and C. Hirai, “Deterioration mechanism of direct internal reforming catalyst”, *J. Chem. Eng. Jap.*, (1998), vol. 31, p. 734–740.
- [344] L. Zhang, B. Zhang, Z. Yang and M. Guo, “The role of water on the performance of calcium oxide-based sorbents for carbon dioxide capture: A review”, *Energy Technol.*, (2015), vol. 3, p. 10–19.
- [345] J. Juan-Juan, M. C. Román-Martínez and M.J. Illán-Gómez, “Catalytic activity and characterization of Ni/Al₂O₃ and NiK/Al₂O₃ catalysts for CO₂ methane reforming”, *Appl. Catal. A Gen.*, (2004), vol. 264, p. 169–174.
- [346] M. Demicheli, D. Duprez, J. Barbier, O. Ferretti and E. Ponzi, “Deactivation of steam reforming model catalysts by coke formation. II. Promotion with potassium and effect of water”, *J. Catal.*, (1994), vol. 145, p. 437–439.
- [347] F. Polo-Garzon, D. Pakhare, J.J. Spivey, and D.A. Bruce, “Dry reforming of methane on Rh-doped pyrochlore catalysts: A steady-state isotopic transient kinetic study”, *ACS Catal.*, (2016), vol. 6, p. 3826–3833.
- [348] V. Balcaen, R. Roelant, H. Poelman, D. Poelman and G. B. Marin, “TAP study on the active oxygen species in the total oxidation of propane over a CuO-CeO₂/γ-Al₂O₃ catalyst”, *Catal. Today*, (2010), vol. 157, p. 49–5.
- [349] D. Dayton, “A review of the literature on catalytic biomass tar destruction”, *Milestone Completion Report*, U.S. Nat. Renew. Energy Lab., (2002).
- [350] J. Gallego, C. Batiot-Dupeyrat, J. Barrault and F. Mondragón, “Severe deactivation of a LaNiO₃ perovskite-type catalyst

- precursor with H_2S during methane dry reforming”, *Energy & Fuels*, (2009), vol. 23, p. 4883–4886.
- [351] M.T. Azizan, “*Steam reforming of oxygenated hydrocarbons for hydrogen Production*”, PhD Thesis, Imperial College London, (2014).
- [352] A.L. Alberton, M.M.V.M. Souza and M. Schmal, “*Carbon formation and its influence on ethanol steam reforming over Ni/Al₂O₃ catalysts*”, *Catal. Today*, (2007), vol. 123, p. 257–264.
- [353] Renewable Energy Policy Network for the 21st Century, “*Renewables 2014, Global status report*”, REN 21 Report, (2014).
- [354] International Renewable Energy Agency, “*Renewable Power Generation Costs in 2012: An Overview*”. Available: http://costing.irena.org/media/2769/Overview_Renewable-Power-Generation-Costs-in-2012.pdf
- [355] D.Y.C. Leung, X. Wu and M.K.H. Leung, “*A review on biodiesel production using catalyzed transesterification*”, *Appl. Energy*, (2010), vol. 87, p. 1083–1095.
- [356] Z. Khan and A. K. Dwivedi, “*Fermentation of biomass for production of ethanol: A review*”, *Univers. J. Environ. Res. Technol.*, (2013), vol. 3, n^o. 1, p. 1–13.
- [357] E. Aydemir, S. Demirci, A. Aytekin and F. Sahin, “*Genetic modifications of saccharomyces cerevisiae for ethanol production from starch fermentation: A review*”, *J. Bioprocess. Biotech.*, (2014), vol. 4, n^o.7, p. 1–8.
- [358] A.V. Herzog, T.E. Lipman and D.M. Kammen, “*Renewable energy sources*”, Energy and Resources Group, Renewable and Appropriate Energy Laboratory.
- [359] A. Effendi, H. Gerhauser and A.V. Bridgwater, “*Production of renewable phenolic resins by thermochemical conversion of biomass: A review*”, *Renew. Sustain. Energy Rev.*, (2008), vol. 12, p. 2092–2116.
- [360] A.V. Bridgwater, “*Biomass fast pyrolysis*”, *Therm. Sci.*, (2004), vol. 8, n^o2, p. 21–49.
- [361] T. Hanaoka, S. Inoue, S. Uno, T. Ogi and T. Minowa, “*Effect of woody biomass components on air-steam gasification*”, *Biomass and Bioenergy*, (2005), vol. 28, p. 69–76.
- [362] A. Barneto, J. Carmona, A. Galvez and J. Conesa, “*Effects of the composting and the heating rate on biomass*”, *Energy and Fuels*, (2009), vol. 23, p. 951–957.
- [363] C. Wu, X. Yin, L. Ma, Z. Zhou and H. Chen, “*Operational characteristics of a 1.2-MW biomass gasification and power generation plant*”, *Biotechnol. Adv.*, (2009), vol. 27, p. 588–592.
- [364] A. Kumar, K. Eskridge, D.D. Jones and M.A. Hanna, “*Steam-air fluidized bed gasification of distillers grains: Effects of steam to biomass ratio, equivalence ratio and gasification temperature*”, *Bioresour. Technol.*, (2009), vol. 100, p. 2062–2068.
- [365] L.P.L.M. Rabou, R.W.R. Zwart, B.J. Vreugdenhil and L. Bos, “*Tar in biomass producer gas, the Energy research Centre of The Netherlands (ECN). Experience: An enduring challenge*”, *Energy & Fuels*, (2009), vol. 23, p. 6189–6198.
- [366] Q. Yu, C. Brage, G. Chen, K. Sjostrom, “*Temperature impact on the formation of tar from biomass pyrolysis in a free-fall reactor*”, *J. Anal. Appl. Pyrolysis*, (1997), vol. 40–41, p. 481–489.
- [367] B. Moghtaderi, “*Effects of controlling parameters on production of hydrogen by catalytic steam gasification of biomass at low temperatures*”, *Fuel*, (2007), vol. 86, p. 2422–2430.
- [368] P.M. Lv, Z.H. Xiong, J. Chang, C.Z. Wu, Y. Chen and J.X. Zhu, “*An experimental study on biomass air-steam gasification in a fluidized bed*”, *Bioresour. Technol.*, (2004), vol. 95, p. 95–101.
- [369] M. Campoy, A. Gómez-Barea, F.B. Vidal and P. Ollero, “*Air-steam gasification of biomass in a fluidised bed: Process optimisation by enriched air*”, *Fuel Process. Technol.*, (2009), vol. 90, p. 677–685.
- [370] Y.H. Qin, J. Feng and W.Y. Li, “*Formation of tar and its characterization during air-steam gasification of sawdust in a fluidized bed reactor*”, *Fuel*, (2010), vol. 89, p. 1344–1347.
- [371] A.V. Bridgwater, “*The technical and economic feasibility of biomass gasification for power generation*”, *Fuel*, (1995), vol. 14, n^o. 5, p. 631–653.
- [372] P. Von Hippel, “*Mean, Median, and Skew: Correcting a Textbook Rule*”, *J. Stat. Educ.*, (2005), vol. 13, p. 1–4.
- [373] “*Statistical parameters: Measures of central tendency and variation*”. Available: http://www.sagepub.com/sites/default/files/upm-binaries/47775_ch_3.pdf
- [374] A.L. Patterson, “*The scherrer formula for X-Ray particle size determination*”, *Phys. Rev.*, (1939), vol. 56, p. 978–982.
- [375] B. Akbari, M.P. Tavandashi and M. Zandrahimi, “*Particle size characterization of nanoparticles- a practical approach*”, *Iran. J. Mater. Sci. Eng.*, (2011), vol. 8, n^o. 2, p. 48–56.
- [376] V. Mukundan, J. Yin, P. Joseph, J. Luo, S. Shan, D. N. Zakharov, C.-J. Zhong and O. Malis, “*Nanoalloying and phase transformations during thermal treatment of physical mixtures of Pd and Cu nanoparticles*”, *Sci. Technol. Adv. Mater.*, (2014), vol. 15, p. 1–16.
- [377] Z. Wei, E. Kowalska and B. Ohtani, “*Influence of post-treatment operations on structural properties and photocatalytic activity of octahedral anatase titania particles prepared by an ultrasonication-hydrothermal reaction*”, *Molecules*, (2014), vol. 19, p. 19573–19587.
- [378] X. Gao, M.R. Bonilla, J.C.D. Da Costa and S.K. Bhatia, “*The transport of gases in a mesoporous γ -alumina supported*

- membrane”, *J. Memb. Sci.*, (2013), vol. 428, p. 357–370.
- [379] M.H. Halabi, M.H.J.M. de Croon, J. van der Schaaf, P.D. Cobden and J.C. Schouten, “*Modeling and analysis of autothermal reforming of methane to hydrogen in a fixed bed reformer*”, *Chem. Eng. J.*, (2008), vol. 137, p. 568–578.
- [380] L.G. Felix, C.W. Choi, D.M. Rue, L.E. Weast and T.P. Seward, “*Robust glass-ceramics catalysts for biomass gasification*”, (2009), vol. 28, p. 336–346.
- [381] T. Borowiecki, A. Denis, W. Gac, R. Dziembaj, Z. Piwowarska and M. Drozdek, “*Oxidation-reduction of Ni/Al₂O₃ steam reforming catalysts promoted with Mo*”, *Appl. Catal. A Gen.*, (2004), vol. 274, p. 259–267.
- [382] D.M. Hercules, A. Proctor and M. Houalla, “*Quantitative analysis of mixed oxidation states in supported catalysts*”, *Acc. Chem. Res.*, (1994), vol. 27, n^o. 12, p. 387–393.
- [383] F.Kapteijn, D.van Langeveld, J.Moulijn, A.Andreini, M.Vuurman, A.Turek, J.M. Jehng and I.E. Wachs, “*Alumina supported manganese oxide catalysts. I. Characterization: Effect of precursor and loading*”, *Journal of Catalysis*, (1994), vol. 150, p. 94–104.
- [384] K. Prodromou and A. Pavlatou-Ve, “*Formation of aluminum hydroxides as influenced by aluminum salts and bases*”, *Clays Clay Miner.*, (1995), vol. 43, n^o. 1, p. 111–115.
- [385] M. Mahé, P. Reynders, A. Demourgues and J.M. Heintz, “*Influence of a ceramic substrate on aqueous precipitation and structural evolution of alumina nano-crystalline coatings*”, *J. Am. Ceram. Soc.*, (2007), vol. 90, n^o. 1, p. 217–224.
- [386] B. Gawel, K. Gawel and G. Øye, “*Sol-gel synthesis of non-silica monolithic materials*”, *Materials*, (2010), vol. 3, p. 2815–2833.
- [387] P. Munnik, P.E. de Jongh and K.P. de Jong, “*Recent developments in the synthesis of supported catalysts*”, *Chem. Rev.*, (2015), vol. 115, p. 6687–6718.
- [388] N.A. Lange, J.A. Dean, “*Lange’s handbook of chemistry*”, McGraw-Hill, New York, 10th Ed., (1967).
- [389] G.B. Manelis, “*Thermal decomposition and combustion of explosives and propellants*”, CRC Press, (2003).
- [390] J. Srinakruang, “*Highly efficient sulfur and coking resistance catalysts for tar gasification with steam*”, *Fuel*, (2006), vol. 85, n^o 17–18, p. 2419–2426.
- [391] G.L.M. Léonard, C.M. Malengreux, Q. Mélotte, S.D. Lambert, E. Bruneel, I. Van Driessche and B. Heinrichs, “*Doped sol-gel films vs. powders TiO₂: On the positive effect induced by the presence of a substrate*”, *J. Environ. Chem. Eng.*, (2016), vol. 4, p. 449–459.
- [392] P. Paoletti, “*Formation of metal complexes with ethylenediamine: a critical survey of equilibrium constants, enthalpy and entropy values*”, *Pure Appl. Chem.*, (1984), vol. 56, n^o. 4, p. 491–522.
- [393] H. Jiang, X. Sun, Y. Du, R. Chen and W. Xing, “*Catalytic activity of palladium nanoparticles immobilized on an amino-functionalized ceramic membrane support*”, *Chinese J. Catal.*, (2014), vol. 35, p. 1990–1996.
- [394] X. Vu, R. Eckelt, U. Armbruster and A. Martin, “*High-temperature synthesis of ordered mesoporous aluminosilicates from ZSM-5 nanoseeds with improved acidic properties*”, *Nanomaterials*, (2014), vol. 4, p. 712–725.
- [395] F. Lónyi and J. Valyon, “*On the interpretation of the NH₃-TPD patterns of H-ZSM-5 and H-mordenite*”, *Microporous Mesoporous Mater.*, (2001), vol. 47, p. 293–301.
- [396] R.N. Widyaningrum, T.L. Church, M. Zhao and A. T. Harris, “*Mesocellular-foam-silica-supported Ni catalyst: Effect of pore size on H₂ production from cellulose pyrolysis*”, *Int. J. Hydrogen Energy*, (2012), vol. 37, p. 9590–9601.
- [397] W. Cai, L. Ye, L. Zhang, Y. Ren, B. Yue, X. Chen and H. He, “*Highly dispersed nickel-containing mesoporous silica with superior stability in carbon dioxide reforming of methane: The effect of anchoring*”, *Materials*, (2014), vol. 7, p. 2340–2355.
- [398] S.L. Pirard, J.G. Mahy, J.P. Pirard, B. Heinrichs, L. Raskinet and S.D. Lambert, “*Development by the sol-gel process of highly dispersed Ni-Cu/SiO₂ xerogel catalysts for selective 1,2-dichloroethane hydrodechlorination into ethylene*”, *Microporous Mesoporous Mater.*, (2015), vol. 209, p. 197–207.
- [399] A. Kamyabi-Gol, S. M. Zebarjad and S.A. Sajjadi, “*A study on the effect of synthesis parameters on the size of nickel particles in sol-gel derived Ni-SiO₂-Al₂O₃ nanocomposites*”, *J. Sol-Gel Sci. Technol.*, (2009), vol. 51, p. 92–101.
- [400] A. Cybulsky and J.A. Moulijn, “*Structured catalysts and reactors*”, 2nd edn, Focus Catal., (2006).
- [401] F. Kapteijn, T.A. Nijhuis, J.J. Heiszwolf and J.A. Moulijn, “*New non-traditional multiphase catalytic reactors based on monolithic structures*”, *Catal. Today*, (2001), vol. 66, p. 133–144.
- [402] T.A. Nijhuis, A.E. W. Beers, T. Vergunst, I. Hoek, F. Kapteijn and J. Moulijn, “*Preparation of monolithic catalysts*”, *Catal. Rev. Sci. Eng.*, (2001), vol. 43, n^o. 4, p. 345–380.
- [403] P. Avila, M. Montes and E.E. Miró, “*Monolithic reactors for environmental applications: A review on preparation technologies*”, *Chem. Eng. J.*, (2005), vol. 109, p. 11–36.
- [404] H. Elmer, “*Applications of refractories: Ceramic engineering and science proceedings*”, vol. 7, John Wiley & Sons, Inc., Hoboken, NJ, USA, (1986).
- [405] C. Agrafiotis and A. Tsetsekou, “*Deposition of meso-porous γ -alumina coatings on ceramic honeycombs by sol-gel methods*”, *J. Eur. Ceram. Soc.*, (2002), vol. 22, p. 423–434.

- [406] A. Cybulski and J. A. Moulijn, "Monoliths in Heterogeneous Catalysis", *Catal. Rev. Sci. Eng.*, (1994), vol. 36, n° 2, p. 179–270.
- [407] J.L. Williams, "Monolith structures, materials, properties and uses", *Catal. Today*, (2001), vol. 69, p. 3–9.
- [408] R.E. Hayes, B. Liu, R. Moxom and M. Votsmeier, "The effect of washcoat geometry on mass transfer in monolith reactors", *Chem. Eng. Sci.*, (2004), vol. 59, p. 3169–3181.
- [409] G.I. Taylor, "Deposition of a viscous fluid on a plane surface", *J. Fluid Mech.*, (1961), vol. 10, n° 2, p. 161–165.
- [410] F. Fairbrother and A.E. Stubbs, "Studies in electro-endosmosis. Part VI. The 'bubble-tube' method of measurement", *J. Chem. Soc.*, (1935), p. 527–529.
- [411] W.B. Kolb and R.L. Cerro, "Coating the inside of a capillary of square cross section", *Chem. Eng. Sci.*, (1991), vol. 46, n° 9, p. 2181–2195.
- [412] W.B. Kolb, A.A. Papadimitriou, R.L. Cerro, D.D. Leavitt and J.C. Summers, "Ins and outs of coating monolithic structures", *Chem. Eng. Prog.*, (1993), vol. 89, n° 2, p. 61–67.
- [413] D.A.W.E. Keita, P. Faure, S. Rodts and P. Coussot, "Evaporation from a capillary tube: Experiment and modelisation", in 5th Int. Conf. Porous Media Their Appl. Sci. Eng. Ind., ECI symposium series, Kona, Hawaii, (2014).
- [414] C. Agrafiotis, A. Tsetsekou and A. Ekonomakou, "Effect of particle size on the adhesion properties of oxide washcoats on cordierite honeycombs", *J. Mater. Sci. Lett.*, (1999), vol. 18, p. 1421–1424.
- [415] S. Mueller, E. Lillewellin and H. Mader, "The rheology of suspensions of solid particles", *Proc. R. Soc. A*, (2010), vol. 466, p. 1201–1228.
- [416] D.R. Rector and B.C. Bunker, "Effect of colloidal aggregation on the sedimentation and rheological properties of tank waste", U.S. Department of energy, Batelle memorial institute, (1995).
- [417] C. Agrafiotis and A. Tsetsekou, "The effect of powder characteristics on washcoat quality. Part I: Alumina washcoats", *J. Eur. Ceram. Soc.*, (2000), vol. 20, p. 815–824.
- [418] "dielectric constantes and absolute viscosities". Available: <http://www.ddbst.com/>
- [419] D. Troy and P. Beringer, "The science and practice of pharmacy", Lippincott Williams & Wilkins, (2006).
- [420] A.F.M. Leenaars and A.J. Burggraaf, "The preparation and characterization of alumina membranes with ultra-fine pores", *J. Memb. Sci.*, (1984), vol. 19, p. 1077–1088.
- [421] R.W. Rice, "Mechanical properties of ceramics and composites: grain and particle effects", CRC Press, (2000).
- [422] "Biomass gasification plants", Volund report, (2011). Available: http://www.volund.dk/en/Biomass_energy/References/
- [423] Xylowatt Website. Available: <http://www.xylowatt.com/>
- [424] Hudol Website. Available: <http://www.hudol.co.uk/>
- [425] J. Hansson, A. Leveau and C. Hulteberg, "SGC Report N°234", (2011). Available: <http://www.sgc.se/ckfinder/userfiles/files/SGC234.pdf>
- [426] B. Van der Drift, "Biomass gasification in the Netherlands", ECN report, (2013).
- [427] K. Stahl, M. Neergaard and J. Nieminen, "Progress Report: Varnamo Biomass Gasification Plant", Gasification technology conference, San Francisco, California, (1999), vol. 16, p. 1–16.
- [428] Gussing renewable energy Website. Available: <http://www.gussingrenewable.com/htcms/en/wer-was-wie-wo-wann/wie/thermische-vergasungficfb-reaktor.html>